# Quantum Assisted Sensing, Simulation and Control

by

Ashok Ajoy

Submitted to the Department of Nuclear Science and Engineering
in partial fulfillment of the requirements for the degree of

Doctor of Philosophy in Nuclear Science and Engineering

at the

MASSACHUSETTS INSTITUTE OF TECHNOLOGY

September 2016





Signature redacted

Author .....
Department of Nuclear Science and Engineering
August 24, 2016

Signature redacted

Certified by .....
Paola Cappellaro
Esther & Harold Edgerton Associate Professor of Nuclear Science and Engineering
Thesis Supervisor

Signature redacted

Certified by .....
Ju Li
Battelle Energy Alliance Professor of Nuclear Science and Engineering
Thesis Reader

Signature redacted

Accepted by ...
Ju Li
Battelle Energy Alliance Professor of Nuclear Science and Engineering
Chair, Department Committee on Graduate Students

# Quantum Assisted Sensing, Simulation and Control

by

Ashok Ajoy

Submitted to the Department of Nuclear Science and Engineering
on August 24, 2016, in partial fulfillment of the
requirements for the degree of
Doctor of Philosophy in Nuclear Science and Engineering

## Abstract

This thesis describes experimental and theoretical work making contributions with the aims of improving and advancing techniques of quantum metrology, simulation and control. Towards this goal, we engineer novel devices for quantum sensing, particularly the measurement of rotations, magnetic fields, and single spins towards the reconstruction of single-molecule structures. We also develop new methods that aid these tasks. For instance, we demonstrate how versatile quantum control of spin systems can be achieved via Hamiltonian engineering based on the creation of dynamical filters and/or the use of a quantum actuator, with novel implications in quantum simulation. We also enhance the available quantum control, sensing and simulation methods by the use of ancillary systems, for instance an electronic quantum actuator and a nuclear quantum memory. Finally, by revisiting old techniques in nuclear magnetic resonance, we develop novel insights and measurement protocols on single-spin quantum systems.

Thesis Supervisor: Paola Cappellaro
Title: Esther & Harold Edgerton Associate Professor

*In Loving Memory of K.G. Raman.*

# Acknowledgments

MIT and Boston have been an exhilarating ride, and I am grateful to many people for the experience. Thanks to my advisor, Paola Cappellaro for being a balanced and inspirational group leader amongst many other things. She gave me the proverbial 'creative license', allowing me a free hand in the conception and implementation of various ideas, while always being there to refine them and make them more rigorous. This led to a very creative time working in her group. I would also like to thank her for letting me build an experiment from scratch, arranging for lab space and putting together resources at a difficult time. It was an incredible and formative experience. Some things break down, others have long lead times, making various hardware devices work reliably in consort take many hours. These and other small frustrations, however, are trumped by the fun in designing a capability that can probe an interesting new direction. Thanks Paola for your trust in me!

Thanks to members of my thesis committee: Ronald Walsworth, Seth Lloyd, Ju Li and Alan Jasanoff. I am grateful to Ron Walsworth for his generosity. I used to hang out in his lab and attend both his group meetings every week. The necessity to come up with ideas that might be of use to his group were the origin of some of the work presented in this thesis. Ron has also assembled an incredible team of skilful and helpful researchers from whom I have benefited greatly. From the Walsworth group, I would like to thank David Glenn, Francesco Casola, Nir Bar-Gill, Keigo Arai, Chinmay Belthangady, Stephen DeVience, J-C. Jaskula and Alexei Trifonov for many lunches and discussions over the years.

Thanks to Seth Lloyd for the numerous interactions. Many ideas in this thesis have an origin in some old paper from Seth. I have admired his forward-looking

papers, being able to spot a new direction many years in advance of anyone else. His work, and the style and elegance of his research have been an inspiration for me, and one that I seek to emulate.

Thanks to Ju Li for many meetings and interactions. Ju is an inspiring figure for the sheer breadth of his research. Everytime I met with him, he had some new insight to offer from which I benefited greatly. From his group, I would like to thank Xiaofeng Qian and Zongyou Yin.

Thanks to Alan Jasanoff for insightful conversations over the years. I want to especially thank Aviad Hai from Alan's group for many discussions about microcoils and applications in neuroscience.

I am also grateful to my mentors at MIT and beyond who have encouraged me. Thanks to Anil Kumar, for his personal mentorship and guidance. Anil pioneered many aspects of NMR, including NOESY and Fourier MRI. My career path was inspired by the numerous coffee discussions I had with him. Thanks to Dieter Suter for taking me into his lab as a student although I had little experience. It was a wonderful period in Dortmund, where I enjoyed working with Gonzalo Alvarez for early experiments and interpretations of dynamical decoupling. Dieter and Gonzalo have remained mentors and friends through the years at MIT.

Thanks to Suresh Ramaswamy for his kindness. He was an exceptional professor and teacher. He once offered a whole course on field theory although I was the only registered student. Suresh trained me to be a good theorist, yet encouraged me to be grounded in experiment. His guidance was crucial for me choosing a career in Science. His untimely passing in 2012 was a personal blow.

Thanks to Fedor Jelezko for his personal mentorship. My visits to Ulm were always full of discovery, learning new tricks and techniques. Fedor's wealth of experimental knowledge is remarkable. He is also a prime example that one could be both

extremely successful as well as very generous. His group is always brimming with guests from all around the world, freely exchanging and brainstorming ideas, a great example of collaborative research. From Ulm I would like to thank Boris Naydenov, Liam McGuinness, Jochen Scheuer, as well as Gopi Balasubramanian and Phil Hemmer with whom I interacted with there.

Thanks to Sunil Bhave for being such a great mentor and friend. I accidentally landed in Sunil's optomechanics and MEMS class, but it turned out to be the best I took at MIT. By mid semester the class was held at Area 4, and it was great fun! Sunil's personal mentorship was the genesis of the NV gyroscope work.

MIT is a great place rich with ideas, and I am grateful to have had a chance to interact with leaders in many fields. Thanks to Ed Boyden for many discussions, and for being an inspiration in coming up with creative ideas. Thanks to Bob Griffin, for his time and generosity. Meeting with John Waugh was a memorable and inspiring experience. I am still in awe of his work in developing average Hamiltonian theory that I used heavily in my thesis. Thanks to Terry Orlando for his class and mentorship. Thanks finally to Alex Pines for his old MIT stories, and for influencing my future career path.

The Quantum Engineering Group has been a great place to work. Thanks to all members old and new for fun times. Thanks especially to the Batman team: Luca Marseglia and Kasturi Saha for building the experiment together. I had a great time collaborating with YiXiang Liu, a brilliant and talented coworker. We made a great team together. I wish her all the success ahead. Thanks to Ulf Bissbort, friend and mentor. I have learnt so much from Ulf. Even after he left, we have chatted almost every alternate day despite the time difference. Thanks to Masashi Hirose, Alex Cooper and Clarice Aiello for being the first set of QEGers, classes taken together and happy times that are too many to put on paper. Thanks to Gurneet Kaur,

Easwar Magesan and Honam Yum for being great first QEG postdocs.

Thanks to the staff at MIT and RLE without whom this thesis would not have been possible. Thanks to Al McGurl and Bill Gibbs who built our lab from scratch and helped solving innumerable problems along the way. Thanks to Kurt Broderick for teaching me how to do fab. Thanks to Laura von Bosau for ordering everything we ever needed for our experiments. Thanks to Clare Egan and Heather Barry for always being there to help.

Thanks to friends from CUA, a great community to be part of. Thanks especially to Ed Chen, Rajibul Islam, Sebastian Will and Alex Sushkov for many corridor chats.

Thanks to my family who have been my greatest support and inspiration. My dad is the most creative engineer I know, and my mother the most inspiring physicist for her pure love for the subject. My brother is the kindest, most skilful engineer. Finally, thanks to my lovely wife Niharika for the wonderful journey together. She is a brilliant computer engineer, and was the prime force behind 'NVAutomizer' now used by the entire group. I became far more creative and productive after I met her, in no small measure because I also became so much happier!

This doctoral thesis has been examined by a Committee of the Department of Nuclear Science of Engineering as follows:

Professor Alan Jasanoff .....
Chairman, Thesis Committee
Professor of Biological Engineering, Brain & Cognitive Sciences and Nuclear Science & Engineering

Professor Paola Cappellaro .....
Thesis Supervisor
Esther and Harold Edgerton Associate Professor of Nuclear Science and Engineering

Professor Ju Li .....
Thesis Reader
Battelle Energy Alliance Professor of Nuclear Science & Engineering and Materials Science & Engineering

Professor Seth Lloyd .....
Member, Thesis Committee
Nam Pyo Suh Professor of Mechanical Engineering

Professor Ronald L. Walsworth .....
Member, Thesis Committee
Senior Lecturer, Harvard-Smithsonian Center for Astrophysics and Harvard University Department of Physics

# Contents

# List of Figures

# Citations to Published Work

Chapter 1 is based on the following paper:

- *Atomic-scale nuclear spin imaging using quantum-assisted sensors in diamond*, A. Ajoy, U. Bissbort, M.D. Lukin, R.L. Walsworth and P. Cappellaro, Phys. Rev. X 5, 011001 (2015).

Large portions of Chapter 2 have appeared in the following paper:

- *Quantum Interpolation for High Resolution Sensing*, A. Ajoy, Y. X. Liu, K. Saha, L. Marseglia, J.-C. Jaskula, U. Bissbort and P. Cappellaro, arXiv:1604.01677 (2016).

Chapter 3 is based on the following paper:

- *Sensitive DC Magnetometry Approaching $T_2$ via Ancilla Assisted Bandwidth Narrowing*, A. Ajoy, Y. X. Liu and P. Cappellaro, arXiv:16xx (2016).

Large portions of Chapter 4 have appeared in the following paper:

- *Stable three-axis nuclear-spin gyroscope in diamond*, A. Ajoy and P. Cappellaro, Phys. Rev. A 86, 062104 (2012).

Large portions of Chapter 6 have appeared in the following paper:

- *Quantum simulation via filtered Hamiltonian engineering: application to perfect quantum transport in spin networks*,
  A. Ajoy and P. Cappellaro, Phys. Rev. Lett. 110, 220503 (2013).

Chapter 7 is based on the following paper:

- *Selective nuclear decoupling by actuator control*,
  G. Kaur, A. Ajoy and P. Cappellaro, New J. of Phys. 15, 093035 (2013).

Chapter 8 is based on the forthcoming paper:

- *Selective nuclear decoupling by actuator control*,
  A. Ajoy, U. Bissbort and P. Cappellaro, arXiv:16xx (2016).

Chapter 9 is based on the following paper:

- *Mixed-state quantum transport in correlated spin networks*,
  A. Ajoy and P. Cappellaro, Phys. Rev. A 85, 042305 (2012).

Chapter 10 is based on the following paper:

- *Perfect quantum transport in arbitrary spin networks*,
  A. Ajoy and P. Cappellaro, Phys. Rev. B 87, 064303 (2013).

# Part I

# High Resolution Nanoscale Magnetic Resonance Imaging

# Preface

In this part of the thesis we consider the use of quantum sensors for the task of high-resolution nuclear magnetic resonance imaging (MRI) at nanometer length scales. The quantum sensor we consider is the nitrogen vacancy (NV) center in diamond, which is a single electronic spin that at can be optically polarized and read-out. Current technology has allowed NV centers to be implanted very close to the surface of the diamond, indeed less than 5nm below the diamond surface. One can now imagine placing a single molecule or protein above the diamond surface and mapping out its three-dimensional structure by determining the strength of the interactions of the quantum sensor to nuclear spins in the molecule. In chapter 1, we consider this problem in detail theoretically, including a new method to selectively transfer polarization from the quantum sensor to nuclear spins in its environment with high resolution. The proposal was made possible by exploiting the coupling of the NV center to an intrinsic quantum memory associated with the $^{14}$N nuclear spin, to reach a tenfold improvement in spatial resolution, down to atomic scales. More precisely, under microwave dressing by Rabi field $\Omega S_x \cos\omega t$, the Hamiltonian of the NV center coupled to a nuclear spin is of the form, $H_1 = \Omega S_x + \omega_L I_z + A S_z I_z + B S_z I_x$. Now when in addition, the NV center is put to state $|1\rangle$ it produces a Zeeman field on the nuclear spins of the form $H_2 = (\omega_L + A) I_z$. A combined evolution, $L$ times under these two Hamiltonians, along with the use of the ancilla qubit as a memory leads to an effective

evolution under an average Hamiltonian $H_{eff} = \Omega S_x + \omega_L I_z + A S_z I_z + B\mathcal{G} S_z I_x$, where $\mathcal{G} = \sum_{k=0}^{L-1} e^{ik\tau(\omega_L + A)}$. This creates a dynamic frequency filter selecting only a few nuclear spins at a time. We showed that this method could not only sense individual spins in a complex biomolecule, but also unravel couplings *among* them – thus elucidating local characteristics of the molecule structure to within a few angstroms of spatial resolution.

In chapter 2 of the thesis we consider a complementary approach for high-resolution sensing, whereby spins which are normally not resolvable due to certain hardware limitations. To be more concrete, many quantum metrology techniques involve an interferometric detection of a weak signal as the build up of a phase shift $\vartheta$ with the parameter being sensed. This is true right from the simplest Sagnac interferometers, down to more exotic proposals like quantum illumination [1] – where the power of quantum phase estimation can be put to full use. However, in all practical experiments, due to limitations in hardware, there is always a finite resolution $\Delta\vartheta$ that limits the smallest step in phase space one can reliably measure. This limit might also bound the minimum resolution that could be achieved by the quantum sensor. This is also the case for sensing the positions of nuclear spins with an NV center – interferometric detection is achieved via precisely timed refocused evolution periods of the NV center starting from the state $\frac{1}{\sqrt{2}}(|0\rangle + |1\rangle)$ – and finite timing resolution $\Delta\tau$ set by hardware, often limits the sensitivity and resolution of the metrology protocol (here $\Delta\vartheta = \omega_L \Delta\tau$). The essential idea presented in Chapter 2 is to construct, through an appropriate control method, a linear interpolation of the quantum sensor dynamics in the interval $\Delta\vartheta$ in such a way that inherent hardware resolution limitations can no longer limit the achievable sensor resolution. This allows one to use the quantum sensor to obtain extremely narrow spectral lines from nuclear spins of interest, and through the spectral narrowing, resolve them.

We study this technique experimentally in chapter 2 of the thesis, and demonstrate that resolution boosts by over a factor of 100 are possible for NV based spin sensing. However, the technique is more general, with potentially wide ranging applications across different platforms in quantum metrology [2]. In chapter 3, we develop in detail the theoretical basis behind the method of quantum interpolation, and point out extensions of this approach for a high-resolution sensing of quantum and classical fields, including nuclear chemical shifts, and high frequency magnetic fields from ferromagnetic resonances.

# Chapter 1

# Atomic-Scale Nuclear Spin Imaging using Quantum-Assisted Sensors

## 1.1 Introduction

Proteins are the most important building blocks of life. The ability to obtain high-resolution protein structures is the keystone of drug discovery, since structure naturally reveals binding sites that can be targeted by drugs. Several methods exist for determining high resolution protein structure, primarily X-ray crystallography [3], transmission electron microscopy [4] and nuclear magnetic resonance (NMR) [5]. While each method has greatly contributed to our understanding of protein structure, none of them can sense individual molecules. Of particular interest would be imaging of small active sites of a protein in its natural environment and conditions.

The advent of novel nano-scale sensors has given hope of achieving the long-standing goal of single-protein, high spatial-resolution structure determination in their natural environment and ambient conditions. In particular, quantum sensors based on the spin-dependent photoluminescence of Nitrogen Vacancy (NV) centers

in diamond[6] have shown the potential to provide few $\mathrm{nT}/\sqrt{\mathrm{Hz}}$ sensing and nanoscale resolution at ambient conditions. NV-based magnetometers[7,8] can be transformative tools in quantum information, material science and bio-imaging[9,10,11], allowing for example high-resolution magnetic imaging of living cells[12].

NV centers in bulk diamond have mapped the location of single $^{13}C$ nuclear spins inside the diamond crystal[13,14,15], while shallow-implanted NVs have recently demonstrated the ability to sense a small number of nuclear spins in various organic materials[16,17,18,19,20], as well as single and small ensembles of electronic spins outside the diamond sensor[21,22,23,24]. While NV sensitivity is approaching single-spin levels, extracting relevant information from a very complex structure is a further challenge, since it requires not only the ability to sense the magnetic field of an isolated nuclear spin, but also to achieve atomic-scale spatial resolution. Here we propose a method that, by exploiting the coupling of the NV center to an intrinsic quantum memory associated with the Nitrogen nuclear spin, can reach a tenfold improvement in spatial resolution, down to atomic scales. The spatial resolution enhancement is achieved through coherent control of the sensor spin, which creates a dynamic frequency filter selecting only a few nuclear spins at a time. We propose and analyze a protocol that would allow not only sensing individual spins in a complex biomolecule, but also unraveling couplings among them, thus elucidating local characteristics of the molecule structure.

Each nuclear spin in samples of interest creates a magnetic field that depends on its position relative to the NV center. For spins 2-5nm away from the NV spin, this magnetic field is within range of the sensitivity of the NV quantum probe[6] (see Fig. 1-1.A), can be made possible by the long coherence time achieved by careful material preparation[26,18,27] and by using pulsed[17] or continuous[28,29] dynamical decoupling (DD) sequences, which can extend the sensing time to hundreds of microseconds. The

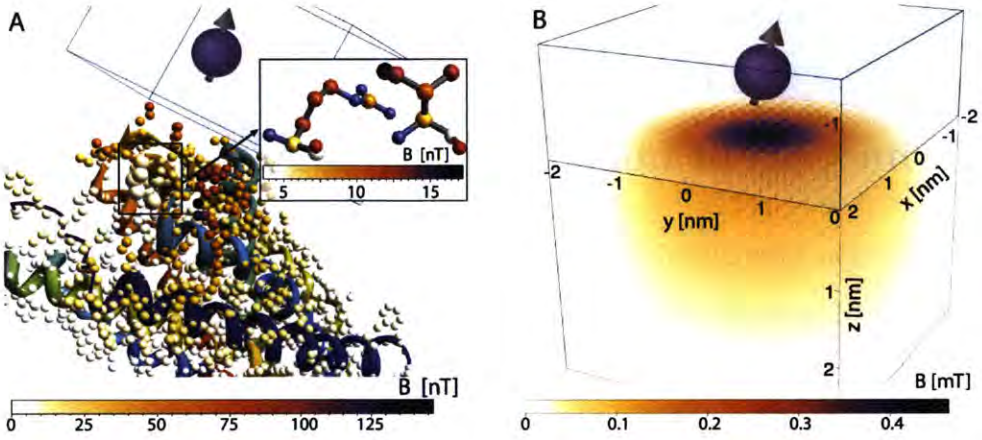


Figure 1-1: **Nuclear spin imaging with a shallow NV center in diamond.** (a) A single NV spin (purple) at 1-2nm from the diamond surface can sense single nuclear spins in a molecule (the chemokine receptor CXCR4[25], ribbon diagram) anchored to the diamond. The magnetic field produced by individual $^{13}$C (spheres with color scale given by $B_{\perp}^{j}/\gamma_e$) is in the range of nT, within reach of NV sensitivity. In the inset: the binding site of interest (atoms other than $^{13}$C are blue (O) and red (N)). (b) A shallow NV center (2nm from the surface) creates a magnetic field gradient ($A(\vec{r})/\gamma_n$) above the [111] surface of the diamond. Note the azimuthal symmetry of the field, which causes degeneracy of the frequency shift at many spatial locations.

decoupling cancels low-frequency dephasing noise, but by appropriately selecting the control timing to match the nuclear spin Larmor frequency, the NV spin can sense the magnetic field created by the nuclear spins, even in the absence of a net nuclear polarization (spin noise). For sparse nuclear spin ensembles, such as encountered in natural diamond, this effect is enough to distinguish individual spins and thus to reconstruct their position[13,14,15]. For dense samples, the frequency resolution is inadequate to distinguish individual spins. In addition, the intrinsic NMR linewidth in a dense molecule might exceed the NV sensing linewidth.

In the following we describe a method to improve the frequency, hence spatial, resolution of NV sensing. We evaluate the method performance with simulations on typical bio-molecules and discuss the experimental resources needed to achieve

atomic-scale reconstruction of nuclear spin positions.

## 1.2 Principles of nuclear spin imaging

We assume that the biomolecule to be probed is attached to the surface of a diamond at the location of a single NV center that is within 3 nm of the diamond surface (Fig. 1-1). To achieve enhanced spatial resolution for NV sensing of the nuclear spins within the biomolecule, we use three critical ingredients: (i) an effective strong magnetic field gradient across the biomolecule due, e.g., to the rapid spatial variation of the magnetic dipolar field from the NV electronic spin; (ii) Hamiltonian engineering of the NV and multi-nuclear spin system[30] – which creates a very sharp dynamical frequency filter for NV sensing and controls the effect of NV spin polarization leakage through the coupled nuclear spin network; and (iii) a quantum memory – the *nuclear* $^{15}$N spin associated with the NV center – which enables long acquisition times and hence an even sharper frequency filter.

The sensing protocol works by following the leakage of polarization from the NV center (which is optically polarized) toward on-resonance nuclear spins. The resonance condition is in principle different for each nuclear spin, as it is given by its position-dependent coupling to the NV center. However, simply implementing cross-polarization does not yield enough frequency resolution for single-spin sensing. By alternating periods of cross-polarization with evolution under a magnetic field gradient –while the NV spin state is preserved by mapping onto the quantum memory– the interaction Hamiltonian is modulated and only couplings of the NV to resonant nuclear spins are retained. Evolution under the gradient thus acts as a sharp frequency filter, thereby increasing the spatial selectivity. The gradient evolution time can be long, limited only by the quantum memory (the *nuclear* $^{15}$N spin associated

with the NV center) coherence time, which at a few milliseconds translates to a high frequency resolution, $\delta A \sim 100$Hz.

Using the NV polarization leakage as a signature of the nuclear spin position provides two advantages over measurement of NV frequency shifts due to specific nuclear spins. First, it is easy to embed nuclear decoupling sequences within the sensing protocol; nuclear decoupling is essential to narrow the NMR spectrum intrinsic linewidth and thus detect signal arising from individual nuclear spins. Second, once the polarization is transferred to a nuclear spin, this spin itself becomes a sensitive probe of its local environment. In the following we propose a three-step protocol for nuclear spin imaging. In a first step, we observe polarization transfer from the NV center to one (or a few) nuclear spin(s), providing partial information about their positions. The nuclear spins can then evolve freely, and polarization diffuses in the nuclear spin network. The polarization is then transferred back to the NV center, revealing the nuclear spin connectivity. We can thus acquire multi-dimensional spectra that not only decrease frequency crowding, but can also resolve degeneracies related to the intrinsic symmetry of the dipolar coupling.

Next we describe in detail the proposed method and its application to biomolecule structure reconstruction.

## 1.3 Results

### 1.3.1 Nuclear Spin Detection via NV centers in diamond

The electronic spin $S = 1$ associated with the negatively charged Nitrogen Vacancy center in diamond is a sensitive probe of magnetic fields at the nano-scale [6]. The good sensitivity of NV spins is due to the long coherence time achieved under dynamical

decoupling. Pulsed decoupling sequences – a train of $\pi$-pulses such as CPMG[31] – not only cancel low-frequency dephasing noise, but also act as sharp band-pass filters at selected frequencies set by the pulse timing[32,33].

Nuclear spins on the surface of the diamond couple to the NV electronic spin via the magnetic dipolar interaction $\vec{\mu}$,

$$\vec{\mu}(\vec{r}) = \frac{\mu_0}{4\pi}\frac{\hbar}{2\pi}\frac{\gamma_e\gamma_n}{r^5}\left[(3r_z^2 - r^2)\hat{z} + 3r_z(r_x\hat{x} + r_y\hat{y})\right], \tag{1.1}$$

where the NV is at the origin and we aligned the coordinate system with the NV symmetry axis. Here $\gamma_{e,n}$ are the gyromagnetic ratios of the electronic and nuclear spins respectively. For shallow NVs, this interaction exceeds the nuclear-nuclear dipolar coupling and is strong enough to allow coherent coupling to individual nuclear spins, via the Hamiltonian:

$$\mathcal{H}_{dip}^j = S_z\vec{\mu}(\vec{r}_j)\cdot\vec{I}^j = S_z[A^jI_z^j + B_\perp^j(\cos\varphi^jI_x^j + \sin\varphi^jI_y^j)], \tag{1.2}$$

where $S_\alpha$ and $I_\alpha^j$ are the NV electronic spin and external nuclear spin operators, respectively. Here $A^j = \mu_z(\vec{r}^j)$ and $B_\perp^j = \sqrt{\mu_x^2 + \mu_y^2}$ are the longitudinal and transverse components of the dipolar coupling at the location of the $j^{th}$ spin.

The normalized signal due to the net phase shift imparted to the NV spin after a train of $2n$ $\pi$-pulses spaced by a time $\tau$ is given by $S = \frac{1}{2}\left(1 + \prod_j \mathcal{S}^j\right)$, where the pseudo-spin signal from the $j^{th}$ nuclear spin is

$$\mathcal{S}^j = 1 - 2\vec{\omega}_0^j \times \vec{\omega}_1^j \sin^2\left(\frac{\Omega_0^j\tau}{4}\right)\sin^2\left(\frac{\Omega_1^j\tau}{4}\right)\frac{\sin(n\alpha^j)^2}{\cos(\alpha^j/2)^2}, \tag{1.3}$$

$$\cos(\alpha^j) = \cos\left(\frac{\Omega_0^j \tau}{2}\right)\cos\left(\frac{\Omega_1^j \tau}{2}\right) - \vec{\omega}_0^j \cdot \vec{\omega}_1^j \sin\left(\frac{\Omega_0^j \tau}{2}\right)\sin\left(\frac{\Omega_1^j \tau}{2}\right).$$

Here the vectors $\vec{\Omega}_i^j = \Omega_i^j \vec{\omega}_i^j$ represent the nuclear spin Hamiltonian in the two subspaces of the NV electronic spin. In general we have $\vec{\Omega}_0^j = \omega_L^j \hat{z}$, where $\omega_L = \gamma_n B$ is the nuclear spin Larmor frequency. Then the signal shows "dips" around $\tau_k = (2k+1)\pi/\omega_L$ marking the presence of nuclear spins. However, the dip times are specific for each nuclear spin because of the differences in dipolar coupling, $\vec{\Omega}_1^j = (\omega_L + A^j)\hat{z} + B_\perp^j[\cos\phi^j \hat{x} + \sin\phi^j \hat{y}]$. The dip minimum is achieved when $\alpha^j = \pi$; for $\vec{\omega}_0^j \cdot \vec{\omega}_1^j \approx 1$ (as is the case for large enough magnetic field); this is obtained at $\tau_k^j = 2\pi(2k+1)/(\Omega_0^j + \Omega_1^j) \approx (2k+1)\pi/(\omega_L + A^j/2)$. At long times, the signal dips arising from different nuclear spins become discernible, as one can separate contributions from spins having dipolar couplings $A^j - A^i = \delta A \gtrsim \omega_L/[(2k+1)n]$. The linewidth of this sensing scheme is thus limited by the coherence time, $\delta A \sim 4\pi/(T_2) \approx (2-50)2\pi$ kHz. While the signal contrast at the dips, $S^j \sim \cos\left(\frac{2B^j n}{\omega_L + A^j/2}\right)$, would be enough to measure protons 2-5nm from the NV center, the frequency resolution is not enough to distinguish individual spins separated by $\sim 0.1$nm in a dense molecule. In addition, the intrinsic NMR linewidth of dense samples (tens of kHz) can exceed the NV sensing linewidth and it is challenging to embed homonuclear decoupling in the NV decoupling-based sensing scheme (see Appendix 1.B).

An alternative approach to nuclear spin sensing is to observe the polarization leakage from the NV center to the nuclear spins [34,35]. We first rotate the NV spin to the transverse axis and then apply a continuous driving along that same axis (spin-locking). The driving decouples the NV from noise and the nuclear spin bath. Setting however the NV Rabi frequency $\Omega$ close to the target nuclear spin energy, $\Omega \approx \pm\omega_L$, polarization is transferred to the nuclear spins [36,37], resulting in a signal

dip:

$$S^j = 1 - \frac{B_\perp^{j2} \sin^2\left(\frac{t}{2}\sqrt{B_\perp^{j2} + [\Omega \mp (A^j + \omega_L)]^2}\right)}{2\left[B_\perp^{j2} + [\Omega \mp (A^j + \omega_L)]^2\right]}. \tag{1.4}$$

The energy matching condition depends on the nuclear spin dipolar coupling $A^j$, but the frequency resolution is limited by the hyperfine transverse component, $\delta A \sim B^j$. Even if homonuclear decoupling can be embedded within cross-polarization, it is not possible to distinguish spins in a dense sample. Also, cross polarization is often plagued by power fluctuation in the driving field, which leads to imperfect energy matching and broadens the effective frequency resolution.

### 1.3.2 Quantum-enhanced spatial resolution

To increase the frequency –and thus spatial– resolution, we exploit the presence of an ancillary qubit associated with the Nitrogen nuclear spin ($^{15}$N with $I = \frac{1}{2}$). This long-lived ancillary spin can store information about the state of the NV electronic spin, while the external nuclear spins evolve under the action of a magnetic field gradient, which creates a further frequency filter, thereby increasing the spatial selectivity.

The gradient evolution time can be as long as a few milliseconds, limited only by the *nuclear* $^{15}$N spin coherence time, yielding a sharp frequency filter. The gradient field could be provided by a strong magnetic tip[21,38], micro-fabricated coils[39] or dark spins[40] on the diamond surface. Even more simply, the NV itself can create the gradient, when set to the $|1\rangle$ state (see Fig. 1-1.B). In the following, we will assume this strategy, as this does not require any additional experimental resource.

The method can proceed as follows. After a period of evolution under the spin-lock Hamiltonian, the NV state is mapped onto the nuclear ancillary spin –initially in the $|1\rangle$ state – by a SWAP gate[41] (see Fig. 1-2). High fidelity SWAP operations

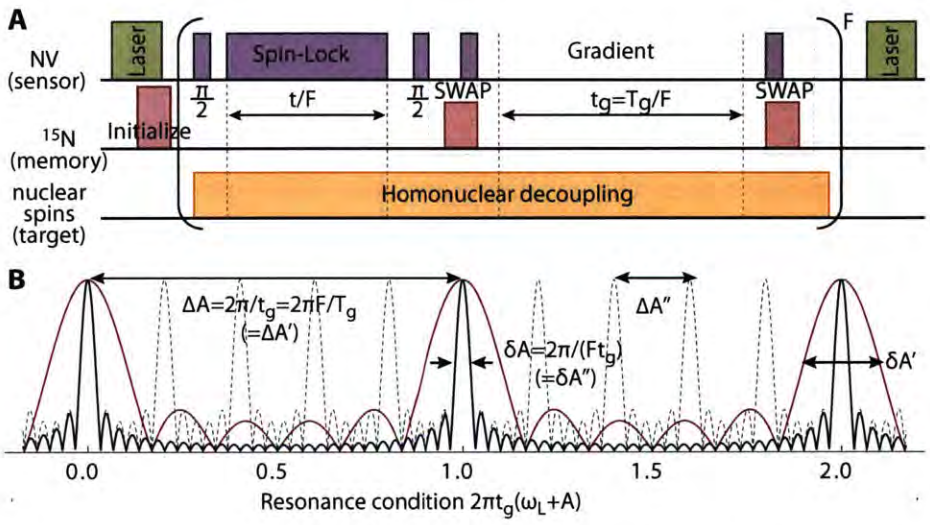


Figure 1-2: **Control scheme for filtered cross-polarization nuclear spin sensing. (A)**: Polarization is transferred from the NV electronic spin to the target nuclear spins in the bio-molecule for a time $t/F$. To increase spatial resolution, the nuclear spins are let to evolve under a magnetic field gradient for a time $t_g = T_g/F$, while the NV state is stored in the nuclear $^{15}$N spin. The scheme is repeated $F$ times to create a sharp filter. For reverse-sensing the two $\pi/2$ pulses are omitted. **(B)**: Filter created by the control scheme as a function of the normalized time $2\pi t_g(\omega_L + A)$. The filter peaks are sharper for higher $F$ (dark line, $F = 30$, red line, $F' = 6$), yielding a smaller linewidth $\delta A$. While it is possible to achieve sharper peaks at longer times (dashed line, $F'' = 6$, $t''_g = 5t_g$), this results in a smaller bandwidth $\Delta A''$.

can be constructed by successive RF and microwave irradiation [42], by free evolution under a misaligned field or via the use of decoherence protected gates [43,44]. The electronic spin is thus left in the $|1\rangle$ state, thereby creating a magnetic field gradient. Inverting these operations after a time $t_g$ effectively implements an evolution of the external nuclear spins under the Hamiltonian

$$H_G = \mathbb{1}_{NV} \otimes \sum_j H_G^j, \quad H_G^j \approx (\omega_L + A^j) I_z^j. \tag{1.5}$$

Alternating evolution under the gradient and the spin-lock Hamiltonian (in the dressed-state basis),

$$H_{\mathrm{SL}} = \Omega S_z + \sum_j \left[ (\omega_L + A^j) I_z^j + B_\perp^j (e^{i\varphi_j} S_+ I_-^j + \mathrm{h.c.}) \right], \tag{1.6}$$

where $I_\pm = I_x \pm i I_y$, we obtain the effective evolution:

$$\left[ e^{-iH_G t_g} e^{-iH_{\mathrm{SL}} t/F} \right]^F \equiv e^{-iH_G t_g F} e^{-it\overline{H}_{\mathrm{F}}} \tag{1.7}$$

Here we define the filtered Hamiltonian $\overline{H}_{\mathrm{F}} = \sum_j \overline{H}_{\mathrm{F}}^j$, with

$$\overline{H}_{\mathrm{F}}^j = \Omega S_z + (\omega_L + A^j) I_z^j + B_\perp^j (\mathcal{G}^j e^{i\varphi_j} S_+ I_-^j + \mathrm{h.c.}), \tag{1.8}$$

$$\mathcal{G}^j(t_g) = \frac{1}{F} \sum_{k=0}^{F-1} e^{ikt_g(\omega_L + A^j)}, \quad |\mathcal{G}^j| = \frac{\left| \sin\left( \frac{F t_g (A^j + \omega)}{2} \right) \right|}{F \left| \sin\left( \frac{t_g (A^j + \omega)}{2} \right) \right|} \tag{1.9}$$

(see 1.A). This control scheme creates a time-domain Bragg grating [33] around the frequencies $\omega_f = 2n\pi/t_g$, with very sharp peaks for large $F$ (see Fig. 1-2.B). Then, only for on-resonance nuclear spins the dipolar coupling transverse component, $B_\perp^j$,

is retained and polarization is transferred, yielding $S^j < 1$ in Eq. (1.4). The filter linewidth, $\delta A = 2\pi/(Ft_g)$, is determined by the gradient-evolution time, which can be made very long since it is only limited by the ancillary nuclear spin dephasing time, $Ft_g \lesssim T^*_{2n} \sim 8 - 10\text{ms}$[45]. The bandwidth $\Delta A$ over which it is possible to distinguish different spins is instead set by the condition $(A \pm \Delta A + \omega_L)t_g \lesseqgtr 2\pi(n \pm 1)$. The scheme can thus achieve a frequency resolution of about $\delta A \sim 2\pi 100\text{Hz}$ over a bandwidth $\Delta A = 2\pi/t_g \sim F \times 2\pi 100\text{Hz}$, which can be 10-50 times larger than $\delta A$. The bandwidth can be further improved by over five times using a novel control strategy that effectively creates anti-aliasing filters[30] (see Appendix 1.F). Since it is possible to embed homonuclear decoupling[46] during both the spin-lock and the gradient evolution, the linewidth is not limited by the spin-spin coupling. We note that a similar filtering scheme could be embedded with the DD-based sensing strategy (Eq. 1.3), increasing its frequency resolution while also allowing homonuclear decoupling during the gradient evolution.

The ancillary $^{15}$N nuclear spin, by acting as a memory, thus achieves two goals: it increases the coherence time and it enables using the NV center as a source of magnetic field gradient. The resulting dynamic Bragg grating reaches high spatial resolution (sub-angstrom for protons and a NV 2-3nm below the diamond surface). As shown in Fig. 1-4, the frequency resolution is much better than for DD-based sensing protocols.

A further advantage of the proposed filtered cross-polarization scheme is that it can be used not only to sense individual nuclear spins, but also to polarize them. The nuclear spins, as explained below, then become local probes of their environment, providing essential structural information.

### 1.3.3 Protocol for nuclear spin imaging

A protocol for nuclear spin imaging involving three steps is illustrated in Fig. 1-3. First, we acquire a 1D NMR spectrum using the filtered cross-polarization method described above ("*sense/polarize*" step), sweeping the filter time $t_g$ and the driving frequency $\Omega$. For each time point, only one (or a few) nuclear spin(s) becomes polarized and thus contributes to the signal. In the second step, the nuclear spins are left to evolve freely for a time $t_d$ ("*diffuse*") prior to transferring polarization back to the NV electronic spin for detection in the third step ("*reverse sense*"). During the diffusion time $t_d$, nuclear polarization migrates to neighboring spins under the action of the homonuclear dipolar Hamiltonian[47]. To sense the new location of the polarization the NV is again driven at the nuclear spin frequency (alternating with the gradient field for enhanced spatial resolution). By omitting the initial rotation to the transverse plane, the NV is now only sensitive to polarized nuclear spins. For a fixed diffusion time $t_d$ one thus obtain a 2D, correlated spectrum, similar to NMR 2D spectroscopy[48]. The spectrum (Figure 1-4) encodes information about the couplings between nuclear spins and thus constrains their relative positions. Note that we could further obtain 3D spectra by sweeping the diffusion time $t_d$ (Appendix 1.E), which would provide additional information about the nuclear spin system correlations[49]. The spectra yield an over-constrained system for the spin positions, as for $N$ nuclear spins we can obtain up to $2N + N(N-1)/2$ equations (Appendix 1.E). By using the polarized nuclear spins as probes of their own environment, this protocol can thus break the symmetry of the dipolar coupling and overcome the phase problem that plagues other experimental techniques.

Indeed, the 1D NMR spectrum acquired in the first step provides information on the dipolar couplings to the NV spin. Using a peak-picking procedure, we directly

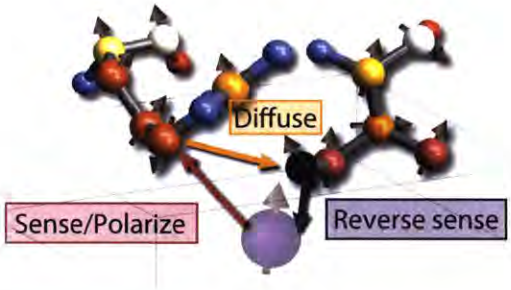


Figure 1-3: **Protocol for quantum-enhanced nuclear spin imaging.** First the NV measures a 1D NMR spectrum (sense). During this step, polarization is selectively transferred from the NV to a particular nuclear spin in the protein (polarize). Polarization is then allowed to spread (diffusion), driven by the nuclear spin-spin dipolar coupling. The polarization now localized on a different nuclear spin is transferred back to the NV spin and measured optically (reverse-sense).

read out the longitudinal dipolar couplings from the frequency position $\omega_p$ of the dips, $A = 2(\omega_p - \omega_L)$. The dip height determines the transverse coupling, as $S^p = 1 - \frac{1}{2}\sin^2(B_\perp t/2)$ (Eq. 1.4). Given a pair of parameters $A_p, B_p$ for each dip, the spin position is found by inverting Eq. (1.1). This yields a pair of solutions for $r_z$ and $r_\perp = \sqrt{r_x^2 + r_y^2}$, with only one usually consistent with the NV depth. The nuclear spin positions lie in a region defined by the unknown angle $\varphi = \arctan(r_y/r_x)$ (analogous to the phase problem in x-ray crystallography.) While the NV depth often further constrains this region, the information obtained from the 2D spectrum correlations is essential to unambiguously determine the position. In addition, 2D correlations help in distinguishing spins that might have similar couplings to the NV (because of the phase symmetry) and thus create overlapping signals in the 1D spectrum, but give rise to distinct peaks in the 2D spectra since they couple to different spins.

For an isolated nuclear spin pair, the signal intensity at the diagonal peaks is $S_{ii} = \frac{1}{2}[1 + \sin(B_\perp^j t/2)^4 \cos(D_{ij} t_d/2)^2]$, where $D_{ij}$ is the dipolar coupling strength between the spins. The cross peaks (yielding a cleaner signal for non-isolated pairs) are instead

$S_{ij} = \frac{1}{2}[1 + \sin(B_\perp^j t/2)^2 \sin(B_\perp^i t/2)^2 \sin(D_{ij} t_d/2)^2]$. For each spin pair, knowledge of their mutual dipolar coupling $D_{ij}$ determines the phase difference $\varphi_i - \varphi_j$, thus all relative phases can be determined (up to a global phase) if enough dipolar couplings can be measured. In general, a 2D spectrum might not be sufficient to fully determine the position of a complex structure since couplings between distant nuclear spins might not be visible and because of uncertainties in the estimated parameters. The information can however be supplemented by 3D spectra (varying the diffusion time) and by including prior information, such as the length of chemical bonds, into the reconstruction algorithm.

## 1.4 Discussion

The proposed method would enable NV centers in diamond to sense individual nuclear spins and their mutual couplings with atomic-scale resolution and thereby determine the atomic structure of pockets and local sites close to the surface of large bio-molecules. Experiments can be performed at ambient conditions, without the need to crystallize the molecules, and on single molecules, avoiding the need to synthesize large ensembles. Site-selective isotopic labeling [50] would allow focusing on a small number of $^{13}C$ or Nitrogen spins, or even protons in molecules in a deuterated solution. The molecules could be functionalized and attached to the diamond surface, for example by methods such as the EDC/NHS reaction, which forms a chemical bond stable over a few weeks [51]. Deterministic binding near an NV center may be obtained using co-localization techniques developed in [51].

Measuring the structure of local surface sites in biomolecules, relevant to many biological functions and drug discovery, is within reach of current NV sensitivity, although the mapping of whole bio-molecules is more challenging and requires further

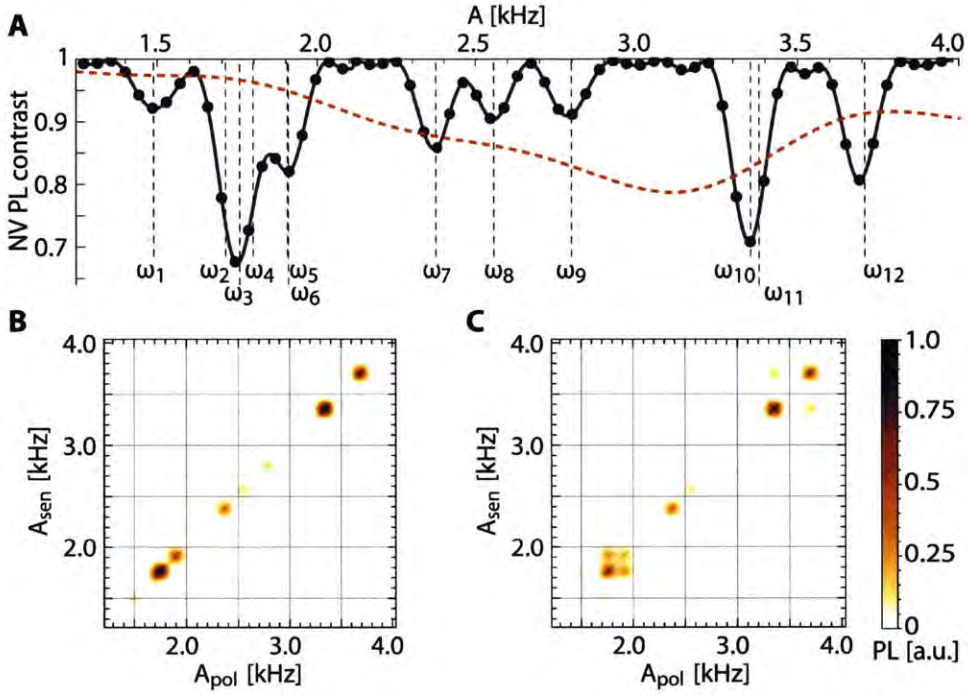


Figure 1-4: **Simulated 1D and 2D NMR spectra** for the binding site in CXCR4, obtained with the NV-based filtered sensing protocol. **(A)**: Simulated normalized spin-dependent NV photoluminescence (PL) after the filtered cross-polarization sequence. The x-axis shows the on-resonance dipolar frequency $A$ at each measurement point, while the driving frequency is $\Omega = A/2/\sqrt{3} + \omega_L$ (with Larmor frequency $\omega_L = 2$MHz) and the gradient time $t_g = 2\pi/(A/\sqrt{3} + \omega_L)$. A homonuclear decoupling sequence was applied to the $^{13}$C spins to narrow their intrinsic linewidth. The PL shows dips when $A$ and the inverse gradient time (simultaneously swept) match the longitudinal dipolar coupling $A^j$ of one nuclear $^{13}$C spin in the protein. We simulated the 12 $^{13}$C spins in the ARG and ILE active site and an NV center 1.75nm below the diamond surface, with the [111] axis aligned around the vertical direction. The gradient time was varied from 201.68 to 201.84$\mu$s (for a maximum total gradient time of $T_g \approx 6$ms in $F = 30$ steps). The total polarization time was $t = 720\mu$s. The dip height is a measure of the transverse dipolar coupling $B^j_\perp$. The spectrum shows 8 dips, with the height indicating overlapping contributions from almost equivalent spins. The dashed line is the spectrum one would obtain with a DD-based protocol distorted by the spin-spin couplings (Appendix 1.B). **(B)**: Simulated 2D NMR spectra from the proposed protocol. After polarization (obtained with the same parameters as for the 1D spectrum) the nuclear spins evolve freely for $t_d = 300\mu$s, allowing polarization diffusion. The polarization is then mapped back to the NV center and measured via its spin-dependent PL. The left plot is the 2D NMR spectrum for no diffusion $t_d = 0$, while the right plot shows the spreading of polarization in the nuclear spin network, as indicated from off-diagonal non-zero terms.

technical advances in quantum metrology[52] or nano-diamonds with enhanced material properties[53]. Our method could complement information acquired via existing techniques, in particular x-ray crystallography and NMR. While x-ray diffraction is able to image whole proteins with Angstrom resolution, the technique requires the ability to produce high quality single crystals of a few hundred of microns, thus restricting the number of proteins that can be studied (e.g., membrane proteins cannot be crystallized); in contrast, NV-based sensing can image single proteins in their natural state. In addition, the imaging protocol we propose can help solve reconstruction issues associated with the phase problem in x-ray diffraction and overcrowded spectra in NMR. While the NV-based scheme has similarities to NMR methods such as NOESY[5], which explore through-space spin-spin correlations, the ability of our NV technique to polarize only one spin at a time allows acquiring more information even in possibly crowded spectra.

We can estimate the resources needed for such tasks by considering the frequency resolution and signal-to-noise ratio (SNR) requirements to distinguish one or few nuclear spins in a dense molecule. For a nuclear spin on-resonance with the NV Rabi frequency, the signal in Eq. (1.4) simplifies to $S^j = 1 - \frac{1}{2}\sin^2(B_\perp t/2)$, where the time $t$ is limited by the coherence time in the rotating frame ($T_{1\rho} \approx 2$ms[29]). The SNR in $M$ measurements is then $SNR \sim \sqrt{M/2}CT_\rho$, where $C \approx 0.01 - 0.3$[6,42] captures the finite contrast and photon collection efficiency. In order to distinguish spins with dipolar couplings differing by $\delta A$, the total gradient time should be $T_g = Ft_g = 2\pi/\delta A$ in $F$ steps. Thus the total time required to measure one spin is $T_s = M(T_g + T_\rho + Ft_a + t_{\rm ro})$, where $t_{\rm ro}$ is the read-out time and $t_a$ is the time needed for the ancillary spin protocol (polarization of the NV, $\sim$500ns, NV $\pi$-pulse, 20ns and SWAP gate, $\sim 4\mu$s). For the 2D protocol, assuming division of the spectral range in $b$ frequency steps and letting the nuclear spin diffuse for a time $t_d$, the total

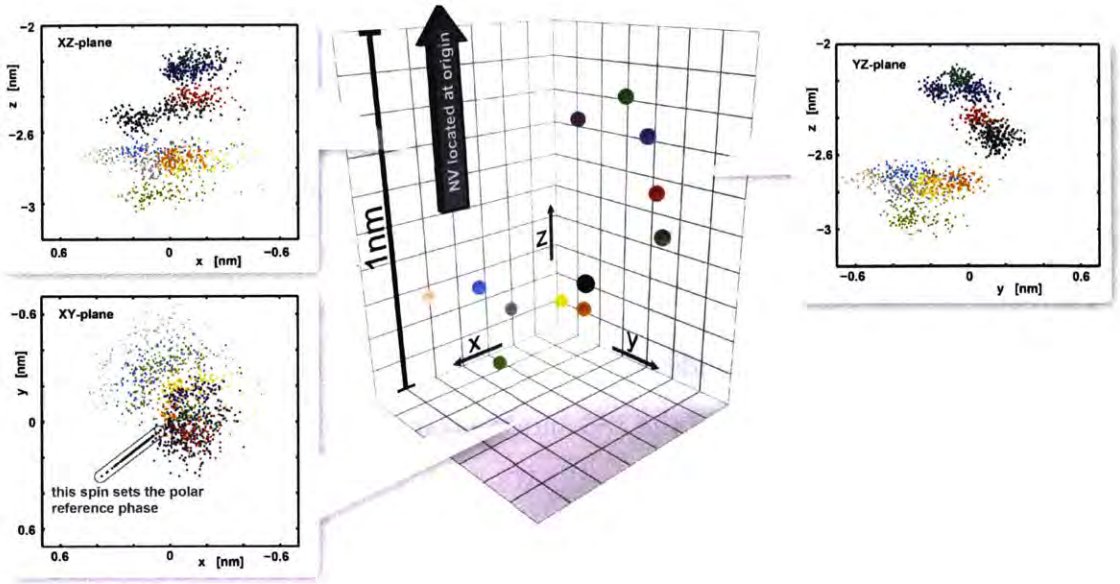


Figure 1-5: Accuracy of the position assignment obtained from our proposed sensing method for the $^{13}$C nuclear spins in the 183 and 185 residues of CXCR4. The spatial reconstruction uncertainty for the positions of the of $^{13}$C nuclear spins is shown as scatter plots in the three planes, where the color defines the nuclear spin it refers to (see 1.C and Appendix 1.E). Specifically, we choose the coordinates of residue 183 and 185 of the 3ODU protein[25] and assume a constant error $\Delta A_j = \Delta B_j = 300$Hz and a relative error $\Delta D_{ij} = 0.5 D_{ij}$.

measurement time becomes $T_{2D} = b(T_{1D} + t_d) = b^2 T_s + b t_d$.

Consider for example the chemokine receptor CXCR4[25]. Chemokine receptors are G protein-coupled receptors found predominantly on the surface of leukocytes and are critical regulators of cell migration for immune surveillance, inflammation, and development. In particular, the CXCR4 receptor (Fig. 1-1.A) is implicated in cancer metastasis and HIV-1 infection. CXCR4 ligand-binding cavities are actively studied as mutations are reported to decrease HIV-1 infectivity. CXCR4 was recently crystallized and its structure determined by x-ray diffraction[25] (we use these data in our simulations). It would be desirable to acquire more information about con-

formational changes in these receptors, resulting in signal transduction and HIV-1 entry process, as well as to obtain information about similar membrane proteins that cannot be crystallized.

In order to estimate the resources required to determine the structure of CXCR4 binding sites, we simulated the dynamics of the NV electronic spin under the action of the proposed control sequences and the protein's nuclear spins. In the simulations we assumed that only the amino-acids ARG and ILE are $^{13}$C-labeled, thus we can focus just on the 12 $^{13}$C nuclear spins of the 183 and 185 residues, as coupling to other spins (e.g., protons) is off-resonance or too weak. We further assumed application of both heteronuclear and homonuclear decoupling sequences to narrow the $^{13}$C linewidth. For an NV 1.75nm below the diamond surface, the minimum dipolar coupling of interest is $B_{\perp} = 250$Hz. Thus we need $M \approx 1000$ acquisitions to see such a spin, assuming a collection efficiency of $C \approx 0.2$ which can be obtained by 100 repeated readouts of the electronic spin, using the ancillary nuclear spin [42,54,55]. Choosing $b = 15$ bins to scan the frequency bandwidth of interest, $W = 2.5$kHz, the gradient time for the target linewidth is $T_g = 6\text{ms} = 1/(166\text{Hz})$. The experimental time to acquire a 1D spectrum is about $T_{1D} \approx 2$ minutes, while mapping the 2D correlations for the 10-12 frequencies of interest requires about $T_{2D} \approx 30$minutes. In Fig. 1-4 we show simulated 1D and 2D spectra for the CXR4 receptor active site; to illustrate the potential of our filtered scheme we increased the number of frequency bins to $b = 64$. The figure shows the high frequency resolution the method can achieve as well as the additional information provided by the local diffusion of polarization in the nuclear spin network, resulting in position estimates for each resolvable spins with good precision. Assuming an uncertainty of $\Delta A = \Delta B = 300$Hz for the dipolar couplings and an error $\sqrt{[\Delta D_{ij} = 0.5 D_{ij}]^2 + [50\text{Hz}]^2}$, the typical volume uncertainty ranges from 1.2Å$^3$ to 10 Å$^3$ for the various spins we considered (see Appendix 1.E

for details), although it increases sharply with the distance from the NV.

We note that these estimates do not include atomic position fluctuations due for example to thermal motion. The assumption that the atoms are quasi-static during the duration of the experiment is nonetheless reasonable, especially for nano/micro-crystalline structures. In general, obtaining a precise estimate of atom fluctuations is difficult, since it depends on several factors, including molecule topology and torsion, binding mechanism to the diamond surface and surrounding molecular environment (liquid hydration layer or ice). However, we can obtain estimates for crystal structures from the Debye-Waller coefficients tabulated in the PDB – at 77K, the disorder in atom positions for most crystals is under 1.5Å, comparable to the sensing resolution of our protocol.

## 1.5 Conclusions and Outlook

We proposed a practical method for atomic-scale nuclear spin imaging in bio-molecules using NV centers in diamond. Recent developments in materials fabrication [56,26], ion implantation [57,58] and coherent control techniques [59,60] have brought diamond magnetometers close to the threshold of single nuclear spin sensitivity. These quantum sensors have the potential to be an important tool in proteomics, as they overcome some of the challenges plaguing other experimental techniques, such as x-ray diffraction and conventional NMR. Most prominently, they would not require crystallization of the sample, a challenge for many classes of bio-molecules such as membrane proteins; nor large sample sizes.

Our novel strategy combines coherent control of the NV sensor with an intrinsic quantum memory to enhance the sensor spectral resolution. This control strategy not only creates a sharp dynamic filter by alternating periods of a spin-lock Hamil-

tonian with evolution under a gradient field, but provides other advantages. The sequence is compatible with homonuclear decoupling, thus allowing sensing beyond the natural bio-molecule NMR linewidth. In addition, our technique allows mapping the couplings among the spins themselves, using them as local probes of their environment. The resulting multi-dimensional NMR spectra highlight spatial correlations in the sample, lift spectral overlaps due to symmetries and aid the structure reconstruction algorithms. This would allow resolving the contributions in the NV signal arising from different nuclear spins in a dense sample and to use the acquired information to determine the nuclear spin positions. Reconstructing a protein local 3D structure in its natural conditions would allow researchers to work backwards and design compounds that interact with specific sites.

By combining the strength of NMR-inspired control techniques with the quantum properties of NV center spins, the proposed strategy for magnetic resonance detection at the nano-scale promises to make diamond-based quantum sensors an invaluable technology for bio-imaging.

# Appendix

## 1.A Hamiltonian Engineering by Dynamic Filter Generation

The creation of a dynamic Bragg grating (spectral filter), which yields high spatial resolution, is obtained from the concatenation of the NV spin-lock Hamiltonian with a gradient field. The resulting evolution can be understood from a first order approximation[61], similar to average Hamiltonian theory[62]. Expanding the product in Eq.( 1.7) of the main text, we obtain $\left[e^{-iH_G t_g} e^{-iH_{\rm SL} t/F}\right]^F = e^{-iH_G t_g F} \prod_{f=0}^{F-1} e^{-ifH_G t_g} e^{iH_{\rm SL} t/F} e^{ifH_G t_g}$. The gradient Hamiltonian only acts on the nuclear spins, rotating the spin-lock Hamiltonian to $\widetilde{H}_{\rm SL}^{(f)} = e^{-ifH_G t_g} H_{\rm SL} e^{ifH_G t_g} = \Omega S_z + (\omega_L + A^j) I_z^j + B_\perp^j (e^{ift_g(\omega_L + A^j)} e^{i\varphi_j} S_+ I_-^j +$ h.c.).

The product $\prod_{f=0}^{F-1} e^{-i\widetilde{H}_{\rm SL}^{(f)} t/F}$ can be approximated to first order by the exponential of the sum $\approx e^{-it/F \sum \widetilde{H}_{\rm SL}^{(f)}}$ and we thus obtained the effective Hamiltonian of Eq. (1.8). The error in the approximation is given by the commutators $[\widetilde{H}_{\rm SL}^{(f)}, \widetilde{H}_{\rm SL}^{(f')}] t^2/F^2 \sim \omega_L B_\perp^j t^2/F^2$. For typical values of the nuclear spin Larmor frequency and the transverse dipolar coupling, $\omega_L \sim 100 - 1000 B_\perp^j$, and setting $t \sim 1/B_\perp^j$, we need $F = 10 - 30$ for the approximation to hold. This can be easily reached and it is usually required anyway to achieve the desired frequency selectivity. Symmetrization of the

sequence[62,63] achieves cancellation of all odd order terms making the filter insensitive to slow fluctuations in the microwave driving power at the cost of longer sequences (Appendix).

## 1.B Decoupling Under Selective Polarization

As the frequency selectivity of the NV sensing protocols increases, the spectral resolution is no longer limited by the filter itself but by the finite linewidth of the nuclear signal. A major source of line broadening are the couplings among nuclear spins, which can be as large as tens of kHz between neighboring spins in a protein. Simple steps to mitigate this problems include reducing the spin density by isotopic labeling[50] and decoupling the spins of interest from different spin species (heteronuclear decoupling), using well-established methods in the NMR community[62].Contrary to DD-based sensing techniques, homonuclear decoupling sequences can be embedded in the cross-polarization scheme. Consider, e.g., one of the simplest decoupling sequences, WAHUHA[46], which works by averaging to zero the secular homonuclear dipolar coupling over the cycle time. Assuming the sequence is applied during the NV driving, the effective Hamiltonian averaged over one cycle becomes $H_{\mathrm{SL}}=\Omega S_z+\sum_j\left[(\omega_L+\frac{A^j}{2\sqrt{3}})I^j_{z_m}-B^j_m S_x I^j_{x_m}+iC^j S_x I^j_{y_m}+\mathrm{h.c.})\right]$, where $B^j_m=B^j_\perp\frac{(2+\sqrt{3})\sin(\varphi)+\cos(\varphi)}{3\sqrt{2}(\sqrt{3}-3)}$, $C^j_m=B^j_\perp\frac{(2+\sqrt{3})(\cos(\varphi)-\sin(\varphi)}{3\sqrt{2}(\sqrt{3}-3)}$ and the operators $\vec{I}_m$ are defined in a frame where the nuclear spin z axis is rotated to the [111] direction. In this frame, the dynamics is equivalent to what observed in the absence of homonuclear decoupling; thus polarization is transferred from the NV electronic spin to the nuclear spin under the resonant condition, $\Omega=\omega_L+A^j_m/(2\sqrt{3})$, at a rate set by the transverse coupling, $B^j_\perp\frac{\sqrt{7+4\sqrt{3}}}{3\sqrt{3}}$. More generally, other decoupling sequences can be applied during the spin-locking periods (as well as during evolution under the gradients in the filtered

scheme). The sequences narrow the nuclear spin linewidth, at the cost of a reduction in the dipolar coupling strength on the order of the homonuclear sequence scaling factor[62] (e.g. $1/\sqrt{3}$ for WAHUHA).

## 1.C Volume Uncertainty Estimation

The explicit functional dependence of the spins' reconstructed positions is intractable for any, but the fewest number of spins. Furthermore, if more coupling constants (both spin-NV and intra-spin) than spatial degrees of freedom are accessible, the system is overspecified and a unique solution compatible with all measured coupling will generally not exist, if the latter contain an error. Given $N$ nuclear spins, we aim at finding their spherical coordinates, denoted by a $3N$-dimensional vector $\mathbf{R} = [r_1, \ldots, r_N, \vartheta_1, \ldots \vartheta_N, \varphi_1, \ldots, \varphi_N]^T$. The measurement protocol allows determining an $L$-dimensional vector of couplings $\mathbf{P} = [A^1, \ldots, A^N, B^1, \ldots, B^N, D_{(1,2)}, \ldots, D_{(N-1,N)}]^T$, which are generally non-linear functions $\mathbf{F_P}(\mathbf{R})$ of the positions. Note that if measuring 1D spectra only, we have $L < 3N - 1$ and it is is impossible to reconstruct $\mathbf{R}$ without additional information. Thanks to the polarization protocol, instead, and given the scaling of the number of couplings with $N$ (even if not all inter-spin couplings are measured), we typically have $L > 3N - 1$ and the system is overdetermined: There may be no configuration compatible with all the values in $\mathbf{P}$, but one can determine an *optimal* solution from the information given.

The set of measured parameters $\mathbf{P}$ may generally contain an error $\delta\mathbf{P}$, composed of a statistical and a systematic component. In turns, this lead to an error in the reconstructed positions, $\delta\mathbf{R}$. To estimate and quantify the uncertainty induced in the position reconstruction for a given uncertainty in the measured couplings, we perform a linear regression analysis around the true spatial positions and subsequently

determine the error propagation within this framework, as described in detail the Appendix.

## 1.D Simulations

### 1.D.1 CXCR4 Receptor

As an example of the potential of our sensing protocol, in the main text we consider the G protein-coupled chemokine receptor CXCR4 [25] (Protein Data Bank code 3ODU). The positions of the protein atoms have been downloaded from PDB, as obtained by x-ray diffraction with 2.5Å resolution [25]. Of particular interest are the CXCR4 ligand-binding cavities for the small molecule IT1t, a druglike isothiourea derivative[7] . We focused on the residues 183 and 185 of the binding site, assuming that the protein has been synthesized with only the desired amino acids (Arginine, ARG, for 183 and isoleucine, ILE for 185) had been $^{13}C$ isotopically labeled. The protein was thus first rotated to minimize the distance from this residues to the NV center (positioned at a depth of 1.75nm), with the constraint that the whole protein should lie above the diamond surface. We then considered only the $^{13}C$ of the two residues of interest (6 $^{13}C$ in each residue), since all other labeled amino acid are far away and would not contribute (nor distort) the signal.

We simulated the 1D and 2D spectra recorded by the NV center using the cross-polarization method. We choose the frequency bandwidth of interest to be $1.25 - 4$kHz and subdivided this range in 64 bins to achieve a very smooth spectrum (note that this is not necessary in the experiments, indeed, a good spectrum is already obtained with 25 bins and this could be improved by using more advanced sampling techniques, instead of a uniform sampling). The magnetic field was set

to 0.185T ($\omega_L \approx 2$MHz) to keep the gradient time small enough and to reduce the dipolar coupling to its secular components only. The polarization time was set to $t = 720\mu$s and the gradient time to at most $T_g = 6$ms, achieved over $F = 30$ cycles. We varied the spin-lock frequency over the selected frequency range, while also varying the corresponding gradient time in order to optimally select the desired hyperfine coupling strength (see Fig. 4.A of the main text). Since the nuclear spin-spin dipolar coupling are quite strong (up to 658Hz) we considered that homonuclear decoupling was applied during both the cross-polarization and gradient evolutions. Specifically, we simulated the effects of 1 (during polarization) and 10 (during the gradient) cycles of the WAHUHA decoupling sequence[46], where the time-delay between pulses was on the order of $3\mu$s. In turn, the decoupling affects the resonant frequencies as explained in the methods and reduces the effective polarization rate, thus we set the NV Rabi frequency to $\Omega = \omega_A/(2\sqrt{3})$ and the corresponding gradient time to $T_g = 2k\pi/(\omega_A/\sqrt{3}+\omega_L)$ (with $k = 400$), where $\omega_A$ is the targeted hyperfine frequency.

To obtain the 2D spectra we simulated the reverse sensing control sequence over the same frequency range and with the same parameters as the sensing/polarizing step, after letting evolve the nuclear spins for a time $300\mu$s (see Fig. 4.C of the main text). For comparison, we also show in Fig. 4.B the 2D spectrum with zero diffusion time. We note that this 2D spectrum highlights the polarization transfer in the nuclear spin network and the corresponding spatial proximity; however, the spectrum has not been optimized to extract the relevant information.

Indeed, once the spins have been identified with a 1D spectrum (Sense/Polarize step) further information about their position can be better extracted by focusing on their frequencies only. The 1D spectrum provides high precision information on the longitudinal hyperfine couplings $A_j$, thanks to the high frequency selectivity of the

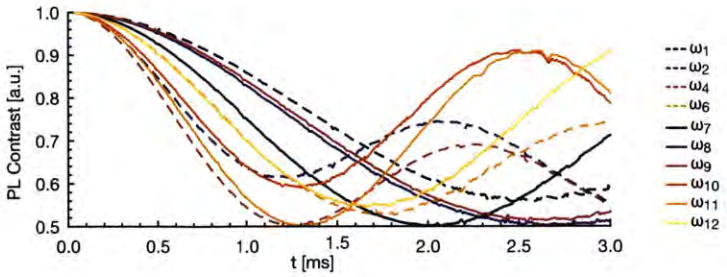


Figure 1-6: **Cross polarization transfer.** NV photoluminescence contrast (a.u.) as a function of the cross polarization time $t$ under rf driving at the target spin frequencies. The transverse hyperfine coupling to the target spins can be inferred with more precision from these curves. Note that the dynamics reveals additional information about the spin system: for example, driving at slightly different frequencies ($\omega_2$ and $\omega_4$, $\omega_9$ and $\omega_{10}$) one reveals the presence of additional spins, that have very similar longitudinal hyperfine coupling (see Fig. 4 of the main textfor the frequency labeling). In the 1D spectrum (Fig. 4 of the main text), the presence of these spins was only hinted to by the size of the dip at that frequency.

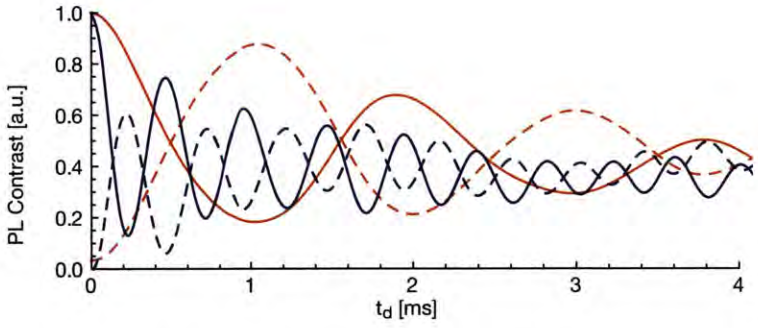


Figure 1-7: Normalized NV photoluminescence contrast as a function of the diffusion time $t_d$ for two pairs of excitation frequencies. The selected frequencies (for polarization and reverse sensing) excite two $^{13}$C in the 185 residue which are each strongly coupled by the dipole-dipole interaction to two other spins. Thus polarization excited with driving at 2.5kHz (violet) and 3.3kHz (orange) during the polarization step (solid lines) is transferred to other spins and read out (dashed lines) at 2.8kHz and 3.7kHz respectively, during the reverse polarization step. From the spin dynamics as a function of $t_d$ one can infer the strength of the coupling, 658Hz and 143Hz, respectively.

gradient filter. While the 1D spectrum also provides information of the transverse hyperfine couplings $B_j$, their estimated value might be less precise, if e.g. spin-spin couplings have not been precisely refocused or if there are spins with close-by $A_j$ values. A more precise estimate of the transverse hyperfine couplings can be obtained by fixing the target frequency $\omega_A = A_j$ and varying the polarization time. In order to estimate the dipole-dipole couplings, instead of considering the 2D spectrum as depicted in figure 4 of the main text, a better strategy is to only select pairs of frequencies (as determined by the 1D spectrum) and vary the mixing time. This enables following the flow of polarization from one spin to another, thus determining their dipolar coupling. The couplings can be estimated by fitting to a model of evolution under the full dipolar Hamiltonian.

### 1.D.2 Peripheral anionic site in acetylhydrolase

In order to show the potential of the sensing scheme to provide information about a variety of molecules, we provide another example of simulated spectra.

We consider the peripheral anionic site (PAS) in acetylcholinesterase (AChE [64,65,66]), a key enzyme in the nervous system. AChE binding sites are actively studied to develop targeted inhibitors that can improve cognitive abilities in Alzheimer's disease patients[67]. Bivalent AChE inhibitors, which can interact with both the PAS and catalytic anionic binding sub-site, can produce more potent AD drugs, thus the PAS sub-site structure has been fully characterized and can serve as an example of how the NV-based protocol would extract information from similar, yet to be characterized, molecules.

To reconstruct the structure of PAS with the proposed scheme, we simulated the

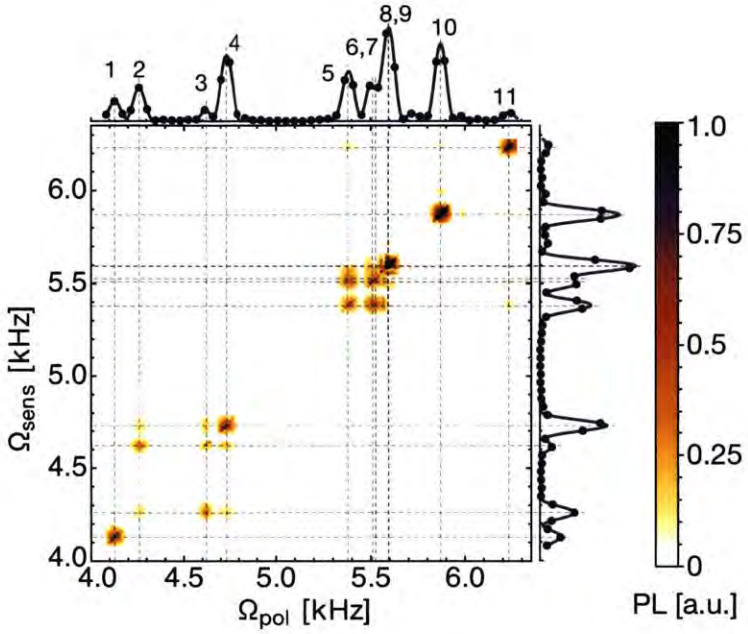


Figure 1-8: **Simulated spectra for peripheral anionic site in acetylhydrolase**. Figure describes 1D and 2D simulated spectra for acetylhydrolase obtained with the NV-based filtered sensing protocol. We plot the normalized spin-dependent photoluminescence (PL) of NV center. The 1D spectrum (on the sides of the 2D map, showing 1-PL) displays peaks when the driving frequency and the gradient time (which are swept simultaneously) match the longitudinal dipolar coupling $A^j$ of one nuclear $^{13}$C spin in the protein. The axes show the on-resonance dipolar frequency $A$ at each measurement point, while the driving frequency is $\Omega = A/2+\omega_L$ (with Larmor frequency $\omega_L = 1.6$MHz in the simulation) and the gradient time $t_g = 2\pi/(A+\omega_L)$. The simulated 2D spectra are obtained from the proposed protocol: After polarization (obtained with the same parameters as for the 1D spectrum) the nuclear spins are let to evolve freely for $500\mu$s, allowing polarization diffusion. The polarization is then mapped back to the NV center and measured via its spin-dependent PL. The 2D spectrum shows the spreading of polarization in the spin network, as indicate from off-diagonal non-zero terms.

dynamics of the NV electronic spin under the action of the control sequences and the protein's nuclear spins. In the simulations we assumed that only the amino-acid TRP is $^{13}$C-labeled, thus we can focus just on the 11 $^{13}$C nuclear spins in the PAS binding site, as coupling to other spins (e.g. protons) is off-resonance. We further assumed to apply both heteronuclear and homonuclear decoupling sequences, so that the $^{13}$C linewidth is narrowed.

To obtain the 1D spectrum, we simulated the 11 $^{13}$C spins in the PAS binding site and an NV center 2nm away from it, with the [111] axis aligned around the vertical direction. The gradient time was varied from 204.6 to 204.9$\mu$s (for a maximum total gradient time of $T_g$ = 6ms in $F$ = 30 steps) while also varying the NV driving frequency accordingly. The polarization time was $t = 300\mu$s for the first 4, more far away, spins and $t = 180\mu$s for the other spins. The dip height is a measure of the transverse dipolar coupling $B_\perp^j$. The spectrum shows 9 dips, but it cannot resolve almost equivalent spins.

In Fig. 1-8 we show simulated 1D and 2D spectra for the PAS for an NV 2nm from it. Note that this corresponds to an NV only 1nm below the diamond surface (because of the AChE geometry) but this constraint could be reduced by fabricating a small diamond pillar containing the NV center. To illustrate the potential of our filtered scheme we increased the number of frequency bins to $b = 50$ in order to highlight the frequency resolution. The figure show the high frequency resolution the method can achieve as well as the additional information provided by the local diffusion of the polarization in the nuclear spin network.

## 1.E Position Reconstruction and Error Estimation

Here we describe the procedure used to estimate the error in the reconstructed spatial coordinates induced by errors in the coupling constants $A_j$, $B_j$, $D_{i,j}$ that would naturally arise from the sensing protocol due to finite frequency resolution and sensitivity.

We consider $N$ nuclear spins and denote their combined spherical coordinates by a $3N$-dimensional vector $\mathbf{R} = [r_1, \ldots, r_N, \vartheta_1, \ldots \vartheta_N, \varphi_1, \ldots, \varphi_N]^T$. Furthermore, we define the $L$-dimensional vector of couplings $\mathbf{P} = [A^1, \ldots, A^N, B^1, \ldots, B^N, D_{(1,2)}, \ldots, D_{(N-1,N)}]^T$, which are generally non-linear functions $\mathbf{F_P}(\mathbf{R})$ of the positions. The true positions $\overline{\mathbf{R}}$, possibly unknown, correspond to the true coupling constants $\overline{\mathbf{P}}$.

### 1.E.1 Reconstruction Fitting Procedure

The task of a spatial reconstruction procedure is to determine the spatial coordinates $\mathbf{R}$ of the individual spins for a given set of measured parameters $\mathbf{P}$. Here, we have to distinguish three cases:

- For $L < 3N - 1$ it is is impossible to reconstruct $\mathbf{R}$ without additional information.

- For $L = 3N - 1$ there may be a countable number of unique solutions $\mathbf{R}$, which exactly reproduce the given $\mathbf{P}$.

- For $L > 3N - 1$ the system is overdetermined. There may be no configuration compatible with all the values in $\mathbf{P}$, but one can determine an *optimal* solution from the information given.

When measuring 1D spectra only, we have the first situation; thus any scheme that does not allow measuring intra-spin couplings (as our proposed protocol) will require additional information on the molecule structure to achieve a full reconstruction.

Thanks to the polarization protocol, instead, and given the scaling of the number of couplings with $N$ (even if not all inter-spin couplings are measured), one is typically in the last regime. To find an optimal $\mathbf{R}$ for a given $\mathbf{P}$, one defines a deviation function

$$D_{\mathbf{P}}(\mathbf{R}) := \left| \sum_i \frac{\mathbf{P}_i - [\mathbf{F}_{\mathbf{P}}(\mathbf{R})]_i}{\Delta P_i} \mathbf{e}_i \right|, \tag{1.10}$$

which is a measure (metric) in $\mathbf{P}$-space for how strongly the couplings $\mathbf{F}_{\mathbf{P}}(\mathbf{R})$ resulting from a configuration $\mathbf{R}$ deviate from the given set $\mathbf{P}$. Here $|\ldots|$ is a norm defining a metric, such as the $L^p$ norm $||\hat{\mathbf{x}}||_p = (\sum_j |x_j|^p)^{-1/p}$, and $\mathbf{e}_i$ is the unit vector in the $j$-th dimension. The optimal position is now determined by the value of $\mathbf{R}$ obtained by minimizing $D_{\mathbf{P}}(\mathbf{R})$. Additionally, any prior information about the magnitude of the error $\Delta P_j$ in each individual coupling (both statistical and systematic) enters as an additional ingredient in Eq. (1.10). This gives a higher weight to the information we know to a higher degree of accuracy and has the appealing feature that the it makes each component in the metric of $D_{\mathbf{P}}$ dimensionless. Furthermore, due to the linearity of a norm, only the relative ratios of the errors affect the result. If no perfect $\mathbf{R}$ reproducing all the measured couplings $\mathbf{P}$ exists, which is generally the case in the presence of experimental errors, the specific choice of the metric in $D_{\mathbf{P}}(\mathbf{R})$ influences the optimal position determined by this procedure, although for small errors this should not be of significance.

## 1.E.2 Alleviating the Phase Problem

The information obtained from a 1D spectrum allows determining the longitudinal $A^j$ and transverse $B^j$ dipolar coupling to the NV center for each nuclear spin. The knowledge of both the longitudinal and transverse couplings confines the position of each nuclear spin to a ring (and an additional to reflection on the $z = 0$ plane). The polar angle thus remains undetermined and is referred to a as the *phase problem* - also inherent to NMR spectroscopy and x-ray diffraction. Using the reverse sensing protocol gives access to the dipolar inter-spin coupling, revealing information about the relative positions of the spins. Hence, some of the polarizable spins in an entire ensemble can be used as antennas to sense other spins in their vicinity, as shown in Fig. 1-9(a). In an ensemble of $N$ spins there are $N(N-1)/2$ independent pairs of couplings $D_{ij}$. Hence, the number of $D$-couplings typically exceeds the number of unknown phases, allowing a reconstruction of the relative polar phases (up to a reflection on a plane through the $z$-axis) and hence the entire spatial structure. This can be substantiated by analyzing the deviation potential $D_{\mathbf{P}}(\mathbf{R})$ for two spins as a function of the two polar angles $\varphi_1, \varphi_2$. If the coupling $D_{1,2}$ is (artificially) set to zero, $D_{\mathbf{P}}$ is independent of $\varphi_1$ and $\varphi_2$, reflecting the phase problem for both spins. If, in contrast, $D_{1,2}$ is set to a non-zero value, this independence is lifted and $D_{\mathbf{P}}$ takes on a minimum value of zero along lines of constant $|\varphi_2 - \varphi_1|$, as shown in Fig. 1-9(b).

Still, there always remains a global phase uncertainty, as a closer inspection of the couplings reveals. If the position of all spins is rotated by an arbitrary angle around the $z$-axis, all couplings remain unchanged. This is however of no significance for the proposed sensing scheme, since one is only interested in the relative coordinates of the protein spins in any structure determining procedure.

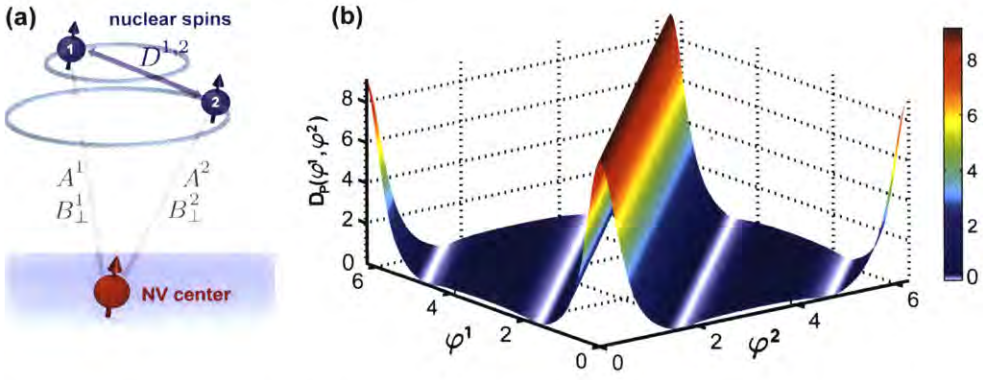


Figure 1-9: **Alleviating the phase problem.** The deviation metric $D_{\mathbf{P}}(\varphi_1 - \varphi_2)$ for two spins at constant $z_1$, $z_2$, $r_{x,y,1}$, $r_{x,y,2}$. The knowledge of the inter-spin coupling $D_{ij}$ contains the information about the relative polar phase between the two spins, leading to a continuous minimum of $D_{\mathbf{P}} = 0$ along $|\varphi_1 - \varphi_2|$ =const.

### 1.E.3 Linear Regression and Error Estimation

The set of measured parameters $\mathbf{P} = \overline{\mathbf{P}} + \boldsymbol{\delta}\mathbf{P}$ may generally contain an error $\boldsymbol{\delta}\mathbf{P}$, composed of a statistical and a systematic component. Here we want to estimate and quantify the uncertainty induced in the position reconstruction for a given uncertainty in the measured couplings. Here $\overline{\mathbf{P}} = \mathbf{F}_{\mathbf{P}}(\overline{\mathbf{R}})$ are the (possibly unknown) true couplings, corresponding to the true positions $\overline{\mathbf{R}}$.

For sufficiently small $\boldsymbol{\delta}\mathbf{P}$, the equations $\mathbf{F}(\mathbf{R})$, where $\mathbf{R} = \overline{\mathbf{R}} + \boldsymbol{\delta}\mathbf{R}$, can be linearized around $\overline{\mathbf{R}}$

$$\mathbf{F}_{\mathbf{P}}(\mathbf{R}) = \mathbf{F}_{\mathbf{P}}(\overline{\mathbf{R}}) + J \cdot \boldsymbol{\delta}\mathbf{R} + \mathcal{O}(\boldsymbol{\delta}\mathbf{R}^2). \tag{1.11}$$

This yields the deviation in the parameters $\boldsymbol{\delta}\mathbf{P} = J \cdot \boldsymbol{\delta}\mathbf{R}$ for a given deviation in the positions $\boldsymbol{\delta}\mathbf{R}$ to linear order, where $J$ is the Jacobi matrix with elements $J_{i,j} = \frac{\partial[\mathbf{F}_{\mathbf{P}}(\mathbf{R})]_i}{\partial R_j}\Big|_{\overline{\mathbf{R}}}$. To estimate the position accuracy, we are however interested in

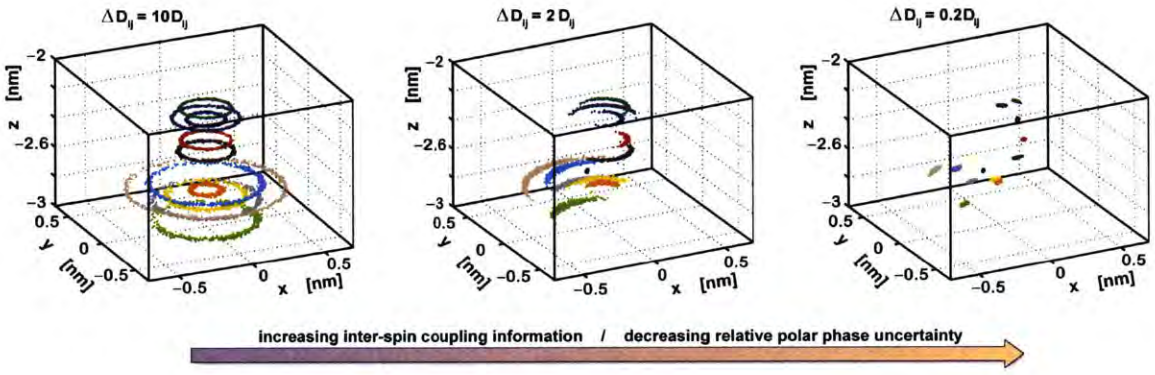


Figure 1-10: **Alleviation of the phase problem obtained from measuring intra-spin couplings.** A sequence of 3D uncertainty distributions for different relative error strength in the inter-spin couplings at $\Delta A = \Delta B = 10Hz$, for the configuration of nuclear spins in the ligand binding site of the chemokine receptor CXCR4. For a very large error of $\Delta D_{ij} = 10D_{ij}$ there is essentially no information available on the relative phases and the knowledge of the positions can only be restricted to radially symmetric rings, shown in the left figure. As these couplings are determined with increasing precision, this information on the relative angles (chosen relative to the spin shown in black) rotational symmetry is broken and the effective volume is reduced and eventually confined to small oval-shaped regions. The position reconstruction is performed using the procedure described in the following subsections.

the inverse case, i.e. we want to determine the deviation in the position $\boldsymbol{\delta}\mathbf{R}$ for a given deviation in the parameters $\boldsymbol{\delta}\mathbf{P}$.

For the simple case that $\dim(\mathbf{R}) = \dim(\mathbf{F})$, i.e. $L = 3N - 1$, the error $\boldsymbol{\delta}\mathbf{R}$ could be calculated using the inverse of the Jacobi matrix $J_{i,j} = \frac{\partial F_i}{\partial R_j}\Big|_{\overline{\mathbf{R}}}$.

However, for $\dim(\mathbf{F}) > \dim(\mathbf{R})$, if the number of known couplings exceeds the number of relevant spin coordinates (which is possible as soon as $N > 2$), the system of equations becomes overdetermined and does not necessarily possess a solution fulfilling all requirements. In this regime we resort to linear regression, which, for a given error $\boldsymbol{\delta}\mathbf{P}$, yields the most compatible set of $\delta\mathbf{R}$ by minimizing the deviation measure $|\boldsymbol{\delta}\mathbf{F} - J\boldsymbol{\delta}\mathbf{R}|^2$.

Here we extend upon the standard linear regression approach, which assumes an identical uncertainty for all input parameters. We present a short derivation of this extended approach and start by defining the diagonal and Hermitian matrix

$$S := \begin{pmatrix} \Delta P_1 & 0 & 0 \\ 0 & \Delta P_2 & 0 \\ 0 & 0 & \ddots \end{pmatrix}. \tag{1.12}$$

with the standard deviation (or more generally the uncertainty, including a possible systematic error) of the $j$-th parameter $\Delta P_j$ as the $j$-th diagonal element, the deviation of the linearized argument can be written in matrix form as

$$D_{\mathbf{P}}(\mathbf{R}) \approx \left| \sum_i \frac{\boldsymbol{\delta}\mathbf{P}_i - (J \cdot \boldsymbol{\delta}\mathbf{R})_i}{\Delta P_i} \mathbf{e}_i \right|_p = \left| S^{-1}(\boldsymbol{\delta}\mathbf{P} - (J \cdot \boldsymbol{\delta}\mathbf{R})) \right|. \tag{1.13}$$

Specifically choosing the $L^2$-norm (as is the standard procedure in linear regression), the uncertainty-weighted linear regression equations are derived by minimizing

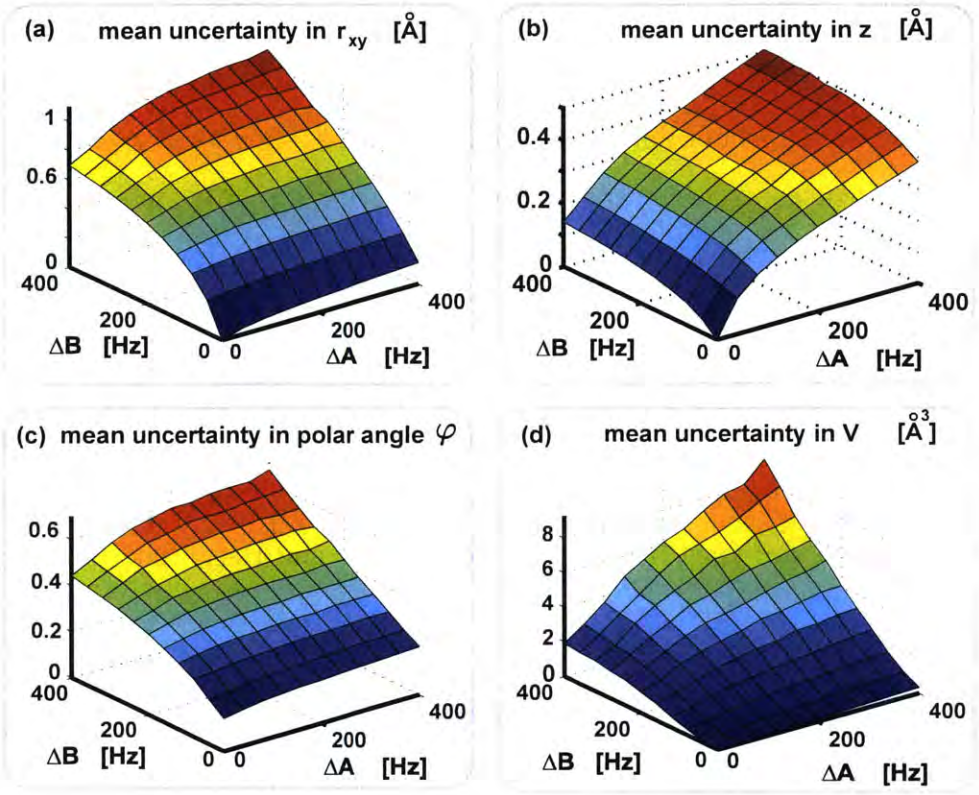


Figure 1-11: **Uncertainty in parameter estimation.** The uncertainty (standard deviation) induced in the cylindrical coordinates as a function of a Gaussian distributed random error with standard deviation $\Delta A$ and $\Delta B$ for the associated couplings. A relative Gaussian error $\Delta D_{ij} = 0.5 D_{ij}$ and $\Delta D_{ij}^{(bg)} = 50$Hz is used for the inter-spin couplings. The volume corresponding to the 90th percentile, obtained from a separable integration in cylindrical coordinates, is shown in the rightmost plot.

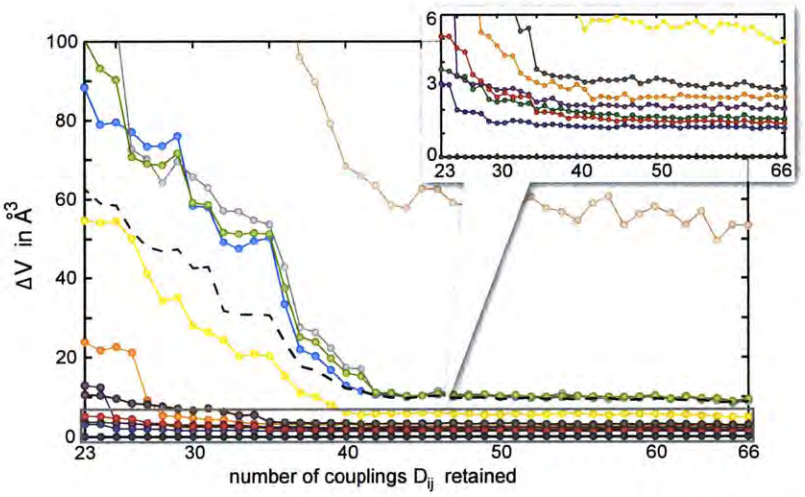


Figure 1-12: **Estimation of volume uncertainty as a function of the number of couplings extracted.** Volume uncertainty of individual spins (color coding corresponds to the colors used in Fig. (5) in the main text) and average volume uncertainty (black line) as a function of the number of couplings $D_{ij}$ used in the reconstruction procedure. $\Delta A = \Delta B = 300$Hz, and a relative error of 0.5 in conjunction with a constant background uncertainty $\Delta D_{ij}^{(bg)} = 50$Hz was used for the fluctuation in the inter-spin couplings, i.e. $\Delta D_{ij} = \sqrt{(0.5 D_{ij})^2 + (50\text{Hz})^2}$. For $N = 12$ spins, there are $N(N-1)/2 = 66$ independent couplings. Here, we fixed the position of the spin shown in black in Fig. (5) in the main text.

the deviation $D_{\mathbf{P}}(\mathbf{R})$ for a given set of data points $\mathbf{P}_i$, leading to the necessary condition

$$0 \stackrel{!}{=} \frac{\partial D_{\mathbf{P}}(\mathbf{R})^2}{\partial \delta \mathbf{R}_j} \tag{1.14}$$

for all components $j$. If the matrix $J^\dagger S^{-2} J$ is non-singular, this can be written in matrix form as

$$\delta \mathbf{R} = \left[J^\dagger S^{-2} J\right]^{-1} J^\dagger S^{-2} \delta \mathbf{P}. \tag{1.15}$$

This equation describes to linear order how the optimal fit, i.e. the position of the minimum of $D(\mathbf{R})$, changes if the parameters $\mathbf{P}$ deviate slightly from the true values (as induced for instance by a measurement error). To estimate the spatial uncertainty for a given uncertainty $\delta \mathbf{F}$ in the parameters, we proceed as follows:

- From the positions $\overline{\mathbf{R}}$ of the spins (assumed to be exact), we calculate the true couplings $\mathbf{F}_{\mathbf{P}}(\overline{\mathbf{R}})$.
- We simulate the statistical measurement error by sampling each element of $\delta \mathbf{P}$ from a Gaussian distribution with standard deviation chosen as the respective given error.
- For the resulting single realization $\mathbf{P} = \overline{\mathbf{P}} + \delta \mathbf{P}$, we calculate the corresponding optimal position $\mathbf{R}$ using the linear regression procedure described above.
- This is repeated over many realizations, leading to distributions in the reconstructed coordinates, from which the uncertainty can be estimated and the effective uncertainty volume element can be calculated.

The positions of the spins of the protein pocket we considered and scatter plots resulting from the above simulation procedure for feasible experimental parameters are shown in Fig. (5) in the main text. The uncertainty in the cylindrical coordinates

and the effective 90th percentile volume is estimated from the standard deviation of the sample distributions and shown as a function of $\Delta A$ and $\Delta B$ in Fig. 1-11.

### 1.E.4 Dependence on the number of inter-spin couplings

An important feature of our proposed method is the capability to measure the inter-spin couplings $D_{ij}$, of which there are $N(N-1)/2$ for a system consisting of $N$ nuclear spins. Under realistic conditions, not all of these couplings are will be measured, nor do they have to be. Furthermore, many of these couplings will be rather small, as they fall off as $r^{-3}$, where $r$ is the distance between the respective spins.

The dependence of the spins volume uncertainty on the number of measured couplings is shown in Fig. (1-12) for the same spatial configuration as shown in Fig. (5) in the main text. The largest $D_{ij}$ in magnitude are retained for a given number of values. To account for the fact that the uncertainty in $D_{ij}$ scales with its magnitude for large $D_{ij}$, but is also bounded from below, we sample the deviation $\delta D_{ij}$ from the true value from a Gaussian with a standard deviation

$$\Delta D_{ij} = \sqrt{(\eta\, D_{ij})^2 + (\Delta D_{ij}^{(bg)})^2} \tag{1.16}$$

containing both a relative uncertainty $\eta$ and a constant background uncertainty $\Delta D_{ij}^{(bg)}$.

Clearly, the volume uncertainty of the individual spins decreases as the available information from an increasing number of couplings is included, featuring jumps when important couplings connecting different clusters are included. This volume uncertainty differs significantly for different spins and is primarily determined by two factors: the distance of the respective spin to the NV (which sets the uncertainty in $r_\perp$ and $z$) as well as the distance between the respective spin and the reference

nuclear spin, relative to which the polar phase is specified. The volume uncertainty for the majority of the favorable spins ranges from $1.2^3$ to $10^3$ once the most relevant couplings have been included.

### 1.E.5 Volume Uncertainty Dependence on Distance from NV

Since the interaction between the nuclear spins and the NV center depends strongly on distance, this parameter – and in particular the depth of the NV below the diamond surface – is critical in determining the spatial resolution.

To estimate the volume uncertainty as a function of the distance from the NV center, we consider a simple model, where only the parameters $A$ and $B$ are measured. The uncertainty in the volume is then given by $\Delta V = \langle r \rangle (2\Delta r_\perp)(2\Delta z)(2\Delta\varphi) = 2\pi \langle r \rangle 4\Delta r_\perp \Delta z$, assuming the maximum uncertainty in the phase $\varphi$.

From the relationships linking $\{r_\perp, z\}$ and $\{A, B\}$, we can calculate $\Delta z$ and $\Delta r_\perp$ in the linear regime (assuming small errors $\Delta A$, $\Delta B$) as a function of the nuclear spin position. In figure 1-13 we plot the error uncertainty for hydrogen nuclear spins as a function of the distance from the NV.

### 1.E.6 Single Spin Detectability

Let us first consider the sensing capabilities for a single spin, for which case distinguishability issues do not arise. The sensing volume is given by the set of all spatially accessible points above the diamond surface, for which $B_\perp(\hat{\mathbf{r}}) > \Delta B_\perp$, i.e. where the peak height is larger than the error and thus identifiable as a peak. The value of the coupling $A$, which sets the peak's position, does not affect its detectability in the case of a single spin. For both possible NV orientations [111] and [001], the dipolar coupling constants and the single spin sensing volumes are shown in (a,b) and (c) of

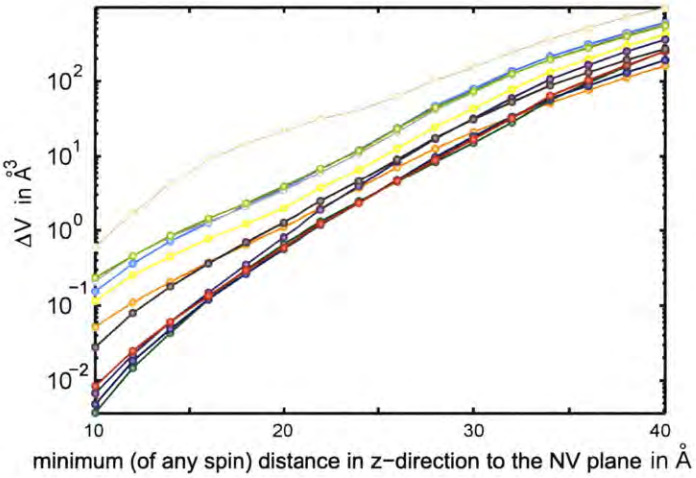


Figure 1-13: **Estimation of volume uncertainty function of the distance from the NV.** The volume uncertainty $\Delta V$ as a function of the distance from the NV assuming a statistical uncertainty of $\Delta D = \Delta B$=300Hz and $\Delta D = \sqrt{(D/2)^2 + (50Hz)^2}$. The NV is assumed to be aligned along the z axis ([111] crystal) and at the origin of the coordinate axes. The color coding with respect to the spins is identical to the plots above, and as shown in Fig. (5) in the main text.

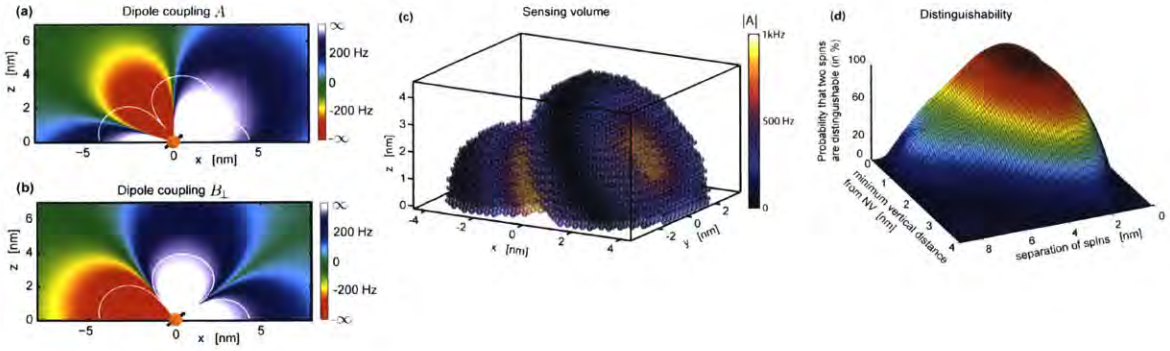


Figure 1-14: **Sensing Volume for a [100] diamond.** For a NV oriented in the $\sqrt{2}\mathbf{e}_x + \mathbf{e}_z$ direction (a) and (b) show the dipolar coupling constants for a $^{13}$C spin in the $y = 0$ plane as a function of distance from the NV, which is located at the origin. The diamond surface is assumed to be parallel to the $x$-$y$-plane (i.e. of the [001] type) at the $z$-value of the NV implantation height. The sensing volume, within which a single spin can be directly detected, is given by the 3D volume within which the dipolar coupling constant $B_\perp$ is of the order or larger than the uncertainty $|B_\perp| \geq \Delta B_\perp$. This sensing volume is given by the area bounded by the white lines in (a) and (b) and the structure of the 3D sensing volume is explicitly shown in (c), where the spatial dependence of the coupling $A$ is color coded. Subfigure (d) shows the a priori two-spin distinguishability (i.e. without utilizing an additional external magnetic field) as a function of the distance from the NV and the inter-spin separation. We assume an uncertainty of $\Delta A = \Delta B = 300\text{Hz} \cdot h$.

Fig.1-14 and Fig.1-15 respectively.

Above, we have considered the detectability of a single spin. With the presence of multiple spins in the potential sensing volume, ambiguities may arise if different spins have a very similar coupling $A$, making them indistinguishable within a single spectrum. Clearly, the occurrence of such a case depends on the specific spatial configuration at hand. For the general case, the distinguishability can at best be quantified in a statistical sense, i.e. for random spatial distributions of the spins, what is the probability that the two spins are indistinguishable and how does this depend on the distance of the spins from the NV. To give quantitative insight to this

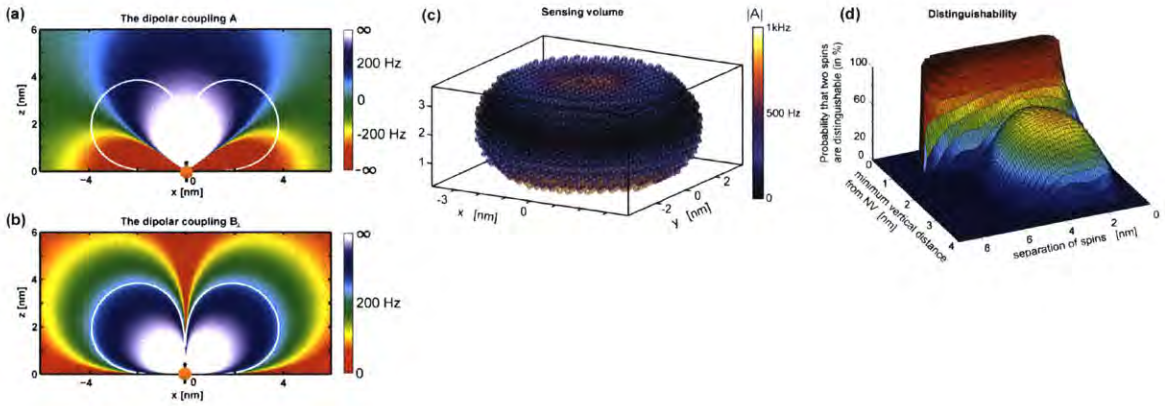


Figure 1-15: **Sensing Volume for a [111] diamond.** The same quantities as in Fig.1-14 are shown with the difference that the NV is oriented in the $\mathbf{e}_z$ direction, i.e. the diamond is of the [111] type.

question, we analyze the probability that two randomly chosen spins are distinguishable for the typical NV orientations. Furthermore, we include the dependence of the distinguishability on the distance to the NV by the following procedure: For a given distance $z$ of the plane in the $x$-$y$-direction, the position of the first spin is randomly sampled in this plane. If it is detectable, i.e. if its coupling $B$ at that position is larger than the threshold uncertainty $\Delta B$, it is accepted, otherwise the procedure is repeated. Once a valid spin in the plane has been chosen, the position of the second spin is randomly sampled from the entire volume above the plane at height $z$. For every coordinate, it is checked analogously if the spin is detectable and the procedure is again repeated until a valid detectable position has been found. Once two valid positions have been found, it is checked whether the two spins are distinguishable, i.e. whether their values of $A$, defining the peaks' positions on the frequency axis, are sufficiently different to be identified as separate peaks. This criterion is chosen as $|A^{(1)} - A^{(2)}| > \Delta A$. This Monte Carlo sampling scheme thus yields the probability

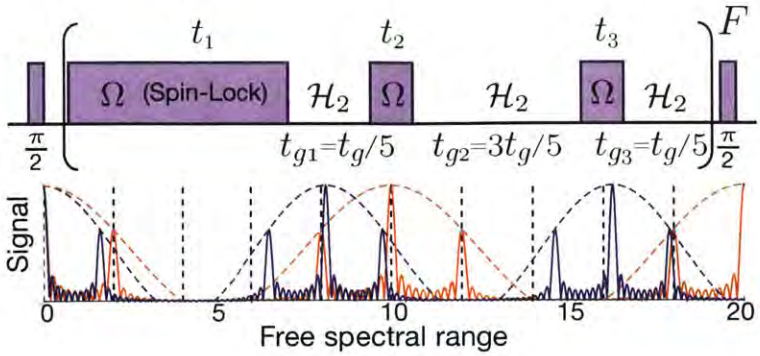


Figure 1-16: **Anti-aliasing filter.** (a) The engineered filter sequence consists of $F$ cycles of unequal time-blocks of polarization driving (for times $t_k$) and gradient evolution ($t_{gk}$). The timings are chosen to engineer a slow envelope modulation of the grating. (b) Dynamic filters for two frequencies $\omega_j$ differing by the unmodulated filter bandwidth. Under the anti-aliasing sequence, the peak heights become a function of the spectral range number $m$ and it is possible to distinguish aliased peaks from their amplitudes. The filter bandwidth is now effectively extended to the period of $\mathcal{A}$ (dashed lines).

that two randomly chosen spins (assuming an a priori constant spatial probability distribution) lead to independent, clearly resolved peaks, which can be distinguished by eye. This probability is shown as a function of the inter-spin separation and the minimum distance of the two spins to the NV for the two different NV orientations in FIG.1-14 and FIG.1-15 (d).

## 1.F Extension and improvements to the filtered cross-polarization sensing method

### 1.F.1 Anti-aliasing by engineered filters

The filtered sensing method achieves high spatial resolution thanks to the longer evolution times afforded by using the nuclear ancillary spin. Indeed, the filter linewidth scale as $\delta A \sim 1/(Ft_g)$. Unfortunately, the improvement in resolution comes at the cost of a reduced bandwidth which also scales as $\Delta A \sim 1/t_g$. Note that in principle since we sweep the Rabi frequency $\Omega$ in the Hartmann-Hahn sensing experiments, the sensing bandwidth is infinite. However, the "bandwidth" we shall be concerned with here is that of the sensing filter – which becomes relevant if for instance $\Omega$ is kept constant and the filter period alone is swept to sense over some frequency range. We can however overcome this resolution-bandwidth tradeoff by employing a dynamical implementation of an anti-aliasing filter.

Aliasing occurs due to the periodicity of the filter $\mathcal{G}$ over different spectral regions $\Delta A$. Here we propose a novel strategy for anti-aliasing methods that can beat this aliasing problem and boost the effective sensing bandwidth while still maintaining the high resolution afforded by the filter. The method involves making the maxima of the filter dependent on the spectral region number $m = \omega t_g/(2\pi)$, so that peaks belonging to different spectral region can be distinguished, even when they are folded over. Our approach is to introduce a slow modulation of the filter, with frequency $f_a$, thus increasing by a factor $f_a$ the bandwidth.

Fig. 1-16 shows the construction of the anti-aliasing filter. In one cycle, we employ $F$ cycles of $M$ alternating blocks of polarization driving with periods $\{t_k/F\}$ and free

evolution with delays $\{t_{gk}\}$, with $F\sum_{k=1}^{M} t_{gk} = T_g = 2\pi F/\omega_j$. Consider for simplicity a single nuclear spin. One cycle of the sequence gives the propagator

$$\begin{aligned} U &= e^{i\omega_j I_z t_g}\left[e^{i\sum_{k=1}^{M} t_{gk}\omega_j I_z} e^{-iHt_{M-1}/F} e^{-i\sum_{k=1}^{M} t_{gk}\omega_j I_z}\right] \\ &\times \left[e^{i(t_{g1}+t_{g2})\omega_j I_z} e^{-iHt_2/F} e^{-i(t_{g1}+t_{g2})\omega_j I_z}\right]\cdots \\ &\times \left[e^{it_{g1}\omega_j I_z} e^{-iHt_1/F} e^{-it_{g1}\omega_j I_z}\right] e^{-iHt_0/F} \end{aligned} \tag{1.17}$$

Taking the zeroth order average Hamiltonian approximation, and considering $F$ cycles we obtain an effective Hamiltonian

$$\overline{H} = \Omega S_x + \omega_j I_z + \frac{B_\perp}{2}\mathcal{A}(\omega_j)\mathcal{G}(\omega_j) S_z I_x \tag{1.18}$$

with the filter

$$\mathcal{A}(\omega_j)\,\mathcal{G}(\omega_j) = \frac{1}{F}\left(\sum_{m=1}^{M} t_m e^{i\sum_{k=1}^{m} t_{gk}\omega_j}\right)\left(\sum_{k=0}^{F-1} e^{ikt_{gj}\omega_j}\right) \tag{1.19}$$

The function $\mathcal{A}$ thus modulates the grating $\mathcal{G}$ and its parameters (the timings $\{t_k, t_{gk}\}$) can be set to achieve anti-aliasing. For example, in Fig.1-16 we set $M = 3$, $t_{gk} = t_g/5\{1,1,0\}$ and $t_k = t\{0.4472, 0.4472, 0.7236\}$ to engineer zeros at two consecutive positions of $\mathcal{G}_j$ maxima. This provides a sharp contrast in the amplitude of the filter, and allows one to easily discern aliased peaks. The tradeoff is a loss of 37% in the filter peak amplitude, but with an increases of the sensing bandwidth by a factor 5 (the periodicity of the function $\mathcal{A}$).

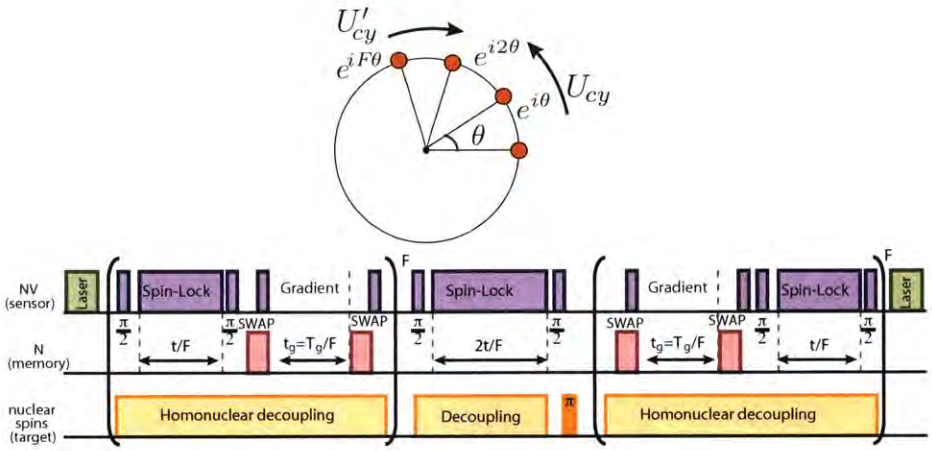


Figure 1-17: **Symmetrized cross-polarization sequence.** Left: Phasor representation of the symmetrization. In order to make the toggling frame Hamiltonians mirror antisymmetric, it is necessary to concatenate the normal propagator $U_{cy}$, which produces the grating filter $\mathcal{G}_j$, with ,an effective propagator in the opposite direction $U'_{cy}$ producing $\mathcal{G}'_j$. Here we denote the phases of each term of $\mathcal{G}_j$ and $\mathcal{G}'_j$ as a phasor on a unit circle. Right: sequence used to construct a symmetrized sequence.

### 1.F.2 Symmetrization and robustness to power fluctuations

The zeroth order average Hamiltonian approximation can be made accurate to first order if the toggling frame Hamiltonians are mirror anti-symmetric with respect to the center of the sequence in time. We shall refer to this as symmetrization. This would entail the situation shown in 1-17(a) where the grating $\mathcal{G}_j = 1+e^{i\tau_j\omega_j}+e^{i2\tau_j\omega_j}+\cdots+e^{i(F-1)\tau_j\omega_j}$ is followed by the grating, $\mathcal{G}'_j = e^{i(F-1)\tau_j\omega_j}+e^{i(F-2)\tau_j\omega_j}+\cdots+1$ in a total of $2L$ cycles. Fig. 1-17 shows example of how this can be obtained in practice, for $F=3$. This yields the propagator,

$$\begin{aligned} U &= e^{itH_1}\left(e^{i\tau_j H_2}e^{itH_1}e^{-i\tau_j H_2}\right)\left(e^{i(2\tau_j)H_2}e^{itH_1}e^{-i(2\tau_j)H_2}\right) \\ &\times \left(e^{i(2\tau_j)H_2}e^{itH_1}e^{-i(2\tau_j)H_2}\right)\left(e^{i\tau_j H_2}e^{itH_1}e^{-i\tau_j H_2}\right)e^{itH_1} \\ &= \left[e^{itH_1}e^{i\tau_j H_2}\right]^{F-1}\times e^{i(2t)H_1}\times\left[e^{-i\tau_j H_2}e^{itH_1}\right]^{F-1}, \end{aligned} \tag{1.20}$$

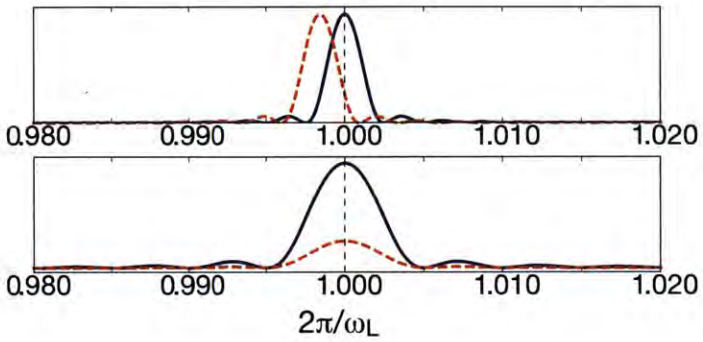


Figure 1-18: **Effects of symmetrization of the selective Hartmann-Hahn sequence.** We compare the unsymmetrized (top panel) and symmetrized (lower panel) sequences for an NV coupled to a single spin with Larmor frequency $\omega_L$. The spin lock frequencies were $\Omega = 0.95\omega_L$ (orange dashed line) and $\Omega = \omega_L$ (violet line). Under the unsymmetrized sequence, there is a shift in the resonance peak when $\Omega \neq \omega_L$. This shift is due to higher order terms in the Magnus expansion, and cannot be explained by the simple zero-order approximation based grating function filter in Eq. 8 of the main text. The symmetrized sequence, on the other hand, has a vanishing first order term, and is immune to shifts in $\Omega$ and hence is robust under power fluctuations.

which yields the desired effective Hamiltonian for filtered polarization. Since now the approximation is valid to second order in the Magnus expansion, the symmetrized sequence is far more robust to fluctuations in the driving power $\Omega$ during cross-polarization. Power fluctuations can be as large as 5% of the drive amplitude [68,69], thus it is critical that the filtering action is invariant to the exact value of $\Omega$. Indeed, if one considers only the zeroth order average Hamiltonian, a slight variation in $\Omega$ should not affect the position of the grating maxima $\mathcal{G}_j$, which should following $\tau_j = 2m\pi/\omega_j$ ideally just depend on the delay periods $\tau$. However, due to the presence of non vanishing higher order terms in the Magnus expansion, we find that there is in fact a dependence on the $\mathcal{G}_j$ maxima on $\Omega$ (see 1-18).

In contrast, the symmetrized sequence is robust against variations on the value of $\Omega$. Thus, even if the Hartmann-Hahn condition is not exactly satisfied the filtering action is unaffected and the positions of the $\mathcal{G}_j$ maxima are determined only by the timing $t_g$. In addition to improved robustness, this could facilitate the experiments, since one could just fix $\Omega = \omega_L$ and achieve the selective polarization transfer by sweeping the filter time $t_g$. The tradeoff for this higher robustness is that one needs twice the number of cycles (and hence twice the experimental time) to achieve the same linewidth as in the unsymmetrized case (1-18).

## 1.G Comparison with other sensing schemes

We compare different NV-based sensing methods that have been proposed. This highlight the advantages of the proposed cross-polarization based sensing protocol. Not only can the method achieve high frequency resolution, as it incorporates the filtering effects of dynamical-decoupling based sensing, but it also offers other benefits. Specifically, it allows the simultaneous application of homonuclear decoupling

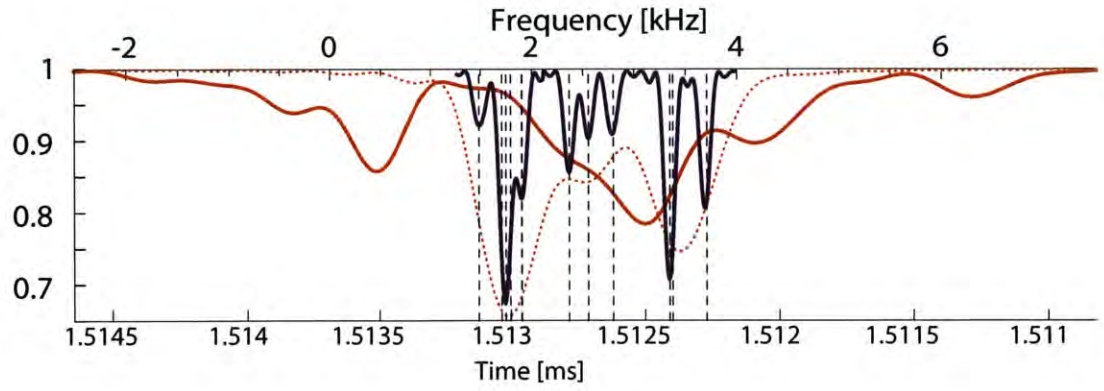


Figure 1-19: **Comparison of DD-based sensing with filtered cross-polarization sensing.** Even assuming very good performances of the dynamical decoupling sequence (1200 pulses and $T_2 > 1.5$ms) and no effect of the spin couplings (dotted line), the frequency resolution is not as good as for the filtered cross-polarization scheme (orange line). When spin couplings are taken into account, the spectrum broadens further (thick solid line) preventing the spatial position reconstruction.

sequences on the nuclear spins and importantly it enables acquiring 2D spectra that encode information about the nuclear spins interconnectivity.

## 1.H Geometrical pictures of the sensing schemes

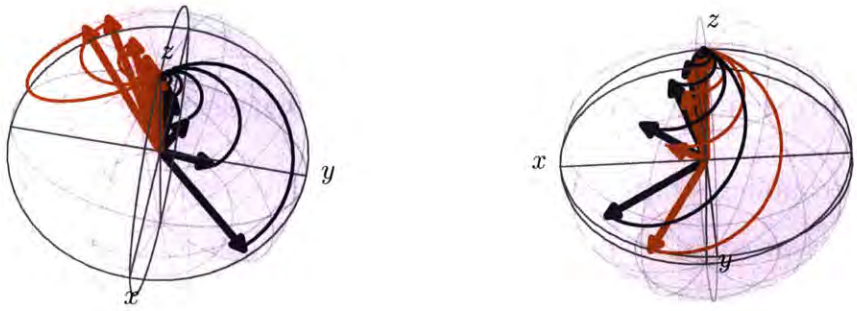


Figure 1-20: **Bloch sphere representation of the dynamical-decoupling based nuclear sensing sequence.** (a) Evolution of one nuclear spin in the $|0\rangle$ (orange) and $|1\rangle$ (violet) subspaces of the electron spin, under the action of $F$ cycles. These effective propagator under such cycles can be considered as concatenated rotations, and the effective nuclear axes move apart with increasing $F$. The final signal contrast depends on $\cos\Phi$, where $\Phi$ is the angle between the two axes. Hence increasing $F$ increases the sensing SNR. Note that the trajectories shown represent the path traversed on the Bloch sphere given the propagator $e^{-iH_a t}e^{-2iH_b t}e^{-iH_a t}$ ($\{a,b\} = \{0,1\}$) and serves as a guide to the eye. (b) Trajectories of different nuclear spins. We consider two nuclear spins separated by 1% in their effective Larmor frequencies and consider the effective nuclear axes (orange and violet arrows) in the $|0\rangle$ subspace for $F$ cycles of the sequence. As F increases, the two arrows move farther apart, signaling that the resolution increases with increasing $F$.

An intuitive understanding of the (filtered) sensing schemes can be gained from a geometric picture of the relevant evolution. In this section we first present this picture

for the dynamical-decoupling based NV sensing, considering in particular the effect of varying the two parameters under the experimenter's control – the period between pulses $\tau_j$ and the number of cycles $L$. We then present an analogous analysis for the filtered cross-polarization sensing.

### 1.H.1 Dynamical decoupling-based spin sensing

Dynamical decoupling sensing sequence works by creating two different axes of rotation of the nuclear spins, conditioned on the $|0\rangle$ or $|1\rangle$ subspace of the NV. Indeed, in the rotating frame of the NV, the Hamiltonian can be written as $H = H = |0\rangle\langle 0| H_0 + |1\rangle\langle 1| H_1$, where $H_0 = \omega_L \sum I_{zj}$ and $H_1 = \sum_j [(\omega_L + A_j) I_{zj} + B_{\perp,j} I_{\perp,j}]$. Consider for simplicity a single nuclear spin under a periodic dynamical decoupling (PDD) sequence. The dips in the signal occur when the PDD pulses are separated by $\tau = (2m+1)\pi/\omega_L$. For $A, B_\perp \ll \omega_L$ this effectively generates $\pi$ rotations about different effective nuclear axes, as shown on a Bloch sphere in Fig (1-20).

Consider the nuclear evolution in the $|0\rangle$ subspace of the NV. The propagator is then,

$$\begin{aligned} U_1^0 &= \exp(iH_1\tau_j)\exp(iH_0\tau_j)\exp(iH_1\tau_j) \approx \exp(i\pi\hat{H}_1)\exp(i\pi\hat{H}_0)\exp(i\pi\hat{H}_1) \\ &= -\exp(i\pi\hat{H}_1)\exp(i\pi\hat{H}_0)\exp(-i\pi\hat{H}_1) = -\exp(i\pi\hat{H}_1') \end{aligned}$$

where the operators with the hat refer to normalized nuclear rotation axes, and we used $e^{i(2\pi)\hat{H}_1} = -1$ in the last line. Here $H_1' = e^{i\pi H_1} H_0 e^{-i\pi H_1}$ is the effective axis formed by rotating $H_0$ around the generator $H_1$ by $\pi$ radians. In the $|1\rangle$ subspace one gets the same expression but with the $H_0, H_1$ reversed.

$$U_1^1 = \exp(i\pi\hat{H}_0)\exp(i\pi\hat{H}_1)\exp(-i\pi\hat{H}_0) = -\exp(i\pi\hat{H}_0') \tag{1.21}$$

Similarly if one considers now the concatenated rotation,

$$U_2^0 = \exp(iH_1'\tau_j)\exp(iH_0\tau_j)\exp(iH_1'\tau_j) \approx \exp(i\pi\hat{H}_1'') \tag{1.22}$$

where now $H_1'' = e^{i\pi H_1'} H_0 e^{-i\pi H_1'}$ is the effective axes formed by rotating $H_0$ around the generator $H_1'$ by $\pi$ radians. Hence with each concatenated rotation, the effective nuclear spin rotation axes in the two subspaces move further out (see 1-20). This leads to the increasing dispersion between the two nuclear axes – and as one increases the number of cycles $n$ these axes move apart further, and the final signal depends on the cosine of the angle between these two final axes. Hence increasing $n$ leads to higher SNR.

One can observe that the frequency resolution improves as the number of cycles is increased (Fig. 1-20(b)). Consider two nuclear spin axes in the $|0\rangle$ subspace, and as $n$ increases the relative angle between them gets magnified. This leads to higher resolution. Resolution can also be improved by going to higher multiples of $\pi/\omega_L$ for the same reason –any difference between the two angles get magnified (because in effect one is close to a $\pi$ rotation but not exactly $\pi$).

The frequency resolution is ultimately limited by the intrinsic NMR linewidth of the target nuclear spins. In principle, one could embed a homonuclear dynamical decoupling sequence (such as wahuha[46] or mrev8[70]) in the sensing scheme. In practice, this might result quite difficult. Ideally one would want the nuclear spin system to evolve under the Hamiltonians $H_0$ and $H_1$ during alternating time periods. Because of spin couplings, the Hamiltonians are instead $H_0' = H_0 + H_0^{(nn)}$ and $H_1' = H_0 + H_1^{(nn)}$, where $H_i^{(nn)}$ describes the nuclear spin-spin interaction (which might be different in the two NV manifolds[71]). A homonuclear sequence during each time period $\tau$ could average this Hamiltonian to zero. However this implies that

the nuclear spin pulse separation should be $\delta t \leq \tau/6 = (2m+1)\pi/(6\omega_L)$ and the nuclear spin pulse duration itself $t_p$ should be at least 1-2 times smaller. For small $m$, this condition would require violating the rotating wave approximation for the nuclear spin pulses. We would need large $m \geq 100$ to be able pulse on the nuclear spins (which might not be possible given the NV coherence time) and even then, the required driving strength might exceed what is experimentally feasible.

We note that this problem does not arise with cross-polarization based sensing, since there is no requirement to achieve a full decoupling cycle in a given short time $\tau$.

### 1.H.2 Filtered cross-polarization spin sensing

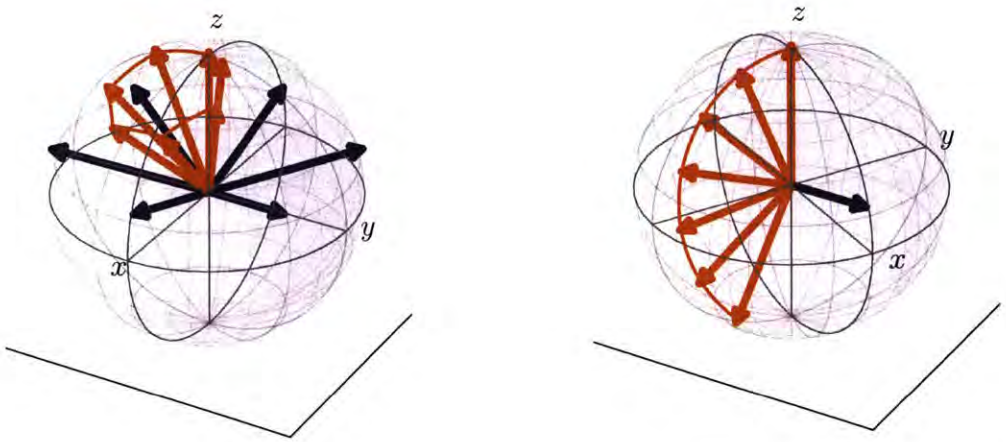


Figure 1-21: **Filtering action in the $\Delta$ subspace.** The violet arrows are the Hamiltonians $H_\Delta$ and the orange arrows trace the evolution of the spin vector $S^\Delta$. (a) Non-resonant case of the filter i.e. when the period $\tau \neq 2m\pi/\omega_L$. As the vector $\Sigma(0) = S_z^\Delta$ starts tipping, the Hamiltonian gets effectively rotated after every cycle of the sequence, and if L is large enough the spin vector returns to the north pole without tipping, leading to no polarization transfer. Hence the filtering action physically exploits the coherence on the nuclear spin. (b) Resonant case when $\tau \approx 2m\pi/\omega_L$. Now the Hamiltonian gets rotated in such a manner that it always returns to the same position on the Bloch sphere after every cycle. The effect is that the tipping of the spin vector adds up coherently, and there is effective polarization transfer.

We now consider a similar geometric picture for the filtering effects of cross polarization protocol that causes the narrower linewidth. In contrast to the previous section, cross-polarization under spin locking involves two spins and cannot be directly visualized on a Bloch sphere. To aid the geometric visualization of the polarization

exchange between the NV and a nuclear spin we employ the $\{\Sigma, \Delta\}$ Hamiltonian decomposition[? 72]. For simplicity, let us consider the Hamiltonian,

$$H = \omega S_z + \omega_L I_z + B S_x I_x \tag{1.23}$$

which is the active part of the Hartmann-Hahn Hamiltonian in the frame of reference that is tilted with respect to the NV spin locking frame. In the $\{\Sigma, \Delta\}$ basis defined by,

$$S_z^\Sigma = \tfrac{1}{2}(S_z + I_z) \qquad S_z^\Delta = \tfrac{1}{2}(S_z - I_z)$$

$$S_x^\Sigma = \tfrac{1}{2}(S^+I^+ + S^-I^-) \;\; S_x^\Delta = \tfrac{1}{2}(S^+I^- + S^-I^+)$$

$$S_y^\Sigma = \tfrac{1}{2i}(S^+I^+ - S^-I^-) \; S_y^\Delta = \tfrac{1}{2i}(S^+I^- - S^-I^+)$$

this Hamiltonian can be written as $H = H_\Sigma + H_\Delta$ with

$$H_\Sigma = (\omega_L + \omega) S_z^\Sigma + B S_x^\Sigma = \omega^\Sigma \left[ S_z^\Sigma \cos(\vartheta_\Sigma) + S_x^\Sigma \sin(\vartheta_\Sigma) \right]$$

$$H_\Delta = (\omega_L - \omega) S_z^\Delta + B S_x^\Delta = \omega^\Delta \left[ S_z^\Delta \cos(\vartheta_\Delta) + S_x^\Delta \sin(\vartheta_\Delta) \right]$$

where $\omega^\Sigma = \sqrt{(\omega_L + \omega)^2 + B^2}$, $\omega^\Delta = \sqrt{(\omega_L - \omega)^2 + B^2}$ and $\sin(\vartheta_{\Sigma,\Delta}) = B/\omega^{\Sigma,\Delta}$. In this basis, the initial state is fully polarized along the north pole in both subspaces,

$$\Sigma(0) = S_z = S_z^\Sigma + S_z^\Delta$$

Close to the Hartmann-Hahn matching condition, the $\Sigma$ subspace does not evolve and full polarization transfer occurs when the $S_z$ operator starting at the north pole

ends up at the south pole of the $\Delta$-space Bloch sphere (see 1-21).

The filtering action of the sequence can now be visualized in this basis, focusing on the $\Delta$ subspace. For a sequence of alternating period of evolution under the polarization and gradient Hamiltonians, we achieve an effective polarization Hamiltonian modulated by the grating. In the $\Delta$ subspace, this Hamiltonian for instance has the form $H_\Delta = (\omega_L - \omega)S_z^\Delta + B\cos\vartheta S_x^\Delta + B\sin\vartheta S_y^\Delta$. If the filter is off-resonance, $\vartheta \neq 2\pi$ and the axes of the effective rotation keeps changing at each cycle of the sequence, thus the state $S_z^\Delta$ is unable to flip completely (1-21(a)). For instance, if $\vartheta = \pi$ the effective Hamiltonians in alternate cycles is $\omega S_z + \omega_L I_z \pm BS_xI_x$, and polarization is fed into and removed from the nuclear spins in alternate cycles. In contrast when $\vartheta = 2\pi$, the filter is resonant and the action of every cycle adds coherently leading to an inversion in $\Delta$ subspace and polarization transfer (Fig. 1-21(b)).

# Chapter 2

# Quantum Interpolation for High Resolution Sensing

## 2.1 Introduction and Fundamental Principles

### 2.1.1 Introduction

Precision metrology often needs to strike a compromise between signal contrast and resolution, since the hardware apparatus sets limits on the precision and sampling rate at which the data can be acquired. In nanoscale magnetic resonance probes, for instance, finite sampling times greatly limit the achievable sensitivity and spectral resolution. In some cases, classical supersampling techniques have become a standard tool to achieve a significantly higher resolution than the bare recorded data. For instance, the Hubble Space Telescope uses classical digital image processing algorithms like variable pixel linear reconstruction (also known as Drizzle [73]) to construct a supersampled image from multiple low resolution images captured at slightly different angles. This technique amounts to effectively interpolating to a higher number of

pixels than in the native sensor. Unfortunately, this classical interpolation method would fail for signals obtained from a quantum sensor, where the information is encoded in its quantum phase [74].

Quantum systems such as trapped ions [75], superconducting qubits [76,77] and spin defects [78,79] have been shown to perform as excellent spectrum analyzers and lock-in-detectors for both classical and quantum fields [80,81,82].

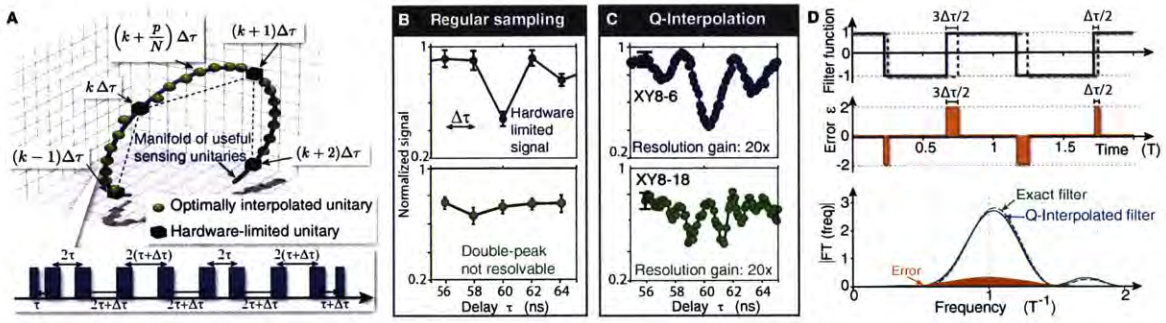


Figure 2-1: **Quantum Interpolation scheme.** (**A**) *Conceptual picture of quantum interpolation.* The unitary evolution of a quantum sensor can only be probed at discrete intervals $\tau_k = k\Delta\tau$ (black cubes) and classical reconstruction would miss an accurate description (dashed black line). Quantum interpolation faithfully approximates the evolution at arbitrary small fractional intervals (green spheres) by coherent combination of pulse sequences. (**B-C**) *NMR signal from a single $^{14}N$ spin associated with the NV quantum sensor.* Left: sensing with conventional sequences limited to $\Delta\tau$=2ns. Right: quantum interpolation, improving the resolution to 110 ps. The lower panels show that only quantum interpolation can reveal details of signal (the appearance of a double peak) linked to the quantum evolution of the $^{14}$N spin. (**D**) *Filter function description of quantum interpolation.* Top: Time domain filter function $f(t)$ for the desired (dashed green lines) and interpolated pulse sequence (solid blue lines) for the simplest case of a half-time interpolation with total sequence time $T$. The deviation between these filters is the error function $\epsilon$ (middle panel) that needs to be minimized for an optimal interpolation construction. Bottom: Frequency domain representation of both filter functions and the FT of their difference.

Here we introduce a technique, that we call quantum interpolation, to overcome

these limitations in sensing resolution. In analogy to classical interpolation, our method aims at capturing data points on a finer mesh than they are directly accessible because of experimental limitations. The method relies on quantum interference to achieve high-fidelity interpolation of the quantum dynamics between hardware-allowed time samplings, thus allowing high resolution sensing. We demonstrate over two orders of magnitude resolution gains, and discuss applications of our work to high resolution nanoscale magnetic resonance imaging. Not only is quantum interpolation an enabling technique to extract structural and chemical information from single biomolecules, but it can be directly applied to other quantum systems for super-resolution quantum spectroscopy.

### 2.1.2 Principle

The key idea is presented in Fig. 2-1A. The result of any quantum sensing experiment, implemented for example, by a dynamical decoupling sequence with fixed evolution time $\tau$, can be represented as a point in a continuous manifold of evolution operators. Unfortunately, the timing resolution $\Delta\tau$ limits sampling to only a discrete subset of points in this manifold. Simply acquiring data at two or more time points and interpolating the results, as done in classical sensing, yields no new information. Indeed, the information is stored in the quantum sensor phase, which is then read in an incoherent manner. Instead, we achieve quantum interpolation by manipulating the quantum sensor dynamics in a coherent way, effectively *supersampling* the ideal sensing manifold at arbitrarily small fractional intervals. More precisely, given discrete propagators $\mathcal{U}(\tau_k)$ describing the quantum probe evolution under a control sequence block of $\pi$-pulses separated by a time $\tau_k = k\Delta\tau$, we construct the

interpolated propagators

$$U^N(\tau_{k+p/N}) = \mathcal{P}\left\{\prod_{m=1}^{N-p}\mathcal{U}(\tau_k)\prod_{n=1}^{p}\mathcal{U}(\tau_{k+1})\right\} \approx \mathcal{U}^N(\tau_{k+p/N}), \tag{2.1}$$

suitably ordering the pulse sequence for interpolation, reflected by the permutation $\mathcal{P}$.

We exploit quantum interpolation to perform high spectral resolution magnetometry of quantum and classical fields using the electronic spin of the Nitrogen Vacancy (NV) center in diamond[6] as a nanoscale probe[79,83,82]. Using a conventional XY8-6 dynamical decoupling sequence[17,16] to measure the $^{14}$N nuclear spin of the NV center, we obtain a low resolution signal where the expected sinc-like dip is barely resolved (Fig. 2-1B). Upon increasing the number of pulses, this narrow dip is completely lost. To enhance the signal resolution we use an optimized interpolation sequence (Fig. 2-1C) that completely mitigates the deleterious effects of timing resolution. Indeed, the number of points that can be sampled via quantum interpolation scales linearly with the number of pulses $N$, while the filter bandwidth decreases as $1/N$. The sensing resolution is now determined only by the quantum probe coherence time $T_2$ (simultaneously extended due to dynamical decoupling) and the number of pulses that can be reliably applied.

The ordering of the different pulse sequence blocks is a crucial step in achieving an interpolated propagator that remains the most faithful approximation of $\mathcal{U}^N(\tau_{k+p/N})$ even at large $N$. For instance, a naive construction, $\mathcal{P} = \mathbf{1}$ in Eq. (3.3), leads to fast error accumulation. We tackle this problem by minimizing the deviation $\epsilon = |f_U - f_\mathcal{U}|$ of the time domain modulation (shaded regions in Fig. 2-1C), since we find that this also minimizes the filter function error and maximizes the fidelity of the interpolated propagator with the ideal one.

We can thus design a simple procedure to determine the *optimal* control sequence to approximate any desired unitary $\mathcal{U}^N(\tau_{k+p/N})$. Intuitively, the optimal construction compensates the error at each decoupling sequence block to achieve for any number $N$ of pulses a constant error that depends only on $\Delta\tau$. We show analytically and numerically that the error for interpolated propagators of all $p/N$ samples is approximately equal, and bounded by the error of $U^2(\tau_{k+1/2}) = \mathcal{U}^2(\tau_{k+1/2}) + \mathcal{O}(\Delta\tau^2)$ (see Appendix).

## 2.2 Interferometric spin sensing via the NV center

Although the principle of nuclear spin sensing by NV centers has been discussed extensively, the method is very often presented with a semi-classical picture of the nuclear spin noise and the filter formalism. For a better understanding of quantum interpolation, we need instead to more precisely evaluate this interferometric method by considering the full quantum mechanical evolution of the the nuclear spins [14,13].

### 2.2.1 Coupled system of NV center and nuclear spins

NV centers have shown to be sensitive probes of their nuclear spin environment. The NV center interacts with the nuclear spins via the anisotropic hyperfine interaction given by

$$\mathcal{H}_{\text{hf}} = \sum_j \mathbf{S} \cdot \mathbf{A}^{(j)} \cdot \mathbf{I}_j = \sum_j \frac{g}{r_N^3} \left[3(S \cdot \hat{\mathbf{r}}_N)(I_j \cdot \hat{\mathbf{r}}_N) - \mathbf{S} \cdot \mathbf{I}\right],$$

where $g = \frac{\hbar\mu_0\gamma_N\gamma_e}{4\pi}$, with the gyromagnetic ratios of nuclear and electron spins respectively $\gamma_N$ and $\gamma_e$, and the vector $\vec{\mathbf{r}}_N^{(j)} = (r_{xj}, r_{yj}, r_{zj})$ joins the center of the NV and the nuclear spin [84,9]. In the presence of a magnetic field, one can consider on the NV the pseudo two level system formed by the $\{0, -1\}$ levels. Apply-

ing now a secular approximation and retaining terms that commute with $S_z$ gives $\mathcal{H}_{\rm hf} = \sum_j \frac{g_N}{(r_N^{(j)})^3} S_z \left[3r_z(r_{xj}I_{xj} + r_{yj}I_{yj}) + (3r_{zj}^2 - 1)I_{zj}\right]$. The overall Hamiltonian of the coupled system is then,

$$\mathcal{H} = \Delta S_z + |0\rangle\langle 0| H_{|0\rangle} + |-1\rangle\langle -1| H_{|-1\rangle} \tag{2.2}$$

with $\Delta = \Delta_0 - \gamma_e B_z$, where $\Delta_0 = 2.87$GHz is the zero field NV splitting, and

$$H_{|0\rangle} = \omega_L I_{zj} \tag{2.3}$$

$$H_{|-1\rangle} = [(\omega_L + A_j)I_{zj} + B_j I_{xj} + C_j I_{yj}] \tag{2.4}$$

represent the effective nuclear spin Hamiltonians conditioned on the state of the NV. Here, we have used the common spectroscopic notation [85], $A_j \equiv A_{zz}^{(j)} = (3r_{zj}^2 - 1), B_j \equiv A_{zx}^{(j)} = 3r_{zj}r_{xj}, C_j \equiv A_{zy}^{(j)} = 3r_{zj}r_{yj}$ to represent the magnitude of the hyperfine interactions to spin $j$, that are contained in the hyperfine tensor $\mathbf{A}^{(j)} = A_{\mu,\nu}^{(j)}$.

### 2.2.2 NV nuclear spin sensing from a geometric perspective

In the sensing pulse sequences, the NV is prepared initially in the state $|\psi\rangle = \frac{1}{\sqrt{2}}(|0\rangle + |-1\rangle)$, while given the low magnetic field and high temperature, the nuclear spins are in the mixed state $\mathbb{1}_j/2$. Due to different evolutions of the nuclear spins conditioned on the $|0\rangle$ or $|-1\rangle$ of the NV center (following Eq. (2.2)), the evolution in the two NV manifolds gives rise to a destructive interference that is detected as a an apparent decay of the NV coherence.

We now provide a geometric perspective to spin sensing sequences with the aim of describing the origin of the increasing sensitivity and the decreasing linewidth with

the number of cycles $N$.

We first define the unitary rotation operator $\mathcal{R}^j(\Theta_j, \hat{\mathbf{n}}_j) := e^{-i\Theta_j \vec{\sigma}^j \cdot \hat{\mathbf{n}}_j/2}$, describing a rotation of the *nuclear* spin $j$ around the axis $\hat{\mathbf{n}}_j$ by an angle $\Theta_j$ (the *flip* angle).

The fundamental units of the CPMG and XY8 spin sensing sequences are described by a unitary transformation composed of three successive rotations

$$\mathcal{U}_{\text{tot}} : = \mathcal{R}(\Theta_a, \hat{\mathbf{n}}_a)\, \mathcal{R}(\Theta_b, \hat{\mathbf{n}}_b)\, \mathcal{R}(\Theta_a, \hat{\mathbf{n}}_a), \tag{2.5}$$

that, in turn, can be described as a rotation about a new rotation axis $\hat{\mathbf{n}}_{\text{tot}}$ by a flip angle $\Theta_{\text{tot}}$, $\mathcal{U}_{\text{tot}} = e^{i\varphi_{\text{tot}}}\, \mathcal{R}(\Theta_{\text{tot}}, \hat{\mathbf{n}}_{\text{tot}})$, where $\varphi_{\text{tot}}$ is an unimportant global phase. Some algebra yields the total effective flip angle

$$\Theta_{\text{tot}} = 2 \arccos\left( \left| 2b \cos\left(\frac{\Theta_a}{2}\right) - \cos\left(\frac{\Theta_b}{2}\right) \right| \right) \tag{2.6}$$

and the effective rotation axis

$$\mathbf{n}_{\text{tot}} = 2b \sin\left(\frac{\Theta_a}{2}\right) \hat{\mathbf{n}}_a + \sin\left(\frac{\Theta_b}{2}\right) \hat{\mathbf{n}}_b \tag{2.7}$$

with

$$b = \cos\frac{\Theta_a}{2} \cos\left(\frac{\Theta_b}{2}\right) - (\hat{\mathbf{n}}_a \cdot \hat{\mathbf{n}}_b) \sin\left(\frac{\Theta_a}{2}\right) \sin\left(\frac{\Theta_b}{2}\right). \tag{2.8}$$

For CPMG-like sequences, the rotation axis associated with $\mathcal{U}_{\text{tot}}$ lies in the plane spanned by the original rotation axes $\hat{\mathbf{n}}_a$ and $\hat{\mathbf{n}}_b$, i.e. $\hat{\mathbf{n}}_{\text{tot}}$ always has the same azimuth angle as $\hat{\mathbf{n}}_b$ if we choose a coordinate system with $\hat{\mathbf{z}} = \hat{\mathbf{n}}_a$. We shall use this property later to visualize trajectories of metrology Hamiltonians in a three-dimensional visualization in Fig. 2-13. This is not the case for periodic dynamical

decoupling sequences[86] (such as the spin echo[87]).

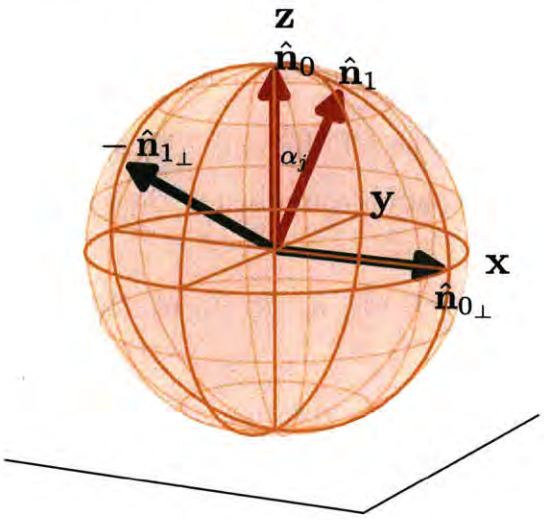


Figure 2-2: **Geometry of interferometric CPMG sensing.** Bloch sphere description of the simple interferometric CPMG control sequence that is employed for sensing nuclear spins in the environment of an NV center. Here $\hat{\mathbf{n}}_0$ and $\hat{\mathbf{n}}_1$ are the two axes of the nuclear spin conditioned on the state of the NV. At the signal peak, obtained for $2\tau \approx \pi/\omega_L$, the result of the sequence are the two effective axes $\hat{\mathbf{n}}_{0_\perp}$ and $-\hat{\mathbf{n}}_{1_\perp}$ (see Eq. (2.9)).

We can now use these results for the system described in Sec. 2.6.3, where the two axes of rotations are defined by the Hamiltonians $H_{|0,1\rangle}$ in Eq. (2.4).

Here we chose the coordinate system such that $\hat{\mathbf{z}} = \hat{\mathbf{n}}_0$, i.e. the $z$-axis is aligned with the external magnetic field. We consider the coupling of the NV with a single spin $j$ at a time, which furthermore allows us to choose the coordinate system such that $\varphi_j = 0$ and the hyperfine coupling $C_j = 0$. Specifically, using the geometric notation[72] to represent the normalized Hamiltonians in Eq. (2.4), we have $\hat{H}_{|0\rangle} = \hat{\mathbf{n}}_0 = \hat{\mathbf{z}}$ and $\hat{H}^j_{|-1\rangle} = \hat{\mathbf{n}}_1 = \cos(\alpha_j)\hat{\mathbf{z}} + \sin(\alpha_j)\hat{\mathbf{z}}_{j\perp}$, where $\hat{\mathbf{z}}_{j\perp} = \cos(\varphi_j)\hat{\mathbf{x}} + \sin(\varphi_j)\hat{\mathbf{y}}$.

We refer to the angle $\alpha_j = \tan^{-1}\left[\frac{B_j}{\omega_L + A_j}\right]$ as the *tilt* angle of spin $j$.

The simplest protocol for spin sensing is the interferometric CPMG-N technique[88,31], which consists of $2N$ refocusing $\pi$ pulses. For spin sensing, we sweep the delay between pulses $2\tau$, and the sensing signal dip appears when $2\tau \approx \pi/\omega_L$. At this time, the nuclear spin sees two different evolutions conditioned on the state of the NV center, that for $\omega_L \gg A_j, B_j$ can be approximated as

$$\begin{aligned}\mathcal{U}_{|0\rangle} &= \mathcal{R}(\pi/2, \hat{\mathbf{n}}_0)\mathcal{R}(\pi, \hat{\mathbf{n}}_1)\mathcal{R}(\pi/2, \hat{\mathbf{n}}_0) = \mathcal{R}(\hat{\mathbf{n}}_{|0\rangle}, \Theta_{|0\rangle}) \\ \mathcal{U}_{|-1\rangle} &= \mathcal{R}(\pi/2, \hat{\mathbf{n}}_1)\mathcal{R}(\pi, \hat{\mathbf{n}}_0)\mathcal{R}(\pi/2, \hat{\mathbf{n}}_1) = \mathcal{R}(\hat{\mathbf{n}}_{|-1\rangle}, \Theta_{|1\rangle}).\end{aligned} \tag{2.9}$$

(see Sec. 2.2.3 for the exact expression.) The effective axes of rotation are

$$\hat{\mathbf{n}}_{|0\rangle} = \frac{\hat{\mathbf{n}}_0 - \hat{\mathbf{n}}_1 \cos\alpha_j}{\sin\alpha_j} = -\hat{\mathbf{n}}_{1_\perp} \tag{2.10}$$

$$\hat{\mathbf{n}}_{|1\rangle} = \frac{\hat{\mathbf{n}}_1 - \hat{\mathbf{n}}_0 \cos\alpha_j}{\sin\alpha_j} = \hat{\mathbf{n}}_{0_\perp}. \tag{2.11}$$

Note that both axes lie in the plane span($\hat{\mathbf{n}}_0$, $\hat{\mathbf{n}}_1$) and are orthogonal to $\hat{\mathbf{n}}_1$ and $\hat{\mathbf{n}}_0$ respectively. Thus they retain the same mutually spanned angle $\hat{\mathbf{n}}_0 \cdot \hat{\mathbf{n}}_1 = \cos\alpha_j$ in magnitude. The effective flip angles are found to be $\Theta_{|0\rangle} = \Theta_{|-1\rangle} = 2\alpha_j$, which leads to the to a simple *geometric* interpretation (see Fig. 2-2): effectively the control protocol translates the initial tilt angle $\alpha_j$ to twice the *flip* angle, while the effective axes are perpendicular to the initial axes are still separated by $\alpha_j$.

We can now formally derive the dip signal from a CPMG/XY8 experiment[1], and interpret it geometrically using Eq. (2.9). The time evolution operator for the entire

[1]CPMG and XY8 sequences just differ in the phases of the pulses employed, and the resulting signal in both cases is quantitatively the same.

control sequence with $N$ cycles is

$$U = |0\rangle\langle 0| \otimes \mathcal{U}_{|0\rangle}^N + |-1\rangle\langle -1| \otimes \mathcal{U}_{|-1\rangle}^N, \tag{2.12}$$

Note that for $\mathcal{U}_{|0/-1\rangle}^N = \mathcal{R}(N\Theta_{|0\rangle}, \hat{\mathbf{n}}_{|0\rangle})$ the rotation angles are amplified by $N$, whereas the rotation axes remain unchanged.

Initially, we prepare the NV in the $\frac{|0\rangle+|-1\rangle}{\sqrt{2}}$ state by applying a $\frac{\pi}{2}$ pulse. The initial state of the system is thus described by the density matrix $\rho_{\text{ini}} = \frac{1}{4}(\mathbb{1}+\sigma_x)\otimes\mathbb{1}$, where the first operator acts on the NV space and the second on the nuclear spin space. After the decoupling pulse sequence, the system is thus in the state

$$\rho_{\text{final}} = U\rho_{\text{ini}}U^\dagger = \frac{1}{4}(\mathbb{1} + U(\sigma_x \otimes \mathbb{1})U^\dagger). \tag{2.13}$$

After the sequence, another $\frac{\pi}{2}$ pulse is applied, which maps the phase onto a population of the NV state. We can therefore define the signal as the expectation value $S = \langle\sigma_x \otimes \mathbb{1}\rangle$ before the last $\frac{\pi}{2}$ pulse. The signal can be interpreted as the overlap of the initial and final density matrix

$$S = \text{Tr}(\sigma_x\rho_{\text{final}}) = 4\text{Tr}(\rho_{\text{ini}}^\dagger\rho_{\text{final}}) - 1. \tag{2.14}$$

Using Eq. (2.12) and Eq. (2.13), a straightforward calculation yields

$$\begin{aligned} S &= \frac{1}{4}\text{Tr}[(\sigma_x \otimes \mathbb{1})(|0\rangle\langle -1| \otimes \mathcal{U}_{|0\rangle}^N {\mathcal{U}_{|-1\rangle}^N}^\dagger + |-1\rangle\langle 0| \otimes \mathcal{U}_{|-1\rangle}^N {\mathcal{U}_{|-0\rangle}^N}^\dagger)] \\ &= \frac{1}{4}\text{Tr}(\mathcal{U}_{|0\rangle}^N {\mathcal{U}_{|-1\rangle}^N}^\dagger + \mathcal{U}_{|-1\rangle}^N {\mathcal{U}_{|-0\rangle}^N}^\dagger). \end{aligned} \tag{2.15}$$

Since the trace of any SU(2) rotation operator is real, the last two terms are equal and the signal can be expressed in geometric terms

$$
\begin{aligned}
S &= \frac{1}{2}\mathrm{Tr}\Big\{ \left[ \mathbb{1}\cos\left(\frac{N\Theta_{|0\rangle}}{2}\right) - i\hat{\mathbf{n}}_{|0\rangle}\cdot\boldsymbol{\sigma}\,\sin\left(\frac{N\Theta_{|0\rangle}}{2}\right)\right] \\
&\times \left[ \mathbb{1}\cos\left(\frac{N\Theta_{|-1\rangle}}{2}\right) - i\hat{\mathbf{n}}_{|-1\rangle}\cdot\boldsymbol{\sigma}\,\sin\left(\frac{N\Theta_{|-1\rangle}}{2}\right)\right] \Big\} \\
&= 1 - \sin^2(N\alpha_j)\cos^2(\alpha_j/2) \qquad (2.16)
\end{aligned}
$$

To obtain the last line, we used $(\hat{\mathbf{n}}_{|0\rangle}\cdot\boldsymbol{\sigma})(\hat{\mathbf{n}}_{|-1\rangle}\cdot\boldsymbol{\sigma}) = \hat{\mathbf{n}}_{|0\rangle}\cdot\hat{\mathbf{n}}_{|-1\rangle}\mathbb{1} + i\boldsymbol{\sigma}\cdot(\hat{\mathbf{n}}_{|0\rangle}\times\hat{\mathbf{n}}_{|-1\rangle})$ and $\mathrm{Tr}(\sigma_j) = 0$ for all terms containing a single Pauli matrix.

Geometrically, the signal in Eq. (2.16) is just the overlap of the rotations $\mathcal{U}^N_{|0\rangle} = \mathcal{R}(N\alpha_j, -\hat{\mathbf{n}}_{1_\perp})$ and $\mathcal{U}^N_{|-1\rangle} = \mathcal{R}(N\alpha_j, \hat{\mathbf{n}}_{0_\perp})$. It also becomes evident that amplification of the flip angle from $\alpha_j$ to $N\alpha_j$ upon application of $N$ cycles explains why the peak signal intensity grows quadratically with the number of cycles $N$ – an important feature for external spin sensing. Equivalently, the application of $N$ cycles leads to a longer evolution path length and hence larger phase accumulation in the interferometric detection.

### 2.2.3 Exact analysis of the signal dip

To evaluate the exact expression for the peak signal from a CPMG/XY8 experiment we consider the propagators $\mathcal{U}_{|0\rangle} = \mathcal{R}(\eta\pi/2, \hat{\mathbf{n}}_1)\mathcal{R}(\pi, \hat{\mathbf{n}}_0)\mathcal{R}(\eta\pi/2, \hat{\mathbf{n}}_1)$, and $\mathcal{U}_{|-1\rangle} = \mathcal{R}(\pi/2, \hat{\mathbf{n}}_0)\mathcal{R}(\eta\pi, \hat{\mathbf{n}}_1)\mathcal{R}(\pi/2, \hat{\mathbf{n}}_0)$, where $\eta = \left[\left(1 + \frac{A_j}{\omega_L}\right)^2 + \left(\frac{B_j}{\omega_L}\right)^2\right]^{1/2}$ takes into account that the nuclear spin Hamiltonian norm in the two NV manifolds is different.

This gives for $N$ cycles of the experiment,

$$\begin{aligned}
\mathcal{U}^N_{|0\rangle} &= -\mathbb{1}\cos N\alpha_j + i\frac{\sin N\alpha_j}{\sin \alpha_j}\boldsymbol{\sigma}\cdot[-\hat{\mathbf{n}}_{1_\perp}\sin\alpha_j \\
&\quad +\hat{\mathbf{n}}_1\cos\alpha_j\cos(\eta\pi/2)] \\
\mathcal{U}^N_{|-1\rangle} &= -\mathbb{1}\cos N\alpha_j + i\frac{\sin N\alpha_j}{\sin \alpha_j}\boldsymbol{\sigma}\cdot[\hat{\mathbf{n}}_{0_\perp}\sin\alpha_j\sin(\eta\pi/2) \\
&\quad +\hat{\mathbf{n}}_0\cos(\eta\pi/2)]\,,
\end{aligned} \tag{2.17}$$

where $\cos(\alpha_j) = \cos(\alpha_j)\sin(\eta\pi/2)$. Note that when the interactions are weak, $\omega_L \gg A_j, B_j$, we have $\eta \to 1$ and $\cos\alpha_j \to \cos\alpha_j$, and one exactly recovers the expressions Eq. (2.9) above. The exact signal including the hyperfine terms is now,

$$\begin{aligned}
1-S &= \cos^2 N\alpha_j + \frac{\sin^2 N\alpha_j}{\sin^2\alpha_j}\left[\sin^2\alpha_j\cos^2\alpha_j\left(\cos(\eta\pi/2)-1\right)\right. \\
&+ \left.\cos^2\alpha_j - \cos^2\alpha_j + \sin^2\alpha_j\cos(\eta\pi/2)\right]
\end{aligned}$$

### 2.2.4 Linewidth of the nuclear spin sensing signal

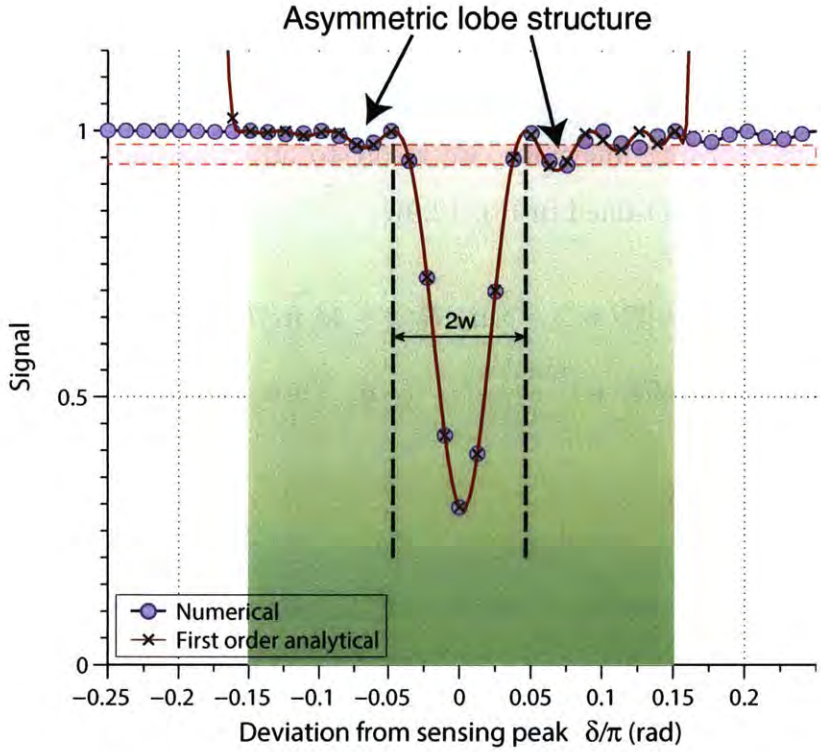


Figure 2-3: **Lineshape in spin sensing experiments.** Here we compare the analytic expressions for the lineshape of spin sensing experiments with the numerically obtained result for a small deviation $\delta$ about the sensing peak. We considered $\alpha_j = 0.1$ rad and $N = 10$ cycles of the CPMG experiment. The result demonstrates that the first order expression obtained in Eq. (2.21) does indeed capture the lineshape accurately, including the asymmetry in the sidelobes on either side of the sensing peak (red dashed lines). The green shading represents the region over which the first order expression is a good approximation. The dashed lines describe the evaluation of the signal linewidth $w$ following Eq. (2.22).

The previous sections considered the peak signal obtained as a result of the spin sensing experiment. However, it is also of critical importance to quantify the linewidth of the sensing signal since by falling as $1/N$ it allows sensing spins at higher resolution as $N$ increases.

To derive the sensing linewidth, we resort to an expansion in the deviation $\delta$ about the signal peak obtained in Eq. (2.9),

$$\begin{aligned} \mathcal{U}_{|0\rangle}^{N}(\pi+\delta) &= [\mathcal{R}(\pi/2+\delta,\hat{\mathbf{n}}_0)\mathcal{R}(\pi+2\delta,\hat{\mathbf{n}}_1)\mathcal{R}(\pi/2+\delta,\hat{\mathbf{n}}_0)]^N \\ &\approx \mathbb{1}\cos N\alpha_j' + i\frac{\sin N\alpha_j'}{\sin\alpha_j'}\boldsymbol{\sigma}\cdot[-\hat{\mathbf{n}}_{1_\perp}\sin\alpha_j - \delta(1+\cos\alpha_j)\hat{\mathbf{n}}_1] \end{aligned} \tag{2.18}$$

where to first order in $\delta$,

$$\sin^2\alpha_j' = \sin^2\alpha_j + \delta^2(1+\cos\alpha_j)^2\,. \tag{2.19}$$

which incorporates an effective destructive interference in the flip angle. It is also instructive to compare Eq. (2.18) with Eq. (2.9): the expressions are identical except for a corruption factor proportional to $\delta$ in Eq. (2.18). This can be visualized as a slight mixing of the perfect vector $\hat{\mathbf{n}}_{1_\perp}$ with a term $\delta(1+\cos\alpha_j)\hat{\mathbf{n}}_1$. Crucially this is the same factor that causes the interference in Eq. (2.19). Similarly in the $|-1\rangle$ manifold of the NV center one has,

$$\begin{aligned} \mathcal{U}_{|-1\rangle}^{N}(\pi+\delta) &= [\mathcal{R}(\hat{\mathbf{n}}_1,\pi/2+\delta)\mathcal{R}(\hat{\mathbf{n}}_0,\pi+2\delta)\mathcal{R}(\hat{\mathbf{n}}_1,\pi/2+\delta)]^N \\ &\approx \mathbb{1}\cos N\alpha_j' + i\frac{\sin N\alpha_j'}{\sin\alpha_j'}\boldsymbol{\sigma}\cdot[\hat{\mathbf{n}}_{0_\perp}\sin\alpha_j - \delta(1+\cos\alpha_j)\hat{\mathbf{n}}_0] \end{aligned} \tag{2.20}$$

This gives the signal similar to Eq. (2.16), but now as a function of the deviation

from the sensing peak $\delta$,

$$\begin{aligned} S &= \cos^2 N\alpha'_j + \frac{\sin^2 N\alpha'_j}{\sin^2 \alpha'_j}\left[-\sin^2\alpha_j\,\cos\alpha_j\right. \\ &+ \left.\delta^2\cos\alpha_j\,(1+\cos\alpha_j)^2 - 2\delta\sin^2\alpha_j\,(1+\cos\alpha_j)\right]. \end{aligned} \tag{2.21}$$

Figure 2-3 compares the analytical expression in Eq. (2.21) to an exact numerical calculation. It is evident that for most of the region close to the sensing peak (shaded region), the agreement is very close.

Importantly then the insight offered by Eq. (2.18) allows one to intuitively understand the origin of the sensing linewidth: with increasing $\delta$, there is destructive interference of the flip-angle $\alpha_j$ to $\alpha'_j$ (Eq. (2.19)). As the number of cycles is increased, the destructive interference effect is magnified by $N$ (Eq. (2.21)) and leads to a decreasing linewidth $\propto 1/N$.

To quantify the linewidth $w$ exactly, let us define it as the first *zero* of sensing signal $S$ in Eq. (2.21). This happens when the function $\sin(N\alpha'_j)$ vanishes, i.e. $\alpha'_j = \pi/N$, giving the linewidth in units of *angle*,

$$w^2 \approx \frac{\sin^2(\pi/N) - \sin^2\alpha_j}{2\cos^2(\alpha_j/2)} \tag{2.22}$$

Similarly, the sensing linewidth in units of time can be evaluated as $w/\omega_L$, giving for small $\alpha_j$,

$$w/\omega_L \approx 1/(\sqrt{2}\omega_L\cos(\alpha_j/2))\cdot\sin(\pi/N) \tag{2.23}$$

that indeed falls as $\propto 1/N$ as we would expect for interferometric detection.

The linewidth directly shows the origin of the *asymmetry* of the sensing peak. This is subtle feature, characteristic of CPMG-like sequences (but not of period sequences) that we are able to discern clearly in our experiments via quantum inter-

polation (Fig. 2-1). This shows that our quantum interpolation expansion is indeed of low error and faithfully represents the true signal.

The asymmetry is manifested by the linear term in $\delta$ in Eq. (2.21), or equivalently the odd $\sin\delta$ term in Eq. (2.21), as it is evident in Fig. 2-3. Indeed, the time $2\tau = \pi/\omega_L$ is not the exact signal minimum; instead, at this time, the effective vectors $[\hat{\mathbf{n}}_{0_\perp}\sin(\alpha) - \delta(1+\cos\alpha)\hat{\mathbf{n}}_0]$ and $[-\hat{\mathbf{n}}_{1_\perp}\sin\alpha - \delta(1+\cos\alpha)\hat{\mathbf{n}}_1]$ in Eq. (2.18) and Eq. (2.20) are not exactly perpendicular to each other away from the sensing peak.

### 2.2.5 $^{14}$N spin sensing and lineshape analysis

In Sec. 2.6.2 we applied quantum interpolation based supersampling to study the lineshape from a single $^{14}$N spin intrinsic to the NV center. We performed experiments close to the ground state anti-crossing of the NV center, $B_z \approx 1000$G, where due to the presence of a weak misaligned magnetic field, one obtains a peak signal under XY8-N of the form

$$S(\delta = 0) = \cos(8N\alpha), \text{ where } \alpha = \tan^{-1}\left[\frac{\gamma_e B_\perp A_{xx}}{\Delta\omega}\right], \tag{2.24}$$

with $A_{xx} = -2.62$MHz, and where $\Delta = \Delta_0 - \gamma_e B_z$ is the resonance frequency of the NV center, and $\omega = P - A_\parallel/2 - \gamma_n B_z$, with the quadrupolar interaction $P = -4.95$MHz, the parallel hyperfine term $A_\parallel = -2.16$MHz, and the gyromagnetic ratio $\gamma_n = 0.31$kHz/G. This signal originates from second order perturbation effects due to a combination of the non-secular terms $B_\perp S_x$ and $\frac{A_\perp}{2}(S_+ I_- + S_- I_+)$ in the

NV center Hamiltonians

$$\begin{aligned} \mathcal{H} &= \mathcal{H}_0 + V \\ \mathcal{H}_0 &= \Delta_0 S_z^2 + B_z(\gamma_e S_z + \gamma_N I_z) + P I_z^2 + A_\parallel S_z I_z \\ V &= \gamma_e B_\perp S_x + \frac{A_\perp}{2}(S_+ I_- + S_- I_+) \end{aligned} \tag{2.25}$$

that yield a term $\propto S_z I_x$. The signal thus becomes stronger close to the avoided crossing, where the energy denominator $\Delta$ becomes small. For typical values of misaligned fields,$\alpha$ is small, and the signal is approximately $S \propto \cos\left[\frac{8\gamma_e B_x A_\perp N}{\Delta\,\omega}\right]$. In Fig. 2-1, and in Fig. 2-19 we perform XY8 sensing while sweeping the number of cycles $N$. In Fig. 2-19 we fit the data to the theoretical lineshape, numerically evaluated following Eq. (2.16), where the operators $\mathcal{U}_{|0\rangle}$ and $\mathcal{U}_{|1\rangle}$ are now defined with the tilt angle $\alpha_j = \alpha$ from Eq. (2.24) above. We find a remarkable match with the theoretical model in Fig. 2-19, and from the data we extract a value of $B_\perp$ which corresponds to an misalignment of 1.14G at the bare field of 954.71G. One is also able to discern the asymmetry in the lineshape (see Sec. 2.2.4).

## 2.3 Bound on Interferometric spin sensing due to finite sampling

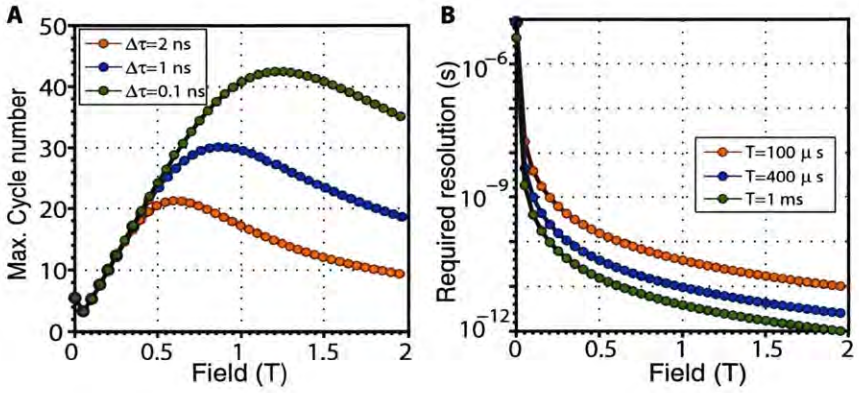


Figure 2-4: **Effects of finite timing resolution. (A)** Panel denotes the maximum number of CPMG cycles $N$ before one becomes sensitive to finite timing resolution effects. Here we consider a single $^1$H spin that is 2.45nm away from the NV center at relative coordinates [1,1,2]nm to the NV center. As is evident, at moderately high magnetic fields $> 0.5$T, one quickly becomes prone to subsampling effects. **(B)** Panel denotes the largest $\Delta\tau$ required to still be not prone to subsampling effects, i.e. the largest $\Delta\tau$ required to still efficiently sample the signal peak. We consider here different total times of the sequence, limited by the maximum $T_2 \approx 1$ms. Even for moderately high magnetic fields, one requires a timing resolution of a few picoseconds, which is at the limit of current hardware (see Table 2.1). Quantum interpolation based supersampling allows us to achieve a small effective $\Delta\tau$ from modest available hardware.

### 2.3.1 Loss in sensing contrast

Often we are interested in resolving spins that are very close together in frequency, for instance to be able to reconstruct their positions and the structure of the spin network of which they are part. The differences in frequency arising for instance from chemical shifts could be as small as $10^{-6}\omega_L$. In a real experimental scenario however, the rotations on the nuclear spins via the NV are effectively achieved through delayed evolution as in Fig. 2-2, and the construction of Eq. (2.21) is prone to finite-sampling effects, leading to a loss of signal contrast and resolution. In this section, we quantify these deleterious effects in detail.

Consider for interferometric spin sensing, we would like ideally to construct the CPMG sequence by matching the delay $2\tau = \pi/\omega_L$; however given a finite sampling resolution $\Delta\tau$, one has a finite error that directly translate to a deviation from the ideal signal peak. For instance in Eq. (2.9), this translates to errors in the rotation flip angles of $\pi/2$ and $\pi$ that constitute a perfect CPMG spin sensing sequence – instead, these angles can now only be achieved to within the sampling interval $\Delta\vartheta = \omega_L\Delta\tau$ (see Fig. 2-6).

In the following, we shall quantify the deleterious effects of the this finite timing resolution:

1. Due to the fact that the signal linewidth decreases with the number of cycles $N$, finite sampling resolution $\Delta\vartheta$ might cause the sensing peak to be *lost* beyond a threshold) $N_{\max}$. This is experimentally demonstrated for instance in the left panels of Fig. 2-1**(B)**, where the sensing peak is just a single point or less and is not efficiently sampled.

2. For a deviation away $\delta_0$ from the perfect interferometric construction, we will

show below that the signal falls away quadratically with $\delta_0$ and the number of cycles $N$. This leads, very quickly, to the underestimation of the sensing peak contrast, that can lead to significant error in reconstructing the hyperfine term $B_j$ for spin sensing experiments.

3. Finite resolution also leads to a decrease in the maximum achievable peak signal, directly affecting the *sensitivity* of the NV based spin sensor.

Let us first evaluate the maximum number of cycles $N_{\max}$ such that the linewidth $w/\omega_L \leq \Delta\vartheta$, i.e. after which we become susceptible to finite sampling effects. From Eq. (2.22),

$$N_{\max} \approx \frac{\pi}{\sqrt{(\omega_L \Delta\tau)^2(1+\cos\alpha_j)^2 + \sin^2\alpha_j}} \tag{2.26}$$

For instance for a hardware set timing limitation of $\Delta\tau$=1ns (see Fig. 2-4(**A**)), for a weakly coupled $^1$H spin at 0.5T and $\alpha_j = 0.05$rad, we have that the maximum XY8-N experiment that can be applied is $N_{\max} \approx 12$. This is a very small number of cycles, and increasing $N$ beyond $N_{\max}$ leads to subsampling of the peak signal, leading to a substantial loss of contrast.

Let us now in determine in detail the loss in signal contrast and resolution. Let us define sampling error $\delta_0 = \pi - k\Delta\vartheta$ where $k$ is integral (Fig. 2-6), and which denotes the deviation from the perfect CPMG sensing sequence (the perfect sequence in Eq. (2.9) refers to $\delta_0 = 0$). The signal contrast $C(\delta_0) = \frac{1}{2}[1 - S(\delta_0)]$ is now,

$$C(\delta_0) = \frac{1}{2}\sin^2 N\alpha_j' \,(1-\cos\alpha_j') + \frac{\sin^2 N\alpha_j'}{\sin^2\alpha_j'}\sin^2\alpha_j\cos\alpha_j \tag{2.27}$$

while the perfect contrast $C(0) = \sin^2(N\alpha_j)[1+\cos(\alpha_j)]$. For small sampling error

$\delta_0$, one can now evaluate the effective loss in contrast,

$$\epsilon = C(0) - C(\delta_0) = \frac{1}{4}(N\alpha_j)^2\delta_0^2\left(2 - \frac{\alpha_j^2}{2}\right)^2 \tag{2.28}$$

This expression is good upto second order in $\delta_0$, and captures the scaling of the contrast loss $\epsilon \propto N^2\delta_0^2$, i.e. as the number of cycles $N$ increases or as one improperly samples the signal peak (larger $\Delta\tau$), the loss in contrast increases quadratically. This is also evident in the experimental data shown in the left panels of Fig. 2-1 **(B)**– the sensing peak is improperly sampled, and the structure in the peaks cannot be resolved.

While Eq. (2.28) considered the loss in contrast for small $\delta_0$, let us consider now the maximum bound on the contrast $C_j(\delta_0)$. We will show that the signal not only grows quadratically slowly following Eq. (2.28), but is also upper bounded to a significantly lower level. Consider that maximum contrast at the peak $C(0)|_{\max} = 1 + \cos\alpha_j$, while at finite $\delta_0$ we have,

$$C(\delta_0)|_{\max} = 1 + \frac{\cos(\alpha_j)\left[\sin^2(\alpha_j) - \delta_0^2(1+\cos\alpha_j)^2\right]}{\sin^2(\alpha_j) + \delta_0^2(1+\cos\alpha_j)^2} \tag{2.29}$$

It is quite easy to see that $C(\delta_0)|_{\max} < C(0)|_{\max}$. For instance, for $\delta_0 \gg \sin\alpha_j$ (meaning one is away from the sensing peak), we have $C(\delta_0)|_{\max} = 1 - \cos(\alpha_j) \to 0$ since $\alpha_j$ by definition is small. This quantifies the intuition of destructive interference affecting the flip angle $\alpha_j$ into $\alpha_j'$ (see Eq. (2.19)) as one moves away from the sensing peak. In contrast in the perfect case $C(0)|_{\max} = \frac{1}{2}(1+\cos\alpha_j) \to 1$. Hence, in summary, one can quantify the deleterious effects of limited timing resolution $\Delta\tau$ with regards to signal contrast: not only does the signal grow quadratically slower with $N$ and $\delta_0$, but it is also upper bounded to a lower level.

### 2.3.2 Loss in sensing resolution

In addition to a loss of signal contrast, in this section we show that finite timing resolution $\Delta\tau$ also leads to a loss of sensing *resolution*. Consider that the effective linewidth in time units (Eq. (2.22)) is given by $\Delta\tau_{\text{lw}} = w/\omega_L = \frac{[\sin^2(\pi/N)-\sin^2(\alpha_j)]^{1/2}}{2\omega_L \cos(\alpha_j/2)}$, however the hardware limits us to effectively a resolution of $\Delta\tau$. In order to resolve the signal peak faithfully we have the requirement that $\Delta\tau \leq \frac{1}{2}\tau_{\text{lw}}$. Along with the fact that the number of pulses is bounded by the coherence time, $N_{\max} = \frac{T_2\omega_L}{2\pi}$, this translates to

$$\Delta\tau \lesssim \frac{1}{2\sqrt{2}\omega_L \cos(\alpha_j/2)} \sin\left(\frac{2\pi^2}{T_2\omega_L}\right) \tag{2.30}$$

Eq. (2.30) quantifies the fact that one needs a better timing resolution (smaller $\Delta\tau$) as one goes to higher magnetic fields, or higher number of cycles. For instance (see Fig. 2-4**(B)**), for a $^1$H nuclear spin at a field of 0.5T, assuming $T_2 = 1$ms and $\alpha_j = 0.05$rad typical for a weakly coupled spin, Eq. (2.30) sets the requirement $\Delta\tau \leq 15.83$ps, which is a very small required timing resolution (Table 2.1). If $\Delta\tau$ does not satisfy Eq. (2.30), then the sensing peak can be completely lost. This is demonstrated also in the left panels of Fig. 2-1**(B)**, where poor sampling resolution does not allow us to resolve the structure in the $^{14}$N signal (that follows Eq. (2.21)).

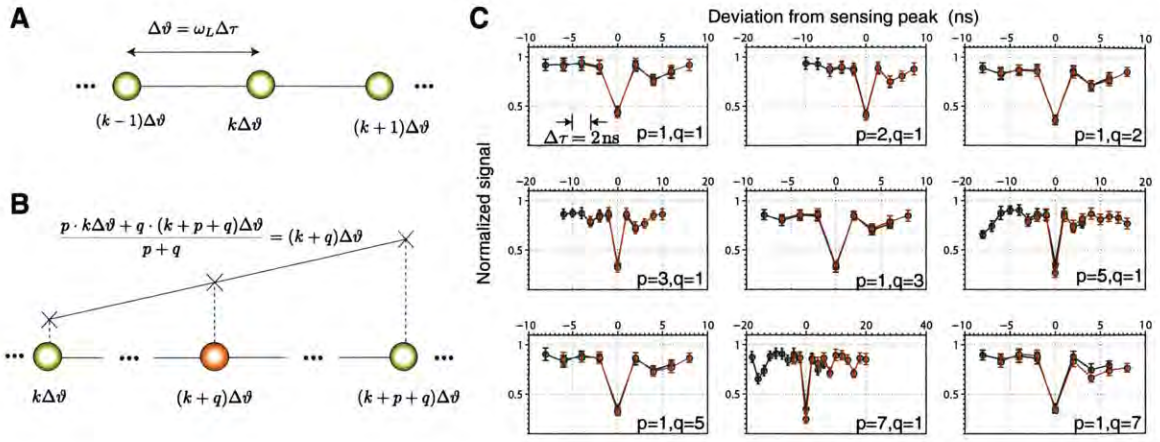


Figure 2-5: **Evaluating quantum interpolation via explicit subsampling.** In these experiments, we deliberately undersample the signal from a $^{14}$N spin using a timing resolution that is larger than the intrinsic $\Delta\tau = 2$ns set by hardware. The experiments are schematically described in **(A-B)**. In **(C)**, we construct for different values of $(p, q)$ (the legend shows $q/(p+q)$) in an XY8-6 sequence, the approximate supersampled point $\left[U^p_{|0\rangle}(k\Delta\vartheta + \delta)U^q_{|0\rangle}((k+p+q)\Delta\vartheta + \delta)\right]^{N/(p+q)}$ (orange circles) and compare it against the ideal one $U^N_{|0\rangle}((k+q)\Delta\vartheta + \delta)$ (green circles). Both these propagators can be separately and individually constructed experimentally, allowing us to characterize the supersampling error with no free parameters (i.e. model independent). In these experiments $k$ is swept, and the sensing peak corresponds to the closest value of $k$ such that $k\Delta\vartheta \approx \pi$. If the construction has high fidelity error than the two lines should be identical and shifted, and hence should overlap in the panels. The results demonstrate that the construction error is low for most values of $(p, q)$, and this can be further improved by means of an optimal interpolation construction (see Sec. 2.5.1).

## 2.4 Theory of Quantum Interpolation

The key power of the interferometric CPMG spin sensing protocol is that as the number of cycles $N$ increases the signal strength increases $\propto N^2$ and the linewidth falls as $w \propto 1/N$, yielding the double advantages of higher sensitivity and higher resolution for increasing number of pulses. To achieve the goal of single protein structure reconstruction, we need to apply the sensing protocol in its optimal conditions, that is, at large $N$ and high field (high frequency $\omega_L$). Indeed, at high field, one also gains additionally in sensitivity and resolution because of an increase in statistical polarization of the nuclear spins being sensed[38], and the fact that parameters of interest like chemical shifts scale with magnetic field, thereby allowing an effective gain in sensing resolution.

Quantum interpolation overcomes hardware finite-timing resolution limits (see Table 2.1) to dramatically gain in both sensitivity and resolution.

### 2.4.1 Theory of quantum interpolation

To make things concrete, consider that the nuclear signal obtained via the NV center is interferometrically obtained by sweeping the delay $2\tau$ between pulses, and $S = \frac{1}{2}\mathrm{Tr}\left(\mathcal{U}^{\dagger}_{|0\rangle}(\tau\omega_L)\mathcal{U}_{|-1\rangle}(\tau\omega_L)\right)$ , where

$$\mathcal{U}_{|0\rangle,|-1\rangle}(\vartheta) = \mathcal{R}(\vartheta/2, \hat{\mathbf{n}}_{0,1})\mathcal{R}(\vartheta, \hat{\mathbf{n}}_{1,0})\mathcal{R}(\vartheta/2, \hat{\mathbf{n}}_{0,1}) \,, \tag{2.31}$$

refer to nuclear rotation operators conditioned on the state of the NV center, with the definition $\mathcal{R}(\vartheta, \hat{\mathbf{n}}_j) = e^{-i\vartheta\vec{\sigma}\cdot\hat{\mathbf{n}}_j/2}$. The signal peak arises when the flip angle $\vartheta = 2\tau\omega_L \approx \pi$, however due to finite timing resolution, one can only sample $\vartheta$ in

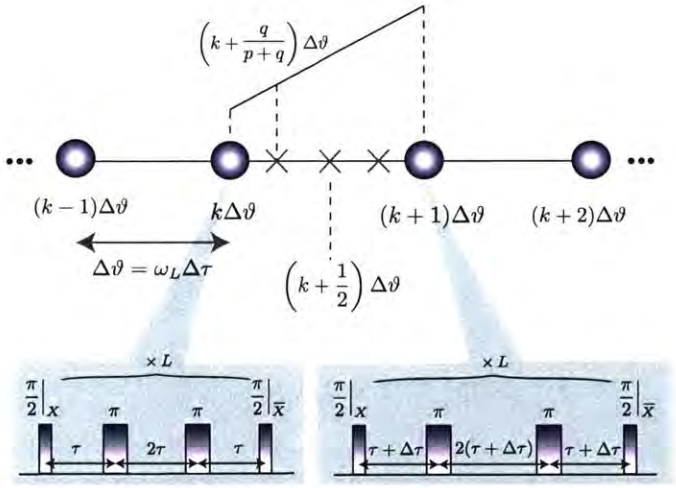


Figure 2-6: **Schematic of quantum interpolation based supersampling.** Consider that we have, due to hardware limitations, a sampling resolution $\Delta\tau$ in the delays $\tau$ that are swept in the usual CPMG sequence. If $\Delta\vartheta = \omega_L\Delta\tau$ this refers to the fact that one can only sample angles $k\Delta\vartheta$, with integral $k$ (purple points). The aim of quantum interpolation based supersampling is to effectively obtain a large number of samples $\left(k+\frac{q}{p+q}\right)\Delta\vartheta$ (crosses) between two neighboring hardware allowed samples. In principle for $N$ cycles of a CPMG sequence, the number of experimentally achievable samples with low error scales $\propto N$, allowing the effective sensing resolution to be limited only by the number of pulses that can be reliably applied.

steps of $\Delta\vartheta = \omega_L \Delta\tau$. Our technique allows one to effectively mitigate this problem through the *supersampling* of points, leading to a far finer grid than the $\Delta\tau$ resolution barrier. To develop this notion mathematically, we denote by $U_0$ and $U_1$ two hardware defined nuclear unitaries in the $|0\rangle$ manifold of the NV center,

$$U_0 := \mathcal{U}_{|0\rangle}(\pi + \delta_0 - \Delta\vartheta/2)\ ;\ U_1 := \mathcal{U}_{|0\rangle}(\pi + \delta_0 + \Delta\vartheta/2) \tag{2.32}$$

Here $\Delta\vartheta$ refers to the effective sampling interval in angle, $\Delta\tau = \Delta\vartheta/\omega_L$, and $\delta_0$ is the parameter that describes how far away we are from the sensing peak – in essence $\pi + \delta_0 - \Delta\vartheta/2 = k\Delta\vartheta$ for an integral $k$. A similar definition for Eq. (2.32) also exists in the $|-1\rangle$ subspace. Let us now assign $U_{1/2}$ the unitary arising from the product,

$$U_{\frac{1}{2}} := [U_0 U_1]^{\frac{1}{2}} \approx \mathcal{U}_{|0\rangle}(\pi + \delta_0) \tag{2.33}$$

where the subscript on $U_{1/2}$ refers to the fact we are effectively constructing a unitary, good to first order in $\Delta\vartheta$, that lies exactly "in-between" the two hardware defined unitaries $U_0$ and $U_1$, and crucially which leads to the same signal as the ideal unitary $\mathcal{U}_{|0\rangle}(\pi+\delta_0)$ to second order in $\Delta\vartheta$. The high fidelity of the approximation would imply that the signal obtained is a *faithful* representation of the signal interferometrically obtained employing $\mathcal{U}_{|0\rangle}(\pi + \delta_0)$ and $\mathcal{U}_{|-1\rangle}(\pi + \delta_0)$, which cannot be accessed due to finite sampling resolution. This can be explicitly quantified as the requirement, to second order in $\Delta\vartheta$,

$$\begin{aligned}\mathrm{Tr}\left\{\mathcal{U}^{\dagger}_{|0\rangle}(\pi + \delta_0 + \Delta\vartheta/2)\,\mathcal{U}^{\dagger}_{|0\rangle}(\pi + \delta_0 - \Delta\vartheta/2)\,\mathcal{U}_{|-1\rangle}(\pi + \delta_0 - \Delta\vartheta/2)\,\mathcal{U}_{|-1\rangle}(\pi + \delta_0 + \Delta\vartheta/2)\right\} \\ \approx \mathrm{Tr}\left\{\mathcal{U}^{2\dagger}_{|0\rangle}(\pi + \delta_0)\,\mathcal{U}^{2}_{|-1\rangle}(\pi + \delta_0)\right\}\end{aligned} \tag{2.34}$$

We will refer to the construction of Eq. (2.33) as *quantum interpolation* – we

have essentially interpolated the interval $\Delta\tau$ by employing a composite construction of hardware accessible unitaries at the endpoints of this interval. In Fig. 2-13, we develop a geometric interpretation of quantum interpolation and graphically demonstrate how the error in the propagators grow with $\Delta\vartheta$.

Generalizing this further, while hardware limits us only to sample $k\Delta\vartheta$ and $(k+1)\Delta\vartheta$, quantum interpolation allows us to *linearly* interpolate the interval $\Delta\vartheta$ to effective supersample points $\left(k+\frac{q}{p+q}\right)\Delta\vartheta$ (Fig. 2-6). Given $2N$ $\pi$-pulses in the spin sensing sequence, this can expressed as,

$$\begin{aligned} U_{\frac{q}{p+q}} &:= [U_0^p(k\Delta\vartheta+\delta_0)U_0^q((k+1)\Delta\vartheta+\delta_0)]^{\frac{N}{p+q}} \\ &\approx U_0^N\left[\left(k+\frac{q}{p+q}\right)\Delta\vartheta+\delta_0\right] \end{aligned} \tag{2.35}$$

Importantly, as $N$ increases, the number of points $q/(p+q)$ that can be supersampled ideally scales $\propto N$. This is remarkable because although the linewidth decreases $\propto 1/N$, the interpolated resolution scales $\propto N$, allowing one to completely mitigate the deleterious effects of timing resolution $\Delta\tau$. The sensing resolution is now determined only the number of pulses that can be reliably applied, and the NV coherence time $T_2$, and experimental gains in resolution approaching three orders of magnitude are now achievable. However, for this to be true, it is crucial that the approximation infidelity in Eq. (2.35) is minimized. This infidelity limits the number of supersamples one can reliably construct. In the following section, we motivate a method to quantify this infidelity, and later develop an optimal construction of $U_{\frac{q}{p+q}}$.

One can draw insight about the need for an optimal construction by performing some simple experiments: the approximation becomes worse when $p \approx q \approx N/2$ for the same reason that the construction in Eq. (2.35) has an error that grows with $N$ and $\delta$. In order to study this in detail, we characterize this experimentally in Fig.

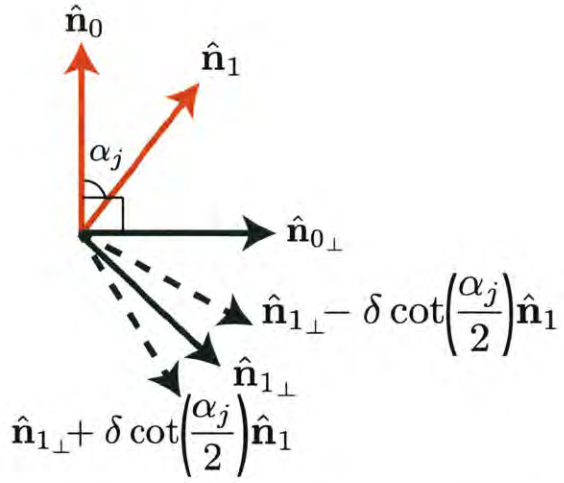


Figure 2-7: **Compensation mechanism in quantum interpolation of $U_{1/2}$.** Compensation mechanism in the construction of the quantum interpolated half-way point $U_{1/2}$. We denote the two effective axes corresponding to the operators $\mathcal{U}_{|0\rangle}$ and $\mathcal{U}_{|-1\rangle}$ in Eq. (2.9). Here the red arrows refer to the original nuclear axes $\hat{\mathbf{n}}_0$ and $\hat{\mathbf{n}}_1$ conditioned on the state of the NV, separated by the tilt angle $\alpha_j$. As a result of the CPMG sequence, these axes respectively effectively become $\hat{\mathbf{n}}_{0_\perp}$ and $\hat{\mathbf{n}}_{1_\perp}$ (green arrows). To describe the linewidth of the sensing signal one notices that the propagator $\mathcal{U}_{|0\rangle}(\pi \pm \delta)$ (Eq. (2.18)) are effectively described by the vectors $\hat{\mathbf{n}}_{1_\perp} \mp \delta \cot\left(\frac{\alpha_j}{2}\right) \hat{\mathbf{n}}_1$ (dashed green arrow), and the product $[\mathcal{U}_{|0\rangle}(\pi+\delta)\mathcal{U}_{|0\rangle}(\pi-\delta)]$ points in the direction $\hat{\mathbf{n}}_{1_\perp}$ to second order in $\delta$, forming the basis of quantum interpolation.

2-5 via deliberate undersampling. We construct the propagators,

$$[U_0^p(k\Delta\vartheta + \delta)U_0^q((k+p+q)\Delta\vartheta + \delta)]^{\frac{N}{p+q}} \approx U_0^N((k+q)\Delta\vartheta + \delta) \tag{2.36}$$

Both the left and right hand sides of the equation can be independently constructed experimentally. If the approximation fidelity in Eq. (2.36) is good, the signals should be identical in both cases. The experimental results show a very good overlap, demonstrating that the construction error is low for most values of $(p, q)$. However, the error is found to slightly increase away from the sensing peak. This is an artifact

of the construction of Eq. (2.36) being non-optimal. We shall show below that to minimize the error one needs to obtain a construction is one that minimizes the effective *distance* at which the effective error compensation occurs.

### 2.4.2 Analytical results for quantum interpolated $U_{1/2}$

Let us now evaluate fully analytically the quantum interpolation construction of the half-way-sample $U_{1/2}$, consisting of $2N$ pulses of the form,

$$U_{1/2} = \left[\mathcal{U}_{|0\rangle}(\pi + \Delta\vartheta/2)\mathcal{U}_{|0\rangle}(\pi - \Delta\vartheta/2)\right]^{N/2}. \tag{2.37}$$

This can be effectively translated to a pulse sequence following Fig. 2-1 **(A)**, consisting of pulses that are unequally spaced. To illustrate the mechanism of the interpolation in Eq. (2.37), consider that we had determined that the origin of the finite linewidth of the spin sensing sequence is the fact that away from the signal peak ($\delta = 0$) there is effectively destructive interference in the flip angle $\alpha_j$ into $\alpha'_j$ (see Eq. (2.19)) leading to a loss of signal contrast. Now if the effective flip angle $\alpha'_j$ can be made *independent* of $\delta$, then the signal linewidth is proportional to a constant to second order. This is precisely what occurs through the quantum interpolation construction in Eq. (2.37).

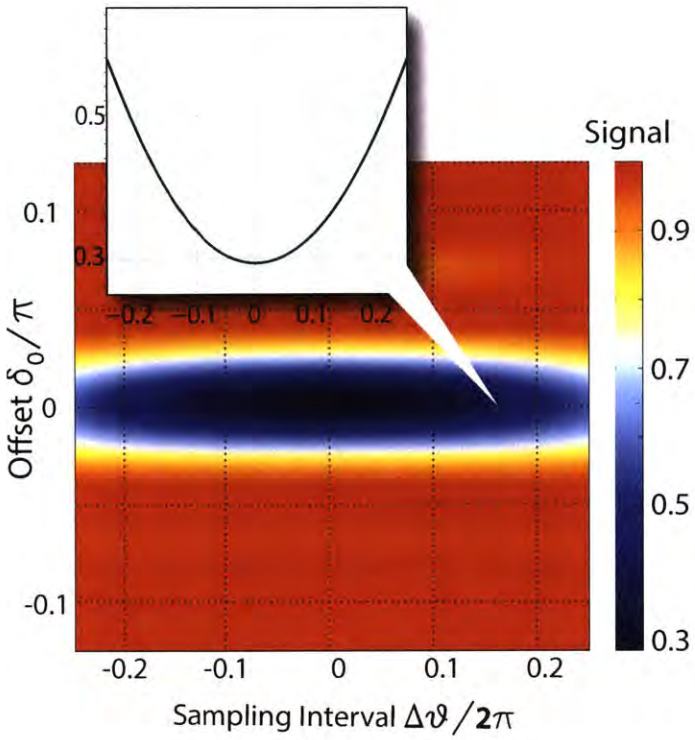


Figure 2-8: **Robustness of quantum interpolation.** In this panel, we numerically study the quantum interpolation construction for different values of $\delta_0$. More specifically, here we consider the signal obtained using the quantum interpolated unitary $U_{1/2} = [U_0 U_1]^{1/2} \approx \mathcal{U}_{|0\rangle}(\pi + \delta_0)$, for different values of $\delta_0$. The signal is calculated with $\alpha_j = 0.1$ rad following Eq. (2.16) and is represented in color. The graph indicates, as is our expectation from Eq. (2.34), that the interpolated unitary faithfully produces the same signal as the target unitary $\mathcal{U}_{|0\rangle}(\pi + \delta_0)$ independent of the choice of $\delta_0$. Moreover, the deviation in the signal goes second order in $\Delta\vartheta$ (inset).

To describe this in detail, for simplicity, once again one can use a first order expansion to discern the physics of the problem. Evaluating the effective propagators, for effectively $N/2$ cycles (keeping the number of pulses the same as in Eq. (2.18)),

we obtain

$$\begin{aligned}
\left[\mathcal{U}_{|0\rangle}(\pi+\Delta\vartheta/2)\mathcal{U}_{|0\rangle}(\pi-\Delta\vartheta/2)\right]^{N/2} &\approx \mathbb{1}\cos N\alpha_j + i\frac{\sin N\alpha_j}{\sin 2\alpha_j}\,\boldsymbol{\sigma}\cdot\left[-\hat{\mathbf{n}}_{1_\perp}(2\cos\alpha_j'\,\sin\alpha_j)\right. \\
&- \left.\Delta\vartheta\sin\alpha_j\,(1+\cos\alpha_j)(\hat{\mathbf{n}}_{1_\perp}\times\hat{\mathbf{n}}_1)\right] \\
\left[\mathcal{U}_{|-1\rangle}(\pi+\Delta\vartheta/2)\mathcal{U}_{|-1\rangle}(\pi-\Delta\vartheta/2)\right]^{N/2} &\approx \mathbb{1}\cos N\alpha_j + i\frac{\sin N\alpha_j}{\sin 2\alpha_j}\,\boldsymbol{\sigma}\cdot\left[\hat{\mathbf{n}}_{0_\perp}(2\cos\alpha_j'\,\sin\alpha_j)\right. \\
&+ \left.\Delta\vartheta\sin\alpha_j\,(1+\cos\alpha_j)(\hat{\mathbf{n}}_{0_\perp}\times\hat{\mathbf{n}}_0)\right]. \qquad (2.38)
\end{aligned}$$

Remarkably, the dependence of $\alpha_j'$ on the $\Delta\vartheta$ and the destructive interference in Eq. (2.19) is now removed (compare with Eq. (2.38) with Eq. (2.18)). The sensing signal as a function of $\Delta\vartheta$ is now

$$\begin{aligned}
S &= \cos^2 N\alpha_j - \sin^2 N\alpha_j\cos\alpha_j \\
&- \frac{\sin^2 N\alpha_j}{\sin^2 2\alpha_j}\left[\Delta\vartheta^2\sin^2\alpha_j\,(1+\cos\alpha_j)^2\,(1-\cos\alpha_j)\right]. \qquad (2.39)
\end{aligned}$$

The first line is exactly the signal magnitude obtained at the signal peak – but now the width is set weakly by the second line that goes as $\Delta\vartheta^2$. This quantum interpolation compensation mechanism has also a simple geometric interpretation (Fig. 2-7) – similar to a spin echo[87], the linear dependence on $\Delta\vartheta$ leading to the destructive interference in Eq. (2.19) is removed by employing another vector with the opposite sign, giving an effective propagator that is independent of $\Delta\vartheta$.

We note that while in the above analysis we considered the case of the offset $\delta_0 = 0$ in Eq. (2.32), we can also numerically evaluate that the quantum interpolation construction for $U_{1/2}$ is robust to different values of offset $\delta_0$. This is shown in Fig. 2-8, where the shading represents the signal obtained as a function of $\Delta\vartheta$ for different $\delta_0$. It is evident that for any slice in the $\delta_0$ dimension, the signal falls off quadratically in

$\Delta\vartheta$, a reflection of the fact that to first order the quantum interpolation compensation mechanism (Fig. 2-7) is still robust.

### 2.4.3 Evaluating the fidelity of quantum interpolation

As a clarifying calculation, let us evaluate how close the unitary out of quantum interpolation is close to the ideal one. Using a trace norm measure, we show that this is approximately second order in $\Delta\vartheta$. The ideal propagator is $U_{id} = \mathcal{U}^2_{|0\rangle}(\pi) = \exp(-i2\alpha_j \sigma \cdot \hat{\mathbf{n}}_{1\perp})$. Comparing with the quantum interpolated expression, we have that the trace norm,

$$\begin{aligned} F &= \mathrm{Tr}\left\{\mathcal{U}_{|0\rangle}(\pi + \Delta\vartheta/2)\mathcal{U}_{|0\rangle}(\pi - \Delta\vartheta/2)U_{id}^{\dagger}\right\} \\ &= \cos 2\alpha_j \left[\sin^2(\Delta\vartheta/2) + \cos^2(\Delta\vartheta/2)\cos 2\alpha_j\right] \\ &+ 2\sin 2\alpha_j \, \sin\alpha_j \, \cos\alpha'_j \cos(\Delta\vartheta/2) \\ &\approx 1 + \mathcal{O}(\Delta\vartheta^2) \end{aligned} \tag{2.40}$$

Note that except the $\cos\alpha'_j$ term, all the other terms are second order or more in $\Delta\vartheta$. The $\cos\alpha'_j$ term too is weighted by $\sin^2\alpha_j$, and for most practical cases of spin sensing where $\alpha_j$ is small, this term has a negligible contribution. Hence to a very good approximation, the quantum interpolation expression is good to first order in $\Delta\vartheta$. A graphical comparison of the unitaries obtained via quantum interpolation to the ideal one is shown in Fig. 2-13.

### 2.4.4 Comparison with Baker-Campbell-Hausdorff result

Let us now demonstrate that the effectiveness of the quantum interpolation construction cannot be seen as a simple manifestation of the zeroth order of the Baker-

Campbell-Hausdorff (BCH) expansion[89,90]. The zeroth order BCH expression does not care for cross terms or commutators between the two unitaries, and can be written down as, $\left[\mathcal{U}_{|0\rangle}(\pi+\Delta\vartheta/2)\mathcal{U}_{|0\rangle}(\pi-\Delta\vartheta/2)\right] \approx U_{\rm BCH}$, with,

$$\begin{aligned} U_{\rm BCH} &= \exp\left[-i\alpha_j'\boldsymbol{\sigma}\cdot(\hat{\mathbf{n}}_{1+}+\hat{\mathbf{n}}_{1-})\right] \\ &= \exp\left[i2\alpha_j'\boldsymbol{\sigma}\cdot\frac{-\hat{\mathbf{n}}_{1\perp}\sin\alpha_j\,\cos(\Delta\vartheta/2)}{\sin\alpha_j'}\right] \end{aligned} \tag{2.41}$$

where $\hat{\mathbf{n}}_{1\pm}$ are the *exact* effective vectors in the expressions for unitaries away from the sensing peak (Eq. (2.18)),

$$\begin{aligned} \hat{\mathbf{n}}_{1+} &= \frac{1}{\sin\alpha_j'}\left[\hat{\mathbf{n}}_{1\perp}\sin\alpha_j - \hat{\mathbf{n}}_0\sin(\Delta\vartheta/2)\,(1+\cos\alpha_j)\right]\cos(\Delta\vartheta/2) \\ \hat{\mathbf{n}}_{0+} &= \frac{1}{\sin\alpha_j'}\left[\hat{\mathbf{n}}_{0\perp}\sin\alpha_j - \hat{\mathbf{n}}_1\sin(\Delta\vartheta/2)\,(1+\cos\alpha_j)\right]\cos(\Delta\vartheta/2) \end{aligned} \tag{2.42}$$

For $N/2$ cycles of the CPMG experiment, this has the form

$$U_{\rm BCH}^{N/2} \approx \exp\left[iN\alpha_j'\cos(\Delta\vartheta/2)\frac{\sin\alpha_j}{\sin\alpha_j'}(\boldsymbol{\sigma}\cdot-\hat{\mathbf{n}}_{1\perp})\right]. \tag{2.43}$$

Eq. (2.43) immediately reveals that the quantum interpolation compensation effect in Eq. (2.38) cannot be captured by a simple BCH analysis. This is because $\Delta\vartheta$ cannot be seen as a perturbative parameter in the expressions, and in general the BCH expansion does not converge[91]. More intuitively, the flip angle compensation in Eq. (2.19) that was crucial to remove the dependence of $\delta$ to bring back the bare flip angle of $\alpha_j$ in Eq. (2.38) is no longer present. Instead the flip angle is now $\alpha_j'\cos(\Delta\vartheta/2)\frac{\sin\alpha_j}{\sin\alpha_j'}$, which only approaches the right expression when $\alpha_j'$ is small. Note however that we have made no assumptions in our analysis about $\alpha_j$ being

| Instrument | Manufacturer | Timing res. $\Delta\tau$ | Jitter | Cost | $\Delta\vartheta$ | Q-value |
|---|---|---|---|---|---|---|
| AWG70001A[92] | Tektronix | 20 ps | 250 fs | $100,000 | $\pi/7378$ | 1174.4 |
| AWG5002C[93] | Tektronix | 1.76 ns | 5.0 ps | $32,300 | $\pi/83$ | 13.3 |
| WX1284C[94] | Tabor | 1 ns | 2.0 ps | $30,000 | $\pi/147$ | 23.5 |
| PulseBlaster ESR-PRO[95] | SpinCore | 2.0 ns | 100 fs | $5,000 | $\pi/73$ | 11.7 |

Table 2.1: **Representative examples of timing instruments** commonly used for spin sensing experiments, and their respective timing resolution $\Delta\tau$. There is a steep increase of instrument price with improved resolution. For the special case of a single $^1$H nuclear spin that is 2nm away from the NV center, and at a field of 0.5T, we specify also the corresponding values of $\Delta\vartheta$ and the bare Q-value. Note that the Q-value is rather poor for instruments with a few nanosecond $\Delta\tau$, while for sensing structural features such as chemical shifts one requires a Q-value approaching atleast $10^5$ (see Table 2.2). Quantum interpolation based supersampling can provide significant boosts in Q over these bare values. In the table, we also specify the RMS timing jitter of these instruments that ultimately might limit the achievable resolution via quantum interpolation.

small, and hence the simple zeroth order BCH analysis leads to a larger error than a more complete analysis that also includes the effect of commutators or cross terms.

### 2.4.5 Survey of hardware and comparison with supersampling

Table 2.1 summarizes a list of hardware used for spin sensing experiments, and their respective timing resolutions. In our experiments we used the SpinCore PulseBlaster[95] and Tabor Arbitrary Waveform Generator[94] with timing resolutions of 2ns and 1ns respectively. Using the latter instrument, through quantum interpolation based supersampling we were able to experimentally demonstrate a resolution of 8.9ps, a boost by a factor of 112 (Fig. 2-17). Note that random timing jitter of these instruments sets the ultimate achievable resolution through supersampling.

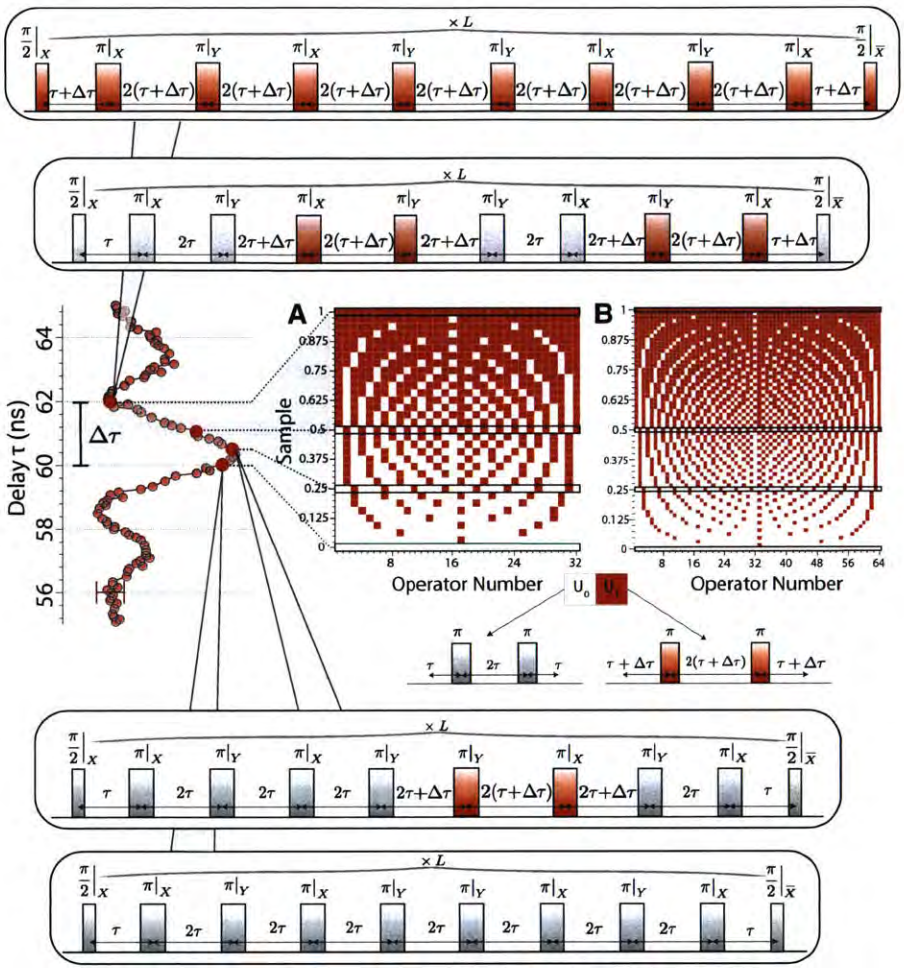


Figure 2-9: **Pulse sequence construction for optimal quantum interpolation.** Shown is the optimal quantum interpolation supersampling construction for different samples for **(A)** N=4 and **(B)** N=8 cycles of an XY8 sensing sequence. Here "sample" refers to point to be interpolated between two hardware limited intervals as the fraction of the timing resolution $\Delta\tau$. For reference example experimental data is shown (red circles, corresponding to Fig. 2-1**(B)**). Here $\Delta\tau = 2$ns, and in each such interval one could effective supersample proportional to the number of pulses applied. To experimentally construct the optimal interpolated sequence for a sample corresponding a particular row of the matrix, one applies the sequence of operators $U_0$ (white) or $U_1$ (red) from left to right. The boxed inset panels denote the pulse sequences corresponding to four example samples – $\{0, 1/4, 1/2, 1\}$.

## 2.5 Optimal Quantum Interpolation construction

### 2.5.1 Optimal supersampling construction

The naive construction based on the approximation of Eq. (2.35) is not optimal, and carries the error that finally limits the number of additional supersamples that reliably constructed. Thus we develop an optimal construction for quantum interpolation to overcome this problem. The optimal construction sets the *order* of operators $U_0$ and $U_1$ used to interpolate a supersample $q\Delta\tau/(p+q)$ with the lowest amount of error.

### 2.5.2 Error in sequence construction: Semiclassical analysis

The simplest method to characterize the error of supersampling sequences is through a semiclassical analysis using the filter formalism of dynamical decoupling [96,97,98], as it enables a simple optical analogy [63]. Here we assume a classical noise field acting on the NV center, yielding the Hamiltonian $\mathcal{H}_n = bE_z(t)S_z$. Here $E_z(t)$ is a classical noise field, assumed to be Gaussian-distributed with zero mean. For instance, $E_z(t)$ might approximate the spin noise for an ensemble of weakly coupled nuclear spins. For stationary noise, the time-correlation is $\langle E_z(t)E_z(t+\tau)\rangle = g(\tau)$, with the noise spectral density $S(\omega) = \frac{1}{\sqrt{2\pi}}\int_{\infty}^{\infty} dt g(t)e^{-i\omega t}$. For example, the spectral density function due to nuclear spin noise is centered at their resonance frequency, with zero linewidth if considering a single nuclear spin. In the toggling frame, each $\pi$ pulse in the control sequence flips the sign of the noise Hamiltonian $\mathcal{H}_n$, leading to the effective time-dependent Hamiltonian $\widetilde{\mathcal{H}} = bf(t)E_z(t)S_z$. The time-domain filter function $f(t)$ switches between $\pm 1$ at each pulse. The decay of the coherence of the

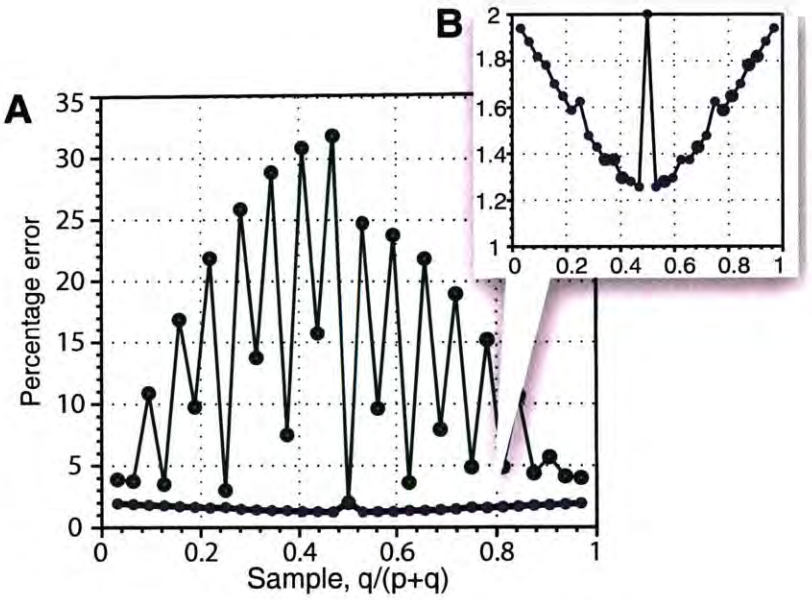


Figure 2-10: **Performance of optimal quantum interpolation.** We represent the percentage errors (specified in units of $\Delta\tau/4\tau$) of the construction of a supersample $[q/(p+q)]\,\Delta\tau$ via quantum interpolation using two hardware defined unitaries $U_0$ and $U_1$, and an time resolution of $\Delta\tau$. Here we consider $N = 16$ cycles of the CPMG sensing sequence, giving a total of 32 possible supersamples. The error is calculated from the effective area under the time domain error function $\epsilon$ following Fig. 2-11. **(A)** The green points denote the naive construction $U_0^p U_1^q$, where the errors accumulate very quickly. The purple line and points instead denote the case of the optimal construction following Fig. 2-16, where the error of all samples is less than the half-way-sample (zoomed in the inset **(B)**). Hence the optimal construction can reliably produce different supersamples with low effective error (see also Fig. 2-12).

NV center is then given by the overlap integral $\chi(t) = \frac{\sqrt{2\pi}|b|^2}{2} \int_{-\infty}^{\infty} |F(\omega)|^2 S(\omega) d\omega$, between the frequency domain filter $F(\omega)$ (the Fourier transform of $f(t)$) and the noise spectrum.

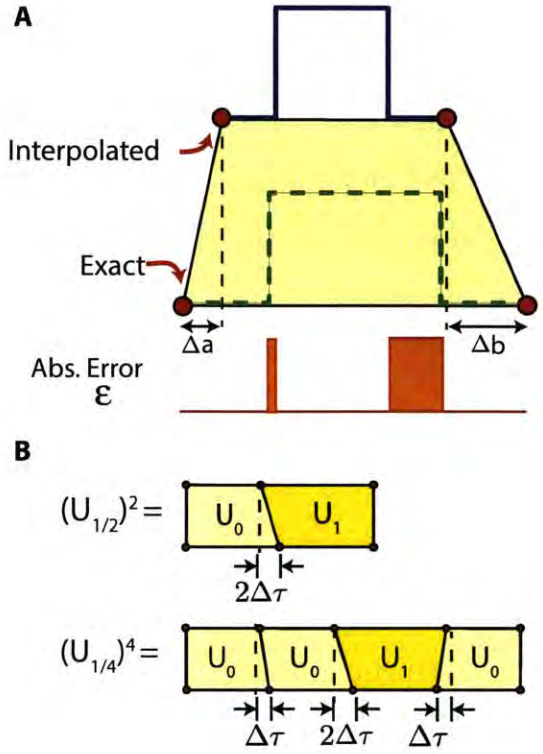


Figure 2-11: **Evaluating construction error via the filter formalism. (A)** Here the upper rail of the trapezium represents the interpolated construction (approximate), and the lower rail represents the target construction (ideal) (see also Fig. 2-16). The circles denote the *total* period of the corresponding interpolated (blue line) and exact time domain filter functions (green dashed lines), corresponding to Fig. 2-1**(C)**. $\Delta a$ and $\Delta b$ denote the deviations of the interpolated filter from the exact one, and the net error is then $\epsilon = \left|-\frac{3}{4}\Delta a + \frac{1}{4}\Delta b\right| + \left|-\frac{1}{4}\Delta a + \frac{3}{4}\Delta b\right|$, which is minimized by the optimal supersampling construction. **(B)** Optimal constructions for the quantum interpolated points one-half and one-quarter between two hardware defined samples.

Now, given the finite timing resolution $\Delta\tau$, we can only obtained two different

time-domain filter functions with total time separated by $4\Delta\tau$. The aim of quantum interpolation is to obtain a filter that leads to the same signal as the effective filter that is "in-between" these two hardware separated filters. While the error arises from differences between the ideal and interpolated $F(\omega)$, to evaluate the how closely this construction is a faithful representation of the ideal filter, by Parseval's theorem, one just needs to determine the deviation $\epsilon$ of the interpolated time-domain filter from the ideal one.

For the case of $U_{1/2}$, the relative error is just $\Delta\tau/2\tau$, which is proportional to the size of the sampling interval. This provides a convenient starting point to determine the *optimal* interpolation construction for any arbitrary sampling point $\frac{q}{p+q}\Delta\tau$: Essentially the optimal construction is the one that minimizes the *net* deviation $\epsilon$ of the time-domain interpolated filter from the ideal one. Fig. 2-11 offers a simple prescription to calculate this error; the upper rail represents the filter corresponding to the quantum interpolation construction out of $U_0$ and $U_1$ operators, while the lower rail represents the ideal filter. The total length for both rails is identical – this ensures that the filter does indeed sample the correct frequency. Comparing each filters for each successive application of operators (i.e. piece wise), one obtains trapezium shaped blocks that can be pieced together to evaluate the error of a supersampling sequence. The net error of each of these blocks has the form (see Fig. 2-11),

$$\epsilon = \left|-\frac{3}{4}\Delta a + \frac{1}{4}\Delta b\right| + \left|-\frac{1}{4}\Delta a + \frac{3}{4}\Delta b\right| \tag{2.44}$$

The optimal constructions, for instance shown in the lower panels of Fig. 2-11 for $U_{1/2}$ and $U_{1/4}$ minimize this error. Note that the error in Eq. (2.44) is maximized in

the situation where $\Delta a$ is negative, and $\Delta b$ positive, giving the bound,

$$\epsilon \leq (\Delta a + \Delta b) \tag{2.45}$$

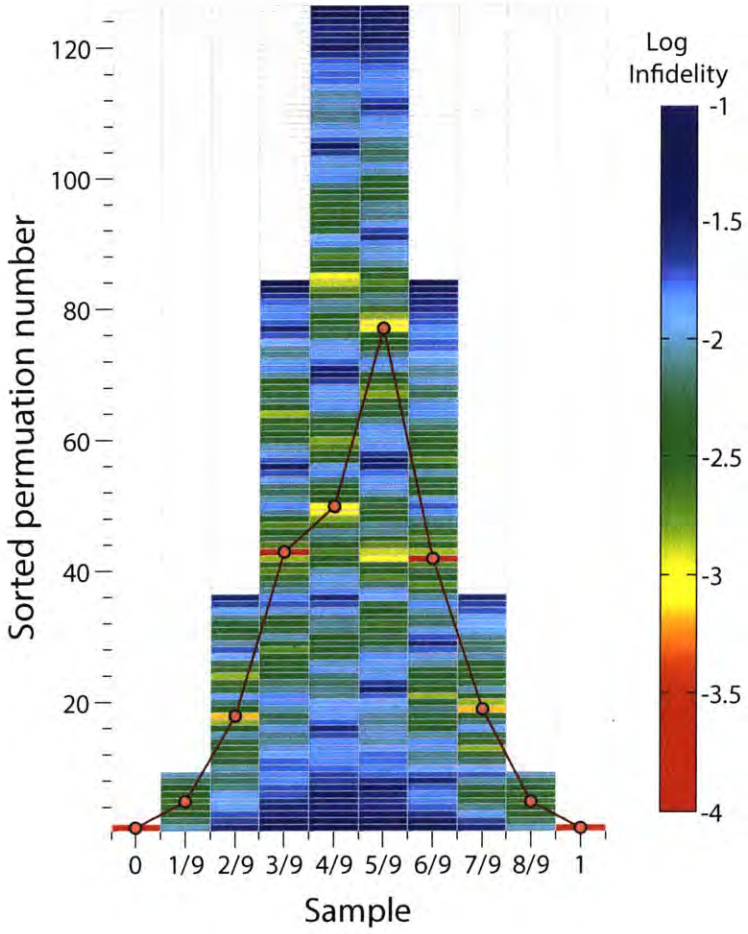


Figure 2-12: **Evaluating optimality of quantum interpolation constructions.** Figure evaluates the optimal quantum interpolation construction for $N = 9$ cycles of the CPMG sequence. For every sample, of the form $p\Delta\tau/N$, for integral $p$, we evaluate the fidelity of the interpolated unitary obtained from hardware defined unitaries $U_0$ and $U_1$ to the target unitary, for *every* possible permutation of $U_0$ and $U_1$. For clarity, for instance, for the sample $1/9$, there are 8 permutations of the sequence $[U_0 U_1^8]$, and we study the infidelity of each of these permutations (second bar). Here we evaluated the mean infidelity over the range $\delta_0 \in [-2\Delta\vartheta, 2\Delta\vartheta]$, for $\Delta\vartheta = \pi/20$ and $\alpha_j = 0.1$ rad. The permutations are sorted down to up by Hamming weight, i.e. in increasing decimal order of their sequence strings. The colors represent the log of the infidelity, and the smaller number represents that the constructed unitary is better, i.e. has lower error. The optimal construction obtained using the Algorithm in Fig. 2-15 are shown in the by the orange circles. Numerically, we find that the construction from Fig. 2-15 does indeed capture the optimal possible permutation.

### 2.5.3 Analysis via quantum mechanical propagators

While in the previous section we derived the optimal construction based on a semi-classical (filter) analysis, here we show that the optimal construction is also a faithful approximation of the desired evolution for the *quantum* systems that the quantum sensor is probing.

Specifically, we consider the infidelity of quantum interpolation operators with respect to the the ideal propagator and perform a numerical analysis of the infidelity of *every* permutation, for a broad range of values of $\delta_0$ close to the sensing peak. In general, we find that the plot is qualitatively similar for different values of $\Delta\vartheta$, the range of $\delta_0$, and the value of $\alpha_j$.

### 2.5.4 Geometric representation of quantum interpolation

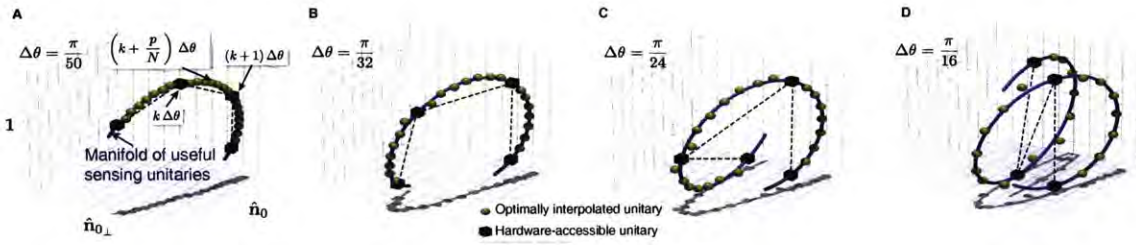


Figure 2-13: **Quantum interpolation from a geometric perspective.** The blue line indicates the ideal manifold of sensing unitaries, while the black squares represent the hardware accessible unitaries (see also Fig. 2-1(**A**)). We represent unitaries as points in the 3D space spanned by the operators $\{\mathbb{1}, \hat{\mathbf{n}}_0, \hat{\mathbf{n}}_{0_\perp}\}$. The projection of the missing dimension, $(\hat{\mathbf{n}}_0 \times \hat{\mathbf{n}}_{0_\perp})$ is small and only causes the norm of the vector to be smaller than one. Without quantum interpolation, the signal obtained upon sweeping $\delta_0$ corresponds to the dashed black line. The green circles are the unitaries resulting from quantum interpolation with two successive hardware accessible samples following the optimal construction, where one seeks to construct the ideal unitaries $\mathcal{U}^N_{|0\rangle}(\pi - \delta_0 + k\Delta\vartheta)$, with $\delta_0 \in \{-\Delta\vartheta, 0, \Delta\vartheta, 2\Delta\vartheta\}$. Here $N = 8$ leading to 8 supersamples in each $\Delta\vartheta$ interval, and we considered $\alpha_j = 0.1$ rad. The different panels denote different values of $\Delta\vartheta$. The success of quantum interpolation is evident from the fact that the two result of interpolation closely matches the target unitaries over the entire manifold, even for large $\Delta\vartheta$.

While in Fig. 2-1 we introduced a geometric picture of quantum interpolation as based only on a simple, visual intuition, here we provide more details of that representation, showing that it is indeed a faithful and quantitative representation of the

unitary operators involved in quantum interpolation. We represent the unitaries obtained from a quantum sensing experiment as vectors in 4D space [99]. As we consider only the *manifold* of the unitaries obtained by CPMG-like sequences as one sweeps through the sensing peak, we can reduce the space to 3 dimensions only (Fig. 2-13 and Fig. 2-1(**A**)). Indeed, from Eq. (2.38), the projection of the unitaries in the $(\hat{\mathbf{n}}_0 \times \hat{\mathbf{n}}_{0_\perp})$ dimension is small, and the unitaries can be represented to a very good approximation in the three dimensional space spanned by the vectors $\{\mathbb{1}, \hat{\mathbf{n}}_0, \hat{\mathbf{n}}_{0_\perp}\}$. Due to finite timing resolution one can only sweep this manifold in discrete steps (black squares in Fig. 2-13), but through quantum interpolation one can sample this manifold almost continuously (green circles). This is shown in Fig. 2-13 for increasing values of $\Delta\vartheta$ from left to right. In these simulations, we consider the construction of the ideal unitaries $\mathcal{U}_{|0\rangle}^{N}(\pi - \delta_0 + k\Delta\vartheta)$ via the optimal quantum interpolation construction, where $\delta_0$ takes values $\delta_0 \in \{-\Delta\vartheta, 0, \Delta\vartheta, 2\Delta\vartheta\}$ about the sensing peak, and we considered $\alpha_j = 0.1$ rad and $N = 8$ CPMG cycles. It is evident that for small $\Delta\vartheta$ quantum interpolation accurately samples the exact manifold (blue line), while for increasing $\Delta\vartheta$ the approximation becomes slightly worse. It is remarkable that even with the rather large $\Delta\vartheta = \pi/16$ (compare with Table 2.1 for those corresponding to usual hardware) quantum interpolation very closely tracks the ideal manifold, a reflection of the second order error in Eq. (2.40).

### 2.5.5 Scaling of number of supersamples

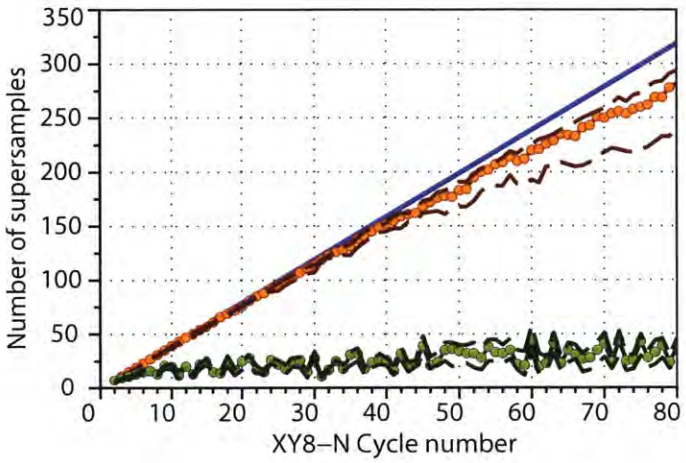


Figure 2-14: **Gains in resolution via supersampling.** Here we consider $\alpha_j = 0.1$ rad and $\Delta\vartheta = \pi/20$, which for conventional magnetic fields used for spin sensing corresponds to a timing resolution $\Delta\tau$ of a few nanoseconds (typical for hardware, for instance in Table 2.1). We consider the scaling of the number of supersamples possible via quantum interpolation constructions for XY8-N sequences. The maximum number of samples (blue line) grows linearly with $N$. The green line quantifies the samples obtained via the construction of Eq. (2.35), where the points indicate a fidelity better than 0.9 over a range of $\delta \in [-\Delta\vartheta/2, \Delta\vartheta/2]$, while the dashed lines indicates fidelity >0.85 (upper dashed line) and >0.95 (lower dashed line). As is evident, the number of samples grows $\propto N$ for small $N$, before saturating. The optimized construction obtained in Sec. 2.5.1 is shown in the red points. Decreasing $\Delta\vartheta$ further (see Fig. 2-13) will lead to an even larger number of supersamples before saturation. The numerical results indicate that one can reliably achieve resolution gains by over three orders of magnitude using quantum interpolation.

Let us now characterize the theoretical number of supersamples one can achieve via quantum interpolation, and the effective boost in sensing resolution. From the geometric construction of the algorithm in Fig. 2-16, it is evident that for $N$ cycles of the CPMG sequence, one has a set of $N$ points on the right half circle, and hence one can obtain a total $N$ supersamples in every $\Delta\tau$ interval. This is also denoted in Fig. 2-9, where for an XY8-N sequence one can theoretically achieve a total of $4N$ supersamples.

However, given an maximum error bound, the number of supersamples will at some point deviate from this linear scaling. To study this in detail, we performed numerical simulations (see Fig. 2-14) considering a spin with $\alpha_j = 0.1$ rad and $\Delta\vartheta = \pi/20$ (typical for hardware, for instance in Table 2.1), and considered the number of supersamples that have a fidelity better than 0.9 (points), 0.95 and 0.85 (dashed lines) over a range of $\delta \in [-\Delta\vartheta/2, \Delta\vartheta/2]$. The fidelity was calculated by evaluating the overlap of the interpolated unitary with the ideal one, similar to Eq. (2.40). In Fig. 2-14, the blue line shows the theoretical maximum number of supersamples grows linearly with $N$, while via the optimal construction one can achieve a linear scaling upto $N = 200$ (green points), allowing for an effective increase in resolution by over two orders of magnitude. Decreasing $\Delta\vartheta$ further (see Table 2.1) will increase the range over which the scaling of supersamples is linear. Note that the naive construction (Eq. (2.35)) also has a linear scaling for small $N$, but it quickly saturates after $N > 15$ due to the accumulation of error, pointing out again the need for the optimal construction.

Ultimately then, through the optimal quantum interpolation construction, the resolution achievable can be made largely dependent only on the number of pulses that can be reliably applied to the system. The linear scaling of the number of samples can exactly and completely mitigate the deleterious effects of finite resolution.

### 2.5.6 Algorithm for optimal supersampling construction

**Algorithm 1** : Construction of the optimal interpolation sequence

**procedure** OPTIMALCONSTRUCTION

Set loop iteration counter $m \leftarrow 0$

Optimal sequence string $U \leftarrow$ null

***loop***:

*Propagate* $m \leftarrow m +$ sample

**if** $|m| \leq 1/2$ **then** Append $U_0$ operator to sequence

**else**

Append $U_1$ operator to sequence

*Reflect* $m \leftarrow m - 1$

**while** $m \neq 0$ **do**

**goto *loop***

**end procedure**

Figure 2-15: **Algorithm for optimal quantum interpolation construction.** The algorithm produces the optimal sequence of $U_0$ and $U_1$ operators to interpolate the desired sampling point. In the algorithm, "sample" stands for a fraction between 0 and 1 corresponding to the desired supersample time. See Sec. 2.A for an explicit MATLAB implementation of this algorithm.

Let us now determine the supersampling construction that minimizes the error $\epsilon$ in Eq. (2.44) – the deviation from the ideal filter. For a sample of the form sample $= q/(p+q)$, we obtain the optimal string of operators $U_0$ or $U_1$ with the minimization

evaluated at the end of each applied operator following Fig. 2-11. We note that while in principle one has to minimize the deviation of the time domain filters edge to edge in Fig. 2-11, however it is sufficient to use a simple approach of minimizing deviations in the total periods. A simple algorithm that achieves this has the pseduocode in Fig. 2-15. The optimal construction is shown in Fig. 2-9, where the colors represent the operators $U_0$ or $U_1$. The panels describe the construction of different supersamples, the total number of which scales linearly with the number of pulses (shown are the examples of XY8-4 and XY8-8).

A geometric interpretation of this algorithm, similar to Householder rotations [100,99] is described in Fig. 2-16. The required sample can be represented as a phasor on a circle, at an angle $\pi \times$ (sample). The algorithm is composed of two steps – *propagate*, or *propagate and reflect*, associated with the application $U_0$ or $U_1$ operators respectively. Geometrically, one keeps propagating along points on the circle that differ by the required sample, and reflect every time when one trespasses into the left half circle (shaded region in Fig. 2-16). The algorithm ends when the phasor returns to the starting point. It is evident then for a sample $\Delta\tau/N$, one needs $N$ operators in the construction.

As the optimal construction compensate the error at each step, it is significantly better than the naive construction $U_0^p U_1^q$ that lets the error accumulate (see Fig. 2-10). Consequently, the number of supersamples achievable via quantum interpolation scale linearly with the number of pulses to a large extent (Fig. 2-14). More interestingly, this also implies that the error of all supersamples is approximately the same and bounded by the error of the $U_{1/2}$ as we shall show below.

### 2.5.7 Error of the Optimal Quantum Interpolation Construction

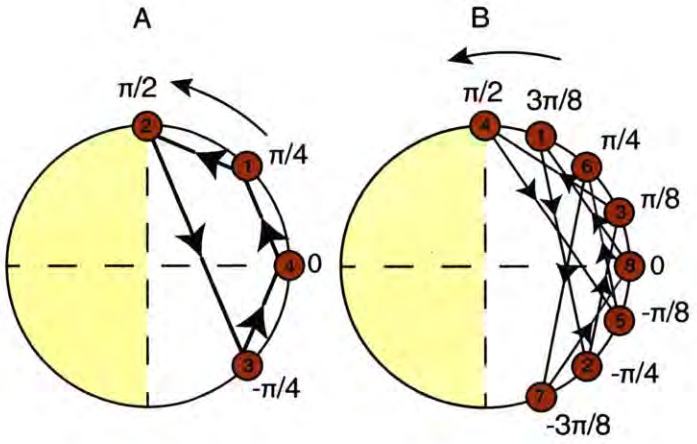


Figure 2-16: **Geometric representation of the optimal construction,** for two particular sampling times **(A)** $\Delta\tau/4$ and **(B)** $3\Delta\tau/8$. We represent the desired sample as phasor at angle $\pi \times$ sample on a circle (orange circles). The left half plane (LHP) of the circle (shaded) is considered forbidden. Starting with an initial loop counter $m = 0$, we propagate the algorithm by forming the phasor $m \to m +$ sample (arrows); and so long as we don't pass into the LHP we assign to this the operator $U_0$. In the opposite case, we assign $U_1$, and reflect the phasor about the origin. The algorithm ends when we finally return to the starting position. The numbers in the orange circles indicate the progression of the algorithm. This geometric representation also allows an intuitive understanding of why the error of all samples is almost the same (see Fig. 2-10).

While in principle we expect that each quantum interpolation construction, achieving supersampling at a different sampling point, might have a different error, here we show that for the same number of pulses, the error is always bounded by the error of $U_{1/2}^N$ (see inset of Fig. 2-10). For clarity, let us first consider the simple case when $N = 2^k$ and calculate the error of any of the supersamples. From the geometric picture in Fig. 2-16, all samples of the form $\ell\Delta\tau/2^k$ for integral $(\ell, k)$ traverse the *same* set of points on the right half circle. Since $\Delta a$ and $\Delta b$ are now constrained to be points on the right half circle in Fig. 2-16 the net error can be calculated from Eq. (2.45) to be

$$\begin{aligned} \epsilon &\leq 2\Delta\tau \times 2(\text{sum of all points on right half circle}) \\ &= 2\Delta\tau \times 2\left(2\sum_{\ell=0}^{2^{(k-1)}-1}\frac{\ell}{2^k}+\frac{1}{2}\right) = 2^k(2\Delta\tau), \end{aligned} \tag{2.46}$$

Hence the net error is bounded by $\epsilon \leq 2^{k-1}(4\Delta\tau)$, exactly the error of $U_{1/2}^{2^k}$, which is the construction of the half-way-sample with the same number of pulses. An analogous calculation and graphical approach can be made for general $N$, and once again it is easy to show that that the error of all supersamples is bounded by that of $U_{1/2}$. This is convenient because it allows a simplification of the error analysis of supersampling, which is bounded by the analytical results obtained in Sec. 2.4.2, where we evaluated the error of $U_{1/2}$ and quantified its dependence on the size of the sampling interval $\Delta\tau$.

## 2.6 Experimental Demonstrations of Quantum interpolation

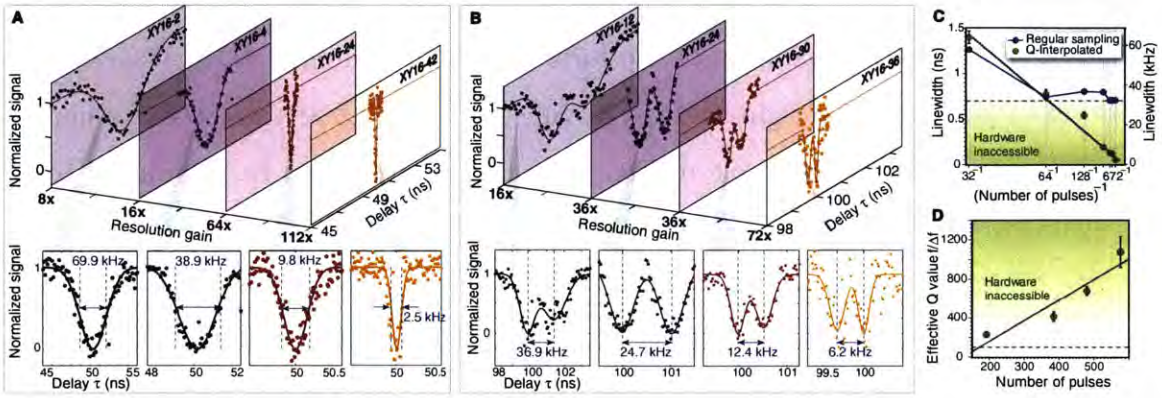


Figure 2-17: **High resolution sensing and spectroscopy.** (**A**) *Detection of the spurious harmonic of an AC magnetic field via quantum-interpolated XY16 sequences.* The incoherent external magnetic field is generated by an AC current at $f_{\mathrm{AC}} = 2.5$MHz through a 20-$\mu$m wire located in the vicinity of the NV center. Our hardware limitation ($\Delta\tau = 1$ns) translates in a frequency resolution of $\Delta f_{\mathrm{AC}} = 35.3$kHz, and would cause a severe suppression of the detected signal as its linewidth decreases linearly with the number of $\pi$-pulses. In the rightmost panel, quantum interpolation enables supersampling at 8.9ps (an effective boost of 112), which still permits to resolve clearly a linewidth of 2.5kHz. (**B**) *Detection of incoherent AC magnetic fields with two distinct frequencies.* Quantum interpolation with a maximum of 672 $\pi$-pulses allows for a gain of a factor 72 and faithfully reconstructs the AC fields, even if the two frequencies are not resolved by regular XY16 sequences with our timing resolution. (**C**) *Linewidth of the detected AC magnetometry signal* (from **A**) with regular sampling (blue) and supersampling (green). The error bars are residuals to a Gaussian fit. (**D**) *Sensing quality factor* $Q = f/\Delta f$ extracted from (**B**). Conventional dynamical decoupling sequences can only achieve $Q \leq 100$. This limit can be surpassed with quantum interpolation, scaling linearly with number of pulses, to reach $Q \approx 1000$.

### 2.6.1 Super-resolution spectroscopy of Classical fields

To demonstrate the power of quantum interpolation we perform high resolution magnetometry of a classical single-tone AC magnetic field at the frequency $f_{\mathrm{AC}} =$

2.5MHz. By applying optimally-ordered quantum interpolated sequences (Fig. 2-17A), we detect the spurious harmonic[101] of frequency $2f_{\mathrm{AC}}$. As the number of $\pi$-pulses is increased, the filter function associated with the equivalent XY-N sequences, and accordingly the measured signal, becomes narrower. The spectral linewidths extracted from a Gaussian fit of these dips are not affected by the finite time resolution as highlighted in Fig. 2-17C. Without quantum interpolation, we reach our experimental resolution limit after applying a sequence of only 64 $\pi$-pulses (see Chapter 3). Quantum interpolation enables AC magnetometry far beyond this limit: we obtain an improvement by a factor 112 in timing resolution, corresponding to sampling time of 8.9ps.

The advantage of quantum interpolation over conventional dynamical decoupling sequences is manifest when the goal is to resolve signals with similar frequencies. Fig. 2-17D shows that our quantum sensor is easily able to detect a classic dual-tone perturbation, resolving fields that are separated by $\Delta f = 6.2$kHz, far below the limit set by our native 1ns hardware time resolution.

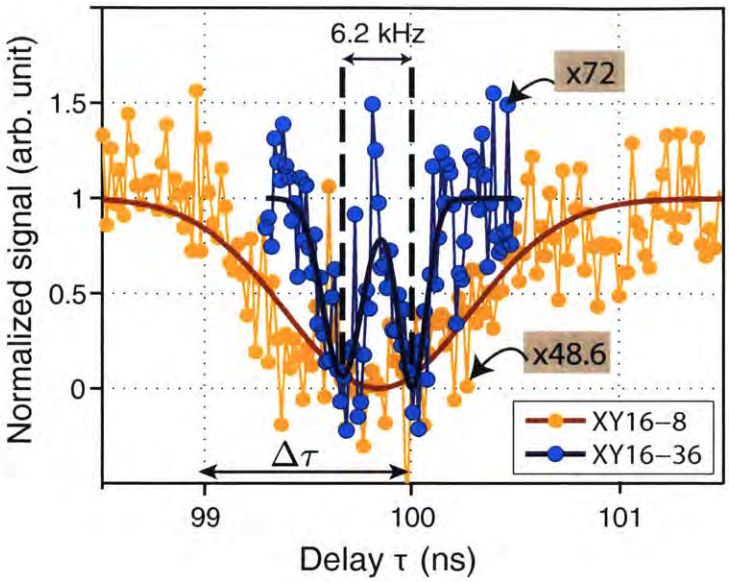


Figure 2-18: **Quantum interpolation for increasing resolution.** Here we demonstrate that quantum interpolation while increasing the number of pulses can allow us to resolve peaks that were normally indistinguishable. We perform AC magnetometry from two distinct incoherent sources, separated by 6.2kHz. The timing resolution here experiments was $\Delta\tau = 1$ns, and without quantum interpolation based supersampling, the entire data would just consist of four points in this plot. The supersampling resolution gains for both experiments are indicated in the boxes. Note that we have normalized the two experimental results so that the peak signal strength is identical for both cases.

We also performed magnetometry of two AC signals separated by 6.2kHz with XY16-8 and XY16-36 (see Fig. 2-18). We observe that the two peaks cannot be resolved by XY16-8, but upon increasing the number of pulses, one is able to resolve them. It is important to note that we employed quantum interpolation for both experiments; indeed given our timing resolution of $\Delta\tau = 1$ns, the entire data in Fig.

2-18 would otherwise just consist of four points.

A useful figure of merit to characterize the resolution enhancement of quantum interpolation, in analogy to band-pass filters, is the Q-value of the sensing peak, $Q = f/\Delta f$. The Q-value for conventional decoupling pulse sequences is set by the finite time resolution, $Q = 1/(2f\Delta\tau)$. Quantum interpolation lifts this constraint, allowing $Q \approx 2N/\pi$, limited only by the coherence time $T_2$, $N_{\max} \leq T_2/(2\tau)$. Our experiments illustrate that the effective sensing Q can be linearly boosted with the pulse number to over 1000 (Fig. 2-17D). Given typical NV coherence time (1ms), $\pi$-pulse length (50ns) and timing resolution (1ns), an impressive gain of about $10^4$ over the hardware limits is achievable. In the Appendix we present a detailed comparison with other high resolution sensing techniques like correlation spectroscopy [49], and Hartmann-Hahn sensing [34,35] and also describe how quantum interpolation could also potentially enhance these methods.

These experiments demonstrate that via quantum interpolation, the effective ability to resolve two closeby spectral frequencies is no longer limited by hardware but only by the number of pulses that can be reliably applied.

### 2.6.2 Super-resolution spectroscopy of quantum fields

Even more remarkably, the coherent construction of quantum interpolation ensures that one can measure not only classical signals, but also quantum systems (e.g. coupled spins [24]) with high spectral resolution. This result is non-trivial, since it implies that we are not only modulating the quantum probe, but also effectively *engineering* an interpolated Hamiltonian for the quantum probed system [30]. Specifically, we consider a quantum probe coupled to the quantum system of interest via an interaction $\mathcal{H} = |0\rangle\langle 0|\mathcal{H}_0 + |1\rangle\langle 1|\mathcal{H}_1$. Here $|0\rangle$, $|1\rangle$ are the two eigenstates of the

quantum probe and $\mathcal{H}_{0,1}$ the target system Hamiltonians in each manifold. Then, the propagator under a $\pi$-pulse train (with timings as in the XY8 sequence) is given by $\mathcal{U}^N(\tau) = |0\rangle\langle 0|\mathcal{U}_0^N(\tau) + |1\rangle\langle 1|\mathcal{U}_1^N(\tau)$, with

$$\mathcal{U}_{0,1}^N(\tau) = (e^{-i\mathcal{H}_{0,1}\tau}e^{-i\mathcal{H}_{1,0}2\tau}e^{-i\mathcal{H}_{0,1}\tau})^N \tag{2.47}$$

Sensing of the target quantum system is achieved via interference between the two evolution paths given by $\mathcal{U}_{0,1}^N(\tau)$, which results in the quantum probe signal $S = \left[1 + \mathrm{Tr}(\mathcal{U}_0^N\mathcal{U}_1^{N\dagger})\right]/2$[13,14]. The interference is enhanced by increasing the number of pulses $N$, and by a careful choice of the time $\tau$, making it susceptible once again to finite timing resolution. Quantum interpolation can overcome this limitation, engineering any propagator $U_{0,1}^N(\tau_{k+p/N})$ by suitably combining $\mathcal{U}_{0,1}^{N-p}(\tau_k)$ and $\mathcal{U}_{0,1}^p(\tau_{k+1})$. It is somewhat surprising that this construction would work: when considering a large number of pulses, one would expect that the non-commutativity of the propagators and the non-convergence of the perturbative Baker-Campbell-Hausdorff expansion would amplify the discrepancy between ideal and interpolated propagator. Fortunately, the construction developed for classical fields still keeps the error small (see Chapter 3).

Consider for example the coupling of a quantum probe (the NV center) to two-level systems (nuclear spins-1/2). NV centers implanted a few nanometers below the diamond surface have recently emerged as the prime technology towards the long-standing goal of obtaining high spatial-resolution structure of single molecules in their natural environment, by performing nano-scale Nuclear Magnetic Resonance (NMR) spectroscopy[17,16,102,103,82]. The outstanding key challenge is resolving the spectral features (and hence positions) of densely packed networks of spins in such molecules. Frequency differences, as small as a few Hz, arise from chemical shifts

and the coupling to the NV. The Hamiltonian of each spin in the molecule is given by $\mathcal{H}_0 = \omega_L I_{zj}$ ; $\mathcal{H}_1 = \omega_L I_{zj} + \sum_\nu A_{z\nu}^{(j)} I_{\nu j}$, where $\omega_L$ is the Larmor frequency of the spins, and $A_{z\nu}^{(j)}$ are the components of the coupling to the NV center. Then, the $\mathcal{U}_{0,1}$ propagators are composed of nuclear spin rotations conditioned on the NV state. The maximum interference signal arises for $\tau = \pi/\left[2(\omega_L + A_{zz}^{(j)})\right]$, when the propagators correspond to rotations around two non-parallel axes separated by an angle $\alpha = \arctan\left[A_{z\perp}^{(j)}/(\omega_L + A_{zz}^{(j)})\right]$. The angle between the nuclear spin rotation axes in the two NV manifolds is amplified with every subsequent application of $\pi$-pulse, giving rise to a signal contrast that grows with $N^2$. The destructive interference is also amplified away from the sensing peak, leading to a sinc linewidth that falls as $1/(N\tau)$, similar to the results obtained using the semi-classical filter picture.

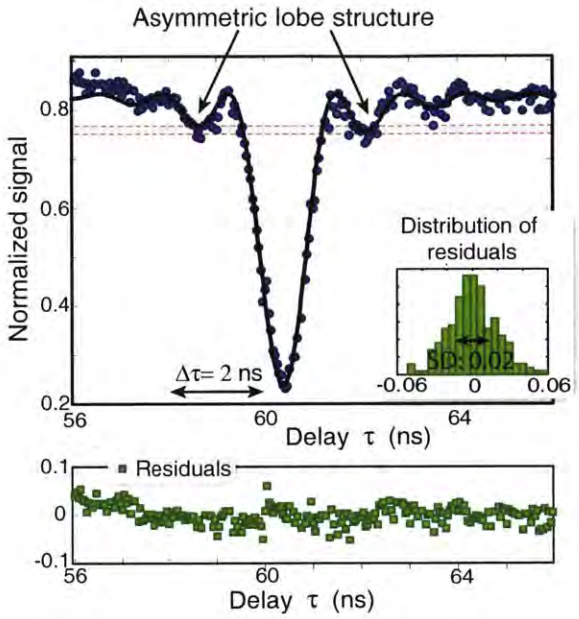


Figure 2-19: **High resolution spin detection.** A modified XY8-12 sequence enables an effective sampling at 48ps (a resolution gain by 41 with respect to the hardware-imposed $\Delta\tau$=2ns). The lineshape of the $^{14}$N NMR signal displays a slight asymmetry in the signal sidelobes, an expected feature (see Chapter 3) of the NMR signal under the XY8 sequence (solid line). The agreement with the theory-fitted curve is very good, reflected by the relative residual standard deviation being 3%.

To experimentally demonstrate the high precision sensing reached by quantum interpolation, we measure the $^{14}$N nuclear spin via its coupling to the NV center electronic spin. Even if the $^{14}$N is strongly coupled to the NV ($A_{zz} = -2.16$MHz), it usually does not give rise to an interferometric signal because of its transverse coupling $A_{zx} = 0$. However, a small perpendicular field $B_\perp = 0.62$G generates an effective transverse coupling $\frac{\gamma_e B_\perp A_{xx}}{(\Delta - \gamma_e B_z)}$, with $A_{xx} = -2.62$MHz [104] and $\gamma_e = 2.8$MHz/G the NV gyromagnetic ratio. This effect becomes sizable at a longitudinal magnetic

field $B_z = 955.7$G that almost compensates the NV zero-field splitting $\Delta = 2.87$GHz. The $^{14}$N nuclear spin frequency is largely set by its quadrupolar interaction $P = -4.95$MHz, a high frequency beyond our timing resolution (Fig. 2-1B). We employed quantum interpolation to supersample the signal at 48ps (a 41-fold gain), revealing precise features of the spectral lineshape (Fig. 2-19), including the expected slight asymmetry in sidelobes(see Chapter 3). Detecting this distinct spectral feature confirms that quantum interpolation can indeed achieve a faithful measurement of the quantum signal, as we find an excellent match of the experimental data with the theoretical model, with the error being less than 3% percent for most interpolated points. The ability to probe the exact spectral lineshape provides far more information than just the signal peaks, especially when there could be overlapping peaks or environment-broadened linewidths.

These results have immediate and far-reaching consequences for nanoscale NV-NMR[105,82,81], where our technique can map spin arrangements of a nearby single protein with a spatial resolution that dramatically improves with the number of pulses. The Q-value provides an insightful way to quantify the resolution gains for these applications. With a $Q \approx 10^4$ that is currently achievable, $^{13}$C chemical shifts of aldehyde and aromatic groups can now be measured[106]. Beyond sensing nuclear spins, we envision quantum interpolation to have important applications in condensed matter, to sense high frequency (hence high Q) signals[107], such as those arising from the excitation of spin-wave modes in magnetic materials like Yittrium Iron Garnett[108].

### 2.6.3 Data fitting and error estimation

To fit the theoretical model to the data, we use a steepest descent minimization algorithm to minimize the $\chi^2$ in conjunction with simulated annealing to avoid local minima and ensure the global best fit. Subsequently, we use a Monte-Carlo approach to estimate the uncertainty of the various fit parameters.

Let us denote the fit parameters for our model by $\mathbf{P}$. For a given set $\mathbf{P}$, our theoretical model provides a non-linear functional relation $y = f(x|\mathbf{P})$. Given a measured set of data points $\{x_n\}$ and $\{y_n\}$, we determine the optimal set of parameters $\mathbf{P}_{\text{opt}}$ by minimizing $\chi^2 = \sum_n [y_n - f(x_n|\mathbf{P})]^2/\sigma_y^2$. Here we have assumed that the statistical error $\sigma_y$ of the measured data points is identical for all points.

For example, the fitting parameters for Fig. 3 in the main article are the tilt angle $\alpha_1$ of the rotation axis of $U_1$, as well as the offsets and scaling factors for both the $x$ and $y$ axes ($x$ and $y$ corresponding to deviation time from the sensing peak and the measured signal intensity in this case).

Once $\mathbf{P}_{\text{opt}}$, the statistical uncertainty of $y_m$ is estimated from the deviation from the optimally fitted function $\sigma_y^2 \approx \sum_n [y_n - f(x_n|\mathbf{P}_{\text{opt}})]^2/(N-1)$, where $N$ is the number of data points. The value of $\sigma_y$ obtained by this procedure yields sets a lower bound for the true statistical uncertainty, as any systematic deviation of the fitted function (i.e. if we have not captured the underlying true functional form in our theoretical model) increases $\sigma_y$. Subsequently the uncertainty in the fit parameters $\mathbf{P}$ can be estimated beyond linear order by generating artificial data sets of points $\{x_n\}$ and $\{y_n\}$ statistically distributed around $f(x_n|\mathbf{P}_{\text{opt}})$, subsequently performing a fit for each data set. We assume a Gaussian distribution for the generation of these data points, an assumption which can be verified by inspecting the distribution of $\delta y_n = y_n - f(x_n|\mathbf{P}_{\text{opt}})$ in the original data. Repeating this procedure yields a

distribution of fit parameters of which the distributional form, confidence intervals and standard deviation for the individual parameters can be extracted.

## 2.7 Advantages and applications of Quantum Interpolation

### 2.7.1 Comparison with other high resolution sensing techniques

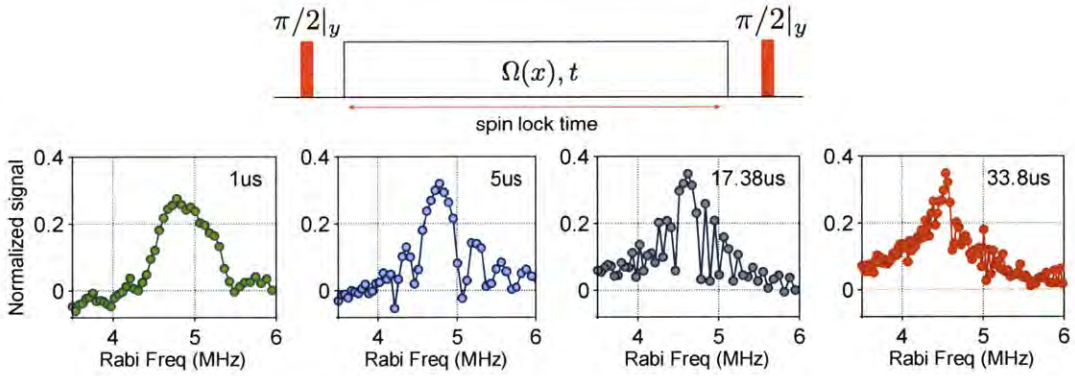


Figure 2-20: **Comparison with Hartmann-Hahn spin sensing.** Here we vary the spin lock period at 1083G and study the sensing peak from a $^{14}$N nuclear spin under the presence of a weak misaligned field. The linewidth is Fourier limited by the spin lock period (shown in panels), and at long lock periods saturates due to amplifier noise. This is a representative example of the problem plaguing the ultimate achievable sensing resolution via the Hartmann-Hahn spin sensing technique.

We now compare the performance of XY8-based sensing, aided by our quantum interpolation technique, with other methods of high-resolution magnetometry. There are two main approaches to NV-based sensing besides XY8-based magnetometry, cross-polarization via resonant driving of the NV [34,105] and correlation spectroscopy [49].

In the first technique, the NV center is spin-locked with a Rabi frequency $\Omega$, and at the Hartmann-Hahn matching condition [109,110] $\Omega = \omega_L + A_j$ there is a flow of polarization from the NV center to the resonant nuclear spin(s), which can be detected as a reduction in the NV polarization. Since this method does not rely on precise delays but instead on amplitude matching, the sensing resolution is set by the precision with which one can set the Rabi frequency. In practice, however, this technique is severely limited by amplifier noise that affects the stability of the spin lock, thus broadening the matching condition. Indeed, given typical amplifier noise of 8dB, corresponding to $T_{2\rho} \approx 40\mu$s for NV centers, the achievable resolution is only 25kHz. To demonstrate this, we performed Hartmann-Hahn experiments (Fig. 3-14) to sense a single $^{14}$N nuclear spin in the presence of a static misalignment, giving rise to a signal similar to Fig. 2-1. The sinc-like linewidth decreases linearly with the spin-lock time; however, the effect of amplifier noise is to relatively quickly saturate the linewidth and reduce signal contrast.

There have been proposals for overcoming amplifier noise, for instance by employing concatenated driving [69]. This relies on going into a doubly dressed basis that is immune to amplifier noise. However, it cannot easily be applied to high resolution sensing of nuclear spins because the modified Hartmann-Hahn condition now involves matching the Larmor frequency to the newly opened second order energy gap that is typically very small. This makes it difficult to match the Hartmann-Hahn condition selectively to few spins species, and hence obtain high resolution spectra. An alternative approach was proposed in Ref. [105]. Spin lock periods are interrupted

by periods of free evolution under a gradient that creates an effective frequency filter, allowing potentially high resolution ≈200Hz. However, even this method is once again susceptible to finite timing resolution, for which quantum interpolation can be effectively employed.

A second important class of techniques is correlation spectroscopy [49]. The experiment consists of two blocks of XY8 sequences separated by a long delay $t$. The delay is swept and the target spin resonant frequency is obtained via Fourier transform. Since the delay $t$ can be very long, $t \approx T_1$, one can achieve very high resolutions, for instance 470Hz in Ref. [111]. Unfortunately, the increased resolution comes at the cost of a great loss in sensitivity (contrast). Indeed for correlation spectroscopy the signal contrast goes $\propto \sin^2(N\alpha)$ , where $N\alpha$ is the phase picked up by the NV during each XY8 interrogation period (Eq. 1 and S14 in [49]), while in XY8 sensing the contrast is $\propto \sin(2N\alpha)$ (assuming the same number of pulses). Thus, it is not possible to make a fair comparison of the two methods based only on frequency resolutions. Moreover, since XY8-sensing is a direct sampling technique as opposed to Fourier sampling in correlation spectroscopy, it is potentially more efficient for sampling sparse signal peaks and does not suffer from aliasing artifacts.

Still, since correlation spectroscopy experiments employ XY8/CPMG building blocks, quantum interpolation could be an important enabling tool in these experiments. More specifically, each XY8 building block should have time-delays that match the resonance frequency of the nuclear spins to be sensed, and is thus susceptible to finite-timing resolution. Quantum interpolation can be applied to mitigate this problem, translating into a potentially large boost in signal contrast (see Sec. 2.3). This enhanced resolution would also translate to a larger sensing bandwidth, allowing the resolution of spectral features without aliasing artifacts.

Finally, let us contrast our method with other proposals that also employ dy-

namical decoupling sequences with unequally spaced pulses. Ref.[112] employed 3 pulse blocks with unequal delays (variants of more general pulse families detailed in Figs. 7 and 8 in Ref.[33]) to resolve hidden spectral features. The sequence works by creating more filter function peaks (quantified by the parameter $r$ in Fig. 2 of Ref.[112]), that however have much smaller amplitude. Indeed the 7/38 harmonic employed in[112] is over 10 times weaker than the primary filter harmonic, leading to a contrast loss in the resulting signal. Other $r$ values have even poorer contrast (see Fig. 2 of Ref.[112]). Similar arguments can be made regarding sequences theoretically proposed in Ref.[113] (Fig. 2 of that paper). In contrast, quantum interpolation introduces *no* loss of signal contrast. The key advance in our work is a deterministic (and optimal) method to move the primary filter harmonic with a very fine step, and with an extremely small error. As a result, all the peaks are of the same amplitude up to second order in $\Delta\tau$. This can be ascribed to employing optimal interferences between spin propagators and is not merely a classical filter construction as considered in Refs.[112,113]. Moreover since the construction is completely deterministic, one can sample only particular chosen samples of interest, a task that is not easily possible in previous proposals.

### 2.7.2 Q-value as figure of merit

#### Gains in Q-value via quantum interpolation

In order to characterize the boost in resolution granted by supersampling, we introduce as figure of merit the Q-value of the sensing peak, $Q = f_{\mathrm{AC}}/\Delta f_{\mathrm{AC}}$. Given that the sensing peak arises at time $\tau = 1/f_{\mathrm{AC}}$, and the sensing linewidth in time units

is $w$, we have the frequency linewdith

$$\Delta f = \frac{1}{\tau - w} - \frac{1}{\tau + w} \approx \frac{2w}{\tau^2} = 2wf_{\mathrm{AC}}^2 \tag{2.48}$$

giving $Q \approx 1/[2wf_{\mathrm{AC}}]$. This definition of $Q$ describes the ability to resolve sensing peaks at different frequencies, where the minimum condition to resolve two sensing peaks is that the peaks are separated by at least $2w$. The Q-value scales linearly with the number of pulses $N$, since ideally $w \propto 1/N$. However, in practice $w$ is bounded by the finite timing resolution $\Delta\tau$. Let us now evaluate the maximum achievable Q-value in this situation of limited $\Delta\tau$. Then, the smallest linewidth one can achieve for sensing is $w = \Delta\tau$, giving the bare Q-value

$$Q_{\mathrm{bare}} = \frac{1}{f_{\mathrm{AC}}(2\Delta\tau)}. \tag{2.49}$$

Quantum interpolation can boost the Q-value by overcoming the limits in sampling time, $\Delta\tau$. This is shown for instance in Fig. 2-17, where $\Delta\tau = 1\mathrm{ns}$ restricts $Q_{\mathrm{bare}}$ to a maximum of 100. Thanks to quantum interpolation, where the number of possible supersamples scales linearly with the pulse number, the Q-value is limited in principle only by the intrinsic linewidith of the sensing peak, given by the total time of the experiment. At the maximum allowed time, that is $T = T_2 \approx 1\mathrm{ms}$, we can estimate the Q-value under quantum interpolation using Eq. (2.23),

$$Q_{\mathrm{supersample}} = \frac{\sqrt{2}\cos(\alpha_j/2)}{\sin\left(\frac{2\pi^2}{T_2\omega_L}\right)}. \tag{2.50}$$

Hence, due to quantum interpolation, one achieves a boost in the sensing $Q$ value by an amount,

$$Q_{\text{boost}} = \frac{Q_{\text{supersample}}}{Q_{\text{bare}}} = \frac{\Delta\tau}{w} = \frac{\sqrt{2}\Delta\tau\omega_L \cos(\alpha_j/2)}{\sin\left(\frac{2\pi^2}{T_2\omega_L}\right)} \tag{2.51}$$

where we have used the expression in Eq. (2.30). Fig. 2-17**(D)**, obtained from the experiments in Fig. 2**(C)**, illustrates that the effective sensing $Q = f/\Delta f$ can be boosted by a factor of 1000. However this experiment was performed with a total time of 115.2$\mu$s. At the $T_2$ of 330$\mu$s experimentally demonstrated for shallow NV centers in[82], $Q \approx 2893$. Given the rapid improvements in coherence times over the past few years, it is reasonable to expect that $T_2 \approx$ 1ms is achievable for shallow NVs in the near future (it is already routine for bulk NVs [26]). This would allow one to approach a Q-value of $10^4$ that, along with quantum interpolation, could allow NV based sensors to measure fields with high resolution from varied sources.

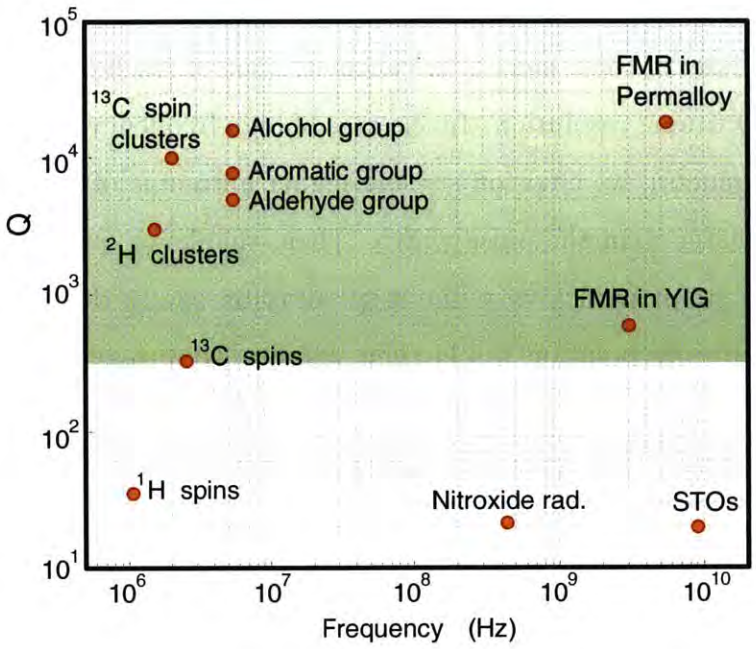


Figure 2-21: **Q-value vs $f$ for different quantum metrology experiments.** In this scatter plot we show representative examples the Q-values from different signal sources plotted against their native frequency $f$ (see Table 2.2). Note that in our experiments, we could obtains gains in Q by about $10^4$ via quantum interpolation, and this might open up the metrology of several signals (green shaded region) that were hitherto extremely challenging.

### 2.7.3 Applications to quantum metrology experiments

The Q-value provides a convenient measure to characterize the gains due to quantum interpolation. In our experiments, we were able to achieve substantial gains in Q-value over the bare limit set by the hardware. More broadly, quantum interpolation is useful for NV-based sensing of signals that have high Q, for instance, signals with extremely small $\Delta f$ (narrow linewidths or frequency differences) such as nuclear spins

and chemical shifts, or signals with high frequency $f$, such as spin wave modes in ferromagnets. Many of these signals are currently out of reach because of the severe constraint set by timing resolution. In the case of high frequency signals (for instance FMR in ferromagnets), we envision sensing higher harmonic of the signal for which the time $\tau$ is greater than the pulse width. Then, thanks to quantum interpolation the time can be swept with a very fine step, allowing one to detect high-Q, high $f$ signals. Quantum interpolation would then significantly broaden the impact of NV center as a probe for condensed matter systems, as we show in detail Table 2.2 and Fig. 2-21, where the Q-values are plotted against frequency.

| Experiment | Signal Source | f | $\Delta f$ | Q-value | Ref. | Notes |
|---|---|---|---|---|---|---|
| Nanoscale NMR/ESR | $^{13}$C spins | 2.5 MHz | 7.5 kHz | 333 | 82 | Nanoscale spin sensing experiments on a single protein of Ubiquitin. |
| | Nitroxide rad. | 430 MHz | 20 MHz | 21.5 | 81 | Electron radicals measured in a single protein. |
| | $^{1}$H spins | 1.06 MHz | 30 kHz | 35.3 | 114 | Proton spins measured in an organic molecule outside diamond. |
| | $^{13}$C spin clusters | 2 MHz | 200 Hz | $10^4$ | 105 | Simulated linewidths requried to resolve clusters of spins in CXCR4. |
| | Nanoscale NQR of $^{2}$H clusters | 1.5 MHz | 500 Hz | 3000 | 82 | Simulated linewidths requried to resolve NQR peaks arising in deuterated phenylalanine. |
| $^{13}$C Chemical shift | Aldehyde group | 5.35 MHz at 0.5T | - | $\sim$ 5000 | 106 | We assume that to be able to resolve chemical shifts, one requires a Q of atleast the shift value. |
| | Aromatic group | | | $\sim$ 7700 | | |
| | Alcohol group | | | $\sim$ 16000 | | |
| Spin waves in Ferromagnets | FMR in Permalloy | 5.5 GHz | 0.3 MHz | $1.8 \times 10^4$ | 115 | Here we consider *spectrally* sensing the spin waves excitations directly via the NV. |
| | FMR in YIG | 3 GHz | 5 MHz | 600 | 115,116 | |
| | STOs | 9 GHz | 450 MHz | 20 | 117 | Spin torque switching in Tantalum. |

Table 2.2: **Examples of Q-values from different sources.** In this table we show representative examples of Q-values required to effectively sense signals from different sources, including single spins, chemical shifts, and spin wave modes in ferromagnets (see also Fig. 2-21). We note that most measurements in the literature are of low Q-value, below 1000 (see also Table 2.1). Given that we can experimentally achieve substantial gains in Q-value due to quantum interpolation, several of the high Q signals are now within the regime of quantum metrology with NV centers.

## 2.8 Conclusions and Outlook

In conclusion, we have developed a quantum interpolation technique that achieves substantial gains in quantum sensing resolution. We demonstrated its advantages by performing high frequency-resolution magnetometry of both classical fields and single spins using NV centers in diamond. The technique allows pushing spectral resolution limits to fully exploit the long coherence times of quantum probes under decoupling pulses. We experimentally demonstrated resolution gains by 112, and Q-value by over 1000, although the ultimate limits of the technique can be at least an order of magnitude larger. Quantum interpolation thus turns quantum sensors into high-resolution and high-Q spectrum analyzers of classical and quantum fields. We expect quantum interpolation to be an enabling technique for nanoscale single molecule spectroscopy at high magnetic fields [118], allowing the discrimination of chemical shifts and angstrom-resolution single molecule structure.

# Appendix

## 2.A Code for the construction of the optimal super-sampling sequence

Here we present a simple code (in MATLAB) that allows constructing the optimal interpolation sequence for a desired sampling time $q/(p+q)\Delta\tau$ (see Fig. 2-9). The algorithm yields an array of time delays for how the basic CPMG building blocks $U_0$ and $U_1$ (each consisting of 3 rotations) should be ordered and the $\pi$-pulses phases chosen according to the XY8 scheme.

Listing 1. Matlab code for the optimal quantum interpolation sequence construction

```
%% Basic blocks of delay time (separation between neighbouring pi pulses).

U_0 = [tau, 2*tau, tau];
U_1 = [tau+delta_tau, 2*(tau+delta_tau), tau+delta_tau];
% tau is the parameter we sweep in experiment and delta_tau is the smallest time step we can
    sweep by

%% Assemble the delay time in the order as in the optimal construction of a supersampling
    sequence.

delay={}; % Initialize cell array 'delay'
count=0; m=0;

for  j = 1: 4*n  %  Here n is XY8 cycle number
       m = m + sample;
   % sample is a fraction number between 0 and 1, rounded to multiples of 1/(4*n);
      if abs(m) <= 1/2
          count = count+1;
          delay{count} = U_0;
      else
          count  = count+1;
          delay{count} = U_1;
          m = m-1;
      end
end

% For instance, for n=1 and sample =1/4, one gets a delay cell array: delay={U_0 U_0 U_1 U_0}.

% Let us take as given functions which add a pulse or delay to a sequence.
% For simplicity, the carrier power and frequency are not shown as inputs and only phase is
    emphasized here.

function add_pi/2_pulse(phase)
function add_pi_pulse(phase)
function add_delay(delay_time)

%% Create a supersampling XY8-n sequence, combining pi pulses with correct phase and delay.

add_pi/2_pulse(0);

for j=1:4*n
 if mod(j,4)==1 || mod(j,4)==2
      add_delay(delay{j}(1,1));
      add_pi_pulse(0);  % pi|x
      add_delay(delay{j}(1,2));
      add_pi_pulse(90); % pi|y
      add_delay(delay{j}(1,3));
else
      add_delay(delay{j}(1,1));
      add_pi_pulse(90);  % pi|y
      add_delay(delay{j}(1,2));
      add_pi_pulse(0); % pi|x
      add_delay(delay{j}(1,3));
end
end

add_pi/2_pulse(0);
```



Figure 2-22: Matlab code for the optimal quantum interpolation sequence construction

# Part II

# Quantum Enhanced Measurement

# Preface

In this part of the thesis we consider how quantum sensors can be employed in new and novel modalities in order to sense DC magnetic fields and rotations with high sensitivity. More specifically, in Chapter 3, we consider a method for sensing DC magnetic fields using quantum sensors that can potentially achieve higher sensitivities than conventional methods, and can be employed for nanoscale vector magnetometry. Sensing such DC magnetic fields is of wide interest since many natural signals in biology and condensed matter are of very low frequency, approaching DC. In such experiments, the signal is a phase that is proportional to the total period allowed for the quantum sensor to interrogate the DC field. Conventional quantum sensing, via the Ramsey method, is usually limited by the sensor dephasing time $T_2^*$ while the intrinsic sensor coherence time $T_2$ can be a few orders of magnitude larger. If one is capable of performing DC magnetometry at $T_2$, then one stands to gain in sensitivity. In chapter 3, we introduced theoretically, and then experimentally demonstrated a method by which the DC sensing can be done at interrogation periods approaching the full coherence time. The technique employs a quantum lock-in principle by which the DC field is first up converted to an AC field and then down converted back to DC by dynamic decoupling, and as a consequence the bandwidth of noise seen by the quantum sensor is effectively suppressed, allowing sensing at $T_2$.

We currently experimentally obtain sensitivities that are comparable to the Ramsey method, although our present experiments are limited by pulse error; in principle though by pulse optimization, our method can allow potentially a gain in sensitivity over the Ramsey method. The technique has other advantages: it senses transverse magnetic fields, and used in conjunction with the Ramsey method can allow the sensing of both the magnitude and complete vector orientation of DC magnetic fields at nanometer length scales.

In chapter 4 of the thesis we proposed a novel spin-mechanical hybrid device for the ultrasensitive detection of rotations[55]. Gyroscopes find wide applications in everyday life from navigation and inertial sensing to rotation sensors in hand-held devices and automobiles. Current devices, based on either atomic or solid-state systems, impose a choice between long-time stability and high sensitivity in a miniaturized system. The proposal involved building a solid-state spin gyroscope associated with the Nitrogen-Vacancy (NV) centers in diamond to overcome these constraints. More specifically, we take advantage of the $^{14}$N nuclear spin coherence properties of NV centers to achieve high rate sensitivity of about 1 mdeg/s/sqrt(Hz mm$^3$). Moreover, by exploiting the four classes of the NV axes, we will be able to determine *axis* of rotation in addition to its rate. The key advantage of the hybrid device comes from the fact that the mechanical gyroscope and the spin gyroscope are on the same device footprint, but sensitive to different sources of noise, allowing for Kalman filtering to achieve highly *stable* rotation sensing, a facet that is especially crucial for inertial navigation.

We are now building an experimental prototype of this device, the design of which is presented in chapter 6. The prototype consists of a diamond with a high density of NV centers $\sim 10^{17}/\text{cm}^3$, and a technique for exploiting the optical waveguiding properties of the diamond[119] to increase the photon collection efficiency and consequently

signal to noise.

# Chapter 3

# Sensitive $T_2$-limited DC Magnetometry via Ancilla Assisted Bandwidth Narrowing

## 3.1 Introduction

Over the past two decades magnetic field sensors have come of age, and several small fields in nature at the few femto-Tesla level are now well within the ambit of detection. These spectacular sensitivities are often a consequence of exploiting a type of *quantum* interference in these sensors, widely evidenced in an array of state-of-the-art technologies including SQUIDs [120], atomic vapor cells [121,122], and Nitrogen Vacancy (NV) centers in diamond [7,8,123]. For the quantum metrology of magnetic fields, one usually draws the distinction between AC fields (usually of a few MHz of higher) and low frequency, static (DC) or quasi-DC fields. Most sensitive performance occurs when the signals of interest are AC, due to the ability to operate

the sensor away from intrinsic $1/f$ noise[124] that often severely plagues sensor performance. However, arguably many more signals of fundamental importance fall in the latter (DC) category, including for instance, magnetic fields from the from the firing of action potentials in single neurons[125,126,127], and from edge currents in topological insulators[128,129].

The conventional method for sensing DC magnetic fields is through the celebrated Ramsey technique[130]; however the presence of noise often limits the sensor interrogation to the dephasing time $T_2^*$. This is far lower than the inherent sensor coherence time $T_2$, often by a few orders of magnitude[131]. Indeed the key sensitivity advantage for AC sensors is derived from the ability to perform phase sensitive (lock-in) detection[132] at the known signal frequency of interest, leading to the effective bandwidth narrowing of sensor noise[133], allowing measurement times at the full $T_2$.

Here we introduce and experimentally demonstrate an ancilla mediated method to implement similar bandwidth narrowing for DC magnetometry. This allows one to achieve significant gains in sensitivity and noise suppression – *both* of sensor noise and noise carried by the signal to be sensed. More precisely, we employ a sensor consisting of the electron spin of a single NV center in diamond, and an ancillary hyperfine-coupled nuclear spin that serves to effectively up-convert our DC field of interest to an AC field (at frequency $\omega_L$) and is subsequently followed by quantum lock-in-detection (rectification[75]) at $\omega_L$ (see Fig. 3-1). This frequency conversion chain from DC-AC-DC enables the effective noise bandwidth narrowing to within $1/T_2$. The AC frequency $\omega_L$, set by the ancillary nuclear spin, can be tuned to well beyond the noise spectrum cut-off. Remarkably, as we shall describe, these same frequency up-conversion ideas can also be applied to the magnetometry of low frequency (1kHz - 1MHz) AC fields, that are out of reach of conventional sensors.

In addition, the long interrogation times make the sensor amenable to highly effi-

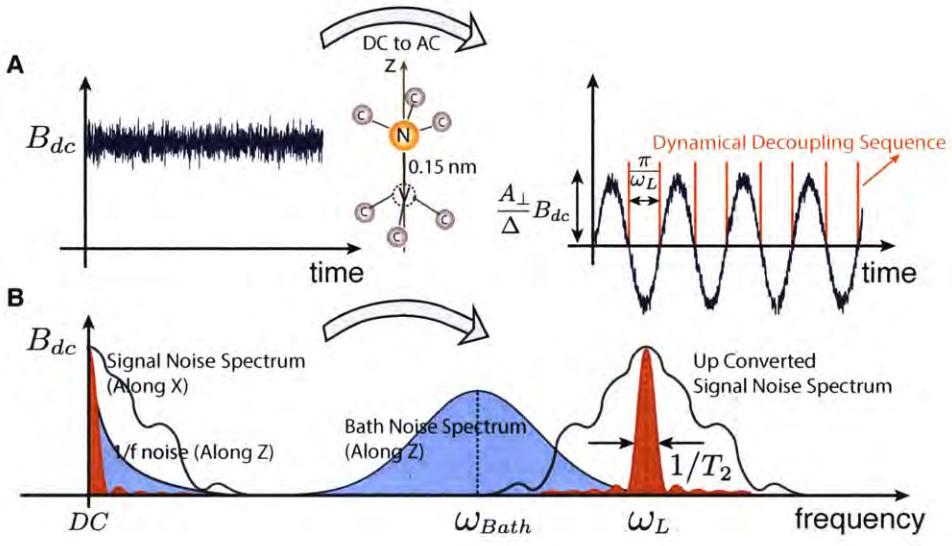


Figure 3-1: **Bandwidth narrowing for sensitive low noise DC magnetometry.** **(A)** Consider a magnetic signal of interest $B_{\rm dc}$ immersed in a low frequency noise spectrum. We would like to reject this noise and measure just the DC component. The ancillary $^{14}$N nuclear spin of an NV center up-converts $B_{\rm dc}$ to an AC signal centered at the frequency $\omega_L$ and with an amplification factor $A_\perp/\Delta$. Rectification by a dynamical decoupling sequence (orange lines indicate position of $\pi$ pulses) now causes a quantum lock-in detection at $\omega_L$, recovering a DC signal of reduced noise bandwidth $\sim 1/T_2$. **(B)** This is illustrated in the frequency domain in the lower panel, where we denote the low-frequency noise carried by the signal (light blue) in the $\hat{\mathbf{x}}$ direction, and the $1/f$ and spin bath noise (dark blue) acting on the NV sensor in the $\hat{\mathbf{z}}$ direction. Ancilla assisted up-conversion leads to a dual noise bandwidth narrowing of both signal and sensor noise. This enables a substantial gain in interrogation time, and consequently magnetometer sensitivity.

cient readout techniques of the NV sensor including charge state readout [134], further providing significant sensitivity gains. Coupled with the inherent advantages of NV center being single point defect sensors, our technique can enable sensitive, low noise, full vector nanoscale magnetometry at $T_2$, and when applied to an ensemble of NV sensors can provide large gains in the sensitivity per unit volume pixel.

This chapter is organized as follows. Sec. 3.2 details our ancilla based magnetometry protocol, including the derivation of the interferometric signal obtained in presence of a DC magnetic field, and Sec. 3.3 contains a detailed sensitivity analysis, including a comparison with the Ramsey method. In Sec. 3.4 we consider the noise filtration ability of our technique, based on frequency up-conversion, leading to an effective low-pass filtering of signal noise and band-pass filtering of sensor noise. Sec. 3.5 evaluates the sensor dynamic and operating range. Finally in Sec. 3.6, we describe a method for full vector magnetometry with our technique opening the door to precision DC field measurement at sub-nm length scales.

## 3.2 Nuclear spin assisted DC field sensing

While more general, here we consider the application of our technique to the sensor based on the electronic spin of the Nitrogen Vacancy (NV) center in diamond, which has shown to have AC field sensitivities better than $1\text{nT}/\sqrt{\text{Hz}}$ [7], and nanoscale spatial resolution [16,17,105]. We consider using a nearby nuclear spin as an ancilla, hyperfine coupled to it with tensor $\mathbf{A}$, and with the tensor principal axis frame coincident with the N-V axis (defined to be $\mathbf{z}$). This could be for instance the $^{14}$N nuclear intrinsic the NV center, or a $^{13}$C spin in the first shell [84,136]. While the $^{14}$N spin is a natural choice since it is a component of every NV sensor, and provides the added benefit of high robustness to magnetic fields (see also Appendix 3.C), an ancillary $^{13}$C spin

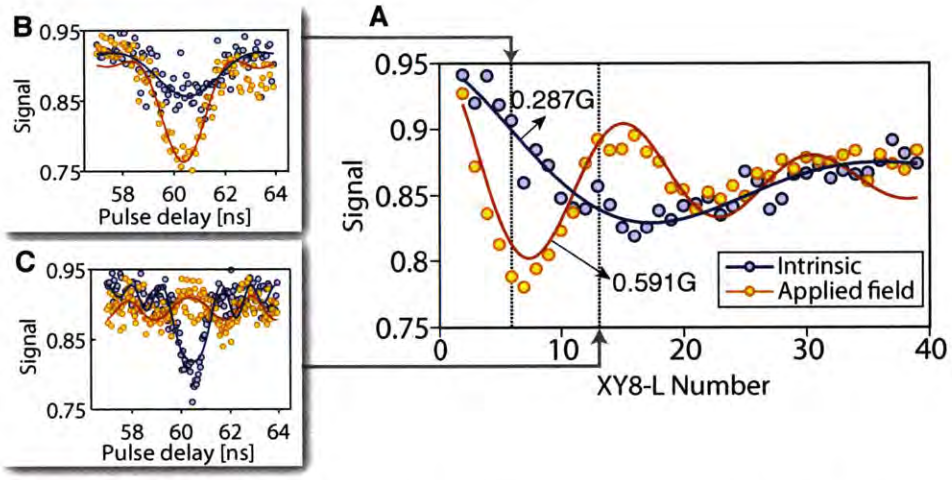


Figure 3-2: **Ancilla assisted DC magnetometry.** **(A)** Peak XY8 signal obtained at $\Delta = 141$MHz from an $^{14}$N ancilla nuclear spin under intrinsic misalignment $B_{\text{int}} \sim 0.287$G (blue points) and under a DC external field $B_e$ (orange points) to be sensed. The field magnitudes are obtained from the frequency of the oscillations. We employed quantum interpolation [135] to efficiently sample the peak (see also Fig. 3-13). The insets show representative time domain traces corresponding to **(B)** XY8-7 and **(C)** XY8-12, sampled respectively at 35.7ps and 20.8ps via quantum interpolation. The signals have the characteristic modified sinc-function lineshapes [135], that open up a larger number of side-lobes as the strength of DC field increases.

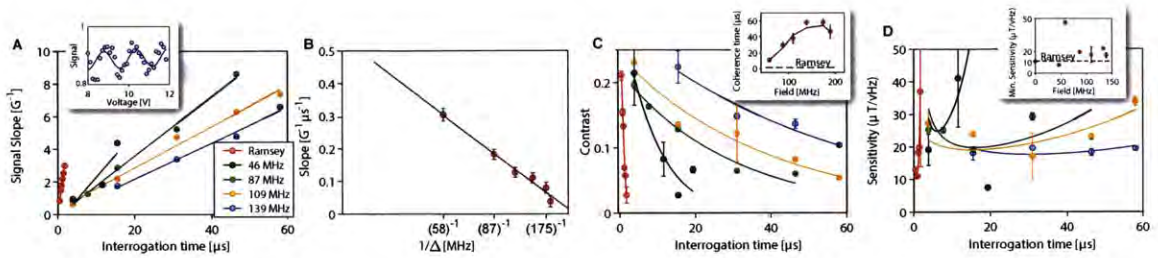


Figure 3-3: **Characterization of magnetometer sensitivity.** We sweep an external DC field $B_e$ and determine the signal sensitivity via a measurement of $dS/dB_e|_{B_0}$, while operating in the optimal (linear) regime of the magnetometer (Fig. 3-5). Inset shows an example trace, and through a Fourier transform we decompose separately the signal slope and decay. **(A)** Signal slope as a function of interrogation time for representative values of field $\Delta$. The error bars are obtained from a Lorentzian fits of the Fourier transforms. **(B)** Slope of the corresponding traces in **(A)**, the data clearly demonstrating the characteristic $1/\Delta$ dependence. The error bars are residuals to the inverse linear fit. **(C)** Decay of the corresponding signals with increasing interrogation time, with the inset showing the extracted coherence times. For the Ramsey experiment we are limited by short $T_2^* \approx 1.15\mu$s (dashed line), while our ancilla assisted protocol is limited only by pulse error. **(D)** Obtained sensitivity for different values $\Delta$ and interrogation time. Inset plots the best experimentally measured sensitivity values. Our technique can experimentally achieve sensitivities comparable to the Ramsey method $\approx 10.99\mu\text{T}/\sqrt{\text{Hz}}$, with additional benefits in noise suppression (Fig. 3-4).

could reduce certain experimental constraints due to its strong hyperfine coupling.

For simplicity first consider the case of a spin-1/2 nuclear ancilla. Upon suitable application of a train of $N$ pulses that are suitably delayed close to the nuclear Larmor frequency $\omega_L = \gamma_n B_z + A_\parallel$, one obtains a interferometric signal proportional to the field strength to be measured. The pulses are applied following the CPMG/XY8 protocol[88,31,137], a method conventionally used for detecting external spins in the environment of the NV center[138,13] (see Appendix 3.B for a detailed derivation of the interferometric signal). More precisely, we detect the component of the field perpendicular to the N-V axis $B_\perp$, and the signal $S = \frac{1}{2}(1+\cos N\alpha)$ arises through a second-order process where $\alpha = \tan^{-1}\left[\frac{B_\perp A_\perp}{\Delta\omega_L}\right]$, and $\Delta = \Delta_0 - \gamma_e B_z$ is the resonance frequency of the NV center ($\Delta_0 = 2.87$GHz is the NV zero field splitting). For small values of fields being measured, $\alpha \ll 1$, and to a good approximation $S = \frac{1}{2}\left(1+\cos\left[\frac{\gamma_e B_\perp A_\perp N}{\Delta\,\omega_L}\right]\right)$; this signal is especially strong close to the NV center ground state anti-crossing (GSLAC) at $B_z \to 1025$G, where $\Delta \to 0$. It is noteworthy that the signal is proportional to the hyperfine field $A_\perp$; with $^{14}$N this coupling is $A_\perp = 2.62$MHz, while for $^{13}$C this could be substantially stronger, $A_\perp > 140$MHz leading potentially to DC field sensing at large values of $\Delta$. In effect, the second order process can be viewed as a frequency up conversion[139,140,141] from the DC field $B_\perp$ to an effective AC field $B_\perp\,(A_\perp/\Delta)\cos(\omega_L t)$ acting at the frequency $\omega_L$ given by the ancillary nucleus; for an $^{14}$N for instance, $\omega_L = Q - A_\parallel/2 - \gamma_n B_z + A_\perp^2/4\Delta$ with the quadrupolar interaction $Q = -4.95$MHz[142,104] (see Appendix 3.C).

Note that while hyperfine mediated fields have been used before to boost the Larmor[84] and Rabi[104] frequencies of the ancillary nuclear spin, here instead we employ these fields for a frequency *mixing* action that aids quantum metrology with the NV electronic spin. We also mention that a method for transverse DC magnetometry was demonstrated in Ref.[143] employing a Ramsey sequence on the $^{14}$N *nuclear* spin, and

is consequently much less sensitive and noise resilient than the technique described in this chapter.

## 3.3 Magnetometer Sensitivity analysis

The sensitivity of our NV center magnetometer can be estimated through the smallest field one could measure in an interrogation time $t$, $\delta B_\perp = \frac{\Delta S}{dS/dB_\perp|_{B_0}}$, where $\Delta S$ is the spin projection noise $\Delta S = \sqrt{\langle S^2\rangle - \langle S\rangle^2}$, and $dS/dB_\perp|_{B_0}$ represents the signal slope obtained at the most sensitive bias point[6]. The sensitivity, then defined as the smallest field that can be measured in one second of averaging is $\eta = \frac{\Delta S}{dS/dB_\perp|_{B_0}}\sqrt{t+t_d}$, where $t_d$ represents the sensor dead time required to prepare and read out the NV sensor. In our experiment, $t_d = 1.3\mu$s, although it could approach ≈350ns with optimization. In practice the sensitivity depends on the collection efficiency of the photons from the NV center fluorescence, quantified by the magnetometer $C$-factor, with $\frac{1}{C} = \sqrt{1+\frac{2(N_0+N_1)}{(N_1-N_0)}}$ for conventional readout, where $N_{0,1}$ are the mean number of photons conditioned on the NV spin state, and leading to $\Delta S = \frac{1}{C}\sqrt{S(1-S)}$.

In order to determine the signal slope $dS/dB_\perp|_{B_0}$, we perform experiments with an $^{14}$N ancilla by sweeping an external voltage $V$ that produces an external field $B_e$ proportional to $V$ (Fig. 3-3), with the slope $\gamma_v = B_e/V = 0.115\pm$ 0.002 G/V being obtained from the experiments described in Fig. 3-5. We operate in the optimal (linear) regime of the magnetometer (see Appendix 3.D), where the field to be measured, perpendicular to the N-V axis, is exactly proportional to the applied field $B_\perp \propto B_e$.

From Sec. 3.2, and considering the NV sensor state dependent contrast of 30%, we expect the experimentally obtained signal to be of the form $S = 0.85 + 0.15e^{-(t/T_2)^p}\cos\left(\frac{B_e A_\perp t}{\Delta}\right)$, where we have imposed that the signal lies between 1 and

0.7, and decays with a timescale set by the effective $T_2$. From a first-order Taylor analysis, one expects $dS/dB_\perp|_{B_0} = 0.3e^{-(t/T_2)^p}(A_\perp t/\Delta)$, i.e. the signal slope varies linearly with the interrogation time, is inversely proportional to the deviation $\Delta$ from the GSLAC, and is weighted by the signal decay. In order to perform an experimental estimation with low error, especially considering that there is a finite minimum field that can be applied via the external source, we perform a Fourier transform of the signal obtained to *separately* extract the signal slope $(A_\perp t/\Delta)$ (from FFT frequency, Fig. 3-3(**A**)) and the signal decay $0.3e^{-(t/T_2)^p}$ (from FFT contrast, Fig. 3-3(**C**)). For a photon shot-noise independent comparison, we also perform conventional Ramsey magnetometry experiments in Fig. 3-3 under the same conditions, and for a fair comparison we have plotted the results suitably weighted to include the $\vartheta = 39.32°$ tilt angle of the applied field (measured via Fig. 3-5). In Fig. 3-3(**B**), one can clearly discern the $1/\Delta$ dependence of the signal slope showing a very good agreement with theory. From Fig. 3-3(**C**) it is evident that in our technique the NV sensor is better protected against noise and much longer interrogation times are possible over the Ramsey experiment for which, in presence of the external voltage, effective $T_2^* \approx 1.16\mu$s (inset in Fig. 3-3(**C**)).

We measured a value of $\Delta S \approx 17.27$ through a binning of photocounts, and estimated the magnetometer sensitivities for different values of $\Delta$ and interrogation times in Fig. 3-3(**D**). At $\Delta = 139$MHz the sensitivity of our ancilla assisted protocol $\approx 17.64\mu\text{T}/\sqrt{\text{Hz}}$ approaches that of the Ramsey technique $\approx 10.99\mu\text{T}/\sqrt{\text{Hz}}$ (inset of Fig. 3-3(**D**)). As we shall describe in Appendix 3.D we are primarily limited in achievable interrogation times $\approx 60\mu$s by pulse error. By employing instead high nuclear harmonics (Fig. 3-10) for magnetometry so that pulse quality is better, or through spin-lock pulse sequences Hartmann-Hahn matched to $\omega_L$ (see Appendix 3.F), or simply by using magnetic shielding that is conventionally employed in sen-

sitive magnetometers[144], one should be able to push the interrogation times to the full $T_2 > 500\mu$s, and far outperform the Ramsey sensitivity.

However, even at the currently demonstrated level, our protocol could provide *additional* sensitivity gains when combined with the recently developed technique of readout via NV spin-to-charge mapping (CSR)[134]. CSR can provide large gains in magnetometer C-factor at the cost of increased dead time $t_d$. For the Ramsey technique $t_d$ is a substantial fraction of the interrogation time and leads to little overall gain in sensitivity. In contrast the long interrogation times in our method make one amenable to longer readout dead-times giving potentially significant sensitivity boosts; indeed for $t_d \approx T_2/4$, $C_{\mathrm{CSR}} \to 10C$ for $T_2 \approx 1$ms[145]. At the current level of $T_2 \approx 60\mu$s as in Fig. 3-3, $C_{\mathrm{CSR}} \approx 2C$.

We also note that for DC magnetometry with an ensemble of NV sensors, the fact that the experiments are performed close to the GSLAC produces an additional boost in $C$-factor by $\approx$1.5, since off-axes NV center classes that do not contribute to the signal have their photoluminescence effectively quenched by $\sim$0.6 (see Appendix 3.A).

## 3.4 Dual suppression of Signal and Sensor Noise

Ancilla assisted frequency up-conversion enables low noise DC magnetometry. We shall draw the distinction between two sources of noise (Fig. 3-1) – that carried by the magnetic field being sensed (*signal noise*), and the noise on the NV center sensor due to its local environment (*sensor noise*). The signal noise originates at the source of the weak magnetic field being measured. For instance for the field from neurons this could be due to the buildup of charge carriers in the action potential[125]. The signal noise is in the $\hat{\mathbf{x}}$ (transverse) direction, and is assumed to have a low frequency noise

spectrum with cut-off $\omega_n$ (see Fig. 3-1), while to a good approximation sensor noise is primarily in the $\hat{\mathbf{z}}$ direction (leading to sensor dephasing), and with a Lorentzian spectral density centered about $\omega_{\text{Bath}}$ and with cut-off frequency determined by the mean coupling to spins/impurities in the sensor environment. As we describe in detail in Appendix 3.B, our technique enables *low-pass* filtering of signal noise, and *band-pass* filtering of sensor noise, tasks that are far less effective in the conventional Ramsey experiment. In analogy with conventional phase-sensitive detectors, the origin of this filtering action can be attributed to the ancilla performing a frequency of up-conversion to $\omega_L$ of the DC field to be measured, allowing us to lock-into this frequency and effectively *narrow* the noise bandwidth seen by the sensor. We also note that in comparison to techniques for ancilla-based quantum error correction which also lead to qualitatively similar gains in interrogation times potentially beyond $T_2$ [52,146] (provided feedback correction is applied faster than the error rate affecting the sensor), in our protocol the ancilla need not be initialized or actively manipulated, and hence greatly reduces the experimental resources required.

In Fig. 3-4 we experimentally *map* this signal filter lineshape, and demonstrate the expected low-pass frequency behavior (Appendix 3.B) with cutoff decreasing linearly with the total interrogation time of the experiment. We demonstrated low-pass signal noise cutoff of 13.32kHz for XY8-13, in contrast to the much larger Ramsey cutoff of 869.6kHz. In most quantum metrology platforms it is extremely beneficial to bring the sensor closest to the signal source, but this also makes it challenging to integrate an intermediary filter stage between them [147]. In our protocol the ancillary nuclear spin inherently performs this filtering task, allowing a tunable low-pass signal filter with no additional footprint.

The dual suppression of sensor noise and signal noise also allows a gain in magnetometer sensitivity as we shall now describe. Consider first that sensitivity $S \propto \frac{1}{\sqrt{n_r}}$,

where $n_r$ is number of repetitions of a single interrogation of the experiment; and assuming one is not limited by drift in the experimental control, this shot-noise regime is bounded by $\omega_n$. This is reflected, for instance, through the measurement of the sensor Allen deviation for a noisy DC field. Hence, in the regime $1/T_2 < \omega_n < 1/T_2^*$, a suppression in signal noise allows a gain in achievable shot-noise repetitions $n_r$, and consequently sensitivity by a factor approaching $\sqrt{\frac{T_2}{T_2^*}}$ over the conventional Ramsey technique.

Consider also that for an ensemble NV magnetometer, $S \propto \frac{1}{\sqrt{N_v}}$, where $N_v$ is the number of sensors per unit volume. However, the increase in $N_v$ is always associated with an increase in other electronic impurities that serve to degrade sensor performance. Indeed the mean dipolar coupling to these impurity spins sets the effective width of the Lorentzian sensor noise spectrum. However, the suppression of spin bath sensor noise via dynamical decoupling [131,148] allows one to maintain $N_v/T_2 \approx 1$, i.e. the sensitivity per unit volume remains approximately constant. In contrast, the scaling of $T_2^*$, and Ramsey sensitivity with sensor and impurity concentration is far more complex; experiments [131,148] indicate that $T_2^*$ saturates at moderate concentrations does not increase thereafter. Overall therefore, one can gain in sensitivity per unit volume for ensemble magnetometer operation through a dual suppression of signal and sensor noise.

## 3.5 Evaluation of magnetometer dynamic range

The dynamic range for our ancilla assisted DC magnetometry protocol is a function of deviation from the GLSAC, $\Delta$; indeed decreasing with smaller $\Delta$. In this section we evaluate in detail the factors affecting our NV sensor dynamic range, including the role of experimental imperfections and pulse errors and how they can be mitigated.

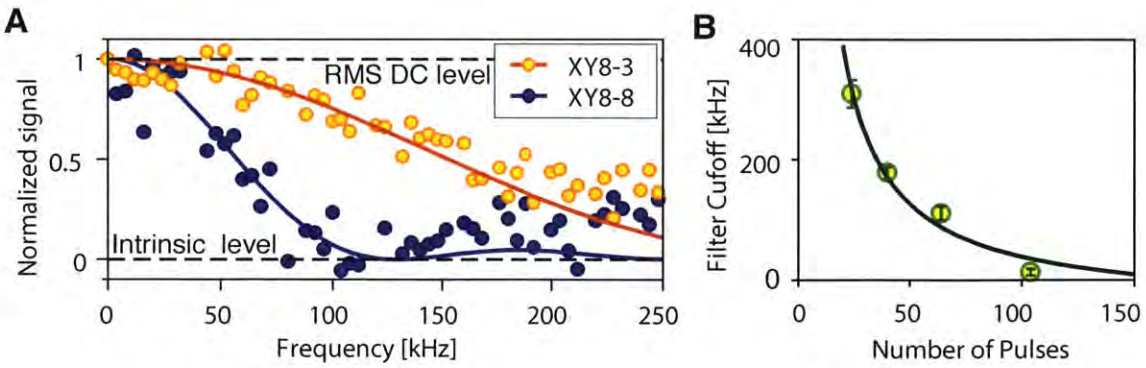


Figure 3-4: **Experimental low-pass filtering of signal noise. (A)** Representative experiments with an $^{14}$N ancilla at $\Delta$ =141 MHz, sweeping a single tone of low frequency magnetic field for increasing XY8-L magnetometry sequences. The signal obtained directly maps the filter function of the protocol. The data is normalized against concurrently measured values for the corresponding RMS DC signal and the signal due to intrinsic misalignment (dashed lines). Solid lines are the theoretical low-pass filters (Eq. (3.2)), and show a very good agreement with the experimental data. **(B)** Experimentally obtained filter cut-off frequency, defined by its first zero crossing. The filter becomes narrower with increasing interrogation times (pulse number) as expected (solid line), with the measured point corresponding to a cut-off of 13.32kHz. In contrast, the filter for the Ramsey technique is much broader, with cutoff $1/T_2^* \approx$ 869.6kHz. The error bars are obtained by fits of the theoretical low-pass filters.

Note that in our experiments, where we have no magnetic shielding, the presence of a residual field $B_i$ from the Earth affects the lower limit of the dynamic range, and sets an optimal operating regime for magnetometer performance. Appendix 3.D has a detailed analysis of this, instead here we consider the upper limit to the operating range, i.e. the maximum field $B_\perp$ that can be applied to our sensor with no loss of sensitivity.

First consider that the presence of $B_\perp$ causes a small tilt of the initial state prepared after the first $\pi/2$ pulse (assumed to be ideal for the moment), and overall

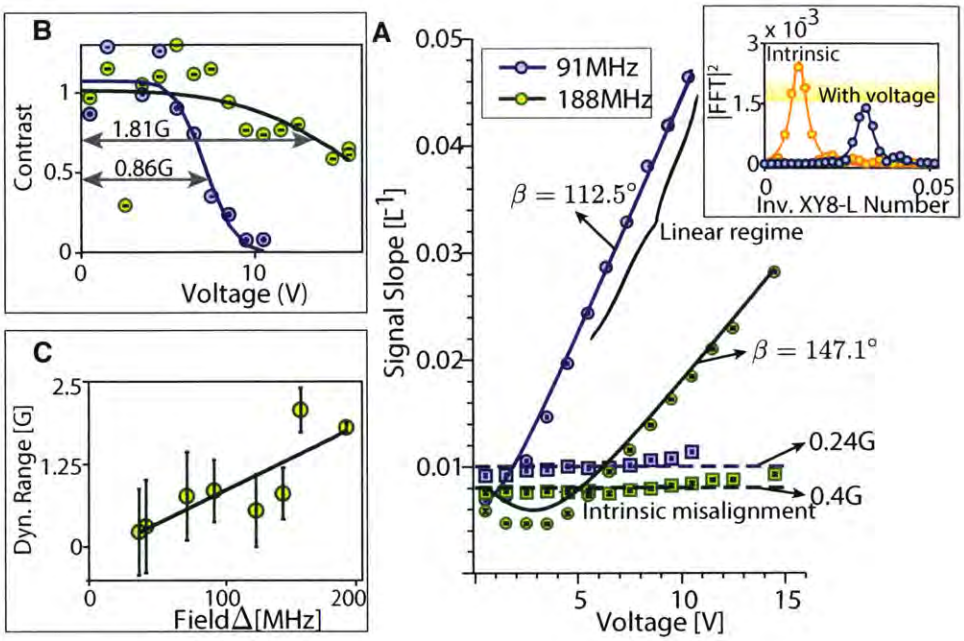


Figure 3-5: **Characterization of optimal sensor operating range.** We perform XY8-L experiments sweeping cycle number L for increasing $B_e$, produced by an external voltage. **(A)** Circles represent measured signal frequency $dS/dL$ for increasing $B_e$ for two values of $\Delta$. These are extracted following the inset, which shows a representative signal FFT, the two traces corresponding to intrinsic misalignment $B_i$ and the external field. Clearly, signal frequency increases on application of $B_e$. The solid lines are fits following Fig. 3-11, from which we discern the optimal (linear) operating regime where $B_e \gg B_i$. We also extract the values of $\beta$ (in-plane angle between $B_e$ and $B_i$) as shown. The squares are the concurrently measured values of $B_i$, and dashed lines represent the mean $B_i$. Error bars are obtained from a Lorentzian fit of the Fourier transform peaks. For field values closer to the GSLAC (decreasing $\Delta$) the signal slope $dS/dB_e dL$ increases, leading to increased magnetometer sensitivity (see Fig. 3-3). The decrease in signal contrast in the inset is an indication of finite sensor dynamic range. **(B)** To quantify this, panel denotes the corresponding normalized signal contrast for the same two fields. There is a sharp turning point (marked), which we refer to as the sensor dynamic range. Solid lines indicate a sigmoidal fit. Note that the normalization is performed with respect to the concurrently measured intrinsic misalignment. **(C)** Fitted dynamic range for different values of $\Delta$, indicating that it decreases with smaller $\Delta$. Solid line is a linear fit. The pulse Rabi frequency 3.57G sets the maximum achievable dynamic range in these experiments.

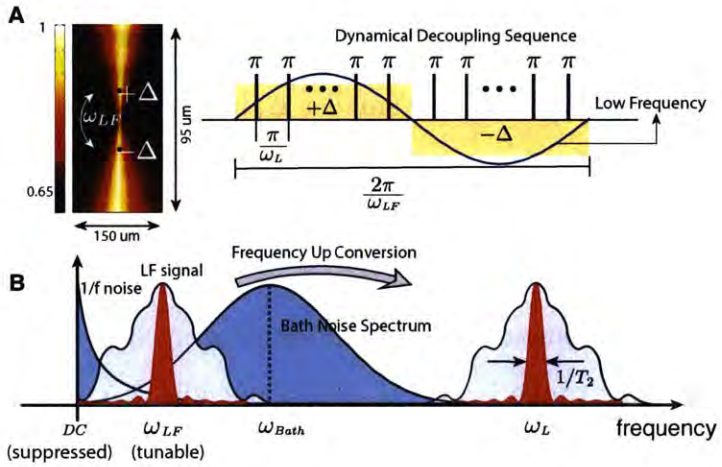


Figure 3-6: **Maytagging for low frequency AC magnetometry.** Schematic illustration of a method for sensing low frequency AC fields $\omega_{\mathrm{LF}}$. **(A)** Experimentally obtained NV photoluminescence in an XZ magnet scan close to the GSLAC (see Fig. 3-7). We propose alternating (maytagging) the field between two values of $\Delta$ symmetrically on either side of the GLSAC at $\omega_{\mathrm{LF}}$ (as low as $1/T_1$), with the right panel showing the pulse sequence. Crucially the pulsing frequency $\omega_L$ is decoupled from the sensing frequency $\omega_{\mathrm{LF}}$, allowing us to suppress $1/f$ and bath noise acting on the sensor, and also the DC component. **(B)** Frequency domain representation, wherein $\omega_{\mathrm{LF}}$ is up-converted to $\omega_L$ and detected via dynamical decoupling.

would lead to a loss in signal contrast (and hence magnetometer sensitivity) by the amount $\Delta^2/(\Delta^2 + B_\perp^2)$. However, this effect can be completely mitigated: for a known bias point of magnetometer operation $B_{0_\perp}$, one can compensate the tilt with a suitable preparation pulse with flip angle $\frac{\pi}{2} - \arctan(B_\perp/\Delta)$. A second factor affecting the dynamic range, especially as one approaches the GSLAC ($\Delta \to 0$), is the fact that the pulses become of lower quality due to the breakdown of the rotating wave approximation (RWA). In general this can be compensated for by decreasing the pulse Rabi frequency with smaller $\Delta$; however the minimum pulse Rabi frequency $\Omega_{\text{min}}$ is bounded by the situation when the pulses overlap, $\Omega_{\text{min}} = \pi/(2\omega_L)$. Imposing $\Omega_{\text{min}} < 5\Delta$ for RWA to hold, then sets a bound on the smallest approach to the GSLAC giving, $\Delta \gtrsim 5\pi/\omega_L \approx 20$ MHz for the $^{14}$N nuclear ancilla used in our experiments. Note that in comparison, for a $^{13}$C ancilla one only requires $\Delta \gtrsim 5$MHz, allowing a wider dynamic range (as detailed in Appendix 3.A, we are reliably able to achieve $\Delta < 6$MHz in our experiments).

Finally consider also that $B_\perp$ also affect pulse quality even within the RWA – the individual flip angle error being $B_\perp^2/(\Omega^2 + B_\perp^2)$, and pulse phase error $\arctan(B_\perp/\Omega)$, where $\Omega$ is the Rabi frequency where we have assumed that $B_\perp \ll \Omega$ so the pulses are still on-resonance. These errors are magnified upon increasing the number of pulses, leading to a loss of magnetometer sensitivity. However, the knowledge of the operating bias point $B_{0_\perp}$ can allow pulses to be suitably calibrated to be of low error. Even otherwise, the use of higher order pulse sequences, widely developed in the NMR[98,149], can suppress these errors to a large extent – the errors in one part of the sequence being exactly compensated by those in another part.

The presence of a finite dynamic range is evident in the decay of the curves in Fig. 3-2, the pulse error compensation being slightly imperfect at high XY8-L number. We perform a detailed experimental characterization (see Fig. 3-5 ) of the sensor

dynamic range by determining this loss in signal contrast of the signal upon sweeping external magnetic field (voltage), for increasing XY8 cycle number, and for different values of $\Delta$. The panel in Fig. 3-5(B) shows a representative example – at high applied voltages, there is a sharp loss of contrast beyond the sensor dynamic range. By performing a fit to a sigmoidal function $\sim \frac{\exp(-B_e - B_{e_0})}{[1+\exp(-B_e - B_{e_0})]}$, we extract the turning point $B_{e_0}$ that we refer to as the sensor dynamic range. From Fig. 3-5(C) it is evident that the dynamic range decreases as one approaches the GSLAC. Note that the Rabi frequency $\Omega = 10$MHz sets the upper bound on the dynamic range in these experiments.

## 3.6 Applications: Nanoscale vector magnetometry

Finally, let us describe a protocol for *full* vector magnetometry of DC fields[150] with a single NV sensor, that might allow the sensing of electric and magnetic fields with sub-nm spatial resolution. First employing the Ramsey technique and our ancilla assisted protocol, one is able to obtain the parallel and perpendicular component of the field. For instance in the experiments in Fig. 3-3, we extracted a tilt angle of the field of $\vartheta = 39.32°$. In order to further decompose the components in the perpendicular plane, one can apply a field in a particular direction (say $\hat{\mathbf{x}}$), and sweeping pulse number then allows the extraction of the in-plane angle $\beta$ through a Fourier transform. Note that this is equivalent to experiments described in Fig. 3-5, where we extracted the values of $\beta$ but with respect to the intrinsic misalignment $B_i$ that in this case acted as the applied field.

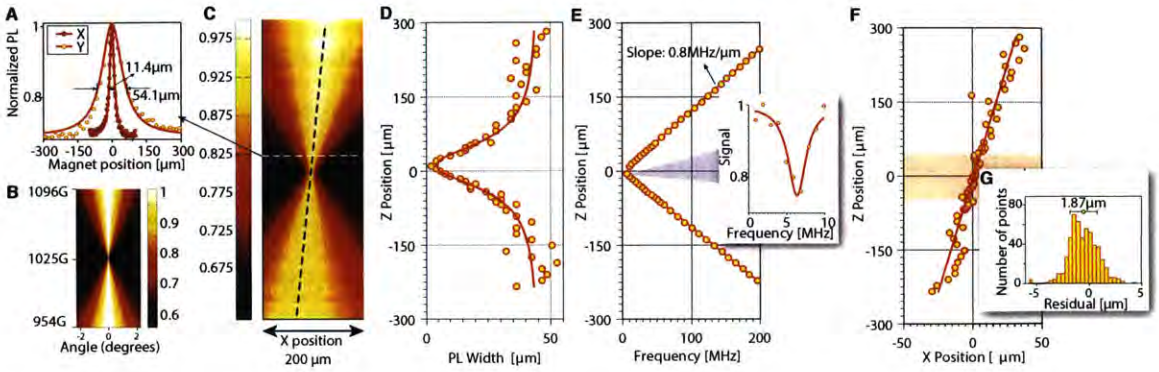


Figure 3-7: **Alignment of magnetic field close to GSLAC. (A)** Representative NV center photoluminescence curves obtained on magnet sweep in X and Y. Clearly one is very sensitive to misalignment close to the GSLAC at 1025G. **(B)** This is demonstrated clearly in simulations of NV photoluminescence as a function of misalignment angle and magnetic field. **(C)** Experimentally obtained NV photoluminescence in an XZ magnet scan. The narrow neck is the anti-crossing point, and the dashed line indicates the position where the fluorescence is maximized and consequently the magnet is close to aligned. **(D)** Experimentally extracted PL widths plotted on the same Z axis. The solid line is a Lorentzian fit. In the GSLAC neck, the PL width is under $5\mu$m. **(E)** Measured NV electronic Larmor frequency $\Delta$ on the same Z axis. Remarkably the frequency varies linearly with Z (the solid line is a linear fit). We are able to align the field to better than $\Delta = 6$MHz. The inset shows this through a pulsed ODMR experiment with a 1MHz linewidth, and also demonstrates the the $^{14}$N nuclear spin is optically polarized. **(F)** Optimization of field alignment via a gradient ascent algorithm. On the same Z axis, the circles are alignment positions for magnet X position, while the solid line is a linear fit only using points near the GSLAC neck (shaded). **(G)** Inset represents a histogram of the residuals to the fit in the shaded region over 36 such datasets, showing that the average error of magnet alignment close to the GSLAC is reproducibly under $1\,\mu$m.

## 3.7 Outlook: Low Frequency AC Magnetometry

Several ubiquitous fields of experimental significance are often of low frequency (30kHz - 1MHz). For instance, this a common occurrence in determine impulse response fields from magnetic materials[151], where the repetition rate is often material limited to $\omega_{\mathrm{LF}} < 1\mathrm{MHz}$. It would be invaluable to have an experimental means of measuring them while still maintaining sensor coherence inspite of noise sources at much higher frequency. Unfortunately the conventional echo based AC field sensing techniques require the pulsing frequency to be exactly matched with the frequency one wants to sense, which is not possible when $\omega_{\mathrm{LF}} < 1/T_2^*$ due to sensor dephasing, and poses a severe experimental constraint. Hence the low frequency regime is a "'blind-spot" for conventional magnetometry[152].

We now propose a method, employing ancilla assisted frequency up-conversion, to overcome this challenge. The basic idea is illustrated in Fig. 3-6, where analogous to field reversals employed in MEMS technology[153], we consider alternating (*maytagging*) the field between two values of $\Delta$ symmetrically situated about the GSLAC, with the maytagging frequency chosen to be the frequency of interest $\omega_{\mathrm{LF}}$ (Fig. 3-6). This can be experimentally arranged for instance by the application of a control voltage causing a $\hat{\mathbf{z}}$ field, and by choosing the initial bias field to be at exactly GSLAC, $\Delta \to 0$. Maytagging leads to the amplitude modulation of the effective field being sensed, $B_\perp A_\perp/(\Delta \cos\omega_{\mathrm{LF}} t)$, and only frequencies in $B_\perp$ that match the maytagging frequency contribute to the signal. All other components, including crucially the DC component, are filtered out in the same manner as the filtering of signal noise in Fig. 3-4 (see Appendix 3.B for a detailed derivation).

Crucially now this sensing frequency is under experimental control, and can be

in principle as low as $1/T_1 \approx 200$ Hz. Importantly this allows us to go away from the zero frequency point where the $1/f$ noise has a potentially significant contribution. Hence a tunable frequency up-conversion from $\omega_{\mathrm{LF}}$ that can be very low, to a high-frequency $\omega_L$, allows us to decouple the pulsing frequency from the sensing frequency. It is also remarkable that since $\omega_L$ is largely independent to the exact value of $\Delta$ (Appendix 3.C), the protocol is robust to finite rise and fall times in the application of the maytag field given sufficiently broadband pulses. We expect that such low frequency magnetometry would enable an important lock-in tool for sensing slowly varying fields that are of wide interest, including sensing neuronal activity and edge currents from topological insulators.

## 3.8 Conclusions

We have demonstrated a new modality for high sensitivity, low noise DC magnetometry through a process of frequency up-conversion via an ancillary nuclear spin, allowing interrogation potentially at the full coherence time $T_2$. The enhanced noise rejection of signal and sensor noise could lead to enhanced sensitivity per pixel size. In conjunction with Ramsey spectroscopy, our technique enables full vector DC magnetometry at the nanoscale. Similar up-conversion ideas can be applied to the magnetometry of low frequency AC fields. We anticipate applications of our sensing technique in many areas of biology and condensed matter physics.

*Acknowledgments* – We gratefully acknowledge discussions with S. Bhave, R. Walsworth and F. Jelezko. This work was supported by xxx.

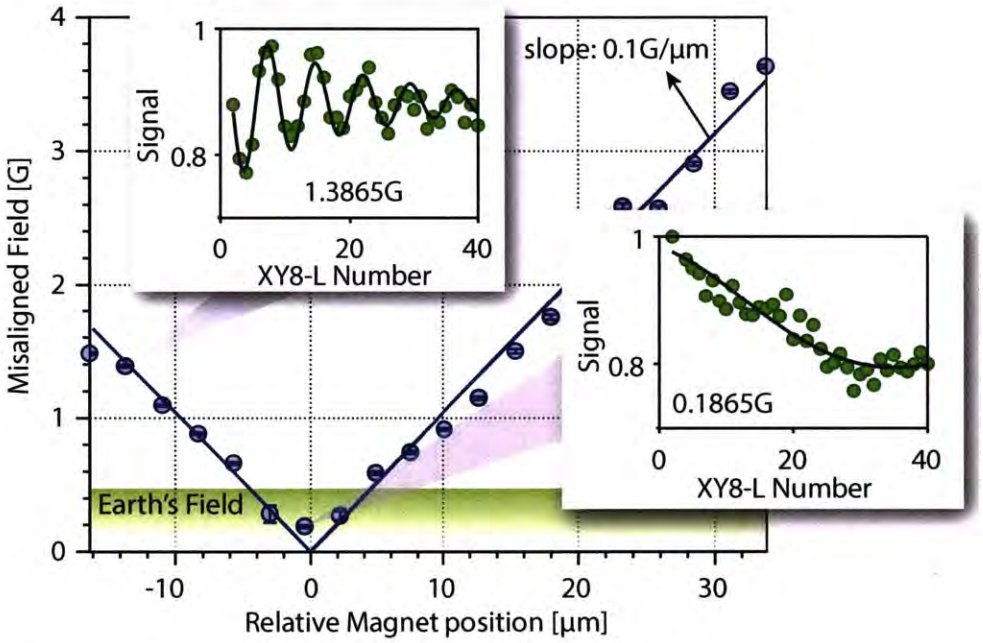


Figure 3-8: **Controlled tuning of intrinsic misalignment.** Transverse misaligned field introduced by translating the magnet in X from the aligned position (Fig. 3-7) at $\Delta = 153$MHz. The dependence is very closely linear (solid lines are a fit with slope 0.1 G/$\mu$m), allowing one to controllably increase intrinsic misalignment (employed in Fig. 3-12) or minimize it. The misaligned field here is estimated by XY8 experiments sweeping the cycle number (insets), with error bars estimated from a Lorentzian fit of their Fourier transforms. The shaded region represents misalignment at the $< 0.5$G level, comparable to the field of the Earth.

# Appendix

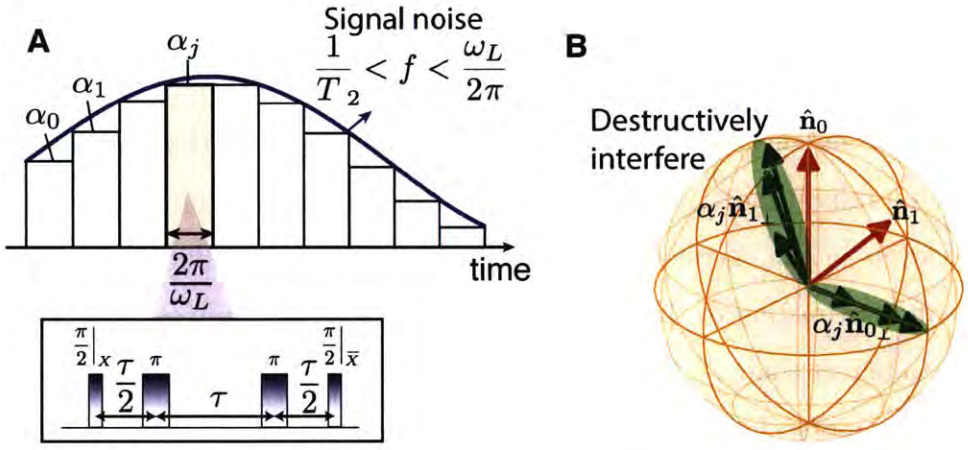


Figure 3-9: **Low frequency noise rejection in ancilla assisted magnetometry.** Schematic derivation of the low-pass signal noise filter inherent to our protocol. **(A)** Consider a low frequency magnetic noise tone of frequency $f \ll \omega_L$. Each rectangular block corresponds to a CPMG pulse sequence (inset) of total time $\tau = 2\pi/\omega_L$. To a good approximation the signal results from the combined effect of the tilt angle $\alpha_j = B_\perp^{(j)} A_\perp/\Delta$, discretized over the $L$ CPMG blocks.**(B)** Geometric visualization of filtering action. Here $\hat{\mathbf{n}}_0$ and $\hat{\mathbf{n}}_1$ (red arrows) are the axes of nuclear rotation. For a *static* DC field, the effective vectors are perpendicular to the original axes and anti-parallel leading to a strong signal through constructive interference. However in the presence of low-frequency signal noise, these open up a fan of vectors (green arrows), for instance $\alpha_j\hat{\mathbf{n}}_{1_\perp^{(j)}}$, over which the effective propagator needs to be evaluated. This leads to destructive interference, and consequently signal noise suppression that increases with $L$.

## 3.A Magnetic field alignment at the GSLAC

In this section, we present details of the magnet construction and alignment procedure close to the GSLAC (see Fig. 3-7). The magnet is a composite assembly of 10 N52 cubic magnets of 9.53mm edge (K&J Magnetics B666-N52) and 1.48T surface magnetization. We define X to be the magnetization axis of the magnet assembly, and is placed parallel to the edge of the [100] diamond. The magnet is a mounted on a stage controlled by motorized actuators (Zaber TNA08A50) for translation in X,Y and Z.

To align the magnet near the GSLAC (1020G), we exploit the fact that the NV center photoluminescence (PL) gets quenched with increasing misalignment due to mixing of levels in the excited state[154,115] (Fig. 3-7(**B**)). Translating the magnet in X and Y, and optimizing to the position of maximum photoluminescence leads to an alignment to better than 1°. An experimental 2D XZ map of NV photoluminescence illustrates this more clearly, (Fig. 3-7(**C**)), the narrow neck corresponding to the GSLAC. Indeed the extracted widths of the PL as a function of the magnet height (Z) (Fig. 3-7(**C**)) indicates that the GSLAC neck could be narrower than $5\mu$m.

The NV center Larmor frequency $\Delta$ changes linearly as a function of the magnet height, and can be made to approach zero close to the GSLAC (Fig. 3-7(**D**)). We attribute this to the approximate linear field lines given the small dimensions of the neck region compared to the size of the magnet. To further optimize the alignment to the level of the Earth's field ($<$ 1G), we employ a gradient ascent algorithm that optimizes to the highest photoluminescence in the GSLAC neck region (shaded), and extrapolate linearly away from this region, once again exploiting the linear dependence of NV Larmor frequency. The small PL variance in the GSLAC

neck ensures that the alignment procedure is reproducible and of low error (Fig. 3-7(**E**)). We note that when aligned the $^{14}$N nuclear spin is completely polarized through a hyperfine mediate optical process [155], further increasing the signal contrast obtained in the magnetometry experiments.

The amount of misalignment can be accurately measured through an XY8 experiment, sweeping the number of pulses and extracting the frequency $f_0$ of the resulting oscillations (Fig. 3-8), following $B_\perp = \tan(f_0/2)\frac{\Delta\omega_L}{\gamma_e A_\perp}$. We are reproducibly able to align the field to better than 0.5G, this $\sim 0.05\%$ residual level largely being set by the magnetic field of the Earth (there is no shielding in our experiment). Translating the magnet in X also allows the controllable addition of misalignment, the amount of which also goes approximately linearly, and enables us to perform experiments to quantify the effect of residual Earth's field on the sensor dynamic range (Appendix 3.D).

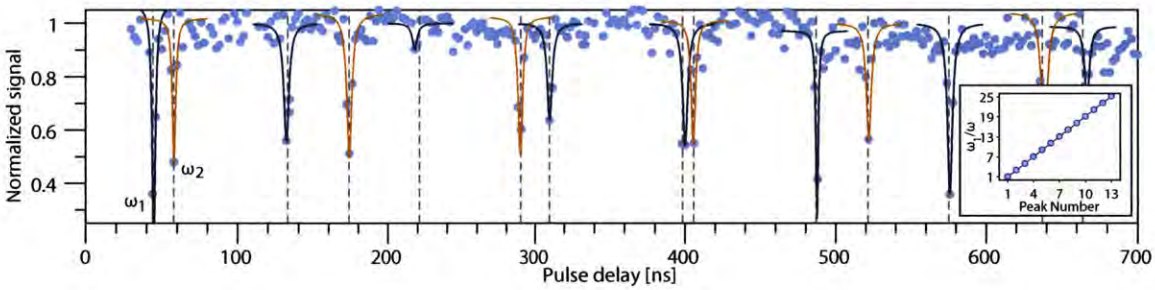


Figure 3-10: **Signal harmonics in $^{14}$N assisted magnetometry.** DC magnetometry signal at 1344G for long inter-pulse times showing families of harmonics from the $^{14}$N ancilla, occurring at $\omega_{1,2} = Q \pm A_\parallel/2 \pm \gamma_n B_z \mp A_\perp^2/4\Delta$. These are indicated respectively by the orange and blue peaks. Gray lines indicate the theoretically expected values of the harmonics, and we find very close experimental agreement. The inset plots the experimentally obtained values of the frequencies of the blue peaks as a function of $\omega_1$, and demonstrate that we measure odd $^{14}$N harmonics as expected. Employing these, one can perform experiments in a suitable duty cycle regime where the pulse error can be minimized.

## 3.B Derivation of low pass signal noise filtering

We now consider the ability of our ancilla assisted DC magnetometry protocol to effectively act as a low pass filter for the noise carried by the field to be sensed (signal noise). This signal noise could be for instance, amplitude modulations in the field originating at the signal source. In this section, we derive the effective filter function of the signal noise employing a first order Magnus expansion [90].

Let us first obtain the interferometric signal obtained under a purely DC field. In the frame of the ancillary nuclear spin there are two effective axes of rotation conditional on the state of the NV electron, that can be represented as the normalized Hilbert-Schmidt vectors [72], $\hat{H}_{|0\rangle} := \hat{\mathbf{n}}_0 = \hat{\mathbf{z}}$ ; $\hat{H}_{|-1\rangle} := \hat{\mathbf{n}}_1 = \cos\alpha\,\hat{\mathbf{z}} + \sin\alpha\,\hat{\mathbf{z}}_\perp$, with the effective Hamiltonian being, $\mathcal{H} = \Delta S_z + |0\rangle\langle 0|\, H_{|0\rangle} + |-1\rangle\langle -1|\, H_{|-1\rangle}$ with $H_{|0\rangle} = \gamma_n B_z I_z$, $H_{|-1\rangle} = \omega_L I_z + \frac{B_\perp A_\perp}{\Delta} I_x$. The delay between pulses $\tau$ is typically swept (Fig. 3-2), and when the delay matches the condition $\tau = \pi/\omega_L$, the signal is now interferometrically obtained as an effective overlap of two propagators conditioned on the NV state: $\mathcal{U}_{|0\rangle} = \exp(-i\alpha\sigma\cdot\hat{\mathbf{n}}_{1_\perp})$ and $\mathcal{U}_{|1\rangle} = \exp(i\alpha\sigma\cdot\hat{\mathbf{n}}_{0_\perp})$, and is of the form $S = \frac{1}{2}\left[1 + \mathrm{Tr}\left\{\mathrm{Re}\left(\mathcal{U}^\dagger_{|0\rangle}\mathcal{U}_{|-1\rangle}\right)\right\}\right]$. With increasing interrogation times, effectively achieved through the application of larger number $L(= N/2)$ of the CPMG cycles, there is a linear phase accumulation in the interferometric detection [135], $\mathrm{Tr}\left\{\mathcal{U}^L_{|0\rangle}\mathcal{U}^{L\dagger}_{|-1\rangle}\right\} = \cos^2 L\alpha + (\hat{\mathbf{n}}_{0_\perp}\cdot\hat{\mathbf{n}}_{1_\perp})\sin^2 L\alpha$. The last term is responsible for the growing signal strength with pulse number, giving $S = \sin^2(L\alpha)\cos^2(\alpha/2) \approx \cos(2L\alpha)$ (see Fig. 3-2). Note that this analysis remains unchanged for spin-1 nuclei, considering we employ a pair of pseudo spin-1/2 levels (Fig. 3-10).

To derive the noise filter function, we decompose the signal noise into low frequency AC tones of frequency $f$ and obtain the signal as a function of $f$. Consider-

ing $L$ cycles of the CPMG experiment and assuming that one works in the regime, $1/T_2 < f < \omega_L/2\pi$, to a very good approximation perturbation theory can be applied piece-wise (Fig. 3-9(**A**)) over each of the $L$ blocks, giving rise to the effective angles $\alpha_j = B_\perp^{(j)} A_\perp/\Delta$ proportional to the field value $B_\perp^{(j)}$ at every mean interval. Note that while considering a $^{14}$N ancilla, $\omega_L/2\pi \approx 3.87$MHz, and $1/T_2 \approx 1$kHz, and hence our analysis is valid for a wide range of signal noise frequencies.

Now, one can evaluate the *effective* propagators $U^{\text{eff}}_{|0,-1\rangle}$ over the entire sequence by taking the product, $U^{\text{eff}}_{|0,-1\rangle} = \prod_j U^{(j)}_{|0\rangle,|-1\rangle}$. For instance, since the axis $\hat{\mathbf{n}}_{0_\perp}$ is the same for all of the cycles, the propagator $U^{\text{eff}}_{|-1\rangle}$ is particularly simple to calculate: $U^{\text{eff}}_{|-1\rangle} = \exp(-i\sum_j \alpha_j \sigma \cdot \hat{\mathbf{n}}_{0_\perp})$. It is evident that for high frequency signal noise components, for which $\sum_j \alpha_j \to 0$, $U^{\text{eff}}_{|-1\rangle} \to \mathbb{1}$, there is *destructive* interference between different CPMG cycles, the signal suppressed, and consequently the noise component effectively filtered out. It is such destructive interference that increases proportional to $L$, and determines the signal noise filter.

To see this in more detail, let us first similarly evaluate $U^{\text{eff}}_{|-1\rangle}$ in a zeroth order Magnus expansion. Then we have that the signal,

$$S \propto \text{Tr}\left\{U^{\text{eff}\dagger}_{|0\rangle} U^{\text{eff}}_{|-1\rangle}\right\} = \cos(L\sqrt{\mathcal{A}^2+\mathcal{B}^2})\cos(L\overline{\alpha}) - \frac{\mathcal{B}}{\sqrt{\mathcal{A}^2+\mathcal{B}^2}}\sin(L\overline{\alpha})\sin(L\sqrt{\mathcal{A}^2+\mathcal{B}^2}) \tag{3.1}$$

where $\overline{\alpha} = \frac{1}{L}\sum \alpha_j$ and $\mathcal{A} = -\frac{1}{L}\sum \alpha_j \sin\alpha_j$ ; $\mathcal{B} = \frac{1}{L}\sum \alpha_j \cos\alpha_j$. For weak noise, $\|\alpha_j\| \ll 1$, and retaining only first order terms $\mathcal{A} \approx 0$ ; $\mathcal{B} \approx \overline{\alpha}$ and to a good approximation we have, $S \propto \text{Tr}\left\{U^{\text{eff}\dagger}_{|0\rangle} U^{\text{eff}}_{|-1\rangle}\right\} \approx \cos 2L\overline{\alpha}$. Let us consider the concrete case of a single noise tone of frequency $f = 1/(\tau L_p)$, where $L_p$ refers to the effective CPMG cycle number required to complete one period. Then, assuming

$\alpha_j = \alpha \cos\left(\frac{\pi j}{L_p} + \varphi\right)$ and small $\alpha$, giving,

$$S \propto \cos\left\{2\alpha \cos\left(\frac{\pi(L+1)}{2L_p} + \varphi\right) \frac{\sin\left(\frac{\pi L}{2L_p}\right)}{\sin\left(\frac{\pi}{2L_p}\right)}\right\} \tag{3.2}$$

Note that $\varphi$ here refers to the phase of the noise tone with respect to the start of the pulse sequence, and to derive the effective filter one has to perform an average over $\varphi$. Importantly, the filter characteristics is set by the second term in the argument of Eq. (3.2) which has the form analogous to a Bragg grating [33,30], with the filter width defined by its first zero given by $f = 1/(2L_p\tau)$, and the filter suppression increases linearly with $L$, giving a low-pass bandwidth of $1/T_2$ in the extreme case.

Geometrically the action of the frequency tone is extremely clear in the space of unitary vectors (see Fig. 3-9**(B)**): for the propagator $U_{|-1\rangle}$ we have an effective shortening of the corresponding vector, while for $U_{|0\rangle}$ we have a fan of vectors over which the effective propagator has to be evaluated. In essence, for purely DC fields the signal terms in each cycle are all fixed strength, leading to a constructive rotation by the same amount. On the other hand AC fields lead to scrambling of the rotations and effectively destructive interference, with the filter suppression increasing with the effective time of the sequence. Hence our ancilla assisted protocol leads effectively to a low pass filter for signal noise and a band-pass filter for sensor noise, both with bandwidth $1/T_2$.

In comparison, for the Ramsey experiment there is poor filtering [156,33]; we have free evolution and all frequencies are allowed to contribute to sensor dephasing, the filter being of the form $F = [\sin(\omega T_2^*)/\omega]^2$, having bandwidth $1/T_2^*$ which could be two orders of magnitude larger than achievable in our experiment (Fig. 3-4). In effect then, the noise on the sensor due to spins in the NV environment set a bound

on the amount of filtering one can achieve for the noise carried by the field being sensed.

## 3.C Robustness of $^{14}$N ancilla to magnetic field drift

While the $^{14}$N has the inherent advantage of being a part of every NV center sensor, it offers significant additional advantages from a noise rejection perspective. First, note that since $\omega_L = Q - A_\parallel/2 - \gamma_n B_z$ is dominated by the large quadrupolar interaction $Q$ =-4.95 MHz, it places the effective frequency to which up-conversion occurs to point that is much higher than possible via the intrinsic Zeeman field $\gamma_n B_z$ ≈300 kHz alone; allowing a significant suppression of the signal noise, falling $\propto 1/\omega_L^2$. Indeed for most DC signals of practical interest, $\omega_L$ far exceeds the cut off frequency $\omega_n$ carried by the signal. More remarkably, the frequency $\omega_L$ is immune to magnetic field drift to first order, since the relative change $\delta\omega_L/\omega_L \approx \gamma_n \delta B_z/(Q - A_\parallel/2) = (7.75\times10^{-5})\cdot\delta B_z$ is suppressed by over four orders of magnitude. This ensures that the effective frequency employed for quantum lock-in detection, and the quantum interpolation used to implement it, is robust against field drift. Indeed drift only causes a change in $\Delta$, and hence an effective amplitude modulation of the up-converted signal at $\omega_L$; however this is exactly the signal noise that can be suppressed to better than $1/T_2$ by our protocol (Sec. 3.4). Hence the $^{14}$N ancilla affords an inherent robustness to magnetic field drift, and provides a enabling experimental advantage.

In order to study this experimentally (Fig. 3-10), we performed experiments at $\Delta = -893$MHz (1344G), and the $^{14}$N harmonic is very closely at the same frequency $\omega_L \approx 3.87$MHz as close to the GSLAC (see Fig. 3-2). Note that close to the GSLAC due to optically mediated nuclear spin polarization [155], we normally detect only one of the two $^{14}$N frequencies ($\omega_2$ in Fig. 3-10); however at large $\Delta$ the two frequencies

and their odd harmonics are clearly discernible.

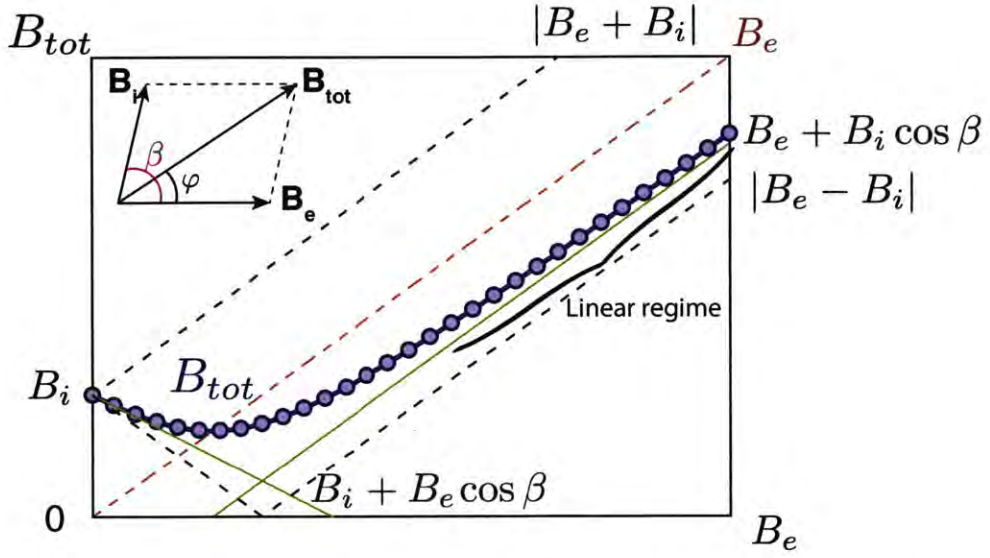


Figure 3-11: **Geometric interpretation of optimal magnetometer operating regime.** Panel denotes the value of the effective field $|B_{\rm tot}|$ formed as a vector sum (inset) of the external field to be measured $B_e$ and the intrinsic misalignment $B_i$, separated by the representative angle $\beta = 3\pi/4$ rad. Green lines denote asymptotes in the extremal regimes $B_e \gg B_i$ and $B_e \ll B_i$, while black dashed lines denote the limits of $|B_{\rm tot}|$. In the regime $B_e \gg B_i$, the total field grows linearly with $B_e$, and there is no loss of sensitivity due to intrinsic misalignment. This is the optimal operating regime for the NV sensor (see also Fig. 3-12). One can clearly discern this lineshape in the experiments of Fig. 3-5, where the signal slope measures $B_{\rm tot}$.

## 3.D Effect of intrinsic misalignment on sensitivity and operating range

We refer to intrinsic misalignment $B_i$ as the residual field away from the ground state anti-crossing, due chiefly to the magnetic field of the Earth. In principle this can be eliminated to about a part per million through magnetic shielding [144], a conventional

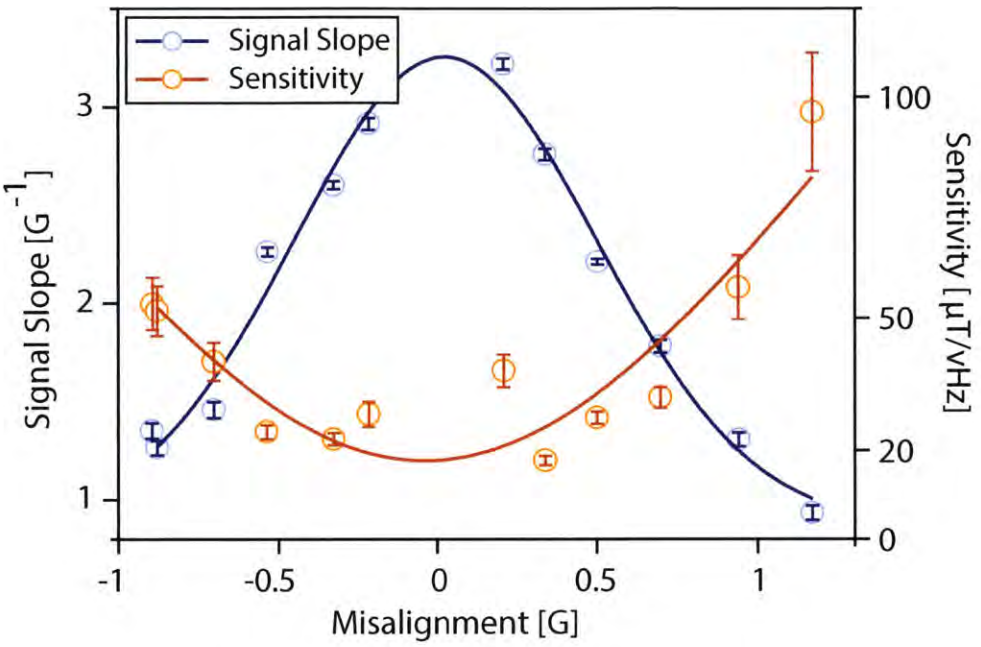


Figure 3-12: **Effect of intrinsic misalignment on sensitivity.** NV magnetometer DC sensitivity (orange) and the signal slope $dS/dB_e|_{B_0}$ excluding signal decay (blue), measured for different values of intrinsic misalignment $B_i$. Experiments correspond to XY8-48 (interrogation time 46.47$\mu$s) at $\Delta = 174.5$MHz. Misalignment is controllably added following Fig. 3-8. Error bars are calculated from Lorentzian fits of the Fourier transforms of the obtained magnetometer fringes. The solid lines are gaussian fits to guide the eye. As is evident, increasing intrinsic misalignment has a deleterious effect on sensitivity, and for optimal sensor performance one would operate the NV sensor in the linear regime $B_e \gg B_i$, or employ magnetic field shielding.

choice for ultra-sensitive magnetometers. However, in our experiments without any shielding, intrinsic misalignment imposes limitations of sensor operating range, effectively setting an optimal bias point for sensor operation as we shall describe below.

More precisely, the field to be measured $B_e$, and $B_i$ are both perpendicular to the N-V axis but are separated by the angle $\beta$; hence the field one measures is the vector sum $\vec{B}_\perp = \vec{B}_{\text{tot}} = \vec{B}_e + \vec{B}_i$, with $B_{\text{tot}} = \sqrt{B_e^2 + B_i^2 + 2B_eB_i\cos\beta}$. An increasing $B_e$, in general, leads to to a nonlinear response of the sensor (see Fig. 3-11). Indeed in the regime when $B_e \ll B_i$, the effective field is approximately given by the asymptote $B_{\text{tot}} = B_i + B_e\cos\beta$ leading to an effective loss of sensitivity by $\cos\beta$. As $\beta \to \pi/2$, the field sensitivity vanishes to first order. Geometrically, this is because increasing $B_e$ goes into changing the direction of $B_{\text{tot}}$ rather than its amplitude. In the opposite regime, when $B_e \gg B_{\text{int}}$, we effectively have the asymptote $B_{\text{tot}} = B_i\cos\beta + B_e$ , for which there is no loss of sensitivity, and which we shall refer to being the *linear regime* of the NV sensor. More generally, we have that the rate of change, $dB_{\text{tot}}/dB_e = \left[\frac{B_e + B_i\cos\beta}{B_{\text{tot}}}\right] = \cos\varphi$, where $\varphi$ is the angle of the resultant vector $\vec{B}_{\text{tot}}$ to $\vec{B}_e$ (Fig. 3-11). This allows us to concretely quantify the onset of the linear regime as being where $\varphi \lesssim \pi/8$. The presence of the linear regime is evident in the experiments of Fig. 3-5**(B)**, where the signal slope upon sweeping XY8-L cycle number immediately reflects $B_{\text{tot}}$; the solid lines being fits to the theoretical result above. Note that the values $\beta$ differ for different $\Delta$ values due to our magnet alignment procedure (Appendix 3.A).

In order to experimentally study the effect of intrinsic misalignment on sensitivity, we increase $B_i$ in a controllable fashion following Fig. 3-8, and perform ancilla assisted DC magnetometry at every point. The results in Fig. 3-12 indicate that intrinsic misalignment leads to a loss in sensitivity, and severely affects sensor performance; thus in experiments to characterize and operate the NV magnetometer (for

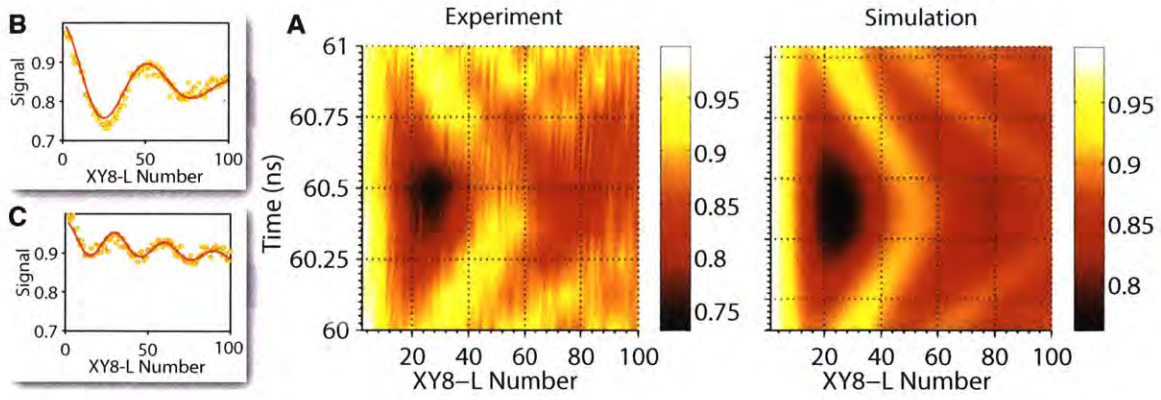


Figure 3-13: **Quantum interpolation to efficiently sample the signal peak.** **(A)** In a $\Delta\tau = 1$ns window about the $^{14}$N signal peak (Y axis), we sweep the XY8-L number (X axis), with $\Delta\tau$ being the timing resolution of our timing hardware (see also Fig. 3-2). These experiments are performed at $\Delta$ =150MHz. We use quantum interpolation effectively supersample 16 slices in this window. The signal obtained matches closely with the expected theoretical lineshape in Sec. 3.2 (right panel), allowing us to estimate the static misaligned field in these experiments $|B_\perp| = 1.46\mu$T. **(B-C)** Lower inset demonstrates that without quantum interpolation there is significant loss of signal contrast, but the full contrast is recovered if one samples the signal peak (upper inset).

instance Fig. 3-3), we always work in the linear regime – by suitable alignment of the magnetic field we can reliably reduce $B_i < 0.5$G (Appendix 3.A).

## 3.E Quantum interpolation to efficiently sample the signal peak

The delay between the $\pi$ pulses in CPMG/XY8 experiments has to be $\pi/\omega_L$, however this makes one susceptible to finite timing resolution $\Delta\tau$ of the hardware used to generate the pulses (in our case $\Delta\tau = 1$ns). Indeed as the number of pulses $N$

increases, the signal peak becomes effectively narrower (see Sec. 3.2), leading to significant loss of contrast if one does efficiently sample the true signal peak. The error goes as[135], $\epsilon \approx \frac{1}{4}(N\alpha)^2\Delta\tau^2\left(2-\frac{\alpha^2}{2}\right)^2$ that scales $\propto N^2(\Delta\tau)^2$, leading consequently to a severe loss of magnetometer sensitivity at large $N$.

We recently introduced quantum interpolation[135] as a means to completely overcome this hardware problem, allowing one to effectively *supersample* the signal peak with arbitrarily high precision even with a finite $\Delta\tau$. If the propagator $\mathcal{U}(\tau_k)$ describes action of a CPMG pulse sequence block, with $\pi$-pulses separated by a time $\tau_k = k\Delta\tau$, then quantum interpolation refers to the construction,

$$U^N(\tau_{k+p/N}) = \mathcal{P}\left\{\prod_{m=1}^{N-p}\mathcal{U}(\tau_k)\prod_{n=1}^{p}\mathcal{U}(\tau_{k+1})\right\} \approx \mathcal{U}^N(\tau_{k+p/N}), \tag{3.3}$$

that allows the construction of supersamples $\tau_{k+p/N}$ that cannot usually be accessed. Here the permutation $\mathcal{P}$ refers to a optimal sequence ordering that minimizes error in the construction, the error going as $\mathcal{O}(\Delta\tau^2)$. Importantly the number of additional timing samples achievable via quantum interpolation scales linearly with the total number of pulses[135], allowing us to completely mitigate the problem of hardware finite hardware resolution for increasing $N$.

In Fig. 3-2 quantum interpolation is used to sample the $^{14}$N signal peak to about 48 times higher resolution (20.8ps) than set by our hardware, allowing us to to determine the exact peak position at $\approx$ 60.45ns. The signal lineshape can be described as a modified sinc function with a slight asymmetry about the peak, and can be evidently discerned in Fig. 3-2. The power of the technique is demonstrated in is described Fig. 3-13, where we obtain the magnetometry signals similar to Fig. 3-2 for 16 different supersamples in the $\Delta\tau$ window set by our hardware. The experimental data closely matches the theoretically expected sinusoidal lineshape.

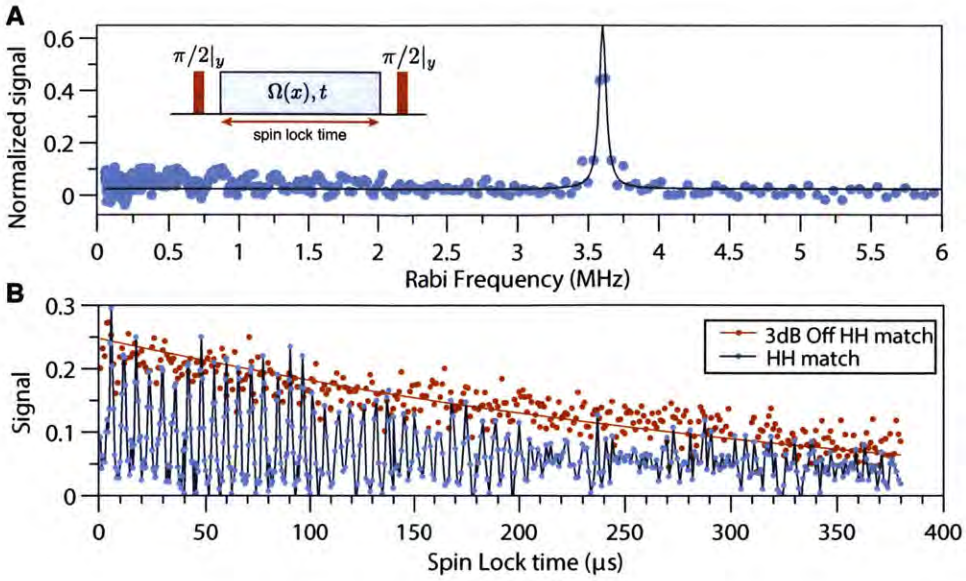


Figure 3-14: **Spin lock ancilla assisted DC magnetometry (A)** Spin lock measurements performed at 717G, with lock length fixed at $10\mu$s, and sweeping Rabi frequency $\Omega$. We obtain a magnetometry signal at the Hartmann-Hahn match $\Omega = \omega_L$. Inset shows the pulse sequence. **(B)** Sweeping spin lock time at $\Delta = 165$MHz at the Hartmann-Hahn match (blue) and 3dB away (orange). The oscillations constitute the DC magnetometery signal, exactly analogous to Fig. 3-5. Crucially we are able to extend the sensor interrogation time $> 350\mu$s.

The obtained *chevron* patterns in Fig. 3-13 are exactly identical to those in two-spin exchange[99]. Overall, this illustrates that the quantum interpolation construction is indeed of low error, and demonstrates that the true signal peak cannot be accounted for without it.

## 3.F Spin lock DC magnetometry

We now consider an alternate strategy for ancilla assisted DC magnetometry via spin locking[34,35] (see inset of Fig. 3-14**(A)**). The NV center is spin locked at a

Rabi frequency $\Omega$, and at the Hartmann-Hahn matching condition[109,110] $\Omega = \omega_L$, there is once again a second-order hyperfine mixing $\propto B_\perp A_\perp/\Delta$ that causes a flow of polarization away from the NV center. This can be interferometrically detected and constitutes the magnetometry signal. In essence this method is a rotating frame analogue of the dynamical decoupling protocol we employed in the main portion of this chapter. The signal has exactly the same form of Sec. 3.2, $S = \frac{1}{2}[1 + \cos(\alpha t)]$, where $t$ is the spin-lock time, and the ancilla assisted frequency up-conversion that enabled signal and sensor noise suppression is also identical. Overall spin lock DC magnetometry might offer some additional inherent advantages: (i) the Hartmann-Hahn matching occurs in drive amplitude, and hence does not require quantum interpolation (ii) since decoupling is applied continuously, a larger amount of the sensor noise spectrum can be effectively suppressed, quantified by the coherence time $T_{1\rho}$ that is usually greater than echo based $T_2$. In practice however, amplifier noise sets the ultimate coherence time achievable. In Fig. 3-14**(B)** we present example spin lock DC magnetometry data at $\Delta = 165$MHz, indicating an interrogation time of over $350\mu$s is achievable. A detailed analysis of magnetometer sensitivity using spin-lock techniques will be presented elsewhere. However we note that Fig. 3-14 indicates that we are primarily limited in the interrogation times in Fig. 3-3 (and hence sensitivities) by pulse error, and can be mitigated through higher order pulse compensation[149].

## 3.G Data analysis

For clarity, we now detail the procedure for the fitting of experimental data that is used to calculate the corresponding error bars, primarily in Fig. 3-3, Fig. 3-4 and Fig. 3-5. We use a Monte-Carlo approach to estimate the uncertainty of the various

fit parameters following Ref.[135].

Let us denote the fit parameters for our model by $\mathbf{P}$. For a given set $\mathbf{P}$, our theoretical model provides a non-linear functional relation $y = f(x|\mathbf{P})$. Given a measured set of data points $\{x_n\}$ and $\{y_n\}$, we determine the optimal set of parameters $\mathbf{P}_{\text{opt}}$ by minimizing $\chi^2 = \sum_n [y_n - f(x_n|\mathbf{P})]^2/\sigma_y^2$. Here we have assumed that the statistical error $\sigma_y$ of the measured data points is identical for all points.

Once $\mathbf{P}_{\text{opt}}$, the statistical uncertainty of $y_m$ is estimated from the deviation from the optimally fitted function $\sigma_y^2 \approx \sum_n [y_n - f(x_n|\mathbf{P}_{\text{opt}})]^2/(N-1)$, where $N$ is the number of data points. The value of $\sigma_y$ obtained by this procedure yields sets a lower bound for the true statistical uncertainty, as any systematic deviation of the fitted function (i.e. if we have not captured the underlying true functional form in our theoretical model) increases $\sigma_y$. Subsequently the uncertainty in the fit parameters $\mathbf{P}$ can be estimated beyond linear order by generating artificial data sets of points $\{x_n\}$ and $\{y_n\}$ statistically distributed around $f(x_n|\mathbf{P}_{\text{opt}})$, subsequently performing a fit for each data set. We assume a Gaussian distribution for the generation of these data points, an assumption which can be verified by inspecting the distribution of $\delta y_n = y_n - f(x_n|\mathbf{P}_{\text{opt}})$ in the original data. Repeating this procedure yields a distribution of fit parameters of which the distributional form, confidence intervals and standard deviation for the individual parameters can be extracted.

# Chapter 4

# Stable Three-Axis Nuclear Spin Gyroscope in Diamond

## 4.1 Introduction

Gyroscopes find wide application in everyday life, from navigation and inertial sensing, to rotation sensors in hand-held devices and automobiles. Current devices, based on either atomic or solid-state systems, impose a choice between long-time stability and high sensitivity in a miniaturize system. For instance, conventional commercial gyroscopes are built using micro electro-mechanical systems (MEMS) technology that allows for sensitivities exceeding $3\text{mdeg/s}/\sqrt{\text{Hz}}$ in a hundreds of micron size footprint[157,158]. Despite several advantages – including low current drives ($\sim 100\mu\text{A}$) and large bandwidths ($\gtrsim 200\text{deg/s}$) – that have allowed MEMS gyroscopes to gain ubiquitous usage, they suffer from one critical drawback: the sensitivity drifts after a few minutes of operation, making them unattractive for geodetic applications[159]. The intrinsic reason for these drifts – formation of charged asperities at the surface of

the capacitive transduction mechanism – is endemic to MEMS, but does not occur in other systems used as gyroscopes, such as atom interferometers [160,161,162] or nuclear spins [163,164,165]. However, to achieve sensitivities comparable to MEMS, these systems require large volumes ($\sim \mathrm{cm}^3$), long startup times, and large power and space overheads for excitation and detection.

Here we propose to overcome the drawbacks of these two classes of gyroscopes by using a *solid-state* spin gyroscope (that we call *nNV-gyro*) associated with the nuclear spin of Nitrogen-Vacancy (NV) [166] centers in diamond (Fig. 4-1). We achieve high sensitivity by exploiting the long coherence time of the $^{14}$N nuclear spin associated with the Nitrogen-Vacancy center in diamond. The *nNV-gyro* combines the efficient optical initialization and measurement offered by the NV electronic spin with the stability and long coherence time of the nuclear spin, which is preserved even at high density. While the gyroscope is based on a simple Ramsey interferometry scheme, we use coherent control of the quantum sensor to improve its coherence time and robustness against long-time drifts. Such a sensor can achieve sensitivity $\eta \sim 0.5\mathrm{mdeg/s}/\sqrt{\mathrm{Hz} \cdot \mathrm{mm}^3}$, while offering enhanced stability in a small footprint. In addition, we exploit the four axes of delocalization of the Nitrogen-Vacancy center to measure not only the rate of rotation, but also its direction, thus obtaining a compact three-axis gyroscope.

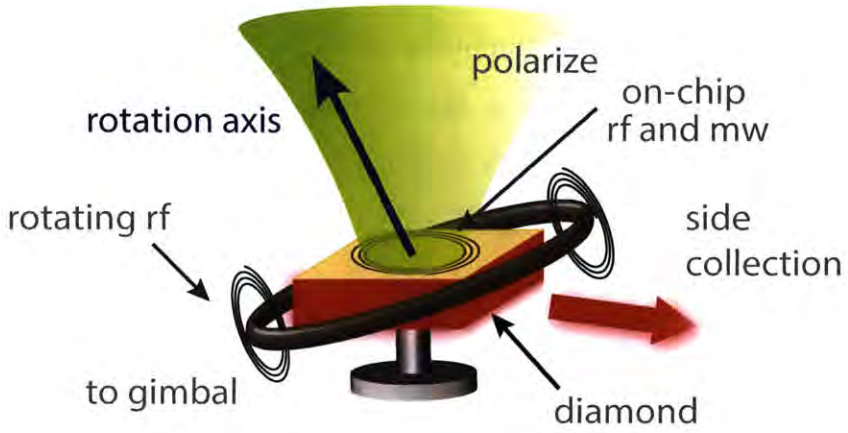


Figure 4-1: **Conceptual design of the nNV-gyro.** A slab of diamond of dimensions $(2.5\times2.5)\text{mm}^2\times150\mu\text{m}$ is anchored to the device body. rf coils and $\mu$w coplanar waveguides are fabricated on the diamond for fast control. NV centers are polarized by a green laser (532nm) and state-dependent fluorescence intensity (637nm) is collected employing a side-collection technique [119]. A second set of rf coils rotate with respect to the diamond chip frame, for example by being attached to one or more rings in a mechanical gimbal gyroscope (not shown). The $^{14}$N nuclear spins are used as probes of the *relative* rotation between the diamond frame and the external rf-coil frame. See Fig. 4-5 for a possible actual implementation.

The operating principles are based on the detection of the phase [1] that the Nitrogen-14 nuclear spin-1 acquires when it rotates around its symmetry axis. Consider an isolated spin-1 with Hamiltonian $\mathcal{H}_0 = QI_z^2 + \gamma_N b I_z$, where $Q$ is the intrinsic quadrupolar interaction ($Q = -4.95$MHz for NV center's $^{14}$N ), $b$ is a small magnetic field, $\gamma_N b \ll Q$ and $\gamma_N = 2\pi \times 3.1\text{MHz/T}$ the $^{14}$N gyromagnetic ratio.

[1] While this manuscript was in preparation, a proposal to utilize the *geometric* phase acquired by the electronic NV spin as a rotation sensor has appeared in [167,168]

The spin is subject to radio-frequency (rf) fields in the transverse plane at the frequency $Q$ and with a (gated) amplitude $2\omega_{\rm rf}(t)$. The diamond rotates around the spin symmetry axis (z-axis) at a rate $\Omega$ with respect to the frame in which the rf field is applied. Thus, the driving field is described by the Hamiltonian $\mathcal{H}_{\rm rf}=2\omega_{\rm rf}(t)\cos(Qt)[I_x\cos(\Omega t)-I_y\sin(\Omega t)]$. We can describe the spin evolution in the interaction frame set by $QI_z^2-\Omega I_z$. The term in $e^{-i\Omega I_z}$ transforms $\mathcal{H}_{\rm rf}$ to

$$2\omega_{\rm rf}\cos(Qt)I_x=\omega_{\rm rf}[e^{-iQI_z^2t}I_xe^{iQI_z^2t}+e^{iQI_z^2t}I_xe^{-iQI_z^2t}],$$

thus in the rotating-wave approximation the dynamics is governed by the Hamiltonian:

$$\mathcal{H}_I=(\gamma_N b+\Omega)I_z+\omega_{\rm rf}(t)I_x \tag{4.1}$$

In a Ramsey sequence (Fig. 8-2) the spin acquires a phase $\phi=(\gamma_N b+\Omega)t$, from which one can extract the rotation rate.

While the nNV-gyro operating principles are somewhat similar to NV-based magnetometers[6] and NMR gyroscopes[165], some critical differences lead to its outstanding performance. In contrast to magnetometry, the sensitivity to rotation rates is independent of the spin's gyromagnetic ratio. Thus, we can exploit the $^{14}$N nuclear spin as sensor, leading to much improved performance because of the isolation of nuclear spins from noise sources. However, this also requires new strategies for the polarization and readout of the nuclear spin, which we illustrate below. There are two critical advantages of the nNV-gyro with respect to NMR-gyros. While certain NMR gyroscope designs use optical pumping for spin polarization[169,170], the nNV-gyro exploits the unique properties of the NV electron spin for optical polarization and readout of the nuclear spins, achieving far better efficiencies, close to 100%. Furthermore,

using a solid-state system allows the application of control fields in the *same* reference frame of the sensor spins, which, as we show below, decouple the spins from low-frequency noise sources such as temperature, stray magnetic fields and strains. Stated equivalently, while NMR-gyros are limited by the *dephasing* time $T_2^*$ of the spins, the nNV-gyro is limited by the much longer *coherence* time $T_2$. In the following we present details of the nNV-gyro operation and analyze its expected performance.

## 4.2 Gyroscope operation

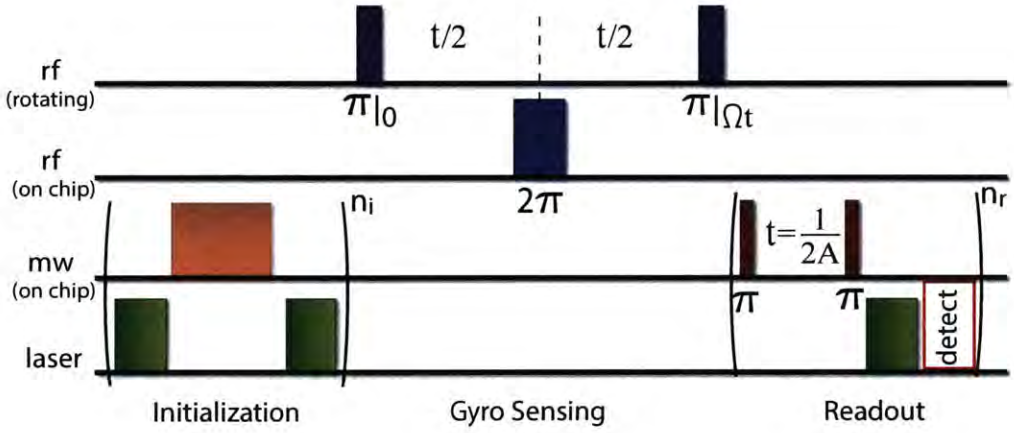


Figure 4-2: **nNV-gyro control sequence.** RF pulses, resonant with the quadrupolar transition of the $^{14}$N nuclear spin, are applied in a frame rotating at a rate $\Omega$ with respect to the diamond, thus inducing a phase $\Omega t$. The nuclear spin is first initialized by polarization transfer from the NV electronic spin. An echo pulse is applied in the diamond frame to refocus static frequency shifts. Finally, $\Omega$ is extracted by mapping the nuclear spin phase shift onto a population difference of the electronic spin and measuring the corresponding fluorescence intensity.

Consider first the operation of a one-axis nNV-gyro. The nuclear spin is first initialized by polarization transfer from the electronic NV spin. Under optical excitation, the electronic $m_s = \pm 1$ levels follow a non-spin preserving transition through metastable levels down to the $m_s = 0$ ground state, yielding high polarization of the electronic spin [171,172]. The polarization can be transferred to the nuclear spin exploiting the hyperfine coupling, $A = 2.2$MHz, in the electron-nuclear spin Hamiltonian

$$\mathcal{H}_{en} = \Delta S_z^2 + \gamma_e b S_z + Q I_z^2 + (\Omega + \gamma_N b) I_z + A \vec{S} \cdot \vec{I}, \tag{4.2}$$

where $\gamma_e = 2.8$MHz/G is the electronic gyromagnetic ratio and $\Delta = 2.87$GHz is the zero-field splitting. Several methods for polarization transfer have been implemented experimentally, including measurement post-selection [45] and exploiting a level anti-crossing in the orbital excited state at $b \sim 500$G (using an adiabatic passage [173] or the resonance between the nuclear and electronic spins [155,174,175]). However all these methods have drawbacks that make them unsuitable for our purpose. The first method is too lengthy while the second prevents the use of repeated readouts and requires precise alignment of a static magnetic field. At low field, polarization transfer between the electronic and nuclear spin is complicated by the fact that both are spin-1. Unlike for spin-1/2, polarization transfer in the rotating frame (under the Hartmann-Hahn matching condition [36]) does not lead to perfect polarization, unless the electronic spin is reduced to an effective spin-1/2 [176]. Instead, here we propose using forbidden two-photon transitions to achieve population transfer. Driving the NV electronic spin at the $\Delta \pm \gamma_e b + Q$ transitions with a field along its *longitudinal* (z) axis [177] modulates its resonance frequency, thus making energy exchange with the nuclear spin possible. This is similar to two-photon transitions described by Floquet theory [178]: while the transition rates are usually small, the ability to drive the NV

electronic spin with very high fields[179] makes the polarization time $t = \pi\frac{\Delta+\gamma_e b+Q}{A\Omega_R}$ short: for a Rabi frequency $\Omega_R = 500\text{MHz}$ and a field $b = 20\text{G}$, the time required is only $1.3\mu\text{s}$ (see Appendix 4.A). We note that this initialization time is far shorter than for other gyroscope types, including the few tens of milliseconds of startup time required for MEMS gyroscopes[157].

For ease of operation, we assume that the rf and microwave ($\mu$w) pulses used for initialization and readout can be delivered by an on-chip circuit, integrated with the diamond. After preparation, the NV electronic spin is left in the $|0\rangle$ state, which does not couple to the $^{14}$N nuclear spin nor to the spin bath. A Ramsey sequence is applied using the off-chip rf driving thus inducing accumulation of a rotation-dependent phase (Eq. 4.1). A $2\pi$-pulse at the center of the sequence, applied with the on-chip rf field, refocuses the effects of stray magnetic fields and provides decoupling from the spin bath [2]. The sensor spin coherence time is limited by $T_2$ (and not by the shorter dephasing time $T_2^*$), which can be exceptionally long for nuclear spins. Thus the additional pulse, made possible by working with a solid-state device, is critical in making the nNV-gyro immune to a host of low frequency drifts that limit the operational time of other gyroscope types.

Moreover, since the echo refocuses the coupling to other electronic spins, the nNV-gyro can operate at very high density of sensor spins. Ion implantation can reach NV density $n_{\text{NV}} \sim 10^{18}\text{cm}^{-3}$. Even assuming a density of residual single nitrogen defects (P1 centers[180,181]) $n_{\text{P1}} \approx 10 n_{\text{NV}} \sim 10^{19}\text{cm}^{-3}$, the $^{14}$N $T_2$ time is not appreciably affected by the P1 bath. Indeed, while at these densities the dipole-dipole interaction $d_{ab} = \frac{\mu_0}{4\pi}\frac{\hbar}{2\pi}\frac{\gamma_a\gamma_b}{r_{ab}^3}$ among P1 centers is large ($d_{\text{P1,P1}} \sim 3\text{MHz}$, with $\gamma_{\text{P1}} = \gamma_e$), the coupling to the nuclear spin is still small, $d_{P1,N} \sim 345\text{Hz}$ (where we estimated the mean spin-spin distance as $r = \sqrt[3]{\log(8)/(4\pi n_{\text{P1}})}$[182]). This leads to motional narrowing and a

[2]The echo is effective even if the on- and off-chip fields cannot be made phase-coherent

very slow exponential decay, as confirmed by simulations (Appendix 4.B). The $^{14}$N coherence time is also affected by the interaction with the close-by NV center [173,45], which induces dephasing when undergoing relaxation with $T_1 \sim 2 - 6$ms at room temperature and low field [183]. While in high purity diamonds the dephasing time $T_2^*$ can be as long as 7ms [45], in the proposed conditions of operation we can conservatively estimate the coherence time of the nuclear spin to be $T_2 = 1$ms. We note that the echo sequence has the added benefit to make the measurement insensitive to many other imperfections, such as temperature variation, strain, background stray fields, variation in the quadrupolar interaction and instability in the applied bias magnetic field. Thus this scheme yields a solid-state gyroscope with stability comparable to that achieved in atomic systems.

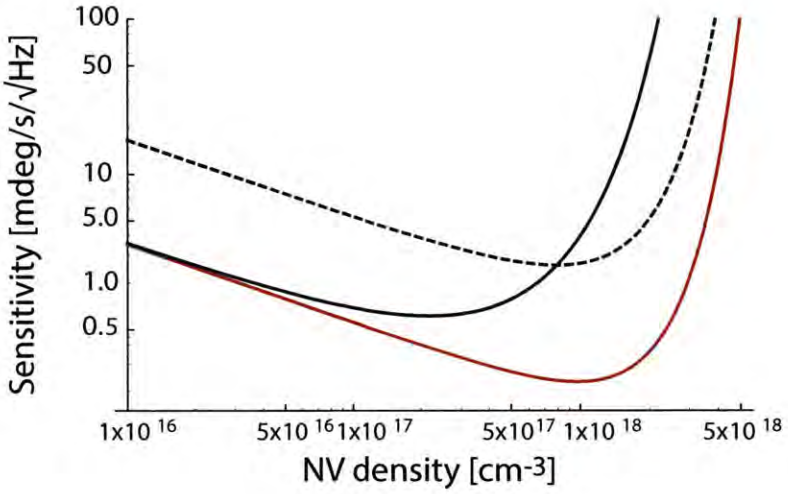


Figure 4-3: **nNV-gyro sensitivity** in mdeg/s/$\sqrt{\text{Hz}}$, as a function of density, $\eta(n) = \frac{e^{t_{\text{map}}/T^*_{2,\text{NV}}} e^{t/T_{2,n}}}{C\sqrt{nV/4}} \frac{\sqrt{t+t_d}}{t}$. Here the exponential factors take into account the sensitivity degradation due to spin decoherence[6], with decay constants that depend on density, $T_{2,n}, T^*_{2,\text{NV}} \propto 1/n$ (Appendix 4.B). We considered a diamond chip of dimensions $V = (2.5 \times 2.5)\text{mm}^2 \times 150\mu\text{m}$ and assumed that only $1/4^{\text{th}}$ of the NV spins are along the desired direction. The interrogation time was $t = 1\text{ms}$ (solid lines) and $t = 0.1\text{ms}$ (dashed line). The sensitivity for a simple Ramsey scheme (black lines) is limited by the nuclear spin $T_{2,n} = T^*_2$. Using an echo scheme (red thick line) improves the sensitivity, which is now limited by the coherence time $T^*_{2,\text{NV}}$ of the NV electronic spin used to read out the sensor spin state, since the nuclear coherence time $T_{2,n} = T_2$ is much longer.

After the sensing sequence, the $^{14}$N spin is left in the state

$$|\psi_n\rangle = \frac{\sin(\Omega t)}{\sqrt{2}}\left(e^{+i\Omega t}|\text{-}1\rangle - e^{-i\Omega t}|+1\rangle\right) - \cos(\Omega t)|0\rangle, \tag{4.3}$$

which can be mapped into a population difference between the NV levels thanks to

the hyperfine coupling (here we only considered the longitudinal component of the isotropic hyperfine interaction $AI_zS_z$ because of the large zero-field splitting $\Delta$).

The readout sequence (Fig. 8-2), with pulses on resonance to both $0 \leftrightarrow \pm 1$ transitions [3], generates the state

$$|\psi_{en}\rangle = \frac{1}{2}\sin(\Omega t)\left[e^{i\Omega t}(|\text{-}1,\text{-}1\rangle + |{+}1,\text{-}1\rangle) + \right. \tag{4.4}$$

$$\left. e^{-i\Omega t}(|{+}1,{+}1\rangle + |\text{-}1,{+}1\rangle)\right] - \cos(\Omega t)\,|0,0\rangle\,, \tag{4.5}$$

where $\left|m_z^S, m_z^I\right\rangle$ indicates an eigenstate of $S_z$ and $I_z$ for the electronic and nuclear spins, respectively. The time required to map the state onto the NV center is $t_{\text{map}} =$ 230ns, which is close to the $T_2^*$ time for the NV at high density, thus we expect a reduction in contrast. Indeed it is the NV dephasing time that ultimately limits the allowed spin densities. A possible solution would be to perform a spin echo on both nuclear and electronic spins to extend the coherence time.

Optical readout extracts the information about the rotation $\Omega$. The measurement step can be repeated to improve the contrast [42,54]: although at low field the nuclear spin relaxation time under optical illumination is relatively short, thus limiting the number of repeated readouts [42], when combined with a side-collection scheme [119] giving high collection efficiency $\eta_m \approx 1$, we can still achieve a detection efficiency $C \sim 0.25$ for $n_r = 100$ repetitions and a total readout time $t_{\text{ro}} \approx 150\mu$s (see Appendix 4.C). The higher detection efficiency will also allow a large dynamic range by exploiting adaptive phase estimation schemes [184,45,185].

[3] the mapping is also possible if only one NV transition is driven, although it requires a longer time.

| Gyroscope Type | Size $mm^3$ | Sensitivity $^\circ/\sqrt{hr}$ | Startup time |
|---|---|---|---|
| Fiber optic (S)[186] | $3.6\times10^4$ | 0.5 | 250ms |
| Ring Laser (G)[187] | $1\times10^6$ | $5\times10^{-3}$ | 1s |
| Cold atoms (G)[188] | $\sim10^9$ | $2.95\times10^{-4}$ | 51ms |
| Atom beam (G)[163] | $1.56\times10^4$ | $2\times10^{-3}$ | |
| MEMS (S)[157] | 147 | 1.6 | 50ms |
| NMR (G)[189,165] | $>10^3$ | $10^{-3}$ | 100s |
| nNV-Gyro (S) | 1 [4] | $3\times10^{-2}$ | $1.3\mu s$ |

Table 4.1: **Representative examples from different gyroscope families**, showing their typical performance parameters. S/G in the first column indicate whether the gyroscope is solid-state (S) or gas-based (G). Note that there is, in general, a wide variance of parameters in each gyroscope family; here we just show typical examples. Moreover, laboratory-based gyroscope setups may not be optimized for compact sizes.

## 4.3 Performance of nNV-gyroscopes

We now consider the performance of the nNV-gyroscope design, with respect to sensitivity and stability, and its potential advantages over competing technologies.

The sensitivity per unit time $\eta$ is ideally shot-noise-limited[122,6]: $\eta \propto 1/\sqrt{tN}$, where $N$ is the number of nitrogen nuclear spins associated with NV centers in the diamond chip. We estimate the expected sensitivity by limiting the interrogation time $t$ to $T_2$ and taking into consideration the preparation and readout dead-times $t_d = t_{\rm pol} + t_{\rm ro}$ and the detection efficiency $C$:

$$\eta = \frac{\sqrt{T_2 + t_d}}{C T_2 \sqrt{N}}. \tag{4.6}$$

For a volume $V = 1\text{mm}^3$ containing $N = n_{\rm NV}V/4 \approx 2.5\times10^{14}$ sensor spins along the rotation axis, the estimated sensitivity for the nNV-gyro is then $\eta \approx$

$0.5(\text{mdeg/s})/\sqrt{\text{Hz}}$, better than current MEMS gyroscopes although in a slightly larger volume (see Fig. 4-3).

More importantly, the *stability* of the nNV-gyro can be much higher than for MEMS and comparable to atomic gyroscopes (see Table 4.1). Indeed, the echo-based scheme makes the nNV-gyro insensitive to drifts due to strain, temperature and stray fields. In addition, the NV spin is a sensitive probe of these effects, capable of measuring magnetic[6] and electric[190] fields, as well as frequency[191] and temperature shifts[192]. Because of almost four orders of magnitude larger sensitivity of the NV spin than the $^{14}$N spin (given by the ratio $\gamma_e/\gamma_N$), the NV can be used to monitor such drifts and correct them via a feedback mechanism.

## 4.4 Operation of the nNV-gyro as a three-axis gyroscope

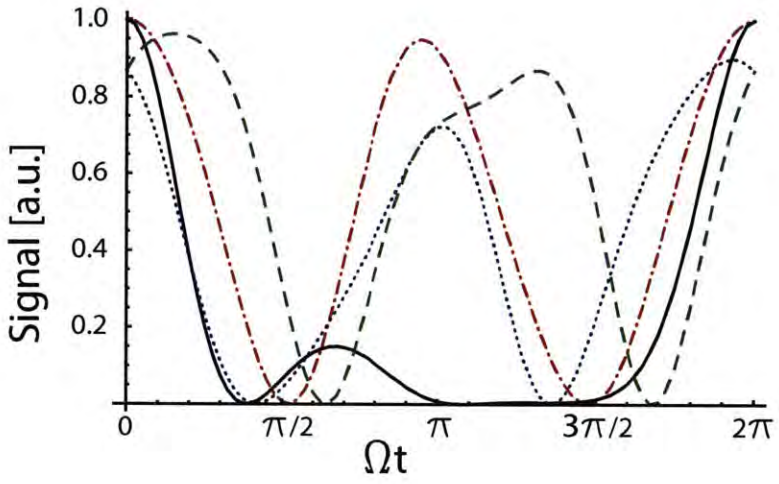


Figure 4-4: **Operation as a three-axis gyroscope**. Signal $S_c$ from the four classes of NV centers, for a rotation $\Omega$ along an axis with angles $\vartheta = \pi/6$ and $\varphi = 2\pi/3$ from the [111] direction (which coincides with the 1st class of NV, dash-dotted line).

The NV center in diamond consists of a substitutional nitrogen adjacent to a vacancy in the lattice. The nitrogen-to-vacancy axis sets the direction of the electronic zero-field splitting and nuclear quadrupolar interaction. The axis can be along any of the four tetrahedral $\langle 111 \rangle$ crystallographic directions of the diamond lattice. This intrinsic symmetry can be exploited to operate the nNV-gyro as a three-axis gyroscope, extracting information about the rotation rate as well as its direction.

While the maximum sensitivity is achieved for rotations aligned with the symmetry axis, if the rotation $\vec{\Omega}$ is about an axis forming an angle $\{\vartheta, \varphi\}$ with respect

to the NV axis, the $^{14}$N still undergoes a complex evolution that depends on $\vec{\Omega}$. The two rf pulses in the Ramsey interferometry scheme differ not only by their phase $\psi_{1,2}$ in the NV x-y plane, but also by their flip angle $\alpha_{1,2}$. If we assume the first pulse to be along the $x$-axis for the first NV class, the second rf pulse is rotated by an angle $\psi_2^1 = \psi(\vartheta, \varphi, \Omega t)$ in the NV x-y plane, with

$$\tan(\psi_2^1) = \frac{\sin^2\vartheta \sin(2\varphi) \sin^2(\Omega t/2) + \cos\vartheta \sin(\Omega t)}{\cos(\Omega t) - \sin^2\vartheta \cos^2\varphi \cos(\Omega t) + \sin^2\vartheta \cos^2\varphi}$$

The flip angle $\alpha_2^1 = \alpha(\vartheta, \varphi, \Omega t)$ is also reduced with respect to the nominal angle $\pi$,

$$\begin{aligned} \alpha_2^1 &= \pi \Big[ \left\{ \cos(\Omega t) - \sin^2\vartheta \cos^2\varphi \cos(\Omega t) + \sin^2\vartheta \cos^2\varphi \right\}^2 \\ &+ \left\{ \sin^2\vartheta \sin(2\varphi) \sin^2(\Omega t/2) + \cos\vartheta \sin(\Omega t) \right\}^2 \Big]^{1/2} \end{aligned}$$

The state at the end of the Ramsey sequence is then given by

$$\begin{aligned} |\psi_n\rangle &= \frac{e^{-i\psi_2} \left[ \sin(\psi_2) - i \cos\left(\frac{\alpha_2}{2}\right) \cos(\psi_2) \right]}{\sqrt{2}} |+1\rangle \\ &- \sin\left(\frac{\alpha_2}{2}\right) \cos(\psi_2) |0\rangle \\ &- \frac{e^{i\psi_2} \left[ \sin(\psi_2) + i \cos\left(\frac{\alpha_2}{2}\right) \cos(\psi_2) \right]}{\sqrt{2}} |-1\rangle \,, \end{aligned}$$

from which one can extract information about the rotation rate $\Omega$. Similar expressions hold for the other NV classes, if it is possible to drive excitation fields in the transverse plane of each family. Then the angles $\alpha_2^c$, $\psi_2^c$ are different for each family of NVs and measuring the signal from three families allows extracting information about $\vec{\Omega}$.

Assuming that the driving field is applied only along one direction for all the four

NV classes, even the first excitation pulse angles $\{\psi_1^c, \alpha_1^c\}$ differ for each class, while for the second pulse $\{\psi_2^c, \alpha_2^c\}$ depend not only on the class but also on the rotation vector $\vec{\Omega}$, via simple trigonometric relationships. We thus obtain the signal for each class

$$\begin{aligned} S^c = &[\cos(\alpha_1^c/2)\cos(\alpha_2^c/2) + \\ &- \sin(\alpha_1^c/2)\sin(\alpha_2^c/2)\cos(\psi_1^c - \psi_2^c)]^2 , \end{aligned} \tag{4.7}$$

which is shown in Figure (4-4). The signal can be measured by sequentially mapping the nuclear spin state onto the corresponding electronic spin via on resonance $\mu$w pulses (a bias field of 10-20G is sufficient to lift the frequency degeneracy among the 4 classes[193,194]). A more efficient scheme would take advantage of repeated readouts and long relaxation times of the nuclear spins, to measure the signal from 3 NV classes without the need to repeat the preparation and echo sequence. Although a driving field along a single direction makes the deconvolution algorithm more complex, the signal arising from three classes of NV centers is still enough to reconstruct the rotation rate and its direction.

## 4.5 Conclusions and Outlook

We proposed a solid-state device able to measure rotation rates with a resolution $\eta \approx 0.5\text{mdeg/sec}/\sqrt{\text{Hz}}$ in a $1\text{mm}^3$ package, while providing great stability. The device performance compare favorably with respect to other current technologies (see Table 4.1). Even smaller devices –at the micron scale– could be useful by exploiting this long-time stability to improve the performance of MEMS gyroscope in a combinatoric device (see Fig. 4-5). High-performance MEMS gyroscopes can be fabricated in diamond using reactive-ion etching tools[195]. While the substrate itself acts as a *mechanical* gyroscope, the nuclear spins inside it act as a *spin* gyroscope.

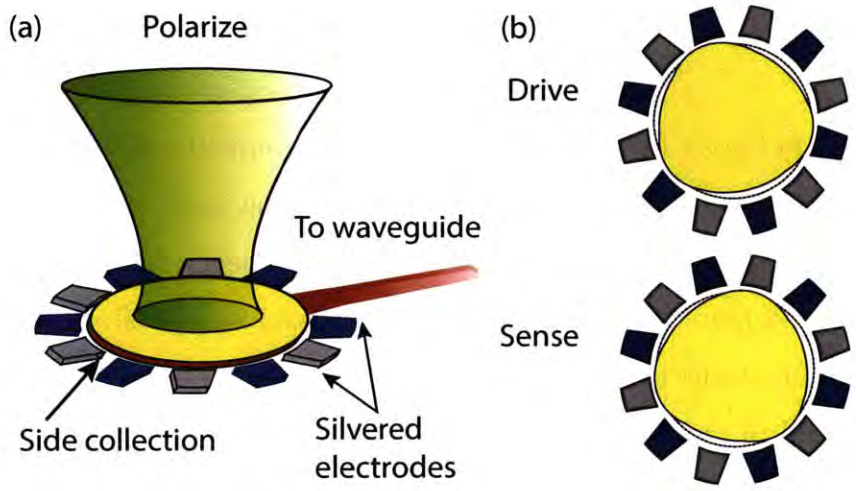


Figure 4-5: **Conceptual design of an integrated nNV-MEMS gyroscope**, comprising a bulk acoustic wave (BAW) single-axis MEMS gyroscope [158] in a $\sim$ 800$\mu$m diamond disk implanted with NV centers, whose nuclear spins form a spin gyroscope. (a) Schematic of the nNV-gyro operation. The spins implanted in the disk are polarized by an on-chip green laser. The electrodes surrounding the disk are silvered to allow for total internal reflection and fluorescence is side-collected [119] by replacing one of them by an on-chip optical waveguide at 638nm. Striplines for rf/ $\mu$w control are fabricated on the disk. (b) Operation of the BAW mechanical gyroscope. The BAW is *electrostatically* driven in the second elliptic mode by a $\sim$ 10kHz sinusoidal signal from the *drive* (blue) electrodes. A rotation out of the plane causes a decrease in the gap near the *sense* (grey) electrodes leading to a capacitive measurement of the rotation [158]. Combinatoric filtering with the nNV measurement leads to noise rejection and improved stability.

These two gyroscopes, employing complementary physical effects, are sensitive to different sources of noise, which can be corrected by Kalman-filter techniques [196]. The integrated device would offer both stability and sensitivity in a small package.

The nNV-gyro takes full advantage of the long coherence time of *nuclear* spins, which is preserved even at very high densities, while exploiting its interaction with the electronic spin of the NV center for efficient initialization and readout. Going beyond our conservative estimates, the nNV-gyro could achieve the performance of inertial-grade gyroscopes with improvements in the coherence time of the nuclear and electronic NV spin, as could be obtained with $\gtrsim$ 50% N to NV conversion efficiency [197], with a preferential alignment of the NV symmetry axis along two directions [198], and with improved collection efficiency, exploiting single-shot measurement of the NV center at low temperature [199,200].

# Appendix

## 4.A Polarization scheme for the $^{14}$N nuclear spin

In the main text we proposed to use two-photon transitions to drive polarization transfer between the electronic and nuclear spins associated with the NV center. These transitions can be accessed by driving the NV electronic spin at the $\omega_{\pm} = \Delta \pm \gamma b + Q$ frequencies with a field *along* its longitudinal (z) axis [177,201]. The longitudinal field effectively modulates the electronic spin resonance frequency thus making energy exchange with the nuclear spin possible. Consider the Hamiltonian in Eq. (4.2). In the interaction frame given by $\mathcal{H}_I = \mathcal{H}_{en} - A\vec{S}\cdot\vec{I}$, the coupling term acquires a time-dependence. For example the term $\mathcal{H}_p = A(|0\rangle\langle+1|_e\,|0\rangle\langle\text{-}1|_n + \text{h.c.})$, which drives the polarization exchange, acquires a phase oscillating at the frequency $\pm(\Delta + \gamma b + Q)$. Adding a longitudinal field, $\mathcal{H}_z = \Omega\cos(\omega_+ t)S_z$ further modulates the time-dependence when evaluating the Hamiltonian in the corresponding interaction picture given by $U_z = e^{i\Omega\sin(\omega_+ t)/\omega_+ S_z}$. For the terms considered above we have for example

$$\begin{aligned}\widetilde{\mathcal{H}}_p &= A\left(e^{-i[\omega_+ t - \Omega\sin(\omega_+ t)/\omega_+]}\,|0\rangle\langle 1|_e\,|0\rangle\langle\text{-}1|_n + \text{h.c.}\right)\\ &= A\left(\textstyle\sum_n J_n\left(\frac{\Omega}{\omega_+}\right)e^{-i\omega_+(1-n)t}\,|0\rangle\langle 1|_e\,|0\rangle\langle\text{-}1|_n + \text{h.c.}\right),\end{aligned}$$

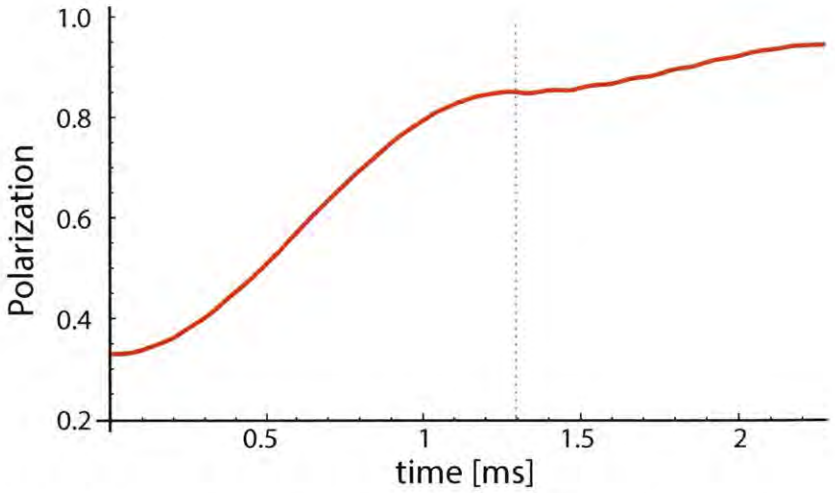


Figure 4-6: **Effect polarization of $^{14}$N nuclear spin.** We consider the polarization of the $^{14}$N nuclear spin under longitudinal driving of the NV electronic transitions, with a Rabi frequency $\Omega_R = 500$MHz, hyperfine $A \approx 2.2$MHz and a static magnetic field of 20G. The simulation includes dephasing of the electronic spin modeled by a Ornstein-Uhlenbeck process yielding a $T_2^*$ time of about 200ns. To achieve high polarization the process is repeated twice by re-polarizing the NV electronic spin (dashed line) via optical illumination.

where we used the properties of the Bessel function $J_n(\cdot)$. In the rotating wave approximation, only the term $n = 1$ is retained, while all the other terms in the Hamiltonian $\widetilde{\mathcal{H}}_I$ that oscillate at a frequency $\neq \omega_+$ are also canceled. In the limit $\Omega \ll \omega_+$ we have $J_n(\Omega/\omega_+) \approx \Omega/(2\omega_+)$, thus the Hamiltonian inducing polarization exchange is $\mathcal{H}_p \approx \frac{A\Omega}{2\omega}(|0\rangle \langle 1|_e |0\rangle \langle -1|_n + \text{h.c.})$

The ability to drive the NV electronic spin with very high fields [179], makes the polarization time $t = \pi \frac{\Delta+\gamma b+Q}{A\Omega_R}$ short: for a Rabi frequency $\Omega_R = 500$MHz, hyperfine $A \approx 2.2$MHz and a field of 20G, the time required is only $1.3\mu$s, thus the forbidden transition is a competitive way of driving nuclear spin transitions. Given the short dephasing time of the NV spin, a two-step process might be required, in which the NV is optically re-polarized before driving the polarization exchange a second time.

To estimate the effects of a spin bath during the longitudinal driving, we simulated the polarization transfer in the presence of dephasing noise (see Fig. 4-6).

## 4.B Coherence time of the $^{14}$N nuclear spins

The $^{14}$N nuclear spin dephasing and coherence time are usually limited by the $T_1$ relaxation time of the electronic NV spin. At high density of paramagnetic impurities, the interaction with other electronic spins could accelerate the decay. To estimate this contribution, we simulated the $^{14}$N nuclear spin evolution under a Ramsey and echo sequence in the presence of an electronic spin bath. The simulation was performed using a cluster expansion[7,202] to model the effects of a P1 electronic spin bath. The spin bath was modeled as an ensemble of electronic spin-1/2, thus omitting the details of the actual bath (such as the strong hyperfine coupling of the P1 to its nuclear spins, as well as shielding effects due to nearby carbon-13 nuclear spins[79] and localization effects due to disorder[203]). Still, the simulations can give rough estimates of the expected $T_2$ times and are consistent with the results of a simple model based on describing the spin bath as a classically fluctuating bath described by a Ornstein-Uhlenbeck process. In particular, we expect that due to motional narrowing, the coherence times are long even at high densities as shown in Figure (4-7).

## 4.C Improved measurement efficiency by repeated readouts

The NV spin state can be read under non-resonant illumination at room temperature using the fact that the $m_s = \pm 1$ excited states can decay into metastable states,

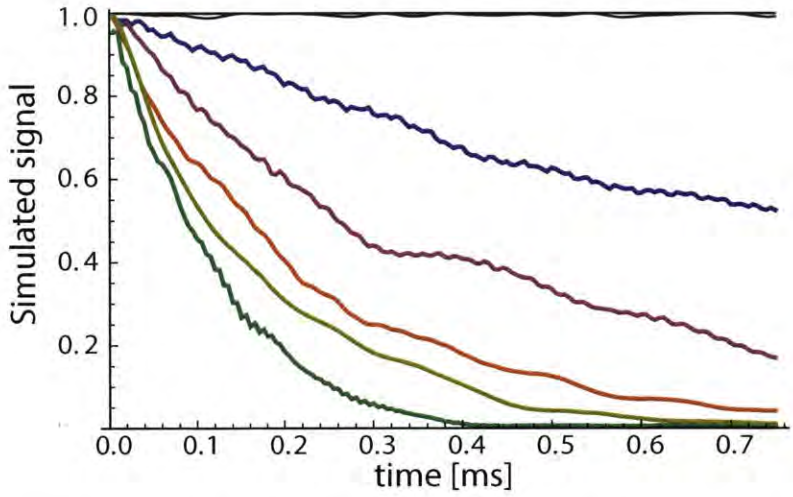


Figure 4-7: **$^{14}$N coherence decay** under a spin-echo sequence (black lines) and a Ramsey sequence. We simulated an ensemble of 100 non-interacting nuclear spin, each subjected to a bath of $\sim 500$ electronic spins, with a density (from bottom to top lines) of $n = (0.35, 1.06, 1.76, 2.47, 3.17) \times 10^{19}\text{cm}^{-3}$ (The lines for the echo are indistinguishable).

which live for ~300 ns. The optical excitation conserves spin as does the direct optical decay which happens in about 12 ns. Thus, a NV in the $m_s = 0$ state will emit, and absorb, approximately 15 photons, compared to only a few for a NV in the $m_s = \pm 1$ states, yielding state discrimination by fluorescence intensity. The complication is that the metastable state decays primarily via spin-non conserving processes into the $m_s = 0$ state thereby re-orienting the spin. This is good for spin polarization, but erases the spin memory and reduces measurement contrast. The detection efficiency of the NV center spin state is thus given by $C = \left(1 + \frac{2(n_0+n_1)}{(n_0-n_1)^2}\right)^{-1/2}$[6], where $n_{1,0}$ is the number of photons collected if the NV spin is in the $m_s = \{0, 1\}$ state, respectively.

In the repeated readout scheme[42,54], the state of the nuclear spin is repetitively mapped onto the electronic spin, which is then read out under laser illumination. The measurement projects the nuclear spin state into a mixed state, but the in-

formation about its population difference is preserved, under the assumption that the measurement is a good quantum non-demolition measurement. We can include the effect of these repeated readout by defining a new detection efficiency, $C_{n_r} = \left(1 + \frac{2(n_0+n_1)}{n_r(n_0-n_1)^2}\right)^{-1/2}$, which shows an improvement $\propto \sqrt{n_r}$, where $n_r$ is the number of measurements. The sensitivity needs of course to be further modified to take into account the increased measurement time. Provided the time needed for one measurement step is smaller than the interrogation time (including the initialization time), it becomes advantageous to use repeated readouts. The maximum number of readouts is set by the nuclear spin relaxation under optical illumination, driven by non-energy conserving flip-flops in the excited states. While at high fields, this time is very long, allowing 2000 measurements in 5ms, in the present conditions we find that $\sim$ 100 measurements would provide a good balance between the improvement in $C$ and the reduction due to longer measurement time.

# Chapter 5

# Experimental design of a prototype nNV gyroscope

## 5.1 Introduction

Let us now consider the design of a prototype NV nuclear spin gyroscope. After considering various constraints, Fig. 5-1 describes the schematic side and top views of the design. For excitation, we will exploit the superior homogeneity and strength offered by circular spiral like geometries. The details of the coil design and fabrication steps are in Fig. 5-4.

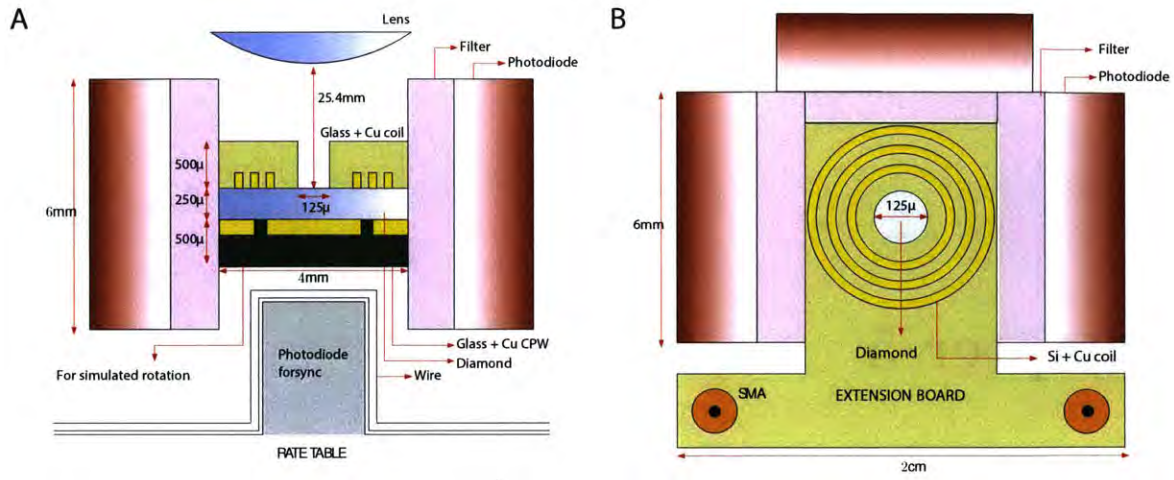


Figure 5-1: **(a) Side and (b) top views schematic of the proposed experimental setup.** A $4 \times 4 \times 0.2$mm [111] sample is arranged in side collection fashion. The Si microwave coil provides the $2\pi$ pulses for the echo. The center of the coil has a slot to allow optical excitation. A cylinder of NVs of diameter $\sim 20\mu$ contribute to the signal. We consider two scenarios: in case of using the rate table to sense mechanical rotation, the wire on the table provides the Ramsey $\pi/2$ pulses. For simulated gyroscopy, the pulses are provided by a glass CPW on the bottom side on the diamond. Note that this arrangement prevents coupling to the coil (mutual inductance is greatly reduced). A photodiode below the wire allows synchronization with electronics on the rate table.

## 5.2 Optical setup

### 5.2.1 Excitation optical setup

In this section we shall detail the optical components and design constraints for the design of the prototype, including the amount of laser power, size of the laser, objective lenses, AOMs and excitation geometry, and photodiodes and the collection geometry.

Let us first consider the amount of laser power required. Ref. [199] estimates laser saturation power is $\sim 6nW/\text{NV}$. Hence, maximum number of NVs that can be excited is $1.6\times10^8/\text{W}$. This corresponds to volume of $1.6\times10^8/N/\text{W}$, where $N$ is the concentration in $\text{cm}^3$, eg. $N = 10^{15}$. In this case, for a height of $200\mu$ this corresponds to $\varphi 16\mu$. Hence for $N = 10^{15}$, and sample height $h = 200\mu$, the maximum beam radius we can employ is $16\mu$m.

Consider now the mount and total space budget for the laser. All lasers come with power supplies that are usually bulky. However, a suitable choice maybe from Lasermate, that offers has 1.4W lasers with laser head $7.75\times2.75\times2$in., and the power supply is $9.37 \times 5.74 \times 4$in. The supply weighs 2.3kg. Hence, given an approximate space budget of $576\text{in}^2$ for a compact solid state gyroscope, the laser and power supply can be budgeted at about $60\text{in}^2$ each.

The excitation optical setup consists of an acousto-optic modulator in single pass configuration, and the collection is through the side collection scheme pioneered in Ref. [119] . Let us now evaluate the signal rise time and collection area. Ref. [119] uses a solderable photodiode Advanced photonix PDB-C609-2, with response time of 30ns, and an active collection area of $6\text{mm}\times7\text{mm}$. Ref. [119] mentions that parasitic capacitance and leakage current leads to about 10 times higher electronic noise in

the readout than expected. Note that in the side collection scheme, $\sim 91\%$ of the photons undergo total internal reflection. Theoretically about 29% of photons are collected in the first pass. Experimentally Ref.[119] finds that about 40% photons are collected, which gives rise to an estimated 11% photons undergoing multiple reflections. The photodiode rise time is 30ns, and about 40% of photons are collected by side collection.

Let us now consider if an objective lens is actually required in our setup. Considering an NA=0.4 microscope air objective ($n = 1$), the depth of focus is given by,

$$\text{DOF} = \frac{n\lambda}{2\text{NA}^2} = 166.2nm \tag{5.1}$$

Hence it does not cover the whole $200\mu$ sample height, and we can do without an objective.

We plan to use a lens to focus down the beam into a $\approx 20\mu$m excitation area. Assuming we use a focal length of $f = 25.4$mm lens, and the sample is placed exactly at the focus using a translation stage. If $D$ is the incoming beam waist, the size of the beam at the focus is given by,

$$x_{1/2} = 1.22f\lambda/D \tag{5.2}$$

For $\lambda = 532$nm, and sample at focus, and assuming $D = 1$mm, this corresponds to $x_{1/2} = 16.4\mu$m.

### 5.2.2 Collection Optical setup

Let us finally consider methods for low noise side collection readout. A possibility is to improve performance by using a low noise amplifier Amptek CoolFET with

dimensions $3.5 \times 2.5 \times 1.375$in. It has a rise time of $2.5ns$, and a capacitance of 8pF. It provides a gain of $64\mu V$/electron charge. In a $T_2 = 35\mu s$, this corresponds to a voltage gain of $1.398 \times 10^4/\mu$ of current. The preamp gain is about $10^4 \mathrm{V}/\mu A$ of photodiode current in the $T_2$ period.[119] finds that this is sufficient to give about a 4% contrast in the $|0\rangle$ and $|1\rangle$ states *per* readout cycle. Assuming we read out in cycles of 300ns, and assuming each NV gives 40kcps and there are $10^8$ NVs contributing, this corresponds to $1.2 \times 10^6$ counts per readout cycle.

Consider also the details of the sample mounting. The sample is placed in contact (glued) to 632nm LP filters Edmund NT 62-979. The filter OD is exceeds 4. The filter is of quartz of refractive index 1.45. The diamond refractive index is 2.42. The PDs are placed in close contact with the back of the filter. In Ref.[119] , the filter is 2mm in height, while the PD active area is 6mm.

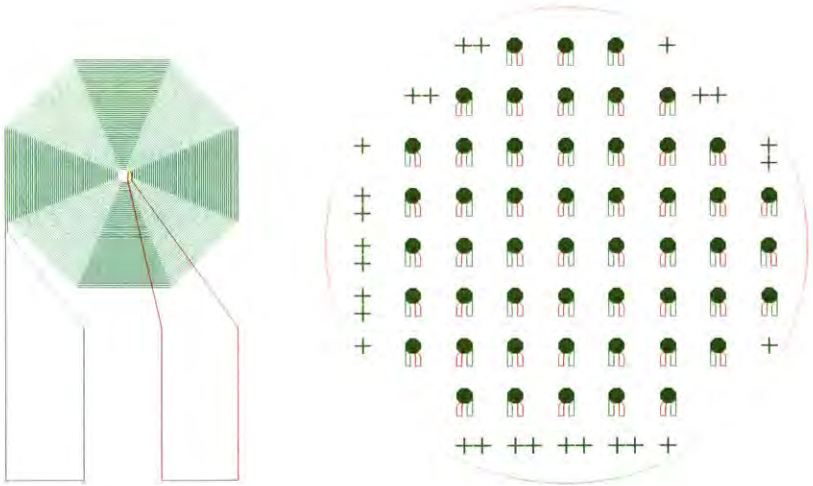

(a) (b)

Figure 5-2: **Microcoil for spin excitation.** (a) Coil design consists of an octagonal spiral with inner diameter $125\mu$, outer diameter $3mm$, pitch $25\mu$, width $25\mu$, and $N = 30$. (b) The mask design consists of 51 spiral coils per 4in glass wafer.

## 5.3 Electronics setup

Now let us consider the excitation scheme for the microwave and RF circuit. In contrast to Ref.[119], where they use a single turn coax, we plan to use a microcoil arrangement (Fig. 5-2) would provide a much stronger field (scaling as number of turns $N$). It will also provide better longitudinal homogeneity. Proper matching circuitry will reduce reflection loss.We will fabricate on glass (Fig. 5-4) because it is insulating, and immune to parasitic capacitances upto $f = 800\text{MHz}$[?] . The thickness of the 4in. glass wafers was $525\mu$m in[?] due to ease of handling. For reference, the glass coverslip is about $125\mu$m in thickness.

## 5.4 Design and fabrication of microcoils

To get an idea of the strength of the fields, we performed simulations of the microcoil fields in Fig. 5-3. Several microcoils have been fabricated before for RF irradiation in NMR. The coil in[?] needed $41\mu$s for a $\pi/2$ pulse at 0dBm, for a remarkably large area of 2.5mm$\times$1.5mm. The RF frequency was $f = 21.3\text{MHz}$. The field strength is about 100G at $750\mu$m (see Fig. 5-3). For the coils in[? ?] , the field strength was 40G/mA at a distance of about $140\mu$m from the coil surface. At $250\mu$m, the field is about 50% of the field at the center of the coil[?] . Here the frequency of interest was 300MHz. The $\pi/2$ pulse widths were $10\mu$s at an excitation current amplitude of 276mA, corresponding to an input power of 38mW[?] .

To consider if coil heating is an important consideration, let us determine the Joule heating in the coil in Fig. 5-2(a). The important parameter is the coil resistance. This can be estimated using $R = \rho l_c / S_{eff}$, where $\rho = 1.68 \times 10^{-8} \Omega m$ is the bulk resistivity of Cu, $l_c = N\pi(r_i + r_e + w) = 15.07\text{cm}$ is the effective coil length

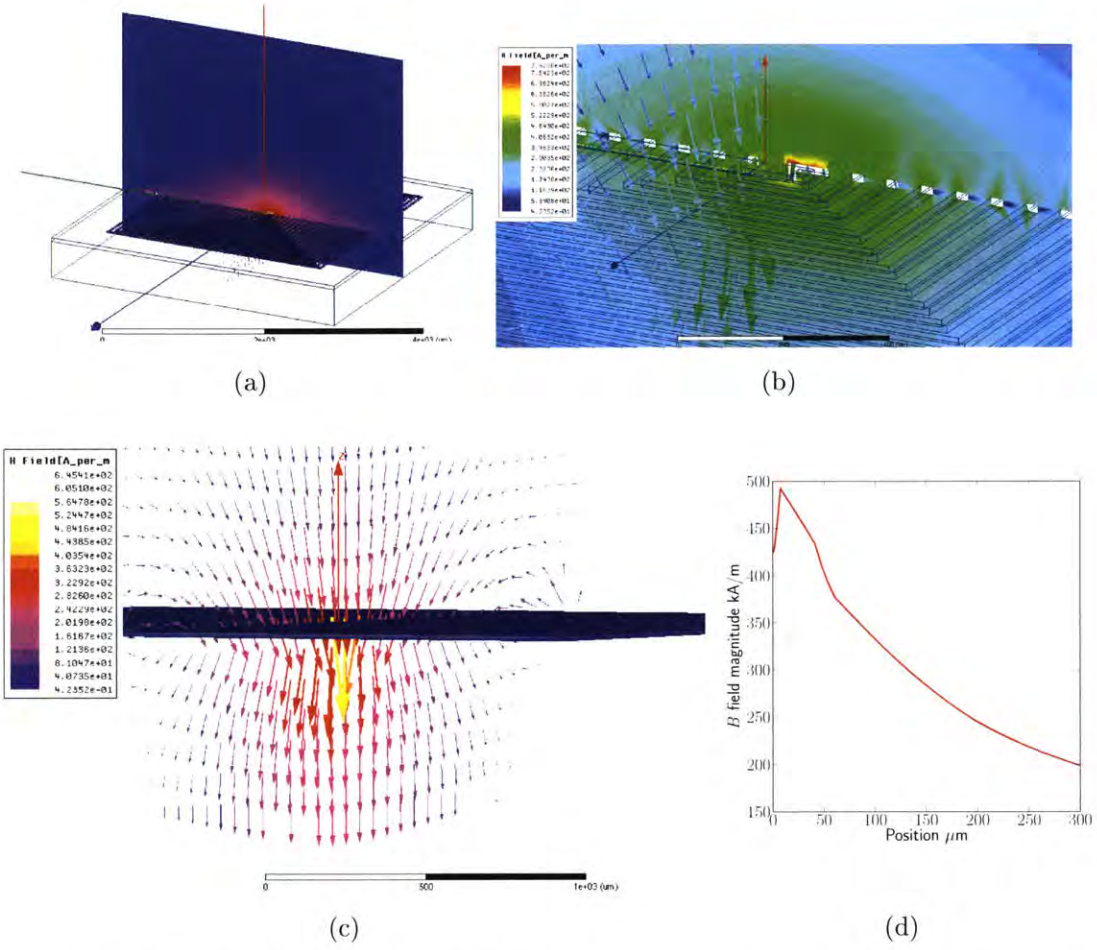


Figure 5-3: **HFSS simulation of fields from a rectangular glass-Cu spiral coil.** (a) Model setup consists of 30 turns, $125\mu$ inner diameter, $3mm$ outer diameter, $25\mu$ pitch and $15\mu$ Cu thickness (b) Distribution of $B$ field strengths. The field is strongest at the center and has better transverse homogeneity than the CPW. (c) Direction of the field lines. The field has predominantly $Z$ character with much better spatial homogeneity than the CPW excitation.(d) Fall off of the field strength with height from the origin. Note that in a $250\mu$ height, the field reduces by a factor of almost two. The slight kink at low height is because of the modeled $15\mu$ thickness of the Cu wire.

where $r_{i,e}$ is the inner and outer coil radius. To calculate the effective cross sectional area, one needs to consider the skin depth which is important at high frequencies,

$$\delta = \sqrt{\frac{2\rho}{2\pi f \mu}} \tag{5.3}$$

where $\mu = 1.25 \times 10^{-6} H/m$ is the permeability of Cu. For $f = 3\text{GHz}$, $\delta = 1.194\mu$ – hence the current only flows in a small shell of this thickness. This leads to $S_{eff} = 2\delta(w + h) = 155.2\mu^2$. Substituting we get $R = 16.31\Omega$. To consider the heating effect, consider that the thermal conductivity of oxide and glass is $\lambda_g = 1.4W/mK$, while that of diamond is $\lambda_d = 10^3 W/mK$. For a rectangular slab of face area $A$ and face separation $l$,

$$P = \frac{\lambda A \Delta T}{L} \tag{5.4}$$

where $\Delta T$ is the temperature difference between the faces. Hence, considering $A = (4mm)^2$, and $L = 250\mu$, because of the high thermal conductivity of diamond if one face of diamond is maintained at room temperature with a big heat sink, then the rise in temperature of the coils is only $\Delta T = 0.25K$ per $1A$ of current. At 3GHz, the skin depth $\delta = 1.194\mu$, and coil resistance $R = 16.31\Omega$, gives a rise of 0.25K in coil temperature per 1A of current if coil is in contact with heat sunk diamond.

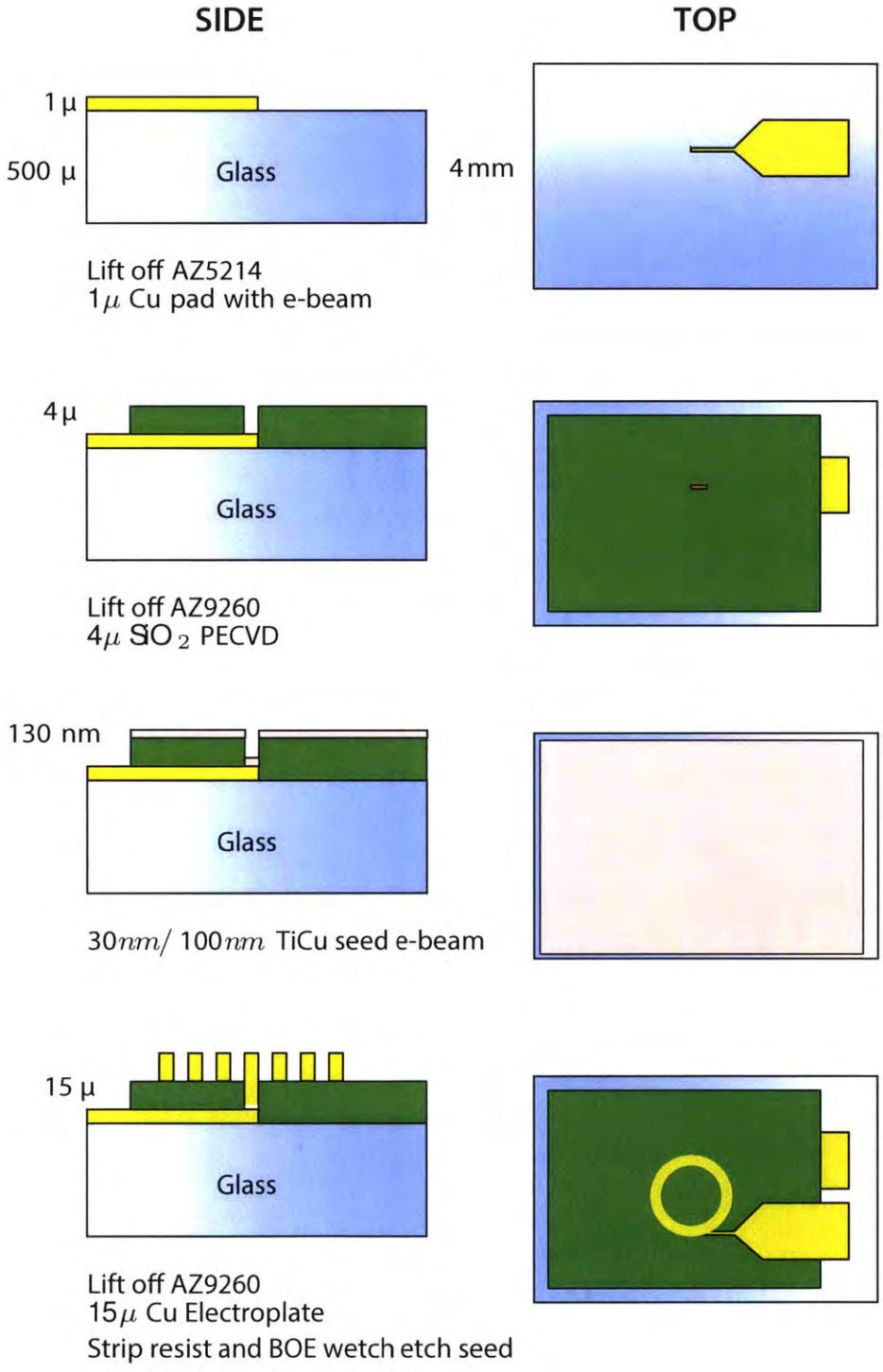


Figure 5-4: **Steps for the fabrication of microcoils used in gyroscope experiment.** In this process we try to fabricate a multi turn coil using a liftoff process. A silicon dioxide layer acts an insulator between the two layers of the coil. A via is fabricated with a cylindrical dimension of one micron that is used connect the two layers of the microcoil.

# Part III

# Quantum Assisted Simulation

# Preface

Ever since the proposal of Richard Feynman of simulating the dynamics of one quantum system with another, quantum simulation is often considered a major goal in the development of quantum information processors (QIPs). In this part of the thesis, we shall concern ourselves with various experimental challenges facing quantum simulation, and propose ways for their mitigation. In its simplest form, quantum simulation considers the ability of turning a naturally occurring system under experimental control into another system that one wants to simulate. Quantum simulation can be achieved with a predefined set of quantum logical gates (for instance Hadamard, CNOT[204]), in the same way that a classical computer would do. However, this *digital* quantum simulation is often quantum simulation is hard to achieve in practice because the number of gate operations scale exponentially with the number of qubits, making the system vulnerable to decoherence. In chapter 6 of this thesis, we have proposed an alternative paradigm for quantum simulation that requires no local qubit control, but only relies on *collective* qubit rotations and static field gradients[205]. Unlike gate based techniques, this *analog* approach to quantum simulation[206] approach achieves the desired coupling engineering via a construction that is akin to a time domain Bragg grating – in essence we perform a *time-domain filtering* action that stroboscopically produces our desired Hamiltonian[33]. The peaks of the

grating maxima can be tuned independently, allowing the method to be very versatile and simulate efficiently several classes of many-body Hamiltonians. For instance, starting with a fully coupled dipolar spin crystal $\mathcal{H}_{\text{natural}} = \sum_{jk} \frac{1}{r_{jk}^3}(3\sigma_j^z\sigma_k^z - \sigma_j \cdot \sigma_k)$, I could demonstrate the engineering of a *nearest neighbor* weighted XY Hamiltonian $\mathcal{H}_{\text{target}} = \frac{1}{2}\sum_j \frac{b}{n}\sqrt{j(n-j)}[\sigma_j^+\sigma_{j+1}^+ + \sigma_j^-\sigma_{j+1}^-]$ that can drive perfect quantum information transport between two separated nodes of a large spin network [63,99], while naturally decoupling all unwanted interactions. One can also naturally *apodize* the Bragg peaks so as to make the quantum simulation robust under decoherence and coupling disorder. We describe this subject in detail including its application for the specific case of engineering a quantum information processor for quantum transport, i.e. transferring information in a ballistic dispersionless manner from one part of the QIP to another, in a sense forming the 'quantum wires' that transmit information between connected processors of the future.

In chapter 7 of this thesis, we will focus on a complementary question. Large scale quantum simulators, and quantum information processing (QIP) systems will require the preparation and control of *multi-qubit* states. These states are harder to control and to model analytically because of their complex many-body dynamics. While some recent works have looked at their decoherence and control schemes via dynamical-decoupling, the decay was usually assumed to be induced by an uncorrelated bath, acting independently on each qubit, while this is often not the case in nature, especially for spatially close spins. Indeed, strategies to protect multi-qubit states against decoherence in large quantum network registers are difficult to formulate because of the complex many body decay dynamics of these states under the decoherence interaction. A better knowledge of the decay dynamics may help in the construction of such control schemes. In chapter 7, we experimentally and theoretically study the decay of such multi-qubit states under the action of a correlated spin

bath, paving the way to the more effective construction of strategies to mitigate such decay.

# Chapter 6

# Quantum Simulation via Filtered Hamiltonian Engineering

## 6.1 Introduction

Controlling the evolution of complex quantum systems has emerged as an important area of research for its promising applications. The control task can be often reduced to Hamiltonian engineering[207] (also extended to reservoir engineering[208,209]), which has enable a variety of tasks, including quantum computation[210], improved quantum metrology[211] and dynamical decoupling[33,32]. The most important application is quantum simulation[206,212], with the ultimate goal to achieve a programmable universal quantum simulator, able to mimic the dynamics of any system. One possible strategy is to use a quantum computer and decompose the desired evolution into unitary gates[72,204]. Alternatively, one can use Hamiltonian engineering by a Suzuki-Trotter factorization of the desired interaction into experimentally achievable Hamiltonians[213,214]. However, experimental implementations of these simulation methods

often require *local* quantum control, which is difficult to achieve in large systems.

We propose a method for Hamiltonian engineering in quantum information processing architectures that requires no local control, but only relies on collective qubit rotations and field gradients. The technique achieves a spatial modulation of the coupling strengths via a dynamical construction of a weighting function combined with a Bragg grating. As an example, we demonstrate how to generate the ideal Hamiltonian for perfect quantum information transport between two separated nodes of a large spin network. We engineer a spin chain with optimal couplings from a large spin network, such as naturally occurring in crystals, while decoupling all unwanted interactions. For realistic experimental parameters, our method can be used to drive almost perfect quantum information transport at room-temperature. The Hamiltonian engineering method can be made more robust under coherence and coupling disorder by a novel apodization scheme. Thus the method is quite general and can be used engineer the Hamiltonian of many complex spin lattices with different topologies and interactions.

Here we present a scheme for Hamiltonian engineering that employs only collective rotations of the qubits and field gradients – technology readily available e.g. in magnetic resonance, ion traps[204] and optical lattices[215]. We consider a qubit network (Fig. 10-1) with an internal Hamiltonian $\mathcal{H}_{\text{int}}$, for example due to dipolar couplings naturally occurring among spins in a crystal lattice. The target Hamiltonian $\mathcal{H}_{\text{tar}}$ is engineered from $\mathcal{H}_{\text{int}}$ by first "removing" unwanted couplings and then "modulating" the remaining coupling strengths. The first step is equivalent to creating a time-domain Bragg grating, a sharp filter that retains only specific couplings[216]. Then, a weighting function allows fine-tuning of their strengths, without the need for local control.

Hamiltonian engineering has a long history in NMR, as described by coherent

averaging[62,91], and field gradients have been proposed to achieve NMR "diffraction" in solid[217,218]. While decades old pulse sequences exist for selective excitation[219], and have been recently extended in the context of dynamical decoupling[33], and turning on couplings one at a time[220,221], our method allows increased control and *simultaneous* tunability of the filtered coupling strengths by exploiting magnetic-field gradients, and a photonics inspired approach for robust filter construction[216]. Hence our method is much broader and more general than previously discussed control techniques and offers an intuitive and quantitative approach for the engineering of Hamiltonians in many physical settings.

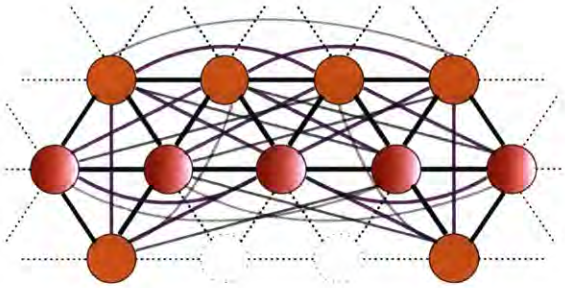

Figure 6-1: **A complex spin network in a trigonal planar lattice.** Only spins considered in simulations are depicted with edges denoting couplings. Hamiltonian engineering preserves only NN couplings inside a chain (red) and eliminates off-chain couplings to the surrounding network (orange), thanks to a linear magnetic field gradient along the chain.

As an example, we show how to apply this filtered engineering method to generate an optimal Hamiltonian for quantum information transfer (QIT). Linear arrays of spins have been proposed as quantum *wires* to link separated nodes of a spin network[222]; engineering the coupling between the spins can achieve perfect QIT[223]. Finally, we will analyze experimental requirements to implement the method in ex-

isting physical architectures.

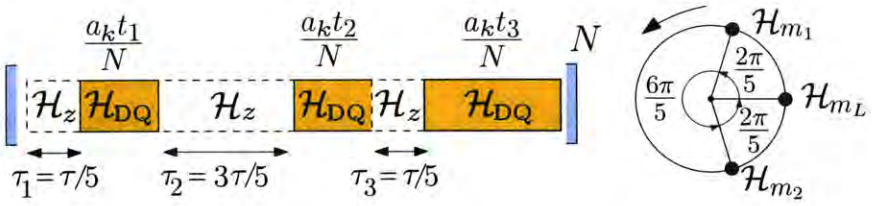


Figure 6-2: **Filtered engineering sequence**, consisting of periods ($\tau_j$) of *free* evolution under the gradient $\mathcal{H}_z$ and *mixing* evolution under $\mathcal{H}_{\rm DQ}$ of duration $t_j/N$. The blocks are applied left to right and the cycle is repeated $N$ times. The sequence can be *apodized* by an appropriate choice of coefficients $a_k$ at the $k^{\rm th}$ cycle. Left: Example sequence for engineering transport in a 5-spin chain in the complex network of Fig. 10-1. , Explicit values of $\mathbf{t_m} = \{t_1, t_2, \cdots\}$ are in[224] and $\tau = \pi/\omega$. Right: Phasor representation[224] of Hamiltonian engineering. In the circle we show the phases $\varphi_j = b_{i,i+1} t_j$ acquired by the $S_i^+ S_{i+1}^+$ term of the toggling frame Hamiltonians $\mathcal{H}_{m_j}$.

## 6.2 Hamiltonian engineering

The goals of filtered Hamiltonian engineering can be summarized as (i) the cancellation of unwanted couplings – often next-nearest neighbor (NNN) – and (ii) the engineering of the remaining couplings to match the desired coupling strengths. We achieve these goals by dynamically generating tunable and independent grating ($\mathcal{G}_{ij}$) and weighting ($F_{ij}$) functions via collective rotations under a gradient. The first step is to create the Hamiltonian operator one wishes to simulate using sequences of collective pulses. Although the initial Hamiltonian $\mathcal{H}_{\rm int}$ restricts which operators can be obtained[224], various control sequences have been proposed to realize a broad set of Hamiltonians[225,226]. These multiple pulse sequences cannot however modu-

late specific coupling strengths, which is instead our goal – this can be achieved by evolution under gradient. Consider for example the XY Hamiltonian, $\mathcal{H}_{XY} = \sum_{ij} b_{ij}(S_i^x S_j^x + S_i^y S_j^y)$. Evolution under the propagator $U(t,\tau) = e^{-i\mathcal{H}_z\tau}e^{-i\mathcal{H}_{XY}t}e^{i\mathcal{H}_z\tau}$, where $\mathcal{H}_z = \sum_i \omega_i S_i^z$ is obtained by a gradient, is equivalent to evolution under the Hamiltonian

$$\begin{aligned}\mathcal{H}'_{XY} = \textstyle\sum_{ij} b_{ij}[&(S_i^x S_j^x + S_i^y S_j^y)\cos(\delta\omega_{ij}\tau) \\ &+(S_i^x S_j^y - S_i^y S_j^x)\sin(\delta\omega_{ij}\tau)],\end{aligned} \tag{6.1}$$

where $\delta\omega_{ij}=\omega_j-\omega_i$. The modulation is repeated to obtain $U_0 = \prod_h U(t_h,\tau_h) \approx e^{i\overline{\mathcal{H}}T}$ over the total time $T$, where the effective Hamiltonian $\overline{\mathcal{H}}$ can be calculated from a first order expansion. Given a desired target Hamiltonian $\mathcal{H}_d = \sum_{ij} d_{ij}^1(S_i^x S_j^x + S_i^y S_j^y) + d_{ij}^2(S_i^x S_j^y - S_i^y S_j^x)$, we obtain a set of equations in the unknowns $\{t_h,\tau_h\}$ by imposing $\overline{\mathcal{H}} = \mathcal{H}_d$.

To simplify the search for the correct timings, we can first apply a filter that cancels all unwanted couplings and use the equations above to only determine parameters for the remaining couplings. The filter is obtained by a dynamical implementation of a Bragg grating: we evolve under $N$ cycles (while reducing the times to $t_h/N$) with a gradient modulation $U = \prod_{k=0}^{N-1}\left(e^{i\mathcal{H}_z\tau k}U_0 e^{-i\mathcal{H}_z\tau k}\right)$ that weights the couplings by a factor $\mathcal{G}_{ij}$, with

$$\mathcal{G}_{ij} = \sum_{k=0}^{N-1} e^{ik\tau\delta\omega_{ij}} = e^{i(N-1)\tau\delta\omega_{ij}/2}\frac{\sin(N\tau\delta\omega_{ij}/2)}{\sin(\tau\delta\omega_{ij}/2)}. \tag{6.2}$$

We now make these ideas more concrete by considering a specific example, the engineering of an Hamiltonian allowing perfect QIT in mixed-state spin chains [227,228,99,229].

### 6.2.1 Filtered engineering for QIT

For lossless transport, the simplest $n$-spin chain consists of nearest-neighbor (NN) couplings that vary as $d_j = d\sqrt{j(n-j)}$[223], ensuring perfect transport at $T = \pi/(2d)$. Manufacturing chains with this precise coupling topology is a challenge due to fabrication constraints and the intrinsic presence of long-range interactions. *Regular* spin networks are instead found ubiquitously in nature: our method can be used to dynamically engineer the optimal Hamiltonian in these complex spin networks. Consider a dipolar-coupled spin network with Hamiltonian

$$\mathcal{H} = \mathcal{H}_{\text{int}} + \mathcal{H}_z = \sum_{ik} b_{ik}(3S_i^z S_k^z - S_i \cdot S_k) + \sum_i \omega_i S_i^z, \tag{6.3}$$

where the spatial frequency *tagging* is achieved by applying a magnetic field gradient. The target Hamiltonian for QIT in a $n$-spin chain is $\mathcal{H}_d = \sum_{i=1}^{n-1} d_i(S_i^x S_{i+1}^x - S_i^y S_{i+1}^y)$. We consider this interaction, instead of the more common XY Hamiltonian, since it drives the same transport evolution[?] and the double-quantum Hamiltonian $\mathcal{H}_{\text{DQ}} = \sum_{i<k} b_{ik}(S_i^x S_k^x - S_i^y S_k^y)$ can be obtained from the dipolar Hamiltonian via a well-known multiple-pulse sequence[225,224]. The sequence cancels the term $\mathcal{H}_z$ and, importantly, allows time-reversal by a simple phase shift of the pulses. We can further achieve evolution under the field gradient only, $\mathcal{H}_z$, by using homonuclear decoupling sequences, such as WAHUHA[46,91] or magic echo[230]. Note that in our scheme, collective pulses are used to create the building blocks $\mathcal{H}_{\text{DQ}}$ and $\mathcal{H}_z$ out of which the simulation is constructed.

The filtered engineering sequence consists of alternating periods of *free* evolution ($\tau_{\mathbf{z}}$) under $\mathcal{H}_z$ and double-quantum excitation $\mathcal{H}_{\text{DQ}}$ (*mixing* periods $\mathbf{t_m}$). We analyze this sequence using average Hamiltonian theory[62,91].Consider for sim-

plicity a sequence with only two mixing and free evolution periods. Then, setting $U_z(\tau) = \exp(i\tau\mathcal{H}_z)$ and $U_{\rm DQ}(t) = \exp(it\mathcal{H}_{\rm DQ})$, the propagator for $N$ cycles is $U_N = \left[U_z(\tau_1)U_{\rm DQ}\left(\frac{t_1}{N}\right)U_z(\tau_2)U_{\rm DQ}\left(\frac{t_2}{N}\right)\right]^N$, or

$$\begin{aligned} U_N &= \left[U_z(\tau_1)U_{\rm DQ}\left(\tfrac{t_1}{N}\right)U_z^\dagger(\tau_1)\right] \times \left[U_z(\tau)U_{\rm DQ}\left(\tfrac{t_2}{N}\right)U_z^\dagger(\tau)\right] \\ &\times \cdots \times \left[U_z(N\tau)U_{\rm DQ}\left(\tfrac{t_2}{N}\right)U_z^\dagger(N\tau)\right], \end{aligned} \tag{6.4}$$

where $\tau = \tau_1 + \tau_2$, and in a sequence (eg. Fig. 6-2) propagators are applied right to left. Now, $U_z(\tau)U_{\rm DQ}(t)U_z^\dagger(\tau) = e^{it\mathcal{H}_m(\tau)}$, where $\mathcal{H}_m(\tau) = \sum_{i<k} b_{ik}(S_i^+S_k^+e^{i\tau\delta_{ik}} + S_i^-S_k^-e^{-i\tau\delta_{ik}})$ is the *toggling* frame Hamiltonian with $\delta_{ik} = \omega_i + \omega_k$. Employing the Suzuki-Trotter approximation[214], $U_N$ is equivalent to evolution under the effective Hamiltonian

$$\overline{\mathcal{H}} = \sum_{i<j} \frac{b_{ij}}{NT} S_i^+S_j^+ \left(t_1e^{i\tau_1\delta_{ij}} + t_2e^{i(\tau_1+\tau_2)\delta_{ij}}\right)\mathcal{G}_{ij} + \text{h.c.} \tag{6.5}$$

with $\mathcal{G}_{ij} = e^{i(N-1)\tau\delta_{ij}/2}\frac{\sin(N\tau\delta_{ij}/2)}{\sin(\tau\delta_{ij}/2)}$, and $T = \sum_k t_k$.

In general, for a sequence of free times $\tau_{\mathbf{z}} = \{\tau_1, \ldots, \tau_L\}$ and mixing times $\mathbf{t_m} = \{t_1, \ldots, t_L\}$, the average Hamiltonian is $\overline{\mathcal{H}} = \sum_{i<j} S_i^+S_j^+F_{ij}(\tau_{\mathbf{z}}, \mathbf{t_m})\mathcal{G}_{ij}(\tau) + \text{h.c.}$, where $\tau = \sum_{j=1}^L \tau_j$ and we define the *weighting* function,

$$F_{ij}(\tau_{\mathbf{z}}, \mathbf{t_m}) = \frac{b_{ij}}{NT}\sum_k t_k \exp\left(i\delta_{ij}\textstyle\sum_{h=1}^k \tau_h\right). \tag{6.6}$$

The grating $\mathcal{G}_{ij}$ forms a sharp filter with maxima at $\tau\delta_{ij} = 2m\pi$. A linear 1D-magnetic field gradient along a selected chain of spins in the larger network sets the $j^{\rm th}$ spin frequency to $\omega_j = j\omega - \omega_0$, where $\omega_0$ is the excitation frequency. Each spin pair acquires a spatial phase under the gradient: if $\omega\tau = \pi$ and $2\omega_0\tau = 3\pi - 2m\pi$

the NN couplings are preserved, while the NNN couplings lie at the minima of the grating and are canceled (Fig. 6-3). Other non-NN, off-chain couplings lie at the grating side-lobes and have greatly reduced amplitudes at large $N$.

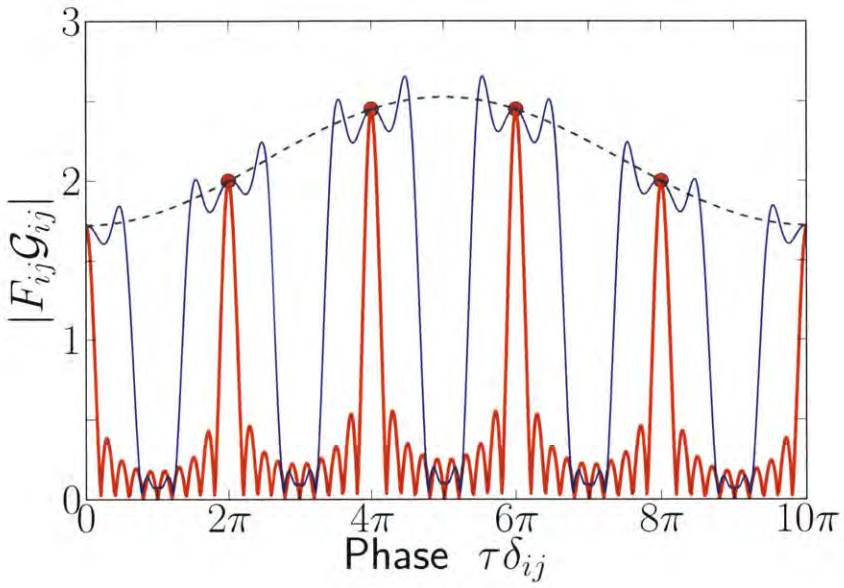


Figure 6-3: **Engineering filter function**, $|F_{ij}\mathcal{G}_{ij}|$ for a 5-spin chain, as a function of the phase $\tau\delta_{ij}$. A single cycle creates the weighting function $F_{ij}$ (dashed line), which is transformed to sharp (red) peaks at the ideal couplings (circles) at larger cycle number (here $N = 10$). The peak widths can be altered by apodization, e.g. sinc-apodization (blue line) $a_k = \sin(W(k - N/2))/(W(k - N/2))$, with $W = (\pi + 1)/2$ and normalized so that $\sum_{k=1}^{N} a_k = N$.

Following the filter, the weighting function $F_{j(j+1)}$ is constructed to yield the ideal couplings for perfect transport. We have a set of $2n$ equations (for an $n$-spin chain),

$$\begin{aligned} &\textstyle\sum_{h=1}^{L} \sin\left[\omega(2j+1)\sum_{k=1}^{h}\tau_k\right] t_h b_{j,j+1} = 0, \qquad \forall j \\ &\textstyle\sum_{h=1}^{L} \cos\left[\omega(2j+1)\sum_{k=1}^{h}\tau_k\right] t_h b_{j,j+1} \propto d_j, \qquad \forall j, \end{aligned} \tag{6.7}$$

with $2L$ unknowns for $L$ time steps. The number of conditions (thus of time steps) can be reduced by exploiting symmetry properties. For example, a gradient symmetric with respect to the chain center would automatically satisfy most of the conditions in Eq. (6.7) and only $L = \lceil n/2 \rceil$ time steps would be required. Unfortunately this solution is practical only for some chain lengths [224]; we thus focus on a suboptimal, but simpler solution. Consider an odd $n$-spin chain. To enforce the mirror symmetry of $d_j$ and ensure that the average Hamiltonian remains in DQ form, we imposes time mirror symmetry, $t_j = t_{L-j}$, while the gradient times are $\tau_j/\tau = 3/n$ for $j = (L+1)/2$ and $\tau_j/\tau = 1/n$ otherwise (Fig. 6-2). This choice yields a *linear* system of equations for $L = n - 2$ mixing periods $\mathbf{t_m}$,

$$F_{j(j+1)}\mathcal{G}_{j(j+1)} = \sum_k t_k \cos\left(\frac{2j\pi k}{n}\right) = d\sqrt{j(n-j)} \tag{6.8}$$

Analogous solutions can be derived for even spin chains. A phasor representation [231] of how the evolution periods exploit the symmetries is presented in Fig. 6-2 and [224].

The tuning action of $F_{j(j+1)}\mathcal{G}_{j(j+1)}$ is very rapid, achieving perfect fidelity, $f = \mathrm{Tr}\left\{U S_1^z U^\dagger S_n^z\right\}/2^n$, in just a few cycles. Increasing N reduces the error in the Trotter expansion by improving $F_{j(j+1)}$ (Fig. 6-4.a) as well as the selectivity of $\mathcal{G}_{j(j+1)}$ (Fig. 6-4.b). The peak width of the grating decreases as $2\pi/N$ [33], improving its selectivity linearly with $N$ [224]. As shown in Fig. 6-4, about $n$ cycles are required for almost perfect decoupling of the unwanted interactions ($f > 0.95$).

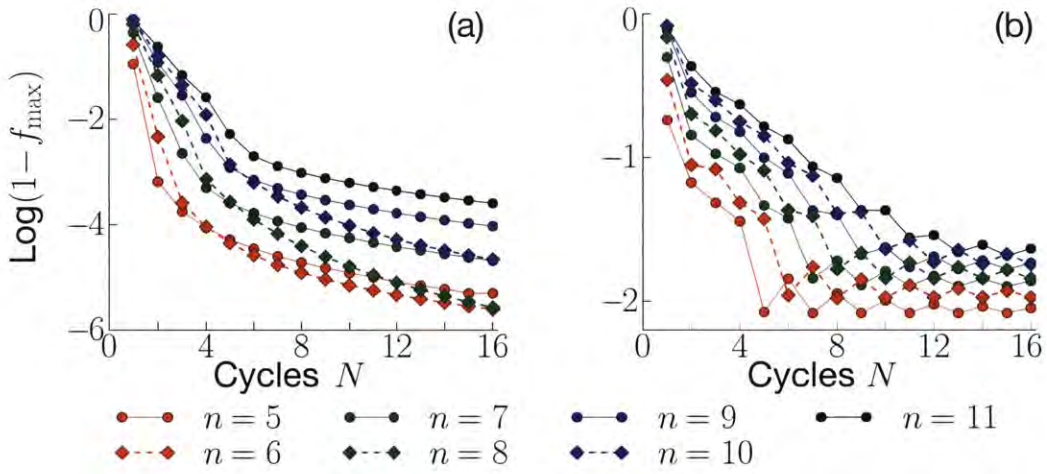


Figure 6-4: **Minimum transport infidelity obtained by filtered engineering**, as a function of cycle number $N$ for a $n$-spin dipolar chain with (a) NN couplings only and (b) all couplings.

The highly selective grating also avoids the need to isolate the chain and for the surrounding network to have a regular structure. However, in the presence of disorder in the chain couplings one needs to compromise between broader grating peaks (via small $N$) and poorer decoupling of unwanted interactions (Fig. 6-5). To improve the robustness of our scheme, we can further modulate the mixing times $\mathbf{t_m}$ by coefficients $a_k$; this imposes an apodization of the grating function as $\mathcal{G}_{ij} = \sum a_k e^{ik\tau\delta_{ij}}$. Apodization can counter disorder and dephasing , which destroys the exact phase relationships among spins that enabled our Hamiltonian engineering method. The grating peaks can be made wider by $W$ (Fig. 6-3) and any coupling that is in phase to within $W$ can still be engineered robustly (see Fig. 6-6) at the expenses of a poorer decoupling efficiency of long-range couplings. Apodization has other applications: for instance, it could be used to engineer *non-linear* spin chains in lattices or, quite generally, to select any regular array of spins from a complex network

– allowing a wide applicability of our method to many natural spin networks and crystal lattices[224].

### 6.2.2 Approximation validity

The control sequence is designed to engineer the average Hamiltonian $\overline{\mathcal{H}}$ only to first order. Higher order terms arising from the Trotter expansion yield errors scaling as $\mathcal{O}(t_k t_{k+1}/N^2)$. Consider e.g. the propagator for a 5-spin chain,

$$U_N = [e^{i\frac{t_1}{N}\mathcal{H}_m(\tau_1)} e^{i\frac{t_1}{N}\mathcal{H}_m(\tau_2)} e^{i\frac{t_L}{N}\mathcal{H}_{\mathrm{DQ}}}]^N, \tag{6.9}$$

where $\tau_1 = \pi/(5\omega)$ and $\tau_2 = 3\pi/(5\omega)$. This yields the desired $\overline{\mathcal{H}}$ with an error $\mathcal{O}(t_1^2/N^2)$ for the first product, and $\mathcal{O}(2t_1 t_L/N^2)$ for the second. While increasing $N$ improves the approximation, at the expense of larger overhead times, the even small $N$ achieves remarkably good fidelities , since by construction, $t_j \ll t_L \approx T/N$. In essence, the system evolves under the unmodulated DQ Hamiltonian during $t_L$, yielding the *average* coupling strength, while the $t_j$ periods apply small corrections required to reach the ideal couplings. Symmetrizing the control sequence would lead to a more accurate average Hamiltonian because of vanishing higher orders[232]. However, this comes at the cost of longer overhead times $\tau_{\mathbf{z}}$, thus using a larger number of the unsymmetrized sequence is often a better strategy.

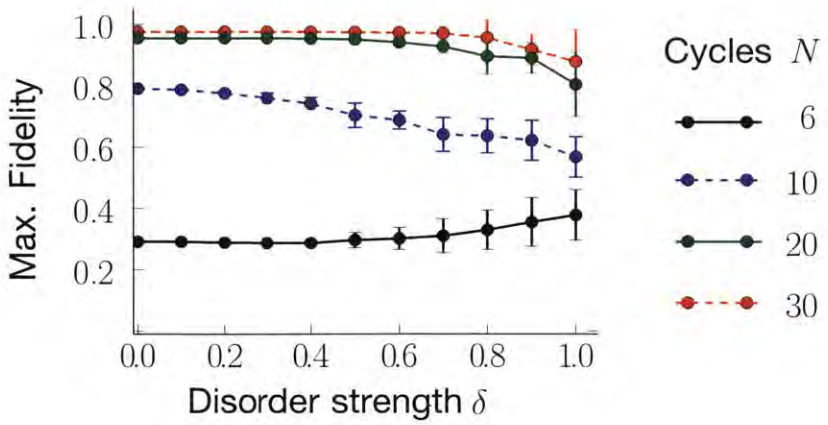


Figure 6-5: **Variation of maximum fidelity with disorder** in the network (Fig. 10-1) surrounding the spin chain. The spins are displaced by $\delta\, r$, where $r$ is uniformly distributed on $[-r_0/2, r_0/2]$ (averaged over 30 realizations) with $r_0$ the NN chain spin separation.

## 6.3 Experimental viability

We consider an experimental implementation and show that high fidelity QIT at room temperature is achievable with current technology.

We assume that a spin lattice of NN separation $r_0$, yielding a NN coupling strength $b = \frac{\mu_0 \hbar}{4\pi} \frac{\gamma^2}{r_0^3}$. If an ideal $n$-spin chain could be fabricated with maximum coupling strength $b$, the transport time would be $T_{\rm id} = \frac{n\pi}{8b}$ [227]. Alternatively, perfect state transfer could be ensured in the weak-coupling regime [229,228], with a transport time $T_{\rm weak} \approx \frac{\Gamma\pi}{b}$, where $\Gamma \gg 1$ ensures that the end-spins are weakly coupled to the bulk-spins. We compare $T_{\rm id}$ and $T_{\rm weak}$ to the time required for $N$ cycles of the engineering sequence, $T_{\rm eng}$. Since $t_L \gg t_j$, to a good approximation the total mixing time is $Nt_L \lesssim \sum_j \sqrt{j(n-j)}/(nb) \approx \pi n/8b$. Adding the overhead time $N\tau$, which

depends on the available gradient strength as $\tau = \pi/\omega$, we have, $T_{\text{eng}} = \frac{n\pi^2}{16b} + \frac{N\pi}{\omega}$. Since we can take $\Gamma \approx n$ for the weak regime[228] and $N \approx n$ for filtered engineering, a gradient larger than the NN coupling strength would achieve faster transport.

For concreteness, consider a crystal of fluorapatite (FAp) $[Ca_5(PO_4)_3F]$ that has been studied for quantum transport[233,234]. The $^{19}F$ nuclear spins form parallel linear chains along the $c$-axis, with intra-chain spacing $r_0 = 0.344$nm ($b = 1.29$kHz), while the inter-chain coupling is $\approx 40$ times weaker. Maxwell field coils[235] can generate sufficient gradient strengths, such as a gradient of $5.588 \times 10^8$G/m over a 1 mm$^3$ region[236], corresponding to $\omega = 0.7705$kHz. Far stronger gradients are routinely used in magnetic resonance force microscopy; for example, dysprosium magnetic tips[237] yield gradients of 60G/nm, linear over distances exceeding 30nm, yielding $\omega = 82.73$kHz. Setting $\omega = 25$kHz would allow $\pi/2$-pulse widths of about $0.5\mu$s to have sufficient bandwidth to control chains exceeding $n = 50$ spins. Homonuclear decoupling sequences[91,230] can increase the coherence time up to $T_{\text{eng}}$. volution under the DQ Hamiltonian has been shown to last for about 1.5ms[238] in FAp; decoupling during the $U_z$ periods could increase this to 15ms[230]. While pulse errors might limit the performance of Hamiltonian engineering, there exist several methods to reduce these errors[239]. With $\omega = 25$kHz and 30 cycles, nearly lossless transport should be possible for a 25-spin chain.

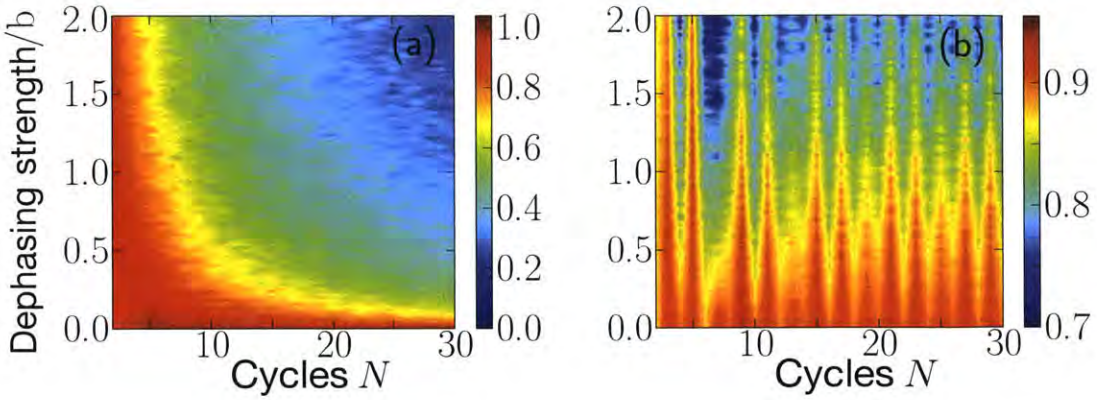


Figure 6-6: **Transport fidelity** for a 5-spin chain with dipolar couplings (NN coupling strength $b$). The spins are subject to dephasing noise, modeled by an Ornstein-Uhlenbeck process of correlation time $\tau_c = 2/b$ and strength $2b$, averaged over 100 realizations. (a) No apodization. (b) With sinc-apodization ($W = (\pi + 1)/2$ as in Fig. 6-3).

Filtered Hamiltonian engineering could as well be implemented in other physical systems, such as trapped ions[204] or dipolar molecules[240] and atoms[215] in optical lattices. For instance, Rydberg atoms in optical lattices[241,242] could enable simulations at low temperature, thanks to the availability of long-range couplings and the ability to tune the lattice to create gradients. The scheme could also be extended to more complex 2D and 3D lattices ([224]).

## 6.4 Conclusions and Outlook

We have described a method for quantum simulation that does not require local control, but relies on the construction of time domain filter and weighting functions via

evolution under a gradient field. The method achieves the engineering of individual spin-spin couplings starting from regular, naturally occurring Hamiltonian. We presented a specific application to engineer spin chains for perfect transport, isolating them from a large, complex network. We showed that robust and high fidelity quantum transport can be driven in these engineered networks, with only experimental feasible control.

# Appendix

## 6.A Operator engineering

An important ingredient of any Hamiltonian engineering scheme is the ability to obtain the Hamiltonian operator form desired, before engineering the coupling strengths. Nuclear Magnetic Resonance has a long tradition of control sequences able to modify the naturally occurring Hamiltonians into desired operators; the most prominent application is in the refocusing of unwanted interactions, which has been further developed and is now a common technique in quantum information under the name of "dynamical decoupling"[243]. Here we briefly review these decoupling sequences and extend them to more general two-body Hamiltonians as well as to the task of creating a desired operator.

We consider a general Hamiltonian for 2 spin-$\frac{1}{2}$ particles:

$$H = \vec{\omega}_1 \cdot \vec{\sigma}_1 + \vec{\omega}_2 \cdot \vec{\sigma}_2 + \vec{\sigma}_1 \cdot \mathbf{d} \cdot \vec{\sigma}_2, \tag{6.10}$$

which can be rewritten in terms of spherical tensors $T_{l,m}$[244] (see Table 6.1):

$$H = \sum_{l,m} (-1)^m A_{l,-m} T_{l,m} \tag{6.11}$$

| | |
|---|---|
| $\mathbb{1}$ | $T_{00}=(\sigma_x^a\sigma_x^b+\sigma_y^a\sigma_y^b+\sigma_z^a\sigma_z^b)/\sqrt{3}$ |
| $T_{10}^a=\sigma_z^a/2$ | $T_{10}^b=\sigma_Z^b/2$ |
| $T_{11}^a=\sigma_+^a/\sqrt{2}$ | $T_{1-1}^a=\sigma_-^a/\sqrt{2}$ |
| $T_{11}^b=\sigma_+^b/\sqrt{2}$ | $T_{1-1}^b=\sigma_-^b/\sqrt{2}$ |
| $T_{11}=(\sigma_+^a\sigma_z^b-\sigma_z^a\sigma_+^b)/2$ | $T_{1-1}=(\sigma_-^a\sigma_z^b-\sigma_z^a\sigma_-^b)/2$ |
| $T_{10}=(\sigma_+^a\sigma_-^b-\sigma_-^a\sigma_+^b)/2$ | $T_{20}=(2\sigma_z^a\sigma_z^b-\sigma_x^a\sigma_x^b-\sigma_y^a\sigma_y^b)/\sqrt{6}$ |
| $T_{21}=(\sigma_+^a\sigma_z^b+\sigma_z^a\sigma_+^b)/2$ | $T_{2-1}=(\sigma_-^a\sigma_z^b+\sigma_z^a\sigma_-^b)/2$ |
| $T_{22}=\sigma_+^a\sigma_+^b/2$ | $T_{2-2}=\sigma_-^a\sigma_-^b/2$ |

Table 6.1: **Spherical tensor operators** for two spin-1/2 ($a$ and $b$)[244]. $\sigma_\alpha$ are the usual Pauli operators.

| Chain Length | Mixing periods $\mathbf{t_m}$ |
|---|---|
| 4 | $\{-0.1340,-0.1340,1.7321\}$ |
| 5 | $\{-0.201,-0.201,2.1242\}$ |
| 6 | $\{-0.2962,-0.0415,-0.0415,-0.2962,2.4907\}$ |
| 7 | $\{-0.369,-0.0652,-0.0652,-0.369,2.8806\}$ |
| 8 | $\{-0.4533,-0.1024,-0.0194,-0.0194,-0.1024,-0.4533,3.2594\}$ |
| 9 | $\{-0.5269,-0.1298,-0.0316,-0.0316,-0.1298,-0.5269,3.6492\}$ |
| 10 | $\{-0.6065,-0.1638,-0.0517,-0.0109,-0.0109,-0.0517,-0.1638,-0.6065,4.0330\}$ |
| 11 | $\{-0.6801,-0.1920,-0.0666,-0.0183,-0.0183,-0.0666,-0.1920,-0.6801,4.4231\}$ |

Table 6.2: **Mixing times $\mathbf{t_m}$** in units of $1/d$ (as used in Fig. 5 and Fig. 6 of the main text). Note that $t_L \gg t_j$ for $j \neq L$. Negative times are easily achieved by a $\pi/2$ shift of the DQ sequence pulses, which implements a time-reversal version of the DQ Hamiltonian.

where the coefficients $A_{l,-m}$ depend on the type of spin-spin interaction and the external field. This notation is useful when considering rotations of the Hamiltonian. We consider only collective rotations – that is, rotations applied to all the spins together, which are easily achievable experimentally. Note that they also conserve the rank $l$[91].

The goal of Hamiltonian engineering by multiple pulse sequence is to obtain a desired Hamiltonian from the naturally occurring one by piece-wise constant evolution under rotated versions of the natural Hamiltonian. We thus want to impose the

condition

$$\sum_k R_k \mathcal{H}_{nat} R_k^\dagger = \mathcal{H}_{tar}, \tag{6.12}$$

where $R_k$ are collective rotations of all the spins, which achieves the desired operator to first order in a Trotter expansion. Rotations can be described by the Wigner matrices $D^l_{m,n}(R_k)$ as:

$$R_k T_{l,m} R_k^\dagger = \sum_n (-1)^m D^l_{m,n}(R_k) T_{l,n} \tag{6.13}$$

thus Eq. (6.12) can be written using the spherical tensors as

$$\sum_{k,n} \sum_{l,m} (-1)^m A^{nat}_{l,-m} D^l_{m,n}(R_k) T_{l,n} = \sum_{l,m} (-1)^m A^{des}_{l,-m} T_{l,m}, \tag{6.14}$$

yielding the set of equations

$$\sum_{k,m} (-1)^m A^{nat}_{l,-m} D^l_{m,n}(R_k) = (-1)^n A^{des}_{l,-n}. \tag{6.15}$$

We note that since collective pulses cannot change the rank $l$, there are limitations to which Hamiltonians can be engineered. In particular, $T_{00}$ commutes with collective rotations: its contribution is thus a constant of the motion and, conversely, it cannot be introduced in the desired Hamiltonian if it is not present in the natural one. For example, an Ising Hamiltonian $H_I = \sigma_z^a \sigma_z^b$ is expanded as $H_I = (T_{00} + \sqrt{2} T_{20})/\sqrt{3}$, so that only the second part can be modulated. Conversely, the secular dipolar Hamiltonian is given by $T_{20}$, thus it cannot produce an Hamiltonian containing $T_{00}$ (although it can be used the create the DQ-Hamiltonian, $\mathcal{H}_{\rm DQ} = T_{22} + T_{2,-2}$). Group theory methods can be used to help solving Eq. (6.15) by reducing the number of

conditions using symmetries. For example, the DQ Hamiltonian can be prepared from the secular dipolar Hamiltonian by using a simple sequence consisting of two time intervals, $t_1 = t_2/2$ with the Hamiltonian rotated by $R_2 = \frac{\pi}{2}\big|_y$ in second time period, to yield: $T_{2,0}t_1 + \left[\sqrt{\frac{3}{128}}(T_{2,2} + T_{2,-2}) - \frac{1}{2}T_{2,0}\right] t_2 \propto \mathcal{H}_{DQ}$. Symmetrized versions of this simple sequence are routinely used in NMR experiments [225,226].

## 6.B Phasor representation of the engineering sequence

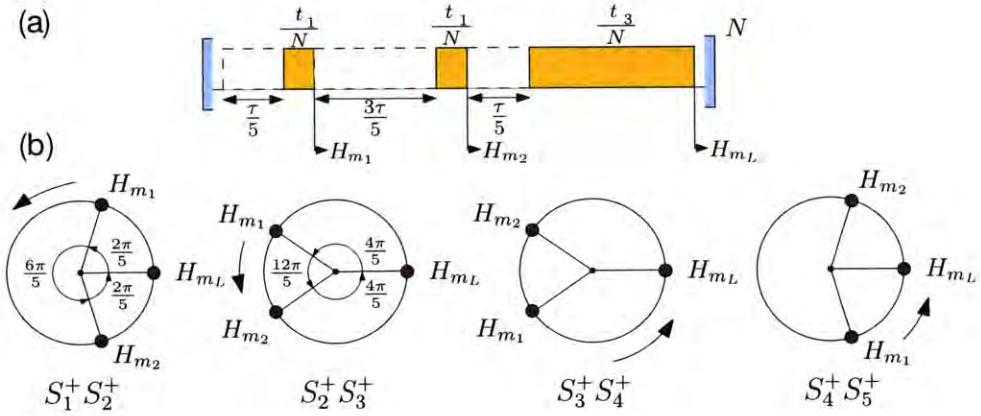


Figure 6-7: **Phasor representation of the Hamiltonian engineering sequence** for $n = 5$. The phase acquired by the toggling frame Hamiltonians $H_{m_j}$ after each mixing period in the sequence (a) is depicted on a unit circle for each of the NN terms $S_j^+ S_{(j+1)}^+$ in (b). The unit circle is traversed anti-clockwise from $H_{m_1}$ to $H_{m_L}$. Mirror symmetry of the engineered couplings about the center of the chain is ensured since $\{S_1^+ S_2^+, S_4^+ S_5^+\}$ and $\{S_2^+ S_3^+, S_3^+ S_4^+\}$ have identical phasor representations. The DQ form of the average Hamiltonian is ensured by forcing that the phasors for each of the $S_j^+ S_{(j+1)}^+$ terms have reflection symmetry about $2\pi$.

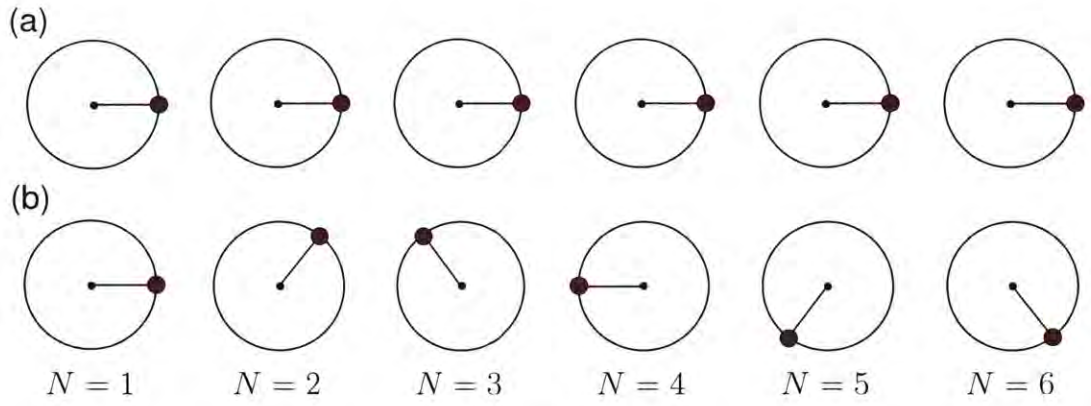


Figure 6-8: **Phasor representation of the grating's filtering action upon cycle iteration.** (a) The effective phasor of a nearest-neighbor neighbor coupling traverses a $2\pi$ rotation with each cycle, and is perfectly refocussed (constructive interference). (b) However, the phasor corresponding to long range couplings do not complete a full rotation (the figure shows an example of a long range coupling for which $\delta_{ij} = \pi/3$). Hence cycle iteration leads to destructive interference and reduced average amplitudes of these couplings.

The filtered engineering sequence presented in the main text has an intuitive geometric visualization in terms of phasors, which demonstrates the symmetries involved in the QIT Hamiltonian and the subsequent choice of free evolution periods $\tau_{\mathbf{z}}$. Let us consider for example the 5-spin sequence (Fig. 6-7a), and the toggling frame Hamiltonians $H_{m_j}$ during each mixing period. The phases acquired by the Hamiltonians are represented on a unit circle for each of the $S_j^+ S_{j+1}^+$ terms (Fig. 6-7b). The phasor representation makes clear the symmetries involved in the $F_{ij}$ filter engineering. Since the ideal couplings $d_j$ are mirror symmetric about the center of the chain, the construction of the filter $F_{j(j+1)}$ should match this symmetry. This can be ensured in two ways.

We could select a gradient centered around the middle spin in the chain. Then $\omega_j = -\omega_{n-j}$, and the set of equations in (4) of the main text reduces to only $n-1$ equations (instead of $2(n-1)$) if $t_k = t_{L-k}$ and $\mathcal{H}_m(\tau_k) = \mathcal{H}_m(\tau_{L-k})^\intercal$. This second condition further ensures that the first set of equations in Eq. (4) are always satisfied (the condition is easily satisfied by setting $t_k^z = -t_{L-k}^z$ with $t_k^z = \tau_k - \tau_{k-1}$ and $t_1^z = \tau_1$). Thus we only have $\lceil (n-1)/2 \rceil$ equations to be satisfied and correspondingly only $\lceil (n-1)/2 \rceil$ mixing periods. Although solutions can be found with this scheme, only for $n = 4, 5$ all the times are real. For larger spin chains it is possible to find all real solutions for $L = \lceil (n-1)/2 \rceil + 2$ mixing periods, although the system of equations quickly becomes intractable.

A second strategy is to use a gradient with minimum at the first spin in the chain, $L = n-2$ mixing periods (for $n$ odd) and choose $\tau_j/\tau = 3/n$ for $j = (L+1)/2$ and $\tau_j/\tau = 1/n$, and $t_j = t_{(L-j)}$. Moreover, since we want to retain the DQ form of the average Hamiltonian $\overline{H}$, the toggling frame Hamiltonians $H_m(\tau_k)$ and $H_m(\tau_{L-k})$ are such that their phasors have reflection symmetry about $2\pi$ for each $S_j^+ S_{j+1}^+$ term. This ensures that only the $(S_j^+ S_{j+1}^+ + S_j^- S_{j+1}^-)\cos[\tau\delta_{j(j+1)}]$ term survives, leading to an effective DQ form (see Fig. 6-7).

The filtering action of the grating can also be visualized quite simply by the phasor diagrams in Fig. 6-8: nearest-neighbor couplings undergo constructive interference upon cycle iteration and are retained, while long range couplings vanish on average.

## 6.C Characterizing grating selectivity

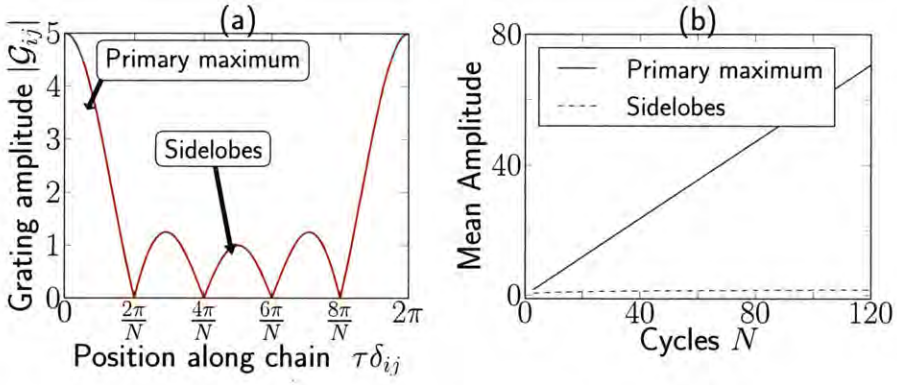


Figure 6-9: **Characteristics of the dynamic Bragg grating.** (a) The amplitude of the dynamic Bragg grating, $|\mathcal{G}_{ij}|$ for $N = 5$ cycles. There are $N-1$ minima at $2j\pi/N$, and $N-2$ secondary maxima (*sidelobes*). The width of the primary maximum is $2\pi/N$, and decreases with the number of cycles making the grating more selective. (b) Right panel characterizes the decoupling efficiency in terms of the mean amplitude of grating $|\mathcal{G}_{ij}|$ in the primary maxima (i.e the range $[0, \pi/N] \cup [2(N-1)\pi/N, 2\pi/N]$), and the side lobes (the range $[\pi/N, 2(N-1)\pi/N]$). Increasing the number of cycles decreases the relative sideband power, and hence increases the grating selectivity.

Let us now characterize the selectivity of $N$-cycles of the Bragg grating $\mathcal{G}_{ij} = \sum_{k=0}^{N-1} e^{ik\tau\delta_{ij}}$. Fig. 6-9(a) shows the grating amplitude $|\mathcal{G}_{ij}|$ for $N = 5$ cycles. In general, the width of the primary maximum, $2\pi/N$, decreases with $N$ and this increases the selectivity of the grating. Concurrently, the relative amplitude of the $N-2$ sidelobes decreases with $N$. Specifically, consider Fig. 6-9(b), which compares the mean grating amplitude in the primary maxima i.e. in the range $[0, \pi/N] \cup [2(N-1)\pi/N, 2\pi/N]$, and the sidelobes in the range $[\pi/N, 2(N-1)\pi/N]$.

From the properties of the Bragg grating, we find that the decoupling efficiency, characterized by the relative amplitude of the amplitude in the primary maxima with respect to the sidelobes, increases linearly with $N$.

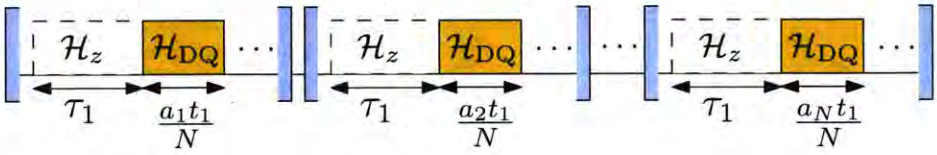


Figure 6-10: **Schematic of apodized Hamiltonian engineering sequences.** Each cycle of the sequence is enclosed in blue brackets, and the sequence consists of $N$ cycles. The DQ evolution period in each cycle is weighted by the apodization coefficients $a_k$, where $k$ is the cycle number. Note that the net evolution period in this case remains almost identical to the case of non-apodized sequences. Sinc-apodization can be used to broaden the Bragg maxima, making the sequence more robust to dephasing; for this case we choose $a_k = \sin(W(k - N/2))/(W(k - N/2))$, and normalize it such that $\sum a_k = N$. Here $W$ denotes the width of the maxima.

## 6.D Construction of apodized sequences

We now describe more in the detail the apodized sequences we introduced in Fig. 6-6 in order to make the Hamiltonian engineering more robust under decoherence. Apodized fiber Bragg gratings (FBGs) are widely used in photonics for suppression of sidelobe amplitudes (eg. [216]). However, the novelty of our formalism is to demonstrate (i) that the same underlying principles can be applied in the *time domain* as opposed to the spatial construction in FBGs, (ii) that they have the extremely beneficial effect of making Hamiltonian engineering *robust* under environmental noise, and (iii) that they can be used to engineer *non-linear* crystal lattices where conventional comb-like

gratings would fail.

The schematic of the apodized sequences are illustrated in Fig. 6-10, where $a_k$ denote the apodization coefficients with $k$ being the cycle number. In this case, the grating function gets modified as

$$\mathcal{G}_{ij} = \sum_{k=0}^{N-1} a_k e^{ik\tau\delta_{ij}} = a_0 + a_1 e^{i\tau\delta_{ij}} + a_2 e^{i2\tau\delta_{ij}} + \cdots + a_{N-1} e^{i(N-1)\tau\omega_{ij}}, \tag{6.16}$$

which is just the N-point discrete Fourier transform of the apodization window function whose samples are $a_k$. Hence choosing the appropriate apodization coefficients $a_k$ allow one to engineer the grating.

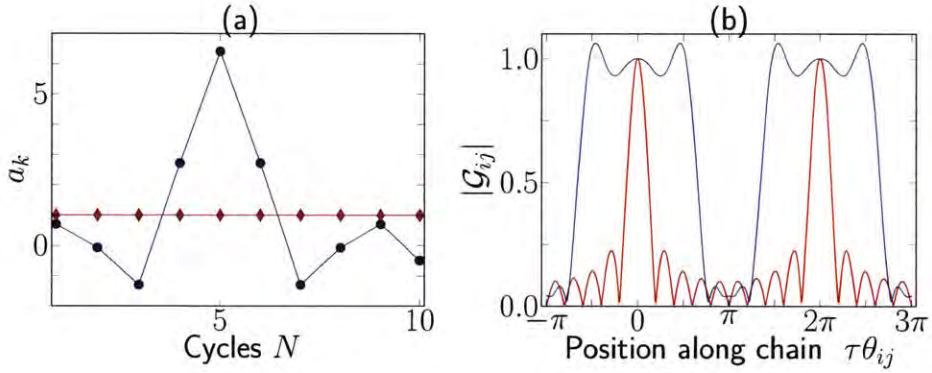


Figure 6-11: **Constructing an apodized dynamic Bragg grating.** (a) The blue circles show the apodization window $a_k$ upon sinc-apodization for $N = 10$ cycles with $W = \pi/2 + 1/2$. The red diamonds show the case without apodization, i.e. $a_k = 1$. Note that the DQ evolution period in the former case is about 1.65 times longer than without apodization; however this is only a marginal increase. (b) The grating function $\mathcal{G}_{ij}$ in case of sinc-apodization (blue) consists of broad square peaks of width $W$, compared to the sinc peaks in the non-apodized case (red).

For example, in the non-apodized case $a_k = 1$, the window function is a rectangle, and the grating consists of sharp sinc-peaks (see Fig. 6-11(a)). Under sinc-apodization, $a_k = \sin(W(k - N/2))/(W(k - N/2))$, the grating consists of square peaks of width $W$ (Fig. 6-11(b)). Note that we normalize the window such that $\sum a_k = N$. This leads to a net DQ evolution period that is about 1.65 times longer than in the non-apodized case (for $N = 10$); however, this is a marginal increase since the total length of the sequence depends more strongly on the free evolution period $N\pi/\omega$ (more precisely $T_{eng} \approx \frac{n\pi^2}{16b} + \frac{N\pi}{\omega}$). In the apodized case, all couplings in $W$ satisfy the maxima condition and are refocussed. More importantly, the average sidelobe amplitude remains the same as that of the non-apodized case, leading to the same decoupling efficiency that grows linearly with $N$ (see Fig. 6-9). Hence this leads to robustness under dephasing, since even couplings that have dephased by an amount $W/2$ are refocussed and amenable to Hamiltonian engineering. However, the mismatch to the exact engineered strengths due to the falling square profiles of the resulting $F_{ij}\mathcal{G}_{ij}$ functions leads to reduced fidelities in this case (see Fig. 6-6).

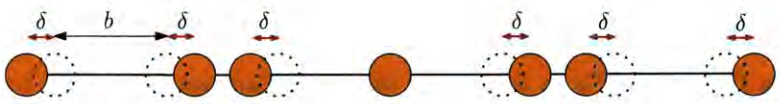


(a)

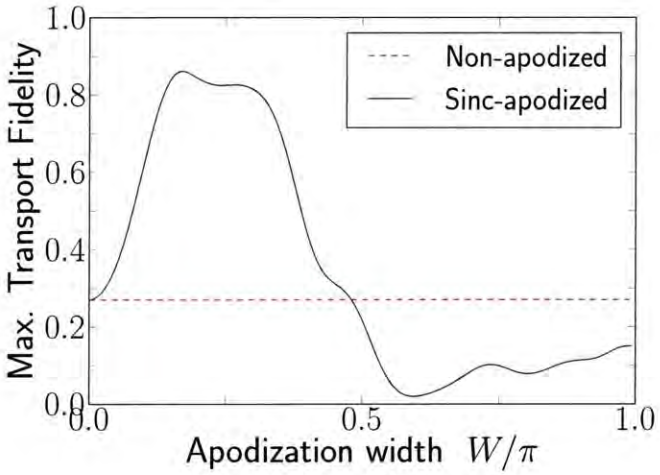


(b)

Figure 6-12: **Apodized sequences can also aid in the engineering of a non-linearly spaced array of spins.** For instance, panel (a) shows a non-linearly spaced $n = 7$ spin chain (orange) obtained by perturbing a regular chain (dotted), with perturbation strength $\delta/b = 0.15$. For simplicity we consider a mirror symmetric perturbation; however this is not necessary in general. The strengths of the couplings for perfect transport are calculated by modifying the usual parabolic strengths $d_{j(j+1)} = b\sqrt{n(n-j}$ by also considering the different dipolar strengths between neighboring spins. However, even when perfectly engineered, the sequence would not work efficiently since the spins are non-linearly spaced while the usual grating is linear. (b) Sinc- apodization provides a possible solution. The blue line shows the transport fidelity for different apodization widths $W$ considering all couplings included and $N = 20$ cycles, and demonstrates high fidelity $> 0.85$. For large $W$, the fidelity drops because certain long-range couplings now get refocussed. Without apodization, the fidelity is far lower (red dashed) especially for large $N$.

In Fig. 6-13, we study in more detail the case considered in Fig. 6-6 of the portion of this Chapter of a $n = 5$ spin chain embedded in a spin bath and under the influence of Ornstein-Uhlenbeck noise due to it. The results clearly show that apodization leads to more robust performance even under strong noise fields (for instance, strengths exceeding the nearest-neighbor coupling $b$, Fig. 6-13(a)), and long application times of the sequence (Fig. 6-13(b)).

The apodization scheme has other interesting applications. Fig. 6-12(a) shows a particular example of a *non-linearly* spaced spin array, with all couplings included. Note that even if one were to calculate the appropriate periods $(\tau_{\mathbf{z}}, \mathbf{t_m})$ for engineering the modified chain, it would be difficult to refocus only the nearest-neighbor couplings since the usual grating function $\mathcal{G}_{ij}$ consists of linearly-spaced peaks. An option would be to use a small value of $N$, leading to broad peaks; however, this has the disadvantage of greater amplitude in the sidelobes (see Fig. 6-9) and poor decoupling of long-range interactions (especially in more complex networks). Sinc-apodization provides a useful workaround by allowing the use of large $N$ (and consequently low side-band power), and broader grating maxima that might refocus the NN couplings. Fig. 6-12(b) demonstrates that reasonably effective Hamiltonian engineering, and high transport fidelities can be achieved even for such non-linear spin arrays.

## 6.E Off resonance DQ excitation to construct $U_z$

In the main text, we assumed that the free evolution propagators $U_z$ were constructed by employing a homonuclear decoupling sequence (for eg. WAHUHA [46]) during the $\tau_z$ intervals to refocus the internal Hamiltonian couplings, while leaving the action of the gradient. An alternative method is to use the DQ excitation sequence even during these periods, but shifting the offset frequency $\omega_0$ far off-resonance. This is possible

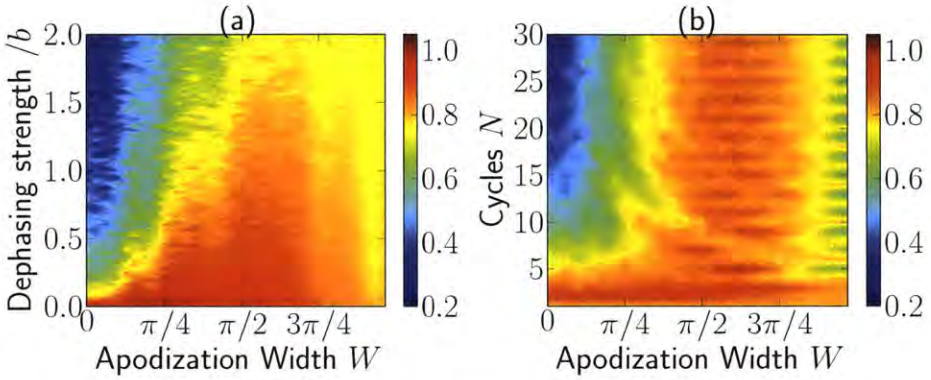


Figure 6-13: **Maximum transport fidelity $f$ for a fully coupled $n = 5$ spin dipolar chain embedded in a spin bath.** We consider that the bath produces a purely dephasing noise field on the chain, modelled by an Ornstein-Uhlenbeck (OU) process of correlation time $\tau_c = 2/b$, and maximum dephasing strength $2b$, where $b$ is the NN coupling strength (see also Fig. 6-6). (a) Here we consider $N = 20$ cycles, and study the variation of transport fidelity with sinc-apodization width $W$, averaged over 100 manifestations of the OU noise. When $W = 0$ (no apodization), the fidelity rapidly decreases even under small noise fields. As $W$ increases, the broader Bragg maxima lead to more robust performance. There exists an optimal $W$ that maximizes fidelity – in this case $W \approx 5\pi/8$ produces fidelity exceeding 0.9 even for noise strengths $\approx b$. (b) In the right panel, we study the variation of maximum fidelity under a fixed dephasing strength $= b$, for varying $W$ and number of cycles $N$. Without apodization, increasing $N$ leads to sharper Bragg peaks and poor performance under noise. At the optimal $W \approx 5\pi/8$, there is extremely robust performance even for large $N$, demonstrating that the sequence can be applied for long times without loss of performance. Note that the figure also shows that even cycles perform slightly better than when $N$ is odd, due to better symmetrization.

since the recoupling filter is periodic with a period $2m\pi$ thus we can shift $\omega_0$ while retaining identical filter characteristics. Fig. 6-14 shows that an offset a few times larger than the coupling is sufficient to reach almost free evolution. Still, employing a decoupling sequence requires almost the same control requirements, and has the added advantage of enhancing the net decoherence time of the system, allowing for transport in longer engineered spin chains.

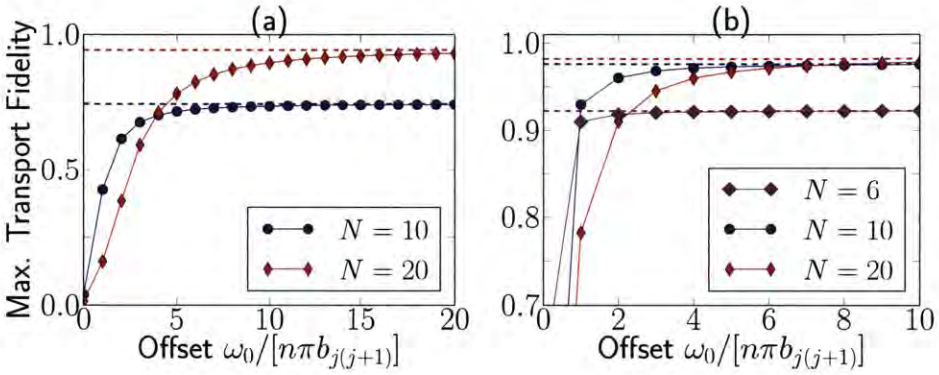


Figure 6-14: **Off-resonance construction of dynamic Bragg grating.** A possible implementation of the $U_z$ blocks is by shifting the offset frequency of the DQ excitation $\omega_0$ to $mn\pi b_{j(j+1)}$. Secular truncation ensures that even an offset by a few filter periods is sufficient to obtain fidelities (solid lines) comparable to when the $U_z$ blocks are created by dipolar decoupling (dashed lines). We considered in (a) the network in Fig. 1 of the main text and in (b) a 9-spin chain with all couplings.

## 6.F Extension to more complex lattices

The techniques developed in this paper are not limited to spin chains, but can be directly extended to engineering more complex spin lattices. Fig. 6-15(a) shows one such example of a honeycomb lattice (naturally occurring for example in graphene).

Assuming a *fully-coupled* lattice where spins are coupled by the dipolar interaction, we demonstrate below how one could "extract" from this lattice, parallel nearest-neighbor-only chains of tunable NN coupling strength. A more detailed extension of the filtered Hamiltonian engineering method to 2D and 3D lattices will be presented elsewhere.

Consider the lattice of Fig. 6-15(a), and assume a linear gradient of strength $\omega$ is placed along the X axis (blue line). Fig. 6-15(b) details the principle of operation. When the Bragg condition is satisfied with $\tau = \pi/\omega$, the NN couplings (black) are perfectly refocussed. Following Fig. 6-9, to a good approximation, the NNN couplings are decoupled if we employ greater than 6 cycles. Of course, the NNNN couplings remain refocussed. However for the honeycomb lattice they are 18.52 times weaker than the NN couplings, and this factor sets the decoupling efficiency of the method. Note that different parallel chains can be engineered to have different relative NN coupling strengths $J_j$, by a suitable choice of the weighting function $F_{ij}$.

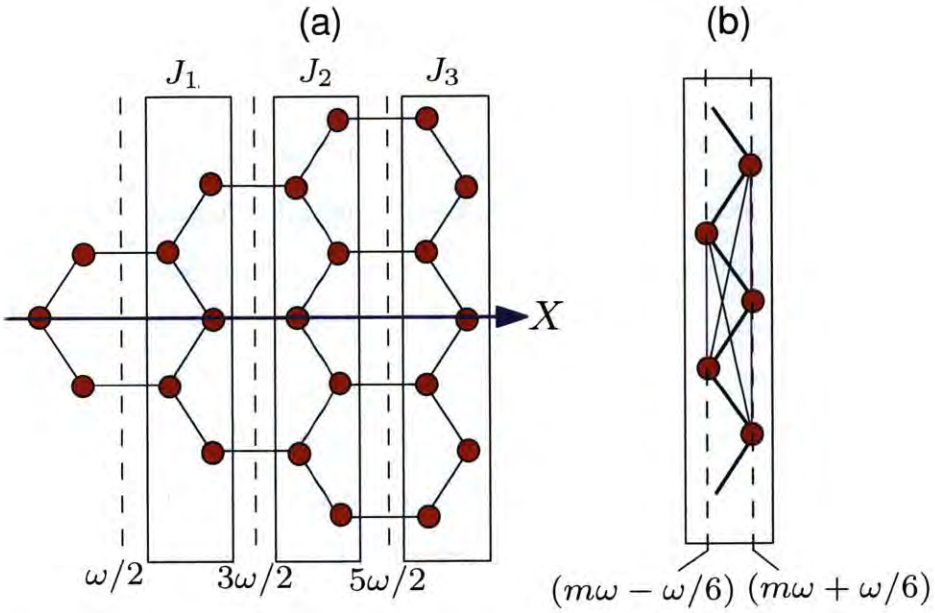


Figure 6-15: **Extension of Hamiltonian engineering to other spin lattices.** (a) Left panel shows a honeycomb lattice, and the blue line along the X axis denotes the gradient direction. The dashed lines denote the magnetic field strengths along the gradient. It is possible to extract from the the *fully-coupled* honeycomb lattice, arrays of nearest-neighbor spin chains (blue boxes). Moreover, the relative nearest-neighbor coupling strength of the different chains $J_j$ can be engineered by filtered engineering. (b) The right panel describes the principle of operation. The nearest-neighbor spins of the chain are at field positions $m\omega \pm \omega/6$, where $m$ is an integer. When $\tau = \pi/\omega$ in the Hamiltonian engineering sequence, NN couplings (dark black) satisfy the Bragg maxima condition and are refocussed. The NNN couplings (magenta) on the other hand pick up a phase $2m\pi \pm 2\pi/3$, and are decoupled when $N > 6$ cycles. The decoupling efficiency is limited by the NNNN couplings (green), which are 18.52 times weaker than the NN couplings.

# Chapter 7

# Simulation of spin coherence decays in one-dimensional spin system

## 7.1 Introduction

Large quantum systems hold the promise to deliver improvements in metrology (e.g. via squeezed or entangled states) or in computation. Unfortunately these quantum systems are usually very fragile and plagued by problems of decoherence [245] – as they undergo irreversible decay [246] due to interaction with their environment. While the decay of single qubits under the effect of various types of environments have been extensively studied and control sequences that could mitigate decoherence effects have been studied (e.g. dynamical decoupling techniques [243,247,248,98]), large scale quantum information processing (QIP) systems will require the preparation and control of *multi-qubit* states. These states are harder to control and to model analytically because of their complex many-body dynamics. While some recent works have looked at their decoherence and control schemes via dynamical-decoupling [249], the decay was

usually assumed to be induced by an uncorrelated bath, acting independently on each qubit, while this is often not the case in nature, especially for spatially close spins. Indeed, strategies to protect multiqubit states against decoherence in large quantum network registers are difficult to formulate because of the complex many body decay dynamics of these states under the decoherence interaction. A better knowledge of the decay dynamics may help in the construction of such control schemes. In this chapter, we experimentally and theoretically study the decay of such multi-qubit states under the action of a correlated spin bath. In particular, we are interested in investigating the decay rate dependence on the correlations in a multi-qubit spin state. Here we use solid-state nuclear magnetic resonance (NMR) to experimentally investigate coherence decay of multispin states of $^{19}$F 1D spin chains in a Fluorapatite crystal due to internal dipole-dipole interactions. We leverage the low dimensionality of the system studied – the linear coupling geometry provided by nuclear spins in apatite crystals[233,234] – to gain insight into both the many-body states created by the coherent Hamiltonian dynamics, as well as their decay. We present a simple analytical model that captures the essential features of the multi-qubit decays, and compares well with the experimental data. These results will be helpful in paving the way for the future design of schemes to mitigate the decay.

Specifically, in the linear spin system – calcium Fluorapatite (FAp) [250] – we consider multi-spin states created by the double quantum Hamiltonian $\mathcal{H}_{\mathrm{DQ}}$, which has been widely studied in quantum transport[251]. We analyze their decay under the natural dipolar Hamiltonian $\mathcal{H}_{\mathrm{dip}}$. Similar decay dynamics were studied in more complex 3D spin systems in a set of pioneering experiments in adamantane by Suter and coworkers [252,253] and extended to other 3D systems[254], and in the study localization phenomena[255,256]. However, in contrast to 3D systems, the highly restricted coupling topology in our experiments leads to analytically tractable solutions for the

Hamiltonian evolution and the decay rates. It is thus possible to have a much better characterization of the multi-spin states we can create than it was possible in more complex 3D systems and thus we can study how the decay rate changes with the state characteristics, such as long-range correlations in extended spin clusters and their degree of coherence. This is also important in light of recent work in creating low-dimensional systems in ion-traps[257], or via Hamiltonian engineering[258] in crystals.

In this work, we further compare the decoherence behavior for different initial states of the spin chain, and demonstrate that certain initial states are intrinsically relatively protected against the decoherence. We also characterize the scaling of the decay rate with the coupling topology in the spin network, and show that a 1D topology (spin chain) has much slower decay than an the 3D case. Our work strongly implies that communication between registers of a quantum computer architecture should be via a linear coupling architecture (chains) for minimum signal loss.

The chapter is organized as follows. We describe the experimental system and methods in Section 7.2 and we present the experimental results. In Section 7.3 we introduce an analytical model (extended details can be found in 7.A) to interpret the experimental results. This leads us to a better insight into the decay rate dependence on the state characteristics that we further explore in Section 7.4 by experimentally studying a diverse set of states.

## 7.2 Experimental Methods and Results

### 7.2.1 The Spin System

The system of interest are $^{19}$F nuclear spins in a single crystal of fluorapatite (FAp) [$Ca_5(PO_4)_3F$]. We use NMR techniques to study the spin dynamics at room temperature in a 300 MHz Bruker Avance Spectrometer ($B_0$=7T) with a probe tuned to 282.4 MHz. In the FAp crystal, six parallel chains lie along the crystal $c$-axis, with a short intra-nuclear spacing within a single chain, $r_0 = 0.3442$nm, and a longer inter-chain separation of $R = 0.9367nm$. The spins interact via the secular dipole-dipole Hamiltonian,

$$\mathcal{H}_{\text{dip}} = \sum_{ij} b_{ij}[2\sigma_z^i\sigma_z^j - (\sigma_x^i\sigma_x^j + \sigma_y^i\sigma_y^j)] \tag{7.1}$$

where $\sigma_\alpha^i$ are the usual Pauli matrices and the couplings are

$$b_{ij} = \frac{\mu_0}{16\pi}\frac{\gamma^2\hbar}{r_{ij}^3}(1 - 3\cos^2\vartheta_{ij}),$$

with $\mu_0$ the standard magnetic constant, $\gamma$ the $^{19}$F gyromagnetic ratio, $r_{ij}$ the distance between nucleus $i$ and $j$ and $\vartheta_{ij}$ the angle between $\vec{r}_{ij}$ and the $z$-axis. When the crystal is aligned with the magnetic field, as in our experiments, the nearest-neighbor inter-chain dipolar coupling is about 40 times weaker than the in-chain coupling. Thus, for short evolution times, couplings across different chains can be neglected and the system can be considered as a collection of one-dimensional spin chains[259,260,261,262,234].

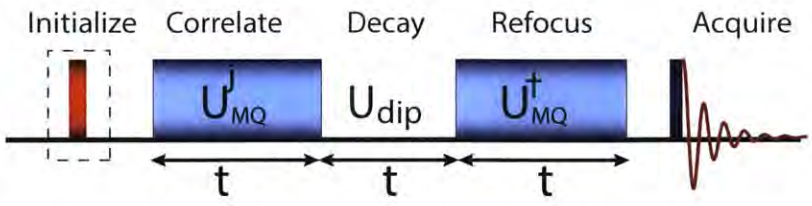


Figure 7-1: **Experimental scheme.** The system is first prepared in an initial state of interest, for example the thermal equilibrium state or $\sum \sigma_x$ using a $\pi/2$-pulse (red bar). Evolution via the DQ Hamiltonian $\mathcal{H}_{\mathrm{DQ}}$ (obtained by a multi-pulse sequence, blue rectangles) creates spin correlations during the time $\tau$. A phase shift $\varphi$ of the propagator encodes information about the multiple quantum coherence intensities created. The state undergoes decay under the dipolar interaction $\mathcal{H}_{\mathrm{dip}}$ during the time $t$. The correlated state is refocused by the inverse propagator $U_{\mathrm{DQ}}^{\dagger}$ before a $\pi/2$ pulse is used to detect the spin free-induction decay.

### 7.2.2 Experimental Protocol

The experimental scheme is shown in Fig. 8-2. The system is first prepared in a suitable initial state $\rho_i$ starting from its equilibrium state. Evolution under a propagator $U_{\mathrm{MQ}}$ for a time $\tau$ creates a complex, multiple-quantum coherence state. The system is then let evolve freely for a time $t$, during which the coherences decay mainly under the effects of the dipolar Hamiltonian. In order to observe this decay, we first refocus the remaining coherences with a propagator $U_{\mathrm{MQ}}^{\dagger}$ before measuring the spin magnetization via the usual free induction decay.

The equilibrium state is the Zeeman thermal state, $\rho_{th}(0) \propto \exp(-\varepsilon\Sigma_z) \approx \mathbb{1} - \varepsilon\Sigma_z$, where $\Sigma_z = \sum_j \sigma_z^j$ and $\varepsilon = \gamma B_0/k_B T \ll 1$ (with $k_B$ the Boltzmann constant and $T$ the temperature). We focus on the evolution and decay of the deviation from identity of this state, i.e. $\delta\rho_{th} \sim \Sigma_z$, and of other initial states that can be created

from $\delta\rho_{th}$ with appropriate manipulation (see Section 7.4). Indeed, the identity does not evolve and does not contribute to the signal.

Starting from the prepared initial state $\rho_i$, we create spin correlations by evolution under the double quantum (DQ) Hamiltonian

$$\mathcal{H}_{\mathrm{DQ}} = \sum_{ij} b_{ij}(\sigma_x^i\sigma_x^j - \sigma_y^i\sigma_y^j), \tag{7.2}$$

which is known to generate quantum coherences among the spins [263]. The primitive pulse cycle is given by, $\mathrm{P}_2 = \frac{\delta t}{2} - \frac{\pi}{2}|_x - \delta t' - \frac{\pi}{2}|_x - \frac{\delta t}{2}$, where $\delta t' = 2\delta t + w$, $\delta t$ is the delay between pulses and $w$ is the width the $\pi/2$ pulse. We used the symmetrized 8-pulse variant of this basic sequence [263,264], $\mathrm{P}_8 = \mathrm{P}_2 \cdot \overline{\mathrm{P}_2} \cdot \overline{\mathrm{P}_2} \cdot \mathrm{P}_2$, where $\overline{\mathrm{P}_2}$ is the time-reversed version of $\mathrm{P}_2$, which simulates $\mathcal{H}_{\mathrm{DQ}}$ to second order in the Magnus expansion [91]. In the experiments, the length of the $\pi/2$ pulse was $w = 1.01\mu$s and the evolution time was incremented by varying inter-pulse delay from $\delta t = 1\mu$s to $6.2\mu$s and the number of loops was increased from 1 to 12 (varying both parameters enabled exploring a wide range of evolution times up to 1ms). A recycle delay of 5s was used to re-equilibrate the system.

The density operator created by evolution under the DQ Hamiltonian can be decomposed into its multiple quantum coherences (MQC) components, $\rho(\tau) = U_{\mathrm{MQ}}(\tau)\rho(0)U_{\mathrm{MQ}}^{\dagger}(\tau) = \sum_m \rho^{(m)}$, where a multiple quantum term of order $m$, $\rho^{(m)}$, acquires a phase $m\varphi$ under a collective $\Sigma_z$ rotation by an angle $\varphi$. The correlated spin states created under $\mathcal{H}_{\mathrm{DQ}}$ evolution contain in general all *even* $M$ coherence orders. However, since standard NMR techniques measure only single-quantum coherences (SQC), in order to probe the higher spin coherences it is necessary to indirectly encode their signatures into SQCs which can be measured inductively [225]. This is achieved by labeling each coherence order with a different phase $\varphi$ by means of collective rota-

tions $U_\varphi = \exp(-i\varphi\sigma_z/2)$ about the z axis, effectively creating the phase shifted DQ Hamiltonian, $\mathcal{H}_{\mathrm{DQ}}^{\varphi} = U_\varphi \mathcal{H}_{\mathrm{DQ}} U_\varphi^\dagger$. Finally, MQC are refocused back to single-spin single-quantum terms and free induction decay is measured. Each measurement is repeated while incrementing $\varphi$ from 0 to $2\pi$ in steps of $\delta\varphi = 2\pi/2K$ where $K$ is the highest order of MQC we wish to encode. If $\delta\rho_i$ is the initial density matrix, the final density matrix $\delta\rho_f$ is given by:

$$\delta\rho_f(t,\tau) = U_{\mathrm{MQ}}^\dagger(\tau) U_{\mathrm{dip}}(t) U_{\mathrm{MQ}}^{\varphi}(\tau) \delta\rho_i U_{\mathrm{MQ}}^{\varphi\dagger}(\tau) U_{\mathrm{dip}}^\dagger(t) U_{\mathrm{MQ}}(\tau),$$

where $U_{\mathrm{MQ}}(\tau) = \exp(-i\mathcal{H}_{\mathrm{DQ}}\tau)$. Since often the observable $\delta\rho_o$ is proportional to the initial state (as it is the case for the thermal equilibrium state and the total magnetization along the z-axis) we can write the measured signal as a correlation $S(t,\tau) = \mathrm{Tr}\{\delta\rho(t,\tau)\delta\rho_o(\tau)\}$, between the state prepared by the DQ evolution, $\delta\rho_o(\tau) = U_{\mathrm{MQ}}(\tau)\delta\rho_o U_{\mathrm{MQ}}(\tau)$ and the same state after decay under the dipolar evolution, $\delta\rho(t,\tau) = U_{\mathrm{dip}}\delta\rho_o(\tau)U_{\mathrm{dip}}^\dagger$. The signal intensities of various coherence orders are thus given by:

$$I^{(m)}(t,\tau) = \mathrm{Tr}\left\{\delta\rho_o^{(m)}(\tau)\delta\rho^{(m)}(t,\tau)\right\} = \sum_{k=1}^{K} S^k(t,\tau) e^{-ikm\delta\varphi}, \tag{7.3}$$

where $S^k(t,\tau) = \mathrm{Tr}\left\{\delta\rho_f^k(t,\tau)\delta\rho_o\right\}$ is the signal acquired in the $k$th measurement when setting $\varphi = \pi k/K$.

### 7.2.3 Results and Data Analysis

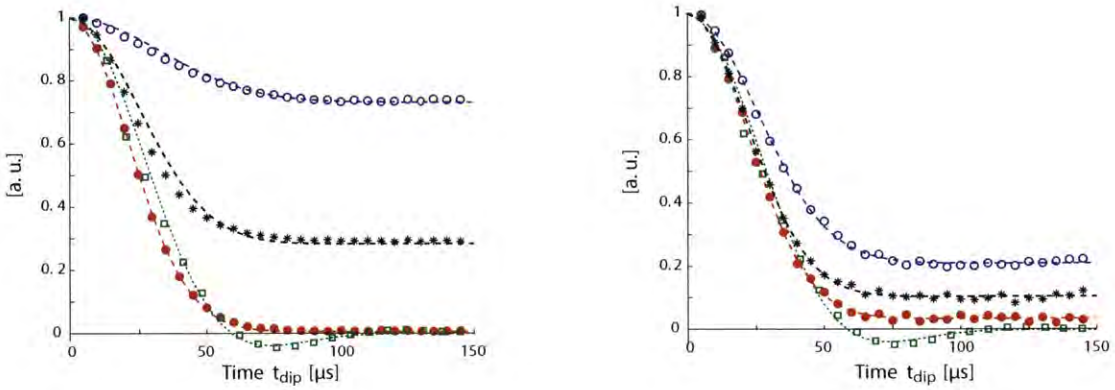


Figure 7-2: **Decay of quantum coherences in Dipolar field for Zeeman initial state.** (ZQ (0Q) blue open circles, DQ (2Q) red dots, Total signal black stars). Data points are the normalized signal intensities for evolution time $48\,\mu$s (left) and $589\,\mu$s (right). The dashed lines are fitting using the function in Eq. (7.4). For comparison we plot the free-induction decay (green squares) that we fit with the function [265] $A\left[(1-C)\mathrm{sinc}(m_2 t)\, e^{-m_1 t^2/2} + C\right]$.

We first studied the decay of MQC intensities created under $\mathcal{H}_{\mathrm{DQ}}$ starting from an initial thermal state ($\delta\rho_{th} \sim \sigma_z$). In a quasi-1D system such as FAp, it is known that the DQ Hamiltonian excites mainly zero- and double-quantum coherences [259,266]. The decay of the total signal, $S(t,\tau) = \mathrm{Tr}\{\rho_f(t,\tau)\rho_i\}$, and of each coherence intensity is shown in Fig. 7-2 as a function of dipolar decay time ($t$) for two exemplary MQC excitation times, $\tau = 48\mu$s and $589\mu$s. The decoherence dynamics was studied by repeating the experimental scheme described above while varying the DQ evolution time ($\tau$) from $36\mu$s to $925\mu$s and the decay time ($t$) from 0 to $145\mu$s. Note that the decay periods are much shorter than the time scale of complete dipolar mixing

(approximately 6ms); hence our experiments are in the short time limit. We fitted the decay curves to Gaussian functions,

$$G(t,\tau) = A(\tau)\left([1 - C(\tau)]e^{-M(\tau)t^2/2} + C(\tau)\right), \tag{7.4}$$

where $A$ (amplitude), $M$ (second moment) and $C$ (asymptote) are used as fitting parameters that vary with the DQ time $\tau$. As shown by the decay curves in Fig. 7-2 and by the behavior of the fitting parameters in Fig. 7-3-7-4, the system exhibits an interesting oscillatory dynamics as a function of the DQ-time evolution. This is in contrast to what was observed in 3D systems[252,254], where the decay simply becomes monotonically faster as the DQ-time is increased. The difference can be traced to the fact that the constrained coupling topology in 1D systems allow for a slower decay dominated by nearest-neighbor interactions, while in 3D systems the decay is more rapid and diffusion-like. In the following, we present a theoretical model of the observed behavior in 1D systems.

## 7.3 Theoretical model and interpretation

To gain insight into the decay behavior, we model both the dipolar Hamiltonian and the DQ Hamiltonian as 1D, nearest-neighbor (NN) interactions, neglecting the smaller contributions from long-range couplings in the chain and between chains. This approximation is justified in the short time limit[260].

### 7.3.1 Decay Amplitude

The nearest-neighbor DQ Hamiltonian is known to be analytically solvable in 1D by means of a Jordan-Wigner mapping[267] onto a system of free fermions. The density

operators for thermal initial state evolving under DQ Hamiltonian can be expressed in terms of canonical fermionic operators as [238,268]:

$$\begin{aligned}\rho_{th}(\tau) = &\sum_{p-q\in\text{even}} i^{-(p+q)} f_{pq}(2\tau)\left(c_p^\dagger c_q + c_q^\dagger c_p - \delta_{p,q}\right) \\ &+i\sum_{p-q\in\text{odd}} i^{-(p+q)} f_{pq}(2\tau)(c_p^\dagger c_q^\dagger - c_q c_p),\end{aligned} \tag{7.5}$$

where the first term describes zero-quantum coherences, $\rho^{(0)}(\tau)$, and the second term double-quantum coherences, $\rho^{(2)}(\tau)$. Here we defined the fermionic operators $c_p = \left(\prod_{k<p}\sigma_z^k\right)\sigma_-^p$ and

$$f_{pq}(\tau) = \frac{2}{n+1}\sum_k (-1)^p \sin(p\kappa)\sin(q\kappa)e^{-2ibt\cos\kappa}, \tag{7.6}$$

where $N$ is the chain length and $\kappa = \frac{\pi k}{N+1}$.

We are interested in following the decay of these states under the dipolar Hamiltonian. We thus consider the normalized signal as a function of decay time $t$,

$$S(t,\tau) = \text{Tr}\left\{\delta\rho_o(\tau)U_{\text{dip}}(t)\delta\rho(\tau)U_{\text{dip}}^\dagger(t)\right\}/\text{Tr}\left\{\delta\rho_o(\tau)\delta\rho(\tau)\right\} \tag{7.7}$$

We first note that the amplitude $A(\tau)$ in Eq. (7.4) is given either by the total signal, $A_S(\tau) = \text{Tr}\left\{\delta\rho_o(\tau)\delta\rho(\tau)\right\}$ or by the MQC intensities, $A_{m\text{Q}}(\tau) = \text{Tr}\left\{\delta\rho_o^{(m)}(\tau)\delta\rho^{(m)}(\tau)\right\}$, at $t = 0$. This is shown in Fig. (7-3a), where we plot $A_{\text{zQ}}(\tau)$ and $A_{\text{DQ}}(\tau)$. Since the total signal decays during the DQ evolution time $\tau$ (due to imperfection in the creation of the NN DQ Hamiltonian because of pulse errors, higher-order corrections in the Magnus expansion as well as errors due to long-range couplings [260]) we normalize these amplitudes by the total signal amplitude $A_S(\tau)$. Upon this correction it is possible to fit the amplitudes to well-known analytical solutions for the zero- ($I^{(0)}$)

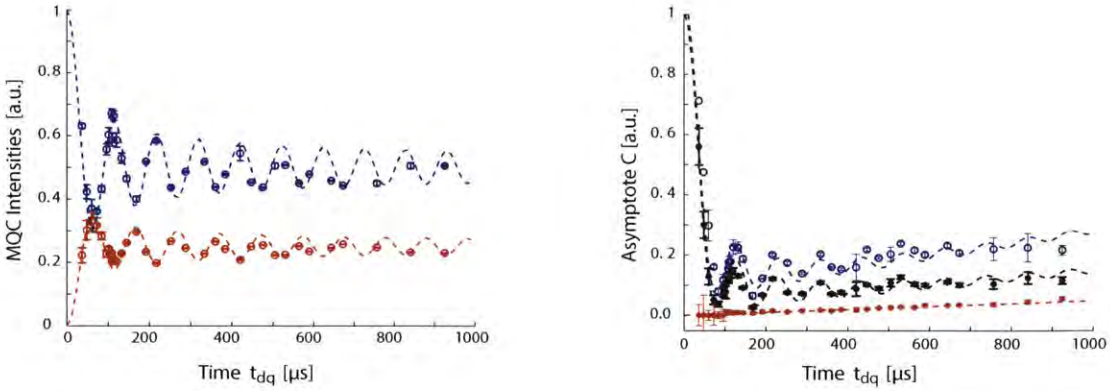


Figure 7-3: **Multiple quantum coherence intensities.** (a):Evolution of multiple quantum coherence intensities ($A_{\mathrm{ZQ}}$ blue, $A_{\mathrm{DQ}}$ red) starting from Zeeman initial state. The experimental data points are fitted by analytical functions (blue and red dashed lines) obtained from DQ Hamiltonian with NN couplings. The error bars are estimated from deviation of 1st order quantum coherence from zero. (b): Experimentally obtained asymptotes ($C_{\mathrm{ZQ}}$ blue, $C_{\mathrm{DQ}}$ red $C_{\mathrm{total}}$ black) fitted by Eq. (7.8) with an additional linear term in $\tau$. Fitting of the data in (a) and (b) gives dipolar coupling: 7.7 $\times 10^3$rad/s and 7.676 $\times 10^3$rad/s respectively.

and double-quantum ($I^{(2)}$) intensities[266] (see also 7.A). From these fits, considering an infinite chain, (Fig. 7-3) we find a NN dipolar constant $b = 7.7 \times 10^3$ rad/s. The value of the dipolar constant $b$ agrees very well with the one obtained from similar measurements done on a different FAp crystal[260,234] and also with the theoretical value $b = 8.17 \times 10^3$rad/s obtained from the known structure of FAp.

### 7.3.2 Long-time Asymptote

The only terms that contribute to the asymptote $C$ are those that commute with the dipolar Hamiltonian, i.e. $C = \mathrm{Tr}\left\{\rho_i^c(\tau)\rho_o^c(\tau)\right\} / \mathrm{Tr}\left\{\rho(\tau)\rho_o(\tau)\right\}$, such that $[\mathcal{H}_{\mathrm{dip}}, \rho^c] = 0$. In the NN approximation, $\rho^c$ contains only the population terms (i.e. $p = q$ in

Eq. 7.5); hence we obtain,

$$C(\tau) = \left(\frac{1}{N}\sum_{p}(-1)^{p} f_{pp}(2\tau)\right)^{2} = \left(\frac{1}{N}\sum_{k}\cos(4\tau\cos\kappa)\right)^{2} \tag{7.8}$$

As $\rho^{c}$ only contains zero-quantum terms, we expect a zero asymptote for the DQ intensities. We use this function with an additional linear term in $\tau$ to fit the experimentally obtained asymptotes. This is shown in Fig. (7-3b). The dipolar coupling (b) is used as a fitting parameter and the best fit value obtained from the fit is $7.676 \times 10^{3}$rad/s, which agrees very well with the MQC fittings. The linear increase of the asymptote with time is due to errors in the implementations of the DQ evolution, as terms which are not zero- and double-quantum coherences appear as an increased population term when normalizing the signal.

### 7.3.3 Decay Rate

To determine the decay rate, we analyze the evolution by a short time expansion [269], $\rho_i(t,\tau) \approx \rho_i(\tau) - it[\mathcal{H}_{\text{dip}}, \rho_i(\tau)] - \frac{t^2}{2}[\mathcal{H}_{\text{dip}}, [\mathcal{H}_{\text{dip}}, \rho_i(\tau)]]$, with a corresponding signal, $S(t,\tau) \propto \text{Tr}\{\rho_i(t,\tau)\rho_o(\tau)\}$. We note that the first order term does not give any contribution to the signal [99], so we calculate the second moment,

$$M = \frac{\text{Tr}\left\{[\mathcal{H}_{\text{dip}}, [\mathcal{H}_{\text{dip}}, \rho_i(\tau)]]\rho_o^{\dagger}(\tau)\right\}}{\text{Tr}\{\rho_i(\tau)\rho_o(\tau)^{\dagger}\}} = \frac{\text{Tr}\left\{[\mathcal{H}_{\text{dip}}, \rho_i(\tau)][\rho_o(\tau), \mathcal{H}_{\text{dip}}]^{\dagger}\right\}}{N2^{N}} \tag{7.9}$$

We can further calculate the contributions to the second moment arising from the zero- and double-quantum terms of the density operator

$$M^{(m)} = \frac{\text{Tr}\left\{[\mathcal{H}_{\text{dip}}, \rho^{(m)}(\tau)][\rho^{(m)}(\tau), \mathcal{H}_{\text{dip}}]^{\dagger}\right\}}{\text{Tr}\{\rho^{(m)}(\tau)\rho^{(-m)}(\tau)\}} \tag{7.10}$$

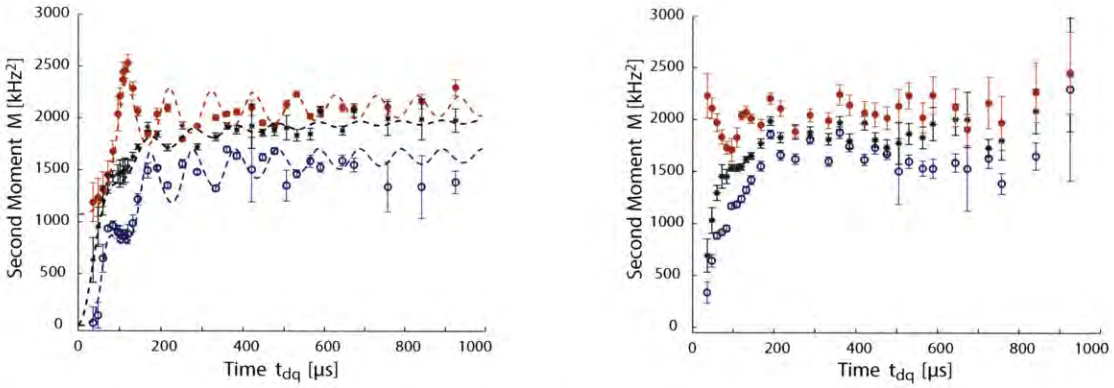


Figure 7-4: **Decay rates of the different MQ components.** Decay rates of the different MQ components as a function of double quantum evolution time $\tau$ for (left) the thermal and (right) end-polarized initial state. Points are experimental results obtained from the fitting of individual decay curves (such as in Fig. 7-2) for each DQ-time $\tau$. Error bars are estimated from fitting of decay curves with 7.4). The dashed lines are $\mu\, M(b,\tau)$, where $M(b,\tau)$ are the analytical curves in 7.A for $N = 100$ with $b = 7.9 \times 10^3$rad/s. The total signal moment (black stars) was scaled by a factor $\mu = 1.7$, the ZQ moment (blue circles) by a factor 1.8 and the DQ moment (red, dots) by 1.5.

These functions can be calculated analytically (see 7.A) thanks to the mapping to fermionic operators. We used these functions to analyze the second moments in Fig. 7-4. We note that while the changes of $M$ with the DQ evolution time $\tau$ can be fitted to these analytical function, yielding a dipolar coupling strength $b = 7.9 \times 10^3$rad/s, the magnitude of the second moment is larger than if it were set by a corresponding $b^2$ by a factor $\mu \approx 1.7$. This indicates that other decay mechanisms are at play, including longer range couplings and control errors.

Some features of the second moments are worth pointing out. At small DQ times, the decay rate of the ZQ intensities (and of the signal) goes to zero, as indeed the initial state is an equilibrium state that commutes with the dipolar Hamiltonian. Instead, $M^{(2)}$ has a finite asymptote, $b^2/12$, for $\tau \to 0$: mathematically, this is

because both the commutator and the DQ intensities go to zero with $\tau$; physically, this means that as soon as some DQ term is created in the state, it will decay with a finite rate under the dipolar Hamiltonian.

The second moments of both MQC intensities then oscillate in time with $\tau$, with the DQ moment always being larger than the ZQ one, $M^{(2)} > M^{(0)}$. This can be understood by their different behavior under the dipolar Hamiltonian. Consider the ZQ state, $\rho_{th}^{(0)}(\tau)$ (first line in Eq. 7.5) and the "flip-flop" term of the dipolar Hamiltonian, $\mathcal{H}_{xx} = b\sum_j (c_j^\dagger c_{j+1} + c_{j+1}^\dagger c_j)$. If we had considered periodic boundary conditions (instead of an open chain), these two operators would have commuted. Thus we expect their contribution to the second moment to be small and decreasing with the chain length $N$. In contrast, the contribution of $\mathcal{H}_{xx}$ to the second moment of $\rho^{(2)}(\tau)$ is on the same order as the contribution from $\mathcal{H}_{zz} = b\sum_j \sigma_z^j \sigma_z^{j+1}$, thus yielding an overall faster decay rate. We can understand this behavior more intuitively. Here we defined quantum coherence with respect to the total magnetization along the z-axis[270], $\Sigma_z$, which also sets the quantization axis of the system. Indeed, we only retained the part of the dipolar interaction that commutes with $\Sigma_z$. Thus we expect terms in the system state that commutes with $\Sigma_z$ (such as ZQ terms) to decay more slowly than state that do not.

It is interesting to note that both the ZQ and DQ second moments are higher when the corresponding MQC intensity is smaller. By analyzing the state in Eq. 7.5, we can see that times $\tau$ of local maxima for $I^{(0)}(\tau)$ correspond to maxima for the function $f_{pp}(2\tau)$, which indicates that the state is localized around single-spin polarization states, $\sigma_z^j$, while at other times the ZQ intensities have stronger contributions from many-spin correlations (three and higher). Correspondingly, local maxima for $I^{(2)}(\tau)$ correspond to higher contributions from localized two-spin double quantum states in $\rho(\tau)$, $\sigma_+^j \sigma_-^{j+1}$. We thus found that the decay rates depends not only on the coherence

order of the state, but also on whether the state is localized or contains a larger number of spin correlations. While these two effects could not be distinguished clearly in 3D experiments, as it was not possible to determine the precise states created, the one-dimensional case provides further insights into the decay dynamics. We can further explore these differences by studying the decay of other correlated states.

## 7.4 Comparison of initial states

In order to study the dependence of the decay rate on the coherence order and the number of correlated spins, we evolved different initial states under the DQ Hamiltonian. Besides the thermal state, we considered two other initial states: the "end-polarized" state $\delta\rho_{\text{end}} \propto (\sigma_z^1 + \sigma_z^N)$[233,234] and a state rotated in the transverse plane, $\Sigma_x = \sum_j \sigma_x^j$. We prepared the first state by the two-pulse scheme introduced in Ref.[233], while the second state can be prepared by a simple collective rotation of the spins.

The end-polarized state exhibits a transport-like dynamics under the DQ Hamiltonian[251]; although the transport is dispersive[227,238], we expect the state to remain fairly localized at short times and thus to show similar decay behavior as the thermal state. In contrast, the initial state $\delta\rho_x \sim \Sigma_x$ quickly evolves into many-spin correlations. Indeed, if we consider for example evolution of the first spin in the chain $\delta\rho_{x_1} \sim \sigma_x^1$, we obtain:

$$\delta\rho_{x_1}(\tau) = \sum_{p\,\in\,\text{odd}} \text{Im}[i^{-p} f_{1p}(\tau)](c_p^\dagger + c_p) - i \sum_{p\,\in\,\text{even}} \text{Im}[i^{-p} f_{1p}(\tau)](c_p^\dagger - c_p) \tag{7.11}$$

Here we note that the fermionic operators $c_p$ represent highly delocalized states,

since we have e.g. $c_p^\dagger + c_p = \sigma_z^1 \cdots \sigma_z^{p-1} \sigma_x^p$. Similar expressions can be found for the evolution of the other spins in the chain and thus for $\delta\rho_x(\tau)$. While this state presents large spin correlations, its coherence number is still quite low, with mostly one- and three-quantum coherences[238]. In order to investigate the decay of larger coherence orders, we thus rotate the state $\delta\rho_x(\tau)$ with a $\pi/2$-pulse around the y-axis before letting it evolve freely. The resulting state, $\delta\rho_{xx}$, contains all even quantum coherence orders with a binomial distribution and it is thus more similar to the states that can be obtained in 3D systems[225].

We compare the decay rates (second moment) of these four different states in Fig. (7-5). When the evolution under the DQ-Hamiltonian is short, the decay rate of $\delta\rho_{\text{th}}$ and $\delta\rho_{\text{end}}$ is small, as expected. Although $\delta\rho_{xx}$ has a small decay rate at short times, since it has main contributions from ZQ coherences, the second moment increases quickly with $\tau$. In comparison, $\delta\rho_x$ has a fast decay even when it has not evolved under the DQ-Hamiltonian (indeed for $\tau = 0$ we recover the second moment of the free-induction decay); even at larger $\tau$ the second moment remains slightly larger than the second moments of $\delta\rho_{\text{th}}$ and $\delta\rho_{\text{end}}$. Indeed at larger $\tau$ all the states becomes fairly delocalized because of the dispersive character of the equal-coupling DQ Hamiltonian[227]. Thus these different states highlight different behaviors of multi-spin correlated states, which depend on the number of spins in the correlated state (with faster decay for larger spin correlation number) and separately on the coherence number.

## 7.5 Conclusions

In this chapter we investigated the dependence of decoherence rate on the state characteristics of a many-spin system. Since the decay process is non-Markovian,

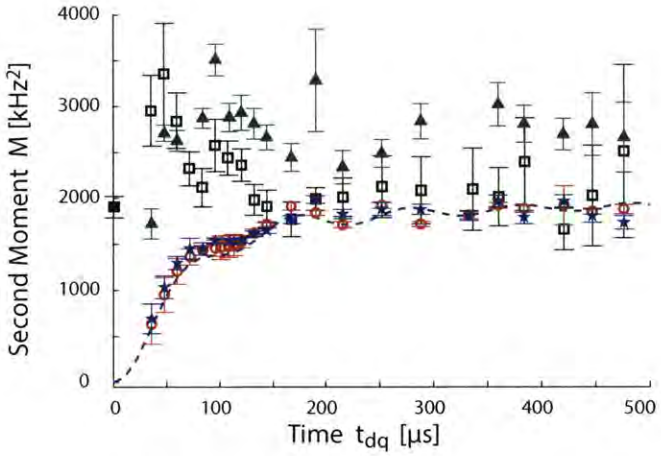


Figure 7-5: **Decay rates of the total signal** as a function of evolution time $\tau$ for different initial states: thermal state $\delta\rho_{th}$ (blue stars), end-polarized state $\delta\rho_{\text{end}}$ (red circles); transverse polarization, $\delta\rho_x$ (black squares) and the state presenting a broader distribution of MQC, $\delta\rho_{xx}$ (green triangles). The black filled square is the second moment of the free-induction decay. As the $\delta\rho_x(\tau)$ states present oscillations in the decay (similar to the free-induction decay, see Fig. 7-2) we fitted their decay to the function[265] $A\left[(1-C)\text{sinc}(m_2 t)\, e^{-m_1 t^2/2} + C\right]$, with the second moment given by $M = m_1 + m_2^2/3$. The dashed line is the analytical model for the thermal state second moment, as in Fig. 7-4.

but it is due to a highly correlated spin bath, we found a very rich dynamics, where decoherence rates (quantified by the second moment of the decay) depend in a non-trivial way on the degree of localization of the state as well as on its coherence with respect to the quantization basis. In particular we found that large spin clusters, with correlations established among many spins, decay faster under a correlated bath, even if their coherence order is not very large. This is in contrast to the decay under simple dephasing, where the coherence order (and for pure states, the entanglement) is critical in determining the decay rate [271]. While it was not possible to separate the coherence order and the number of correlated spins in the dynamics of 3D spin systems (as they grow at the same time), here we were able to get a

deeper insight by using spin chains and exploring different initial states. In addition we found that restricting the dynamics in one dimension slows down the decay, which could be beneficial to create larger coherent quantum states.

# Appendix

## 7.A Calculation of the second moment

Here we provide explicit expressions for the second moment of the decay under the dipolar Hamiltonian of the thermal state evolved under the DQ Hamiltonian for a time $\tau$. Using the second moment to estimate the decay rate is justified by a a short time expansion of the signal,

$$S(t,\tau) \approx S(\tau)(1 - Mt^2/2) = \mathrm{Tr}\left\{\delta\rho(\tau)^2\right\}\left(1 - \frac{\mathrm{Tr}\left\{[\mathcal{H}_{\mathrm{dip}}, \rho(\tau)][\rho(\tau), \mathcal{H}_{\mathrm{dip}}]^\dagger\right\}}{\mathrm{Tr}\left\{\delta\rho(\tau)^2\right\}}\right) \tag{7.12}$$

We can calculate the contributions to the second moment arising from the zero- and double-quantum terms of the density operator

$$M^{(m)} = \frac{\mathrm{Tr}\left\{[\mathcal{H}_{\mathrm{dip}}, \rho^{(m)}(\tau)][\rho^{(m)}(\tau), \mathcal{H}_{\mathrm{dip}}]^\dagger\right\}}{\mathrm{Tr}\left\{\rho^{(m)}(\tau)\rho^{(-m)}(\tau)\right\}}, \tag{7.13}$$

Further, writing the dipolar Hamiltonian as

$$\mathcal{H}_{\mathrm{dip}} = 2\mathcal{H}_{zz} - \mathcal{H}_{xx}, \quad \mathcal{H}_{zz} = \sum_{ij} b_{ij}\sigma_z^i\sigma_z^j, \quad \mathcal{H}_{xx} = \sum_{ij} b_{ij}(\sigma_x^i\sigma_x^j + \sigma_y^i\sigma_y^j) \tag{7.14}$$

we can also separate the contributions from the $\mathcal{H}_{zz}$ and $\mathcal{H}_{xx}$ parts of the dipolar

Hamiltonian, as they simply add up (there are no contributions from cross-terms). We can thus define each contribution as

$$M_{aa}^{(n)} = \mathrm{Tr}\left\{[\mathcal{H}_{aa}, \rho^{(n)}(\tau)][\mathcal{H}_{aa}, \rho^{(n)}(\tau)]^{\dagger}\right\}/(N2^N), \tag{7.15}$$

yielding the total second moment:

$$M = M_{zz} + 2M_{xx} = I^{(0)}(M_{zz}^{(0)} + 2M_{xx}^{(0)}) + I^{(2)}(2M_{zz}^{(2)} + 4M_{xx}^{(2)})/(N2^N), \tag{7.16}$$

where $I^{(m)}$ are the MQC intenties[266]

$$I^{(0)}(\tau) = \frac{1}{N}\sum_{k}\cos(4\tau\cos\kappa)^2 \tag{7.17}$$

$$I^{(2)}(\tau) = \frac{1}{2N}\sum_{k}\sin(4\tau\cos\kappa)^2. \tag{7.18}$$

Using the state in Eq. 7.5 we find the contribution from $\mathcal{H}_{zz}$:

$$M_{zz} = \frac{16}{N}\left[\sum_{p\neq q}|f_{p,q}(2\tau)|^2 - \sum_{q=2}^{N}\left(|f_{q,q-1}(2\tau)|^2 + |f_{q,q-2}(2\tau)|^2 + |f_{1,q}(2\tau)|^2\right)\right], \tag{7.19}$$

which is given by the sum of the ZQ and DQ contributions:

$$M_{zz}^{(0)}I^{(0)} = \frac{16}{N}\left[\sum_{\substack{p\neq q,\\ p-q\in\text{ even}}}|f_{p,q}(2\tau)|^2 - \sum_{q=2}^{N}|f_{q,q-2}(2\tau)|^2 - \sum_{\substack{p\neq 1,\\ p\in\text{ odd}}}|f_{1,q}(2\tau)|^2\right] \tag{7.20}$$

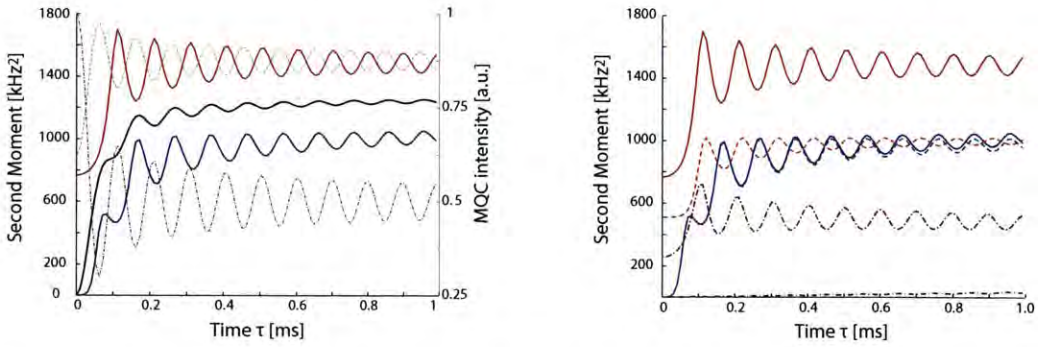


Figure 7-6: **Analytical solutions to second moments for $N = 400$ spins.** Left: second moment for the ZQ intensities (blue), DQ (red) and total signal (black). In lighter gray: MQC intensities (ZQ dash-dotted line, DQ dashed line, shifted by 0.625) highlighting the anti-correlation with the momentum oscillations. Right: Contributions of the $\mathcal{H}_{xx}$ Hamiltonian (dash-dotted) and $\mathcal{H}_{zz}$ Hamiltonian (dashed) to the total (solid) second momenta for ZQ (blue lines) and DQ (red lines) intensities. We note that the second moment from $\mathcal{H}_{xx}$ is almost zero for the ZQ intensities. The small increase at larger DQ times $\tau$ is due to finite-length chain effects.

$$M_{zz}^{(2)} I^{(2)} = \frac{8}{N} \left[ \sum_{p-q \in \text{ odd}} |f_{p,q}(2\tau)|^2 - \sum_{q=1}^{N} |f_{q,q-1}(2\tau)|^2 - \sum_{p \in \text{ even}} |f_{1,p}(2\tau)|^2 \right] \tag{7.21}$$

From the commutator with $\mathcal{H}_{xx}$ we obtain

$$M_{xx} = \frac{4(N-1)}{N} - \frac{2}{N} \sum_{p,q} \left[ f_{p+1,q}(2\tau) - f_{p-1,q}(2\tau) \right] \left[ f_{p,q+1}(2\tau) - f_{p,q-1}(2\tau) \right], \tag{7.22}$$

which can be further decomposed into the ZQ and DQ components:

$$M_{xx}^{(0)} I^{(0)} = M_{xx}(\tau) - I^{(2)}(\tau) M_{xx}^{(2)}(\tau) \tag{7.23}$$

$$M_{xx}^{(2)} I^{(2)} = \frac{2}{N} \sum_{p-q \in \text{ odd}} |f_{p,q}(2\tau) - f_{q-1,p+1}(2\tau)|^2, \tag{7.24}$$

# Part IV

# Quantum Control

# Preface

In this final part of the thesis, we consider problems in quantum control – that are geared towards the control of a large quantum system with external fields in order to perform a suitable information processing task.

In chapter 8 of this thesis, we present a quantum control technique for engineering the Hamiltonian of a nuclear spin network. More precisely, we consider a hybrid system consisting of an NV center (electron spin defect in diamond) and a network of dipolarly coupled nuclear spins[272]. The NV center spin can be manipulated optically and through microwave fields. The idea is to use the NV center to *selectively* decouple (destroy) or recouple (keep) inter-spin couplings, and engineer the form of the interaction. Specifically, the natural Hamiltonian of the system is $\mathcal{H} = \omega_e S_z + |0\rangle\langle 0| H_0 + |1\rangle\langle 1| H_1 + H_{dd}$, where $H_{dd}$ is the dipolar coupling *between* nuclear spins. The nuclear Hamiltonians $H_0 = \sum_j \omega_L I_{zj}$ ; $H_1 = \sum_j [(\omega_L + A_j) I_{zj} + B_j I_{xj} + C_j I_{yj}]$ are *conditioned* on the state of the NV. Essentially, now by just toggling the NV spin state, one can rotate (*actuate*) nuclear spins to achieve something similar to magic angle spinning in conventional NMR – a technique whereby the dipolar interaction that couples the nuclear spins can be averaged close to zero[273]. This quantum control technique can also potentially be extended to more exotic Hamiltonian engineering. For instance, one could create a class of

transverse Ising Hamiltonians of the form $\mathcal{H} = \frac{1}{r_{jk}^3}[d_{jk}^{(z)} I_{zj} I_{zk} + d_{jk}^{(x,y)}(I_{xj} I_{xk} + I_{yj} I_{yk})]$. Since the NV center couples differently to different spins, through NV-driven rotations one can effectively tune $d_{jk}^{(z)}$ and $d_{jk}^{(x,y)}$ to different values for each spin pair. This would enable constructing a broad class of exotic many-body Hamiltonians, as needed for symmetry protected topological states in spin ladders [274], and topological quantum computation models [275].

Chapter 9 and 10 of this thesis present strategies for quantum control in arbitrary and complex spin networks in order to transmit quantum information from between two separated nodes of the network in a dispersionless manner. Such transport of quantum information between distant qubits is an essential task for quantum communication [276] and quantum computation [277]. Linear spin chains have been proposed [222] as quantum wires to connect distant computational units of a distributed quantum processor. This architecture would overcome the lack of local addressability of naturally occurring spin networks by separating in space the computational qubit registers while relying on free evolution of the spin wires to transmit information among them. Engineering the coupling between spins in the linear chain can improve the transport fidelity [223], even allowing for *perfect* quantum state transport (QST), but it is difficult to achieve in experimental systems. Unfortunately, the challenges in manufacturing linear chains with engineered couplings have hindered experimental implementations.

In chapter 10 we present strategies to achieve perfect quantum information transport in *arbitrary* spin networks. Our proposal is based on the weak coupling limit for pure state transport, where information is transferred between two end-spins that are only weakly coupled to the rest of the network.

# Chapter 8

# Selective nuclear decoupling mediated by electronic actuator control

The problem of Hamiltonian engineering has widespread applications in quantum information processing and metrology[207,208,209]. In essence, it describes the action of turning one, naturally occurring Hamiltonian that couples spins in a quantum network, into another synthetic one that is more amenable to simulation and/or measurement[206,213,212]. Quantum control techniques developed over several decades have been used for this task including the use of collective rotations (global spin manipulations) to convert one Hamiltonian into another, for eg. in ion traps[204], optical lattices[215] and magnetic resonance[205]. Instead here, we take an opposite view: we shall try to employ strong coupling to a spin (*actuator*) to selectively make and break couplings in its vicinity.

Specifically, in this chapter, we propose a method for Hamiltonian engineering

that involves the selective decoupling of spin-spin interactions. This refers to manipulating the couplings of some selected spins in a quantum network, and has interesting implications in quantum metrology as we shall demonstrate below. Our protocol is based on a hybrid quantum system consisting of a spin actuator (eg. single electron spins [278,166,279]) and a network of nuclear spins to be engineered. The actuator couples differently to spins of the network, and by suitable control operations on the actuator, one can bring some selected spins of the network into an effectively decoupled state. Since different couplings can engineered to be weighted differently, this has ready applications in quantum simulation; however in this chapter we will focus instead on applications in quantum metrology.

More precisely, we will consider the problem of the determination of the structure of a single molecule placed on top of a diamond containing shallow implanted nitrogen vacancy (NV) centers [280,51,281]. In previous work [105] we had studied in detail a method by which single molecule structure could be reconstructed using the NV center by employing Hartmann-Hahn like polarization techniques [36] to and from the nuclear spins in the molecule. A key part of the method involved using the NV center to determine couplings between different nuclear spins (call them $D_{ij}$'s), hence making the system overspecified, and allowing the efficient reconstruction of molecular structure [105]. In general, increasing the number measurable $D_{ij}$ constrains the sensing volume more, reaching $< 0.1\text{nm}^3$ volume sensing resolution if 50% of the $D_{ij}$'s are measured (for $N$ nuclear spins, this scales as $\sim N^2/2$ couplings), even to 100% error.

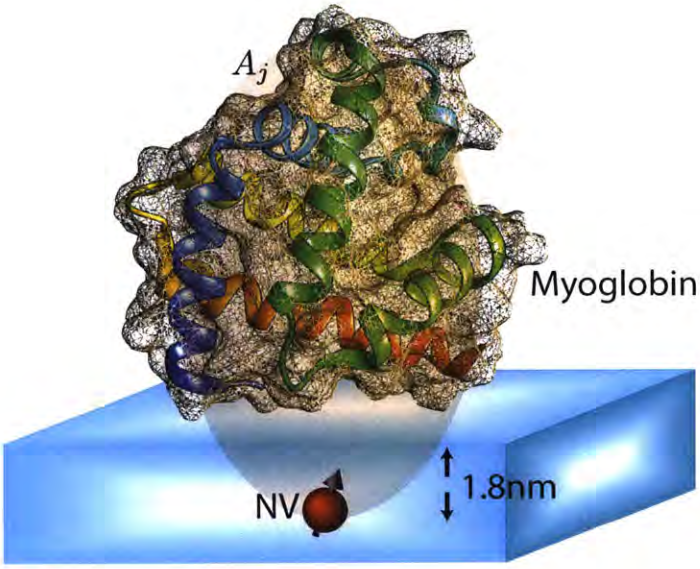


Figure 8-1: **Schematic representation of NV center based actuator control.** Figure shows the schematic arrangement where a single molecule of myoglobin is placed above a 1.8nm NV center [102]. Through an NV based actuator protocol (Fig. 8-2) that relies on the hyperfine fields $\{A_j, B_j, C_j\}$ (Eq. (8.1)), one can selectively decouple spins in the molecule in a window $W$ about a spin of interest (Fig. 8-10) The window $W$ is tunable allowing control over the number of spins that are decoupled (see Fig. 8-11). Our results are also easily extended to actuator control via paramagnetic impurities on the diamond surface [21].

However, in general determining such a large number of the couplings is a challenge because the method relies on the diffusion of spin polarization under the natural nuclear dipolar coupling, which rapidly dies away because of the emergence of higher order correlation terms which cannot be easily probed by the experiment [282]. In this chapter, we seek to ask the question: can the number of couplings $D_{ij}$'s one can

measure be effectively enhanced? As we shall show, this can be achieved by engineering the nuclear coupling Hamiltonian so that there is selective decoupling NV spins in a window $W$ are decoupled from each other allowing one to study the diffusion of polarization to spins outside this window, enhancing the number of measurable couplings. This selective decoupling is achieved just by suitable toggling of the NV center state (with no direct control on the nuclear spins), and relies on the fact that the anisotropic hyperfine interaction to the NV center discriminates different nuclear spins.

This chapter is organized as follows. In Sec. 8.1 we describe the system consisting of a shallow NV center and nuclear spins, and we summarize the protocol in Ref. [105] for the determination of single molecule structure, and describe in detail the sensing volume as a function of the number of couplings one can measure. In Sec. 8.2 we describe the basis of an NV-actuator protocol to rotate the nuclear spin state to achieve selective decoupling, the details of which are in Sec. 8.3. Crucially, one can quantify a window of spins $W$ that are decoupled via the NV – this window is tunable and spatially correlated; details of which are in Sec. 8.3.4. We then consider the enhancement in nuclear sensing volume as a result. Finally, we consider experimental implementations, and the robustness of the protocol to control errors.

## 8.1 System

Nitrogen vacancy (NV) centers in diamond have been recently demonstrated to be sensitive sensors of nuclear spins in their environment [138,13,283]. We consider a ~2nm shallow implanted NV center [284,17,20] and a single target molecule is placed above it [51]. The NV center interacts with the nuclear spins via the anisotropic hyperfine interactions given by, $H_{hf} = \frac{g_N}{r_N^3}\left[3(S\cdot\hat{\mathbf{r}}_N)(I\cdot\hat{\mathbf{r}}_N) - \mathbf{S}\cdot\mathbf{I}\right]$ where $g_N = \frac{\hbar\mu_0\gamma_N\gamma_e}{4\pi}$, and

the vector $r_N = (r_x, r_y, r_z)$ is the line joining the center of the NV and the nuclear spin. Applying a secular approximation and only retain terms that commute with $S_z$ gives $H_{hf} = \frac{g_N}{r_N^3} S_z \left[3r_z(r_x I_x + r_y I_y) + (3r_z^2 - 1)I_z\right]$. Hence for a homonuclear system consisting of $N$ nuclear spins of Larmor frequency $\omega_L = \gamma_N B$, the overall Hamiltonian of the coupled system can be written as,

$$\begin{aligned} H &= \omega_e S_z + |0\rangle\langle 0| H_0 + |1\rangle\langle 1| H_1 + H_{dd} \\ H_0 &= \sum_j \omega_L I_{zj} \; ; \; H_1 = \sum_j \left[(\omega_L + A_j) I_{zj} + B_j I_{xj} + C_j I_{yj}\right] \end{aligned} \tag{8.1}$$

where $A_j = (3r_{zj}^2 - 1), B_j = 3r_{zj}r_{xj}, C_j = 3r_{zj}r_{yj}$, and $H_{dd} = \sum_{i<j} D_{ij}(3I_{zi}I_{zj} - \mathbf{I_i} \cdot \mathbf{I_j})$ is the dipolar coupling between nuclear spins, where $D_{ij} = \frac{(3\cos^2\Theta_{ij} - 1)}{2} \frac{\hbar\mu_0\gamma_N^2}{4\pi r_{ij}^3}$, where $r_{ij}$ is the internuclear distance and $\Theta_{ij} = \cos^{-1}(\hat{\mathbf{r}}_{ij} \cdot \hat{\mathbf{z}})$.

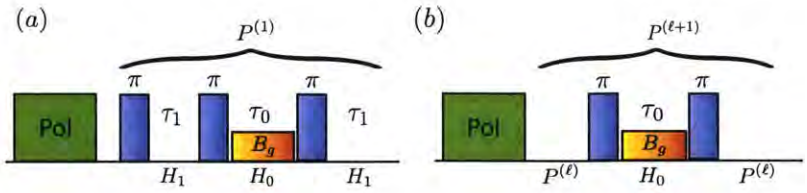


Figure 8-2: **Schematic of the actuator protocol.** Here the NV is polarized in the $|0\rangle$ state by a $\sim 1\mu$s pulse of 532nm laser light, and toggled repeatedly in the $|0\rangle$ and $|1\rangle$ states through microwave $\pi$ pulses. A gradient field $B_g \approx 20$G is applied during the $H_1$ periods. This creates two effective angles for the nuclear spins – $\vartheta_0 = \pi\tau_0/(\omega_L + A_j)$, and $\vartheta_1 = \pi\tau_0/(\omega_L + A_j)$. (a) When $\alpha_0 = \pi$ this creates the operator $\mathcal{P}^{(1)}$ as in Eq. (8.13). (b) This basic construction can be concatenated to yield higher order propagators as in Eq. (8.15). As a result, the nuclear spins in a frequency window $W$ of interest are rotated close to the magic angle, causing them to be decoupled with respect to the nuclear spins outside this window (see Fig. 8-10), allowing long range nuclear couplings to be discerned.

## 8.2 Actuator control with shallow NV centers

For shallow NV centers, the hyperfine fields $A_j, B_j$ are quite strong, and can far exceed the dipolar coupling $\|D_{jk}\|$ – this allows for the *actuator* control of the nuclear spins via the NV. This refers to the coherent rotation of the nuclear spins via the NV electronic spin. Note importantly that the antenna-like hyperfine field $A_j$ of the NV separates different nuclear spins in frequency-space in a manner that is spatially correlated with position in the molecule [105].

Employing electron spins as actuators to control nuclear spins was introduced by Lloyd [285], and this was extended to time optimal actuator control constructions in

Ref.[286] . Refs.[287,279,288] considered the use of actuators for fast nuclear-nuclear gates, including an electron mediated gate in malonic acid that is 100 times faster than bare nuclear gates. More recently they have been employed to construct optimized gates for $^{13}C$ spins in an NV diamond system[289].

However, in contrast to these works, where actuator control was primarily considered for constructing nuclear spin *gates*, in this chapter we consider its application for Hamiltonian engineering. By only toggling the NV center, certain nuclear spin couplings of interest can be destroyed, and others retained – allowing the indirect manipulation of the nuclear spin network. As we shall show below, this allows the metrology of long range nuclear-nuclear couplings that are otherwise hard to discern.

### 8.2.1 Basic protocol: toggling of NV center state

The basic actuator protocol consists of the NV being cast to the $|0\rangle$ state (through polarization with $\sim 1\mu s$ laser light[166]), and subsequent delayed toggling (by $\tau$) of the NV state between $\{|0\rangle, |1\rangle\}$ via resonant $\pi-$ flips. In this chapter, we will consider a more general variant – a $\pi$ flip of the NV is accompanied with the turning on of a small static perpendicular field $B_g < 20G$ (*"dc pulses"*[290]). As we shall see below $B_g$ allows us to set a *tunable* effective decoupling window on nuclear spins above the NV. Hence, depending on the spin state of the NV we then have two Hamiltonians for the nuclear spin $j$,

$$H_0 = \omega_L I_z \; ; \; H_1^j = (\omega_L + A_j) I_z + (B_j + B_g) I_x \tag{8.2}$$

Note we have assumed $C_j = 0$, since for a single spin $j$, this just refers to a convenient choice of coordinate system.

It is convenient in what follows to introduce a geometric notation to represent

the single spin Hamiltonians above. A vector symbol above an operator denotes the effective Hamiltonian in the Hilbert-Schmidt Bloch sphere [72,99], for instance – $\vec{H}_{\{0,1\}} = \|H_{\{0,1\}}\|\hat{H}_{\{0,1\}}$, and $\hat{H}_0 = \hat{\mathbf{z}}$ ; $\hat{H}_1^j = \cos\vartheta_j\hat{\mathbf{z}} + \sin\vartheta_j\hat{\mathbf{z}}_{j\perp}$ where $\hat{\mathbf{z}}_{j\perp} = \cos\varphi_j\hat{\mathbf{x}} + \sin\varphi_j\hat{\mathbf{y}}$ (here $\varphi_j = 0$). The *tilt* angle $\vartheta_j = \tan^{-1}\left[\frac{B_j+B_g}{\omega_L+A_j}\right]$ sets the degree of actuation of each spin Hamiltonian $H_1^j$ due to the coupling to the NV center. Note that $\vartheta_j$ is usually very small, for instance for $^{13}$C nuclear spins at 1000G, and $B_g = 20G$, $\vartheta_j < 1.5°$. However, this actuation angle can be effectively *amplified* by a concatenated application of delayed toggling controls on the NV, the technical details of which we will describe in more detail in the following.

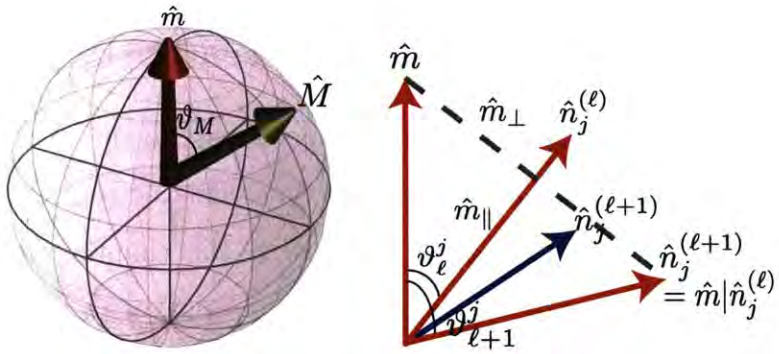


(a) (b)

Figure 8-3: **Toggling the NV center to reach the nuclear magic angle condition.** (a) The decoupling protocol requires the nuclear spin axis starting from $\hat{\mathbf{n}}_0 = \hat{\mathbf{z}}$ (red arrow) to approach the magic axis $\mathbf{M}$ at the angle $\vartheta_M = 54.7°$. This can be achieved by a concatenated toggling of the NV spin state (see Eq. (8.15)). (b) Figure graphically denotes the approach to the magic angle $\vartheta_M$. The two nuclear spin axes for a spin $j$ corresponding to the NV spin state are $\hat{\mathbf{n}}_0$ and $\hat{\mathbf{n}}_1^{(\ell)}$. The index $\ell$ denotes the $\ell^{th}$ concatenated rotation following Eq. (8.15). Upon application of the propagator $\mathcal{P}^{(\ell)}(\pi)\mathcal{R}(\pi,\hat{\mathbf{n}}_0)\mathcal{P}^{(\ell)}(\pi)$, the new axes become $\hat{\mathbf{n}}_0$, and $\hat{\mathbf{n}}_1^{(\ell+1)} = \hat{\mathbf{n}}_0|\hat{\mathbf{n}}_1^{(\ell)}$ (red arrow), which is just the reflection of $\hat{\mathbf{n}}_0$, about $\hat{\mathbf{n}}_1^{(\ell)}$, and in this case $\vartheta_{\ell+1} = 2\vartheta_\ell$. In the general case $\mathcal{P}^{(\ell)}(\alpha_1^{(\ell)})\mathcal{R}(\pi,\hat{\mathbf{n}}_0)\mathcal{P}^{(\ell)}(\alpha_1^{(\ell)})$ one instead gets the blue arrow $\hat{\mathbf{n}}_1^{(\ell+1)} = (\hat{\mathbf{n}}_0|\hat{\mathbf{n}}_1^{(\ell)})\sin^2\alpha_1^{(\ell)} + \hat{\mathbf{n}}_0\cos^2\alpha_1^{(\ell)}$.

Let us define the unitary rotation operator

$$\mathcal{R}^j(\alpha_j,\, \hat{\mathbf{n}}_j) := e^{-i\alpha^{(j)}\vec{\sigma}_j\cdot\hat{\mathbf{n}}_j/2} \tag{8.3}$$

which rotates any state of the nuclear spin $j$ around the axis of normalized 3D unit vector $\hat{\mathbf{n}}_j$ by an angle $\alpha^{(j)}$. In this section, where we are considering a single spin only, we omit all spin indexes $j$. Consider the total unitary transformation composed of the control blocks of successive rotations under $H_1$ and $H_0$ (see Fig. 8-2)

$$\begin{aligned}\mathcal{U}_{\text{tot}} :&= \exp(-i\tau_1 H_1)\exp(-i\tau_0 H_0)\exp(-i\tau_1 H_1)\\ &= e^{i\varphi_{\text{tot}}}\mathcal{R}(\alpha_1,\, \hat{\mathbf{n}}_1)\,\mathcal{R}(\alpha_0,\, \hat{\mathbf{n}}_0)\,\mathcal{R}(\alpha_1,\, \hat{\mathbf{n}}_1)\end{aligned} \tag{8.4}$$

where $\hat{\mathbf{n}}_{0,1} = n_{0,1}/|n_{0,1}|$ are the normalized axes of rotation under $H_{0,1}$ with $n_{0,1} = [\text{Tr}\,\{\sigma_1 H_{0,1}\}\,,\, \text{Tr}\,\{\sigma_2 H_{0,1}\}\,,\, \text{Tr}\,\{\sigma_3 H_{0,1}\}]$. The flip angle around the respective axes are given by

$$\begin{aligned}\alpha_0 &= \tau_0\,\omega_L\\ \alpha_1 &= \tau_1\sqrt{(\omega_L + A_j + B_{g\parallel})^2 + (B_j + B_{g,\perp})^2}.\end{aligned} \tag{8.5}$$

$\varphi_{\text{tot}}$ is an unimportant global phase, which we shall omit. We are now interested in the effective rotation axis $\hat{\mathbf{n}}_{\text{tot}}$ and flip angle $\alpha_{\text{tot}}$ associated with $\mathcal{U}_{\text{tot}} = \mathcal{R}(\hat{\mathbf{n}}_{\text{tot}}, \alpha_{\text{tot}})$ under the above sequence. These can be expressed completely analytically by, firstly, writing the three propagators in the form

$$e^{-i\alpha\vec{\sigma}\cdot\hat{\mathbf{n}}/2} = \cos\frac{\alpha}{2}\mathbb{1} - i(\hat{\mathbf{n}}\cdot\vec{\sigma})\sin\frac{\alpha}{2}. \tag{8.6}$$

Multiplying them out and subsequently using the relations $(\hat{\mathbf{n}}_0\cdot\vec{\sigma})(\hat{\mathbf{n}}_1\cdot\vec{\sigma}) = \hat{\mathbf{n}}_0\cdot\hat{\mathbf{n}}_1 +$

$i\vec{\sigma}\cdot(\hat{\mathbf{n}}_0\times\hat{\mathbf{n}}_1)$ and $(\hat{\mathbf{n}}_1\times\hat{\mathbf{n}}_0)\times\hat{\mathbf{n}}_1=\hat{\mathbf{n}}_0-\hat{\mathbf{n}}_1(\hat{\mathbf{n}}_1\cdot\hat{\mathbf{n}}_0)$, one obtains

$$\mathcal{U}_{\text{tot}}=(2b\cos\frac{\alpha_1}{2}-\cos\frac{\alpha_0}{2})\mathbb{1}-i[2b\sin\frac{\alpha_1}{2}\hat{\mathbf{n}}_1+\sin\frac{\alpha_0}{2}\hat{\mathbf{n}}_0]\cdot\vec{\sigma} \tag{8.7}$$

with

$$b=\cos\frac{\alpha_0}{2}\cos\frac{\alpha_1}{2}-(\hat{\mathbf{n}}_0\cdot\hat{\mathbf{n}}_1)\sin\frac{\alpha_0}{2}\sin\frac{\alpha_1}{2} \tag{8.8}$$

By comparison with Eq. (8.6), the total effective flip angle is

$$\alpha_{\text{tot}}=2\arccos(\left|2b\cos\frac{\alpha_1}{2}-\cos\frac{\alpha_0}{2}\right|) \tag{8.9}$$

and the effective rotation axis is $\hat{\mathbf{n}}_{\text{tot}}=n_{\text{tot}}/|n_{\text{tot}}|$ with

$$n_{\text{tot}}=2b\sin\frac{\alpha_1}{2}\hat{\mathbf{n}}_1+\sin\frac{\alpha_0}{2}\hat{\mathbf{n}}_0. \tag{8.10}$$

Importantly, the rotation axis associated with $\mathcal{U}_{\text{tot}}$ and the effective Hamiltonian lies in the plane spanned by rotation axes $\hat{\mathbf{n}}_0$ and $\hat{\mathbf{n}}_1$ of the original Hamiltonians, i.e. $\hat{\mathbf{n}}_{\text{tot}}$ always has the same azimuth angle as $\hat{\mathbf{n}}_1$ (Fig. 8-3). The polar angle $\vartheta_{\text{tot}}=\arccos(\hat{z}\cdot\hat{\mathbf{n}}_{\text{tot}})$ on the other hand, may however be different and can be effectively amplified.

Let us now consider the special case of $\alpha_0=\alpha_1=\pi$, in which case $b=-\hat{\mathbf{n}}_0\cdot\hat{\mathbf{n}}_1$ and the effective flip angle (8.9) is also $\alpha_{\text{tot}}=\pi$. Experimentally, this is easily achieved by choosing the respective timings $\tau_0$ and $\tau_1$ accordingly. The effective propagator in this case becomes

$$\mathcal{U}_{\text{tot}}=\mathcal{R}(\pi,\,\hat{\mathbf{n}}_{\text{tot}}), \tag{8.11}$$

where the effective rotation axis

$$\hat{\mathbf{n}}_{\text{tot}} = \hat{\mathbf{n}}_0|\hat{\mathbf{n}}_1 = -2(\hat{\mathbf{n}}_1 \cdot \hat{\mathbf{n}}_0)\hat{\mathbf{n}}_1 + \hat{\mathbf{n}}_0 \tag{8.12}$$

is geometrically just the *reflection* of $\hat{\mathbf{n}}_0$ within the plane span($\hat{\mathbf{n}}_0$, $\hat{\mathbf{n}}_1$) about $\hat{\mathbf{n}}_1$ (see Fig. 8-3). Thus the application of Eq. (2.9) "pushes" the effective nuclear axis from $\hat{\mathbf{n}}_1 \rightarrow \hat{\mathbf{n}}_0|\hat{\mathbf{n}}_1$, doubling the polar tilt angle to $\vartheta_{\text{tot}} = 2\vartheta_1 = 2\arccos(\hat{\mathbf{n}}_0 \cdot \hat{\mathbf{n}}_1)$. The control in this situation just corresponds to that applied during periodic dynamic decoupling (PDD) of the NV center [243], and it is this pushing of nuclear axes that forms the basis of several experiments to *sense* the presence of nuclear spins [138,13,17,16] via the NV center. Note that in contrast to PDD experiment, the NV center is initially prepared in the population eigenstate, and is hence limited by $T_1 \sim 7$ms.

More generally, if $\alpha_0 = \alpha_1$, the effective propagator $\mathcal{R}(\alpha_e, \hat{\mathbf{n}}_e)$ corresponds to the rotation about the Hamiltonian having direction $2\hat{\mathbf{n}}_1 b + \hat{\mathbf{n}}_0$, by the effective flip angle $\alpha_e = \tan^{-1}\left[\tan\alpha_1 \left|\frac{2\hat{\mathbf{n}}_1 b + \hat{\mathbf{n}}_0}{2b-1}\right|\right]$. For most of what follows in this chapter however, we will be interested in the case when $\alpha_0 = \pi$, and $\alpha_1$ is variable. For instance, the situation when $\alpha_1 = \pi/4$ corresponds to the CPMG control sequence [88,31] (see Appendix 8.A for a geometric comparison between the CPMG and PDD control sequences). One can calculate the effective propagator as function of $\alpha_1$,

$$\begin{aligned} & \mathcal{R}(\alpha_1, \hat{\mathbf{n}}_1)\mathcal{R}(\pi, \hat{\mathbf{n}}_0)\mathcal{R}(\alpha_1, \hat{\mathbf{n}}_1) \\ = \; & \mathbb{1}2b\cos\alpha_1 + i\vec{\sigma} \cdot [2\hat{\mathbf{n}}_1 b \sin\alpha_1 + \hat{\mathbf{n}}_0] = \mathcal{P}^{(1)} \end{aligned} \tag{8.13}$$

and clearly, as before, when $\alpha_1 = \pi$, in which case we just have the reflection $\hat{\mathbf{n}}_0|\hat{\mathbf{n}}_1$. In Eq. (8.13) we designate the propagator $\mathcal{P}^{(1)}$, for as we shall see below, the nuclear

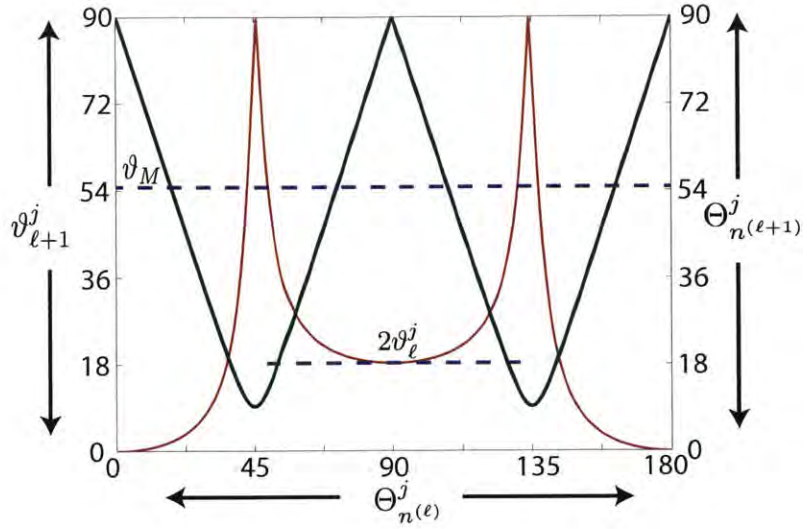


Figure 8-4: **Flip and tilt angles under toggling control.** Figure represents (in degrees) the flip angle $\alpha_1^{(\ell+1)}$ (green) and effective nuclear axes tilt angle $\vartheta_{\ell+1}$ (red) as a function of the flip angle $\alpha_1^{(\ell)}$ in the three-operator propagator $\mathcal{P}^{(\ell)}(\alpha_1^{(\ell)})$. It is clear that at $\alpha_1^{(\ell)} = \pi$, the action of the propagator is an effective reflection $\hat{\mathbf{n}}_0|\hat{\mathbf{n}}_1^{(\ell+1)}$ (see Fig. 8-3), and the flip angle remains $\pi$. It is possible to reach the magic angle $\vartheta_M$ in a single step, but with a much reduced flip angle; however, a more efficient and tunable concatenated protocol to reach the magic angle is in Fig. 8-5.

axes can be pushed apart further by a concatenated applications of propagator similar to Eq. (8.13).

Fig. 8-4 describes the effective flip-angle and tilt angle caused by the resulting propagator such as Eq. (8.13). Note that when $\alpha_1 = \pi/2$, it is possible to push the nuclear axes apart by $\pi/2$ at the cost of reduced flip angle (see Appendix 8.A), while when $\alpha_1 = \pi$ the nuclear axes are apart by $2\vartheta_j$, with the flip-angle maintained at $\pi$. These two situations are just the CPMG and PDD protocols (see Appendix 8.A for a detailed comparison).

### 8.2.2 Iterative amplification of tilt angle: concatenated toggling

The three-sequence propagator in Eq. (8.13) can be iteratively extended in a concatenated manner to further increase the effective nuclear axes tilt angle, following $\mathcal{P}^{(\ell+1)} = \mathcal{P}^{(\ell)}\mathcal{R}(\pi, \hat{\mathbf{n}}_0)\mathcal{P}^{(\ell)}$, where we have used the superscript $(\ell)$ to indicate the concatenation order (see Fig. 8-2). For clarity, let us rewrite Eq. (8.13), and describe the construction of the geometric vector corresponding to higher order concatenations $\mathcal{P}^{(\ell)}$,

$$\mathcal{P}^{(1)} = \mathbb{1}2b^{(0)}\cos\alpha_1^{(0)} + i\vec{\sigma}\cdot(2b^{(0)}\hat{\mathbf{n}}_1^{(0)}\sin\alpha_1^{(0)} + \hat{\mathbf{n}}_0) \tag{8.14}$$

where as before, $b^{(0)} = -\hat{\mathbf{n}}_1^{(0)}\cdot\hat{\mathbf{n}}_0\sin\alpha_1^{(0)}$. It is evident that for instance when $\alpha_1^{(0)} = \pi$, we obtain $\hat{\mathbf{n}}_1^{(1)} = -2(\hat{\mathbf{n}}_1^{(0)}\cdot\hat{\mathbf{n}}_0)\hat{\mathbf{n}}_1^{(0)} + \hat{\mathbf{n}}_0$, and this is just the reflection $\hat{\mathbf{n}}_0|\hat{\mathbf{n}}_1 = \hat{\mathbf{n}}_0 - 2\hat{\mathbf{n}}_{0_\perp}$ where $\hat{\mathbf{n}}_{0_\parallel} = (\hat{\mathbf{n}}_1^{(0)}\cdot\hat{\mathbf{n}}_0)\hat{\mathbf{n}}_1^{(0)}$, and $\hat{\mathbf{n}}_{0_\perp} = \hat{\mathbf{n}}_0 - \hat{\mathbf{n}}_{0_\parallel}$ are the parallel and perpendicular components of the vector $\hat{\mathbf{n}}_0$ in the direction set by $\hat{\mathbf{n}}_1^{(0)}$ (see Fig. 8-3).

Now this can be recursively extended (see Fig. 8-2), for instance as,

$$\begin{aligned}
\mathcal{P}^{(\ell+1)} &= \mathcal{P}^{(\ell)}\mathcal{R}(\pi, \hat{\mathbf{n}}_0)\mathcal{P}^{(\ell)} \\
&= \mathbb{1}2b^{(\ell)}\cos\alpha_1^{(\ell)} + i\vec{\sigma}\cdot(2b^{(\ell)}\hat{\mathbf{n}}_1^{(\ell)}\sin\alpha_1^{(\ell)} + \hat{\mathbf{n}}_0) \\
&= \mathbb{1}2b^{(\ell)}\cos\alpha_1^{(\ell)} \\
&+ i\vec{\sigma}\cdot\left[(\hat{\mathbf{n}}_0|\hat{\mathbf{n}}_1^{(\ell)})\sin^2\alpha_1^{(\ell)} + \hat{\mathbf{n}}_0\cos^2\alpha_1^{(\ell)}\right]
\end{aligned} \tag{8.15}$$

and,

$$\sin^2\alpha_1^{(\ell+1)} = 1 - 2\sin^2\alpha_1^{(\ell)}\cos^2\alpha_1^{(\ell)}\left[1 - \hat{\mathbf{n}}_0\cdot(\hat{\mathbf{n}}_0|\hat{\mathbf{n}}_1^{(\ell)})\right] \tag{8.16}$$

The iterative action of Eq. (8.15) is also graphically described in Fig. 8-5. In essence, a concatenated application of blocks like $\mathcal{P}^{(\ell)}$ leads to the iterated amplification of

the relative angle between the nuclear axes $\hat{\mathbf{n}}_0$ and $\hat{\mathbf{n}}_1^{(\ell)}$. This amplification can be used to push the nuclear tilt angle to $\vartheta_M$ and achieve selective decoupling. If $\alpha_1^{(\ell)} = \pi$, then successive perfect reflections just lead to the expression for the vector $\hat{\mathbf{n}}_1^{(\ell+1)} = (\hat{\mathbf{n}}_0|\hat{\mathbf{n}}_1^{(\ell)})$ and the effective nuclear angles $\vartheta_{\ell+1} = 2\vartheta_\ell$ (see Fig. 8-5). If however, $\alpha_1^{(\ell)} \neq \pi$, the effective direction of the nuclear vector can be specified in terms of the perfect reflection $\hat{\mathbf{n}}_1^{(\ell+1)} \sin\alpha_1^{(\ell+1)} = (\hat{\mathbf{n}}_0|\hat{\mathbf{n}}_1^{(\ell)}) \sin^2\alpha_1^{(\ell)} + \hat{\mathbf{n}}_0 \cos^2\alpha_1^{(\ell)}$, where the second term just describes the leakage away from a perfect reflector – geometrically represented by the blue arrow in Fig. 8-3(b).

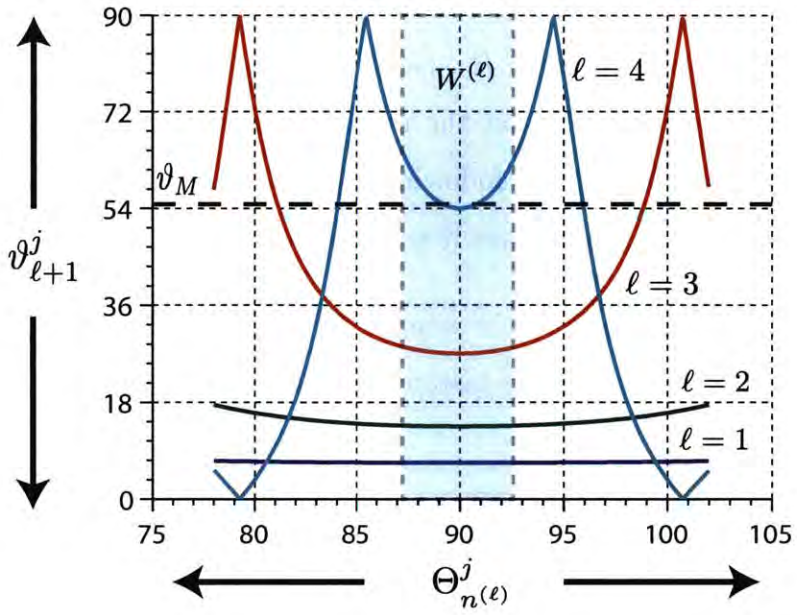


Figure 8-5: **Iterative approach to the magic angle via toggling.** Here, following from Fig. 8-4 we consider the effective hyperfine angle $\vartheta^j_{\ell+1}$ (in degrees) of a spin $j$ on iterating the basic block of Eq. (8.13) $\ell$ times with flip-angle $\alpha_1^{(\ell)}$. One can then quantify the decoupling window $W^{(\ell)}$, inside which nuclear spins are decoupled from one another (Sec. 8.3.4). From Fig. 8-8 the decoupling window is a region approximately 15° around the magic angle $\vartheta_M$. As $\ell$ is increased the effective decoupling window $W^{(\ell)}$ goes down as $W^{(\ell)} = W/2^\ell$, where $W$, the decoupling window on the first iteration can be exactly calculated from Eq. (8.15). The shaded region indicates $W^{(\ell)}$ with $\ell = 4$.

### 8.2.3 Exact approach to the magic angle

Most of the nuclear decoupling effects (Sec. 8.3) we shall be concerned with in this chapter occur at the magic angle when the effective nuclear axes $\hat{\mathbf{n}}_1^{(\ell)}$ are at the tilt

angle $\vartheta_M = \cos^{-1}(1/\sqrt{3})$ (defining the magic axis **M**), which is a symmetry direction for the nuclear dipolar Hamiltonian $H_{dd}$ (see Fig. 8-7)[291,292]. We shall leave a detailed discussion of *selective* decoupling at the magic angle to the following section (Sec. 8.3), and instead here answer the following question: Given an initial nuclear axis $\hat{\mathbf{n}}_1^{(\ell)}$ at angle $\vartheta^{(\ell)}$, how could one take it as close as possible to $\vartheta_M$?

Note that the magic angle can be reached in a single step ($\ell = 1$) following Eq. (8.13), as is evident in Fig. 8-4, for instance by the choice of $\alpha_1$ for a given $\vartheta_j$,

$$\sin^2 \alpha_1^{(\ell)} = \frac{\sqrt{2}}{2\cos\vartheta_j^{(\ell)}(\sqrt{2}\cos\vartheta_j^{(\ell)} - \sin\vartheta_j^{(\ell)})} \tag{8.17}$$

However, since the slope of $\vartheta^{(\ell)}$ is very high except in the region around $\alpha_1^{(\ell)} = \pi$, the *selectivity* of the construction Eq. (8.17) is very high – two nuclear axes $\hat{\mathbf{n}}_{1j}^{(\ell)}$ and $\hat{\mathbf{n}}_{1k}^{(\ell)}$ will both approach the magic angle only if they are very close to start with. As we shall show in Sec. 8.3, this implies that only very closeby spins can be decoupled using the construction of Eq. (8.17).

Instead a more robust and less selective method is by employing concatenated cycles following Eq. (8.15), and operating in the region around $\alpha_1^{(\ell)} = \pi$ . First, we apply the concatenated operators in Eq. (8.15) for $\ell = \text{ceil}\,[\log_2(\vartheta_M/\vartheta_0) - 2]$, to obtain an effective propagator $\mathcal{P}^{(\ell)}$ and angle $\vartheta_\ell$. Now, since each step just leads to the doubling of the effective nuclear angle, $\vartheta_\ell = 2\vartheta_{\ell-1}$, bringing $\vartheta_\ell$ close to the magic angle. For most of the selective decoupling protocols we shall develop in Sec. 8.3, this approach close to the magic angle is sufficient. This is for instance quantified in Fig. 8-8, which describes the scaling of the dipolar interaction for two spins at different tilt angles $\vartheta_\ell^j$ and $\vartheta_\ell^k$. There is a broad window close to $\vartheta_M$ over which decoupling can occur.

However, it is also possible to make $\vartheta_\ell$ *exactly* attain $\vartheta_M$ on the spin of interest, by just rotating $\vartheta_\ell$ in a cone following,

$$[\mathcal{P}^{(\ell)}\mathcal{R}(\alpha_0^{(\ell)}, \hat{\mathbf{n}}_0)\mathcal{P}^{(\ell)}]\mathcal{R}(\alpha, \hat{\mathbf{n}}_0)[\mathcal{P}^{(\ell)}\mathcal{R}(2\pi - \alpha_0^{(\ell)}, \hat{\mathbf{n}}_0)\mathcal{P}^{(\ell)}] \equiv \mathcal{R}(\mathbf{M}, \alpha), \tag{8.18}$$

where the angle $\alpha_0^{(\ell)}$ is given by,

$$\alpha_0^{(\ell)} = \cos^{-1}\left[\frac{\cos\vartheta_M - \cos^2(2\vartheta_\ell)}{\sin^2(2\vartheta_\ell)}\right] \tag{8.19}$$

and the resulting direction $\mathbf{M} = \cos\vartheta_M\hat{\mathbf{z}} + \sin\vartheta_M\hat{\mathbf{z}}_\perp$ being the magic axis (Fig. 8-3(a)). Note that this application of Eq. (8.18) leads to a change in the angle $\varphi_\ell^j$. However given the broad decoupling window (see Fig. 8-8(b)), and the fact that spatially close spin rotate almost identically under actuation from the NV center, this does not have a significant effect in what we shall consider.

### 8.2.4 Including interactions

Thus far, we have neglected nuclear-nuclear interactions in the construction of Eq. (8.13) and its iterative extension $\mathcal{P}^{(\ell)}$. This allows the simple and geometric construction of sequences that rotate the nuclear spin axes in the desired manner. Here, we attempt quantifying the error of this process by including the interactions to first order, and demonstrate numerically that for regimes of experimental interest, engineered actuation of the nuclear spins via the NV is possible even with interactions.

Let us consider the propagator of Eq. (8.13), following the Baker-Campbell-

Hausdorff formula[89] with $H_{\hat{\mathbf{n}}_1} = \sum_j H_{\hat{n}_j}$,

$$\begin{aligned} & e^{i(\Theta_n H_{\hat{\mathbf{n}}_1} + H_{dd})} e^{i(\alpha_0 H_{\hat{m}} + H_{dd})} e^{i(\Theta_n H_{\hat{\mathbf{n}}_1} + H_{dd})} \\ \approx\ & \left[ e^{iH_{dd}/2} e^{i\Theta_n H_{\hat{\mathbf{n}}_1}} e^{iH_{dd}/2} \right] \\ \times\ & \left[ e^{iH_{dd}/2} e^{i\alpha_0 H_{\hat{m}}} e^{iH_{dd}/2} \right] \left[ e^{iH_{dd}/2} e^{i\Theta_n H_{\hat{\mathbf{n}}_1}} e^{iH_{dd}/2} \right] \\ \approx\ & \exp(i\Theta_n H_{\hat{\mathbf{n}}_1} + 3H_{dd}) \end{aligned} \tag{8.20}$$

where the first approximation is to second order, and the second to first order. This can now be extended to the concatenated constructions of Eq. (8.15). For a concatenation order $\ell$ we have,

$$\mathcal{P}^{(\ell+1)} = \mathcal{P}^{(\ell)} \mathcal{R}(\pi, \hat{\mathbf{n}}_0) \mathcal{P}^{(\ell)} = \exp(i\alpha_1^{(\ell)} H_{\hat{\mathbf{n}}_1^{(\ell)}} + 2^{\ell-1} H_{dd}) \tag{8.21}$$

Hence the effect of the couplings can be made insignificant for a spin $j$ if $\|\alpha_1^{(\ell)} H_{\hat{n}_j{}^{(\ell)}}\| \gg \sum_k 2^{\ell-1} |D_{jk}|$. We will show below that this is in fact true for many practical cases of experimental interest (see Fig. 8-6).

### 8.2.5 Experimental considerations

Let us now consider the experimental feasibility of NV driven nuclear spin actuation to the magic angle including the effects of interactions. From Eq. (8.21), it is necessary that the entire rotation to $\vartheta_M$ is carried out faster than the time scale of interactions between spins (set by $\|H_{dd}\|$). Note that we primarily exploit the strong hyperfine coupling ($\gtrsim$ 10kHz) of the shallow NV center to the nuclear spins to rotate them.

We note finally that while in this chapter we consider in detail nuclear spin ac-

tuation via a shallow NV center, our results and protocol can be directly extended for actuation via paramagnetic impurities (*dark spins*) on the surface of the diamond[24,21]. Note that in this case, the hyperfine couplings to the nuclear spins are much stronger (exceeding 100KHz for nuclear spins in a $1\text{nm}^3$ volume around the dark spins), and actuation is less constrained.

Consider that the total time for the construction of $\mathcal{R}(\mathbf{M}, \alpha)$,

$$T \approx \frac{\pi}{\omega_L} 2^{\ell+2} = \frac{\pi}{\omega_L}(\vartheta_M/\vartheta_0) \approx \frac{\pi\vartheta_M}{B+\gamma B_g}, \tag{8.22}$$

since $\vartheta_0 \approx (B+\gamma B_g)/\omega_L$. Since, $B_g$ is a DC transverse magnetic field[290], it is possible that $B_g$ far exceeds the NV Rabi frequency (there are reduced impedence mismatch losses) – Ref.[294] for instance demonstrated $B_g > 20\text{G}$.

In Fig. 8-6 we study the regime where the NV driven actuation of a spin $j$ can bring it to the magic angle $\vartheta_M$ including the effects of the internuclear dipolar interactions. Here $\langle r \rangle$ is the minimum distance between $^{13}\text{C}$ nuclear spins (for comparison a single $^{13}\text{C} - ^{13}\text{C}$ bond length is 0.1nm). As is evident, for experimentally feasibile values of $B_g$ and NV depth, for $\langle r \rangle \gtrsim 2$, it is possible to drive spins selectively to the magic angle and achieve selective decoupling (see Fig. 8-9 and Fig. 8-13). Note that $\langle r \rangle$ sets an experimentally controllable parameter – for instance $\langle r \rangle = 2$ refers to a molecule in which every alternate carbon on average has been labelled as $^{13}\text{C}$, which is possible with recent advances in NMR labeling techniques[295,296].

## 8.3 Selective nuclear decoupling

### 8.3.1 Basic Principle

Using NV driven actuator control, one can *selectively* decouple certain nuclear spins of interest – this shall the focus of this section. Given the dipolar Hamiltonian between the nuclear spins $H_{dd} = \sum_{j<k} D_{jk}(3I_{zj}I_{zk} - \mathbf{I_j} \cdot \mathbf{I_k})$, let us assume that $H_M = \sum_j H_M^j$, where following our geometric notation, $\hat{H}_M^j = \mathbf{M} = \cos\vartheta_M \hat{\mathbf{z}}_j + \sin\vartheta_M(\hat{\mathbf{x}}_j \cos\varphi_j + \hat{\mathbf{y}}_j \sin\varphi_j)$ is the magic axis on spin $j$. Now it is possible to decouple spins of interest at the magic angle, following the simple construction [297],

$$[\exp(i\Theta\hat{H}_M)\exp(i\tau H_{dd})]^L \approx \exp(iL\tau\overline{H}_{dd}) \tag{8.23}$$

where $\Theta$ is the flip angle assumed (for now) to be the same for all spins, and $L$ indicates the number of *cycles* in the construction of Eq. (8.23). In effect, since one has evolution during the actuator control (see Eq. (8.21)), Eq. (8.23) can be just experimentally implemented as $[\exp(i\Theta\hat{H}_M)]^L$. The approximation in Eq. (8.23) denotes a Magnus expansion [90], and we consider the average Hamiltonian to zeroth order [91],

$$\overline{H}_{dd} = \left(\sum_{\ell=1}^{L} e^{i\ell\Theta\hat{H}_M} H_{dd} e^{-i\ell\Theta\hat{H}_M}\right) e^{iL\Theta\hat{H}_M} \tag{8.24}$$

When $L\beta > 2\pi$, it is easy to show that the average Hamiltonian $\overline{H}_{dd} \to 0$, and there is nuclear decoupling. Eq. (8.23) is in fact a recasting of the four-decade-old phase alternating tetrahedral decoupling (PAT) sequence in NMR [297,298], and is related to several early magic angle spinning (MAS) decoupling schemes [291,299,300,46,301]. Note that since we have assumed the magic axis $H_M$ in Eq. (8.23) to be the same for all

spins $j$, there is global decoupling – all spins of the network are decoupled from one another to zeroth order.

The key idea of this chapter is to revisit the original PAT sequence in the context of the incredible versatile system offered by the shallow NV center coupled to the nuclear spins (Fig. 8-1). Through the actuator control of the NV center (Sec. 8.2) one can now effectively engineer the magic axis $H_M$ to be reached only for some particular spins of interest – leading to *selective* nuclear decoupling (Fig. 8-5). Crucially, spins that are spatially close rotate similarly under NV actuation – allowing us to tune the "window" $W$ in which the spins are decoupled (Fig. 8-12) by an appropriate choice of $B_g$ (Fig. 8-13). The NV center hence not only acts as the means to rotate spins, but also to spatially correlate them. We will describe this in detail in the following sections.

### 8.3.2 Geometric interpretation

Let us first describe a nice geometric interpretation of the averaging procedure in Eq. (8.24) as averaging over a cone at the magic angle (see Fig. 8-7). Consider,

$$H_{dd}^{(\ell)} = e^{i\ell\Theta\hat{H}_M} H_{dd} e^{-i\ell\Theta\hat{H}_M} = \sum_{j<k} 3I_{zj}^{(\ell)} I_{zk}^{(\ell)} - \mathbf{I_j}\cdot\mathbf{I_k} \tag{8.25}$$

where for instance, $I_{zj}^{(\ell)} = \left(e^{i\ell\Theta_j \hat{H}_M^j} I_{zj} e^{-i\ell\Theta_j \hat{H}_M^j}\right)$, and $\Theta_j = \Theta_k$. The last term in Eq. (8.25) is a scalar and does not transform under rotations, and we can represent the first term geometrically as $I_{zj}^{(\ell)} I_{zk}^{(\ell)} \to \hat{\mathbf{z}}_j^{(\ell)} \hat{\mathbf{z}}_k^{(\ell)}$. For different $\ell$, these terms can be represented as phasors[205] around the cone tilted at the angle $\vartheta_M$ (yellow circles in Fig. 8-7), and if $L$ is large enough that one traverses the entire cone, the average Hamiltonian prescription is just to take the average vector subtended by the individ-

ual vectors around the cone. This is just the projection of the dipolar Hamiltonian about the symmetry (magic) axis $H_{dd} \cdot \mathbf{I}_{[111]} = 0$[302,303,292]. Moreover, one can make the construction of Eq. (8.24) valid to the second order in the Magnus expansion by symmetrization – i.e. if the phasors on the cone are traversed alternatively clockwise and anticlockwise[293,231,205,105]. Note that the construction Eq. (8.23) assumes that $L\tau > \|1/D_{jk}\|$.

In what follows, through actuation via the NV center, only spins in a window $W$ are engineered to satisfy the geometric averaging of Fig. 8-7, leading to selective decoupling (Fig. 8-8).

### 8.3.3 Selective decoupling via actuator control

In Eq. (8.23) the operator $H_M$ was the same for all spins, let us instead consider the case when it is created following the actuator action of the NV center following Sec. 8.2. Note that in this case different nuclear spins have *different* nuclear actuation axes (say $\hat{\mathbf{n}}_1$), and we now have, similar to Eq. (8.25),

$$H_{dd}^{(\ell)} = \sum_{\ell=1}^{N} U_{\hat{\mathbf{n}}_1}^{j}(\ell\Theta_j) U_{\hat{n}_k}^{k}(\ell\Theta_k) H_{dd} U_{\hat{n}_k}^{k\dagger}(\ell\Theta_k) U_{\hat{\mathbf{n}}_1}^{j\dagger}(\ell\Theta_j) \tag{8.26}$$

and the average Hamiltonian,

$$\overline{H}_{dd} = \sum_{\ell=1}^{L} H_{dd}^{(\ell)} = \sum_{j<k} D_{jk}(\mathbf{I}_j \cdot \mathbf{M} \cdot \mathbf{I}_k) \tag{8.27}$$

where $\mathbf{M}$ is a tensor that now describes the rotated Hamiltonian. Retaining only the secular parts of the Hamiltonian leads to,

$$\begin{aligned}\overline{H}_{dd} &= \sum_{j<k} D_{jk}\Big[M_{zz}I_{zj}I_{zk} + \frac{1}{2}(M_{xx}+M_{yy})(I_{xj}I_{xk} \\ &+ I_{yj}I_{yk}) + \frac{1}{2}(M_{xy}-M_{yx})(I_{xj}I_{yk}-I_{yj}I_{xk})\Big], \end{aligned} \tag{8.28}$$

which then allows us to quantify how the dipolar couplings $D_{jk}$ are *scaled* as a result of the selective actuation,

$$D_{jk}^{(s)} \approx D_{jk}\left[M_{zz} + \left|\frac{1}{2}(M_{xx}+M_{yy})\right| + \left|\frac{1}{2}(M_{xy}-M_{yx})\right|\right] \tag{8.29}$$

where $s = \sum_{j,k} \|D_{jk}^{(s)}\|/\|D_{jk}\|$ sets the metric (scaling factor) that quantifies decoupling performance (see Fig. 8-9 and Fig. 8-13).

Eq. (8.29) forms the basis of selective decoupling (see Fig. 8-8). If $\cos^{-1}(\hat{\mathbf{z}}\cdot\hat{\mathbf{n}}_{1j}) = \cos^{-1}(\hat{\mathbf{z}}\cdot\hat{\mathbf{n}}_{1k} = \vartheta_M$, then $D_{jk}^{(s)} = 0$ and the $j-k$ coupling is effectively decoupled; however if $\{\hat{\mathbf{n}}_{1j}, \hat{\mathbf{n}}_{1k}\}$ are far away from the magic axis $\mathbf{M}$, then $D_{jk}^{(s)}$ is just a rescaling of the dipolar coupling, but it does not vanish (Fig. 8-8). Hence if one selects a spin $j$, and applies the actuator rotation so that the axes $\hat{\mathbf{n}}_1$ to reach the magic angle $\vartheta_M$, then it is plausible to expect that all spins $k$ that are spatially close (in a window $W$) to spin $j$ also rotate similar to it, and approach $\vartheta_M$; hence the couplings $D_{jk}^{(s)}$ inside $W$ are effectively decoupled (see Fig. 8-11 and Fig. 8-12). On the other hand, a spin $i$ that is far outside this window has a negligible rescaling $D_{ij}^{(s)}$, and these long-range couplings can be discerned although $D_{ij} \ll D_{jk}$. Following this, it is most convenient to define the *decoupling window* $W$ in frequency space, such that all couplings $D_{jk}^{(s)}\Big|_{j,k\in W} \leq D_{ij}^{(s)}\Big|_{j\in W,\ell\notin W}$. As a consequence, the long range coupling of

spins in $W$ to other spins is more discernible, for instance if $D^{(s)}_{A_j \to A_j + \Delta A} \leq D^{(s)}_{A_j \to A_k}$. As we shall show, this allows one to reconstruct structure more effectively (see Fig. 8-14). In the following section, we shall quantify the decoupling window $W$ in more detail.

### 8.3.4 Tuning the decoupling window

In the previous section, we described how selective decoupling could be attained by pushing a selected spin $j$ towards the magic angle. A window of spins that are spatially close to spin $j$ get decoupled, while spins that are relatively far away are unaffected. Let us define an effective decoupling window $W$, with the definition that all spins inside $W$ can be considered to be effectively decoupled. We will provide an explicit numerical estimate of $W$ and show that it is *tunable* with parameters under experimental control.

First, consider that different spins are made different under NV actuation because they differ in two parameters, tilt angle $\vartheta^j_\ell$ and flip angle $\Theta^j_{n(\ell)}$. For $\ell = 1$, let $\vartheta^j = \vartheta^j_\ell$, then the effective hyperfine angle $\vartheta^j = \tan^{-1}[\sqrt{(B_j + B_g)^2 + C_j^2}/(\omega_L + A_j)]$ can be controlled by the static field applied $B_g$, which in turn also sets the number of iterations $\ell$ required to reach the magic angle (Fig. 8-5). The flip-angle $\Theta^j$ on the other hand differs for different spins according to $\Theta^j/\Theta^k = \mathcal{N}_j/\mathcal{N}_k$, where $\mathcal{N}_j \approx (\omega_L + A_j) + \frac{1}{2}\frac{(B_j+B_g)^2+C_j^2}{(\omega_L+A_j)}$ to second order. For most experimental situations, $A_j, B_j, B_g \ll \omega_L$, in which case a first order approximation is sufficient, $\mathcal{N}_j \approx (\omega_L + A_j)$.

Let $W$ be the window in $\Theta^j$ that allows an "acceptable" deviation in the hyperfine angle $\vartheta^j_{\ell+1}$ (see Fig. 8-4). For instance, from Fig. 8-8 it is evident that a 15% deviation in $\vartheta^j_{\ell+1}$ from the magic angle still permits almost complete decoupling (in

this case by about a factor of 50). Now, upon cycle iteration $\ell$, Fig. 8-5 provides a qualitative picture on how the situation changes. As $\ell$ in increased one has to move vertically on the traces in Fig. 8-5 – it is evident that the acceptable window of angles in $\Theta^j$ (say $W^{(\ell)}$) decreases; in fact, $W^{(\ell)} \approx W/2^\ell$. This explains why the decoupling window is tunable – for instance, with a small $B_g \approx 0$, $\ell$ is large and the decoupling window $W^{(\ell)}$ is smaller leading to more selective decoupling (see Fig. 8-13). This equation allows us to precisely quantify the decoupling window, since following Eq. (8.15), it is possible to analytically solve for $W$ (in radians),

$$\sin^2\left(\frac{\pi - W}{2}\right) = \frac{\tan\vartheta'^j}{2\tan\vartheta'^j\cos^2\vartheta^j - \sin 2\vartheta^j} \tag{8.30}$$

where $\vartheta'^j = 2.3\vartheta^j$ to allow for a 15% deviation in the hyperfine angle. For small $\vartheta^j < 10°$, the window $W$ is very weakly dependent on $\vartheta^j$ (since the slope of $\vartheta^j_{\ell+1}$ vanishes at $\Theta^j = \pi$), and one can estimate $W \approx 56°$. Hence the decoupling window after $\ell$ iterations is $W^{(\ell)} \approx 56°/2^\ell$. To first order, this allows us to quantify this as an effective decoupling window in the longitudinal hyperfine field of the NV,

$$\Delta A = (1 - \eta)(\omega_L + A_j) \tag{8.31}$$

where $\eta = 1/2\left(1 - W^{(\ell)}/\frac{\pi}{2}\right)$ and $j$ denotes the spin that is brought close to the magic angle. This is an effective decoupling window in frequency space, one can now obtain from Eq. (8.31) a *real-space* window of spins that is decoupled, $\left[\frac{g_N(3\cos^2\vartheta_j - 1)}{A_j + \Delta A}\right]^{1/3} < r_j < \left[\frac{g_N(3\cos^2\vartheta_j - 1)}{A_j}\right]^{1/3}$ To summarize, we have determined that to first order, the region of spins that are effectively decoupled can be expressed just in terms of the hyperfine coupling to the NV. In the high field limit, $\eta \to 1$, and there is selective decoupling; however in the low field limit, or when $B_g \gg A_j$, $\eta \to 0$, and we have

global decoupling of all spins (see Fig. 8-13). The latter regime is similar to that reached during MAS decoupling[291,300] in conventional NMR; however crucially, using the NV center as the actuator allows a tunable, and *spatially correlated* decoupling window (Fig. 8-12), not easily accessible in other systems.

## 8.4 Conclusions

In conclusion, we have considered the task of Hamiltonian engineering via actuator control. In particular, we studied the versatile system of a shallow NV center coupled to nuclear spins in a single molecule, and where the NV center could be used as an actuator to selectively decouple the interspin interactions in an experimentally tunable window. The Hamiltonian engineering protocol just relies on a suitable toggling on the NV center state, with no direct control on the nuclear spins. The tunability of the decoupling window allows one to discern long range internuclear couplings in order to aid in the metrology of single molecule structures placed above the diamond.

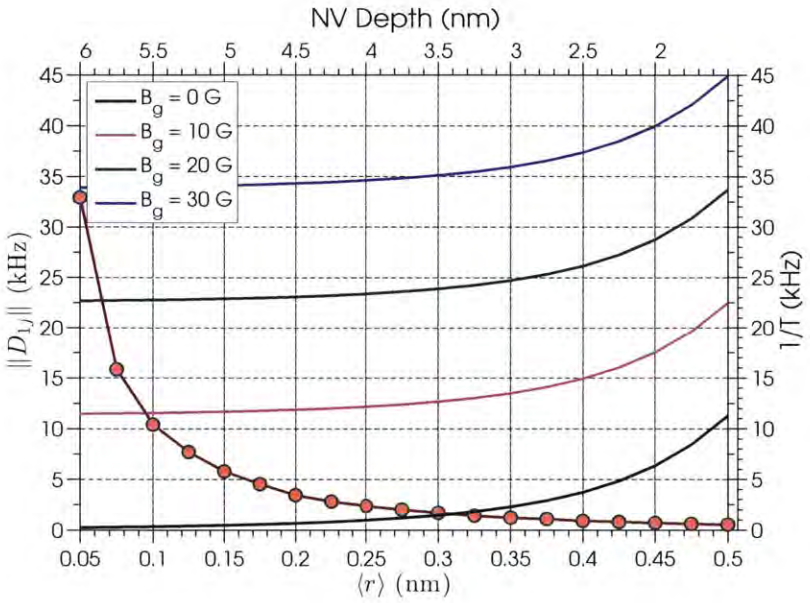


Figure 8-6: **Regime of validity of the NV actuation protocol.** Figure illustrates the regime of validity of the NV actuation protocol Fig. 8-2 while including internuclear dipolar interactions (see Sec. 8.2.4). Here we study the actuation of a single $^{13}$C nuclear spin (labeled spin 1) via the NV center. We consider a random network of 20 $^{13}$C spins (labeled spins j) with minimum inter-nuclear distance $\langle r \rangle$ in a 1nm$^3$ spherical volume around spin 1. The average dipolar coupling $\|D_{1j}\|$ for 150 manifestations of the network by the red points. The solid lines indicate the time $T$ (see Eq. (8.22)) to rotate spin 1 to the magic angle $\vartheta_M$ for different values of $B_g$, and as a function of the depth of the NV (upper axis). For the geometric formalism of Eq. (8.15) to hold we require that $1/T \gg \|D_{1j}\|$, which is clearly satisfied for even small values of $B_g$ (see also Fig. 8-9).

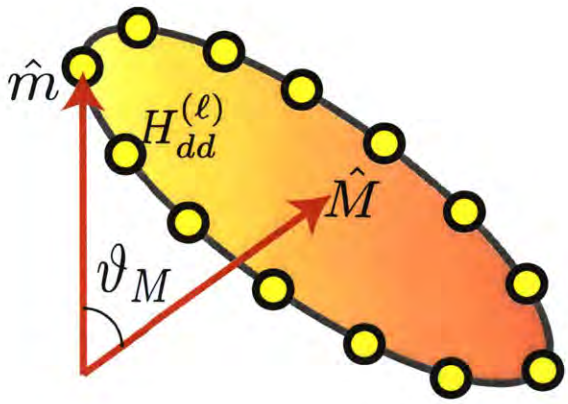


Figure 8-7: **Schematic representation of the decoupling of the average Hamiltonian at the magic angle.** **M** refers to the effective nuclear spin axes of spin $j$ at the magic angle $\vartheta_M$. Each circle represents the effective Hamiltonian $H_{dd}^{(\ell)}$ in Eq. (8.25). If $\ell$ is large enough then the Hamiltonians trace the cone shown, and the average Hamiltonian is the projection of the dipolar Hamiltonian along the axes set by the magic angle, which vanishes to zeroth order in the Magnus expansion. The decoupling can be made perfect up to second order by symmetrization [91,205] – the cone traversed clockwise and anticlockwise in alternating cycles [293,231].

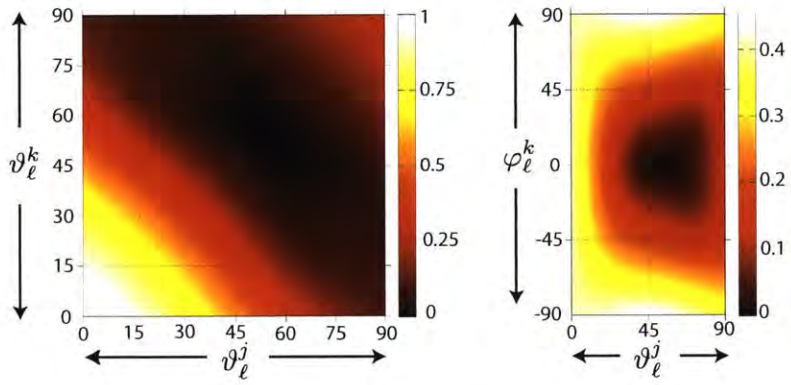


Figure 8-8: **Scaling factor of the dipolar Hamiltonian under actuator mediated selective decoupling.** Figure demonstrates the scaling factor of the dipolar Hamiltonian $\|D_{jk}^{(s)}/D_{jk}\|$ (Eq. (8.29)) as a function of the tilt angle of the effective nuclear axes $\vartheta_\ell^{\{j,k\}}$ (shown here in degrees). (a) In the left panel, we consider $\Delta\varphi_\ell^{jk} = 0$, and the scaling factor vanishes when $\vartheta_\ell^j = \vartheta_\ell^k = \vartheta_M$. Note that $D_{jk}^{(s)}$ also vanishes more generally for $\vartheta_\ell^k = 2\vartheta_M - \vartheta_\ell^j$. (b) In the right panel, we consider $\vartheta_\ell^j = \vartheta_M, \varphi_\ell^j = 0$. Note that optimally in this case we require $\Delta\varphi_\ell^{jk} = 0$.

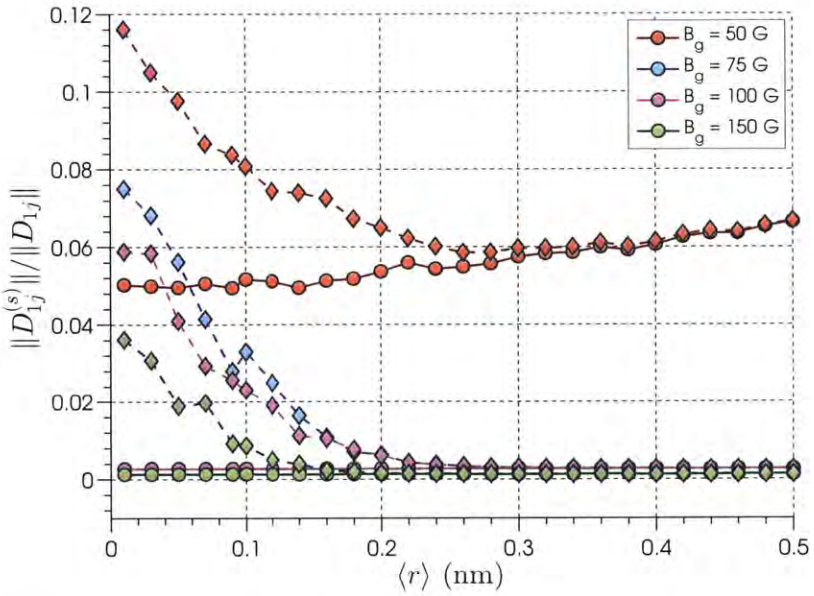


Figure 8-9: **Effect of internuclear dipolar couplings on NV driven selective decoupling.** We study the actuation of a single $^{13}$C nuclear spin (labeled spin 1) via the NV center 2.76nm away from it. We consider a random network of 20 $^{13}$C spins (labelled spins j) with minimum inter-nuclear distance $\langle r \rangle$ in a 1nm$^3$ spherical volume around spin 1 (see also Fig. 8-6 and Appendix 8.B)[63]. As a metric for decoupling performance, we consider the quantity $s = \|D_{1j}^{(s)}\|/\|D_{1j}\|$ (averaged over 150 manifestations of the network) for different values of $B_g$ (Eq. (8.29)). The solid lines (circles) and dashed lines (diamonds) indicate $s$ without and with couplings included respectively. As is evident, for densely packed networks (small $\langle r \rangle$) the dipolar couplings cause a deviation from the desired NV-driven actuation; however, for values of $B_g \gtrsim 50G$, selective decoupling is possible even for network with $\langle r \rangle \lesssim 2$. Note that since $B_g$ that sets the effective decoupling window $W$, for increasing $B_g$, the metric $s \to 0$ indicating that the spin 1 is completely decoupled from the network (see Fig. 8-5 and Fig. 8-13).

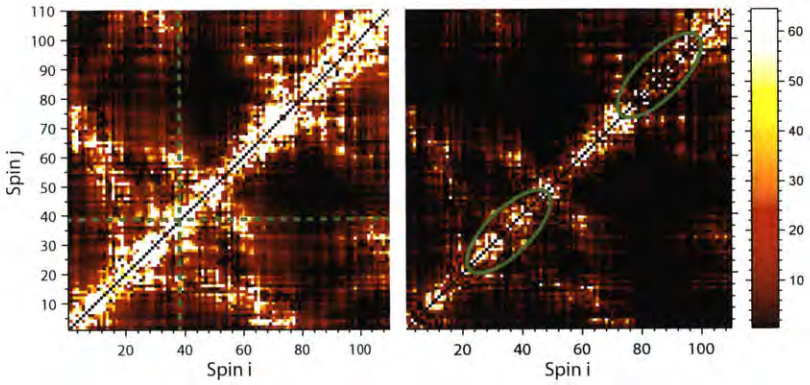


Figure 8-10: **Scaling of the dipolar Hamiltonian under selective decoupling.** The left panel denotes the dipolar matrix $D_{ij}$ (in Hz) for myoglobin placed on top of a diamond containing a 1.8nm shallow NV center (see Fig. 8-1 and Fig. 8-12). We assume $^{13}$C spins at the $\alpha-$carbon locations, with every $^{13}$C spin having on average three $\alpha$ $^{12}$C unlabeled spins, and the spins are numbered arbitarily. The actuator driven decoupling with $B_g = 20$G is applied tuned to spin number 38 (green dashed lines), which is 3.03nm away from the NV center. The right panel denotes the scaled dipolar matrix $D_{ij}^{(s)}$ as a result (see Eq. (8.29)). Note that we did consider the interactions between the $^{13}$C spins during the actuator evolution (Appendix 8.B). As is evident spins close in real space to spin 38 are decoupled (green ovals).

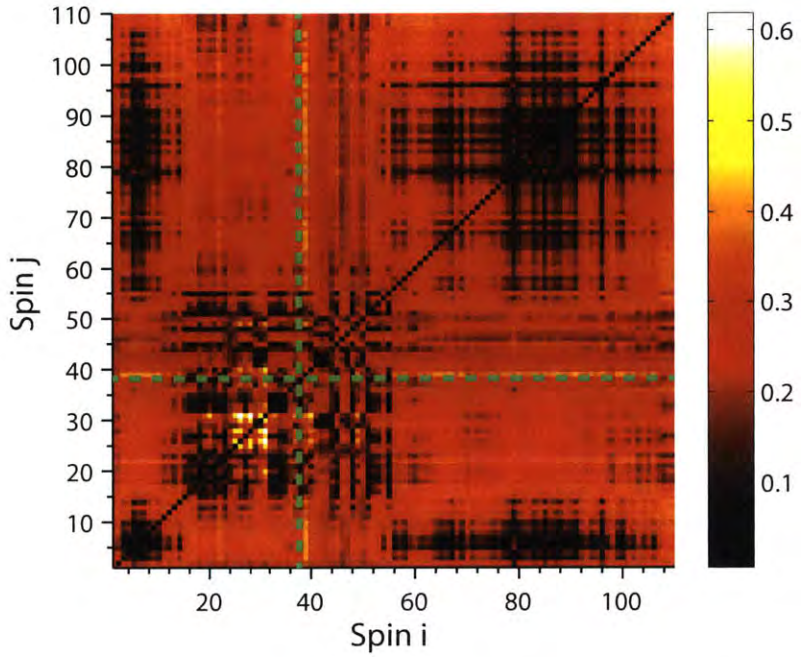


Figure 8-11: **Representative example of selective decoupling.** Figure plots the scaling of the dipolar Hamiltonian $\|D_{jk}^{(s)}\|/\|D_{jk}\|$ for the case considered in Fig. 8-10 and including the interactions during NV actuation (Appendix 8.B). Spin 38 (green lines) is brought near the magic angle, and spins spatially close to this spin are decoupled, and one can quantify a decoupling window. Note that since the spins are numbered arbitrarily in Fig. 8-10. As $B_g$ is increased the effective decoupling window increases (see Fig. 8-5 and Fig. 8-13).

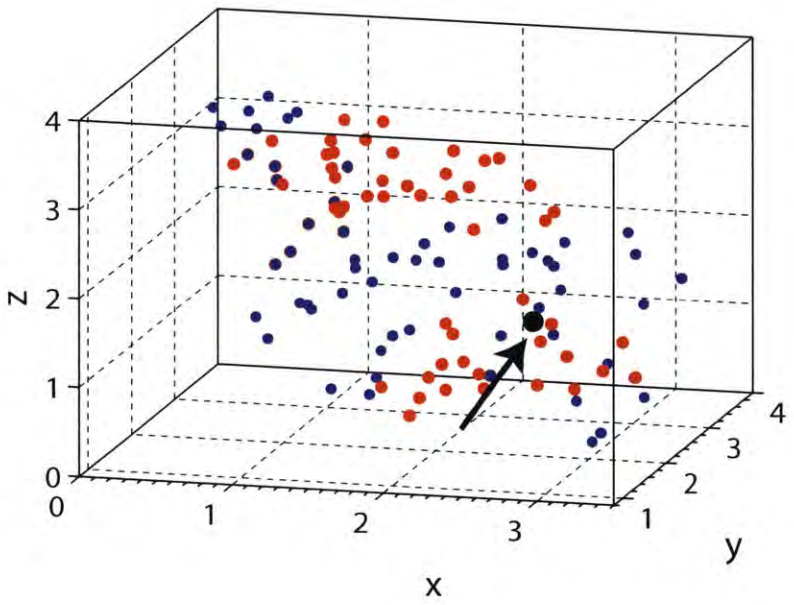


Figure 8-12: **Selective decoupling in real space.** Figure shows (in nm) the positions of the spins in myoglobin considered in Fig. 8-1 (small blue circles). Here the NV center is located at position $(0.5, 1.45, -1.8)$nm. The spin 38 which is brought to the magic angle via NV actuation at $B_g = 20$G in Fig. 8-10 is denoted by the black circle and arrow. The larger red circles indicate spins $j$ for which $s = \sum_k \|D_{jk}^{(s)}\|/\|D_{jk}\| < 0.15$ (Fig. 8-11). As is evident, a window of spins in the molecule can be decoupled that is spatially correlated to the position of the spin brought to the magic angle (see Fig. 8-5), and this window is tunable via $B_g$ (see Fig. 8-13).

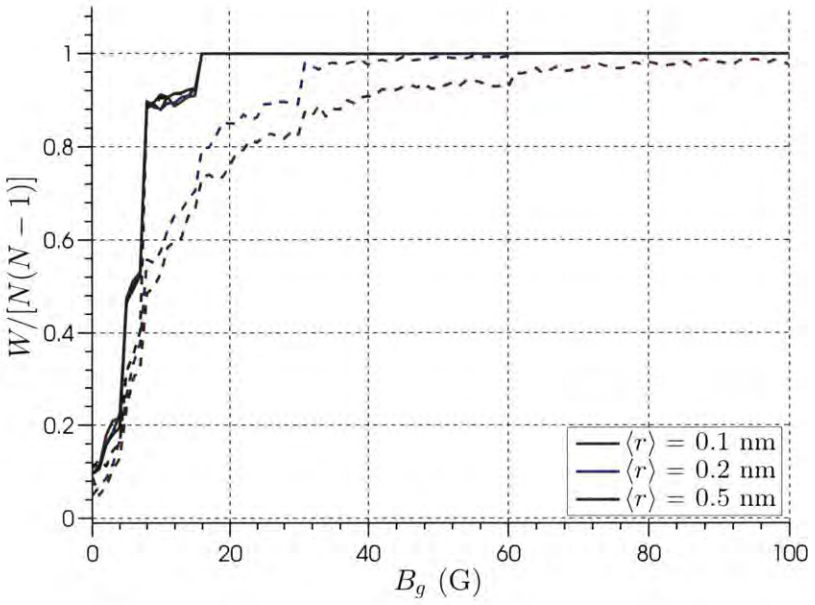


Figure 8-13: **Tunable window for selective decoupling.** Figure demonstrates the effect of increasing $B_g$ on the decoupling window $W$, without (solid lines) and with (dashed lines) the effects of internuclear dipolar couplings being included during NV driven actuation . In particular, similar to Fig. 8-6 and Fig. 8-9, we study the actuation of a single $^{13}$C nuclear spin (labelled spin 1) via the NV center 2.76nm away from it, for different minimum inter-nuclear distances $\langle r \rangle$ for a network of $N = 20$ $^{13}$C spins (see also Appendix 8.B). The decoupling window $W$ is quantified as the number of couplings $\{j, k\}$ that are decoupled by $\|D_{jk}^{(s)}\|/\|D_{jk}\| \leq 0.1$. The normalized quantity $W/N(N-1) \to 1$ when the full network is decoupled. Evidently, the decoupling window is tunable with $B_g$ – increasing the value of $B_g$ increases the decoupling window (Fig. 8-5). Moreover, for reasonable densities of spin networks $\langle r \rangle \gtrsim 2$, decoupling protocol is not adversely affected by evolution under the internuclear dipolar interactions during NV actuation (see Fig. 8-9).

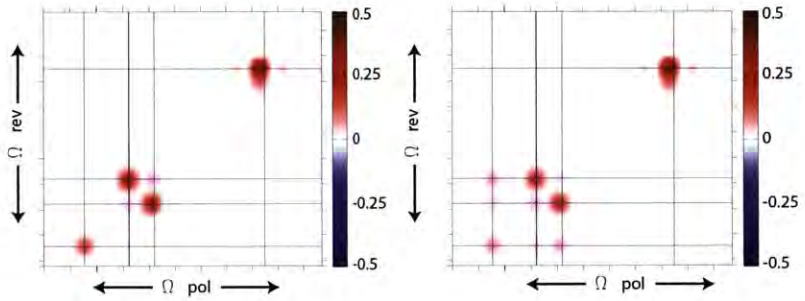


Figure 8-14: **Discerning long range couplings via actuator control.** Panel demonstrates the action of NV driven selective decoupling of nuclear spins to discern a larger number of nuclear couplings. Here we consider a chain of $^{13}$C spins (for instance from an $\alpha$-helix) at position $x = \{2.5, 2.6, 2, 3\}$nm, with $y = 0, z = 2$nm; and the NV at position $(1, 1, 0)$nm. The contour plot shows the reverse sensing signal intensity as a function of spin polarization frequency $\Omega_{pol}$. (a) In the left panel $\Omega_{pol}$ is swept, and the signal is sensed at the frequency $\Omega_{rev}$ after allowing the system to evolve under the natural dipolar Hamiltonian $H_{dd}$ for a time $t = 1/D_{12}$. While there are strong cross peaks that allow us to discern nearest neighbor couplings, the long distance couplings cannot be determined easily. (b) In the right panel, actuator control on the NV center is employed to selectively decouple the spins close to spin 2. As a result there is an effective rescaling of the couplings $H_{dd}$ and the long distance couplings can now be discerned in the cross peaks.

# Appendix

## 8.A CPMG and PDD sensing from a geometric perspective

The formalism we have developed in Sec. 8.2 of this chapter allows us to make a nice geometric interpretation of several NV based spin sensing experiments. In this appendix, we study in particular spin sensing protocols based on the CPMG and PDD dynamical decoupling sequences (for a comparison of decoupling performance see Refs. [98,33]), and describe the effective propagators in the same geometric perspective as in Sec. 8.2. In contrast to the actuator based protocol we introduced, the NV spin is prepared initially in a coherent state $|+\rangle = \frac{1}{\sqrt{2}}(|0\rangle + |1\rangle)$, and one measures the leakage into the state $|-\rangle = \frac{1}{\sqrt{2}}(|0\rangle - |1\rangle)$ as a result of the sequence of $\pi$-pulses. In this appendix, we describe this geometrically, and explicitly show that the sensitivity of the CPMG and PDD sequences of the same number of pulses is identical.

Let us now consider the basic CPMG-2 [88,31] block on resonance on a single nuclear spin. Similar to Eq. (2.9), one can then write down the effective propagator in our

geometric notation,

$$\begin{aligned} & \mathcal{R}(\pi/2,\hat{\mathbf{n}}_1)\mathcal{R}(\pi,\hat{\mathbf{n}}_0)\mathcal{R}(\pi/2,\hat{\mathbf{n}}_1) = \mathbb{1}\cos\vartheta + i\vec{\sigma}\cdot[-\hat{n_j}\cos\vartheta + \hat{\mathbf{n}}_0] \\ = \;& \mathbb{1}\cos\vartheta + i\vec{\sigma}\cdot\hat{\mathbf{n}}_{0_\perp}\sin\vartheta = \mathcal{R}(\vartheta,\hat{\mathbf{n}}_{0\perp}) \end{aligned} \tag{8.32}$$

where we have considered $\hat{\mathbf{n}}_1\cdot\hat{\mathbf{n}}_0 = \cos\vartheta$, where $\tan\vartheta = B_j/(\omega_L + A_j)$ for a single nuclear spin of interest, and $\hat{\mathbf{n}}_{0_\perp}$ is the vector perpendicular to $\hat{\mathbf{n}}_0$. Hence, interestingly, as a result of one cycle of the CPMG propagator, the effective flip angle goes is transformed to $\vartheta$ which is the deviation between the two nuclear axes.

Similarly for one cycle of the PDD sequence [243] we have,

$$\begin{aligned} \mathcal{R}(\pi,\hat{\mathbf{n}}_1)\mathcal{R}(\pi,\hat{\mathbf{n}}_0)\mathcal{R}(\pi,\hat{\mathbf{n}}_1) &= i\vec{\sigma}\cdot[-2\hat{n_j}\cos\vartheta + m] \\ &= \mathcal{R}(\pi,\hat{\mathbf{n}}_0|\hat{\mathbf{n}}_1) \end{aligned} \tag{8.33}$$

where $\hat{\mathbf{n}}_0|\hat{\mathbf{n}}_1$ geometrically just refers to a reflection of the nuclear axis $\hat{\mathbf{n}}_0$ about $\hat{\mathbf{n}}_1$ (see Fig. 8-3).

Comparing Eq. (8.32) and Eq. (8.33), one notices there is a geometric difference between the two propagators – PDD retains the (maximum) flip-angle $\pi$ with a much smaller effective tilt angle $2\vartheta$, while CPMG leads to the maximum tilt angle $\pi/2$ at the cost of the reduced flip angle $\vartheta$ (see Fig. 8-4). While both sequences appear to be vastly different geometrically, as we shall show below for spin sensing the signal obtained is identical in both cases.

Consider a sensing sequence consisting of alternating blocks, for CPMG-2, depending on whether one starts from the $|0\rangle$ or $|1\rangle$ subspace, one gets $\mathcal{U}_0 = U_{\hat{\mathbf{n}}_{0_\perp}}(\vartheta)$ or $\mathcal{U}_1 = U_{\hat{\mathbf{n}}_{1_\perp}}(\vartheta)$. Similarly for PDD we have, $\mathcal{U}_0 = U_{\hat{\mathbf{n}}_0|\hat{\mathbf{n}}_1}(\pi/2)$ or $\mathcal{U}_1 = U_{\hat{\mathbf{n}}_1|\hat{\mathbf{n}}_0}(\pi/2)$. Let us consider the sensing contrast in these two experiments, we have the contrast

is $(1+M)/2$ where $M = \Re\mathrm{Tr}\left\{\mathcal{U}_0\mathcal{U}_1^\dagger\right\}$. Solving we have that after $L$ cycles for a CPMG experiment,

$$\begin{aligned}\mathrm{Tr}\left\{U_0U_1^\dagger\right\} &= \cos^2 L\vartheta + (\hat{\mathbf{n}}_{0_\perp}\cdot\hat{\mathbf{n}}_{1_\perp})\frac{\sin^2 L\vartheta}{\sin^2\vartheta} \\ &= \cos^2 L\vartheta - \cos\vartheta\sin^2 L\vartheta \approx \cos 2L\vartheta \end{aligned} \tag{8.34}$$

and the last part of the function has a sinc form as expected for the filter function. For a comparison with the concatenated form of PDD, we have $L = 2^M$, hence the contrast $\approx \cos 2^{M+1}\vartheta$.

On the other hand, for PDD sensing, and we will show that it has the same form. For one cycle,

$$\mathrm{Tr}\left\{U_0U_1^\dagger\right\} = \cos 3\vartheta \tag{8.35}$$

which is exactly what one would expect geometrically, but now for $M$ concatenations we have the contrast is exactly $\cos 2^{M+1}\vartheta$ which is geometrically equivalent to the angles formed by successive reflections.

## 8.B Simulations including interactions

In this section, we provide additional details of the simulations including the effect of internuclear dipolar interactions during the NV driven actuation (for example in Fig. 8-9 and Fig. 8-10). Since it is in general difficult to simulate the many body Hamiltonians as in Eq. (8.21) that include all interactions, we shall instead follow a hierarchical approach, only retaining the significant couplings for each spin [304].

In particular, for each spin $j$ of the network, we consider a subnetwork of $N_{neigh} \sim$

9 neighboring spins, for which the couplings $\|D_{jk}\|$ are maximum. This physically refers to truncating the dipolar matrix by only considering the strongest interspin interactions for each spin. The simulation is then performed for each spin on the network of $N_{neigh} + 2$ spins (including spin $j$ and the NV) and the zeroth order average Hamiltonian is calculated following Eq. (8.28).

# Chapter 9

# Engineering Quantum Transport in Correlated Spin Networks

## 9.1 Introduction

In the quest toward a scalable quantum computer[305], a promising model comprises distributed computing units connected by passive wires that transmit quantum information[306,307,308,276,309]. This architecture would provide several advantages, since the wires require no or limited control, easing the fabrication requirements and improving their isolation from the environment. For a simpler integration in a solid-state architecture, the wires can be composed of spins. Indeed, quantum spin networks can be used to transport information between separated registers in a quantum information processor.

Following seminal work by Bose[222], which showed that spin chains enable transporting quantum states between the ends of the chain, the dynamics of quantum state transfer has been widely studied (see Ref. [310] for a review), and protocols for im-

proving the fidelity by coupling engineering [223,311,312,313,314,315,316,317], dual-rail topologies [318], active control on the chain spins [221] or on the end spins only [319,320,321,322] have been proposed.

To find a practical implementation, the strict requirements of ideal perfect state transfer models need to be relaxed, allowing for complex coupling topologies and general initial states. Recently there have been extensions to mixed state spin chains [251,323,227,228], which are more easily obtained in high-temperature laboratory settings – making them important protagonists in practical quantum computing. A further challenge to experimental implementation of quantum transport is the lack of chains with the desired coupling strengths, since coupling engineering is limited by fabrication constraints and by the presence of long-range interactions. These challenges highlight the need for a systematic study of mixed state transport in quantum systems beyond chains, including more complex network topologies. These topologies reflect more closely actual experimental conditions as well as systems occurring in nature. For example, there is remarkable recent evidence [324,325] that coherent quantum transport may be the underlying reason for the high efficiency (of over 99%) of photosynthetic energy transfer [326].

To derive explicit conditions for perfect transport we quantify geometric constraints on the unitary propagator that drives transport in an arbitrary network. As a consequence, we find that transferring some mixed states in a network in general requires fewer conditions than pure state transfer. Transport conditions for pure states have been previously quantified [327], however, our method – relying on decomposing the propagator in orthogonal spaces – is fundamentally different and more suitable for mixed states.

Perfect transport occurs when the bulk of the network acts like a lens to *focus* transport to its ends. To make this physical picture more concrete, we describe

mixed state transport as a continuous quantum walk over the network [328,225,329] which progressively populates its nodes. Through this formalism, we derive constructive conditions on the coupling Hamiltonian that results in the *correlation* of transport processes through different possible paths in the network. The correlation of transport processes leads to their constructive interference at the position of the two end-spins, giving perfect transport. While similar walk models have been applied to coherent transfer before (see [330] for a review), our work provides their first extension to transport involving mixed states.

The insight gained by describing quantum transport as correlated quantum walks can be used to construct larger networks where perfect transport is possible. Here we show a strategy to achieve this goal by engineering the coupling strengths between different nodes of the network to construct *weighted* spin networks that support perfect mixed state transport. Feder [331] had considered a similar problem for pure states by mapping the quantum walk of $N$ spinor bosons to a single particle; this has been extended in more recent work [332,333,334].

Here we analyze transport in complex quantum spin networks in the maximally mixed state and derive explicit conditions that should be satisfied by propagators for perfect state transport. Using a description of the transport process as a quantum walk over the network, we show that it is necessary to phase correlate the transport processes occurring along all the possible paths in the network. We provide a Hamiltonian that achieves this correlation, and use it in a constructive method to derive engineered couplings for perfect transport in complicated network topologies.

We also find far more relaxed weighting requirements for mixed state transport, thanks in part to a fermionic instead of bosonic mapping. In turn, this could ease the fabrication requirements for coupling engineering.

The chapter is organized as follows. In Sec. 9.2 we define the problem of mixed

state transport. Sec. 9.3 provides the geometric conditions on the propagator for perfect transport in arbitrary networks. We finally present in Sec. 9.4 the quantum walk formalism, which allows the correlation of transport processes over different paths and the construction of families of weighted networks that support perfect transfer.

## 9.2 Transport in mixed-state networks

Consider an $N$-spin network $\mathcal{N}$, whose vertices (nodes) $\mathcal{V}$ represent spins and whose edges $\mathcal{E} = \{\alpha_{ij}\}$ describe the couplings between spins $i$ and $j$ (see Fig. 9-1). The system dynamics is governed by the Hamiltonian $H = \sum_{i<j} \alpha_{ij} H_{ij}$, where $H_{ij}$ is the operator form of the interaction. In the most general case, a spin of $\mathcal{N}$ may be coupled to several others, for instance, in a dipolar coupled network, $\alpha_{ij} \sim 1/r_{ij}^3$ is a function of the distance between the spins in the network.

We assume that we can identify two nodes, labeled 1 and $N$, that we can (partially) control and read out, independently from the "*bulk*" of the network, and thus act as the "*end*" spins between which transport will occur. The rest of the spins in the network can at most be manipulated by collective control. This also imposes restrictions on the network initialization [227,228]. To relax the requirements for the network preparation, we assume to work in the infinite-temperature limit [227] – a physical setting easily achievable for many experimental systems – where the bulk spins are in the maximally mixed state, $\rho \propto \mathbb{1}$. We will then consider the transport of a slight excess polarization from node 1 to node $N$. The initial state is $\rho_i \sim (\mathbb{1} + \delta Z_1)$, where $Z_1$ is the Pauli matrix acting on spin 1 and $\delta \ll 1$ denotes the polarization excess. Since only the traceless part of the density matrix evolves in time, we will monitor the transport from $\rho_i^{\Delta} = Z_1$ to a desired final state $\rho_f^{\Delta} = Z_N$. The *fidelity* of the transport

process is then defined as $F(t) = \mathrm{Tr}(\rho^{\Delta}(t)Z_N)/\mathrm{Tr}(Z_1^{\dagger}Z_1)$, with $\rho^{\Delta}(t) = U(t)\rho_i^{\Delta}U^{\dagger}(t)$ being the evolved state.

The polarization behaves like a wave-packet traveling over the network $\mathcal{N}$[335,336]. In most cases, the Hamiltonian $H$ drives a rapidly dispersive evolution, where the wave-packet quickly spreads out into many-body correlations among the nodes of $\mathcal{N}$, from which it cannot be recovered[329]. This is for example the case of evolution under the naturally occurring dipolar Hamiltonian, which induces a fast-decay of the spin polarization as measured in solid-state NMR, even if many-body correlations can be detected at longer times[270].

In order to drive a dispersionless transport, thus ensuring perfect fidelity, the network Hamiltonian should satisfy very specific conditions. In this chapter we will investigate these conditions by answering the questions: (i) What are the possible operator forms of the Hamiltonian $H_{ij}$ for dispersionless transport? (ii) What are the coupling topologies and (iii) strengths $\alpha_{ij}$ that support perfect transport?

## 9.3 Conditions for perfect transport

### 9.3.1 Fidelity of mixed-state transport

The condition for perfect transport, $F = 1$, can be expressed in a compact form by using the product-operator (PO) basis[337]. For the $N$-spin network system there are $2^{2N}$ basis elements,

$$\mathbf{B} = \mathbf{B}_1 \otimes \mathbf{B}_{\mathrm{bulk}} \otimes \mathbf{B}_N = \{\mathbb{1}, X_1, Y_1, Z_1, X_2, \ldots, X_1X_2, \ldots, Z_1Z_2, X_1X_2X_3, \ldots, \ldots, Z_1Z_2\cdots Z_{N-1}Z_N\}, \quad (9.1)$$

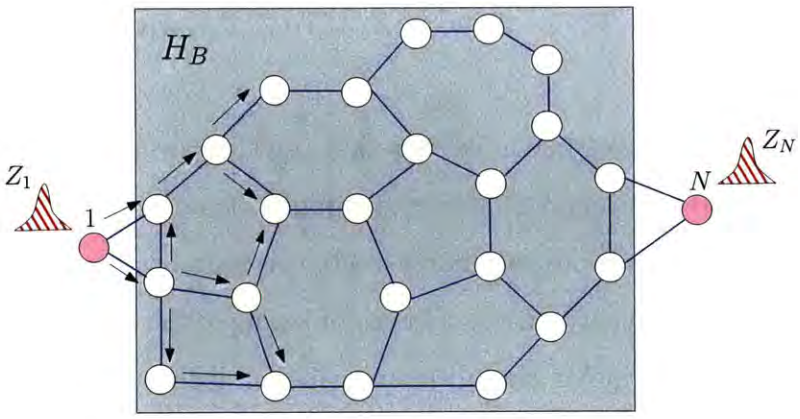


Figure 9-1: **Transport in a spin network**. The network edges represent the interaction among spins (nodes). The pink (dark) nodes represent the *end* spins between which transport should occur. The shaded region comprising yellow (light) nodes is the *bulk* network, $H_B$. An initial polarization packet (hatched) is prepared on spin 1 and allowed to propagate on the network through various possible paths (arrows). For perfect transport, the polarization refocuses at spin $N$.

where $\mathbf{B}_{1,N}$ and $\mathbf{B}_{\text{bulk}}$ are the basis for the end and the bulk spins, respectively.

Using the PO basis, the propagator $U(t) = e^{-iHt}$ can be represented by a vector $|U\rangle = [c_{B_1}, c_{B_2}, \ldots, c_{B_{4^N}}]^T$ in the $2^{2N}$ dimensional Hilbert-Schmidt (HS) operator space spanned by $\mathbf{B}$[72]:

$$U(t) = \textstyle\sum_i c_{B_i}(t) B_i, \quad \text{with} \quad c_{B_i} = \dfrac{\text{Tr}(B_i^\dagger U)}{\text{Tr}(B_i^\dagger B_i)}$$

From an initial state with a polarization excess on spin 1, $\rho_i^\Delta = Z_1$, the system evolves to

$$\rho_f^\Delta = U \rho_i^\Delta U^\dagger = \textstyle\sum_{i,j} c_{B_i} c_{B_j}^* B_i Z_1 B_j \,, \tag{9.2}$$

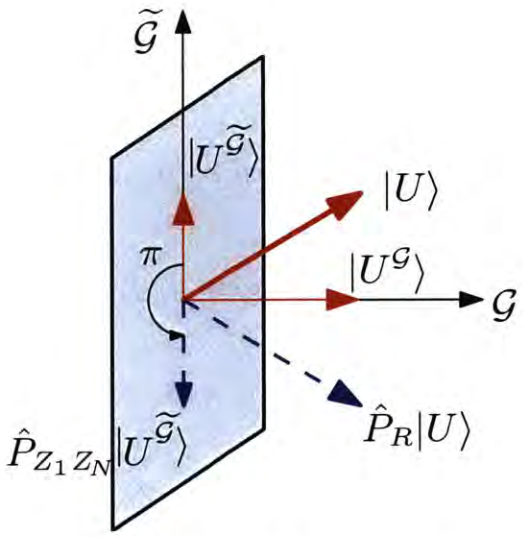


Figure 9-2: **Geometric interpretation** of the condition for maximum $Z_1 \to Z_N$ transport fidelity. The unitary $U$ is represented as a vector $|U\rangle$ (red thick arrow) in the HS space, with components $\left|U^{\mathcal{G}}\right\rangle$ and $\left|U^{\widetilde{\mathcal{G}}}\right\rangle$ in the subspaces $\mathcal{G}$ (represented by an axis) and $\widetilde{\mathcal{G}}$ (represented by the shaded grey plane). $\hat{P}_R\,|U\rangle$ (blue dashed arrow) is the reflection of $|U\rangle$ about the $\mathcal{G}$ axis. Maximum fidelity occurs only when the $\hat{P}_{Z_1 Z_N}$ causes a $\pi$-rotation of $\left|U^{\widetilde{\mathcal{G}}}\right\rangle$.

yielding the transport fidelity to spin $N$

$$
\begin{aligned}
F \;=\; & \frac{1}{\mathrm{Tr}(Z_1^\dagger Z_1)}\mathrm{Tr}\left[\textstyle\sum_{i,j} c^*_{B_i} c_{B_j} B_i Z_1 B_j Z_N\right] = \textstyle\sum_i c_{B_i} c^*_{B_j}, \\
& \text{with } B_j = \pm Z_1 Z_N B_i, \quad \text{for} \quad [B_i, Z_N]_\mp = 0.
\end{aligned}
\tag{9.3}
$$

The last equation follows from the property that all elements of $\mathbf{B}$, except $\mathbb{1}$, are traceless.

The fidelity derived in Eq. (9.3) has a simple form in the HS space. Note that in this operator space, the product $B_i U$ is a linear transformation, $\mathbf{T} : |U\rangle \to \hat{P}_{B_i}\,|U\rangle$, where $\hat{P}_{B_i}$ is a permutation matrix corresponding to the action of $B_i$[99] (here and in

the following we denote operators in the HS space by a hat). The unitarity of $U$ yields the conditions:

$$\|U\| = \langle U|U\rangle = 1 \qquad \langle U|\,\hat{P}_{B_i}\,|U\rangle = 0\,,\ B_i \neq \mathbb{1}. \tag{9.4}$$

Let us partition the HS space in two subspaces $\mathcal{G}$, $\widetilde{\mathcal{G}}$, spanned by the basis $G$ and $\widetilde{G}$,

$$G = \mathbf{B}_1 \otimes \mathbf{B}_{\text{bulk}} \otimes \{\mathbb{1}, Z_N\}, \quad \widetilde{G} = \mathbf{B}_1 \otimes \mathbf{B}_{\text{bulk}} \otimes \{X_N, Y_N\},$$

and note that all elements of $G$ commute with $Z_N$, while all elements of $\widetilde{G}$ anti-commute with $Z_N$. We will label by superscripts $\mathcal{G}$ and $\widetilde{\mathcal{G}}$ the projections of operators in these subspaces. Using this partition, we can simplify the expression for the fidelity of Eq. (9.3) to obtain

$$F = \langle U|\,\hat{P}_{Z_1Z_N}\hat{P}_R\,|U\rangle\ , \tag{9.5}$$

where $\hat{P}_R$ is a reflection about $\mathcal{G}$ and $\hat{P}_{Z_1Z_N}$ is block-diagonal in the $\{G, \widetilde{G}\}$ basis (since $Z_1Z_N \in \mathcal{G}$):

$$\hat{P}_R = \begin{bmatrix} \mathbb{1}^{\mathcal{G}} & 0 \\ 0 & -\mathbb{1}^{\widetilde{\mathcal{G}}} \end{bmatrix}, \quad \hat{P}_{Z_1Z_N} = \begin{bmatrix} \hat{P}^{\mathcal{G}}_{Z_1Z_N} & 0 \\ 0 & \hat{P}^{\widetilde{\mathcal{G}}}_{Z_1Z_N} \end{bmatrix} \tag{9.6}$$

Rewriting the fidelity as the inner product between two vectors, $F = \langle(\hat{P}_{Z_1Z_N}U)|\hat{P}_RU\rangle$, provides a simple geometric interpretation of the perfect transport condition, as shown in Fig. 9-2. The vector $\hat{P}_{Z_1Z_N}|U\rangle$ should be *parallel* to $\hat{P}_R|U\rangle$, which can be obtained if $\hat{P}_{Z_1Z_N}$ rotates $\left|U^{\widetilde{\mathcal{G}}}\right\rangle$ by an angle $\pi$, while leaving $\left|U^{\mathcal{G}}\right\rangle$ unaffected. Alternatively, since $\hat{P}_{Z_1Z_N}$ just describes the $\pi-$rotation of the vector $|U\rangle$ about the $Z_1Z_N$ axis, for perfect transport the rotation-reflection operation $\hat{S} = \hat{P}_{Z_1Z_N}\hat{P}_R$ should be

a *symmetry* operation for $|U\rangle$.

From Eq. (9.4) we have $\langle U| \hat{P}_{Z_1 Z_N} |U\rangle = 0$ and using Eq. (9.5) we can derive explicit conditions to be satisfied by the propagator to achieve perfect transport, $F = 1$

$$\langle U^{\mathcal{G}}| \hat{P}^{\mathcal{G}}_{Z_1 Z_N} |U^{\mathcal{G}}\rangle + \left\langle U^{\widetilde{\mathcal{G}}}\right| \hat{P}^{\widetilde{\mathcal{G}}}_{Z_1 Z_N} \left|U^{\widetilde{\mathcal{G}}}\right\rangle = 0 \tag{9.7}$$

$$\langle U^{\mathcal{G}}| \hat{P}^{\mathcal{G}}_{Z_1 Z_N} |U^{\mathcal{G}}\rangle - \left\langle U^{\widetilde{\mathcal{G}}}\right| \hat{P}^{\widetilde{\mathcal{G}}}_{Z_1 Z_N} \left|U^{\widetilde{\mathcal{G}}}\right\rangle = 1 \tag{9.8}$$

that simplify to

$$\langle U^{\mathcal{G}}| \hat{P}^{\mathcal{G}}_{Z_1 Z_N} |U^{\mathcal{G}}\rangle = - \left\langle U^{\widetilde{\mathcal{G}}}\right| \hat{P}^{\widetilde{\mathcal{G}}}_{Z_1 Z_N} \left|U^{\widetilde{\mathcal{G}}}\right\rangle = \frac{1}{2}\,. \tag{9.9}$$

When is this equation satisfied? By symmetry, it happens when $\|U^{\mathcal{G}}\| = \|U^{\widetilde{\mathcal{G}}}\| = 1/2$, and $|U^{\mathcal{G}}\rangle$ and $\left|U^{\widetilde{\mathcal{G}}}\right\rangle$ are (up to a phase) eigenvectors of $\hat{P}^{\mathcal{G}}_{Z_1 Z_N}$ and $\hat{P}^{\widetilde{\mathcal{G}}}_{Z_1 Z_N}$ with eigenvalues $\pm 1$ respectively:

$$\hat{P}^{\mathcal{G}}_{Z_1 Z_N} |U^{\mathcal{G}}\rangle = + |U^{\mathcal{G}}\rangle\,; \quad \hat{P}^{\widetilde{\mathcal{G}}}_{Z_1 Z_N} \left|U^{\widetilde{\mathcal{G}}}\right\rangle = - \left|U^{\widetilde{\mathcal{G}}}\right\rangle \tag{9.10}$$

To enable perfect transport, $|U\rangle$ must thus have an equal projection on the two subspaces $\mathcal{G}$ and $\widetilde{\mathcal{G}}$, as shown geometrically in Fig. 9-2. Also, intuitively from the symmetry operation $\hat{S}$, all components of $|U\rangle$ lying on the plane $\mathcal{G}$ should be rotationally symmetric with respect to $Z_1 Z_N$, while components of $|U\rangle$ lying on the plane $\widetilde{\mathcal{G}}$ should have reflection symmetry about $Z_1 Z_N$.

Note that Eq. (9.10) imposes fairly weak constraints on the transport unitaries, as opposed to the constraints for pure state transport [327,338]. In particular Eq. (9.10) provides no explicit constraint on the bulk of the network. For example, the two

propagators,

$$\begin{aligned} U_1 &= B_{\text{bulk}}(\mathbb{1} \pm Z_1 Z_N) + B'_{\text{bulk}}(X_1 X_N \pm Y_1 Y_N), \\ U_2 &= B_{\text{bulk}}(\mathbb{1} \pm Z_1 Z_N) + B'_{\text{bulk}}(X_1 Y_N \mp Y_1 X_N), \end{aligned} \tag{9.11}$$

with $B_{\text{bulk}}$ and $B'_{\text{bulk}}$ arbitrary operators ($\in \text{span}\{\mathbf{B}_{\text{bulk}}\}$) acting on the bulk, support perfect transport. Other propagators can be obtained thanks to an invariance property that we present in the next section. More generally, in Sec. 9.A we explicitly provide a prescription to construct classes of unitaries for perfect mixed state transport.

### 9.3.2 Invariance of transport Hamiltonians

The fidelity $F$ in Eq. (9.3) is invariant under a transformation $U' = VU$, where $V$ is unitary and commutes with $\hat{S}$, that is,

$$[\hat{V}, \hat{P}_{Z_1 Z_N} \hat{P}_R] = 0. \tag{9.12}$$

This invariance can be used to construct Hamiltonians that support perfect transport starting from known ones. Consider an Hamiltonian $H$ that generates the transport evolution $U = \exp(-iHt)$. Then the transport driven by $H$ is *identical* to that generated by the Hamiltonian $H' = V^\dagger H V$, where $V$ satisfies Eq. (9.12).

Ref.[339] proved similar symmetry requirements for Hamiltonians that transport pure states; here, however, we derived these Hamiltonian properties just from the geometric conditions on $U$. Ref.[340] treated a similar problem, defining classes of Hamiltonians that perform the same action on a state of interest. A special case of this result was used in[251] to study transport in a mixed-state spin chain driven either

by the nearest-neighbor coupling isotropic XY Hamiltonian,

$$H_{\mathrm{XY}} = \sum_i \alpha_i T^+_{ii+1} \text{ with } T^+_{ij} = (S^+_i S^-_j + S^-_i S^+_j) \tag{9.13}$$

or double-quantum (DQ) Hamiltonian

$$H_{\mathrm{DQ}} = \sum_i \alpha_i D^+_{ii+1} \text{ with } D^+_{ij} = (S^+_i S^+_j + S^-_i S^-_j), \tag{9.14}$$

with $S^\pm_j = \frac{1}{2}(X_j \pm iY_j)$. The unitary operator relating the two Hamiltonians, $V = \prod_{k'} X_{k'}$, where the product $k'$ extends over all even *or* odd spins, does indeed satisfy Eq. (9.12).

### 9.3.3 Quantum information transport via mixed state networks

The requirements for perfect transport (Eq. (9.10)) can be easily generalized to the transport between any two elements of $\mathbf{B}$, say from $\mathcal{I}$ to $\mathcal{F}$. One has simply to appropriately construct the subspaces $\mathcal{G}$ and $\widetilde{\mathcal{G}}$ and the corresponding permutation operator $\hat{P}_{\mathcal{I}\mathcal{F}}$.

One could further consider under which conditions this transport (for example, $X_1 \rightarrow X_N$) can occur *simultaneously* with the $Z_1 \rightarrow Z_N$ transport already considered. More generally, the simultaneous transfer of operators forming a basis for $\mathbf{B_1}$ would enable the transport of quantum information [227,311] via a mixed-state network. The unitary $U$ should now not only be symmetric under $\hat{S}$, but should also under a similar operator derived for $X_1 X_N$. The requirements on $U$ thus become more stringent and only a special case of the propagators constructed in Eq. (9.31) in Sec. 9.A is allowed,

$$U = B_{\text{bulk}}(\mathbb{1} \pm Z_1 Z_N + X_1 X_N \pm Y_1 Y_N)\,. \tag{9.15}$$

This is exactly a SWAP operation (up to a phase) between the end-spins, which can also lead to a transfer of arbitrary *pure* states between 1 and $N$. Therefore, we find that perfect transport of non-commuting mixed states between the end-spins also allows transport in pure state networks. We note that quantum information could be encoded in multi-spin states[341,227] that satisfy proper symmetry conditions and thus do not impose additional conditions on the transport propagators.

### 9.3.4 Which Hamiltonians support mixed state transport?

It would be interesting to determine which Hamiltonians can generate propagators $|U(t)\rangle = \exp(-i\hat{H}t)\,|\mathbb{1}\rangle$ for perfect transport. Unfortunately, deriving requirements for the Hamiltonian from the conditions on the unitaries is non-trivial; however, as we show below, one can still extract useful information.

A general Hamiltonian can be decomposed as $H = H^{\mathcal{G}} + H^{\widetilde{\mathcal{G}}}$, where $H^{\mathcal{G},\widetilde{\mathcal{G}}}$ lie in the subspaces $\mathcal{G}$ and $\widetilde{\mathcal{G}}$, respectively. We cannot set $H = H^{\mathcal{G}}$ since the Hamiltonian does need to have a component that is non-commuting with the target operator ( $Z_N$) in order to drive the transport. If $H = H^{\widetilde{\mathcal{G}}}$, odd powers of $H$ are in $\widetilde{\mathcal{G}}$, while even powers of $H$ belong to $\mathcal{G}$. Then the propagator has contributions from $\left|U^{\mathcal{G}}\right\rangle$ and $\left|U^{\widetilde{\mathcal{G}}}\right\rangle$ with

$$\begin{aligned}
\left|U^{\mathcal{G}}\right\rangle &= |\mathbb{1}\rangle + \frac{(it)^2}{2!}\hat{H}\,|H\rangle + \frac{(it)^4}{4!}\hat{H}^3\,|H\rangle + \cdots \\
\left|U^{\widetilde{\mathcal{G}}}\right\rangle &= it\,|H\rangle + \frac{(it)^3}{3!}\hat{H}^2\,|H\rangle + \cdots
\end{aligned} \tag{9.16}$$

We can demonstrate that in this case the Hamiltonian must satisfy two conditions

to drive perfect transport. First, the "vector" form of the Hamiltonian must be an eigenstate of $\hat{P}_{Z_1 Z_N}$, $\hat{P}_{Z_1 Z_N} |H\rangle = -|H\rangle$, which ensures that the second equation in (9.10) is trivially satisfied, as $\hat{P}_{Z_1 Z_N} \left|U^{\widetilde{\mathcal{G}}}\right\rangle = -\left|U^{\widetilde{\mathcal{G}}}\right\rangle$. Second, since we have

$$\hat{P}_{Z_1 Z_N} \left|U^{\mathcal{G}}\right\rangle = |Z_1 Z_N\rangle + \frac{(it)^2}{2!}\hat{H}|H\rangle + \frac{(it)^4}{4!}\hat{H}^3|H\rangle + \cdots,$$

the first equation in (9.10) implies that $H^{2n} = \frac{1}{2}(\mathbb{1} - Z_1 Z_N)$ for any $n$.

These conditions are for example satisfied by the XY-like Hamiltonian, $H = B_{\text{bulk}} T^{+}_{1N}$, where $B_{\text{bulk}}$ is any operator acting on the bulk and $T^{\pm}_{1N} = (S^{+}_1 S^{-}_N \pm S^{-}_1 S^{+}_N)$. In this case, at $t = \pi/4$, all conditions in Eq. (9.10) are satisfied and perfect transport is achieved. Indeed the XY Hamiltonian has been widely studied for quantum transport[222,223] and it is interesting that we could derive its transport properties solely by the symmetry conditions on the propagator.

An Hamiltonian $H = H^{\widetilde{\mathcal{G}}}$ with support only in $\widetilde{\mathcal{G}}$ is however a very restrictive case as it refers to the situation where all nodes of the network are connected to $N$. Hamiltonians with support in both subspaces are more experimentally relevant, as they correspond to a common physical situation, where the ends of the network are separated in space and direct interaction between them is zero or too weak. In the following, we will consider this more general situation, although restricting the study to XY Hamiltonians in order to derive conditions for perfect transport.

## 9.4 Perfect Transport in networks: Correlated Quantum walks

In the following, we will consider the network $\mathcal{N}$ to consist of spins that are coupled by XY-like interaction, $\{T_{ij}^{+}\}$. We focus on this interaction since it has been shown that with appropriate *engineered* coupling strengths, $\alpha_{ij} \propto \sqrt{i(N-i)}\delta_{j,i+1}$, the XY-Hamiltonian can support perfect transport in linear spin chains (see e.g. [312,313,311,342]). Thanks to the invariance property described in Sec. 9.3.2, this analysis applies to a much broader class of Hamiltonians, in particular to the DQ Hamiltonian.

We assume that the end spins of $\mathcal{N}$ are not directly coupled, thus transport needs to be mediated by the bulk of the network. The simplest such topology is a $\Lambda$-type configuration where the end spins are coupled to a single spin in the bulk. The Hamiltonian $\Lambda_j = (T_{1j}^{+} + T_{jN}^{+})/\sqrt{2}$, where $j$ is a spin in the bulk, is enough to drive this transport. In this case, $(\Lambda_j^2)^n = \Lambda_j^2 \; \forall n$, and hence the propagator is

$$U = \exp(-iHt) = \mathbb{1} + [\cos(t) - 1]H^2 - i\sin(t)H, \tag{9.17}$$

where $H^2 = 1/2[(T_{1j}^{+})^2 + (T_{jN}^{+})^2 + T_{1N}^{+}]$. Since $(\mathbb{1} - 2H^2)$ has the form of $U_3$ in Eq. (9.31), setting $t = \pi$ ensures $U = U_3$, yielding perfect transport. This is an expected result, since this simple lambda-network is just a 3-spin linear chain. This result can be extended to longer chains, as long as engineered couplings ensure that the resulting Hamiltonian is mirror-symmetric [338,311,317].

A different situation arises when there is more than one transport *path* possible, that is, the end spins are coupled to more than one spin in the bulk with an Hamiltonian $H = \sum_{j \in \text{bulk}} \alpha_j \Lambda_j$. For example, Fig. 9-3 depicts a network similar to the

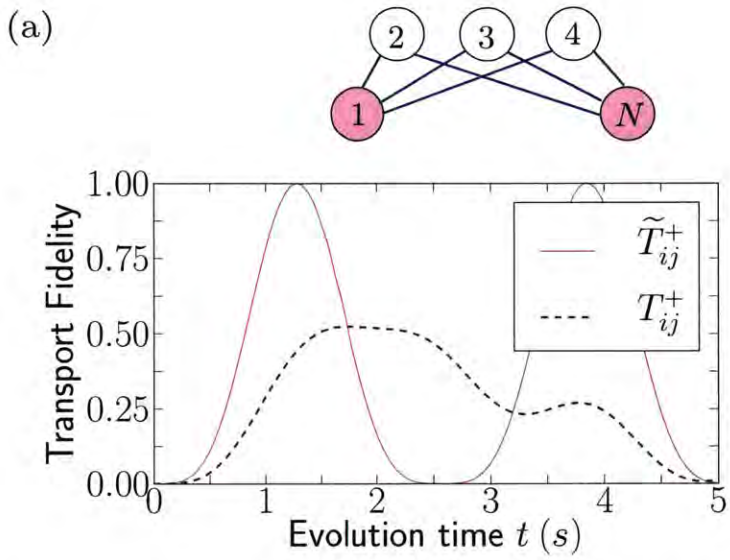


Figure 9-3: **Transport in Λ networks.** Λ-type network with three Λ paths between the bulk and end-spins. (b) Transport fidelity for the Λ-network coupled by the XY-Hamiltonian $T_{ij}^{+}$ (blue dashed) and the modified XY-Hamiltonian $\widetilde{T}_{ij}^{+}$ (red solid). In the latter case, correlated quantum walks lead to perfect transport.

one considered in[228,343] where there are three Λ paths between the end-spins. Even if each path *individually* supports perfect transport, evolution along different paths may not be *correlated*, leading to destructive interference reducing the fidelity (see Fig. 9-3).

Perfect fidelity can be achieved only if different paths can be *collapsed* into a single "effective" one that supports perfect transport (Fig. 9-8). This strategy not only allows us to determine if an Hamiltonian can support perfect transport, but it also gives a recipe to build allowed Hamiltonians, by combining simpler networks known to support perfect transport into more complex ones.

To this end, we use the fact that linear chains enable perfect transport with appropriate engineered couplings. Our first step will then to give conditions under which two chains of the same length (with end-spins in common) can be combined.

To obtain these conditions, we describe the evolution of the spin polarization as a quantum walk over the operators in the network[225,329]. This description reveals the need to *correlate* the parallel paths over the network, in order to achieve a constructive refocusing of the polarization at the other end of the network. We then generalize the conditions by a recursive construction to quite general networks.

### 9.4.1 Transport as a quantum walk over $\mathcal{N}$

We describe the transport evolution as a quantum walk over the network, which progressively populates operators in the HS space. We first expand the transport fidelity $F(t)$ (Eq. 9.5) in a time series,

$$\begin{aligned} F(t) &= \left\langle U_0 \middle| \hat{P}_{Z_1 Z_N} \hat{P}_R \middle| U_0 \right\rangle - it \langle U_0 \left| [\hat{H}, \hat{P}_{Z_1 Z_N} \hat{P}_R] \right| U_0 \rangle \\ &+ \frac{i^2 t^2}{2!} \left\langle U_0 \middle| \left[ \hat{H}, \left[ \hat{H}, \hat{P}_{Z_1 Z_N} \hat{P}_R \right] \right] \middle| U_0 \right\rangle + \cdots \end{aligned} \tag{9.18}$$

with $|U_0\rangle = |\mathbb{1}\rangle$. This process of progressively populating different parts of the HS space upon continuous time evolution under the Hamiltonian can be considered as a quantum *walk*[225,329,344]. Defining the nested commutators,

$$\mathcal{C}_0 = \hat{P}_{Z_1 Z_N} \hat{P}_R \; ; \; \mathcal{C}_n = [\hat{H}, \mathcal{C}_{n-1}] \, , \tag{9.19}$$

Eq. (9.18) takes the form

$$F(t) = \sum_{n=0}^{\infty} \frac{(it)^n}{n!} \langle \mathcal{C}_n \rangle, \tag{9.20}$$

where the expectation value is taken with respect to $|U_0\rangle$.

A large part of the Hamiltonian commutes with $\hat{P}_{Z_1 Z_N} \hat{P}_R$ and can be neglected. We can isolate the non-commuting part by defining the operator $\hat{A}$ via the relation-

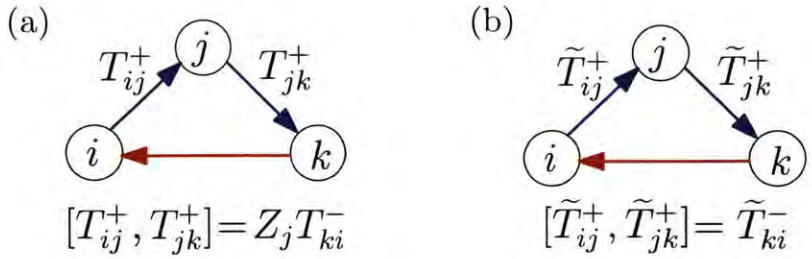


Figure 9-4: **Graphical representation of commutators** for (a) the XY and (b) the modified XY Hamiltonian. The commutator between two top legs (blue) of the directed graph is the third edge (red). In case of the XY Hamiltonian, the commutator is conditioned on node $j$.

ship

$$[\hat{H}, \hat{P}_{Z_1 Z_N} \hat{P}_R] = \hat{A} \hat{P}_{Z_1 Z_N} \hat{P}_R \,. \tag{9.21}$$

The operator $\hat{A}$ and its nested commutators $\mathcal{C}^A_n = [\hat{H}, \mathcal{C}^A_{n-1}]$ (with $\mathcal{C}^A_0 = \hat{A}$) have a simple graphical construction. The commutation relations,

$$\left[T^+_{ij}, T^{\pm}_{jk}\right] = -Z_j T^{\mp}_{ik}; \qquad \left[T^+_{ij}, T^+_{kl}\right] = 0\,, \tag{9.22}$$

(see Fig. 9-4) can be used to provide a simple prescription to graphically determine the flip-flop terms in $\mathcal{C}^A_n$. For any two edges, one in $\mathcal{C}^A_{n-1}$ and one in $H$, that share a common node, $\mathcal{C}^A_n$ contains the edge required to complete the triangle between them. Thus, each higher order in the commutation expansion creates a link between nodes in the network, progressively populating it. We will refer to the operators $\mathcal{C}^A_n$ as quantum walk operators, since as we show below, the nested commutators $\mathcal{C}_n$ in Eq. (9.20) can be built exclusively out of them.

Consider the network of Fig. 9-5(a), with coupling strengths $\alpha_{ij} = 1$: $\hat{A}$ contains only the edges of $\mathcal{N}$ that connect to node 1, as represented by the red lines in Fig. 9-5(b). Fig. 9-5(c-d) represent the higher order commutators, with a red line

linking two nodes denoting a term $T_{ij}^{\pm}$ between them. We note that the graphical construction only predicts the presence of a flip-flop term $T_{ij}^{\pm}$ linking two nodes in the commutator $\mathcal{C}_n^A$, while the explicit forms of the commutators is generally more complex, as shown in Table 9.1, with additional appropriate weights for arbitrary coupling strengths $\alpha_{ij}$. Still, as we now show, only the $T_{ij}^{\pm}$ terms are important to determine the fidelity, and the presence of a $T_{1N}^{\pm}$ term in the graphical series is an indication that transport can occur between the end-nodes.

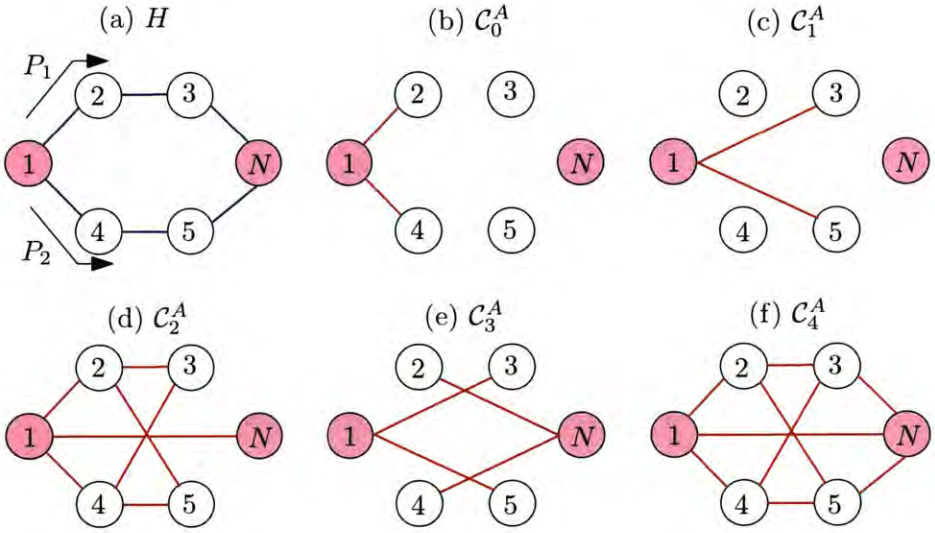


Figure 9-5: **Quantum walk interpretation of quantum transport.** (a) A six spin network with two paths $P_1$ and $P_2$ between the end spins. (b)-(f) represent graphically the successive orders of the quantum walk operators $\mathcal{C}_n^A$: A red line linking two nodes indicates that there is a flip-flop term $T_{ij}^{\pm}$ between them, while path-dependent prefactors are not depicted. Once the walk has covered the entire network, successive orders in $\mathcal{C}_n^A$ reproduce $\mathcal{C}_3^A$ and $\mathcal{C}_4^A$. The explicit expressions for the commutators are shown in Table 9.1.

The commutators $\mathcal{C}_n$ can indeed be written in terms of the $\mathcal{C}_n^A$ nested commutators,

$$\mathcal{C}_n = \sum_{k=0}^{n-1} \binom{n-1}{k} \mathcal{C}_{n-1-k}^A \mathcal{C}_k, \tag{9.23}$$

yielding an expression for the fidelity containing only products of the nested commutators $\mathcal{C}_n^A$:

$$\mathcal{C}_n = \sum_{k_1=0}^{n-1} \sum_{k_2=0}^{k_1-1} \cdots \sum_{k_n=0}^{k_{n-1}-1} \binom{n-1}{k_1} \binom{k_1-1}{k_2} \cdots \binom{k_{n-1}-1}{k_n} \mathcal{C}_{n-k_1-1}^A \mathcal{C}_{k_1-k_2-1}^A \cdots \mathcal{C}_{k_{n-1}-k_n-1}^A \hat{P}_{Z_1 Z_N} \hat{P}_R. \tag{9.24}$$

For a commutator $\mathcal{C}_n$ to yield a non-zero contribution to the fidelity, the product of the operators $\mathcal{C}_k^A$ should be proportional to $Z_1 Z_N$, that is, it should evaluate to even powers of $T_{1N}^{\pm}$. Hence very few terms appearing in Eq. (9.24) actually contribute to the transfer fidelity $F$.

| Walk Operator | XY Hamiltonian | Modified XY Hamiltonian |
|---|---|---|
| $\mathcal{C}_0^A$ | $T_{12}^+ + T_{14}^+$ | $\widetilde{T}_{12}^+ + \widetilde{T}_{14}^+$ |
| $\mathcal{C}_1^A$ | $Z_2 T_{13}^- + Z_4 T_{15}^-$ | $\widetilde{T}_{13}^- + \widetilde{T}_{15}^-$ |
| $\mathcal{C}_2^A$ | $T_{12}^+ - T_{23}^+ - Z_1 Z_2 T_{34}^+ + Z_2 Z_3 T_{1N}^+$<br>$+T_{14}^+ - T_{45}^+ - Z_1 Z_4 T_{25}^+ + Z_4 Z_5 T_{1N}^+$ | $\widetilde{T}_{12}^+ - \widetilde{T}_{23}^+ - \widetilde{T}_{34}^+ + \widetilde{T}_{1N}^+$<br>$+\widetilde{T}_{14}^+ - \widetilde{T}_{45}^+ - \widetilde{T}_{25}^+ + \widetilde{T}_{1N}^+$ |
| $\mathcal{C}_3^A$ | $(Z_4 Z_5 Z_N + 4Z_2) T_{13}^- + (Z_2 Z_3 Z_N + 4Z_4) T_{15}^-$<br>$-2(Z_1 Z_4 Z_5 + Z_3) T_{2N}^- - 2(Z_1 Z_2 Z_3 + Z_5) T_{4N}^-$ | $5\widetilde{T}_{13}^- - 4\widetilde{T}_{2N}^-$<br>$+5\widetilde{T}_{15}^- - 4\widetilde{T}_{4N}^-$ |
| $\mathcal{C}_4^A$ | $(4\mathbb{1} + Z_3 Z_4 Z_5 Z_N) T_{12}^+ + (4\mathbb{1} + Z_2 Z_3 Z_5 Z_N) T_{14}^+ + 9(Z_2 Z_3 + Z_4 Z_5) T_{1N}^+$<br>$-(6\mathbb{1} + 3Z_1 Z_4 Z_5 Z_N) T_{23}^+ - (6Z_1 Z_4 + 3Z_3 Z_N) T_{25}^+ - (6Z_1 Z_2 + 3Z_5 Z_N) T_{34}^+$<br>$+2(\mathbb{1} + Z_1 Z_2 Z_4 Z_5) T_{36}^+ - (6\mathbb{1} + 3Z_1 Z_2 Z_3 Z_N) T_{45}^+ + 2(\mathbb{1} + Z_1 Z_2 Z_3 Z_4) T_{56}^+$ | $5\widetilde{T}_{12}^+ + 5\widetilde{T}_{14}^+ + 18\widetilde{T}_{1N}^+$<br>$-9\widetilde{T}_{23}^+ - 9\widetilde{T}_{25}^+ - 9\widetilde{T}_{34}^+$<br>$+4\widetilde{T}_{36}^+ - 9\widetilde{T}_{45}^+ + 4\widetilde{T}_{56}^+$ |

Table 9.1: **Nested operators arising in a quantum walk**. Here we denote the nested commutators $\mathcal{C}_n^A$ (walk operators) corresponding to the graphs in Fig. 9-5 if the edges represent the XY Hamiltonian or the modified XY Hamiltonian. In the first case, note the presence of path dependent $Z_j$ prefactors, which are absent if the modified XY Hamiltonian is used. This allows for the correlation of transport through parallel paths.

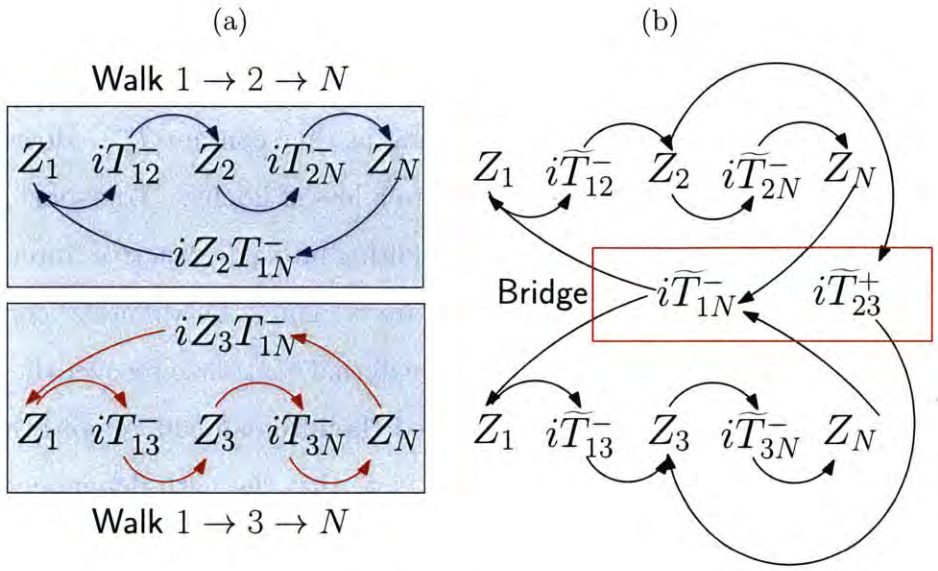


Figure 9-6: **Operators appearing in the quantum walk** of a network consisting of two $\Lambda$ paths, $1 \to 2 \to N$ and $1 \to 3 \to N$. In panel (a), where the transport is driven by the XY-Hamiltonian, the two paths through spins 2 and 3 are different, as they traverse a different set of operators, and are thus depicted in two separated grey panels. In panel (b), where we consider the modified XY Hamiltonian, both walks go through a common set of operators. The previously separate walks are bridged by the operators in the red box, making both walks indistinguishable and hence correlated.

The geometric construction of $\mathcal{C}_n^A$ only yields the XY operators contained in each commutator, but it does not reflect the appearance of prefactors $\propto Z_j$ (due to the commutator in Eq. (9.22)) that are explicitly written out in Table 9.1. Thus, the geometric construction gives a necessary condition for transport, but not a sufficient one.

The operators $\mathcal{C}_n^A$ describe the sum of walks over different paths: for example in

$\mathcal{C}_2^A$, $Z_2 Z_3 T_{1N}^+$ can be interpreted as the information packet reaching node $N$ through path $P_1$ in Fig. 9-5(a), while $Z_4 Z_5 T_{1N}^+$ represents propagation via path $P_2$. These two terms could in principle contribute to the fidelity, as they contain $T_{1N}^+$. However, the additional path dependent factors $\prod_k Z_k$ lead to a loss of fidelity. Transport through different paths yield different $\prod_k Z_k$ factors, resulting into a destructive "interference" effect. Note also that since different paths are weighted by different correlation factors, they cannot be canceled through some external control to recover the fidelity. In the following section we show how a modified Hamiltonian can *remove* this path-conditioning and thus drive perfect transport. Note that the path-dependent factors are as well unimportant in the case of pure states, provided the states reside in the same excitation manifold[345,346,227].

### 9.4.2 Correlating quantum walks over $\mathcal{N}$: Modified XY-Hamiltonian

To remove the path-conditioning one should modify the Hamiltonian so that the $Z_j$ term in the commutator Eq. (9.22) disappears.

This can be done via a modified XY-Hamiltonian

$$\widetilde{T}_{ij}^{\pm} = T_{ij}^{\pm} \prod_{i<u<j} Z_u \tag{9.25}$$

since it satisfies this condition:

$$\left[\widetilde{T}_{ij}^{+}, \widetilde{T}_{jk}^{\pm}\right] = -\widetilde{T}_{ik}^{\mp}\,; \quad \left[\widetilde{T}_{ij}^{+}, \widetilde{T}_{kl}^{+}\right] = 0 \tag{9.26}$$

These operators now depend on the number of nodes between $i$ and $j$, thus introducing a *metric* in the spin-space that distinguishes paths between the two nodes $i$ and $j$. Note that when the network $\mathcal{N}$ is a simple linear chain with nearest-neighbor cou-

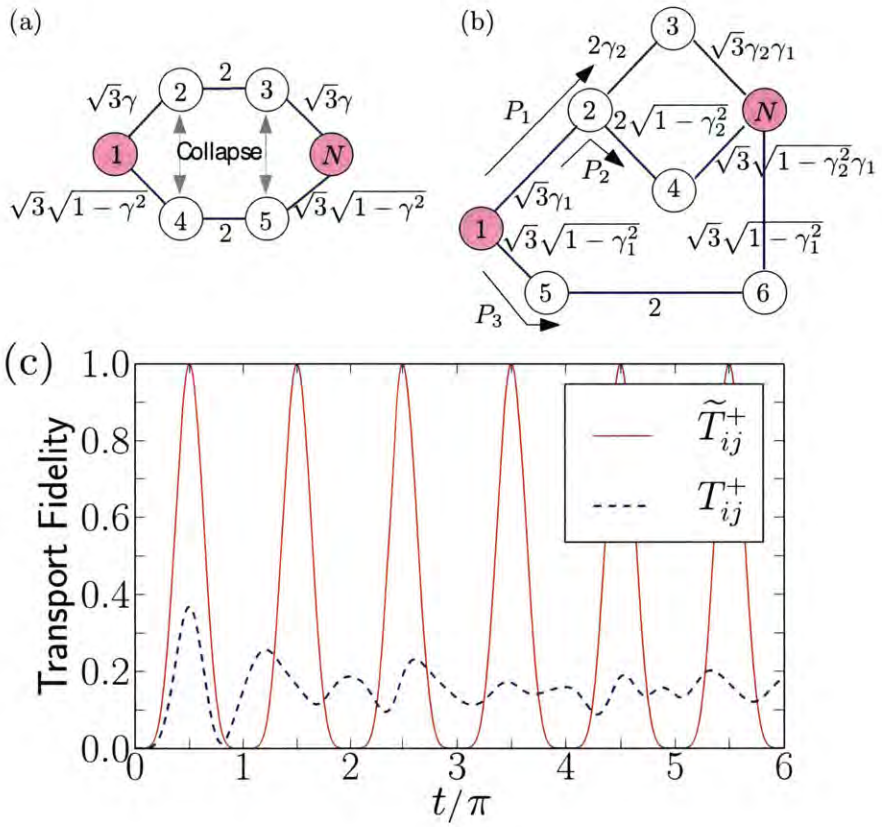


Figure 9-7: **Engineered spin networks.** (a) The network of Fig. 9-5(a), correlated by means of the modified flip-flop Hamiltonian, can be engineered to yield perfect transport. Here, $\gamma$ is any positive parameter, $\gamma < 1$. The two paths $P_1$ and $P_2$ can be collapsed to form a linear chain, since nodes $(2, 4)$ and $(3, 5)$ are equivalent. (b) A more complicated network consisting of three paths $P_1 - P_3$ (black arrows), with engineered strengths paramerized by $0 < \gamma_1, \gamma_2 < 1$. The three paths can be collapsed into an effective 4-spin linear chain, with equivalent nodes (2,5) and (3,4,6). (c) Transport fidelity for the network in (b) with $\gamma_1 = 0.8, \gamma_2 = 0.5$, in case the edges are the XY $\{T^+_{ij}\}$ or modified XY $\{\widetilde{T}^+_{ij}\}$ operators. In this last case perfect fidelity is achieved, while for the usual XY-Hamiltonian the path-conditioned interference leads to poor transport fidelity.

plings the modified Hamiltonian $\widetilde{T}_{ij}^{+}$ is equivalent to the bare XY Hamiltonian. The modification in Eq. (9.25) of the XY-Hamiltonian could also be seen as mapping the spin system into a set of non-interacting fermions[347,348] via a Jordan-Wigner transformation[349], since $C_i = \prod_{u<i} Z_u S_i^{+}$ are operators that satisfy the usual fermionic anti-commutation relationships. When these modified operators are employed in the network $\mathcal{N}$ of Fig. 9-5(a), the two paths $P_1$ and $P_2$ in Fig. 9-5(a) are *indistinguishable* or, equivalently, they become perfectly correlated (see Table 9.1). In effect, the modified XY Hamiltonian drives the quantum walks over different paths through a *common* set of operators of $\mathbf{B}$. This is shown in Fig. 9-6 for a simple $\Lambda$-network consisting of two $\Lambda$ paths.

The graphic construction used to calculate the transport over the network in Fig. 9-5 remains unchanged, except that now the red lines between two nodes denote modified flip-flops $\widetilde{T}_{ij}^{\pm}$ between them. Crucially there are *no* path dependent prefactors and symmetric nodes in each path become *equivalent* in each of the operators $\mathcal{C}_n^A$. It is then possible to collapse different paths into a single effective one, until a complex network $\mathcal{N}$ is collapsed into a linear chain. This is depicted in Fig. 9-7(a).

We can express this result more formally, by defining *collapsed* XY operators, where we denote in parenthesis equivalent nodes in two parallel paths:

$$\widetilde{T}_{i(j,k)}^{\pm} = \frac{1}{\sqrt{\gamma_{ij}^2 + \gamma_{ik}^2}} \left( \gamma_{ij} \widetilde{T}_{ij}^{\pm} + \gamma_{ik} \widetilde{T}_{ik}^{\pm} \right) , \tag{9.27}$$

where $\gamma_{ij}$ and $\gamma_{ik}$ are arbitrary parameters, $0 < \gamma_{ij}, \gamma_{ik} < 1$ (see also Sec. 9.B). Remarkably, these operators satisfy the same path-independent commutation relations as in Eq. (9.26)

$$\left[ \widetilde{T}_{i(j,k)}^{+}, \widetilde{T}_{(j,k)\ell}^{\pm} \right] = -\widetilde{T}_{i\ell}^{\mp} , \tag{9.28}$$

thus showing that intermediate equivalent nodes can be neglected in higher order commutators. In addition the nested commutators $\mathcal{C}_n^A$, and the graphical method to construct them (Fig. 9-4), remain invariant when substituting the modified XY operator with the collapsed operators $\widetilde{T}^{\pm}_{i(j,k)}$.

Using the collapsed operators, the network of Fig. 9-5(a) can thus be reduced to a simpler linear chain (Fig. 9-7). Analogous arguments for path-collapsing were presented in[350], and have been applied before to some classes of graphs[223,333]. In the following we show that path-equivalence could be constructed even for more complex network topologies, since, as we described, path collapsing can be derived just from the commutation relationships between the edges of the network.

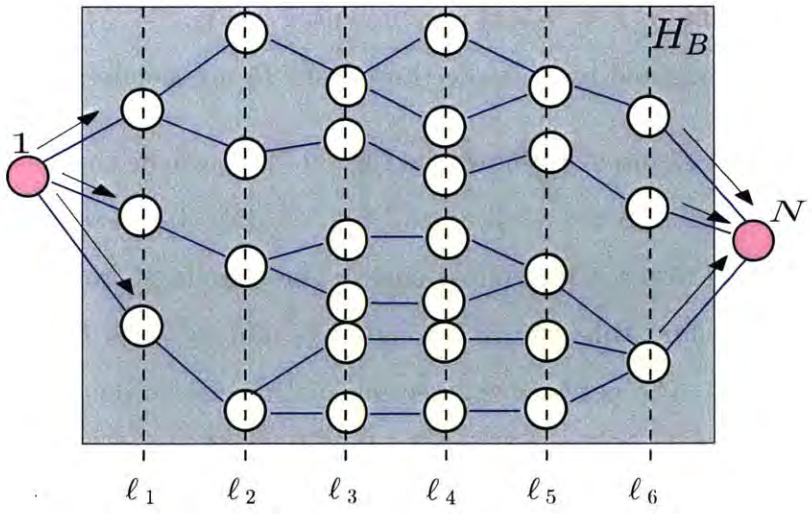


Figure 9-8: **Engineering complex networks for transport.** A complex network topology that can be engineered for perfect transport with the modified XY Hamiltonian. Collapsing the equivalent nodes along the lines $\ell_2 - \ell_5$ leads to three equivalent paths that can be suitably engineered for perfect transport.

### 9.4.3 Engineered spin networks

The path collapsing described in the previous section provides a constructive way to build networks, with appropriate coupling geometries and strengths, that achieve perfect transport. Alternatively, given a certain network geometry, the method determines all the possible coupling strength distributions that leave its transport fidelity unchanged.

For example, starting from a linear chain, any node can be substituted by two equivalent nodes, thus giving rise to two equivalent paths. Then, within the subspace of the equivalent nodes, the couplings can be set using Eq. (9.27) with arbitrary weights $\gamma$, thus giving much flexibility in the final allowed network. The engineered network corresponding to Fig. 9-5(a) is represented in Fig. 9-7(a), where equivalent nodes from $P_1$ are weighted by $\gamma$, while those from $P_2$ are weighted by $\sqrt{1-\gamma^2}$.

A more complex example is shown in Fig. 9-7(b), where the network is built combining the networks in Fig. 9-3(a) and Fig. 9-5(a). It consists of three paths and can be collapsed into a 4-spin linear chain. The couplings shown lead to perfect $Z_1 \to Z_N$ transport for arbitrary path weights $\gamma_1$ and $\gamma_2$, with $0 < \gamma_1, \gamma_2 < 1$, as shown in Fig. 9-7(c). The network engineering scheme can be recursively integrated to construct larger and more complicated network topologies (see for example Fig. 9-8).

Similar weighted networks have been consider before for bosons [331]. The engineered couplings derived by mapping quantum walks of $N$ spinor bosons to the walk of a single particle are however much more restricted than what we found here via the mapping of spins to non-interacting fermions.

## 9.5 Conclusions and Outlook

Experimental implementation of quantum information transport requires relaxing many of the assumptions made in ideal schemes. In this chapter we analyzed a physical situation that is closer to experimental settings – information transport in mixed-state spin networks with complex topologies. We first derived general conditions on propagators that allow perfect transport in these mixed-state spin networks. We used the conditions on the propagators to show that there exist classes of symmetry transformations on the Hamiltonians driving the transport for which the transport fidelity is invariant. We also showed that the propagator conditions also imply that transporting some mixed states requires fewer control requirements than pure state transport, an added advantage to using mixed-state channels in quantum information architectures.

In order to study quantum transfer in complex spin networks, we described the dynamics as a continuous quantum walk over the possible paths offered by the network. This description provided a graphical construction to predict the system evolution, which highlighted the need of correlating the transport processes occurring along different paths of the network to obtain perfect transport. We thus introduced a modified XY-Hamiltonian, based on Jordan-Wigner fermionization, that achieves correlation among paths by establishing a metric for the quantum walks occurring on the network. Conversely, the graphical construction could be as well used to study the generation from the usual XY-Hamiltonian of states of interest in measurement-based quantum computation[351].

Finally, the quantum-walk picture and the graphical construction lead us to define a constructive method to build complex networks from simpler ones, with appropriate

coupling geometries and strengths, that achieve perfect transport. We thus found that there is considerable freedom in the choice of topology and interaction strength that still allows perfect transport in complex networks. While the requirement of a well-defined network topology could be further relaxed [229], the precise construction proposed in this chapter would provide faster transport and the freedom in the coupling distributions could make these networks implementable in experimental systems.

# Appendix

## 9.A Constructing perfect transport unitaries

Here we show how the conditions specified in Eq. (9.10) could be used to construct perfect transport propagators. Our motivation for this is to demonstrate that the conditions of Eq. (9.10) are very *weak*, in the sense that is possible to construct an infinite classes of unitaries that support $Z_1 \to Z_N$ transport.

Consider the matrix forms of $\hat{P}^{\mathcal{G}}_{Z_1 Z_N}$ and $\hat{P}^{\widetilde{\mathcal{G}}}_{Z_1 Z_N}$ in the two-dimensional $\{1, N\}$ subspace of $\mathcal{G}$ and $\widetilde{\mathcal{G}}$:

$$\begin{aligned} \mathcal{G} \sim & \Big\{\{\mathbb{1}, Z_1 Z_N\}, \{Z_1, Z_N\}, \{X_1, Y_1 Z_N\}, \{Y_1, X_1 Z_N\}\Big\} \\ \widetilde{\mathcal{G}} \sim & \Big\{\{X_1 X_N, Y_1 Y_N\}, \{X_1 Y_N, Y_1 X_N\}, \{X_N, Z_1 Y_N\}, \\ & \{Y_N, Z_1 X_N\}\Big\} \end{aligned} \tag{9.29}$$

where the $\sim$ refers to the restriction in the $\{1, N\}$ subspace. Then, for this order of basis, the matrix forms are block diagonal

$$\begin{aligned} \hat{P}^{\mathcal{G}}_{Z_1 Z_N} &= \mathrm{diag}([X, X, -Y, Y]) \\ \hat{P}^{\widetilde{\mathcal{G}}}_{Z_1 Z_N} &= \mathrm{diag}([-X, X, -Y, Y]) \end{aligned} \tag{9.30}$$

where $X$ and $Y$ are the standard Pauli matrices, whose eigenvectors with eigenvalues $\pm 1$ are respectively $[1, \pm 1]^T$ and $[1, \pm i]^T$; this imposes a restriction on $U$. If $B_{\text{bulk}}, B'_{\text{bulk}} \in \text{span}\{\mathbf{B}_{\text{bulk}}\}$, one can explicitly list from Eq. (9.10) possible forms of $U$ for perfect transport,

$$\begin{aligned}
U_1 &= B_{\text{bulk}}(\mathbb{1} \pm Z_1 Z_N) + B'_{\text{bulk}}(X_1 X_N \pm Y_1 Y_N), \\
U_2 &= B_{\text{bulk}}(\mathbb{1} \pm Z_1 Z_N) + B'_{\text{bulk}}(X_1 Y_N \mp Y_1 X_N), \\
U_3 &= B_{\text{bulk}}(Z_1 \pm \mathbb{1} Z_N) + B'_{\text{bulk}}(X_1 X_N \pm Y_1 Y_N), \\
U_4 &= B_{\text{bulk}}(Z_1 \pm Z_N) + B'_{\text{bulk}}(X_1 Y_N \mp Y_1 X_N), \\
U_5 &= B_{\text{bulk}}(X_1 \pm i Y_1 Z_N) + B'_{\text{bulk}}(X_N \mp i Z_1 Y_N), \\
U_6 &= B_{\text{bulk}}(X_1 \pm i Y_1 Z_N) + B'_{\text{bulk}}(Y_N \pm i Z_1 X_N), \\
U_7 &= B_{\text{bulk}}(Y_1 \pm i X_1 Z_N) + B'_{\text{bulk}}(X_N \pm i Z_1 Y_N), \\
U_8 &= B_{\text{bulk}}(Y_1 \pm i X_1 Z_N) + B'_{\text{bulk}}(Y_N \mp i Z_1 X_N),
\end{aligned} \tag{9.31}$$

Note that the bulk of the network specified by $B_{\text{bulk}}$ and $B'_{\text{bulk}}$ can be in any arbitrary state. In fact, the invariance described in Sec. 9.3.2 could be used to show that the eight forms of $U$ in Eq. (9.31) are equivalent to $U_1$ or $U_2$.

Of course, one can combine the forms in Eq. (9.31) to form larger propagators that continue to support perfect transport. Consider for example a propagator constructed out of $U_1$ and $U_2$ in Eq. (9.31), with $B_{\text{bulk}}, B'_{\text{bulk}} = \mathbb{1}$

$$U = \lambda_1(1 \pm Z_1 Z_N) + \lambda_2(X_1 X_N \pm Y_1 Y_N) + \lambda_3(X_1 Y_N \mp Y_1 X_N)$$

where $\lambda_j$ are coefficients to be determined. Then, from Eq. (9.4) we have

$$\begin{aligned} \langle U|U\rangle = 1 &\Rightarrow |\lambda_1|^2 + |\lambda_2|^2 + |\lambda_3|^2 = 1 \\ \langle U|\,\hat{P}_{Z_1 Z_N}\,|U\rangle = 0 &\Rightarrow |\lambda_1|^2 = |\lambda_2|^2 + |\lambda_3|^2 \\ \langle U|\,\hat{P}_{Z_N}\,|U\rangle = 0 &\Rightarrow \mathrm{Im}(\lambda_2^* \lambda_3) = 0 \end{aligned} \tag{9.32}$$

Other conditions in Eq. (9.4) are satisifed trivially. Eq. (9.32) can be solved exactly; for example $\lambda_j = \{1/\sqrt{2}, 1/2, 1/2\}$ is a solution. Importantly however, if $B_{\text{bulk}}$ and $B'_{\text{bulk}}$ were different from each other, the set of equations Eq. (9.32) becomes far simpler.

In summary, achieving $Z_1 \to Z_N$ transport requires weak conditions on the propagator driving the transport. This is as opposed to perfect pure state transport, that requires the propagators to be isomorphic to permutation operators [327] that are mirror symmetric [338] about the end spins of the network.

## 9.B Properties of flip-flop and double-quantum Hamiltonians

In this appendix, we present simple relations satisfied by the flip-flop (XY) operators that will be used in the preceeding main text. Note that the double-quantum (DQ) operators in Eq. (9.14) follow analogous equations. In what follows, distinct indices label distinct positions on the spin network unless otherwise specified. We start with the definition of the operators $S$ and $E$:

$$E_j^{\pm} = \frac{1}{2}(\mathbb{1} \pm Z_j)\,, \qquad S_j^{\pm} = \frac{1}{2}(X_j \pm iY_j). \tag{9.33}$$

These operators satisfy the following product rules:

$$\begin{aligned} &Z_j S_j^{\pm} = \pm S_j^{\pm}, \quad (S_j^{\pm})^2 = E_j^{\pm} E_j^{\mp} = 0, \\ &S_j^{\pm} S_j^{\mp} = (E_j^{\pm})^2 = E_j^{\pm}. \end{aligned} \tag{9.34}$$

We define the flip-flop operators $T_{ij}^{\pm}$ and $L_{ij}^{\pm}$:

$$T_{ij}^{\pm} = (S_i^{+} S_j^{-} \pm S_i^{-} S_j^{+}); \quad L_{ij}^{\pm} = (E_i^{+} E_j^{-} \pm E_i^{-} E_j^{+}) \tag{9.35}$$

From the definition in Eq. (9.35) it follows that

$$T_{ij}^{\pm} = \pm T_{ji}^{\pm} \; ; \; Z_j T_{ij}^{+} = T_{ij}^{-}.$$

We have then the following product relations:

$$\begin{aligned} &\left(T_{ij}^{\pm}\right)^2 = \pm L_{ij}^{+}, \quad T_{ij}^{\pm} L_{ij}^{+} = L_{ij}^{\pm} T_{ij}^{+} = T_{ij}^{\pm}, \\ &\left(L_{ij}^{\pm}\right)^2 = L_{ij}^{+}, \quad T_{ij}^{\pm} T_{jk}^{+} = \tfrac{1}{2}\left(T_{ik}^{\pm} - Z_j T_{ik}^{\mp}\right) \end{aligned} \tag{9.36}$$

and the commutation relations:

$$\begin{aligned} &\left[T_{ij}^{+}, T_{jk}^{+}\right] = -Z_j T_{ik}^{-}, \quad \left[T_{ij}^{+}, Z_j T_{ik}^{+}\right] = T_{kj}^{-}, \\ &\left[T_{ij}^{+}, Z_i\right] = -2T_{ij}^{-}, \quad \left[T_{ij}^{-}, Z_i\right] = -2T_{ij}^{+}. \end{aligned} \tag{9.37}$$

We define the *modified* flip-flop operators $\widetilde{T}_{ij}^{\pm}$,

$$\widetilde{T}_{ij}^{\pm} = T_{ij}^{\pm} \prod_{i<u<j} Z_u, \tag{9.38}$$

obtained by multiplying the flip-flop operator in Eq. (9.35) by a factor of $Z_u$ for all nodes between $i$ and $j$. The modified flip-flop operators follow especially simple

commutation rules

$$\left[\widetilde{T}^{+}_{ij}, \widetilde{T}^{\pm}_{jk}\right] = -\widetilde{T}^{\mp}_{ik} \; ; \; \left[\widetilde{T}^{+}_{ij}, \widetilde{T}^{\pm}_{k\ell}\right] = 0 \tag{9.39}$$

Note that crucially, these commutators only depend on the initial and final nodes ($i$ and $k$), and are independent of intermediate nodes. In a physical analogy, the modified operators $\widetilde{T}^{+}_{ij}$ behave as if they were *path independent.* Thus, when considering two (or more) paths, we could omit any intermediate node, since it would not enter in the ensuing commutators. We then denote *equivalent* nodes in parenthesis –for example, $(j,k)$ means nodes $j$ and $k$ are equivalent– and define the *collapsed* operators:

$$\widetilde{T}^{\pm}_{i(j,k)} = \frac{1}{\sqrt{\gamma^2_{ij} + \gamma^2_{ik}}} \left(\gamma_{ij}\widetilde{T}^{\pm}_{ij} + \gamma_{ik}\widetilde{T}^{\pm}_{ik}\right), \tag{9.40}$$

where $\gamma_{ij}$, $\gamma_{ik}$ are arbitrary parameters, $0 < \gamma_{ij}, \gamma_{ik} < 1$. The collapsed operators satisfy commutation relations similar to Eq. (9.39):

$$\begin{aligned} &\left[\widetilde{T}^{+}_{i(j,k)}, \widetilde{T}^{\pm}_{(j,k)\ell}\right] = -\widetilde{T}^{\mp}_{i\ell} \; , \quad \left[\widetilde{T}^{+}_{(j,k)i}, \widetilde{T}^{\pm}_{i\ell}\right] = -\widetilde{T}^{\mp}_{(j,k)\ell}, \\ &\left[\widetilde{T}^{+}_{(j,k)i}, \widetilde{T}^{\pm}_{i(m,n)}\right] = -\widetilde{T}^{\mp}_{(j,k)(m,n)} \end{aligned} \tag{9.41}$$

The collapsed operators in Eq. (9.40) can be generalized. If $\mathbf{I} = (a_1, a_2, \cdots, a_m)$ and $\mathbf{J} = (b_1, b_2, \cdots, b_n)$ denote two sets of equivalent nodes, we have the collapsed operator

$$\widetilde{T}^{\pm}_{\mathbf{IJ}} = \frac{1}{\sqrt{\sum_{i=1}^{m}\sum_{j=1}^{n}\gamma^2_{a_i b_j}}} \sum_{i=1}^{m}\sum_{j=1}^{n} \gamma_{a_i b_j}\widetilde{T}^{\pm}_{a_i b_j} \; , \tag{9.42}$$

which satisfies the commutation relationships:

$$\left[\widetilde{T}^{+}_{\mathbf{IJ}}, \widetilde{T}^{\pm}_{\mathbf{JK}}\right] = -\widetilde{T}^{\mp}_{\mathbf{IK}} \; ; \; \left[\widetilde{T}^{+}_{\mathbf{IJ}}, \widetilde{T}^{\pm}_{\mathbf{KL}}\right] = 0. \tag{9.43}$$

# Chapter 10

# Engineering Quantum Transport in Arbitrary Spin Networks

## 10.1 Introduction

Transport of quantum information between distant qubits is an essential task for quantum communication[276] and quantum computation[277]. Linear spin chains have been proposed[222] as quantum wires to connect distant computational units of a distributed quantum processor. This architecture would overcome the lack of local addressability of naturally occurring spin networks by separating in space the computational qubit registers while relying on free evolution of the spin wires to transmit information among them. Engineering the coupling between spins can improve the transport fidelity[223], even allowing for *perfect* quantum state transport (QST), but it is difficult to achieve in experimental systems. Unfortunately, the challenges in manufacturing linear chains with engineered couplings has hindered experimental implementations.

Remarkable work[315,316] found relaxed coupling engineering requirements – however, even these proposals still required linear chains with nearest-neighbor couplings[314,228] or networks will all equal couplings[352]. These requirements remain too restrictive to allow an experimental implementation, since manufacturing highly regular networks is challenging with current technology[353,354,355,72].

Here we present strategies to achieve perfect quantum information transport in arbitrary spin networks. Our proposal is based on the weak coupling limit for pure state transport, where information is transferred between two end-spins that are only weakly coupled to the rest of the network. This regime allows disregarding the complex, internal dynamics of the bulk network and relying on virtual transitions or on the coupling to a single bulk eigenmode. We further introduce control methods capable of tuning the transport process and achieve perfect fidelity with limited resources, involving only manipulation of the end-qubits. These strategies could be thus applied not only to engineered systems with relaxed fabrication precision, but also to naturally occurring networks; specifically, we discuss the practical implementation of quantum state transfer between two separated nitrogen vacancy (NV) centers through a network of nitrogen substitutional impurities.

More precisely, we describe strategies for achieving QST between separated "end"-spins in an *arbitrary* network topology. This allows the use of natural spin networks (e.g. in crystals) with almost no fabrication requirements. In large networks, the end-spins are intrinsincally weakly coupled to the bulk network, allowing the use of a perturbative approach to describe the transport dynamics in this weak-coupling regime[315,316,314,228,352,356]. We identify two different scenarios for engineering perfect transport: the end-spins could be set far off-resonance from the rest of the network – transport is then driven by a second-order process and hence is slow, but it requires no active control. Alternately, faster transport is achievable by bringing the end-

spins in resonance with a mode of the bulk of the network, effectively creating a $\Lambda$-type network[99], whose dynamics and bandwidth we characterize completely. We further introduce a simple control sequence that ensures perfect QST by properly *balancing* the coupling of the end-spins to the common bulk mode, thus allowing perfect and fast state transfer. Finally, we investigate the scaling of QST in various types of networks and discuss practical implementations for QST between separated nitrogen vacancy (NV) centers in diamond[357,166] via randomly positioned electronic Nitrogen impurities[358,180,227,359].

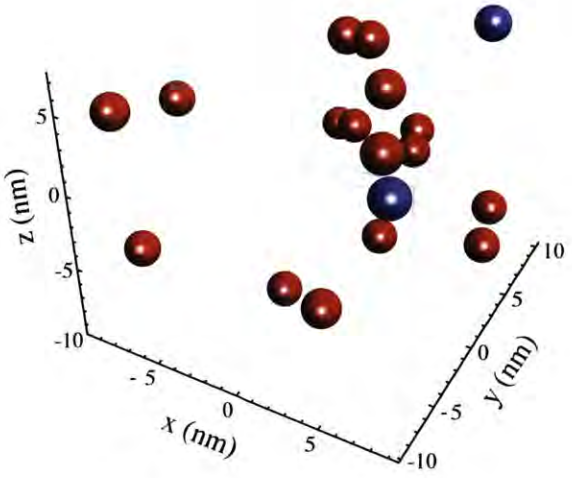


Figure 10-1: **Example of a spin network**, consisting of NV centers (blue spheres) and P1 centers (red) in a diamond lattice. The network is given by randomly positioned P1 centers in the diamond lattice with a concentration of 0.2 ppm and a 5% conversion efficiency to NV. The proposed strategies enable perfect quantum state transfer between the two NV spins in this naturally occurring topology of P1 centers[227,359].

## 10.2 Spin Network

The system (Fig. 10-1) is an $N$-spin network, whose nodes represent spins-$\frac{1}{2}$ and whose edges $H_{ij}$ are the Hamiltonian coupling spins $i$ and $j$. We consider the isotropic XY Hamiltonian, $H_{ij} = (S_i^+ S_j^- + S_i^- S_j^+)$, with $S_j^{\pm} = \frac{1}{2}(S_j^x \pm iS_j^y)$, which has been widely studied for quantum transport[99,251,222,342]. We further assume that two nodes, labeled 1 and $N$, can be partially controlled and read out, independently from the *bulk* of the network: we will consider QST between these *end* spins. For perfect transport, an excitation created at the location of spin 1 should be transmitted without distortion to the position of spin $N$ upon evolution under $H$. We characterize the efficiency of transport by the fidelity, $F(t) = |\langle N| e^{-iHt} |1\rangle|^2$, where $|j\rangle$ represents a single excitation $|1\rangle$ at spin $j$, while all other spins are in the ground state $|0\rangle$.

## 10.3 Weak-coupling regime

The system Hamiltonian can be subdivided into a part, $H_B$, that describes the couplings in the bulk network, and a part, $H_e$, that contains the couplings of the end-spins to the bulk. While optimal fidelity has been obtained for specific, engineered networks (mainly 1D, nearest-neighbor chains), here we consider a completely arbitrary bulk network $H_B$. To ensure perfect transport, we work in the weak-coupling regime for the end-spin coupling $H_e$. We set the total Hamiltonian to

$$H = \beta H_B + \epsilon H_e, \tag{10.1}$$

where we impose $\epsilon \|H_e\| \ll \beta \|H_B\|$, by engineering appropriate weights $\epsilon, \beta$. (Here $\|\cdot\|$ is a suitable matrix norm[360]).

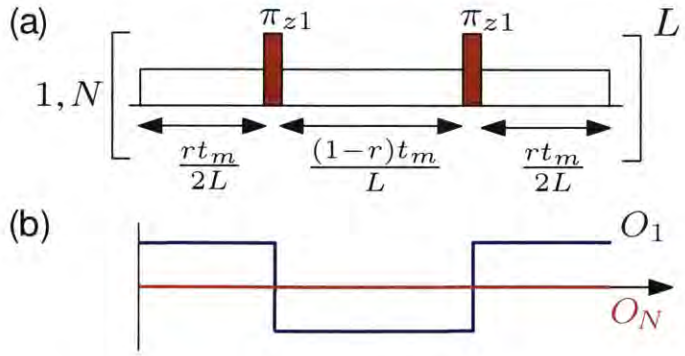


Figure 10-2: **Balancing for perfect quantum transport.** (a) On-resonance balancing sequence applied to the end spins for perfect quantum transport. Yellow blocks indicate microwave irradiation that brings the end spins on resonance with the bulk network. The resulting $\Lambda$-network is in general unbalanced, but appropriately placed $\pi$-pulses (orange) on the end-spin with higher mode overlap (here spin 1) can balance the overlaps $O_{(1,N)}$[33]. (b) The $\pi$-pulses invert the sign of the coupling of spin at node 1 to the bulk mode in the toggling frame such that $O_{1,N}$ become equal on average. For the network of Fig. 10-1, $|O_1| > |O_N|$ and $r = 1/2(1+|O_N/O_1|) = 0.5501$. The sequence is symmetrized[232,214] and repeated for $L$ cycles.

Intuitively, we expect the weak coupling regime to achieve perfect transfer since it imposes two rates to the spin dynamics: the bulk spins evolve on a "fast" time scale while the end-spin dynamics is "slow". The end spins inject information into the network bulk, which evolves so quickly that information spreads everywhere at a rate much faster than new information is fed in, allowing an adiabatic elimination[361] of the information quantum walk in the bulk network[99]. Although high fidelity can be reached, this *off-resonance* transport is slow.

A different strategy for information transport, and a faster rate, is achieved by bringing the end-spins *on resonance* with an eigenmode of the bulk – the weak coupling ensuring greater overlap with a single (possibly degenerate) mode. The system reduces to a $\Lambda$-network[99], where coupled-mode theory ensures perfect transport if both ends have equal overlaps with the bulk mode[362,363], a condition that we will

show can be engineered by the control sequence in Fig. B-9.

To make more rigorous our intuition of the weak regime, we describe transport via a perturbative treatment. Transport in the single excitation subspace is fully described by the adjacency matrix $A$[223], defined via $H = \sum_{i<j} A_{ij}(S_i^+ S_j^- + h.c.)$. For convenience we consider normalized matrices, $\|H_B\| = \|H_e\| = 1$, and introduce the network adjacency matrix, $A = \boldsymbol{\beta} A^B + \epsilon A^e$, which describes the coupling networks of the system Hamiltonian Eq. (10.1); in the weak-coupling regime $\gamma = \boldsymbol{\beta}/\epsilon \gg 1$.

The fidelity can then be written as $F(t) = |\langle N| e^{-iAt} |1\rangle|^2$, where the vectors $|j\rangle$ now represent the node basis in the $N \times N$ network space. We use a Schrieffer-Wolff transformation[364,365,366] and its truncation to first order in $1/\gamma$ to define an effective adjacency matrix, $A' = e^S A e^{-S} \approx A + \frac{1}{2}[S, A]$, which drives the evolution. Setting $S$ so that $[A^B, S] = \frac{\epsilon}{\boldsymbol{\beta}} A^e$, we have $A' \approx \boldsymbol{\beta} A^B + \frac{\epsilon}{2} A^S$, where $A^S = [S, A^e]$ can be evaluated explicitly.

### 10.3.1 Off-resonance QST

Consider first the case where the eigenvalues $\{E_j^B\}$ of $A^B$ are non-degenerate, except for $E_1^B = E_N^B = 0$ (associated with the end-spin subspace). We can fix the energy eigenbasis $\{|v_k\rangle\}$ of $A^B$ by setting $|v_1\rangle = |1\rangle$ and $|v_N\rangle = |N\rangle$. In this basis the structure of the matrix $A^e$ is preserved, non-zero terms connecting only the end-nodes to the bulk, $A^e_{\ell j} = 0$ for $\ell \neq 1, N$. A general element of $A^S$ can be written as

$$A^S_{ij} = \frac{\epsilon^2}{\boldsymbol{\beta}} \sum_k A^e_{ik} A^e_{kj} \left( \frac{1}{E_i^B - E_k^B} + \frac{1}{E_j^B - E_k^B} \right). \tag{10.2}$$

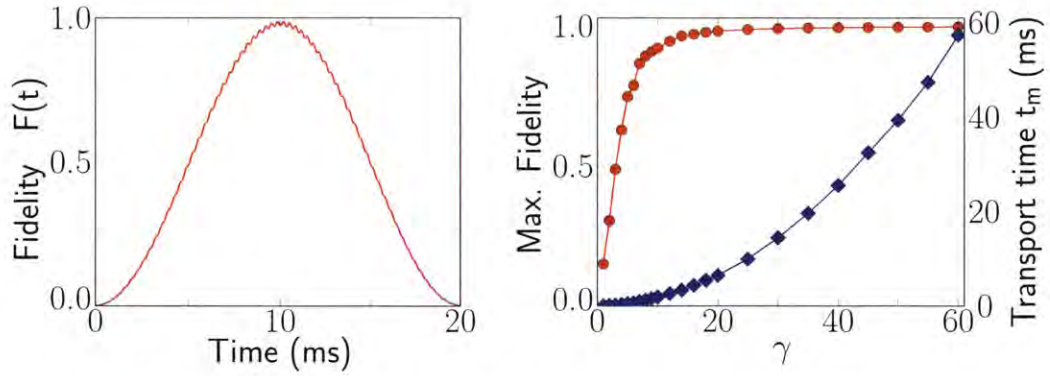


Figure 10-3: **Off-resonance perfect quantum transport.** (a) Off-resonance transport fidelity for the network in Fig. 10-1 for $\gamma = 25$. Perfect transport occurs, but on a slow time scale, an order of magnitude longer than the on-resonance balanced case (Fig. 10-4). (b) Increasing $\gamma$ improves transport fidelity (red circles) but also increases the time required for perfect transport (blue diamonds).

Setting $\{i, j\} \neq 1, N$ and $\{\zeta, \xi\} \in \{1, N\}$, we have

$$A^S_{ij} = \frac{\epsilon^2}{\boldsymbol{\beta}}(A_{i1}A_{1j} + A_{iN}A_{Nj})\left(\frac{1}{E^B_i} + \frac{1}{E^B_j}\right) \tag{10.3}$$

and

$$A^S_{\zeta\xi} = -\frac{2\epsilon^2}{\boldsymbol{\beta}} \sum_{j\neq 1,N} A^e_{\zeta j} A^e_{j\xi} / E^B_j, \tag{10.4}$$

while elements between the end- and bulk-nodes are zero, $A^S_{\zeta j} = 0$, if $A^e_{\xi\zeta} = 0$. Hence $A^S$ can be partitioned into a term with support only in the bulk subspace (Eq. 10.3) and a second term with support only in the end-spin subspace (Eq. 10.4). To first order approximation, it is only this last term that drives QST – the transport happens via a direct coupling between the end-nodes. Since this effective coupling is mediated by the bulk via virtual transitions, its rate is proportional to $\epsilon^2/\boldsymbol{\beta}$. The fidelity of transport is determined entirely by the effective detuning of the two end-

spins, $\alpha = (A^S_{11} - A^S_{NN})/2$:

$$F(t) = \frac{(A^S_{1N})^2}{(A^S_{1N})^2 + \alpha^2} \sin^2\left(t\sqrt{(A^S_{1N})^2 + \alpha^2}\right) \tag{10.5}$$

If we can modify the end-spin Hamiltonian by adding a term $H_{\text{off}} = -2(\omega_1 S^z_1 + \omega_N S^z_N)$, such that $A^S_{11} + \omega_1 = A^S_{NN} + \omega_N$, perfect quantum transport is ensured at $t_m = \pi/(2A^S_{1N})$. This energy shift could be obtained by locally tuning the magnetic field or by applying local AC driving to the end spins, which ensures they have the desired energy in the rotating frame (similar to the Hartman-Hahn scheme [109,110]). Transport fidelity also depends on the goodness of the first order approximation, increasing with $\gamma$ at the cost of longer transport times, as shown in Fig. 10-3(b).

### 10.3.2 On-resonance QST

Transport can be made faster if the end spins are on resonance with one non-degenerate mode of the bulk, $|v_d\rangle$ (we will consider the degenerate case in Appendix 10.A). Resonance happens if the corresponding eigenvalue is $E^B_d = 0$ or it can be enforced by adding an energy shift to the end spins to set $A^e_{11} = A^e_{NN} = \beta/\epsilon E^B_d$. Transport then occurs at a rate proportional to $\epsilon$, as driven by the adjacency matrix $A^d$, the projection of $A^e$ in the degenerate subspace:

$$A^d = \langle 1| A^e |v_d\rangle |1\rangle\langle v_d| + \langle N| A^e |v_d\rangle |N\rangle\langle v_d| + h.c.$$

We note that the goodness of this approximation depends on the gap between the selected resonance mode and the other bulk modes. In the node basis, $A^d$ forms an effective $\Lambda$-*network* [99] (of general form $A^d = \sum_j (A_{1j} + A_{jN}) + h.c.$), coupling the

end-spins with each spin of the bulk:

$$A^d = \sum_j (\delta_{1j} |1\rangle\langle j| + \delta_{Nj} |N\rangle\langle j| + h.c.), \tag{10.6}$$

where $\delta_{(1,N)j} = \langle v_d|j\rangle \langle (1,N)| A^e |v_d\rangle$. Note that importantly we have $\delta_{1j}/\delta_{Nj} =$ cst., $\forall j$. Transport in such $\Lambda$-networks occurs at only four frequencies (see Appendix 10.B), $F(t) = w_0 + \sum_{m=1}^{4} w_m \cos(f_m t)$ with Fourier coefficients $w_m$ defined below, and the frequencies,

$$f_{1,2} = 2\sqrt{S^2 \mp \sqrt{S^4 - \Delta^4}}\,;\; f_{3,4} = \sqrt{2(S^2 \mp \Delta^2)}, \tag{10.7}$$

where,

$$\begin{aligned} S^2 &= \sum_j \frac{1}{2}(\delta_{1j}^2 + \delta_{jN}^2) \\ \Delta^4 &= \sum_{j<k} (\delta_{1j}\delta_{kN} - \delta_{jN}\delta_{1k})^2 \\ \delta^2 &= \sum_j \delta_{1j}\delta_{jN} \end{aligned} \tag{10.8}$$

Physically, $S \sim \|A^d\|$ sets the energy scale of the resonant mode, while $\Delta$ quantifies the *relative* detuning between different $\Lambda$-paths[99] (see Appendix 10.B) .

The Fourier coefficients $w_i$ are found to be $w_0 = -w_3 = -w_4 = \frac{\delta^4}{4(S^4-\Delta^4)}$, $w_1 = w_2 = w_0/2$, giving the analytical expression for QST in a $\Lambda$-network,

$$F(t) = \frac{\delta^4}{S^4 - \Delta^4} \sin^2\left(\sqrt{\frac{S^2+\Delta^2}{2}}t\right) \sin^2\left(\sqrt{\frac{S^2-\Delta^2}{2}}t\right) \tag{10.9}$$

Perfect QST requires $\Delta = 0$ and $\delta = S$. The first condition entails $\delta_{1j}/\delta_{jN} =$ cst.

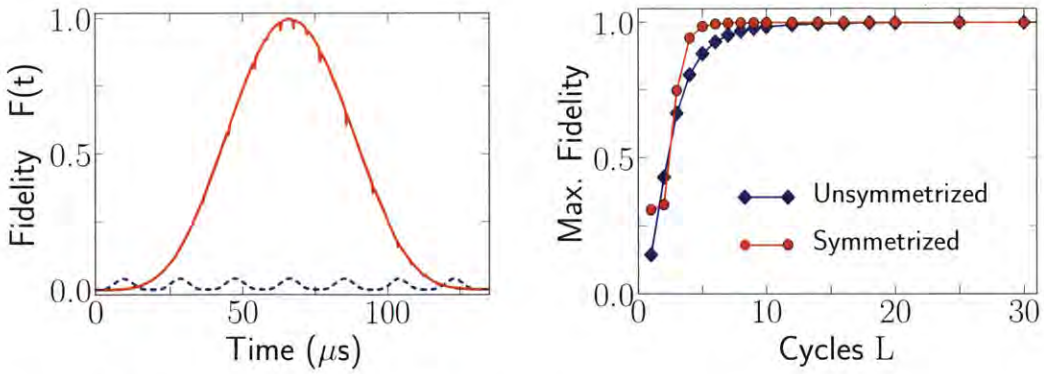


Figure 10-4: **On-resonance perfect quantum transport.** (a) On-resonance transport fidelity for the network of Fig. 10-1, with (red) and without (blue, dotted) balancing, for $\gamma = 1$ and $L = 20$. Almost perfect transport occurs in the balanced case, obtained by the control sequence in Fig. B-9. (b) Increasing the number of cycles $L$ improves the Trotter approximation yielding enhanced fidelity. The symmetrized sequence performs better than the sequence without symmetrization.

$\forall j$, which is always satisfied by $A^d$ if the resonant bulk mode is non-degenerate. We note that in this case there are only two distinct frequencies in Eq. (10.7), which act as signatures of *on-resonance* transport. Thus one could search for a bulk mode experimentally by tuning the end-spin couplings until the appearance of the two frequencies. On the other hand, $\delta = S$ requires a *balanced* network, $\delta_{1j} = \delta_{jN}\ \forall j$. For the reduced adjacency matrix $A^d$ this condition is satisfied when both end-spins have equal overlap with the resonant eigenmode, $\langle 1|\, A^e\, |v_d\rangle = \langle N|\, A^e\, |v_d\rangle$. In the balanced case the fidelity simplifies to $F(t) = \sin(St/\sqrt{2})^4$, which leads to perfect QST at $t_m = \pi/(\sqrt{2}S)$, as if it were a 3-spin chain [223].

### 10.3.3 Perfect QST by on-resonance balancing

Unfortunately the overlaps of the two end spins with the on-resonance mode, $O_{(1,N)} = \langle (1,N)|A^e|v_d\rangle$, are in general unequal, and the $\Lambda$-network unbalanced. Still, it is

possible to *balance* the network by a simple control sequence (Fig. B-9). Assume without loss of generality $O_1 > O_N$. We partition $A^d$ into effective adjacency matrices with couplings only to spins 1 and $N$, $A^d = A^d_1 + A^d_N$. A rotation $e^{-iS^z_1\pi}$ on spin 1 produces $\tilde{A}^d = -A^d_1 + A^d_N$. Then, setting $r = \frac{1}{2}(1 + |O_N/O_1|)$, the evolution

$$e^{-iA^d rt} e^{-i\tilde{A}^d(1-r)t} \approx e^{-iA^d_b t}, \quad \text{with} \quad A^d_b = A^d r + \tilde{A}^d(1-r),$$

is balanced on *average* during the period $t$. The approximation improves if one uses $L$ cycles of the control sequence with shorter time intervals (as in a Trotter expansion[367,214]) and appropriately symmetrizes it (see Fig. B-9) to achieve an error $\mathcal{O}(r^2(1-r)t_m^3/L^3)$. Fig. 10-4(a) shows the effect of enhanced, almost perfect, fidelity upon balancing the network of Fig. 10-1.

Note that for the simplest case of spin chains, the symmetry of the modes ensures the network is already balanced[314,228,368]. However, to drive transport in *arbitrary* networks, one does need an active control scheme for balancing. Similar ideas for engineered mode-matching are employed in the photonics community where the formalism is developed using coupled mode theory[362,363].

## 10.4 Requirements for perfect QST

For transport in real spin networks, the achievable fidelity will be strongly affected by decoherence processes in the spin lattice. It is then necessary to reduce as much as possible the time required for transport. This imposes a compromise between the transport time and the validity of the weak-coupling regime, as they both depend on the weak coupling parameter $\gamma$. In addition, constraints in the control achievable may further degrade the fidelity or, conversely, good control on the spin system might

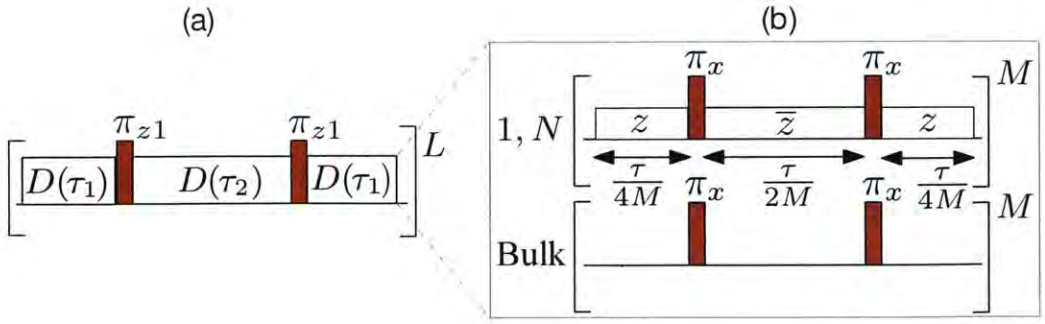


Figure 10-5: **Robust quantum transport.** (a) The control sequence for robust quantum transport under dephasing noise consists of $L$ cycles of a balanced sequence similar to Fig. B-9, but constructed out of decoupling blocks $D(\tau)$. Here $\tau_1 = rt_m/2L$ and $\tau_2 = (1-r)t_m/2L$. Panel (b) details the decoupling block $D(\tau)$, consisting of $M$ cycles. The $\pi_x$ pulses are applied to both the end-spins, and the bulk network. They are accompanied by a toggling of the phase of the microwave irradiation used to bring the end-spins in resonance with the bulk mode. The sequence filters out any dephasing noise field that has a correlation time greater than $\tau/M$; and by appropriately choosing $M$, the transport can be made immune to noise.

improve its coherence properties.

### 10.4.1 Robust transport under decoherence

In many spin systems, the major source of decoherence is dephasing induced by a spin bath[156]. We can be model its effects as a semiclassical dephasing noise field $H_z = \sum_j \omega_j(t) Z_j$, where $\omega_j(t)$ is a stochastic fluctuating field acting on the $j^{\text{th}}$ spin. The noise strength $|\langle \omega_j^2 \rangle|$ is roughly proportional to the mean interaction of the spin to its bath, while the correlation time is approximately the inverse of the bath mean spin-spin coupling.

Simple control methods can greatly reduce the effects of dephasing, without affecting the transport Hamiltonian. Consider for instance the control sequence in Fig.

10-5: A $\pi$ pulse on the full network takes $H_z \rightarrow -H_z$ without changing the coupling Hamiltonian (which is quadratic in the spin operator). If the $\pi$-pulses are applied faster than the correlation time of the noise, the noise Hamiltonian is averaged to zero. This decoupling sequence (the decoupling block $D(\tau)$ in Fig. 10-5) can be embedded in the balancing sequence of Fig. B-9. Even more complex control sequences given by various dynamical decoupling schemes [88,31,243,369] are compatible with the balancing protocol, provided we toggle the phase of the continuous irradiation with each $\pi$-pulse to maintain the end-spins on resonance with the bulk mode. Dynamical decoupling techniques can thus be used to increase the coherence time [98] to be much longer than the transport time, thus reducing the effects of decoherence on the transport fidelity.

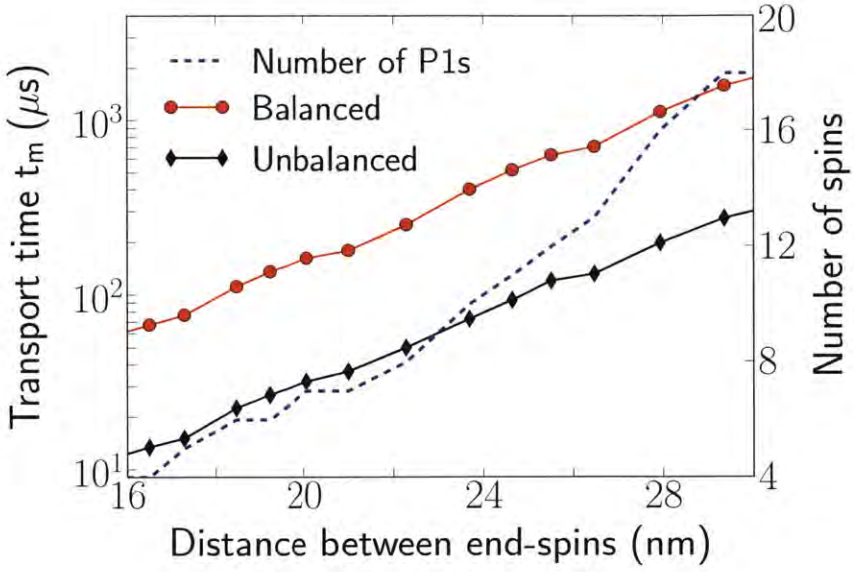


Figure 10-6: **Time for optimal transport** in dipolar coupled spin networks of P1 centers in diamond. The optimal time was calculated from the average over 5000 random lattice realizations of P1 centers of density 10ppm; we considered transport between two NV centers located at increasing distance. The red line (circles) is the time required to achieve a transport fidelity of at least 99% via resonant balancing. The black line (diamonds) is the time at which optimal fidelity is achieved for on-resonant transport without balancing. The fidelity is however quite low ($\sim 15\%$) in this case. The blue dashed line shows the number of P1 centers in the network, $N-2$.

### 10.4.2 Time requirements

We now consider the scaling of the weak coupling parameter $\gamma$ required for the validity of the perturbative approximation. We can fix $\beta = \|H_B\|$ and consider normalized matrices. Then $\beta$ scales as $\sqrt{(N-2)(N-3)/3}$ for a random network where all the couplings are uniformly distributed. For the more realistic case where the coupling strength decreases with distance, the scaling is less favorable, e.g. for a

random dipolar coupled network $\beta$ scales as $\sqrt{2/3(N-3)}/d^3$, where $d$ is the average lattice constant (see Appendix 10.C). Similar scaling occurs for regular spin networks, for example those corresponding to crystal lattices. In general the ratio $\epsilon/\beta$ decreases with the size of the network (usually as $\mathcal{O}(\sqrt{N})$), averting the need to reduce the end-couplings by engineering $\epsilon$, which had been previously deemed necessary[366,368]. For example, $\epsilon = 1$ is sufficient to drive perfect quantum transfer in the network of Fig. 10-1.

In the case of on-resonance balancing, the time at which perfect QST is achieved is $t_m = \gamma\pi/(\sqrt{2}S)$, where $S = \min\{O_1, O_N\}$ scales linearly with $\gamma$. The time is shorter the more symmetrical the end-spins are with respect to the resonant mode, since then $|O_1| \approx |O_N|$. For the off-resonance case the time is $t_m = (\pi\beta/2\epsilon^2)[E^B_\ell/(A^e_{1\ell}A^e_{k\ell})]$, where $E^B_\ell = \min\{|E^B_k|\}$ is the minimum eigenvalue of the bulk. In general this second order transport process takes an order of magnitude longer time than the on-resonance case (Fig. 10-3).

### 10.4.3 Control requirements

Finally, let us estimate the resources needed to impose the end-spin energy shifts as required for perfect QST, for example by a continuous irradiation during $t_m$ (Fig. B-9). In the on-resonance case, the end-spin energy should be set equal to a bulk mode, $E^B_d$. Selecting the highest bulk eigenmode, which has usually the largest gap to the other modes, $E^B_d$ scales as $\mathcal{O}(N)$ for random networks, but it is constant, $\sim 1.6/d^3$, for dipolar coupled networks (Appendix 10.C). Off-resonance transport requires instead a shift of $A^S_{11} - A^S_{NN}$, where $A^S_{11,NN} = \langle A^e_{1,N}|\ell\rangle^2/\gamma^2 E^B_\ell$, where $E^B_\ell$ is the minimum bulk eigenmode. Hence the control required in this case is about an order of magnitude lower than in the resonant case.

## 10.5 Conclusions and outlook

In this section, we showed that perfect quantum state transfer can be engineered even in the case of arbitrarily complicated network topologies. The protocols we presented can thus be used to achieve perfect QST even in naturally-occurring, disordered spin systems.

An experimentally important quantum computing architecture is that of nitrogen vacancy (NV) centers in diamond. Fig. 10-6 shows the scaling of the transport time between two separated NV centers via a bulk network consisting of randomly positioned nitrogen impurities (P1 centers). Transport fidelity loss could occur due to dipolar induced decoherence[310,370]. Dephasing times in excess of $100\mu s$ are routinely achievable in diamond[371,26]. Hence from Fig. 10-6, robust quantum communication is possible in the NV-diamond architecture.

Some experimental challenges remain, although steps to address them have already been taken. In general spins in crystals are coupled by the natural dipolar Hamiltonian and not the isotropic XY Hamiltonian that we assumed here. Thus, we require additional active control to achieve Hamiltonian engineering, for example combining linear gradients with a mixing pulse sequence[372,221,359]. The limitation to pure state transfer requires that the system is polarized at low temperature and high fields. For instance, Ref.[373] demonstrated 99% polarization of a large P1 network ($\sim 10^{16}$ spins) at 2K and 8T. We note that smaller P1 subnetworks could be strongly polarized via the NV centers using cross-polarization[109,374,375,35].

Thanks to the transport strategies we introduced, many other spin systems can be amenable to act as quantum wires for information transport. Provided the end-spins are detuned off-resonance from the bulk network (as it would naturally occur

in most cases), it is possible to achieve unit transport fidelity with minimal control requirements, although on a somewhat long time scale. Transport speed can be improved by bringing the end-spins on resonance with a common mode of the bulk network. These transport strategies may thus present an alternative to the interlinking of quantum registers with little or no fabrication overhead [376,377]. More generally, the in-depth description of the weak-coupling dynamics for a general network might yield more refined strategies for some specific network topologies.

# Appendix

## 10.A Transport for end-spins on-resonance with a degenerate mode

In the main text we described transport when the end spins are on resonance with an eigenmode of the bulk with eigenvalue $E_d^B$. Here we generalize to the situation where the eigenvalue is degenerate, with eigenvectors $|\alpha_m\rangle$. The projector onto the degenerate eigenspace is then,

$$\begin{aligned} P &= (|1\rangle\langle 1| + |N\rangle\langle N|) + \sum_{m\in M} |\alpha_m\rangle\langle\alpha_m| \\ &\equiv (|1\rangle\langle 1| + |N\rangle\langle N|) + P_M, \end{aligned} \tag{10.10}$$

and, to first order, transport is driven by the projection of the adjacency matrix $A^e$ into the this subspace, i.e., $A^d = P^\dagger A^e P$. Now we consider that $A^e$ and $A^B$ have the

following forms, where "$\times$" denotes a non-zero element:

$$A^e = \begin{bmatrix} & \times & \times & \times & \times & \\ \times & & & & & \times \\ \times & & & & & \times \\ \times & & & & & \times \\ \times & & & & & \times \\ & \times & \times & \times & \times & \end{bmatrix}; \qquad A^B = \begin{bmatrix} & & \times & \times & \times \\ \times & & & \times & \times \\ \times & \times & & & \times \\ \times & \times & \times & & \\ & & & & \end{bmatrix}.$$

It follows that

$$\langle 1|A^e|1\rangle = 0\,;\ \langle N|A^e|N\rangle = 0\,;\ \langle \alpha_{m'}|A^e|\alpha_m\rangle = 0, \tag{10.11}$$

yielding

$$\begin{aligned} A^d &= \sum_m \langle 1|A^e|\alpha_m\rangle (|1\rangle\langle\alpha_m| + |\alpha_m\rangle\langle 1|) \\ &+ \sum_m \langle N|A^e|\alpha_m\rangle (|N\rangle\langle\alpha_m| + |\alpha_m\rangle\langle N|), \end{aligned} \tag{10.12}$$

where we have used the fact that $A^e$ is real, and hence $\langle 1|A^e|\alpha_m\rangle = \langle \alpha_m|A^e|1\rangle$. Let us define the end connection vectors,

$$A^e\,|1\rangle = |n_1\rangle\ ;\ A^e\,|N\rangle = |n_N\rangle\,. \tag{10.13}$$

Then,

$$\begin{aligned} A^d &= \sum_m \langle n_1|\alpha_m\rangle (|1\rangle\langle\alpha_m| + |\alpha_m\rangle\langle 1|) \\ &+ \sum_m \langle n_N|\alpha_m\rangle (|N\rangle\langle\alpha_m| + |\alpha_m\rangle\langle N|) \\ &= \sum_j \sum_m \langle n_1|\alpha_m\rangle \left(\langle\alpha_m|j\rangle |1\rangle\langle j| + \langle j|\alpha_m\rangle |j\rangle\langle 1|\right) \\ &+ \sum_j \sum_m \langle n_N|\alpha_m\rangle \left(\langle\alpha_m|j\rangle |N\rangle\langle j| + \langle j|\alpha_m\rangle |j\rangle\langle N|\right) \end{aligned}$$

or simplifying,

$$A^d = \sum_j (\delta_{1j} |1\rangle\langle j| + \delta_{jN} |N\rangle\langle j| + h.c.), \tag{10.14}$$

where $\delta_{(1,N)j} = \langle n_{(1,N)}|P_M|j\rangle$ is the overlap of the end vector $n_1$ and the node $j$ in the resonant subspace.

To achieve balanced on-resonance transport we require that $\delta_{1j} = \delta_{jN}$ for all $j$, which implies that both the end-vectors have equal projections in the resonant subspace,

$$P_M |n_1\rangle = P_M |n_N\rangle . \tag{10.15}$$

## 10.B Transport Fidelity for Λ-networks

Here we derive the maximum transport fidelity for a Λ-type network. Λ-type networks are interesting because the effective Hamiltonian of more complex networks reduces to Λ-network Hamiltonian in the weak-coupling regime (as shown in the previous section), but we will consider here the general case.

For any network of adjacency matrix $A$, the fidelity function $F(t) = |\langle N| e^{-iAt} |1\rangle|^2$

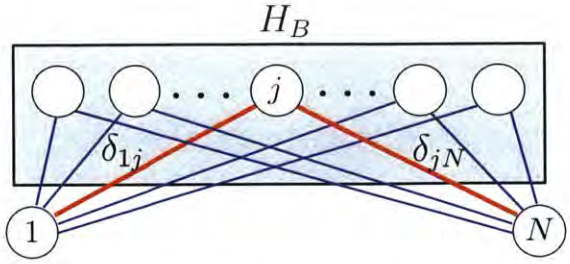


Figure 10-7: **Example of a $\Lambda$ network.** Figure shows a general detuned $\Lambda$-network with multiple $\Lambda$-paths between the end spins. Each leg of any of these $\Lambda$-paths may have an arbitrary detuning. For the representative case of the $\Lambda$-path going through node $j$ (red), these detunings are $\delta_{1j}$ and $\delta_{jN}$.

has a simple expression in the eigenbasis of $A$,

$$F(t) = \sum_{k,\ell} \langle \ell | N \rangle \langle N | k \rangle \langle k | 1 \rangle \langle 1 | \ell \rangle \cos\left(E_k - E_\ell\right) t. \tag{10.16}$$

This shows that the fidelity can be written as the sum

$$F(t) = \sum_n w_n \cos(f_n t), \qquad \text{with} \quad f_n = E_k - E_\ell, \tag{10.17}$$

that is, the frequencies are differences between eigenvalues of $A$, for which the corresponding eigenvectors $|\ell\rangle$ and $|k\rangle$ have non-zero overlap with $|1\rangle, |N\rangle$.

We now consider a general $\Lambda$-network with multiple $\Lambda$-paths that connect the end-spins (see Fig. 10-7) and we will restrict the analysis to the adjacency matrix obtained in the *on-resonance* case only later. We write the adjacency matrix in terms of the coupling strength $\delta_{1j}$ and $\delta_{jN}$ between the end spin and each $j^{th}$ spin in the

bulk, which form the $\Lambda$ path:

$$\begin{aligned} A^d &= \sum_j \Lambda_j \\ \Lambda_j &= \delta_{1j}\left(|j\rangle\langle 1| + |1\rangle\langle j|\right) + \delta_{jN}(|j\rangle\langle N| + |N\rangle\langle j|). \end{aligned} \tag{10.18}$$

Our strategy for finding the transport fidelity in $\Lambda$-networks is to first determine the eigenvalues of the adjacency matrix in Eq. (10.18) and hence the possible frequencies at which information transport can occur. Then, we will use a series expansion to find an explicit expression for the fidelity.

## 10.B.1 Frequencies of Transport

The eigenvalues of the adjacency matrix in Eq. (10.18) are

$$\begin{aligned} \lambda_0 &= 0, \qquad (N-4) \text{ degenerate} \\ \lambda_{1,2} &= \pm\sqrt{S^2 - \sqrt{S^4 - \Delta^4}}, \\ \lambda_{3,4} &= \pm\sqrt{S^2 + \sqrt{S^4 - \Delta^4}}, \end{aligned} \tag{10.19}$$

where we defined,

$$\begin{aligned} S^2 &= \sum_j S_j^2 = \sum_j \frac{1}{2}(\delta_{1j}^2 + \delta_{jN}^2) \\ \Delta^4 &= \sum_{j<k} \Delta_{jk}^4 = \sum_{j<k} (\delta_{1j}\delta_{kN} - \delta_{jN}\delta_{1k})^2 \\ \delta^2 &= \sum_j \delta_{1j}\delta_{jN} \end{aligned} \tag{10.20}$$

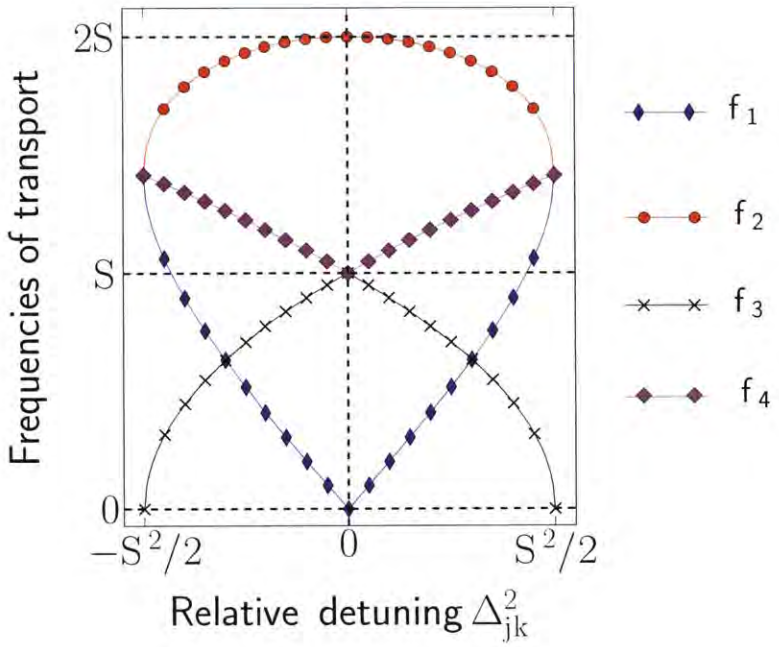


Figure 10-8: **Frequencies of quantum transport**. Figure shows the positive frequencies of transport fidelity for a $\Lambda$-network (Fig. 10-7) consisting of two $\Lambda$-paths, $1 \to j \to N$ and $1 \to k \to N$. The frequencies are plotted as a function of the relative detuning between the paths, $\Delta^2_{jk} = (\delta_{1j}\delta_{kN} - \delta_{jN}\delta_{1k})$. The actual transport also contains symmetric negative frequencies and a DC (zero frequency) component. In general there are four frequencies of transport, derived in Eq. (10.21). Note that when $\delta_{jN}/\delta_{1j}$ is a constant for both paths, there are only two frequencies, $S$ and $2S$, that carry the transport.

While for a general network the frequencies of transport are differences between the eigenvalues of $A^d$, here there are only four distinct frequencies because of the

symmetries in the eigenvalues:

$$f_0 = 0, \qquad f_1 = 2\lambda_1, \qquad f_2 = 2\lambda_3,$$

$$f_3 = \lambda_1 - \lambda_3 = \sqrt{2(S^2 - \Delta^2)},$$

$$f_4 = \lambda_1 + \lambda_3 = \sqrt{2(S^2 + \Delta^2)}.$$

## 10.B.2 Series expansion

With the frequencies found above, equation Eq. (10.17) reduces to $F(t) = \sum_{i=0}^{4} w_i \cos(f_i t)$. To find the parameters $w_i$, we equate the Taylor expansion of Eq. (10.17) and of the fidelity $F(t) = |\langle N| e^{-iAt} |1\rangle|^2$. We only need the first five even power coefficients to fully determine $\{w_i\}$, giving the series of equations,

$$\begin{aligned}
\sum_{i=0}^{4} w_i &= |\langle N|1\rangle|^2 = 0 \\
\sum_{i=1}^{4} w_i f_i^2 &= -|\langle N|A^d|1\rangle|^2 = 0 \\
\frac{1}{4!}\sum_{i=0}^{4} w_i f_i^4 &= \frac{1}{4}|\langle N| \left(A^d\right)^2 |1\rangle|^2 = \mathcal{C}_4 \\
\frac{1}{6!}\sum_{i=0}^{4} w_i f_i^6 &= -\frac{1}{24}\mathrm{Re}[\langle N| \left(A^d\right)^2 |1\rangle\langle N| \left(A^d\right)^4 |1\rangle] = \mathcal{C}_6 \\
\frac{1}{8!}\sum_{i=0}^{4} w_i f_i^8 &= \frac{1}{4!}|\langle N| \left(A^d\right)^4 |1\rangle|^2 \\
&+ \frac{1}{2\cdot 6!}\mathrm{Re}[\langle N| \left(A^d\right)^2 |1\rangle\langle N| \left(A^d\right)^6 |1\rangle] = \mathcal{C}_8
\end{aligned} \tag{10.21}$$

The expectation values can be evaluated exactly, yielding

$$\begin{aligned} \mathcal{C}_4 &= \frac{1}{4}\delta^4, \qquad \mathcal{C}_6 = -\frac{1}{12}S^2\delta^4 \\ \mathcal{C}_8 &= \frac{1}{720}\delta^2\left[9S^4 - \Delta^2\right] \end{aligned} \tag{10.22}$$

For general frequencies $f_i$, the coefficients $w_i$ are

$$\begin{aligned} w_0 &= -\sum_{j=1}^{4} w_j; \\ w_j &= \frac{\mathcal{C}_8 - \sum_{k\neq j} f_k^2\mathcal{C}_6 + \sum_{\ell<m;\ell,m\neq j} f_\ell^2 f_m^2 \mathcal{C}_4}{f_j^2\prod_{k\neq j}(f_k^2 - f_j^2)}, \qquad j > 0 \end{aligned} \tag{10.23}$$

Using the expressions for the frequencies in Eq. (10.21), we find their explicit expressions in terms of $S, \Delta$ and $\delta$:

$$w_0 = \frac{\delta^4}{4(S^4 - \Delta^4)},\ w_1 = w_2 = \frac{w_0}{2},\ w_3 = w_4 = -w_0 \tag{10.24}$$

The fidelity is thus further simplified to

$$\begin{aligned} F(t) &= \frac{\delta^4}{S^4 - \Delta^4}\left[\sin\left(t\sqrt{(S^2 + \Delta^2)/2}\right)\right. \\ &\times \left.\sin\left(t\sqrt{(S^2 - \Delta^2)/2}\right)\right]^2 \end{aligned} \tag{10.25}$$

### 10.B.3 Fidelity for random and degenerate networks

Consider the case when the number of nodes is large, and the detunings $\delta_{1j}$ and $\delta_{jN}$ are sampled from the same distribution, as it would be in a random network. Then,

$$\sum_j \delta_{1j}^2 \approx \sum_j \delta_{jN}^2 \tag{10.26}$$

since the second moments of the random distribution should be equal. In this situation we have

$$S^4 - (\Delta^4 + \delta^4) = \frac{1}{4}\left[\sum_j (\delta_{1j}^2 - \delta_{jN}^2)\right]^2 = 0 \tag{10.27}$$

Then the condition

$$\delta^4 = S^4 - \Delta^4 \tag{10.28}$$

is satisfied and the fidelity becomes

$$F(t) = \left[\sin\left(t\sqrt{(S^2+\Delta^2)/2}\right)\sin\left(t\sqrt{(S^2-\Delta^2)/2}\right)\right]^2$$

In the case of resonance to a non-degenerate mode, we have $\Delta = 0$ and the fidelity can reach its maximum $F(t) = \sin(St/\sqrt{2})^4 = 1$, for $t = \pi/\sqrt{2}S$.

For the case of interest in this work, a network where the end-spins are on resonance with a non-degenerate mode, the adjacency matrix of relevance in the weak regime is the reduced adjacency matrix, $A^d$. As shown above, in this case we have $\Delta = 0$ and the fidelity reduces to

$$F(t) = \left[\frac{\delta}{S}\sin\left(\frac{St}{\sqrt{2}}\right)\right]^4, \tag{10.29}$$

thus maximum fidelity can be reached only if the condition Eq. (10.28) is satisfied.

For example, the mirror-symmetric case $\delta_{1j} = \delta_{jN}$, $\forall j$ yields the optimal fidelity $F = 1$ since then $\delta = S$.

## 10.C Estimating matrix norms for different network topologies

### 10.C.1 Different kinds of networks

In this section, we consider different classes of networks, and estimate the norms of the corresponding adjacency matrices $A$. As described in the main text, the matrix norm of the bulk adjacency matrix is important in predicting the transport time. For example, the scaling of transport time is linear with $\gamma$ in the on-resonance case; and the value of $\gamma$ implicitly depends on the norm of the bulk matrix. Hence a large bulk matrix causes an intrinsically high $\gamma$, and reduces the control requirements on the end-spins. All the networks considered are of $N$ spins, and hence the adjacency matrices are $N \times N$ matrices.

1. *Random network* – The matrix $A$ has random entries in the range $[0, 1]$ (with appropriate symmetrization). The random entries follow a uniform distribution, with no site-to-site correlation. Overall, this case represents a rather unphysical scenario, but will be useful in the computations that follow.

2. *Random network with* $1/d^3$ *scaling* – $A$ contains random entries from a uniform distribution scaled by $1/(hd)^3$, where $h$ is the Hamming distance between two nodes. It represents a network similar to a spin chain where all neighbor connectivities are allowed, and there is a possible spread in the position of the nodes from their lattice sites.

3. *Dipolar scaled regular (symmetric) network* – We consider the network to be regular (symmetric) in two and three dimensions. With an appropriate choice of basis, this can be converted to a Bravais lattice. Special cases of interest are the graphene (honeycomb) lattice and the CNT (rolled honeycomb) lattices.

4. *Dipolar scaled regular network with vacancies* – Here we consider the regular network above and introduce vacancies that are binomially distributed with parameter $p$. This approximately maps to the NV diamond system, where we consider transport through a P1 lattice.

Note that the generalized adjacency matrix $A$ of a network consists of positive numbers in the range $[0, 1]$. This matrix is symmetric and Hermitian.

For the norm, we will use the Frobenius norm, which is the generalized Euclidean norm for matrices.

$$\|A\| = \sqrt{\sum_{i,j}^{N} |a_{ij}|^2} = \sqrt{\sum_{i}^{N} \sigma_i^2} \tag{10.30}$$

where $\sigma_i$ are the singular values of $A$.

## 10.C.2 Random network

Consider the right triangular form (R-form) of $A$,

$$A = \begin{bmatrix} 0 & \times & \times & \times & \times & \times \\ & 0 & \times & \times & \times & \times \\ & & 0 & \times & \times & \times \\ & & & 0 & \times & \times \\ & & & & 0 & \times \\ & & & & & 0 \end{bmatrix} \tag{10.31}$$

Here $\times$ refers to random numbers uniformly distributed in the range $[0, 1]$. We have $E[X^2] = \mathrm{Var}[X] + (E[X])^2 = 1/12 + 1/4 = 1/3$. The total number of elements in the R matrix is,

$$n = \sum_{j=1}^{N}(N-j) = \frac{N(N-1)}{2} \tag{10.32}$$

Hence, since the random numbers are assumed to be uncorrelated from site to site, we have,

$$\|A\| = \sqrt{\frac{N(N-1)}{3}} \tag{10.33}$$

Fig. 10-9(a) shows the linear scaling of the norm in Eq. (10.33), compared to the numerically obtained average of 100 manifestations of random networks. The highest eigenvalue of $A$, $E_{\max}$ also scales linearly with $N$.

### 10.C.3 Dipolar coupled random network

Now we consider the case where there is $1/d^3$ scaling with the Hamming distance between two nodes. This represents a network similar to a spin chain where all neighbor connectivities are allowed, and there is a possible spread in the position of the nodes from their lattice sites. The adjacency matrix has the form,

$$A = \begin{bmatrix} 0 & \frac{\times}{d^3} & \frac{\times}{(2d)^3} & \frac{\times}{(3d)^3} & \frac{\times}{(4d)^3} & \frac{\times}{(5d)^3} \\ & 0 & \frac{\times}{d^3} & \frac{\times}{(2d)^3} & \frac{\times}{(3d)^3} & \frac{\times}{(4d)^3} \\ & & 0 & \frac{\times}{d^3} & \frac{\times}{(2d)^3} & \frac{\times}{(3d)^3} \\ & & & 0 & \frac{\times}{d^3} & \frac{\times}{(2d)^3} \\ & & & & 0 & \frac{\times}{d^3} \\ & & & & & 0 \end{bmatrix} \tag{10.34}$$

As before, assuming that the sites are uncorrelated for the uniform distribution of random numbers $\times$, we have,

$$\begin{aligned} \|A\|^2 &= \frac{2}{3}\left[\frac{N-1}{d^6} + \frac{N-2}{(2d)^6} + \frac{N-3}{(3d)^6} + \cdots + \frac{1}{[(N-1)d]^6}\right] \\ &= \frac{2}{3}\left[\frac{N}{d^6}\sum_{j=1}^{N-1}\frac{1}{j^6} - \frac{1}{d^3}\sum_{j=1}^{N-1}\frac{1}{j^5}\right] \end{aligned} \tag{10.35}$$

Consider that,

$$\sum_{j=1}^{N-1}\frac{1}{j^6} \approx \frac{\pi^6}{945} = 1.01734, \sum_{j=1}^{N-1}\frac{1}{j^5} \approx 1.036 \tag{10.36}$$

and the convergence is very rapid, i.e. it is true even for small $N$. Then,

$$\|A\| \approx \frac{1}{d^3}\sqrt{\frac{2}{3}(N-1)} \tag{10.37}$$

Fig. 10-9(b) shows that the $\sqrt{N}$ scaling matches very well with the numerically obtained average norm of 100 manifestations of random dipolar networks. The highest eigenvalue $E_{\max}$ approaches a constant $1.6/d^3$.

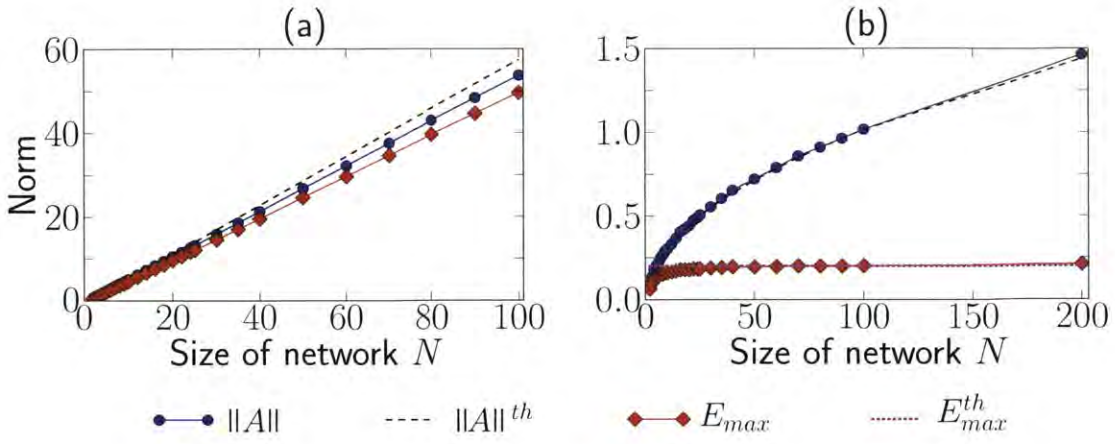


Figure 10-9: **Scaling of network norm with network size.** Figure shows the scaling with network size $N$ of the matrix norms and largest eigenmodes of the adjacency matrices corresponding to (a) a random network and (b) a dipolar random network. The solid lines are average values obtained from 100 manifestations of the networks. The dashed lines are theoretical results. For the dipolar network, the largest eigenmode $E_{\max}$ approaches a constant $1.6/d^3$ (dashed magenta line).

### 10.C.4 Dipolar coupled regular network

Here we consider a regular, symmetric network in two or three dimensions. To a good approximation, we can assume,

$$\|A\| = n\|A\|_{\text{cell}} \tag{10.38}$$

where $||A||_{\text{cell}}$ is the adjacency matrix of the unit cell of the underlying lattice, and $n$ is the number of tilings of this unit cell,

$$n \approx \frac{N}{N_{\text{cell}}} \tag{10.39}$$

where $N_{\text{cell}}$ is the number of nodes per unit cell.

$||A||_{\text{cell}}$ depends on the choice of lattice in the particular network. Let us consider the case of a honeycomb lattice, where we assume only nearest neighbor interactions. This network is found naturally in graphene and CNTs. Then, $||A||_{\text{cell}} = 24/d^3$. Hence, for graphene,

$$||A|| = \frac{2\sqrt{N}}{d^3} \tag{10.40}$$

### 10.C.5 Dipolar coupled regular network with vacancies

Let the probability of a vacancy occurring be $p$. Once again we assume a binomial distribution. We also assume, that we can estimate the norm in this case by using tiling – i.e. we consider the vacancies only in the unit cells. Consider for simplicity the special case of graphene. For $j$ vacancies, we have,

$$P_j = {}^{N_{\text{cell}}}C_j p^j (1-p)^{N_{\text{cell}}-j} \tag{10.41}$$

The corresponding adjacency matrix,

$$||A||_j = \frac{4N_{\text{cell}} - j}{d^3} \tag{10.42}$$

Hence the mean,

$$\|A\|_{\text{cell}} = \sum_j P_j \|A\|_j = \frac{4N_{\text{cell}}(1-p)}{d^3} \tag{10.43}$$

Hence,

$$\|A\| = \frac{2\sqrt{N(1-p)}}{d^3} \tag{10.44}$$

# Part V

# Appendix

# Appendix A

# The Nitrogen Vacancy Center in Diamond

### A.0.6 Optical and Coherence properties of the NV spin

The Nitrogen-Vacancy (NV) center is a localized impurity in diamond, consisting of a nitrogen substitutional atom close to a vacancy (Fig. A-1.A). High densities can be reached by implanting diamond with nitrogen ions and subsequently annealing to recombine the nitrogens with vacancies. Spin-dependent fluorescence, optical polarization and good coherence properties even at room temperature [378,379] have elicited much interest in NV centers for their applications as sensors, fluorescent biomarkers and qubits. The negatively charged $NV^-$ ground state was identified as a spin triplet in ensemble ESR experiments [380,381].

Room temperature optically detected magnetic resonance (ODMR) of a single NV spin was demonstrated in groundbreaking experiments [382,383]. Single NV centers are addressed by optical scanning confocal microscopy with excitation at 532nm and fluorescence detection over the range 650-800nm (Fig.A-1.D). The NV spin state can

be read under non-resonant illumination at room temperature using spin-dependent decay into metastable states (Fig. A-1.B). The optical excitation conserves spin as does the direct optical decay that happens in $\approx$12 ns. However, the $|\pm 1\rangle$ states can undergo spin-orbit induced inter-system crossing[384], decaying in $1/3^{\text{rd}}$ of the cases. The metastable singlet states live for $\sim$300 ns, followed by non-radiative decay to the ground state. Thus, a NV in the $|0\rangle$ state will emit approximately 15 photons, compared to only a few for a NV in the $|\pm 1\rangle$ states, yielding state discrimination by fluorescence intensity. The metastable state decays via spin-non conserving processes into the $|0\rangle$ state thereby re-orienting the spin. This reduces measurement contrast, although it allows spin polarization: laser illumination for 0.5-1$\mu$s easily achieves polarizations in excess of 95%.

The ground state of the NV electronic spin can be manipulated by on-resonance microwave fields (Fig. A-1.C). The $|0\rangle$ and $|\pm 1\rangle$ levels are separated by a zeros field splitting $\Delta \approx 2.87$GHz. A small magnetic field aligned with the NV axis splits the degeneracy between the $|\pm 1\rangle$ levels, allowing addressing one transition

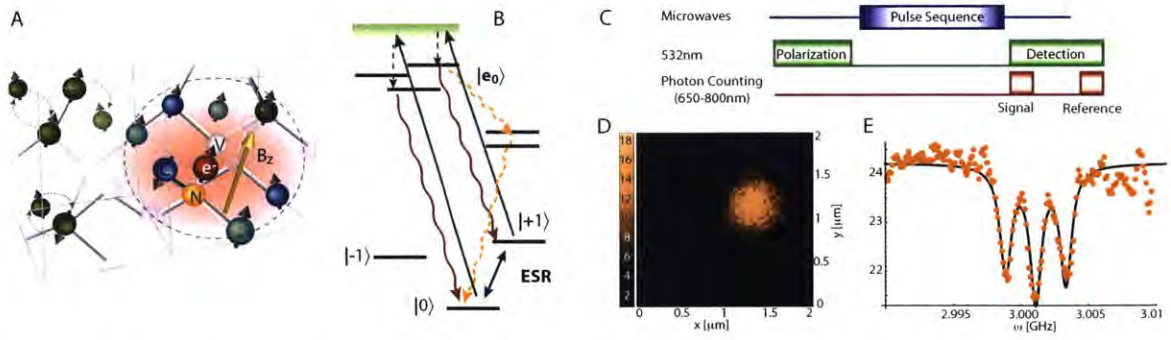


Figure A-1: **Overview of NV centers in diamond.** **(A)** NV center in the diamond lattice and nuclear and electronic spin bath. **(B)** Level structure of the NV center, showing spin and optical transitions responsible for spin polarization and readout, including metastable singlet states. **(C)** Typical experiment scheme. **(D)** Fluorescence image of NV centers by confocal spectroscopy and ODMR spectrum.

at a time. The interest in the NV center stems also from its very good coherence properties. For ultra-pure diamond, the main source of decoherence is the nuclear $^{13}C$ spin bath (1.1% natural abundance), which can be further suppressed in isotopically engineered diamonds[26,385,386]. While the free precession (Ramsey signal) dephases on a fast timescale, $T_2^* \approx 2\mu s$[84], the coherence time can be extended by using dynamical decoupling techniques[87,96] to $T_2 \approx 600\mu s$ in natural diamond[387,84,7] and up to a few milliseconds in isotopically purified diamonds[26,385,386]). The limiting factor is the $T_1$ relaxation process of NV centers. The process is generally slow thanks to low coupling to phonons . At high temperature, the dominant relaxation mechanism is due to two-phonon Orbach-type process and two-phonon Raman process, yielding relaxation times of $T_1$ ≈5-10 ms (depending on the NV and other paramagnetic impurity density). At low temperatures $T_1$ becomes temperature independent since then relaxation is mainly determined by cross relaxation with neighboring spins.

### A.0.7 Improved measurement efficiency by repeated readouts

The NV spin state can be read under non-resonant illumination at room temperature using the fact that the $m_s = \pm 1$ excited states can decay into metastable states, which live for ~300 ns. The optical excitation conserves spin as does the direct optical decay which happens in about 12 ns. Thus, a NV in the $m_s = 0$ state will emit, and absorb, approximately 15 photons, compared to only a few for a NV in the $m_s = \pm 1$ states, yielding state discrimination by fluorescence intensity. The complication is that the metastable state decays primarily via spin-non conserving processes into the $m_s = 0$ state thereby re-orienting the spin. This is good for spin polarization, but erases the spin memory and reduces measurement contrast. The detection efficiency

of the NV center spin state is thus given by $C = \left(1 + \frac{2(n_0+n_1)}{(n_0-n_1)^2}\right)^{-1/2}$[6], where $n_{1,0}$ is the number of photons collected if the NV spin is in the $m_s = \{0, 1\}$ state, respectively.

In the repeated readout scheme[42,54], the state of the nuclear spin is repetitively mapped onto the electronic spin, which is then read out under laser illumination. The measurement projects the nuclear spin state into a mixed state, but the information about its population difference is preserved, under the assumption that the measurement is a good quantum non-demolition measurement. We can include the effect of these repeated readout by defining a new detection efficiency, $C_{n_r} = \left(1 + \frac{2(n_0+n_1)}{n_r(n_0-n_1)^2}\right)^{-1/2}$, which shows an improvement $\propto \sqrt{n_r}$, where $n_r$ is the number of measurements. The sensitivity needs of course to be further modified to take into account the increased measurement time. Provided the time needed for one measurement step is smaller than the interrogation time (including the initialization time), it becomes advantageous to use repeated readouts. The maximum number of readouts is set by the nuclear spin relaxation under optical illumination, driven by non-energy conserving flip-flops in the excited states. While at high fields, this time is very long, allowing 2000 measurements in 5ms, at intermediate fields considered here $\sim$ 100 measurements can be easily achieved. Given typical values for the number of photons collected[42] ($n_0 = 0.016$, $n_1 = 0.011$, which already includes a reduction in the signal due to photoionization to the neutrally charged NV defect[388]) the collection efficiency can be improved from $C \approx 0.02$ to $C \approx 0.2$ with only a marginal increase in the readout time.

# Appendix B

# Details of Experimental Setup

## B.1 Optical Setup

Nitrogen-vacancy (NV) centers in diamond are substitutional nitrogen atom close to a vacancy in the carbon lattice[166]. The spin state of the negatively charged NV center has an exceptionally long coherence time and its electronic level structure allows efficient, all-optical spin polarization. The NV can be optically excited by a 532 nm laser light and it emits at 637 nm.

In our experiments, single NV centers are addressed using a home-built confocal microscope. The entire optical setup is drawn to scale in Fig. B-2. The setup consists of two parts: a collection circuit and an excitation circuit. For the excitation circuit, a collimated 532 nm laser (SPROUT from Lighthouse Photonics) beam is first sent through an acousto-optic modulator (AOM, Isomet Corporation, M113-aQ80L-H) for switching and then focused using an oil immersion objective (Thorlabs N100X-PFO Nikon Plan Flour 1.3NA). The AOM is is used in single pass configuration. The optical pointspread function is approximately 1 $\mu$m in X and Y and 1.5 $\mu$ m

and Z.

Note that the sample is mounted on a 3D-piezo scanner (Npoint) to position at the microscope focus with nm precision. Fig. B-1 has a detailed description of the optics around the sample state. The golden color stages refer to the coarse stage on which the sample is mounted, and below it is the Nikon 1.3 NA oil objective and a 45° mirror. The objective is mounted on a linear stage with a actuator for fine control (Zaber T-LA series). The actuator has a 12 mm working range. Above the sample stage is a three axis motorized stage for the precise alignment of the magnet.

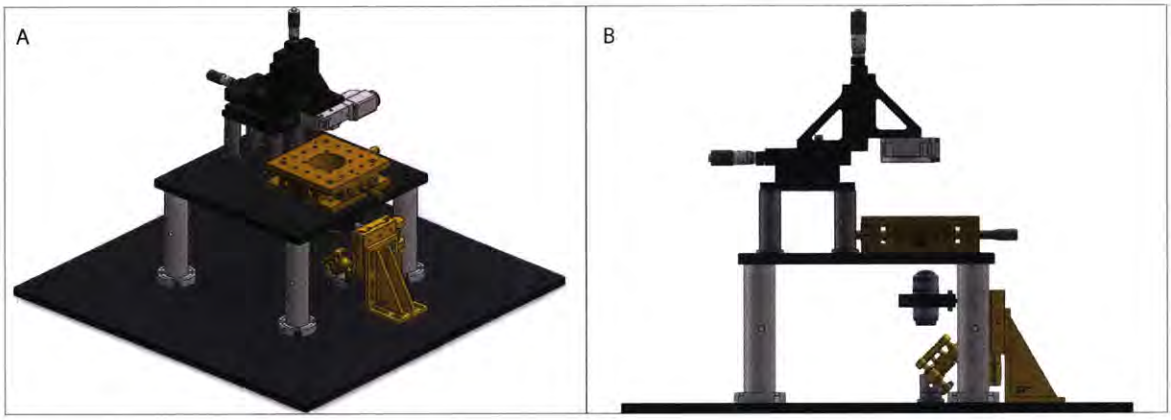


Figure B-1: **Sample mount setup.**Figures describes a detailed view of the setup near the sample mount.

For the collection circuit, the fluorescence from the nitrogen vacancy center is collected by the same objective, collimated, filtered from the 532 nm beam using a dichroic mirror (Chroma NC338988) and then focused onto a 25 $\mu$m pinhole for spatial filtering. The NV center fluorescence was filtered with a 532 nm notch filter (Semrock, BLP01-594R-25) and a 594 nm long-pass filter (Semrock, BLP01-594R-25) and collected using a single-photon counting module (Perkin Elmer SPCM-AQRH-

14). The optical setup in Fig. B-2 also contains a circuit used for sharing the laser between two optical tables.

Fig. B-3 has a detailed parts list, including manufacturers, for the various parts of the optical setup.

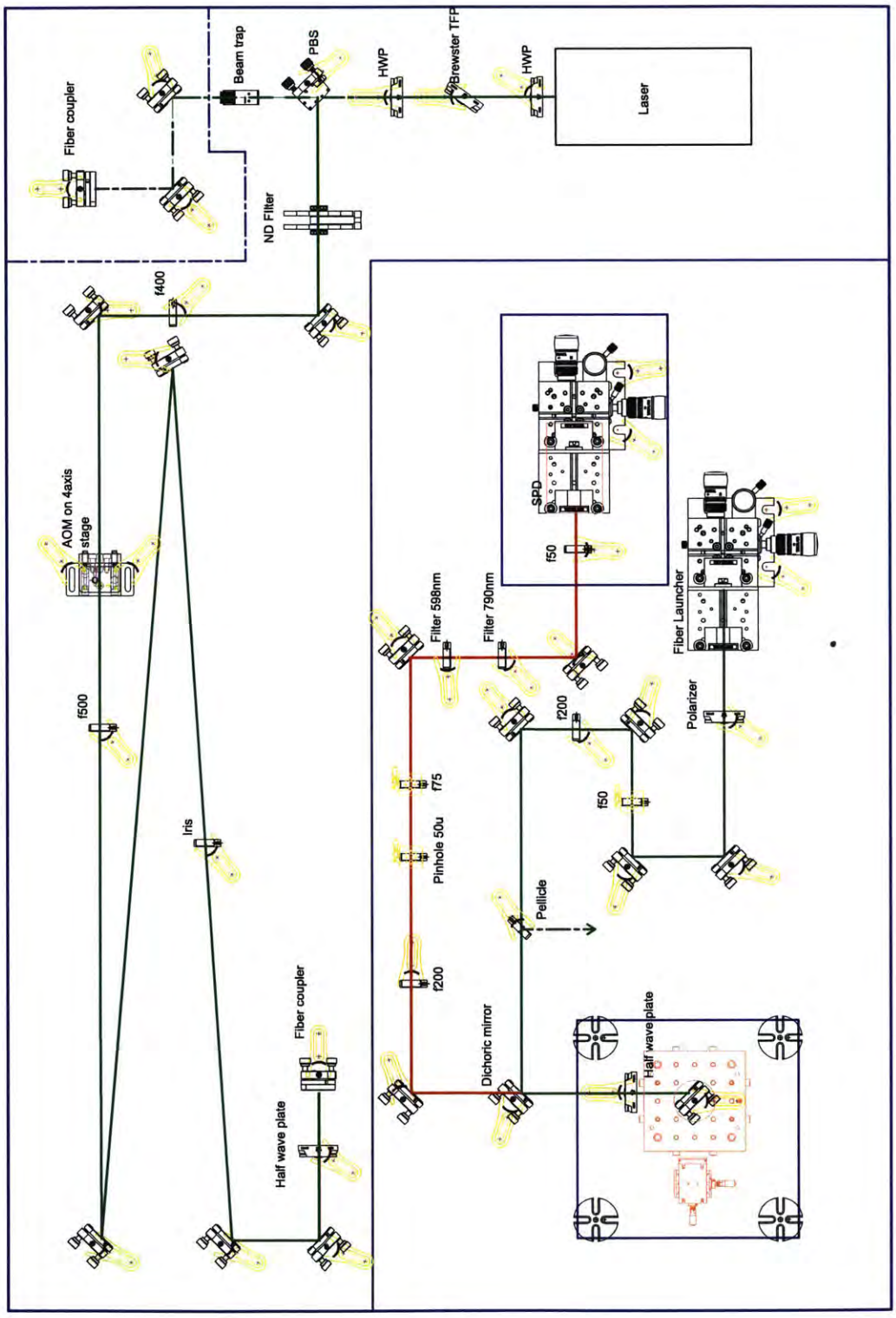




Figure B-2: **Optical setup.** Figure describes the optical set up used for single spin confocal microscopy, drawn approximately to scales with one gid point corresponding to 1 in.

| | |
|---|---|
| TOTAL for Laser Attenuation | $1,989 |
| TOTAL for Excitation circuit | $3,494 |
| TOTAL for Collection circuit | $7,366 |

| PARTS FOR LASER ATTENUTATION | Quantity | Cost/unit | Total Cost |
|---|---|---|---|
| Thorlabs WPH10M-532 Half wave plate | 1 | $ 503.00 | $ 503.00 |
| Thorlabs PBS251 Polarizing beam splitter | 1 | $ 203.00 | $ 203.00 |
| Thorlabs BT610 Beam trap | 1 | $ 290.00 | $ 290.00 |
| Thorlabs RSP1X15 Rotation mount | 1 | $ 125.00 | $ 125.00 |
| Thorlabs KM100PM Prism mount | 1 | $ 69.00 | $ 69.00 |
| Thorlabs PM3 Clamping arm for prism mount | 1 | $ 18.00 | $ 18.00 |
| Thorlabs FW1AND ND Filter wheel with 5 filters | 1 | $ 272.00 | $ 272.00 |
| Thorlabs LMR1 Lens mount | 1 | $ 15.70 | $ 15.70 |
| Thorlabs ID25 Iris | 4 | $ 53.00 | $ 212.00 |
| Thorlabs RS1P8E Pillar post | 4 | $ 21.00 | $ 84.00 |
| Thorlabs PH082E Post holder | 5 | $ 22.50 | $ 112.50 |
| Thorlabs TR1 1/2" Post | 5 | $ 4.74 | $ 23.70 |
| Thorlabs CF125 Clamping fork | 7 | $ 8.75 | $ 61.25 |
| Total | | | $1,989 |

| PARTS FOR SHARING LASER (Order Later) | Quantity | Cost/unit | Total Cost |
|---|---|---|---|
| Thorlabs CFC-5X-A FC/PC Fiber collimator | 1 | $ 225.00 | $ 225.00 |
| Thorlabs KM100T Fiber mount | 1 | $ 64.00 | $ 64.00 |
| Thorlabs AD11F Fiber mount adapter | 1 | $ 27.80 | $ 27.80 |
| Thorlabs Polaris-K1 Mirror mount | 2 | $ 129.00 | $ 258.00 |
| Thorlabs RS1P8E Pillar post | 3 | $ 21.00 | $ 63.00 |
| Thorlabs CF125 Clamping fork | 3 | $ 8.75 | $ 26.25 |
| Total | | | $664 |

| PARTS FOR EXCITATION CIRCUIT | Quantity | Cost/unit | Total Cost |
|---|---|---|---|
| Newport NewFocus 9071 4 axis stage | 1 | $ 488.00 | $ 488.00 |
| Thorlabs KM100PM Prism mount | 1 | $ 69.00 | $ 69.00 |
| Thorlabs PM3 Clamping arm | 1 | $ 18.00 | $ 18.00 |
| Thorlabs WPMH05M-532 Mounted multi-order HWP | 1 | $ 230.00 | $ 230.00 |
| Thorlabs RSP1X15 Rotation mount | 1 | $ 125.00 | $ 125.00 |
| Thorlabs C280TME-A Aspheric lens NA=0.15, f=18.4mm | 1 | $ 79.00 | $ 79.00 |
| Thorlabs SM1Z Z-axis Translation stage | 1 | $ 176.00 | $ 176.00 |
| Thorlabs CP02 Cage plate | 1 | $ 16.00 | $ 16.00 |
| Thorlabs SM1FCA FC/APC Fiber adapter plate | 1 | $ 27.00 | $ 27.00 |
| Thorlabs ER2-P4 2" Cage rod set | 1 | $ 23.20 | $ 23.20 |
| Thorlabs P3-488PM-FC-2 Single mode PM fiber FC/APC | 1 | $ 218.00 | $ 218.00 |
| Thorlabs KM100 Mirror mount | 4 | $ 39.90 | $ 159.60 |
| Thorlabs BB1-E02-10 Mirror set | 1 | $ 675.90 | $ 675.90 |
| Thorlabs BB1-E02 Mirror | 3 | $ 75.10 | $ 225.30 |
| Thorlabs LA1461-A f250 Lens | 1 | $ 27.70 | $ 27.70 |
| Thorlabs LA1433-A f150 Lens | 1 | 28.1 | $ 28.10 |
| Thorlabs LA1708-A f200 Lens | 2 | $ 27.90 | $ 55.80 |
| Thorlabs LMR1 Lens mount | 2 | $ 15.70 | $ 31.40 |
| Thorlabs ID25 Iris | 4 | $ 53.00 | $ 212.00 |
| Thorlabs RS05P8E Pillar post | 4 | $ 18.90 | $ 75.60 |
| Thorlabs RS1P8E Pillar post | 10 | $ 21.00 | $ 210.00 |
| Thorlabs PH082E Post holder | 8 | $ 22.50 | $ 180.00 |
| Thorlabs TR1 1/2" Post | 8 | $ 4.74 | $ 37.92 |
| Thorlabs CF125 Clamping fork | 12 | $ 8.75 | $ 105.00 |
| Total | | | $3,494 |

| | |
|---|---|
| TOTAL for Sample Stage | $4,466 |
| TOTAL for Optics tools and equipment | $2,594 |
| GRAND TOTAL | $19,909 |

| PARTS FOR COLLECTION CIRCUIT | Quantity | Cost/unit | Total Cost |
|---|---|---|---|
| Thorlabs MBT613D Fiber launch 3axis stage | 1 | 1,083.87 | $1,083.87 |
| Thorlabs WPH10M-532 Half wave plate | 1 | $ 503.00 | $ 503.00 |
| Thorlabs LPVISE100-A 1" Linear polarizer | 1 | $ 89.00 | $ 89.00 |
| Thorlabs RSP1X15 Rotation mount | 2 | $ 125.00 | $ 250.00 |
| Thorlabs DMLP567 dichoric mirror | 1 | $ 165.00 | $ 165.00 |
| Semrock BLP01-594R-25 594nm Long pass filter | 1 | $ 358.95 | $ 358.95 |
| Thorlabs ST1XY-D Lens mount (for pinhole) | 1 | $ 467.78 | $ 467.78 |
| Thorlabs P25S 25um pinhole | 1 | $ 63.00 | $ 63.00 |
| Thorlabs RMS20X 0.4NA Olympus Plan Achromat Objective | 1 | $ 472.00 | $ 472.00 |
| Newport 9123NF Objective holder | 1 | $ 55.88 | $ 55.88 |
| Thorlabs KM100 Mirror mount | 2 | $ 39.90 | $ 79.80 |
| Thorlabs Polaris-K1 Mirror mount | 5 | $ 129.00 | $ 645.00 |
| Newport SN100-F3K Suprema mount (for 45 deg mirror) | 1 | $ 160.00 | $ 160.00 |
| Newport PS-45-SUP 45 degree adapter | 1 | $ 30.00 | $ 30.00 |
| Thorlabs AC254-100-B Achromatic doublet f100 | 1 | $ 83.00 | $ 83.00 |
| Thorlabs AC254-075-B Achrmoatic doublet f75 | 2 | $ 83.00 | $ 166.00 |
| Thorlabs AC254-050-B Achormatic doublet f50 | 1 | $ 83.00 | $ 83.00 |
| Thorlabs LMR1 Lens mount | 6 | $ 15.70 | $ 94.20 |
| Thorlabs ID25 Iris | 8 | $ 53.00 | $ 424.00 |
| Thorlabs RS05P8E Pillar post | 4 | $ 18.90 | $ 75.60 |
| Thorlabs RS05 Pillar post extension | 3 | $ 17.00 | $ 51.00 |
| Thorlabs RS3P8E Pillar post | 8 | $ 25.50 | $ 204.00 |
| Thorlabs PH2E Post holder | 8 | $ 23.50 | $ 188.00 |
| Thorlabs TR2 1/2" Post | 8 | $ 5.19 | $ 41.52 |
| Thorlabs CF125 Clamping fork | 8 | $ 8.75 | $ 70.00 |
| Total | | | $5,904 |

| PARTS FOR SAMPLE STAGE | Quantity | Cost/unit | Total Cost |
|---|---|---|---|
| Newport M-406 XY Translation stage | 1 | $630 | $ 629.99 |
| Newport SM-13 13mm Linear travel vernier | 2 | $65.99 | $ 131.98 |
| Thorlabs PB2 post base | 4 | $26.80 | $ 107.20 |
| Thorlabs P8 8" Pillar post | 4 | $54.00 | $ 216.00 |
| Newport 360-90 90 degree bracket | 1 | $70.00 | $ 70.00 |
| Newport 423 Linear translation stage | 1 | $250.00 | $ 250.00 |
| Newport SM-25 25mm Linear travel vernier | 1 | $104.99 | $ 104.99 |
| Thorlabs MB12 12"x12" breadboard | 1 | $161.00 | $ 161.00 |
| Thorlabs N100X-PFO Nikon Plan Flour 1.3NA Objective | 1 | $2,112.00 | $2,112.00 |
| Thorlabs MOIL-30 Microscope objective oil | 1 | $45.00 | $ 45.00 |
| Edmund 58-672-RCD-05P Linear Actuator (for objective) | 1 | $638.21 | $ 638.21 |
| Total | | | $4,466 |

| GENERAL OPTICS TOOLS and EQUIPMENT | Quantity | Cost/unit | Total Cost |
|---|---|---|---|
| Thorlabs SPW301 Spanner wrench for aspheric lens | 1 | $ 14.00 | $ 14.00 |
| Thorlabs SPW602 SM1 wrench | 1 | $ 26.00 | $ 26.00 |
| Thorlabs TC2 Balldriver and hex key set | 1 | $ 88.30 | $ 88.30 |
| Thorlabs HK050 0.05" Hex key pack | 2 | $ 3.10 | $ 6.20 |
| Thorlabs 564HK 5/64" Hex key pack | 2 | $ 3.10 | $ 6.20 |
| Thorlabs HW-KIT2 1/4"-20 Capscrew kit | 1 | $ 106.10 | $ 106.10 |
| Thorlabs HW-KIT4 1/4"-20 Setscrew kit | 1 | $ 94.30 | $ 94.30 |
| Thorlabs HW-KIT1 8-32 Screw kit | 1 | $ 53.60 | $ 53.60 |
| Thorlabs HW-KIT3 8-32 Setscrew kit | 1 | $ 106.10 | $ 106.10 |
| Thorlabs TB5 Black posterboard | 2 | $ 44.00 | $ 88.00 |
| Thorlabs TB4 Black hardboard | 1 | $ 60.90 | $ 60.90 |
| Thorlabs XE25L09 9" Construction rail | 20 | $ 14.00 | $ 280.00 |
| Thorlabs MC-5 Lens tissues | 1 | $ 9.80 | $ 9.80 |
| Total | | | $940 |

Figure B-3: **Parts list for the construction of a single spin confocal microscope optical setup.** It consists of an excitation and collection circuit, sample stage for the precise alignment of the magnets and samples, and a part for the shading of the laser between optical tables. Note that this parts list also has some components for the attenuation of the 5W laser used in experiments.

## B.2 Electronics Setup

The electronic set up has undergone several modifications depending upon the particular experiments described in this thesis, and here we give a basic overview of the different instruments and how they can be interfaced.

For spin control close to zero field we use the amplifier, Miniciruicts ZHL-16W. However at high fields, we amplifiers Minicircuits LZY22+ (10-200MHz) and Minicircuits (), which provide quite easily Rabi drives exceeding 30 MHz. In order to interface this amplifier to the NV center, we use a small copper wire of diameter 25$\mu$m (Alfa Aeasr), placed about 30$\mu$m away. The wire has to be properly impedance matched, otherwise as described below and in Fig. B-6, improper matching leads to an effective differentiation of the control fields. For better impedance matching we use after the wire a 40 dB attenuator and a 50 ohm oscilloscope that acts as the effective load in the circuit.

The microwave pulses are generated by a either a combination of a pulse blaster for precise timing, microwave switch and signal generators (Stanford Research Systems SRS SG384), or alternatively by directly synthesizing the pulses using an arbitrary waveform generator (Model WX1284C, Tabor Electronics Ltd.). Fig. B-4 shows a representative example of the connections to interface the various devices. Note that while using the signal generators can we need to take into account the finite insertion loss in the channels including two switches, that are used for the X and Y channels, and connected as shown in Fig. B-4. To calibrate the pulses to a high degree of quality we use flip-flop sequences that effectively amplify the pulse error with increasing number of pulses as shown in Fig. B-5 to optimize the flip angle. Similar sequences can be derived in order to make the X and Y channels exactly

90Âř apart. Note that for this the two SRS signal sources are these locked and share a common clock and the phase of one of the signature is swept with respect to the other.

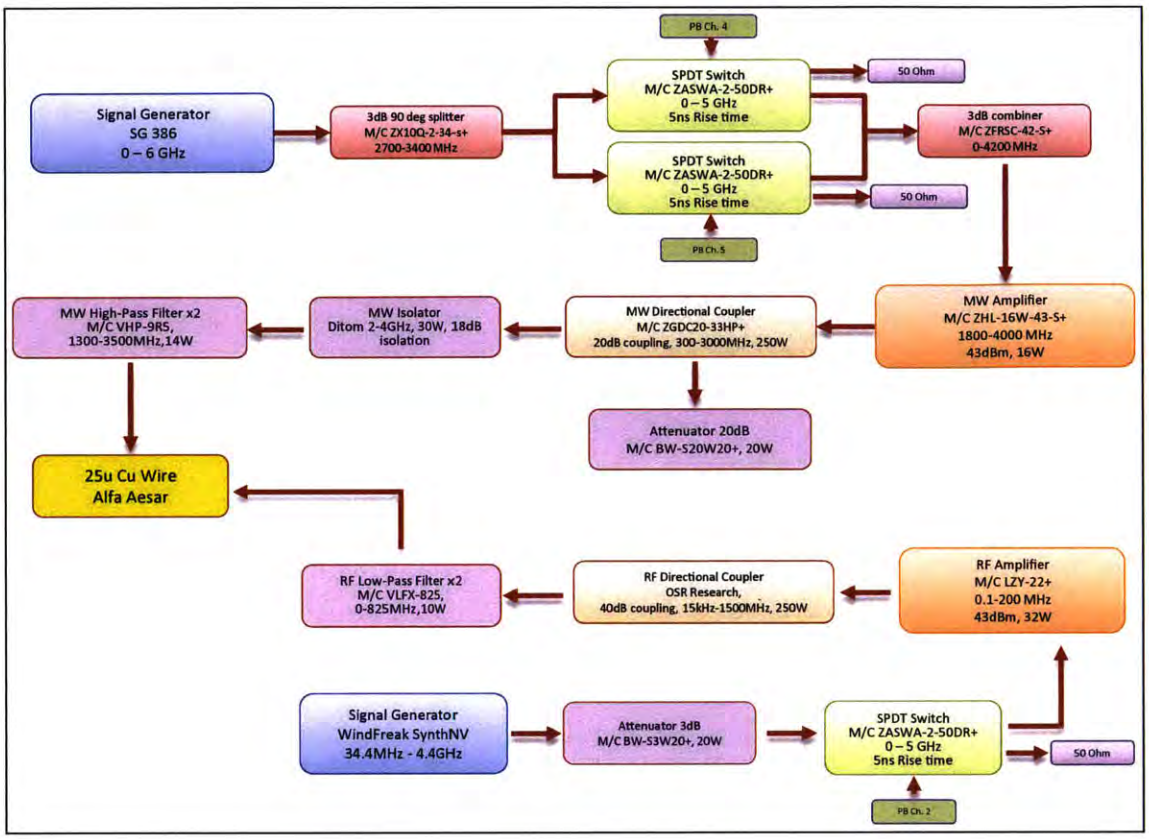


Figure B-4: **Electronics setup.** Figure shows the schematic of the electronics set up used for single spin confocal microscopy.

Direct synthesis by employing the 1.25 GS/s four channel arbitrary waveform generator allows complete phase control of the pulses, to make higher order XY8 sequences and also for KDD sequences. This also effectively eliminates the microwave switch from the circuit, and as a result the switch bouncing which is the primary cause of pulse error in the former situation can be mitigated. Note that the AWG, the AOM and the single-photon counting module are gated using TTL pulses produced

by a 500 MHz PulseBlaster (SpinCore).

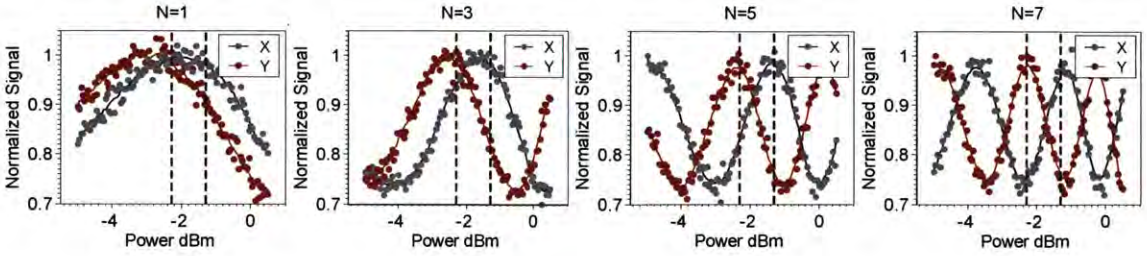


Figure B-5: **Calibration of pulses by flip-flop sequences.** Panel demonstrates the imbalance in amplitude in X and Y channels by using a 90 degree splitter. In these experiments we consider flip-flop sequences of the form $\pi/2 - [\tau - \pi - \tau]^N - \pi/2$, where $\tau$ is a sufficiently small value, $\tau = 12$ns. The pulse length is fixed at the resolution set by the pulse blaster latency, and the pulse power is swept. We expect a maximum at the optimal pulse power for all $N$ odd. The optimal power values (dashed lines) for the X and Y channels are found to differ by $\approx$ 1dB, which is a significant amplitude imbalance for increasing $N$ (panels on the right). I quantify the corresponding flip angle error to be 15%.

In order to debug impedence mismatches, we monitor the pulses on the scope 50 ohm load that allows us to monitor the pulses after they have passed through the entire circuit, and secondly we use a directional coupler with a 40 dB coupling to monitor reflections of the pulses before the wire. Note that to determine the both differentiation effect we go to close to the excited state anti-crossing point (ESLAC 510G), where we are sensitive to effective misalignment but there is no evolution of the eigenstate. Sweeping the magnetic field generated by the DC pulses through the laser readout one is able to effectively map out the control field seen by the NV

center (see Fig. B-6).

For the XY8 magnetometry experiments, the DC magnetic fields using in the evaluation of sensitivity are created through voltage source (BNC 575) driven on the same wire and combined with a bias tee (Minicircuits Z3BT-2R15G+). The experiments are done in a pulsed manner with a pulse rate about 0.5Hz, which ensures we operate within the bandwidth of the bias tee, and importantly also allows a concurrent measurement of intrinsic misalignment in alternate cycles to monitor thermal magnet drift. The applied voltage $V$ produces a proportional magnetic field used to characterize the magnetometer, $B_e = \gamma_v V$, where from the experiments in Fig. 3-5 we extract the value of $\gamma_v = 0.115 \pm 0.002$ G/V. This value also is in good agreement with an independent measurement of $\gamma_v = 0.0939$ G/V from the measured NV center Rabi frequency at 91MHz, where we ascribe the slight discrepancy to transmission loss of the wire at RF frequencies.

For the experiments to determine the low pass filter function to signal noise (Fig. 3-4), we drive a single tone of low frequency voltage from a Rigol 1000D Arbitrary function generator through the same wire, and normalize the obtained filter with the corresponding magnetometer signal under the RMS DC voltage and intrinsic misalignment (zero voltage).

In the NV spin-radar experiment, we are interested in producing very high pulsed DC magnetic fields. Note that pulsing is required because close to the GSLAC the NV florescence is quenched because of state mixing. This is demonstrated in the figure that shows the level anticrossing in an XZ scan with and without a small DC voltage. One can see that the GSLAC neck region opens up is completely quenched. To apply the strong DC pulses, we high-power MOSFETs switches that are able to provide an extremely fast rising edges of under 15 ns and falling edge of under 150ns for voltages in excess of 80V. Because of the presence of this high-voltage pulse, the

eigenstate of the NV center is effectively modified.

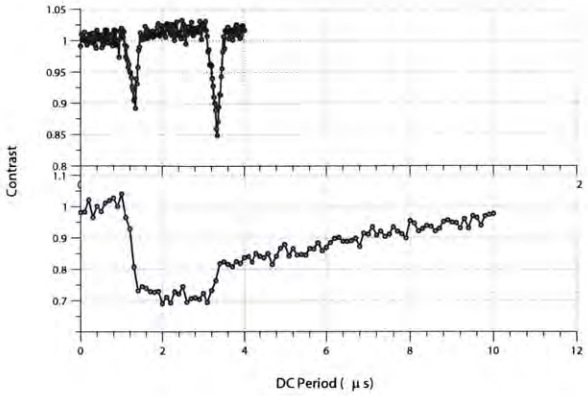


Figure B-6: **Measurements at 500G sweeping the readout laser across the DC field.** We get a differentiated output (red trace). This was because of impedence mismatch, which when fixed reflects the DC field in the PL.

## B.3 Magnet Setup

In this section, we present details of the magnet construction and alignment procedure close to the GSLAC (see Fig. 3-7). The magnet is a composite assembly of 10 N52 cubic magnets of 9.53mm edge (K&J Magnetics B666-N52) and 1.48T surface magnetization. We define X to be the magnetization axis of the magnet assembly, and is placed parallel to the edge of the [100] diamond. The magnet is a mounted on a stage controlled by motorized actuators (Zaber TNA08A50) for translation in X,Y and Z.

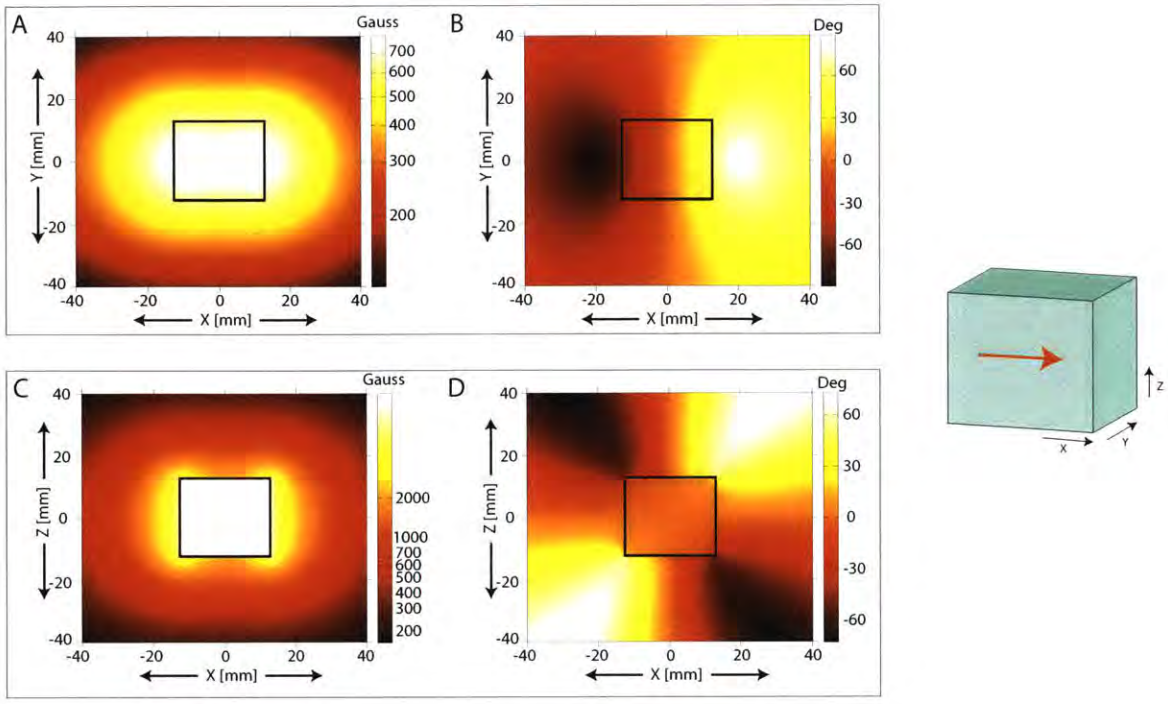


Figure B-7: **Simulated magnetic field lines in XY and XZ plots for a cubic 1 inch magnet.** In the left panels are plotted the the strength of the magnetic field (in gauss) and the right panels show the corresponding angle of the field in degrees. The origin is assumed to be the center of the magnet

To align the magnet near the GSLAC (1020G), we exploit the fact that the NV center photoluminescence (PL) gets quenched with increasing misalignment due to mixing of levels in the excited state[154,115] (Fig. 3-7(**B**)). Translating the magnet in X and Y, and optimizing to the position of maximum photoluminescence leads to an alignment to better than 1°. An experimental 2D XZ map of NV photoluminescence illustrates this more clearly, (Fig. 3-7(**C**)), the narrow neck corresponding to the GSLAC. Indeed the extracted widths of the PL as a function of the magnet height

(Z) (Fig. 3-7(**C**)) indicates that the GSLAC neck could be narrower than 5$\mu$m.

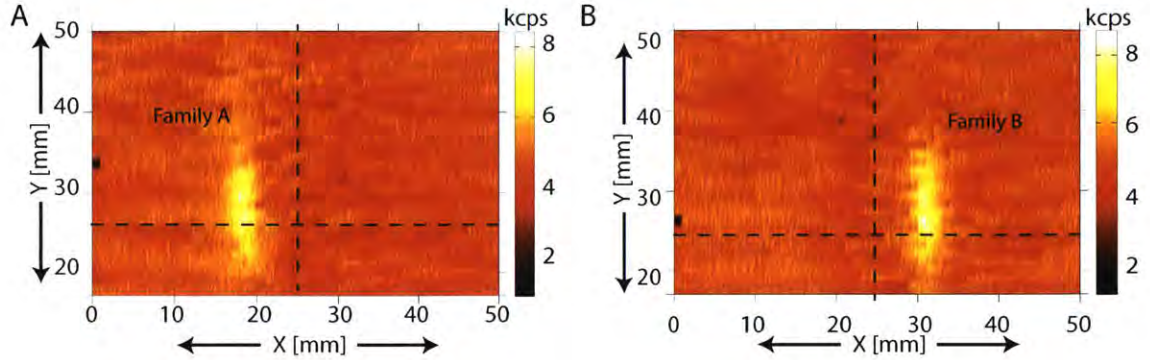


Figure B-8: **Experimentally obtained photoluminescence for two different families of NV centers in an XY scan.** Note that the center of the magnet is approximately at (25.4, 25.4). The NV families arise on either side of the center since we employ infringing fields in order to align the magnetic field. The field in these plots is approximately 700G.

The NV center Larmor frequency $\Delta$ changes linearly as a function of the magnet height, and can be made to approach zero close to the GSLAC (Fig. 3-7(**D**)). We attribute this to the approximate linear field lines given the small dimensions of the neck region compared to the size of the magnet. To further optimize the alignment to the level of the earth's field ($<$ 1G), we employ a gradient ascent algorithm that optimizes to the highest photoluminescence in the GSLAC neck region (shaded), and extrapolate linearly away from this region, once again exploiting the linear dependence of NV Larmor frequency. The small PL variance in the GSLAC neck ensures that the alignment procedure is reproducible and of low error (Fig. 3-7(**E**)). We note that when aligned the $^{14}$N nuclear spin is completely polarized

through a hyperfine mediate optical process [155], further increasing the signal contrast obtained in the magnetometry experiments.

The amount of misalignment can be accurately measured through an XY8 experiment, sweeping the number of pulses and extracting the frequency $f_0$ of the resulting oscillations (Fig. 3-8), following $B_\perp = \tan(f_0/2)\frac{\Delta\omega_L}{\gamma_e A_\perp}$. We are reproducibly able to align the field to better than 0.5G, this $\sim 0.05\%$ residual level largely being set by the magnetic field of the earth (there is no shielding in our experiment). Translating the magnet in X also allows the controllable addition of misalignment, the amount of which also goes approximately linearly, and enables us to perform experiments to quantify the effect of residual earth's field on the sensor dynamic range (Appendix 3.D).

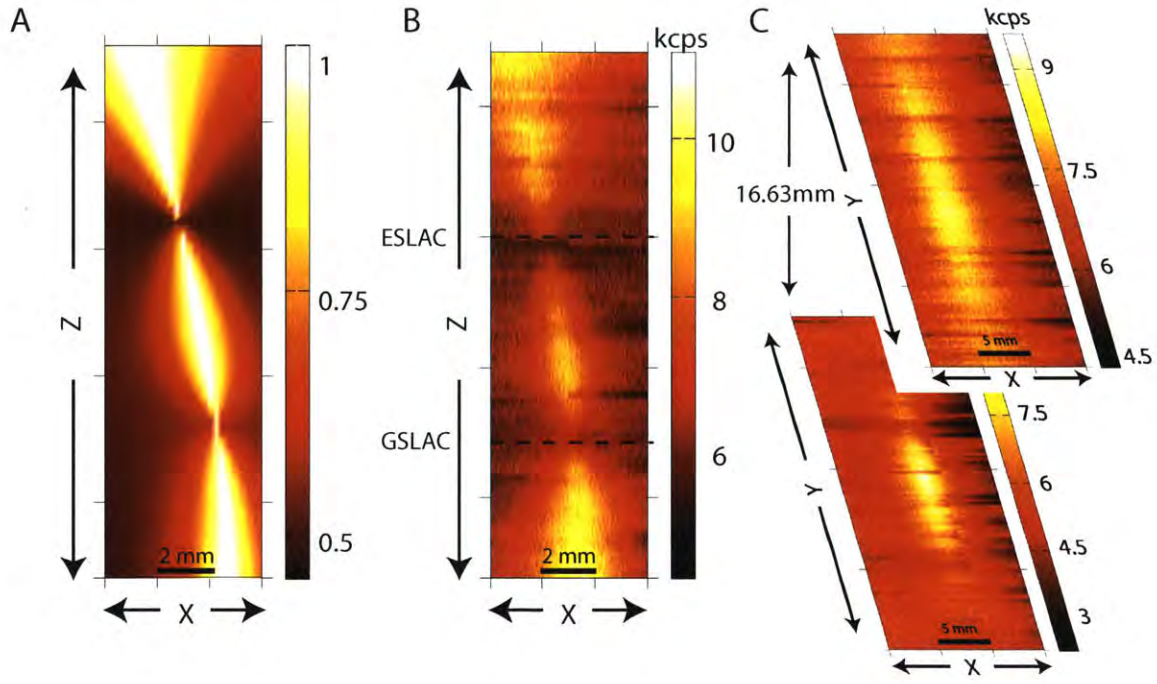


Figure B-9: **Photoluminescence (PL) from a single nitrogen vacancy center under a magnet XZ scan.** (A) Panel describes the theoretically estimated PL, where the where the two necks correspond to the excited state anti-crossing point (ESLAC) at 510G and the the ground state anti crossing (GSLAC) at 1020G. (B) Panel B shows the experimentally obtained PL. (C) Figure describes the XY PL scans for two different slices separated by 16.63 mm. We notice that the photoluminescence becomes broader as one moves away from the anti-crossing points, allowing one to align the fee very precisely at the LACs.

# Bibliography


1. S. Lloyd, Science **321**, 1463 (2008).

2. A. Ajoy, Y. Liu, J.-C. Jaskula, K. Saha, L. Marseglia, and P. Cappellaro, (to be published) (2015).

3. B. T. Wimberly, D. E. Brodersen, W. M. Clemons, R. J. Morgan-Warren, A. P. Carter, C. Vonrhein, T. Hartsch, and V. Ramakrishnan, Nature **407**, 327 (2000).

4. M. Auer, Journal of molecular medicine **78**, 191 (2000).

5. K. Wuthrich, *NMR of proteins and nucleic acids* (Wiley, 1986).

6. J. M. Taylor, P. Cappellaro, L. Childress, L. Jiang, D. Budker, P. R. Hemmer, A. Yacoby, R. Walsworth, and M. D. Lukin, Nature Phys. **4**, 810 (2008).

7. J. R. Maze, P. L. Stanwix, J. S. Hodges, S. Hong, J. M. Taylor, P. Cappellaro, L. Jiang, A. Zibrov, A. Yacoby, R. Walsworth, and M. D. Lukin, Nature **455**, 644 (2008).

8. G. Balasubramanian, I.-Y. Chan, R. Kolesov, M. Al-Hmoud, C. Shin, C. Kim, A. Wojcik, P. R. Hemmer, A. Krüger, F. Jelezko, and J. Wrachtrup, Nature **445**, 648 (2008).

9. J. Cai, F. Jelezko, M. B. Plenio, and A. Retzker, New Journal of Physics **15**, 013020 (2013).

10. L. T. Hall, G. C. G. Beart, E. A. Thomas, D. A. Simpson, L. P. McGuinness, J. H. Cole, J. H. Manton, R. E. Scholten, F. Jelezko, J. Wrachtrup, S. Petrou, and L. C. L. Hollenberg, Sci. Rep. **2**, (2012).

11. A. Cooper, E. Magesan, H. Yum, and P. Cappellaro, Nat Commun **5**, 3141 (2014).

12. D. Le Sage, K. Arai, D. R. Glenn, S. J. DeVience, L. Pham, L. M .and Rahn-Lee, M. D. Lukin, A. Yacoby, A. Komeili, and R. L. Walsworth, Nature **496**, 486 (2013).

13. T. H. Taminiau, J. J. T. Wagenaar, T. van der Sar, F. Jelezko, V. V. Dobrovitski, and R. Hanson, Phys. Rev. Lett. **109**, 137602 (2012).

14. S. Kolkowitz, Q. P. Unterreithmeier, S. D. Bennett, and M. D. Lukin, Phys. Rev. Lett. **109**, 137601 (2012).

15. N. Zhao, S.-W. Ho, and R.-B. Liu, Phys. Rev. B **85**, 115303 (2012).

16. H. J. Mamin, M. Kim, M. H. Sherwood, C. T. Rettner, K. Ohno, D. D. Awschalom, and D. Rugar, Science **339**, 557 (2013).

17. T. Staudacher, F. Shi, S. Pezzagna, J. Meijer, J. Du, C. A. Meriles, F. Reinhard, and J. Wrachtrup, Science **339**, 561 (2013).

18. K. Ohashi, T. Rosskopf, H. Watanabe, M. Loretz, Y. Tao, R. Hauert, S. Tomizawa, T. Ishikawa, J. Ishi-Hayase, S. Shikata, C. L. Degen, and K. M. Itoh, Nano Letters **13**, 4733 (2013).

19. H. J. Mamin, M. H. Sherwood, M. Kim, C. T. Rettner, K. Ohno, D. D. Awschalom, and D. Rugar, ArXiv e-prints (2014), arXiv:1404.7480 [cond-mat.mes-hall] .

20. M. Loretz, T. Rosskopf, J. M. Boss, S. Pezzagna, J. Meijer, and C. L. Degen, Science (2014).

21. M. Grinolds, M. Warner, K. De Greve, Y. Dovzhenko, L. Thiel, R. Walsworth, S. Hong, P. Maletinsky, and A. Yacoby, Nature Nanotechnology **9**, 279 (2014).

22. A. Ermakova, G. Pramanik, J.-M. Cai, G. Algara-Siller, U. Kaiser, T. Weil, Y.-K. Tzeng, H.-C. Chang, L. P. McGuinness, M. B. Plenio, *et al.*, Nano letters **13**, 3305 (2013).

23. S. Kaufmann, D. A. Simpson, L. T. Hall, V. Perunicic, P. Senn, S. Steinert, L. P. McGuinness, B. C. Johnson, T. Ohshima, F. Caruso, *et al.*, Proceedings of the National Academy of Sciences **110**, 10894 (2013).

24. A. O. Sushkov, I. Lovchinsky, N. Chisholm, R. L. Walsworth, H. Park, and M. D. Lukin, Phys. Rev. Lett. **113**, 197601 (2014).

25. B. Wu, E. Y. T. Chien, C. D. Mol, G. Fenalti, W. Liu, V. Katritch, R. Abagyan, A. Brooun, P. Wells, F. C. Bi, D. J. Hamel, P. Kuhn, T. M. Handel, V. Cherezov, and R. C. Stevens, Science **330**, 1066 (2010).

26. G. Balasubramanian, P. Neumann, D. Twitchen, M. Markham, R. Kolesov, N. Mizuochi, J. Isoya, J. Achard, J. Beck, J. Tissler, V. Jacques, P. R. Hemmer, F. Jelezko, and J. Wrachtrup, Nat Mater **8**, 383 (2009).

27. T. Staudacher, F. Ziem, L. Häussler, R. Stöhr, S. Steinert, F. Reinhard, J. Scharpf, A. Denisenko, and J. Wrachtrup, Appl. Phys. Lett. **101**, 212401 (2012).

28. M. Hirose, C. D. Aiello, and P. Cappellaro, Phys. Rev. A **86**, 062320 (2012).

29. M. Loretz, T. Rosskopf, and C. L. Degen, Phys. Rev. Lett. **110**, 017602 (2013).

30. A. Ajoy and P. Cappellaro, Phys. Rev. Lett. **110**, 220503 (2013).

31. S. Meiboom and D. Gill, Rev. Sc. Instr. **29**, 688 (1958).

32. M. J. Biercuk, A. C. Doherty, and H. Uys, J. of Phys. B **44**, 154002 (2011).

33. A. Ajoy, G. A. Álvarez, and D. Suter, Phys. Rev. A **83**, 032303 (2011).

34. P. London, J. Scheuer, J.-M. Cai, I. Schwarz, A. Retzker, M. Plenio, M. Katagiri, T. Teraji, S. Koizumi, J. Isoya, *et al.*, Physical review letters **111**, 067601 (2013).

35. C. Belthangady, N. Bar-Gill, L. M. Pham, K. Arai, D. Le Sage, P. Cappellaro, and R. L. Walsworth, Phys. Rev. Lett. **110**, 157601 (2013).

36. S. R. Hartmann and E. L. Hahn, Phys. Rev. **128**, 2042 (1962).

37. A. Henstra, P. Dirksen, J. Schmidt, and W. Wenckebach, J. Mag. Res. **77**, 389 (1988).

38. C. L. Degen, M. Poggio, H. J. Mamin, C. T. Rettner, and D. Rugar, Proc. Nat. Acad. Sc. **106**, 1313 (2009).

39. K. Arai, D. Le Sage, S. J. DeVience, D. R. Glenn, L. M. Pham, L. Rahn-Lee, M. D. Lukin, A. Yacoby, A. Komeili, and R. L. Walsworth, Biophysical Journal **104**, 193a (2013).

40. M. Schaffry, E. M. Gauger, J. J. L. Morton, and S. C. Benjamin, Phys. Rev. Lett. **107**, 207210 (2011).

41. M. A. Nielsen and I. L. Chuang, *Quantum computation and quantum information* (Cambridge University Press, Cambridge; New York, 2000).

42. L. Jiang, J. S. Hodges, J. R. Maze, P. Maurer, J. M. Taylor, D. G. Cory, P. R. Hemmer, R. L. Walsworth, A. Yacoby, A. S. Zibrov, and M. D. Lukin, Science **326**, 267 (2009).

43. P. Cappellaro, L. Jiang, J. S. Hodges, and M. D. Lukin, Phys. Rev. Lett. **102**, 210502 (2009).

44. T. van der Sar, Z. Wang, M. Blok, H. Bernien, T. Taminiau, D. Toyli, D. Lidar, D. Awschalom, R. Hanson, and V. Dobrovitski, Nature **484**, 82 (2012).

45. G. Waldherr, J. Beck, P. Neumann, R. Said, M. Nitsche, M. Markham, D. J. Twitchen, J. Twamley, F. Jelezko, and J. Wrachtrup, Nat Nano **7**, 105 (2012).

46. J. Waugh, L. Huber, and U. Haeberlen, Phys. Rev. Lett. **20**, 180 (1968).

47. G. R. Khutsishvili, Sov. Phys. Uspekhi **8**, 743 (1966).

48. W. P. Aue, E. Bartholdi, and R. R. Ernst, J. Chem. Phys. **64**, 2229 (1976).

49. A. Laraoui, F. Dolde, C. Burk, F. Reinhard, J. Wrachtrup, and C. A. Meriles, Nature communications **4**, 1651 (2013).

50. M. Kainosho, T. Torizawa, Y. Iwashita, T. Terauchi, A. Mei Ono, and P. Guntert, Nature **440**, 52 (2006).

51. A. O. Sushkov, N. Chisholm, I. Lovchinsky, M. Kubo, P. K. Lo, S. D. Bennett, D. Hunger, A. Akimov, R. L. Walsworth, H. Park, and M. D. Lukin, ArXiv e-prints , 1311.1801 (2013).

52. E. M. Kessler, I. Lovchinsky, A. O. Sushkov, and M. D. Lukin, Phys. Rev. Lett. **112**, 150802 (2014).

53. M. E. Trusheim, L. Li, A. Laraoui, E. H. Chen, O. Gaathon, H. Bakhru, T. Schroder, C. A. Meriles, and D. Englund, Nano Letters **1**, 32 (2013).

54. P. Neumann, J. Beck, M. Steiner, F. Rempp, H. Fedder, P. R. Hemmer, J. Wrachtrup, and F. Jelezko, Science **5991**, 542 (2010).

55. A. Ajoy and P. Cappellaro, Phys. Rev. A **86**, 062104 (2012).

56. K. Ohno, F. Joseph Heremans, L. C. Bassett, B. A. Myers, D. M. Toyli, A. C. Bleszynski Jayich, C. J. Palmstrom, and D. D. Awschalom, Appl. Phys. Lett. **101**, 082413 (2012).

57. C. Osterkamp, J. Scharpf, S. Pezzagna, J. Meijer, T. Diemant, R. Jurgen Behm, B. Naydenov, and F. Jelezko, Appl. Phys. Lett. **103**, 193118 (2013).

58. B. Naydenov, V. Richter, J. Beck, M. Steiner, P. Neumann, G. Balasubramanian, J. Achard, F. Jelezko, J. Wrachtrup, and R. Kalish, App. Phys. Lett. **96**, 163108 (2010).

59. B. Naydenov, F. Dolde, L. T. Hall, C. Shin, H. Fedder, L. C. L. Hollenberg, F. Jelezko, and J. Wrachtrup, Phys. Rev. B **83**, 081201 (2011).

60. G. de Lange, Z. H. Wang, D. RistÃÍ, V. V. Dobrovitski, and R. Hanson, Science **330**, 60 (2010).

61. M. Suzuki, Communications in Mathematical Physics **51**, 183 (1976), 10.1007/BF01609348.

62. U. Haeberlen and J. Waugh, Phys. Rev. **175**, 453 (1968).

63. A. Ajoy and P. Cappellaro, Phys. Rev. B **87**, 064303 (2013).

64. R. B. G. Ravelli, M. L. Raves, Z. Ren, D. Bourgeois, M. Roth, J. Kroon, I. Silman, and J. L. Sussman, Acta Crystallographica Section D **54**, 1359 (1998).

65. H. Haviv, D. M. Wong, H. M. Greenblatt, P. R. Carlier, Y.-P. Pang, I. Silman, and J. L. Sussman, J. Am. Chem. Soc. **127**, 11029 (2005).

66. M. Harel, I. Schalk, L. Ehret-Sabatier, F. Bouet, M. Goeldner, C. Hirth, P. H. Axelsen, I. Silman, and J. L. Sussman, Proc. Nat. Acad. Sc. **90**, 9031 (1993).

67. D. Du and P. Carlier, Curr Pharm Des **10**, 3141 (2004).

68. H. Fedder, F. Dolde, F. Rempp, T. Wolf, P. Hemmer, F. Jelezko, and J. Wrachtrup, Applied Physics B: Lasers and Optics **102**, 497 (2011).

69. J. Cai, B. Naydenov, R. Pfeiffer, L. P. McGuinness, K. D. Jahnke, F. Jelezko, M. B. Plenio, and A. Retzker, New Journal of Physics **14**, 113023 (2012).

70. P. Mansfield, M. J. Orchard, D. C. Stalker, and K. H. B. Richards, Phys. Rev. B **7**, 90 (1973).

71. J. R. Maze, J. M. Taylor, and M. D. Lukin, Phys. Rev. B **78**, 094303 (2008).

72. A. Ajoy, R. K. Rao, A. Kumar, and P. Rungta, Phys. Rev. A **85**, 030303 (2012).

73. A. Fruchter and R. N. Hook, in *Optical Science, Engineering and Instrumentation'97* (International Society for Optics and Photonics, 1997) pp. 120–125.

74. V. Giovannetti, S. Lloyd, and L. Maccone, Phys. Rev. Lett. **96**, 010401 (2006).

75. S. Kotler, N. Akerman, Y. Glickman, A. Keselman, and R. Ozeri, Nature **473**, 61 (2011).

76. F. Yan, J. Bylander, S. Gustavsson, F. Yoshihara, K. Harrabi, D. G. Cory, T. P. Orlando, Y. Nakamura, J.-S. Tsai, and W. D. Oliver, Phys. Rev. B **85**, 174521 (2012).

77. J. Bylander, S. Gustavsson, F. Yan, F. Yoshihara, K. Harrabi, G. Fitch, D. G. Cory, and W. D. Oliver, Nature Physics **7**, 565?570 (2011).

78. G. A. Álvarez and D. Suter, Phys. Rev. Lett. **107**, 230501 (2011).

79. N. Bar-Gill, L. Pham, C. Belthangady, D. Le Sage, P. Cappellaro, J. Maze, M. Lukin, A. Yacoby, and R. Walsworth, Nat. Commun. **3**, 858 (2012).

80. Y. Romach, C. Müller, T. Unden, L. Rogers, T. Isoda, K. M. Itoh, M. Markham, A. Stacey, J. Meijer, S. Pezzagna, *et al.*, Physical review letters **114**, 017601 (2015).

81. F. Shi, Q. Zhang, P. Wang, H. Sun, J. Wang, X. Rong, M. Chen, C. Ju, F. Reinhard, H. Chen, *et al.*, Science **347**, 1135 (2015).

82. I. Lovchinsky, A. Sushkov, E. Urbach, N. de Leon, S. Choi, K. De Greve, R. Evans, R. Gertner, E. Bersin, C. Müller, *et al.*, Science **351**, 836 (2016).

83. B. A. Myers, A. Das, M. Dartiailh, K. Ohno, D. D. Awschalom, and A. B. Jayich, Physical review letters **113**, 027602 (2014).

84. L. Childress, M. V. Gurudev Dutt, J. M. Taylor, A. S. Zibrov, F. Jelezko, J. Wrachtrup, P. R. Hemmer, and M. D. Lukin, Science **314**, 281 (2006).

85. A. Abragam, *Principles of Nuclear Magnetism* (Oxford Univ. Press, 1961).

86. K. Khodjasteh and D. A. Lidar, Phys. Rev. A **75**, 062310 (2007).

87. E. L. Hahn, Phys. Rev. **80**, 580 (1950).

88. H. Y. Carr and E. M. Purcell, Phys. Rev. **94**, 630 (1954).

89. H. Baker, Proc Lond Math Soc **1**, 34 (1902).

90. W. Magnus, Communications on Pure and Applied Mathematics **7**, 649 (1954).

91. U. Haeberlen, *High Resolution NMR in Solids: Selective Averaging* (Academic Press Inc., New York, 1976).

92. *AWG70001A Data Sheet* ().

93. *AWG5002C Data Sheet* ().

94. *wx1284c Data Sheet*.

95. *PB-ESR Pro Data Sheet*.

96. L. Viola and S. Lloyd, Phys. Rev. A **58**, 2733 (1998).

97. L. Cywiński, W. M. Witzel, and S. Das Sarma, Phys. Rev. Lett. **102**, 057601 (2009).

98. G. A. Álvarez, A. Ajoy, X. Peng, and D. Suter, Phys. Rev. A **82**, 042306 (2010).

99. A. Ajoy and P. Cappellaro, Phys. Rev. A **85**, 042305 (2012).

100. A. S. Householder, J. Assoc. Comput. Mach. **5** (1958).

101. M. Loretz, J. Boss, T. Rosskopf, H. Mamin, D. Rugar, and C. Degen, Physical Review X **5**, 021009 (2015).

102. M. Loretz, S. Pezzagna, J. Meijer, and C. Degen, Applied Physics Letters **104**, 033102 (2014).

103. D. Rugar, H. Mamin, M. Sherwood, M. Kim, C. Rettner, K. Ohno, and D. Awschalom, Nature nanotechnology **10**, 120 (2015).

104. M. Chen, M. Hirose, P. Cappellaro, *et al.*, Physical Review B **92**, 020101 (2015).

105. A. Ajoy, U. Bissbort, M. Lukin, R. Walsworth, and P. Cappellaro, Phys. Rev. X **5**, 011001 (2015).

106. R. Ernst, G. Bodenhausen, and A. Wokaun, *Principles of nuclear magnetic resonance in one and two dimensions* (Clarendon Press Oxford, 1987).

107. T. Van der Sar, F. Casola, R. Walsworth, and A. Yacoby, Nature Communications **6** (2015).

108. A. Serga, A. Chumak, and B. Hillebrands, Journal of Physics D: Applied Physics **43**, 264002 (2010).

109. S. R. Hartman and E. L. Hahn, Phys. Rev. **128**, 2042 (1962).

110. A. Pines, M. G. Gibby, and J. S. Waugh, J. Chem. Phys. **59**, 569 (1973).

111. X. Kong, A. Stark, J. Du, L. P. McGuinness, and F. Jelezko, Physical Review Applied **4**, 024004 (2015).

112. W. Ma, F. Shi, K. Xu, P. Wang, X. Xu, X. Rong, C. Ju, C.-K. Duan, N. Zhao, and J. Du, Physical Review A **92**, 033418 (2015).

113. J. Casanova, Z.-Y. Wang, J. Haase, and M. Plenio, Physical Review A **92**, 042304 (2015).

114. T. Staudacher, N. Raatz, S. Pezzagna, J. Meijer, F. Reinhard, C. Meriles, and J. Wrachtrup, Nature communications **6** (2015).

115. T. Van der Sar, F. Casola, R. Walsworth, and A. Yacoby, Nature Communications **6** (2015).

116. L. Trifunovic, F. L. Pedrocchi, S. Hoffman, P. Maletinsky, A. Yacoby, and D. Loss, Nature nanotechnology **10**, 541 (2015).

117. L. Liu, C.-F. Pai, Y. Li, H. Tseng, D. Ralph, and R. Buhrman, Science **336**, 555 (2012).

118. P. Hemmer, Science **339**, 529 (2013).

119. D. Le Sage, L. M. Pham, N. Bar-Gill, C. Belthangady, M. D. Lukin, A. Yacoby, and R. L. Walsworth, Phys. Rev. B **85**, 121202 (2012).

120. J. Clarke and A. I. Braginski, *The SQUID handbook* (Wiley Online Library, 2004).

121. I. Kominis, T. Kornack, J. Allred, and M. Romalis, Nature **422**, 596 (2003).

122. D. Budker and M. Romalis, Nature Phys. **3**, 227 (2007).

123. T. Wolf, P. Neumann, K. Nakamura, H. Sumiya, T. Ohshima, J. Isoya, and J. Wrachtrup, Physical Review X **5**, 041001 (2015).

124. M. S. Keshner, Proceedings of the IEEE **70**, 212 (1982).

125. J. P. Wikswo, J. P. Barach, and J. A. Freeman, Science **208**, 53 (1980).

126. J. Barry, M. Turner, J. Schloss, D. Glenn, Y. Song, M. Lukin, H. Park, and R. Walsworth, ArXiv:1602.01056 (2016).

127. K. Jensen, R. Budvytyte, R. A. Thomas, T. Wang, A. Fuchs, M. V. Balabas, G. Vasilakis, L. Mosgaard, T. Heimburg, S.-P. Olesen, and E. S. Polzik, ArXiv::1601.03273 (2016).

128. Y. Wang, J. Kirtley, F. Katmis, P. Jarillo-Herrero, J. Moodera, and K. Moler, Science **349**, 948 (2015).

129. B. Dellabetta, T. L. Hughes, M. J. Gilbert, and B. L. Lev, Physical Review B **85**, 205442 (2012).

130. N. F. Ramsey, *Molecular Beams* (Oxford University Press, 1990).

131. J. Van Wyk, E. Reynhardt, G. High, and I. Kiflawi, Journal of Physics D: Applied Physics **30**, 1790 (1997).

132. J. H. Scofield, American Journal of Physics **62**, 129 (1994).

133. W. Hill and P. Horowitz, *The art of electronics* (Cambridge University Press, 2015).

134. B. Shields, Q. Unterreithmeier, N. De Leon, H. Park, and M. Lukin, Physical review letters **114**, 136402 (2015).

135. A. Ajoy, Y. Liu, K. Saha, L. Marseglia, J.-C. Jaskula, U. Bissbort, and P. Cappellaro, ArXiv:1604.01677 (2016).

136. J. H. Shim, B. Nowak, I. Niemeyer, J. Zhang, F. D. Brandao, and D. Suter, arXiv:1307.0257 (2013).

137. T. Gullion, D. B. Baker, and M. S. Conradi, J. Mag. Res. **89**, 479 (1990).

138. S. Kolkowitz, Q. P. Unterreithmeier, S. D. Bennett, and M. D. Lukin, Phys. Rev. Lett. **109**, 137601 (2012).

139. J. T. Hill, A. H. Safavi-Naeini, J. Chan, and O. Painter, Nature communications **3**, 1196 (2012).

140. T. Palomaki, J. Harlow, J. Teufel, R. Simmonds, and K. Lehnert, Nature **495**, 210 (2013).

141. S. Sridaran and S. A. Bhave, in *Micro Electro Mechanical Systems (MEMS), 2012 IEEE 25th International Conference on* (IEEE, 2012) pp. 664–667.

142. C. S. Shin, M. C. Butler, H.-J. Wang, C. E. Avalos, S. J. Seltzer, R.-B. Liu, A. Pines, and V. S. Bajaj, Physical Review B **89**, 205202 (2014).

143. X.-D. Chen, F.-W. Sun, C.-L. Zou, J.-M. Cui, L.-M. Zhou, and G.-C. Guo, EPL (Europhysics Letters) **101**, 67003 (2013).

144. T. Kornack, S. Smullin, S.-K. Lee, and M. Romalis, Applied physics letters **90**, 223501 (2007).

145. J.-C. Jaskula, B. Shields, E. Bauch, M. Lukin, R. Walsworth, and A. Trifonov, in *APS Division of Atomic, Molecular and Optical Physics Meeting Abstracts*, Vol. 1 (2015) p. 8010.

146. G. Arrad, Y. Vinkler, D. Aharonov, and A. Retzker, Physical review letters **112**, 150801 (2014).

147. D. Vion, P. Orfila, P. Joyez, D. Esteve, and M. Devoret, Journal of Applied Physics **77**, 2519 (1995).

148. E. Bauch, J. Lee, S. Singh, M. L. Pham, K. Arai, and R. Walsworth, in *APS Division of Atomic, Molecular and Optical Physics Meeting Abstracts*, Vol. 1 (2015) p. 1155.

149. A. M. Souza, G. A. Álvarez, and D. Suter, Physical Review Letters **106**, 240501 (2011).

150. L. M. Pham, D. L. Sage, P. L. Stanwix, T. K. Yeung, D. Glenn, A. Trifonov, P. Cappellaro, P. R. Hemmer, M. D. Lukin, H. Park, A. Yacoby, and R. L. Walsworth, New J. Phys. **13**, 045021 (2011).

151. J. Baker-Jarvis and S. Kim, Journal of research of the National Institute of Standards and Technology **117**, 1 (2012).

152. F. Yan, S. Gustavsson, A. Kamal, J. Birenbaum, A. Sears, D. Hover, T. Gudmundsen, J. Yoder, T. Orlando, J. Clarke, *et al.*, arXiv preprint arXiv:1508.06299 (2015).

153. I. P. Prikhodko, S. A. Zotov, A. A. Trusov, and A. M. Shkel, Microelectromechanical Systems, Journal of **22**, 1257 (2013).

154. J. Tetienne, L. Rondin, P. Spinicelli, M. Chipaux, T. Debuisschert, J. Roch, and V. Jacques, New Journal of Physics **14**, 103033 (2012).

155. V. Jacques, P. Neumann, J. Beck, M. Markham, D. Twitchen, J. Meijer, F. Kaiser, G. Balasubramanian, F. Jelezko, and J. Wrachtrup, Phys. Rev. Lett. **102**, 057403 (2009).

156. L. Cywinski, R. M. Lutchyn, C. P. Nave, and S. DasSarma, Phys. Rev. B **77**, 174509 (2008).

157. *ADXRS624 Data Sheet Rev A*, Analog Devices.

158. H. Johari, J. Shah, and F. Ayazi, in *MEMS 2008. IEEE 21st International Conference on* (2008) pp. 856–859.

159. C. Jekeli, *Inertial Navigation Systems With Geodetic Applications* (Walter de Gruyter, New York, 2000).

160. A. Lenef, T. D. Hammond, E. T. Smith, M. S. Chapman, R. A. Rubenstein, and D. E. Pritchard, Phys. Rev. Lett. **78**, 760 (1997).

161. T. L. Gustavson, P. Bouyer, and M. A. Kasevich, Phys. Rev. Lett. **78**, 2046 (1997).

162. D. S. Durfee, Y. K. Shaham, and M. A. Kasevich, Phys. Rev. Lett. **97**, 240801 (2006).

163. T. W. Kornack, R. K. Ghosh, and M. V. Romalis, Phys. Rev. Lett. **95**, 230801 (2005).

164. T. Havel, P. Cappellaro, C. Ramanathan, and D. Cory, in *Technical Proceedings of the 2005 NSTI Nanotechnology Conference and Trade Show*, Vol. 3 (2005) pp. 161 – 164.

165. J. Kitching, S. Knappe, and E. Donley, Sensors Journal, IEEE **11**, 1749 (2011).

166. F. Jelezko and J. Wrachtrup, Physica Status Solidi (A) **203**, 3207 (2006).

167. M. Ledbetter, K. Jensen, R. Fischer, A. Jarmola, and D. Budker, (2012), arXiv:1205.0093 .

168. D. Maclaurin, M. W. Doherty, L. C. L. Hollenberg, and A. M. Martin, Phys. Rev. Lett. **108**, 240403 (2012).

169. L. Lust and D. Youngner, U.S. Patent No. 7,359,059 B2 (2008).

170. T. G. Walker and W. Happer, Rev. Mod. Phys. **69**, 629 (1997).

171. L. Robledo, H. Bernien, T. van der Sar, and R. Hanson, New J. Phys. **13**, 025013 (2011).

172. G. Waldherr, J. Beck, M. Steiner, P. Neumann, A. Gali, T. Frauenheim, F. Jelezko, and J. Wrachtrup, Phys. Rev. Lett. **106**, 157601 (2011).

173. G. D. Fuchs, G. Burkard, P. V. Klimov, and D. D. Awschalom, Nat Phys **7**, 789 (2011).

174. B. Smeltzer, J. McIntyre, and L. Childress, Phys. Rev. A **80**, 050302 (2009).

175. R. Fischer, A. Jarmola, P. Kehayias, and D. Budker, (2012), arXiv:1202.1072 .

176. B. Luy and S. J. Glaser, Chem. Phys. Lett. **323**, 377 (2000).

177. L. Childress and J. McIntyre, Phys. Rev. A **82**, 033839 (2010).

178. J. H. Shirley, Phys. Rev. **138**, B979 (1965).

179. G. D. Fuchs, V. V. Dobrovitski, D. M. Toyli, F. J. Heremans, and D. D. Awschalom, Science **326**, 1520 (2009).

180. R. Hanson, V. V. Dobrovitski, A. E. Feiguin, O. Gywat, and D. D. Awschalom, Science **320**, 352 (2008).

181. V. M. Acosta, E. Bauch, M. P. Ledbetter, C. Santori, K.-M. C. Fu, P. E. Barclay, R. G. Beausoleil, H. Linget, J. F. Roch, F. Treussart, S. Chemerisov, W. Gawlik, and D. Budker, Phys. Rev. B **80**, 115202 (2009).

182. M. J. R. Hoch and E. C. Reynhardt, Phys. Rev. B **37**, 9222 (1988).

183. A. Jarmola, V. M. Acosta, K. Jensen, S. Chemerisov, and D. Budker, (2011), arXiv:1112.5936 .

184. P. Cappellaro, Phys. Rev. A **85**, 030301(R) (2012).

185. R. S. Said, D. W. Berry, and J. Twamley, Phys. Rev. B **83**, 125410 (2011).

186. SAAB, 8088000-112 Fiber Optic Gyroscope (2012).

187. Honeywell, GG1320AN Digital Ring Laser Gyro (2012).

188. J. K. Stockton, K. Takase, and M. A. Kasevich, Phys. Rev. Lett. **107**, 133001 (2011).

189. L. K. Lam, E. Phillips, E. Kanegsberg, and G. W. Kamin, Proc. SPIE **0412**, 272 (1983).

190. F. Dolde, H. Fedder, M. W. Doherty, T. Nobauer, F. Rempp, G. Balasubramanian, T. Wolf, F. Reinhard, L. C. L. Hollenberg, F. Jelezko, and J. Wrachtrup, Nat Phys **7**, 459 (2011).

191. J. S. Hodges and D. Englund, (2011), http://arxiv.org/abs/1109.3241, arXiv:1109.3241 .

192. V. M. Acosta, E. Bauch, M. P. Ledbetter, A. Waxman, L.-S. Bouchard, and D. Budker, Phys. Rev. Lett. **104**, 070801 (2010).

193. B. J. Maertz, A. P. Wijnheijmer, G. D. Fuchs, M. E. Nowakowski, and D. D. Awschalom, Applied Physics Letters **96**, 092504 (2010).

194. S. Steinert, F. Dolde, P. Neumann, A. Aird, B. Naydenov, G. Balasubramanian, F. Jelezko, and J. Wrachtrup, Rev. Sci. Instr. **81**, 043705 (2010).

195. O. Auciello, S. Pacheco, A. Sumant, C. Gudeman, S. Sampath, A. Datta, R. Carpick, V. Adiga, P. Zurcher, Z. Ma, H.-C. Yuan, J. Carlisle, B. Kabius, J. Hiller, and S. Srinivasan, Microwave Magazine, IEEE **8**, 61 (2007).

196. S. Haykin, *Adaptive filter theory* (Prentice Hall, 2002).

197. S. Pezzagna, B. Naydenov, F. Jelezko, J. Wrachtrup, and J. Meijer, New J. Phys. **12**, 065017 (2010).

198. A. M. Edmonds, U. F. S. D'Haenens-Johansson, M. E. Newton, K.-M. C. Fu, C. Santori, R. G. Beausoleil, D. J. Twitchen, and M. L. Markham, (2011), arXiv:1112.5757 .

199. L. Robledo, L. Childress, H. Bernien, B. Hensen, P. F. A. Alkemade, and R. Hanson, Nature **477**, 574 (2011).

200. E. Togan, Y. Chu, A. Imamoglu, and M. D. Lukin, Nature **478**, 497 (2011).

201. A. M. Zagoskin, J. R. Johansson, S. Ashhab, and F. Nori, Phys. Rev. B **76**, 014122 (2007).

202. W. M. Witzel and S. D. Sarma, Phys. Rev. B **77**, 165319 (2008).

203. W. M. Witzel, M. S. Carroll, L. Cywinski, and S. Das Sarma, ArXiv e-prints (2012), arXiv:1204.2834 .

204. R. Blatt and C. F. Roos, Nat Phys **8**, 277 (2012).

205. A. Ajoy and P. Cappellaro, Phys. Rev. Lett. **110**, 220503 (2013).

206. R. P. Feynman, Inter. J. Th. Phys. **21**, 467 (1982).

207. S. Schirmer, in *Lagrangian and Hamiltonian Methods for Nonlinear Control 2006*, Lecture Notes in Control and Information Sciences, Vol. 366 (Springer, 2007) pp. 293–304.

208. F. Verstraete, M. M. Wolf, and J. Ignacio Cirac, Nat Phys **5**, 633 (2009).

209. B. Kraus, H. P. Büchler, S. Diehl, A. Kantian, A. Micheli, and P. Zoller, Phys. Rev. A **78**, 042307 (2008).

210. D. P. DiVincenzo, D. Bacon, J. Kempe, G. Burkard, and K. B. Whaley, Nature **408**, 339 (2000).

211. P. Cappellaro and M. D. Lukin, Phys. Rev. A **80**, 032311 (2009).

212. J. I. Cirac and P. Zoller, Nat Phys **8**, 264 (2012).

213. S. Lloyd, Science **273**, 1073 (1996).

214. M. Suzuki, Phys. Lett. A **146**, 319 (1990).

215. J. Simon, W. S. Bakr, R. Ma, M. E. Tai, P. M. Preiss, and M. Greiner, Nature **472**, 307 (2011).

216. R. Kashyap, *Fiber Bragg Gratings* (Academic Press, 1999).

217. P. Mansfield and P. Grannell, J. Phys. C **6**, L422 (1973).

218. P. Mansfield and P. Grannell, Phys. Rev. B **12**, 3618 (1975).

219. W. S. Warren, S. Sinton, D. P. Weitekamp, and A. Pines, Phys. Rev. Lett. **43**, 1791 (1979).

220. A. K. Paravastu and R. Tycko, J. Chem. Phys. **124**, 194303 (2006).

221. G. A. Álvarez, M. Mishkovsky, E. P. Danieli, P. R. Levstein, H. M. Pastawski, and L. Frydman, Phys. Rev. A **81**, 060302 (2010).

222. S. Bose, Phys. Rev. Lett. **91**, 207901 (2003).

223. M. Christandl, N. Datta, A. Ekert, and A. J. Landahl, Phys. Rev. Lett. **92**, 187902 (2004).

224. See supplementary online material.

225. J. Baum, M. Munowitz, A. N. Garroway, and A. Pines, J. Chem. Phys. **83**, 2015 (1985).

226. D. Suter, S. Liu, J. Baum, and A. Pines, Chem. Phys. **114**, 103 (1987).

227. P. Cappellaro, L. Viola, and C. Ramanathan, Phys. Rev. A **83**, 032304 (2011).

228. N. Y. Yao, L. Jiang, A. V. Gorshkov, Z.-X. Gong, A. Zhai, L.-M. Duan, and M. D. Lukin, Phys. Rev. Lett. **106**, 040505 (2011).

229. A. Ajoy and P. Cappellaro, ArXiv:1207.5580 (2012).

230. G. S. Boutis, P. Cappellaro, H. Cho, C. Ramanathan, and D. G. Cory, J. Mag. Res. **161**, 132 (2003).

231. E. Vinogradov, P. Madhu, and S. Vega, Chem. Phys. Lett. **314**, 443 (1999).

232. M. H. Levitt, J. Chem. Phys. **128**, 052205 (2008).

233. P. Cappellaro, C. Ramanathan, and D. G. Cory, Phys. Rev. A **76**, 032317 (2007).

234. G. Kaur and P. Cappellaro, New J. Phys. **14**, 083005 (2012).

235. W. Zhang and D. G. Cory, Phys. Rev. Lett. **80**, 1324 (1998).

236. Y. Rumala, BS thesis (CUNY, New York) (2006).

237. H. J. Mamin, C. T. Rettner, M. H. Sherwood, L. Gao, and D. Rugar, App. Phys. Lett. **100**, 013102 (2012).

238. C. Ramanathan, P. Cappellaro, L. Viola, and D. G. Cory, New J. Phys. **13**, 103015 (2011).

239. M. H. Levitt, Prog. Nucl. Mag. Res. Spect. **18**, 61 (1986).

240. N. Y. Yao, A. V. Gorshkov, C. R. Laumann, A. M. Läuchli, J. Ye, and M. D. Lukin, ArXiv:1212.4839 (2012).

241. M. Saffman, T. G. Walker, and K. Mølmer, Rev. Mod. Phys. **82**, 2313 (2010).

242. H. Weimer, M. Muller, I. Lesanovsky, P. Zoller, and H. P. Buchler, Nat Phys **6**, 382 (2010).

243. L. Viola, E. Knill, and S. Lloyd, Phys. Rev. Lett. **82**, 2417 (1999).

244. M. E. Rose, *Elementary Theory of Angular Momentum* (New York: Wiley, 1957).

245. W. H. Zurek, Physics Today **October**, 36 (1991).

246. J. Fischer and D. Loss, Science **324**, 1277 (2009).

247. M. J. Biercuk, H. Uys, A. P. VanDevender, N. Shiga, W. M. Itano, and J. J. Bollinger, Nature **458**, 996 (2009).

248. C. A. Ryan, J. S. Hodges, and D. G. Cory, Phys. Rev. Lett. **105**, 200402 (2010).

249. A. Shukla and T. Mahesh, ArXiv:1110.1473 (2011).

250. K. Teshima, S. Lee, T. Ishizaki, S. Mori, C. Mori, K. Yubuta, T. Ichiki, T. Shishido, and S. Oishi, Cryst. Eng. Comm. **13**, 1749 (2011).

251. P. Cappellaro, C. Ramanathan, and D. G. Cory, Phys. Rev. Lett. **99**, 250506 (2007).

252. H. G. Krojanski and D. Suter, Phys. Rev. Lett. **93**, 090501 (2004).

253. M. Lovrić, H. G. Krojanski, and D. Suter, Phys. Rev. A **75**, 042305 (2007).

254. H. J. Cho, P. Cappellaro, D. G. Cory, and C. Ramanathan, Phys. Rev. B **74**, 224434 (2006).

255. G. A. Álvarez, E. P. Danieli, P. R. Levstein, and H. M. Pastawski, Phys. Rev. A **82**, 012310 (2010).

256. G. A. Álvarez and D. Suter, Phys. Rev. Lett. **104**, 230403 (2010).

257. M. Cetina, A. Bylinskii, L. Karpa, D. Gangloff, K. M. Beck, Y. Ge, M. Scholz, A. T. Grier, I. Chuang, and V. Vuletic, arXiv:1302.2904 (2013).

258. A. Ajoy and P. Cappellaro, ArXiv:1208.3656 (2012).

259. G. Cho and J. P. Yesinowski, Chem. Phys. Lett. **205**, 1 (1993).

260. W. Zhang, P. Cappellaro, N. Antler, B. Pepper, D. G. Cory, V. V. Dobrovitski, C. Ramanathan, and L. Viola, Phys. Rev. A **80**, 052323 (2009).

261. P. Cappellaro, J. S. Hodges, T. F. Havel, and D. G. Cory, Las. Phys. **17**, 545 (2007).

262. E. Rufeil-Fiori, C. M. Sánchez, F. Y. Oliva, H. M. Pastawski, and P. R. Levstein, Phys. Rev. A **79**, 032324 (2009).

263. Y.-S. Yen and A. Pines, J. Chem. Phys. **78**, 3579 (1983).

264. C. Ramanathan, H. Cho, P. Cappellaro, G. S. Boutis, and D. G. Cory, Chem. Phys. Lett. **369**, 311 (2003).

265. A. Abragam and M. Goldman, *Nuclear Magnetism : Order and Disorder.* (Clarendon Press, Oxford, 1982).

266. E. B. Fel'dman and S. Lacelle, Chem. Phys. Lett. **253**, 27 (1996).

267. P. Jordan and E. Wigner, Z. Phys. B **47**, 631 (1928).

268. S. Doronin, I. Maksimov, and E. Fel'dman, JETP **91**, 597 (2000).

269. S. Doronin, E. Fel'dman, and I. Maximov, Journal of Magnetic Resonance **171**, 37 (2004).

270. H. J. Cho, T. D. Ladd, J. Baugh, D. G. Cory, and C. Ramanathan, Phys. Rev. B **72**, 054427 (2005).

271. S. F. Huelga, C. Macchiavello, T. Pellizzari, A. K. Ekert, M. B. Plenio, and J. I. Cirac, Phys. Rev. Lett. **79**, 3865 (1997).

272. A. Ajoy, U. Bissbort, and P. Cappellaro, (to be published) (2015).

273. M. Mehring, *High Resolution NMR Spectroscopy in Solids* (Berlin: Springer-Verlag, 1976).

274. Z.-X. Liu, Z.-B. Yang, Y.-J. Han, W. Yi, and X.-G. Wen, Physical Review B **86**, 195122 (2012).

275. A. Y. Kitaev, Annals of Physics **303**, 2 (2003).

276. H. J. Kimble, Nature **453**, 1023 (2008).

277. J. I. Cirac, P. Zoller, H. J. Kimble, and H. Mabuchi, Phys. Rev. Lett. **78**, 3221 (1997).

278. J. J. L. Morton, A. M. Tyryshkin, A. Ardavan, S. C. Benjamin, K. Porfyrakis, S. A. Lyon, and G. A. D. Briggs, Nature Phys. **2**, 40 (2006).

279. T. W. Borneman, C. E. Granade, and D. G. Cory, Phys. Rev. Lett. **108**, 140502 (2012).

280. J. Wrachtrup, F. Jelezko, B. Grotz, and L. McGuinness, MRS Bulletin **38**, 149 (2013).

281. B. Grotz, J. Beck, P. Neumann, B. Naydenov, R. Reuter, F. Reinhard, F. Jelezko, J. Wrachtrup, D. Schweinfurth, B. Sarkar, and P. Hemmer, New Journal of Physics **13**, 055004 (2011).

282. W.-K. Rhim, A. Pines, and J. S. Waugh, Phys. Rev. B **3**, 684 (1971).

283. N. Zhao, J. Honert, B. Schmid, M. Klas, J. Isoya, M. Markham, D. Twitchen, F. Jelezko, R.-B. Liu, H. Fedder, *et al.*, Nature Nanotechnology **7**, 657 (2012).

284. J. Meijer, S. Pezzagna, T. Vogel, B. Burchard, H. Bukow, I. Rangelow, Y. Sarov, H. Wiggers, I. PlÃijmel, F. Jelezko, J. Wrachtrup, F. Schmidt-Kaler, W. Schnitzler, and K. Singer, App. Phys. A **91**, 567 (2008).

285. S. Lloyd, Phys. Rev. A **62**, 022108 (2000).

286. N. Khaneja, Phys. Rev. A **76**, 032326 (2007).

287. J. S. Hodges, J. C. Yang, C. Ramanathan, and D. G. Cory, Phys. Rev. A **78**, 010303 (2008).

288. J. Zhang, D. Burgarth, R. Laflamme, and D. Suter, Phys. Rev. A **91**, 012330 (2015).

289. G.-Q. Liu, H. C. Po, J. Du, R.-B. Liu, and X.-Y. Pan, Nature communications **4** (2013).

290. C. Lee, D. Suter, and A. Pines, Journal of Magnetic Resonance (1969) **75**, 110 (1987).

291. E. R. Andrew, A. Bradbury, and R. G. Eades, Nature (London) **182**, 1659 (1958).

292. L. Emsley, K. Schmidt-Rohr, and A. Pines, in *NMR and more in honour of Anatole Abragam* (1994).

293. A. Bielecki, A. Kolbert, and M. Levitt, Chemical Physics Letters **155**, 341 (1989).

294. K. Arai, C. Belthangady, H. Zhang, N. Bar-Gill, S. DeVience, P. Cappellaro, A. Yacoby, and R. Walsworth, arXiv preprint arXiv:1409.2749 (2014).

295. S. Ohki and M. Kainosho, Prog NMR Spectrosc **53**, 208 (2008).

296. D. Cowburn and T. Muir, Methods Enzymol **339**, 41 (2001).

297. U. Haeberlen, J. E. Jr, and J. Waugh, Journal of Chemical Physics **55**, 53 (1971).

298. A. Pines and J. Waugh, Journal of Magnetic Resonance **8**, 354 (1972).

299. I. J. Lowe, Phys. Rev. Lett. **2**, 285 (1959).

300. M. Lee and W. Goldburg, Phys. Rev. A **140**, 1261 (1965).

301. M. Mehring and J. S. Waugh, Phys. Rev. B **5**, 3459 (1972).

302. A. Bax, N. M. Szeverenyi, and G. E. Maciel, Journal of Magnetic Resonance (1969) **52**, 147 (1983).

303. A. Samoson, E. Lippmaa, and A. Pines, Molecular Physics **65**, 1013 (1988).

304. W. M. Witzel, M. S. Carroll, A. Morello, L. Cywiński, and S. Das Sarma, Phys. Rev. Lett. **105**, 187602 (2010).

305. T. D. Ladd, F. Jelezko, R. Laflamme, Y. Nakamura, C. Monroe, and J. L. O'Brien, Nature **464**, 45 (2010).

306. J. I. Cirac, A. K. Ekert, S. F. Huelga, and C. Macchiavello, Phys. Rev. A **59**, 4249 (1999).

307. D. K. L. Oi, S. J. Devitt, and L. C. L. Hollenberg, Phys. Rev. A **74**, 052313 (2006).

308. L. Jiang, J. M. Taylor, A. S. Sorensen, and M. D. Lukin, Phys. Rev. A **76**, 062323 (2007).

309. R. V. Meter, W. J. Munro, K. Nemoto, and K. M. Itoh, J. Emerg. Technol. Comput. Syst. **3**, 2:1 (2008).

310. A. Kay, Int. J. of Quantum Info. **8**, 641 (2010).

311. C. Albanese, M. Christandl, N. Datta, and A. Ekert, Phys. Rev. Lett. **93**, 230502 (2004).

312. G. M. Nikolopoulos, D. Petrosyan, and P. Lambropoulos, J. Phys.: Cond. Matt. **16**, 4991 (2004).

313. G. M. Nikolopoulos, D. Petrosyan, and P. Lambropoulos, Europhys. Lett. **65**, 297 (2004).

314. G. Gualdi, V. Kostak, I. Marzoli, and P. Tombesi, Phys. Rev. A **78**, 022325 (2008).

315. A. Wojcik, T. Luczak, P. Kurzynski, A. Grudka, T. Gdala, and M. Bednarska, Phys. Rev. A **72**, 034303 (2005).

316. Y. Li, T. Shi, B. Chen, Z. Song, and C.-P. Sun, Phys. Rev. A **71**, 022301 (2005).

317. Y. Wang, F. Shuang, and H. Rabitz, Phys. Rev. A **84**, 012307 (2011).

318. D. Burgarth and S. Bose, Phys. Rev. A **71**, 052315 (2005).

319. J. Fitzsimons and J. Twamley, Phys. Rev. Lett. **97**, 090502 (2006).

320. D. Burgarth, V. Giovannetti, and S. Bose, Phys. Rev. A **75**, 062327 (2007).

321. T. Caneva, M. Murphy, T. Calarco, R. Fazio, S. Montangero, V. Giovannetti, and G. E. Santoro, Phys. Rev. Lett. **103**, 240501 (2009).

322. D. Burgarth, K. Maruyama, M. Murphy, S. Montangero, T. Calarco, F. Nori, and M. B. Plenio, Phys. Rev. A **81**, 040303 (2010).

323. C. DiFranco, M. Paternostro, and M. S. Kim, Phys. Rev. Lett. **101**, 230502 (2008).

324. G. Panitchayangkoon, D. V. Voronine, D. Abramavicius, J. R. Caram, N. H. C. Lewis, S. Mukamel, and G. S. Engel, Proc. Nat. Acad. Sc. **108**, 20908 (2011).

325. G. S. Engel, T. R. Calhoun, E. L. Read, T.-K. Ahn, T. Mancal, Y.-C. Cheng, R. E. Blankenship, and G. R. Fleming, Nature **446**, 782 (2007).

326. M. Mohseni, P. Rebentrost, S. Lloyd, and A. Aspuru-Guzik, J. Chem. Phys. **129**, 174106 (2008).

327. V. Kostak, G. M. Nikolopoulos, and I. Jex, Phys. Rev. A **75**, 042319 (2007).

328. Y. Aharonov, L. Davidovich, and N. Zagury, Phys. Rev. A **48**, 1687?1690 (1993).

329. M. Munowitz, A. Pines, and M. Mehring, J. Chem. Phys. **86**, 3172 (1987).

330. O. Mï£¡lken and A. Blumen, Physics Reports **502**, 37 (2011).

331. D. L. Feder, Phys. Rev. Lett. **97**, 180502 (2006).

332. H. Krovi and T. A. Brun, Phys. Rev. A **75**, 062332 (2007).

333. A. Bernasconi, C. Godsil, and S. Severini, Phys. Rev. A **78**, 052320 (2008).

334. P. J. Pemberton-Ross and A. Kay, Phys. Rev. Lett. **106**, 020503 (2011).

335. T. J. Osborne and N. Linden, Phys. Rev. A **69**, 052315 (2004).

336. M.-H. Yung, Phys. Rev. A **74**, 030303 (2006).

337. O. Sorensen, G. Eich, M. Levitt, G. Bodenhausen, and R. Ernst, Progress in Nuclear Magnetic Resonance Spectroscopy **16**, 163 (1984).

338. P. Karbach and J. Stolze, Phys. Rev. A **72**, 030301 (2005).

339. A. Kay, Phys. Rev. A **84**, 022337 (2011).

340. I. N. Hincks, D. G. Cory, and C. Ramanathan, ArXiv e-prints (2011), arXiv:1111.0944 .

341. M. Markiewicz and M. Wiesniak, Phys. Rev. A **79**, 054304 (2009).

342. S. C. Benjamin and S. Bose, Phys. Rev. Lett. **90**, 247901 (2003).

343. S. R. Clark, C. M. Alves, and D. Jaksch, New J. Phys. **7**, 124 (2005).

344. C. Di Franco, M. Paternostro, G. M. Palma, and M. S. Kim, Phys. Rev. A **76**, 042316 (2007).

345. S. R. Clark, A. Klein, M. Bruderer, and D. Jaksch, New J. Phys. **9**, 202 (2007).

346. C. Di Franco, M. Paternostro, and M. S. Kim, Phys. Rev. Lett. **102**, 187203 (2009).

347. B. M. Terhal and D. P. DiVincenzo, Phys. Rev. A **65**, 032325 (2002).

348. T. Barthel, C. Pineda, and J. Eisert, Phys. Rev. A **80**, 042333 (2009).

349. E. Lieb, T. Schultz, and D. Mattis, Annals of Physics **16**, 407 (1961).

350. A. M. Childs, Phys. Rev. Lett. **102**, 180501 (2009).

351. R. Raussendorf, D. E. Browne, and H. J. Briegel, Phys. Rev. A **68**, 022312 (2003).

352. A. Wójcik, T. Łuczak, P. Kurzyński, A. Grudka, T. Gdala, and M. Bednarska, Phys. Rev. A **75**, 022330 (2007).

353. F. W. Strauch and C. J. Williams, Phys. Rev. B **78**, 094516 (2008).

354. C. F. Hirjibehedin, C. P. Lutz, and A. Heinrich, Science **312**, 1021 (2006).

355. P. Spinicelli, A. Drau, L. Rondin, F. Silva, J. Achard, S. Xavier, S. Bansropun, T. Debuisschert, S. Pezzagna, J. Meijer, V. Jacques, and J.-F. Roch, New J. Phys. **13**, 025014 (2011).

356. L. Banchi, T. J. G. Apollaro, A. Cuccoli, R. Vaia, and P. Verrucchi, New Journal of Physics **13**, 123006 (2011).

357. M. V. G. Dutt, L. Childress, L. Jiang, E. Togan, J. Maze, F. Jelezko, A. S. Zibrov, P. R. Hemmer, and M. D. Lukin, Science **316**, 1312 (2007).

358. R. C. Barklie and J. Guven, Journal of Physics C: Solid State Physics **14**, 3621 (1981).

359. N. Yao, L. Jiang, A. Gorshkov, P. Maurer, G. Giedke, J. Cirac, and M. Lukin, Nat Commun **3**, 800 (2012).

360. R. Bhatia, *Matrix Analysis* (Springer, 1996).

361. C. W. Gardiner, Phys. Rev. A **29**, 2814 (1984).

362. H. Haus and W. Huang, Proceedings of the IEEE **79**, 1505 (1991).

363. A. Synder and J. Love, *Optical Waveguide Theory* (Springer, 1983).

364. J. R. Schrieffer and P. A. Wolff, Phys. Rev. **149**, 491 (1966).

365. S. Bravyi, D. DiVincenzo, and D. Loss, Ann. Phys. **326**, 2793 (2011).

366. S. Oh, L.-A. Wu, Y.-P. Shim, J. Fei, M. Friesen, and X. Hu, Phys. Rev. A **84**, 022330 (2011).

367. H. F. Trotter, Proc. Amer. Math. Soc. **10**, 545 (1959).

368. T. J. G. Apollaro, L. Banchi, A. Cuccoli, R. Vaia, and P. Verrucchi, Phys. Rev. A **85**, 052319 (2012).

369. G. S. Uhrig, Phys. Rev. Lett. **98**, 100504 (2007).

370. J.-M. Cai, Z.-W. Zhou, and G.-C. Guo, Phys. Rev. A **74**, 022328 (2006).

371. P. L. Stanwix, L. M. Pham, J. R. Maze, D. Le Sage, T. K. Yeung, P. Cappellaro, P. R. Hemmer, A. Yacoby, M. D. Lukin, and R. L. Walsworth, Phys. Rev. B **82**, 201201 (2010).

372. L. Braunschweiler and R. Ernst, J. Mag. Res. **53**, 521 (1983).

373. S. Takahashi, R. Hanson, J. van Tol, M. S. Sherwin, and D. D. Awschalom, Phys. Rev. Lett. **101**, 047601 (2008).

374. E. C. Reynhardt and G. L. High, The Journal of Chemical Physics **109**, 4090 (1998).

375. A. E. Dementyev, D. G. Cory, and C. Ramanathan, Phys. Rev. Lett. **100**, 127601 (2008).

376. P. Rabl, S. J. Kolkowitz, F. H. L. Koppens, J. G. E. Harris, P. Zoller, and M. D. Lukin, Nat Phys **6**, 602 (2010).

377. K. Stannigel, P. Rabl, A. S. Sørensen, P. Zoller, and M. D. Lukin, Phys. Rev. Lett. **105**, 220501 (2010).

378. F. Jelezko, T. Gaebel, I. Popa, A. Gruber, and J. Wrachtrup, Phys. Rev. Lett. **92**, 076401 (2004).

379. J. Wrachtrup and F. Jelezko, J. Phys.: Condens. Matter **18**, S807 (2006).

380. E. van Oort, N. B. Manson, and M. Glasbeek, J. of Physics C: Solid State Physics **21**, 4385 (1988).

381. D. A. Redman, S. Brown, R. H. Sands, and S. C. Rand, Phys. Rev. Lett. **67**, 3420 (1991).

382. A. Gruber, A. Drabenstedt, C. Tietz, L. Fleury, J. Wrachtrup, and C. v. Borczyskowski, Science **276**, 2012 (1997).

383. F. Jelezko, C. Tietz, A. Gruber, I. Popa, A. Nizovtsev, S. Kilin, and J. Wrachtrup, Single Molecules **2**, 255 (2001).

384. N. B. Manson, J. P. Harrison, and M. J. Sellars, Phys. Rev. B **74**, 104303 (2006).

385. N. Mizuochi, P. Neumann, F. Rempp, J. Beck, V. Jacques, P. Siyushev, K. Nakamura, D. J. Twitchen, H. Watanabe, S. Yamasaki, F. Jelezko, and J. Wrachtrup, Phys. Rev. B **80**, 041201 (2009).

386. P. Neumann, R. Kolesov, V. Jacques, J. Beck, J. Tisler, A. Batalov, L. Rogers, N. B. Manson, G. Balasubramanian, F. Jelezko, and J. Wrachtrup, New J. Phys. **11**, 013017 (10pp) (2009).

387. T. Gaebel, M. Domhan, I. Popa, C. Wittmann, P. Neumann, F. Jelezko, J. R. Rabeau, N. Stavrias, A. D. Greentree, S. Prawer, J. Meijer, J. Twamley, P. R. Hemmer, and J. Wrachtrup, Nature Phys. **2**, 408 (2006).

388. G. Waldherr, P. Neumann, S. F. Huelga, F. Jelezko, and J. Wrachtrup, Phys. Rev. Lett. **107**, 090401 (2011).